

SEPTEMBER 2019

AJNR

VOLUME 40 • PP 1437-1607

AJNR

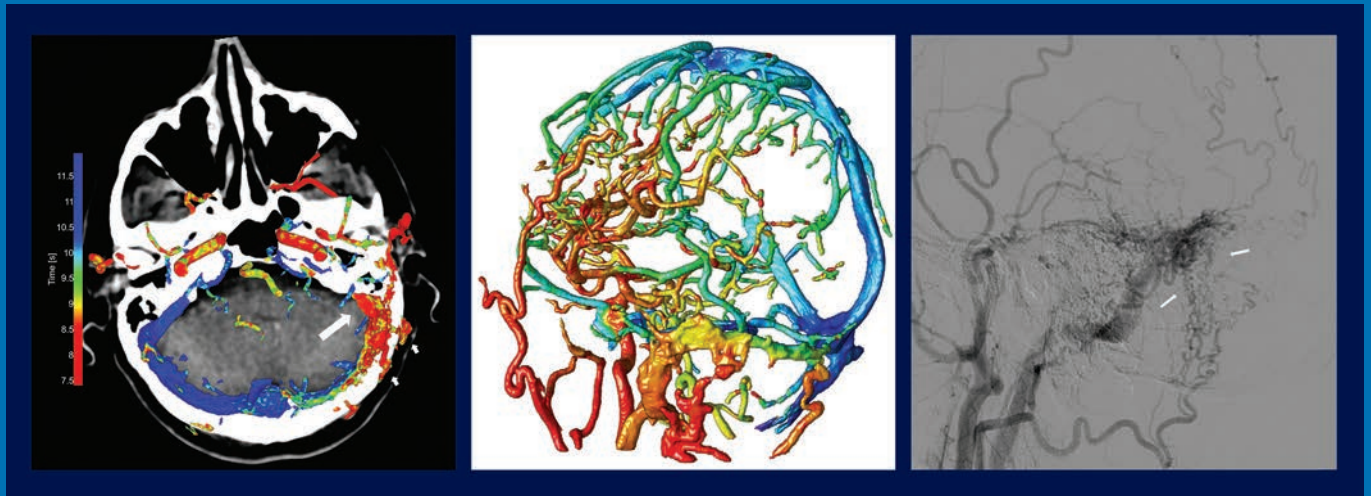
AMERICAN JOURNAL OF NEURORADIOLOGY

SEPTEMBER 2019
VOLUME 40
NUMBER 9
WWW.AJNR.ORG

THE JOURNAL OF DIAGNOSTIC AND
INTERVENTIONAL NEURORADIOLOGY

Color-mapping of 4D-CT in AV shunts
CTA analysis in symptomatic subjects with bilateral
intraplaque hemorrhage
Improved assessment of middle ear cholesteatomas

Official Journal ASNR • ASFNR • ASHNR • ASPNR • ASSR



AJNR

AMERICAN JOURNAL OF NEURORADIOLOGY

SEPTEMBER 2019
VOLUME 40
NUMBER 9
WWW.AJNR.ORG

Publication Preview at www.ajnr.org features articles released in advance of print. Visit www.ajnrblog.org to comment on AJNR content and chat with colleagues and AJNR's News Digest at <http://ajnrdigest.org> to read the stories behind the latest research in neuroimaging.

1437 **PERSPECTIVES** *S.A. Messina*

GENERAL CONTENTS

-   1438 **Altered Relationship between Working Memory and Brain Microstructure after Mild Traumatic Brain Injury** *S. Chung, et al.* **ADULT BRAIN FUNCTIONAL**
-  1445 **Utility of Percentage Signal Recovery and Baseline Signal in DSC-MRI Optimized for Relative CBV Measurement for Differentiating Glioblastoma, Lymphoma, Metastasis, and Meningioma** *M.D. Lee, et al.* **ADULT BRAIN FUNCTIONAL**
- 1451 **Dynamic Contrast-Enhanced MRI in Patients with Brain Metastases Undergoing Laser Interstitial Thermal Therapy: A Pilot Study** *J.I. Traylor, et al.* **ADULT BRAIN FUNCTIONAL**
-  1458 **Molecular Subtype Classification in Lower-Grade Glioma with Accelerated DTI** *E. Aliotta, et al.* **ADULT BRAIN FUNCTIONAL**
-   1464 **Widespread Increased Diffusivity Reveals Early Cortical Degeneration in Huntington Disease** *F. Sampredo, et al.* **ADULT BRAIN FUNCTIONAL**
- 1469 **Usefulness of the Delay Alternating with Nutation for Tailored Excitation Pulse with T1-Weighted Sampling Perfection with Application-Optimized Contrasts Using Different Flip Angle Evolution in the Detection of Cerebral Metastases: Comparison with MPRAGE Imaging** *D. Kim, et al.* **ADULT BRAIN**
- 1476 **Comparison of Unenhanced and Gadolinium-Enhanced Imaging in Multiple Sclerosis: Is Contrast Needed for Routine Follow-Up MRI?** *G. Sadigh, et al.* **ADULT BRAIN**
-   1481 **Optimal Detection of Subtle Gadolinium Leakage in CSF with Heavily T2-Weighted Fluid-Attenuated Inversion Recovery Imaging** *W.M. Freeze, et al.* **ADULT BRAIN**
-   1484 **Validation of Zero TE-MRA in the Characterization of Cerebrovascular Diseases: A Feasibility Study** *S. Shang, et al.* **ADULT BRAIN**
-  1491 **Defining Ischemic Core in Acute Ischemic Stroke Using CT Perfusion: A Multiparametric Bayesian-Based Model** *K. Nael, et al.* **ADULT BRAIN**
-    1498 **Color-Mapping of 4D-CTA for the Detection of Cranial Arteriovenous Shunts** *M. Meijs, et al.* **ADULT BRAIN INTERVENTIONAL**

AJNR (Am J Neuroradiol ISSN 0195–6108) is a journal published monthly, owned and published by the American Society of Neuroradiology (ASNR), 800 Enterprise Drive, Suite 205, Oak Brook, IL 60523. Annual dues for the ASNR include \$170.00 for journal subscription. The journal is printed by Cadmus Journal Services, 5457 Twin Knolls Road, Suite 200, Columbia, MD 21045; Periodicals postage paid at Oak Brook, IL and additional mailing offices. Printed in the U.S.A. POSTMASTER: Please send address changes to American Journal of Neuroradiology, P.O. Box 3000, Denville, NJ 07834, U.S.A. Subscription rates: nonmember \$410 (\$480 foreign) print and online, \$320 online only; institutions \$470 (\$540 foreign) print and basic online, \$935 (\$1000 foreign) print and extended online, \$380 online only (basic), extended online \$825; single copies are \$35 each (\$40 foreign). Indexed by PubMed/Medline, BIOSIS Previews, Current Contents (Clinical Medicine and Life Sciences), EMBASE, Google Scholar, HighWire Press, Q-Sensei, RefSeek, Science Citation Index, SCI Expanded, Meta/CZI and ReadCube. Copyright © American Society of Neuroradiology.

	1505	Quantitative and Qualitative Comparison of 4D-DSA with 3D-DSA Using Computational Fluid Dynamics Simulations in Cerebral Aneurysms <i>S. Lang, et al.</i>	INTERVENTIONAL
  	1511	Analysis of Flow Dynamics and Outcomes of Cerebral Aneurysms Treated with Intracascular Flow-Diverting Devices <i>J.R. Cebral, et al.</i>	INTERVENTIONAL
	1517	Two-Center Experience in the Endovascular Treatment of Intracranial Aneurysms Using the Woven EndoBridge 17 Device Including Midterm Follow-Up Results: A Retrospective Analysis <i>C. Maurer, et al.</i>	INTERVENTIONAL
 	1523	Sentinel Angiographic Signs of Cerebral Hyperperfusion after Angioplasty and Stenting of Intracranial Atherosclerotic Stenosis: A Technical Note <i>M. Ghuman, et al.</i>	INTERVENTIONAL
	1526	Distal Transradial Access in the Anatomic Snuffbox for Diagnostic Cerebral Angiography <i>P. Patel, et al.</i>	INTERVENTIONAL
 	1529	Non-Contrast-Enhanced Carotid MRA: Clinical Evaluation of a Novel Ungated Radial Quiescent-Interval Slice-Selective MRA at 1.5T <i>S. Peters, et al.</i>	EXTRACRANIAL VASCULAR
	1538	Carotid Plaque CTA Analysis in Symptomatic Subjects with Bilateral Intraplaque Hemorrhage: A Preliminary Analysis <i>L. Saba, et al.</i>	EXTRACRANIAL VASCULAR
	1546	Improved Assessment of Middle Ear Recurrent Cholesteatomas Using a Fusion of Conventional CT and Non-EPI-DWI MRI <i>F. Felici, et al.</i>	HEAD & NECK
	1552	A Persistent Foramen of Huschke: A Small Road to Misery in Necrotizing External Otitis <i>W.L. van der Meer, et al.</i>	HEAD & NECK
	1557	Subretinal and Retrolaminar Migration of Intraocular Silicone Oil Detected on CT <i>M. Abdalkader, et al.</i>	HEAD & NECK
	1562	Zero TE MRI for Craniofacial Bone Imaging <i>A. Lu, et al.</i>	HEAD & NECK
  	1567	Global and Regional Changes in Cortical Development Assessed by MRI in Fetuses with Isolated Nonsevere Ventriculomegaly Correlate with Neonatal Neurobehavior <i>N. Hahner, et al.</i>	PEDIATRICS
	1575	Diffusion-Weighted MR Imaging in a Prospective Cohort of Children with Cerebral Malaria Offers Insights into Pathophysiology and Prognosis <i>S.M. Moghaddam, et al.</i>	PEDIATRICS
	1581	Optimizing the Detection of Subtle Insular Lesions on MRI When Insular Epilepsy Is Suspected <i>J. Blustajn, et al.</i>	PEDIATRICS
  	1586	Quantitative Analysis of Spinal Canal Areas in the Lumbar Spine: An Imaging Informatics and Machine Learning Study <i>B. Gaonkar, et al.</i>	SPINE
   	1592	Automatic Spinal Cord Gray Matter Quantification: A Novel Approach <i>C. Tsagkas, et al.</i>	SPINE
  	1601	Comparative Analysis of Volumetric High-Resolution Heavily T2-Weighted MRI and Time-Resolved Contrast-Enhanced MRA in the Evaluation of Spinal Vascular Malformations <i>S.K. Kannath, et al.</i>	SPINE
	1607	35 YEARS AGO IN AJNR	

ONLINE FEATURES

LETTERS

- E44** **Can Trace-Weighted Images Be Used to Estimate Diffusional Kurtosis Imaging-Derived Indices of Non-Gaussian Water Diffusion in Head and Neck Cancer?** *M. Giannelli, et al.*
- E46** **Reply** *N. Tu, et al.*
- E48** **Vendors Used in CT and MRI Neuroradiology Research**
S. Ramezanpour, et al.

BOOK REVIEWS

R.M. Quencer, Section Editor

Please visit www.ajnrblog.org to read and comment on Book Reviews.



Left, 4D-CTA color-mapping in a patient with a dural AVF located in the left sigmoid sinus. Early contrast bolus arrival and arterialization of the left sigmoid sinus are shown in red. *Middle*, 3D rendering of color-mapping. *Right*, conventional angiography.



Indicates Editor's Choices selection



Indicates Fellows' Journal Club selection



Indicates open access to non-subscribers at www.ajnr.org



Indicates article with supplemental on-line table



Indicates article with supplemental on-line photo



Indicates article with supplemental on-line video



Evidence-Based Medicine Level 1



Evidence-Based Medicine Level 2

Official Journal:

American Society of Neuroradiology
 American Society of Functional Neuroradiology
 American Society of Head and Neck Radiology
 American Society of Pediatric Neuroradiology
 American Society of Spine Radiology

EDITOR-IN-CHIEF

Jeffrey S. Ross, MD

Professor of Radiology, Department of Radiology,
 Mayo Clinic College of Medicine, Phoenix, AZ

SENIOR EDITORS

Harry J. Cloft, MD, PhD

Professor of Radiology and Neurosurgery,
 Department of Radiology, Mayo Clinic College of
 Medicine, Rochester, MN

Thierry A.G.M. Huisman, MD

Radiologist-in-Chief, Texas Children's Hospital,
 Houston, TX

Yvonne W. Lui, MD

Associate Professor of Radiology,
 Chief of Neuroradiology,
 New York University School of Medicine,
 New York, NY

C.D. Phillips, MD, FACR

Professor of Radiology, Weill Cornell Medical
 College, Director of Head and Neck Imaging,
 New York-Presbyterian Hospital, New York, NY

Lubdha M. Shah, MD

Associate Professor of Radiology and Director of
 Spine Imaging, University of Utah Department of
 Radiology and Imaging Sciences, Salt Lake City, UT

Charles M. Strother, MD

Professor of Radiology, Emeritus, University of
 Wisconsin, Madison, WI

STATISTICAL SENIOR EDITOR

Bryan A. Comstock, MS

Senior Biostatistician,
 Department of Biostatistics,
 University of Washington, Seattle, WA

ARTIFICIAL INTELLIGENCE DEPUTY EDITOR

Christopher G. Filippi, MD

Professor and Vice Chair of Biomedical and
 Translational Science,
 Donald and Barbara Zucker School of Medicine at
 Hofstra/Northwell,
 Lenox Hill Hospital and Greenwich Village
 Healthplex, New York, NY

EDITORIAL BOARD

Ashley H. Aiken, *Atlanta, GA*
 Lea M. Alhilali, *Phoenix, AZ*
 Kubilay Aydin, *Istanbul, Turkey*
 John D. Barr, *Dallas, TX*
 Ari Blitz, *Baltimore, MD*
 Barton F. Branstetter IV, *Pittsburgh, PA*
 Jonathan L. Brisman, *Lake Success, NY*
 Keith Cauley, *Danville, PA*
 James Y. Chen, *San Diego, CA*
 Asim F. Choudhri, *Memphis, TN*
 Daniel Chow, *Irvine, CA*
 J. Matthew Debnam, *Houston, TX*
 Seena Dehkharghani, *New York, NY*
 Yonghong Ding, *Rochester, MN*
 Clifford J. Eskey, *Hanover, NH*
 Saeed Fakhran, *Phoenix, AZ*
 Massimo Filippi, *Milan, Italy*
 Reza Forghani, *Montreal, Quebec, Canada*
 Nils D. Forkert, *Calgary, Alberta, Canada*
 Wende N. Gibbs, *Phoenix, AZ*
 Christine M. Glastonbury, *San Francisco, CA*
 John L. Go, *Los Angeles, CA*
 Philipp Götz, *Erlangen, Germany*
 Allison Grayev, *Madison, WI*
 Brent Griffith, *Detroit, MI*
 Ajay Gupta, *New York, NY*
 Rakesh Kumar Gupta, *Haryana, India*
 Lotfi Hacein-Bey, *Sacramento, CA*
 Christopher P. Hess, *San Francisco, CA*
 Andrei Holodny, *New York, NY*
 Benjamin Huang, *Chapel Hill, NC*
 Mahesh V. Jayaraman, *Providence, RI*
 Valerie Jewells, *Chapel Hill, NC*
 Christof Karmonik, *Houston, TX*
 Timothy J. Kaufmann, *Rochester, MN*
 Hillary R. Kelly, *Boston, MA*
 Toshihumi Kinoshita, *Akita, Japan*
 Kenneth F. Layton, *Dallas, TX*
 Alexander Lerner, *Los Angeles, CA*
 Michael Lev, *Boston, MA*
 Karl-Olof Lovblad, *Geneva, Switzerland*
 Franklin A. Marden, *Chicago, IL*
 Joseph C. McGowan, *Merion Station, PA*
 Stephan Meckel, *Freiburg, Germany*
 Christopher J. Moran, *St. Louis, MO*
 Takahisa Mori, *Kamakura City, Japan*
 Suresh Mukherji, *Ann Arbor, MI*
 Alexander J. Nemeth, *Chicago, IL*
 Renato Hoffmann Nunes, *Sao Paulo, Brazil*
 Sasan Partovi, *Cleveland, OH*
 Laurent Pierot, *Reims, France*
 Jay J. Pillai, *Baltimore, MD*

Whitney B. Pope, *Los Angeles, CA*
 Joana Ramalho, *Lisbon, Portugal*
 Otto Rapalino, *Boston, MA*
 Álex Rovira-Cañellas, *Barcelona, Spain*
 Paul M. Ruggieri, *Cleveland, OH*
 Amit M. Saindane, *Atlanta, GA*
 Maksim Shapiro, *New York, NY*
 Timothy Shepherd, *New York, NY*
 Mark S. Shiroishi, *Los Angeles, CA*
 Bruno P. Soares, *Baltimore, MD*
 Maria Vittoria Spampinato, *Charleston, SC*
 Khin Khin Tha, *Sapporo, Hokkaido, Japan*
 Krishnamoorthy Thamburaj, *Hershey, PA*
 Cheng Hong Toh, *Taipei, Taiwan*
 Aquilla S. Turk, *Greenville, SC*
 Anja G. van der Kolk, *Utrecht, the Netherlands*
 Willem Jan van Rooij, *Tilburg, Netherlands*
 Arastoo Vossough, *Philadelphia, PA*
 Elysa Widjaja, *Toronto, Ontario, Canada*
 Max Wintermark, *Stanford, CA*
 Ronald L. Wolf, *Philadelphia, PA*
 Kei Yamada, *Kyoto, Japan*
 Carlos Zamora, *Chapel Hill, NC*
 Vahe M. Zohrabian, *New Haven, CT*

EDITORIAL FELLOW

Hediyeh Baradaran, *Salt Lake City, UT*

SPECIAL CONSULTANTS TO THE EDITOR

AJNR Blog Editor

Neil Lal, *Denver, CO*

Case of the Month Editor

Nicholas Stence, *Aurora, CO*

Case of the Week Editors

Juan Pablo Cruz, *Santiago, Chile*
 Sapna Rawal, *Toronto, Ontario, Canada*

Classic Case Editor

Sandy Cheng-Yu Chen, *Taipei, Taiwan*

Health Care and Socioeconomics Editor

Pina C. Sanelli, *New York, NY*

Physics Editor

Greg Zaharchuk, *Stanford, CA*

Podcast Editor

Wende N. Gibbs, *Phoenix, AZ*

Twitter Editor

Jennifer McCarty, *Houston, TX*

Founding Editor
 Juan M. Taveras

Editors Emeriti
 Mauricio Castillo, Robert I. Grossman,
 Michael S. Huckman, Robert M. Quencer

Managing Editor
 Karen Halm
 Assistant Managing Editor
 Laura Wilhelm
 Communications Coordinator
 Rebecca Artz
 Executive Director, ASNR
 Mary Beth Hepp

WEB[®]

Aneurysm Embolization System

MicroVention[®] delivers the first intrasaccular solution for wide neck bifurcation aneurysms.

The **world leader**
and **first**
PMA - approved
device in an
important new
category of
intrasaccular
flow disruptors.

The WEB[®] System is a safe
and effective single-device
solution for treating wide
neck bifurcation aneurysms.



SL Device



SLS Device

Contact a MicroVention sales associate to learn more
about integrating the WEB[®] device into your practice.



**MicroVention Worldwide
Innovation Center**

35 Enterprise
Aliso Viejo, CA 92656 USA

MicroVention UK Limited

MicroVention Europe, S.A.R.L.

MicroVention Deutschland GmbH

microvention.com

PH +1.714.247.8000

PH +44 (0) 191 258 6777

PH +33 (1) 39 21 77 46

PH +49 211 210 798-0

Introducing
Eclipse 2L
DUAL LUMEN BALLOON CATHETER



Balt's Access Portfolio Delivers Unique Solutions



Visit www.balt-usa.com to learn more

Ingest more.



Empowering first pass retrieval
with AXS Vecta 71 Aspiration
Catheter **now powered by** the
Dual Action Aspiration of Medela
Dominant Flex.

AXS Vecta™ 71 Aspiration Catheter

Testing completed by Stryker. Data on file at Stryker.

The AXS Vecta 71 Aspiration Catheter has a larger lumen compared to the AXS Catalyst 6 Distal Access Catheter, which is cleared for use with the Dominant Flex, sold as the AXS Universal Aspiration System. A larger lumen provides more aspiration power and more room for clot ingestion.

ASNR 58th Annual Meeting & The Foundation of the ASNR Symposium 2020

CALL FOR ABSTRACTS

Join us May 30-June 4, 2020 at Caesars Palace in Las Vegas to present the best scientific research in Neuroradiology.

Submission Deadline: Friday, November 1, 2019 (8:00PM EST)

Submit online at [ASNR.org/AnnualMeeting](https://www.asnr.org/AnnualMeeting)

Acceptance notifications will be sent on or before January 15, 2020 upon conclusion of peer review.

Submit an abstract for the ASNR 58th Annual Meeting (May 30 - June 4, 2020, Las Vegas, NV) in one of the following presentation categories:

- Scientific Paper Oral
- Excerpta Oral
- Scientific Poster Print
- Electronic Scientific Poster Electronic
- Electronic Educational Exhibit Electronic
- Educational Exhibit Poster Print

Abstract Submissions Information and Criteria

1. Abstracts should describe the learning objectives of the presentation.
2. The *American Journal of Neuroradiology (AJNR)* encourages presenters to submit manuscripts based on their work to *AJNR* before considering other journals.
3. Presenters of accepted abstracts **must register** for the ASNR 58th Annual Meeting and/or the Foundation of the ASNR Symposium 2020.
4. Published or previously presented works should NOT be submitted.
5. Submission topic areas include: **Adult Brain, Spine, Head and Neck, Pediatrics, Functional/Advanced Imaging, Interventional, Health Policy, AI/ Informatics, and Professional Development.**
6. Submit each abstract in **one** category only.
7. Format abstract text using headings required for submission category.
8. Maximum length: **2,500 characters**, not including title, authors, images, figures.
9. Submission site allows uploading of files into the system.
10. Changes can be made to the abstract until the deadline.

Questions?

Contact the ASNR Education Department at ekruse@asnr.org.

Neuroform Atlas® Stent System

RX ONLY

See package insert for complete indications, contraindications, warnings and instructions for use.

Indications for use

The Neuroform Atlas Stent System is indicated for use with neurovascular embolization coils in the anterior circulation of the neurovasculature for the endovascular treatment of patients ≥ 18 years of age with sacular wide-necked (neck width ≥ 4 mm or a dome-to-neck ratio of < 2) intracranial aneurysms arising from a parent vessel with a diameter of ≥ 2.0 mm and ≤ 4.5 mm.

Contraindications

- Patients in whom the parent vessel size does not fall within the indicated range.
- Patients in whom antiplatelet and/or anticoagulation therapy (e.g., aspirin and clopidogrel) is contraindicated.
- Patients who have not received anti-platelet agents prior to stent implantation.
- Patients with an active bacterial infection.
- Patients in whom angiography demonstrates the anatomy is not appropriate for endovascular treatment due to conditions such as:
 - Severe intracranial vessel tortuosity or stenosis;
 - Intracranial vasospasm not responsive to medical therapy.
- Patients in whom a pre-existing stent is in place in the parent artery at the target intracranial aneurysm location.

Potential adverse events

The potential adverse events listed below, as well as others, may be associated with the use of the Neuroform Atlas Stent System or with the procedure:

- Aphasia
- Allergic reaction to Nitinol metal and medications
- Aneurysm perforation/rupture, leak or contrast extravasation
- Blindness
- Cardiac arrhythmia
- Coil herniation through stent into parent vessel
- Cranial neuropathy
- Death
- Embolus
- Headache
- Hemiplegia
- Hemorrhage (i.e., intracerebral, subarachnoid, retroperitoneal, or in other locations)
- Hydrocephalus
- In-stent stenosis
- Infection
- Ischemia

Stryker or its affiliated entities own, use, or have applied for the following trademarks or service marks:

Neuroform Atlas, Stryker. All other trademarks are trademarks of their respective owners or holders.

The absence of a product, feature, or service name, or logo from this list does not constitute a waiver of Stryker's trademark or other intellectual property rights concerning that name or logo.

Copyright © 2019 Stryker
AF002547 v2.0 | Page 2 of 2

AXS Vecta Aspiration System

RX ONLY

CAUTION: Federal Law (USA) restricts this device to sale by or on the order of a physician.

See package insert for complete indications, contraindications, warnings and instructions for use.

Intended use/indications for use

The AXS Vecta Aspiration Catheter, as part of the AXS Vecta Aspiration System is indicated in the revascularization of patients with acute ischemic stroke secondary to intracranial large vessel occlusive disease (within the internal carotid, middle cerebral – M1 and M2 segments, basilar, and vertebral arteries) within 8 hours of symptom onset.

Patients who are ineligible for intravenous tissue plasminogen activator (IV t-PA) or who failed IV t-PA therapy are candidates for treatment.

Device description

The AXS Vecta Aspiration System is composed of the following components:

- AXS Vecta 71 or 74 Aspiration Catheter
- Medela Dominant Flex Pump
- AXS Universal Aspiration Tubing
- AXS Universal Liner Set.

The AXS Vecta Aspiration Catheter delivers aspiration from the Medela Dominant Flex Pump directly to the site of the occlusion to remove the clot. The AXS Vecta Aspiration Catheter is a single lumen, flexible, variable stiffness catheter. It has a radiopaque marker band on the distal end and a Luer hub at the proximal end. The AXS Vecta Aspiration Catheter shaft has a lubricious hydrophilic coating at the distal end (distal 25cm) to reduce friction during use. It is packaged with one Scout Introducer, one hemostasis valve, and two peel-away introducers.

The Scout Introducer may be used in conjunction with the AXS Vecta Aspiration Catheter to facilitate in the introduction of the AXS Vecta Aspiration Catheter into distal vasculature and aid in navigation to distal anatomy. The Scout Introducer has a lubricious hydrophilic coating at the distal end to reduce friction during use. The inner lumen of the AXS Vecta Aspiration Catheter is compatible with the Scout Introducer, guide wires and microcatheters. The inner lumen of the Scout Introducer is compatible with guide wires and microcatheters of an outer diameter of less than 0.044in.

The AXS Universal Aspiration Tubing serves as a conduit to supply vacuum from the Medela Dominant Flex Pump to the distal tip of the AXS Vecta Aspiration Catheter. The AXS Universal Aspiration Tubing provides a connection between the sterile and non-sterile environments. The proximal end of the AXS Universal Aspiration Tubing is connected to the AXS Universal Liner Set (outside of the sterile environment) while the distal end of the AXS Universal Aspiration Tubing is connected to the AXS Vecta Aspiration Catheter (inside the sterile environment). The AXS Universal Liner Set is connected to the Medela Dominant Flex Pump (also outside of the sterile environment).

The Medela Dominant Flex Pump is designed to generate vacuum for the AXS Vecta Aspiration System. When used as part of the AXS Vecta Aspiration System, the AXS Vecta Aspiration Catheter requires a minimum vacuum pressure of -68 kPa (-20.08 in Hg) from the Medela Dominant Flex Pump.

The Medela Dominant Flex Pump is reusable, non-sterile, and intended to be utilized outside of the sterile environment.

The AXS Universal Liner Set is provided non-sterile and consists of an individually packaged canister liner and a ClotFinder specimen cup. The AXS Universal Liner Set is offered with and without a desiccant. The AXS Universal Liner Set is single-use and the repository for aspirated material.

Dimensions of the AXS Vecta Aspiration Catheter and Scout Introducer are included on the individual device label. The AXS Vecta Aspiration Catheters are available in 3 different lengths, the device configurations including the length of the Scout packaged with each catheter and the recommended Microcatheter length is presented in the table 1.0 below.

Stryker or its affiliated entities own, use, or have applied for the following trademarks or service marks: AXS Universal, AXS Vecta, ClotFinder, Stryker.

Scout is a registered trademark of InNeuroCo, Inc. All other trademarks are trademarks of their respective owners or holders.

The absence of a product, feature, or service name, or logo from this list does not constitute a waiver of Stryker's trademark or other intellectual property rights concerning that name or logo.

Copyright © 2019 Stryker
AF002595 v2.0 | Page 2 of 2

- Mass effect
- Myocardial infarction
- Neurological deficit/intracranial sequele
- Pseudoaneurysm
- Reaction to radiation exposure (i.e., alopecia, burns ranging in severity from skin reddening to ulcers, cataracts, or delayed neoplasia)
- Reactions to anti-platelet/anti-coagulant agents
- Renal failure
- Seizure
- Stent fracture, migration/embolization, or misplacement
- Stent thrombosis
- Stroke
- Transient ischemic attack
- Vasospasm
- Vessel occlusion or closure including parent vessel or non-target side-branches
- Vessel perforation/rupture, dissection, trauma or damage
- Vessel thrombosis
- Visual impairment
- Other procedural complications including but not limited to anesthetic and contrast media risks, hypotension, hypertension, access site complications (including pain, hematoma, local bleeding, local infection, and injury to the artery (i.e. dissection), vein, or adjacent nerves)
- Unplanned intervention

Warnings

Contents supplied STERILE using an ethylene oxide (EO) process. Do not use if sterile barrier is damaged. If damage is found, call your Stryker Neurovascular representative.

For single use only. Do not reuse, reprocess or resterilize. Reuse, reprocessing or resterilization may compromise the structural integrity of the device and/or lead to device failure which, in turn, may result in patient injury, illness or death. Reuse, reprocessing or resterilization may also create a risk of contamination of the device and/or cause patient infection or cross-infection, including, but not limited to, the transmission of infectious diseases from one patient to another. Contamination of the device may lead to injury, illness or death of the patient.

After use, dispose of product and packaging in accordance with hospital, administrative and/or local government policy.

- This device should only be used by physicians who have received appropriate training in interventional neuroradiology or interventional radiology and preclinical training on the use of this device as established by Stryker Neurovascular.
- Persons allergic to nickel titanium (Nitinol) may suffer an allergic response to this stent implant.
- Higher adverse event rates may be experienced for distal aneurysms located in the anterior and middle cerebral arteries.
- Do not use device to treat patients with ruptured intracranial aneurysms within a minimum of 30 days from the aneurysm rupture.

Catheter part number	INC-11129-115	INC-11129-125	INC-11129-132	INC-11129-115	INC-11129-125	INC-11129-132
Catheter inner diameter (in)	0.071	0.071	0.071	0.074	0.074	0.074
Distal catheter outer diameter (in)	0.082	0.082	0.082	0.083	0.083	0.083
Catheter working length (cm)	115	125	132	115	125	132
Scout Introducer length (cm)	133	143	150	133	143	150
Recommended compatible microcatheter length (cm)	150	160	160	150	160	160
Recommended compatible microcatheter outer diameter (in)	0.044	0.044	0.044	0.044	0.044	0.044
Recommended compatible guidewire outer diameter (in)	0.038	0.038	0.038	0.038	0.038	0.038

The AXS Vecta Aspiration System is recommended for use in the following vessel size ranges based on non-clinical testing. Refer to Table 2.0 below.

AXS Vecta Aspiration Catheter	Catheter part number	Vessel size in mm (Vessel size in inches)
AXS Vecta 71	INC-11129-115	2.1-4 mm (0.083in – 0.157in)
	INC-11129-125	2.1-4 mm (0.083in – 0.157in)
	INC-11129-132	2.1-4 mm (0.083in – 0.157in)
AXS Vecta 74	INC-11597-115	2.2-4 mm (0.087in – 0.157in)
	INC-11597-125	2.2-4 mm (0.087in – 0.157in)
	INC-11597-132	2.2-4 mm (0.087in – 0.157in)

Contraindications

The AXS Vecta Aspiration Catheter has not been evaluated for use in the coronary vasculature.

Do not use automated high-pressure contrast injection equipment with the AXS Vecta Aspiration Catheter because it may damage the device.

Adverse events

Potential adverse events associated with the use of catheters or with the endovascular procedures include, but are not limited to:

- Acute Vessel Occlusion
- Air Embolism
- Allergic reaction and anaphylaxis from contrast media
- Arteriovenous fistula
- Death
- Device malfunction
- Distal Embolization
- Emboli
- False Aneurysm Formation
- Hematoma or hemorrhage at the puncture site
- Inability to completely remove thrombus
- Infection
- Intracranial Hemorrhage
- Ischemia
- Kidney damage from contrast media
- Neurological Deficit including Stroke
- Risks Associated with angiographic and fluoroscopic radiation including but not limited to: Alopecia, burns ranging in severity from skin reddening to ulcers, cataracts, and delayed neoplasia
- Sterile inflammation or granulomas at the access site
- Tissue necrosis
- Vessel Spasm, Thrombosis, Dissection or Perforation

Warning

Contents supplied STERILE using an ethylene oxide (EO) process. Do not use if sterile barrier is damaged. If damage is found, call your Stryker Neurovascular representative.

For single use only. Do not reuse, reprocess or resterilize.

Cautions / precautions

- Take all necessary precautions to limit X-ray radiation doses to clinical operators by using sufficient shielding, reducing fluoroscopy times, and modifying X-ray technical factors whenever possible.
- The Neuroform Atlas stent may create local field inhomogeneity and susceptibility artifacts during magnetic resonance angiography (MRA), which may degrade the diagnostic quality to assess effective intracranial aneurysm occlusion.
- Safety and effectiveness of the Neuroform Atlas Stent System in patients below the age of 18 has not been established.
- The benefits may not outweigh the risks of device use in patients with small and medium asymptomatic extracranial intracranial aneurysms, including those located in the cavernous internal carotid artery.
- Carefully weigh the benefits vs. risks of device treatment for each individual patient based on their medical health status and risk factors for intracranial aneurysm rupture during their expected life time such as age, comorbidities, history of smoking, intracranial aneurysm size, location, and morphology, family history, history of prior asymptomatic subarachnoid hemorrhage (aSAH), documented growth of intracranial aneurysm on serial imaging, presence of multiple intracranial aneurysms, and presence of concurrent pathology. The benefits may not outweigh the risks associated with device use in certain patients; therefore, judicious patient selection is recommended based on clinical practice guidelines or tools to assess the life time risk of intracranial aneurysm rupture.

Safety Information Magnetic Resonance Conditional

Non-clinical testing and analysis have demonstrated that the Neuroform Atlas Stent is MR Conditional alone, or when overlapped with a second stent, and adjacent to a Stryker Neurovascular coil mass. A patient with the Neuroform Atlas Stent can be safely scanned immediately after placement of this implant, under the following conditions:

- Static magnetic field of 1.5 and 3.0 Tesla
- Maximum spatial gradient field up to 2500 Gauss/cm (25 Tesla/m)
- Maximum MR system reported whole body averaged specific absorption rate of 2 W/kg (Normal Operating Mode) and head averaged specific absorption rate of 3.2 W/kg.

Under the scan conditions defined above, the Neuroform Atlas Stent is expected to produce a maximum temperature rise of 4 °C after 15 minutes of continuous scanning. The Neuroform Atlas Stent should not migrate in this MRI environment.

In non-clinical testing, the image artifact caused by the device extends approximately 2 mm from the Neuroform Atlas Stent when imaged with a spin echo pulse sequence and 3 Tesla MRI system. The artifact may obscure the device lumen and may be necessary to optimize MR imaging parameters for the presence of this implant. See additional precaution related to the image artifact from the implant in the "Precautions" section of this labeling.



Stryker Neurovascular
47900 Bayside Parkway
Fremont, CA 94538

strykerneurovascular.com

Date of Release: MAY/2019

EX_EN_US

Reuse, reprocessing or resterilization may compromise the structural integrity of the device and/or lead to device failure which, in turn, may result in patient injury, illness or death. Reuse, reprocessing or resterilization may also create a risk of contamination of the device and/or cause patient infection or cross-infection, including, but not limited to, the transmission of infectious diseases from one patient to another. Contamination of the device may lead to injury, illness or death of the patient.

After use, dispose of product and packaging in accordance with hospital, administrative and/or local government policy.

Warnings

- The AXS Vecta Aspiration Catheter has not been evaluated for more than one (1) clot retrieval attempt.
- This device is intended for single use only, do not re-sterilize or reuse. Re-sterilization and/or reuse may result in cross contamination and/or reduced performance.
- When the catheter is exposed to the vascular system, it should be manipulated while under high-quality fluoroscopic observation. Do not advance or retract the catheter if resistance is encountered during manipulation; determine the cause of the resistance before proceeding.
- Operators should take all necessary precautions to limit X-Radiation doses to patients and themselves by using sufficient shielding, reducing fluoroscopy times, and modifying X-Ray technical factors where possible.
- This device is coated with a hydrophilic coating at the distal end of the device for a length of 25 cm. Please refer to the Device Preparation Section for further information on how to prepare and use this device to ensure it performs as intended. Failure to abide by the warnings in this labeling might result in damage to the device coating, which may necessitate intervention or result in serious adverse events.

Precautions

- Do not use kinked, damaged, or opened devices.
- Use the device prior to the "Use By" date specified on the package.
- Exposure to temperatures above 54°C (130°F) may damage device. Do not autoclave.
- Torquing or moving the device against resistance may result in damage to the vessel or device.
- Maintain a constant infusion of appropriate flush solution.
- If flow through the device becomes restricted, do not attempt to clear the lumen by infusion. Remove and replace the device.
- Examine the device to verify functionality and to ensure that its size and shape are suitable for the specific procedure for which it is to be used.
- The AXS Vecta Aspiration System should be used only by physicians trained in percutaneous procedures and/or interventional techniques.
- The Scout Introducer should be used with a guidewire and Microcatheter inserted when in vasculature.
- If using the AXS Vecta Aspiration System for Thrombectomy, monitor the canister fluid level and replace the canister if the fill level reaches 75% of the canister volume.
- Administration of anticoagulants and antiplatelets should be suspended until 24 hours post-treatment. Medical management and acute post stroke care should follow the ASA guidelines.
- Any neurological determination should be evaluated by urgent CT scan and other evaluations as indicated according to investigator/hospital best practice.
- As in all surgical interventions, monitoring of intra-procedural blood loss is recommended so that appropriate management may be instituted.
- Limit the usage of the AXS Vecta Aspiration Catheter to arteries greater than the catheter's outer diameter.
- Excessive aspiration with the distal tip of the AXS Vecta Aspiration Catheter covered by the vessel wall may cause vessel injury. Carefully investigate location of the distal tip under fluoroscopy prior to aspiration.
- There is an inherent risk with the use of angiography and fluoroscopy.
- When transporting the Medela Dominant Flex Pump, utilize the pump handle.



Stryker Neurovascular
47900 Bayside Parkway
Fremont, CA 94538

strykerneurovascular.com

Date of Release: JUN/2019

EX_EN_US



ONE AND DONE

INDICATIONS FOR USE:

The WEB Aneurysm Embolization System is indicated for use at the middle cerebral artery (MCA) bifurcation, internal carotid artery (ICA) terminus, anterior communicating artery (AComm) complex, or basilar artery apex for the endovascular treatment of adult patients with saccular, wide neck bifurcation intracranial aneurysms with dome diameter from 3 mm to 10 mm and either neck size 4 mm or greater or the dome-to-neck ratio is greater than 1 and less than 2.

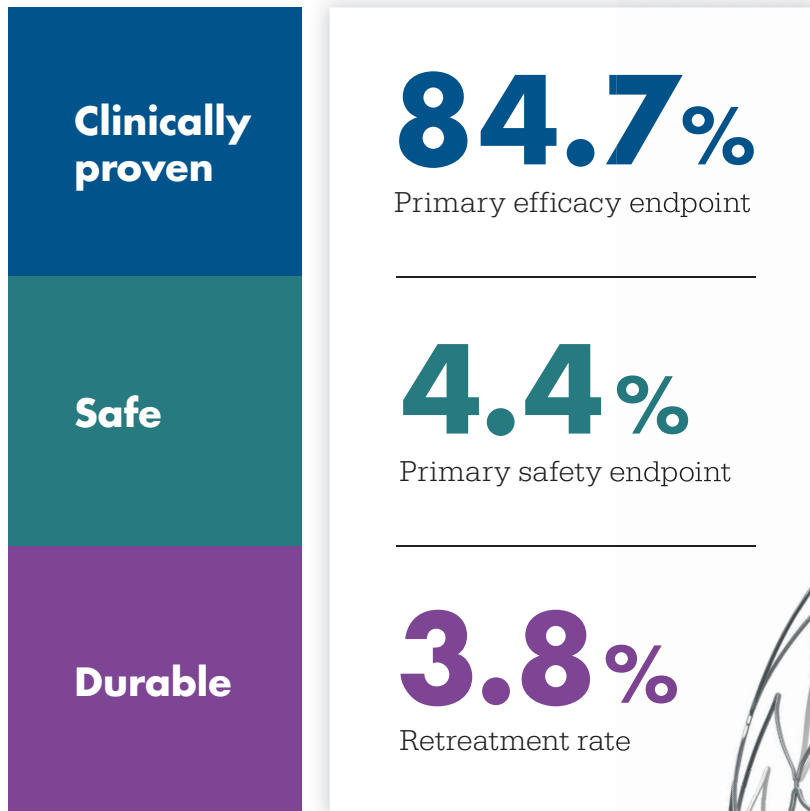
The WEB Aneurysm Embolization System is contraindicated for patients with known bacterial infection that may interfere with or negatively affect the implantation procedure and patients with known hypersensitivity to nickel. For complete indications, contraindications, potential complications, warnings, precautions, and instructions, see instructions for use (IFU provided with the device).

The VIA® Catheter is intended for the introduction of non-liquid interventional devices (such as stents/_ow diverters) and infusion of diagnostic (such as contrast media) or non-liquid therapeutic agents into the neuro, peripheral, and coronary vasculature. The VIA Catheter is contraindicated for use with liquid embolic materials, such as n-butyl 2-cyanoacrylate or ethylene vinyl alcohol & DMSO (dimethyl sulfoxide). The VIA Catheter is contraindicated for use in the pediatric population (<22 yrs of age).

Caution: Federal law restricts these devices to sale by or on the order of a physician.

The results say it all

Now **PMA** approved



The ATLAS IDE Study is the largest of its class with **182 patients treated.**

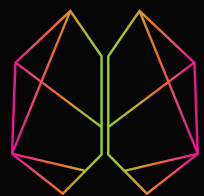
Neuroform Atlas[®]
Stent System



CERENOVUS

#THINKCERENOVUS

Important information: Prior to use, refer to the instructions for use supplied with this device for indications, contraindications, side effects, warnings, and precautions.
Caution: US Law restricts this device to sale by or on the order of a physician
©CERENOVUS 2019. All rights reserved. 114983-190418



CERENOVUS

PART OF THE *Johnson & Johnson* FAMILY OF COMPANIES



Title: Vaulted ceiling of gothic Cathédrale Notre-Dame de Reims, France.

Steven A. Messina, MD, Senior Associate Consultant, Neuroradiology, Assistant Professor of Radiology, Mayo Clinic College of Medicine, Rochester, Minnesota

Altered Relationship between Working Memory and Brain Microstructure after Mild Traumatic Brain Injury

S. Chung, X. Wang, E. Fieremans, J.F. Rath, P. Amorapanth, F.-Y.A. Foo, C.J. Morton, D.S. Novikov, S.R. Flanagan, and Y.W. Lui



ABSTRACT

BACKGROUND AND PURPOSE: Working memory impairment is one of the most troubling and persistent symptoms after mild traumatic brain injury (MTBI). Here we investigate how working memory deficits relate to detectable WM microstructural injuries to discover robust biomarkers that allow early identification of patients with MTBI at the highest risk of working memory impairment.

MATERIALS AND METHODS: Multi-shell diffusion MR imaging was performed on a 3T scanner with 5 b-values. Diffusion metrics of fractional anisotropy, diffusivity and kurtosis (mean, radial, axial), and WM tract integrity were calculated. Auditory-verbal working memory was assessed using the Wechsler Adult Intelligence Scale, 4th ed, subtests: 1) Digit Span including Forward, Backward, and Sequencing; and 2) Letter-Number Sequencing. We studied 19 patients with MTBI within 4 weeks of injury and 20 healthy controls. Tract-Based Spatial Statistics and ROI analyses were performed to reveal possible correlations between diffusion metrics and working memory performance, with age and sex as covariates.

RESULTS: ROI analysis found a significant positive correlation between axial kurtosis and Digit Span Backward in MTBI (Pearson $r = 0.69$, corrected $P = .04$), mainly present in the right superior longitudinal fasciculus, which was not observed in healthy controls. Patients with MTBI also appeared to lose the normal associations typically seen in fractional anisotropy and axonal water fraction with Letter-Number Sequencing. Tract-Based Spatial Statistics results also support our findings.

CONCLUSIONS: Differences between patients with MTBI and healthy controls with regard to the relationship between microstructure measures and working memory performance may relate to known axonal perturbations occurring after injury.

ABBREVIATIONS: AK = axial kurtosis; AWF = axonal water fraction; bCC = body of the corpus callosum; DKI = diffusional kurtosis imaging; DSF = Digit Span Forward; DSB = Digit Span Backward; DSS = Digit Span Sequencing; FA = fractional anisotropy; gCC = genu of the corpus callosum; HC = healthy control; LNS = Letter-Number Sequencing; MTBI = mild traumatic brain injury; pCR = posterior corona radiata; sCC = splenium of the corpus callosum; sCR = superior corona radiata; SLF = superior longitudinal fasciculus; WMTI = white matter tract integrity; WAIS = Wechsler Adult Intelligence Scale; WRAT = Wide Range Achievement Test

Mild traumatic brain injury (MTBI) is an important public health problem with many serious consequences.^{1,2} While most patients with MTBI recover symptomatically within 2–3 weeks after injury, at least 15% of patients report persistent cognitive symptoms that are an important source of distress and disability after injury.^{3–5} Now an important body of work reveals MTBI-related WM injury using DTI^{6–8} and diffusional kurtosis

imaging (DKI).^{9,10} More recently, WM tract integrity (WMTI) metrics derived from an advanced compartmental diffusion WM model¹¹ have been proposed to describe microstructural characteristics in the intra- and extra-axonal environments of WM, including axonal water fraction (AWF), intra-axonal diffusivity, and extra-axonal axial and radial diffusivities.

One of major barriers to applying such findings to clinical cohorts is that the disorder is extremely heterogeneous and most current studies group clinically heterogeneous cohorts of patients with MTBI together, representing a broad spectrum of clinical symptoms. Thus, there is a specific need to understand domain-specific symptoms as they relate to detectable microstructural injuries, to better understand patient-specific injury and recovery.

Received May 15, 2019; accepted after revision June 19.

From the Center for Advanced Imaging Innovation and Research & Bernard and Irene Schwartz Center for Biomedical Imaging, Department of Radiology (S.C., X.W., E.F., C.J.M., D.S.N., Y.W.L.), and Department of Rehabilitation Medicine (J.F.R., P.A., S.R.F.), New York University School of Medicine, New York, New York; and Department of Neurology (F.-Y.A.F.), New York University Langone Health, New York, New York.

This work was supported, in part, by grant funding from the National Institutes of Health/National Institute for Neurological Disorders and Stroke: R01 NS039135–11 and R21 NS090349. This work was also performed under the rubric of the Center for Advanced Imaging Innovation and Research (www.cai2r.net), a National Institute of Biomedical Imaging and Bioengineering, Biomedical Technology Resource Center (NIH P41 EB017183).

Please address correspondence to Sohae Chung, PhD, 660 1st Ave, 4th floor, New York, NY 10016; e-mail: sohae.chung@nyulangone.org

Indicates open access to non-subscribers at www.ajnr.org

<http://dx.doi.org/10.3174/ajnr.A6146>

One of the most common and clinically significant symptoms in patients with MTBI is deficits in working memory,^{3,4,12-15} which often negatively affect quality of life.¹⁶ This result comes as no surprise because working memory, which involves the capacity to temporarily store and manipulate information in pursuit of a goal, is at the core of critical cognitive functions such as comprehension, learning, reasoning, and decision-making.¹⁷ Working memory is conceptualized as comprising 3 main components: the central executive, responsible for manipulation of information and allocation of attention and processing resources, and 2 maintenance systems, the phonologic loop (verbal and auditory information) and the visuospatial sketchpad (visual and spatial information).¹⁸⁻²⁰ There have been a few studies showing associations of working memory performance with measures of WM microstructure such as fractional anisotropy (FA)²¹ and AWF²²⁻²⁴ in healthy individuals, believed to relate to differences in axon volume and myelination. However, such associations have not yet been investigated in patients with MTBI.

Here, we hypothesize that WM injury in patients with MTBI can affect the relationship between microstructural changes to the WM and working memory performance. To test this hypothesis, we investigated the relationship between WM microstructural changes assessed using diffusion MR imaging (DTI, DKI, WMTI) and a set of Wechsler Adult Intelligence Scale, 4th ed (WAIS-IV)²⁵ subtests tapping auditory-verbal working memory functions in patients with MTBI, comparing them against healthy controls (HCs). We also performed subgroup analyses based on working memory performance and time since injury.

MATERIALS AND METHODS

Study Population

This study was approved by our institutional review board at New York University Langone Health. All experiments were performed in accordance with relevant guidelines and regulations, and written informed consent was provided by all subjects before the procedure. We prospectively recruited subjects who were seen for clinical care in the Emergency Department or Institutional Concussion Center. Inclusion criteria were the following: 1) adult individuals in the age range of 18–65 years; 2) diagnostic MTBI criteria defined by the American Congress of Rehabilitation Medicine,²⁶ including either loss of consciousness of <30 minutes or altered consciousness at time of the accident and a Glasgow Outcome Score of 13–15; and 3) injury within 4 weeks. We excluded patients with the following: 1) a history of traumatic brain injury, neurologic illness, or psychiatric disorder; 2) a history of participation in organized contact sports; and 3) any contraindication to MR imaging. We also further excluded non-native English speakers and non-right-handed individuals to avoid any potential confounding effects of language and handedness. We studied 19 patients with MTBI (mean age, 30 ± 7 years; age range, 22–45 years; average time since injury, 16 days; 9 men) and 20 HCs (mean age, 33 ± 10 years; age range, 19–65 years; 9 men). For all subjects, formal neurocognitive tests including the WAIS-IV working memory subtests were performed, and MR images were acquired within 1 day of neurocognitive tests. Additionally, to characterize subjects, the Wide Range Achievement Test, 4th ed, Word Reading subtest (WRAT-4) was performed, and the scores were con-

verted to intelligence quotient scores as a brief measure of intelligence. Subgroups of the subjects in this study were previously included in 2 works with nonoverlapping hypotheses.^{24,27}

MR Imaging Protocol

MR imaging was performed using a 3T MR imaging scanner (Magnetom Skyra; Siemens, Erlangen, Germany). Diffusion imaging was performed with 5 b-values (250, 1000, 1500, 2000, and 2500 s/mm²) using 5 diffusion-encoding direction schemes (6, 20, 20, 30, and 60, respectively). Three images with b=0 s/mm² were also acquired. Multiband (factor of 2)²⁸ EPI was used for accelerated acquisitions with an anterior-posterior phase-encoding direction. Other parameters included the following: FOV = 220 × 220 mm, acquisition matrix = 88 × 88, number of slices = 56, image resolution = 2.5 × 2.5 × 2.5 mm³, TR/TE = 4900/95 ms, bandwidth = 2104 Hz/pixel, a generalized autocalibrating partially parallel acquisition factor of 2. An additional image with b=0 s/mm² with a reversed phase-encoding direction was acquired for geometric artifact correction. The total scan time was 12 minutes.

Working Memory Assessment

Working memory was assessed with age-appropriate WAIS-IV subtests,²⁵ which included Digit Span and Letter-Number Sequencing (LNS). In the Digit Span Forward (DSF) task, examinees repeat a sequence of numbers read to them. In the Digit Span Backward (DSB), the same procedure is followed, except that examinees repeat the numbers in reverse order. In the Digit Span Sequencing (DSS), examinees repeat the numbers in ascending order. In the LNS task, examinees separate numbers from letters and state in ascending/alphabetical order a mixed sequence of numbers and letters read to them. Raw scores were converted into standardized age-corrected z scores with a zero mean and a unitary variation,²⁵ with higher scores indicating better performance.

Image Analyses

Diffusion Image Processing. The diffusion images underwent the preprocessing steps including Marchenko-Pastur principal component analysis denoising,²⁹ Gibbs correction,³⁰ distortion correction with the topup command in FSL (<https://fsl.fmrib.ox.ac.uk/fsl/fslwiki/topup>), eddy current distortion and motion correction with the eddy command in FSL (<https://fsl.fmrib.ox.ac.uk/fsl/fslwiki/eddy>), and outlier detection.³¹ In total, 11 diffusion metrics including DTI (FA, mean diffusivity [MD], axial diffusivity [AD], radial diffusivity [RD]), DKI (mean kurtosis [MK], axial kurtosis [AK], radial kurtosis [RK]), and WMTI (AWF, intra-axonal diffusivity, extra-axonal axial diffusivity, and extra-axonal radial diffusivity) metrics were calculated using in-house software developed in Matlab R2017a (MathWorks, Natick, Massachusetts).

Tract-Based Spatial Statistics. We used the standard Tract-Based Spatial Statistics (TBSS; <http://fsl.fmrib.ox.ac.uk/fsl/fslwiki/TBSS>)³² to reveal possible correlations between working memory test z scores and diffusion metrics. Briefly, subject FA maps were normalized to the FA template through a nonlinear coregistration, and voxelwise statistical analysis was performed on FA val-

ues projected onto the FA skeleton by looking for local maximum values perpendicular to the skeleton using a permutation-based nonparametric testing randomize command in FSL (<https://fsl.fmrib.ox.ac.uk/fsl/fslwiki/Randomise/UserGuide>) with the threshold-free cluster enhancement (TFCE) option. All other parametric maps underwent the same transformations and processes. The tract skeleton was thresholded at an FA of 0.2 for DTI and DKI metrics. For WMTI metrics, analysis was restricted to WM regions consisting of single-fiber orientations (FA threshold of 0.4), as recommended.^{11,33} Age and sex were included as covariates. The number of permutations was set to 5000.

ROI Analysis. ROI analysis was performed on 18 major WM tracts, including genu/body/splenium of the corpus callosum (gCC/bCC/sCC), right and left anterior/posterior limb of the internal capsule, right and left anterior/superior (sCR)/posterior corona radiata (pCR), right and left cingulum, right and left superior longitudinal fasciculus (SLF), and whole WM. ROI regions were generated on the basis of the Johns Hopkins University ICBM-DTI-81 WM labels atlas.³⁴ Briefly, all subjects' FA maps were nonlinearly registered to the FA template; then, a "reversed warping" procedure was performed to assign the atlas labels to each subject's space. The ROIs in each subject's space were manually corrected if necessary. For each ROI, the mean value was obtained only in voxels with FA ≥ 0.2 for DTI and DKI metrics and with FA ≥ 0.4 for WMTI metrics, to restrict analysis to WM regions, as recommended.^{11,33}

Statistical Analysis

The MANCOVA was used to test group differences in the length of education and WRAT-4 intelligence quotient scores, with age and sex as covariates, using SPSS Statistics software, Version 25.0 (IBM, Armonk, New York). Results were considered significant for $P < .05$.

For TBSS, a statistical threshold level of $P < .05$ was applied after family-wise error correction for multiple comparisons.

For ROI analysis, both the Pearson partial correlation and Spearman rank correlation were performed to measure the associations between diffusion metrics and WAIS-IV subtest scores in each ROI, using SPSS. Age and sex were included as covariates. All P values were corrected for multiple comparisons using the Benjamini-Hochberg correction. A statistical threshold level of corrected $P < .05$ was used. Correlation coefficients were calculated. We also used Fisher R-to-Z transformation³⁵ to test for differences in between-group correlations.

On the basis of the ROI analysis results, specific regions demonstrating significant correlations with working memory performance were further interrogated by dividing subjects into subgroups based on their working memory test z scores (<1 , ≥ 1) and time since injury (<2 weeks, 2–4 weeks). Subgroup comparisons were performed using MANCOVA, with age as a covariate. Results were considered significant at $P < .05$.

RESULTS

The average length of education for patients with MTBI was 15.5 ± 1.7 years, not statistically different from that in healthy controls (16.3 ± 1.8 years). Also, WRAT-4 intelligence quotient scores were not statistically different between MTBI ($108.5 \pm$

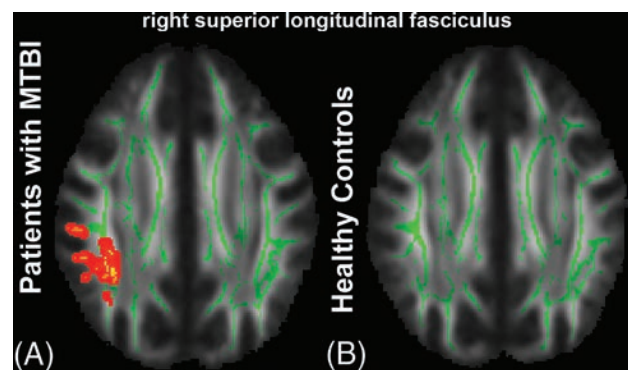


FIG 1. TBSS results show a significant positive correlation between AK and DSB. The mean FA skeleton (green) is overlaid on the mean FA map. Significantly correlated voxels (corrected $P < .05$) are shown in the heat map overlay in the right SLF in the MTBI group (A), but are not seen in the HC group (B).

12.0) and HC (113.6 ± 14.3) groups. WAIS-IV subtests were not significantly correlated with age and length of education for MTBI and HC groups, except for positive correlations between the length of education and DSS in HCs ($P = .03$).

From TBSS analysis, in the MTBI group, we found a significant positive correlation between AK and DSB, primarily in the right SLF (Fig 1A), which was not present in the HC group (Fig 1B). Most interesting, we found complete loss of relationships between FA and LNS in the MTBI group (Fig 2A), while a significant correlation was shown in the HC group (Fig 2B), most notably in parietal WM, sCR/pCR, bCC/sCC, and SLF. We also found no significant correlation between AWF and LNS in the MTBI group (Fig 3A), while there were multiple areas showing a statistically significant positive correlation between AWF and LNS in the HC group, involving parietal WM, sCR/pCR, and bCC/sCC (Fig 3B). No other diffusion metrics showed areas of significant correlation surviving correction for multiple comparisons.

ROI analysis also found a significant correlation between AK and DSB in the right SLF in the MTBI group (Pearson $R = 0.69$, $P = 0.04$; Spearman $\rho = 0.75$, $P = 0.01$) that was not present in the HC group. The correlation coefficients observed in the MTBI and HC groups were significantly different (Fisher R-to-Z transformation, $P = .01$). On the other hand, we also observed loss of relationships between FA and LNS in the MTBI group but found a significant positive correlation in the right pCR in the HC group (Pearson $R = 0.67$, $P = 0.04$; Spearman $\rho = 0.57$, $P = 0.09$). The correlation coefficients observed in the MTBI and HC groups were not significantly different, but there was a trend toward significance (Fisher R-to-Z transformation, $P = .06$). No other significant correlations were found after correction for multiple comparisons. These results are summarized in Table 1.

On the basis of the results of the ROI analysis, subjects were further divided into subgroups according to their working memory test z scores (<1 or ≥ 1) and time since injury (<2 weeks or 2–4 weeks). Details of the subgroup characteristics are given in Tables 2 and 3. With regard to subgroup analysis, we found a significant difference in AK between the MTBI subgroup of 2–4 weeks from injury with DSB <1 and the MTBI subgroup

of 2–4 weeks from injury with DSB ≥ 1 within the right SLF (Fig 4A). Significant differences in FA were shown between the MTBI subgroup of <2 weeks of injury with LNS <1 and the

HC subgroup with LNS <1, and between the HC subgroup with LNS <1 and the HC subgroup with LNS ≥ 1 , within the right pCR (Fig 4B).

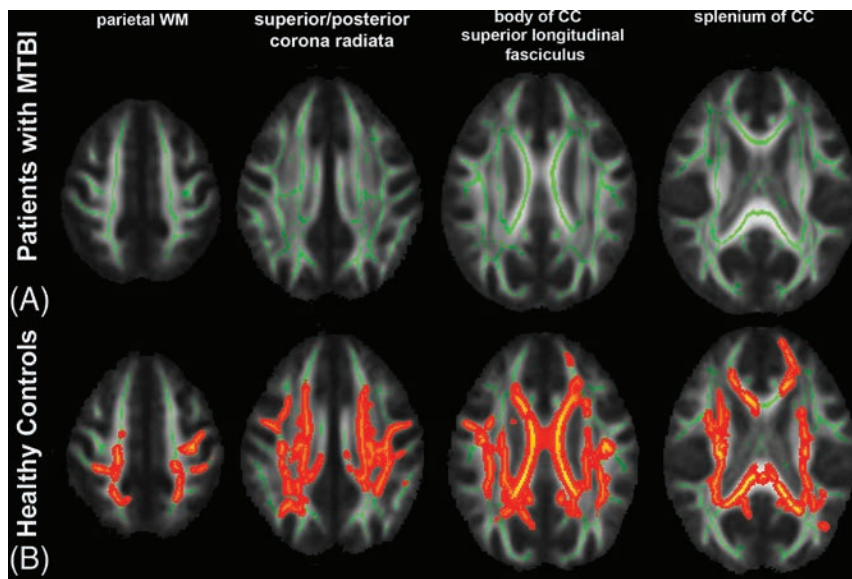


FIG 2. TBSS results show a significant positive correlation between FA and LNS. The mean FA skeleton (green) is overlaid on the mean FA map. Significantly correlated voxels (corrected $P < .05$) are shown in heat map overlay. A, In the MTBI group, no correlation was found. B, In the HC group, significantly correlated voxels involve the parietal WM, SCR/pCR, bCC/sCC, and SLF.

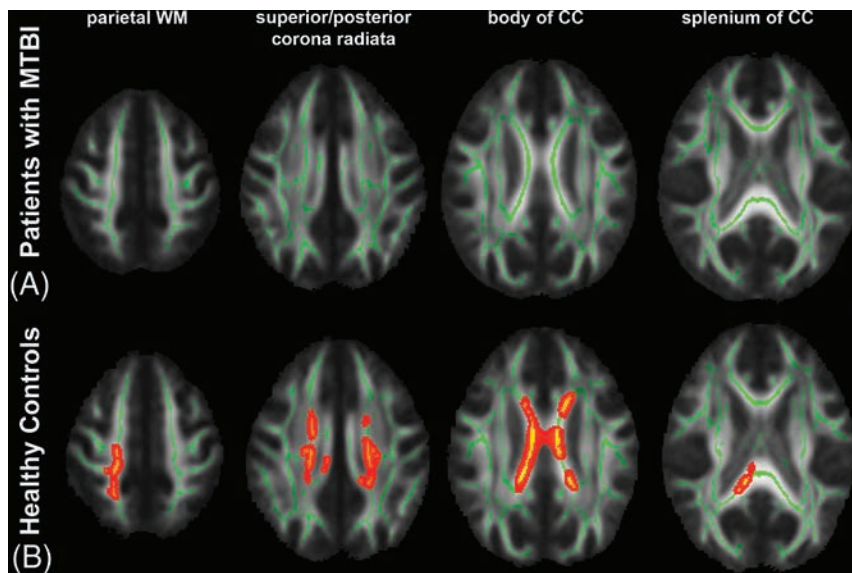


FIG 3. TBSS results show a significant positive correlation between AWF and LNS. The mean FA skeleton (green) is overlaid on the mean FA map. Significantly correlated voxels (corrected $P < .05$) are shown in the heat map overlay. A, In the MTBI group, no correlation was found. B, In the HC group, significantly correlated voxels involve the parietal WM, SCR/pCR, and bCC/sCC.

Table 1: Results of the ROI analysis showing significant positive correlations between AK and DSB in the MTBI group, and between FA and LNS in the HC group

Diffusion Metrics vs Working Memory	ROI	MTBI				HC				Fisher R-to-Z (P)
		Pearson		Spearman		Pearson		Spearman		
		R	P ^a	ρ	P ^a	R	P ^a	ρ	P ^a	
AK vs DSB	Right SLF	0.69 ^b	.04 ^b	.75 ^b	.01 ^b	0.04	1.20	0.11	1.48	2.32 ^b (.01) ^b
FA vs LNS	Right pCR	0.25	2.29	.24	.8	0.67 ^b	.04 ^b	0.57	.09	-1.59 (.06)

^a Corrected P values after Benjamini-Hochberg correction for multiple comparison.

^b Significant results.

DISCUSSION

This study shows significant differences in the relationships between specific WM microstructural markers and auditory-verbal working memory performance between patients with MTBI and healthy controls. Specifically, in the MTBI group, a significant correlation between AK and DSB was present in the right SLF, while the HC group demonstrated no such relationship (Fig 1), a finding observed using both TBSS and ROI analyses. Patients with MTBI also appear to lose the normal associations seen in controls between diffusion metrics (FA, AWF) and LNS (Figs 2 and 3). Furthermore, subgroup analyses also showed a significant difference in AK between the MTBI subgroup of 2–4 weeks of injury with DSB <1 and the MTBI subgroup of 2–4 weeks of injury with DSB ≥ 1 . A significant difference was also found between the MTBI subgroup of <2 weeks of injury and the HC subgroup, both having LNS <1.

Notably, the relationship between AK and DSB in patients with MTBI is mainly present in the right SLF (Fig 1), a structure critical for attention, memory, emotion, and language,^{36,37} linking frontoparietal WM regions critical to working memory.^{38–40} In particular, the right SLF is critical for attention,⁴¹ visuospatial function,⁴² and short-term memory.⁴³ Previously, similar results were reported showing relations between the SLF and working memory deficits assessed by FA and the visual 2-back d-prime index in patients with severe and diffuse traumatic brain injury.⁴⁴ In this study, we found decreased AK in the right SLF, reflecting decreased tissue complexity along the long axis of the axon⁴⁵ in patients with MTBI with

Table 2: Subgroup characteristics defined by their working memory test z scores (LNS <1 or ≥1) and time since injury (<2 weeks or 2–4 weeks)^a

	LNS <1			LNS ≥1		
	MTBI (<2 Weeks)	MTBI (2–4 Weeks)	HC	MTBI (<2 Weeks)	MTBI (2–4 Weeks)	HC
No.	5	10	9	3	1	11
Age	31 ± 6	31 ± 9	31 ± 8	25 ± 3	31	35 ± 12
LNS	-0.13 ± 0.51	0.07 ± 0.41	0.07 ± 0.32	1.55 ± 0.39	2	1.82 ± 0.62

^a Data are means unless otherwise indicated.

Table 3: Subgroup characteristics defined by their working memory test z scores (DSB <1 or ≥1) and time since injury (<2 weeks or 2–4 weeks)^a

	DSB <1			DSB ≥1		
	MTBI (<2 Weeks)	MTBI (2–4 Weeks)	HC	MTBI (<2 Weeks)	MTBI (2–4 Weeks)	HC
No.	4	7	12	4	4	8
Age	30 ± 6	29 ± 8	31 ± 7	37 ± 8	26 ± 4	37 ± 14
DSB	-0.67 ± 0.27	-0.24 ± 0.25	0.08 ± 0.38	1.42 ± 0.5	1.58 ± 0.32	1.79 ± 0.71

^a Data are means unless otherwise indicated.

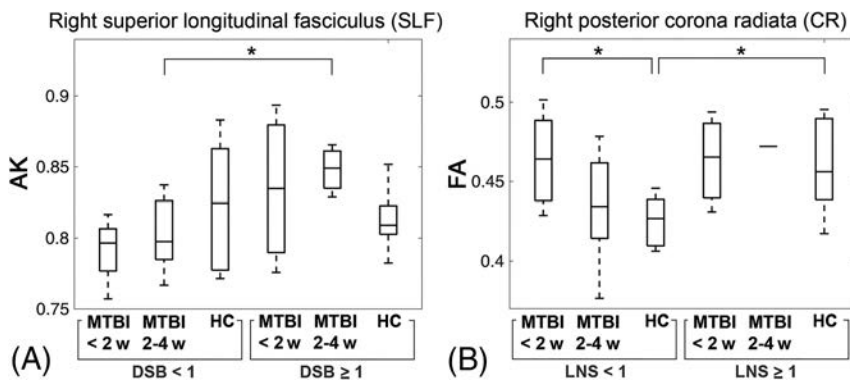


FIG 4. Results of subgroup analysis. *A*, Boxplots of AK show a significant difference between the MTBI subgroup of 2–4 weeks from injury with DSB <1 and the MTBI subgroup of 2–4 weeks from injury with DSB ≥1. *B*, Boxplots of FA show significant differences between the MTBI subgroup of <2 weeks of injury with LNS <1 and the HC subgroup with LNS <1 and between the HC subgroup with LNS <1 and the HC subgroup with LNS ≥1. The asterisk indicates $P < .05$; w, weeks.

poorer performance on DSB. AK is known from animal validation studies to be affected by axonal injury⁴⁶ as well as secondary reactive astrogliosis.⁴⁷

Also differentiating MTBI from HC groups in TBSS analysis was a loss of diffusely present normal associations that we have seen in healthy controls (Figs 2 and 3); in controls, it has been shown that FA and AWF directly correlate with performance on LNS, a complex working memory task.²⁴ However, in patients with MTBI, we found a disruption in this normal relationship, presumed to relate to WM injuries known to occur after MTBI,¹⁴ because AWF is a measure that reflects axonal density and/or myelination.

ROI analyses (Table 1) showed related statistically significant correlations focused in the right SLF in patients with MTBI as well as in the right pCR in healthy controls, compared with the more diffuse TBSS results. TBSS uses maximum values projected onto the WM skeleton, making it more sensitive to maximal deviations in diffusion metrics. Both TBSS and ROI analyses revealed positive correlations in the right SLF and right pCR, suggesting that these regions are strong, potential anatomic landmarks important to working memory performance, and possibly impairment. Along with the SLF, a structure critical to working memory,^{38–40} the corona radiata is also a complex bundle of fibers related to working memory because it consists of several separate pathways connecting the cerebral cortex to

subcortical structures,^{24,48,49} including fiber tracts in the pCR, which connect to the precuneus, a part of the default mode network implicated in working memory performance.^{50,51}

With regard to the subgroup analysis, within the same time-since-injury period of 2–4 weeks, there was a significant difference in AK between the MTBI subgroups with higher and lower working memory performance in the right SLF (Fig 4A). Decreased AK, believed to relate to axonal injury⁴⁶ and/or secondary reactive astrogliosis,⁴⁷ may specifically be a more useful indicator in the MTBI subgroup with lower working memory performance. Also, within the lower LNS range, significantly elevated

FA was observed in the MTBI subgroup within 2 weeks of injury compared with the corresponding HC subgroup with the same lower LNS range (Fig 4B). Elevated FA was reported frequently within 2 weeks of injury, believed to reflect injury-related cytotoxic edema⁵² or reactive astrogliosis.⁵³ We found only a significant difference in FA between the MTBI subgroup within 2 weeks of injury and the HC subgroup, only in the lower LNS range, not in the higher LNS range, suggesting that understanding the relationships between domain-specific symptoms such as working memory deficits and underlying microstructural injuries is important for patient management (eg, pharmacologic intervention to inhibit inflammation and reduce the neurotoxic effects of reactive gliosis).

There are several limitations in the presented study. First, there is a wide age range from 19 to 65 years. Any age effects were minimized using age-corrected WAIS-IV subtest z-scores derived from the published normative sample ($n = 2200$) divided into 13 age bands, spanning ages 16–90.²⁵ Moreover, age is included as a covariate in all statistical analyses. Second, subgroups were defined on the basis of a somewhat arbitrary statistical threshold value for LNS and DSB (Fig 4). Further work could study various performance groups. Third, this study includes a relatively small

number of total subjects and points toward the need for larger studies of working memory dysfunction and brain injury in patients with MTBI. Fourth, this study did not examine the underlying processes that contribute to working memory tasks such as Digit Span and LNS. Further work could focus on component processes such as attention and maintenance of information. Furthermore, as mentioned previously, TBSS uses maximum values projected onto the WM skeleton along an orthogonal line, making it more sensitive to maximal deviations in diffusion metrics but also reducing the need for image smoothing and alleviating any residual misalignment.⁵⁴ In this study, we used both TBSS and ROI approaches to rigorously assess both diffuse and regional WM.

CONCLUSIONS

There are differences between patients with MTBI within 4 weeks of injury and healthy controls in terms of the relationships between brain microstructure and working memory performance. These findings may relate to known WM injury and changes in functional organization occurring after MTBI. Further study on the effect of time since injury on working memory performance may provide insight into the temporal dynamics of working memory deficits in patients with MTBI.

Disclosures: Sohae Chung—RELATED: Grant: National Institutes of Health, Comments: R01 NS039135-II, R21 NS090349, P41 EB017183.* Els Fieremans—UNRELATED: Board Membership: MicSi, Comments: No money has been paid to me or my institution, but for full disclosure, I am an advisory board member of MicSi, a company that provides advanced image-processing and denoising tools; Royalties: GE Healthcare, Comments: I received \$2125 in royalties for patent licensing. My institution, NYU School of Medicine, also received royalties; Stock/Stock Options: MicSi, Comments: No money has been paid to me or my institution for stock, but for full disclosure, I own stock (3%), as well as NYU School of Medicine, in MicSi, a company that provides advanced image-processing and denoising tools. Joseph F. Rath—RELATED: Grant: National Institutes of Health/National Institute for Neurological Disorders and Stroke, Comments: This article reports on grant-funded research, R01 NS039135.* Charles J. Morton—UNRELATED: Employment: Massachusetts General Hospital, Comments: I worked here from September 2013 to August 2016 as a research coordinator. Dmitry S. Novikov—UNRELATED: Board Membership: Microstructure Imaging, Comments: no money paid; Stock/Stock Options: Microstructure Imaging, Comments: no money paid. Steven R. Flanagan—UNRELATED: Consultancy: McGovern School of Medicine, Icahn School of Medicine at Mount Sinai, Comments: Consultant to McGovern School of Medicine for an external review of their Department of Physical Medicine and Rehabilitation. Education sessions were provided to Icahn School of Medicine at Mount Sinai; Grants/Grants Pending: Brain Injury Association of America, Comments: grant support for the development of guidelines for traumatic brain injury*; Royalties: Springer, Comments: royalties from a textbook; Travel/Accommodations/Meeting Expenses Unrelated to Activities Listed: American Academy of Physical Medicine and Rehabilitation, Comments: Travel and accommodations were provided for face-to-face meetings, which I attend as part of my responsibilities as a member of the Board of Governors of the American Academy of Physical Medicine and Rehabilitation. Yvonne Lui—RELATED: Grant: National Institutes of Health, Comments: R01 NS039135-II, R21 NS090349, P41 EB017183.* *Money paid to the institution.

REFERENCES

1. Taylor CA, Bell JM, Breiding MJ, et al. **Traumatic brain injury-related emergency department visits, hospitalizations, and deaths: United States, 2007 and 2013.** *MMWR Surveill Summ* 2017;66:1–16 CrossRef Medline
2. Centers for Disease Control and Prevention. *Report to Congress on Mild Traumatic Brain Injury in the United States: Steps to Prevent a Serious Public Health Problem.* Atlanta: Centers for Disease Control and Prevention; 2003
3. Røe C, Sveen U, Alvsåker K, et al. **Post-concussion symptoms after**

- mild traumatic brain injury: influence of demographic factors and injury severity in a 1-year cohort study.** *Disabil Rehabil* 2009;31:1235–43 CrossRef Medline
4. Chen CJ, Wu CH, Liao YP, et al. **Working memory in patients with mild traumatic brain injury: functional MR imaging analysis.** *Radiology* 2012;264:844–51 CrossRef Medline
5. Ruff R. **Two decades of advances in understanding of mild traumatic brain injury.** *J Head Trauma Rehabil* 2005;20:5–18 Medline
6. Mayer AR, Ling J, Mannell MV, et al. **A prospective diffusion tensor imaging study in mild traumatic brain injury.** *Neurology* 2010;74:643–50 CrossRef Medline
7. Niogi SN, Mukherjee P, Ghajar J, et al. **Extent of microstructural white matter injury in postconcussive syndrome correlates with impaired cognitive reaction time: a 3T diffusion tensor imaging study of mild traumatic brain injury.** *AJNR Am J Neuroradiol* 2008;29:967–73 CrossRef Medline
8. Rutgers DR, Toulgoat F, Cazejust J, et al. **White matter abnormalities in mild traumatic brain injury: a diffusion tensor imaging study.** *AJNR Am J Neuroradiol* 2008;29:514–19 CrossRef Medline
9. Stokum JA, Sours C, Zhuo J, et al. **A longitudinal evaluation of diffusion kurtosis imaging in patients with mild traumatic brain injury.** *Brain Inj* 2015;29:47–57 CrossRef Medline
10. Grossman EJ, Jensen JH, Babb JS, et al. **Cognitive impairment in mild traumatic brain injury: a longitudinal diffusional kurtosis and perfusion imaging study.** *AJNR Am J Neuroradiol* 2013;34:951–57, S1–3 CrossRef Medline
11. Fieremans E, Jensen JH, Helpert JA. **White matter characterization with diffusional kurtosis imaging.** *Neuroimage* 2011;58:177–88 CrossRef Medline
12. Sandry J, Chiou KS, DeLuca J, et al. **Individual differences in working memory capacity predicts responsiveness to memory rehabilitation after traumatic brain injury.** *Arch Phys Med Rehabil* 2016;97:1026–29 e1 CrossRef Medline
13. van der Horn HJ, Liemburg EJ, Scheenen ME, et al. **Post-concussive complaints after mild traumatic brain injury associated with altered brain networks during working memory performance.** *Brain Imaging Behav* 2016;10:1243–53 CrossRef Medline
14. McAllister TW, Flashman LA, McDonald BC, et al. **Mechanisms of working memory dysfunction after mild and moderate TBI: evidence from functional MRI and neurogenetics.** *J Neurotrauma* 2006;23:1450–67 CrossRef Medline
15. McDowell S, Whyte J, D'Esposito M. **Working memory impairments in traumatic brain injury: evidence from a dual-task paradigm.** *Neuropsychologia* 1997;35:1341–53 CrossRef Medline
16. Hoofien D, Gilboa A, Vakil E, et al. **Traumatic brain injury (TBI) 10–20 years later: a comprehensive outcome study of psychiatric symptomatology, cognitive abilities and psychosocial functioning.** *Brain Inj* 2001;15:189–209 CrossRef Medline
17. Kayser AS, Ballard ME, D'Esposito M. **Working memory and TBI.** In: Alloway TP, ed. *Working Memory and Clinical Developmental Disorders: Theories, Debates and Interventions.* Abingdon: Routledge. 2018:180–95
18. Baddeley A. **Working memory: looking back and looking forward.** *Nat Rev Neurosci* 2003;4:829–39 CrossRef Medline
19. Baddeley A. **Working memory: theories, models, and controversies.** *Annu Rev Psychol* 2012;63:1–29 CrossRef Medline
20. Klauer KC, Zhao Z. **Double dissociations in visual and spatial short-term memory.** *J Exp Psychol Gen* 2004;133:355–81 CrossRef Medline
21. Takeuchi H, Taki Y, Sassa Y, et al. **Verbal working memory performance correlates with regional white matter structures in the frontoparietal regions.** *Neuropsychologia* 2011;49:3466–73 CrossRef Medline
22. Golestani AM, Miles L, Babb J, et al. **Constrained by our connections: white matter's key role in interindividual variability in visual working memory capacity.** *J Neurosci* 2014;34:14913–18 CrossRef Medline
23. Lazar M. **Working memory: how important is white matter?** *Neuroscientist* 2017;23:197–210 CrossRef Medline

24. Chung S, Fieremans E, Kucukboyaci NE, et al. **Working memory and brain tissue microstructure: white matter tract integrity based on multi-shell diffusion MRI.** *Sci Rep* 2018;8:3175 CrossRef Medline
25. Wechsler D. *Wechsler Adult Intelligence Scale.* San Antonio: Pearson; 2008
26. Klonoff PS, Costa LD, Snow WG. **Predictors and indicators of quality of life in patients with closed-head injury.** *J Clin Exp Neuropsychol* 1986;8:469–85 CrossRef Medline
27. Chung S, Fieremans E, Wang X, et al. **White matter tract integrity: an indicator of axonal pathology after mild traumatic brain injury.** *J Neurotrauma* 2018;35:1015–20 CrossRef Medline
28. Setsompop K, Gagoski BA, Polimeni JR, et al. **Blipped-controlled aliasing in parallel imaging for simultaneous multislice echo planar imaging with reduced g-factor penalty.** *Magn Reson Med* 2012;67:1210–24 CrossRef Medline
29. Veraart J, Fieremans E, Novikov DS. **Diffusion MRI noise mapping using random matrix theory.** *Magn Reson Med* 2016;76:1582–93 CrossRef Medline
30. Kellner E, Dhital B, Kiselev VG, et al. **Gibbs-ringing artifact removal based on local subvoxel-shifts.** *Magn Reson Med* 2016;76:1574–81 CrossRef Medline
31. Collier Q, Veraart J, Jeurissen B, et al. **Iterative reweighted linear least squares for accurate, fast, and robust estimation of diffusion magnetic resonance parameters.** *Magn Reson Med* 2015;73:2174–84 CrossRef Medline
32. Smith SM, Jenkinson M, Johansen-Berg H, et al. **Tract-based spatial statistics: voxelwise analysis of multi-subject diffusion data.** *Neuroimage* 2006;31:1487–505 CrossRef Medline
33. Jensen JH, McKinnon ET, Glenn GR, et al. **Evaluating kurtosis-based diffusion MRI tissue models for white matter with fiber ball imaging.** *NMR Biomed* 2017;30 CrossRef Medline
34. Mori S, Oishi K, Jiang H, et al. **Stereotaxic white matter atlas based on diffusion tensor imaging in an ICBM template.** *Neuroimage* 2008;40:570–82 CrossRef Medline
35. Fisher RA. *Statistical Methods for Research Workers.* Edinburgh: Oliver and Boyd; 1948
36. Mesulam MM. **From sensation to cognition.** *Brain* 1998;121(Pt 6):1013–52 CrossRef Medline
37. Petrides M, Pandya DN. **Comparative cytoarchitectonic analysis of the human and the macaque ventrolateral prefrontal cortex and corticocortical connection patterns in the monkey.** *Eur J Neurosci* 2002;16:291–310 CrossRef Medline
38. Cohen JD, Perlstein WM, Braver TS, et al. **Temporal dynamics of brain activation during a working memory task.** *Nature* 1997;386:604–08 CrossRef Medline
39. Prabhakaran V, Narayanan K, Zhao Z, et al. **Integration of diverse information in working memory within the frontal lobe.** *Nat Neurosci* 2000;3:85–90 CrossRef Medline
40. Todd JJ, Marois R. **Capacity limit of visual short-term memory in human posterior parietal cortex.** *Nature* 2004;428:751–54 CrossRef Medline
41. Frye RE, Hasan K, Malmberg B, et al. **Superior longitudinal fasciculus and cognitive dysfunction in adolescents born preterm and at term.** *Dev Med Child Neurol* 2010;52:760–66 CrossRef Medline
42. Hoefl F, Barnea-Goraly N, Haas BW, et al. **More is not always better: increased fractional anisotropy of superior longitudinal fasciculus associated with poor visuospatial abilities in Williams syndrome.** *J Neurosci* 2007;27:11960–65 CrossRef Medline
43. Chechlacz M, Gillebert CR, Vangkilde SA, et al. **Structural variability within frontoparietal networks and individual differences in attentional functions: an approach using the theory of visual attention.** *J Neurosci* 2015;35:10647–58 CrossRef Medline
44. Palacios EM, Fernandez-Espejo D, Junque C, et al. **Diffusion tensor imaging differences relate to memory deficits in diffuse traumatic brain injury.** *BMC Neurol* 2011;11:24 CrossRef Medline
45. Jensen JH, Helpert JA. **MRI quantification of non-Gaussian water diffusion by kurtosis analysis.** *NMR Biomed* 2010;23:698–710 CrossRef Medline
46. Andersson G, Orådd G, Sultan F, et al. **In vivo diffusion tensor imaging, diffusion kurtosis imaging, and tractography of a sciatic nerve injury model in rat at 9.4T.** *Sci Rep* 2018;8:12911 CrossRef Medline
47. Zhuo J, Xu S, Proctor JL, et al. **Diffusion kurtosis as an in vivo imaging marker for reactive astrogliosis in traumatic brain injury.** *Neuroimage* 2012;59:467–77 CrossRef Medline
48. Tang CY, Eaves EL, Ng JC, et al. **Brain networks for working memory and factors of intelligence assessed in males and females with fMRI and DTI.** *Intelligence* 2010;38:293–303 CrossRef
49. Long YC, Ouyang X, Liu ZN, et al. **Associations among suicidal ideation, white matter integrity and cognitive deficit in first-episode schizophrenia.** *Front Psychiatry* 2018;9:391 CrossRef Medline
50. Esposito F, Aragri A, Latorre V, et al. **Does the default-mode functional connectivity of the brain correlate with working-memory performances?** *Arch Ital Biol* 2009;147:11–20 Medline
51. Bluhm RL, Clark CR, McFarlane AC, et al. **Default network connectivity during a working memory task.** *Hum Brain Mapp* 2011;32:1029–35 CrossRef Medline
52. Shenton ME, Hamoda HM, Schneiderman JS, et al. **A review of magnetic resonance imaging and diffusion tensor imaging findings in mild traumatic brain injury.** *Brain Imaging Behav* 2012;6:137–92 CrossRef Medline
53. Budde MD, Janes L, Gold E, et al. **The contribution of gliosis to diffusion tensor anisotropy and tractography following traumatic brain injury: validation in the rat using Fourier analysis of stained tissue sections.** *Brain* 2011;134:2248–60 CrossRef Medline
54. Bach M, Laun FB, Leemans A, et al. **Methodological considerations on tract-based spatial statistics (TBSS).** *Neuroimage* 2014;100:358–69 CrossRef Medline

Utility of Percentage Signal Recovery and Baseline Signal in DSC-MRI Optimized for Relative CBV Measurement for Differentiating Glioblastoma, Lymphoma, Metastasis, and Meningioma

M.D. Lee, G.L. Baird, L.C. Bell, C.C. Quarles, and J.L. Boxerman



ABSTRACT

BACKGROUND AND PURPOSE: The percentage signal recovery in non-leakage-corrected (no preload, high flip angle, intermediate TE) DSC-MR imaging is known to differ significantly for glioblastoma, metastasis, and primary CNS lymphoma. Because the percentage signal recovery is influenced by preload and pulse sequence parameters, we investigated whether the percentage signal recovery can still differentiate these common contrast-enhancing neoplasms using a DSC-MR imaging protocol designed for relative CBV accuracy (preload, intermediate flip angle, low TE).

MATERIALS AND METHODS: We retrospectively analyzed DSC-MR imaging of treatment-naïve, pathology-proved glioblastomas ($n = 14$), primary central nervous system lymphomas ($n = 7$), metastases ($n = 20$), and meningiomas ($n = 13$) using a protocol designed for relative CBV accuracy (a one-quarter-dose preload and single-dose bolus of gadobutrol, TR/TE = 1290/40 ms, flip angle = 60° at 1.5T). Mean percentage signal recovery, relative CBV, and normalized baseline signal intensity were compared within contrast-enhancing lesion volumes. Classification accuracy was determined by receiver operating characteristic analysis.

RESULTS: Relative CBV best differentiated meningioma from glioblastoma and from metastasis with areas under the curve of 0.84 and 0.82, respectively. The percentage signal recovery best differentiated primary central nervous system lymphoma from metastasis with an area under the curve of 0.81. Relative CBV and percentage signal recovery were similar in differentiating primary central nervous system lymphoma from glioblastoma and from meningioma. Although neither relative CBV nor percentage signal recovery differentiated glioblastoma from metastasis, mean normalized baseline signal intensity achieved 86% sensitivity and 50% specificity.

CONCLUSIONS: Similar to results for non-preload-based DSC-MR imaging, percentage signal recovery for one-quarter-dose preload-based, intermediate flip angle DSC-MR imaging differentiates most pair-wise comparisons of glioblastoma, metastasis, primary central nervous system lymphoma, and meningioma, except for glioblastoma versus metastasis. Differences in normalized post-preload baseline signal for glioblastoma and metastasis, reflecting a snapshot of dynamic contrast enhancement, may motivate the use of single-dose multiecho protocols permitting simultaneous quantification of DSC-MR imaging and dynamic contrast-enhanced MR imaging parameters.

ABBREVIATIONS: DCE = dynamic contrast-enhanced; FA = flip angle; NAWM = normal-appearing white matter; PCNSL = primary central nervous system lymphoma; PSR = percentage signal recovery; rCBV = relative cerebral blood volume; SI = signal intensity; AUC = area under the curve

Conventional MR imaging cannot always differentiate contrast-enhancing malignant brain tumors, including glioblastoma, primary central nervous system lymphoma (PCNSL), and cerebral metastasis.¹ Meningioma and dural-based metastasis may also appear similar on conventional MR imaging. Because

management differs for these tumors, timely and accurate identification is imperative. Perfusion-weighted MR imaging can help characterize brain tumors, and DSC-MR imaging is the most popular method for measuring brain perfusion with MR imaging.² By tracking T2*-weighted signal changes during the first passage of a gadolinium-based contrast agent bolus, relative cerebral blood volume (rCBV) compared with normal-appearing white matter (NAWM) and percentage signal recovery (PSR) compared with baseline can be calculated.³ rCBV reflects tumor neoangiogenesis

Received March 6, 2019; accepted after revision June 21.

From the Warren Alpert Medical School of Brown University (M.D.L., J.L.B.), Providence, Rhode Island; Department of Diagnostic Imaging (G.L.B., J.L.B.), Rhode Island Hospital, Providence, Rhode Island; and Division of Neuroimaging Research (L.C.B., C.C.Q.), Barrow Neurological Institute, Phoenix, Arizona.

This work was supported by the National Institutes of Health/National Cancer Institute, CA158079-01 (C. Chad Quarles and Laura C. Bell).

Paper previously presented, in part, as an oral scientific presentation (O-35) at: Annual Meeting of the American Society of Neuroradiology and the Foundation of the ASNR Symposium, June 2–7, 2018; Vancouver, British Columbia, Canada.

Please address correspondence to Jerrold L. Boxerman, MD, PhD, FACR, Rhode Island Hospital, Department of Diagnostic Imaging, 593 Eddy St, Providence, RI 02903; e-mail: jboxerman@lifespan.org

Indicates open access to non-subscribers at www.ajnr.org

<http://dx.doi.org/10.3174/ajnr.A6153>

and correlates with glioma grade.⁴ The PSR reflects a complex interplay of capillary permeability related to blood-brain barrier integrity and contrast agent extravasation from tumor capillaries, as well as tumor cell size and cell density.⁵

Because glioblastoma and lymphoma have a disrupted BBB, which is absent in metastases and meningiomas, gadolinium-based contrast agent extravasates in these tumors, inducing T1 and T2* shortening that obfuscates rCBV measurements. Preload contrast agent administration helps mitigate these leakage effects, rendering rCBV measurements more accurate.^{6,7} However, the introduction of a preload dose impacts PSR measurements, because Bell et al⁸ demonstrated that PSR in high-grade gliomas decreases with increasing preload dose. Likewise, Boxerman et al⁹ demonstrated that while T1-sensitive DSC-MR imaging acquisitions with a high flip angle (FA) and short-TE yield increased PSR in high-grade gliomas, preload administration diminishes the variation in PSR measured with different protocols. Therefore, a trade-off exists for DSC-MR imaging acquisition parameters between PSR sensitivity and rCBV accuracy. PSR has been shown to significantly differ among glioblastoma, PCNSL, and metastasis when using a non-leakage-corrected protocol optimized for PSR sensitivity with a high FA, intermediate TE, and without preload at 1.5T.¹⁰ However, DSC-MR imaging performed for rCBV measurement often includes a preload dose of contrast to minimize contrast agent leakage effects.⁷ This study aimed to determine whether the PSR can still differentiate these common contrast-enhancing brain tumors using a preload-based, intermediate-FA, low-TE DSC-MR imaging protocol designed for rCBV accuracy.^{2,6}

MATERIALS AND METHODS

Patients

The institutional review board approved this Health Insurance Portability and Accountability Act-compliant study, and informed consent was waived. We retrospectively queried the neuropathology data base at Rhode Island Hospital for patients with treatment-naïve, biopsy-proved cerebral glioblastoma, metastasis, lymphoma, or meningioma who underwent preoperative DSC-MR imaging with identical field strength and pulse sequence parameters between January 2015 and September 2017. We identified 54 patients: 14 with glioblastomas (9 men; mean age, 62.4 years; range, 47–78 years), 7 with PCNSL (5 men; mean age, 65.9 years; range, 47–82 years), 13 with meningiomas (2 men; mean age, 65.8 years; range, 38–82 years), and 20 with metastases (7 men; mean age, 59.4 years; range, 29–82 years; 12 lung, 2 breast, 2 colon, 2 melanoma, 1 osteosarcoma, 1 ovarian primary).

Image Acquisition

All DSC-MR imaging (gradient-echo EPI: TR = 1290 ms, TE = 40 ms, FA = 60°, matrix size = 128 × 128, slice thickness = 5 mm) was performed at 1.5T (Magnetom Aera; Siemens, Erlangen, Germany) with identical 16-channel head coils. Before image acquisition, a one-quarter-dose (0.025 mL/kg) gadobutrol (Gadavist; Bayer Schering Pharma, Berlin, Germany) preload dose was administered (5 mL/s). After 40–50 baseline acquisitions, a single-dose (0.1 mL/kg) gadobutrol bolus was injected (5 mL/s) and imaging continued for a total of 120 baseline-plus-postbolus im-

age acquisitions (~2.5 minutes). Following DSC-MR imaging, postcontrast spin-echo T1-weighted images (TR = 400 ms, TE = 17 ms, FA = 90°, slice thickness = 5 mm, matrix = 256 × 256, NEX = 1) were acquired at slice positions and orientations identical to those of the DSC-MR imaging to simplify segmentation.

Image Postprocessing

A neuroradiologist with 15 years' post-Certificate of Added Qualification experience semiautomatically segmented contrast-enhancing lesion volumes on postcontrast T1-weighted images using the IB Delta Suite plug-in (Imaging Biometrics, Elm Grove, Wisconsin) for OsiriX-MD (<http://www.osirix-viewer.com>), avoiding necrosis and susceptibility artifacts. For normalization, a 70- to 80-mm² elliptical ROI was placed in the contralateral NAWM. We computed rCBV maps using commercial software (OsiriX Pro Version 2.04 and IB Neuro Version 1.1, Imaging Biometrics) that incorporates a postprocessing leakage-correction algorithm and normalized CBV to mean CBV in NAWM (rCBV).^{4,11} Voxels with subzero rCBV were excluded from the final analysis. PSR was calculated for each voxel using the following formula: $PSR = (S_1 - S_{min}) / (S_0 - S_{min})$, where S_0 is the baseline signal intensity (SI) averaged over the first 10 time points, S_1 is the tail averaged over the last 10 time points, and S_{min} is the minimum SI in the dynamic series. PSR maps were generated without postprocessing leakage correction using Matlab and Statistics Toolbox Release 2017b (MathWorks, Natick, Massachusetts). In addition to rCBV and PSR, we also computed the normalized baseline DSC-MR imaging signal as $S_{0,tumor} / S_{0,NAWM}$. To qualitatively compare signal-time curves for the different tumor types, we computed the population-average relative signal-time curves as $S_{tumor}(t) / S_{0,tumor}$ for each of the 4 tumor types.

Statistical Analysis

All modeling was performed using SAS Software, Version 9.4 (SAS Institute, Cary, North Carolina) with the LOGISTIC and GLIMMIX procedures. Mean and interval estimates were calculated for rCBV, PSR, and normalized baseline signal S_0 by tumor pathology using generalized linear modeling, assuming a log-normal distribution. Receiver operating characteristic analysis was performed for each parameter and each pair-wise comparison to calculate the area under the curve (AUC). The Youden Index was used to examine the diagnostic performance of different thresholds, though empiric thresholds should be interpreted with caution.¹² Somers D, a measure of the correlation between variables that are not both continuous (ranging between -1.0 and 1.0 like the Pearson r), was calculated to estimate the correlation between measured parameters (rCBV, PSR, S_0) and tumor type. All interval estimates were calculated for 95% confidence.

RESULTS

Mean rCBV, PSR, and normalized baseline SI for each tumor type are summarized in Fig 1. The diagnostic performance of these parameters is summarized in the Table. The average normalized signal-time curves for each tumor type are compared in Fig 2.

As indicated with receiver operating characteristic analysis, rCBV differentiated glioblastoma from PCNSL (AUC, 0.79; 95% CI, 0.58–0.99), and meningioma from glioblastoma (AUC, 0.84;

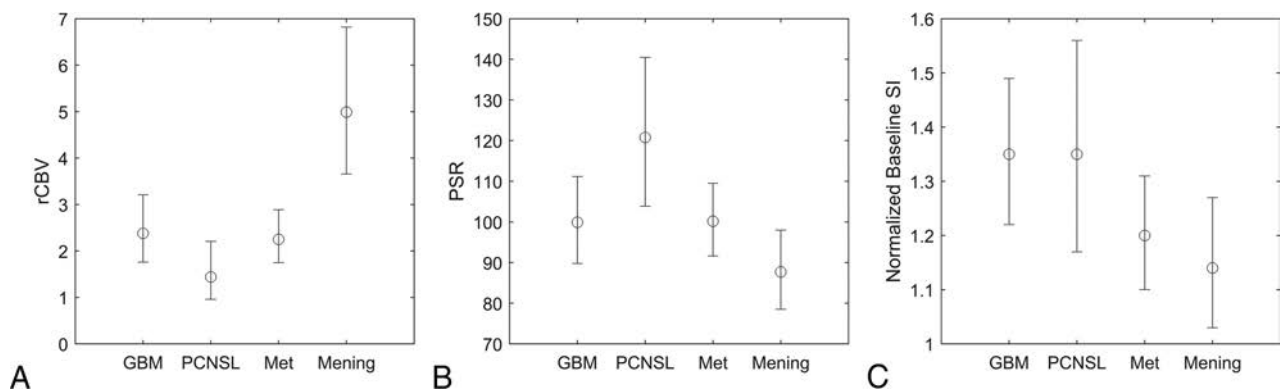


FIG 1. Comparisons of rCBV (A), PSR (B), and normalized baseline SI (C) estimates with 95% confidence intervals for glioblastoma, PCNSL, metastasis (Met), and meningioma (Mening).

Pair-wise discrimination performance (Somers D) of perfusion parameters and baseline SI

Pair-wise Comparison	rCBV	PSR	Baseline SI
GBM vs PCNSL	0.79 (0.58–0.99) D = 0.57	0.83 (0.64–1.00) D = 0.65	0.50 (0.23–0.77) D = 0.00
GBM vs metastasis	0.43 (0.24–0.63) D = -0.14	0.49 (0.28–0.69) D = -0.03	0.66 (0.47–0.84) D = 0.31
GBM vs meningioma	0.84 (0.69–0.99) D = 0.68	0.69 (0.47–0.91) D = 0.37	0.76 (0.56–0.95) D = 0.52
PCNSL vs metastasis	0.66 (0.43–0.88) D = 0.31	0.81 (0.64–0.97) D = 0.61	0.66 (0.43–0.88) D = 0.31
PCNSL vs meningioma	0.97 (0.90–1.00) D = 0.93	0.89 (0.74–1.00) D = 0.78	0.71 (0.46–0.97) D = 0.43
Metastasis vs meningioma	0.82 (0.68–0.96) D = 0.64	0.65 (0.44–0.87) D = 0.31	0.55 (0.35–0.75) D = 0.10

Note:—GBM indicates glioblastoma multiforme; D, Somers D.

^a Data are area AUC and 95% CI).

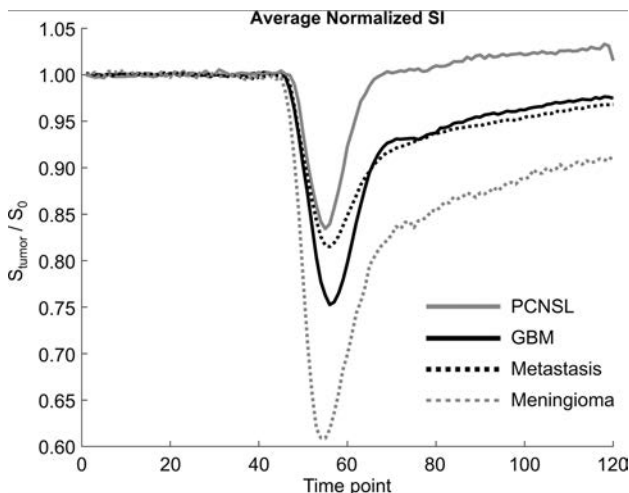


FIG 2. Average normalized signal-time curves for glioblastoma multiforme (solid black), PCNSL (solid gray), metastasis (dotted black), and meningioma (dotted gray). TR = 1290 ms, with a total acquisition time of 2 minutes 35 seconds.

95% CI, 0.69–0.99), PCNSL (AUC, 0.97; 95% CI, 0.90–1.00), and metastasis (AUC, 0.82; 95% CI, 0.68–0.96), with more modest differentiation of PCNSL from metastasis (AUC, 0.66; 95% CI, 0.43–0.88). The PSR differentiated PCNSL from glioblastoma (AUC, 0.83; 95% CI, 0.64–1.00), metastasis (AUC, 0.81; 95% CI, 0.64–0.97), and meningioma (AUC, 0.89; 95% CI, 0.74–1.00), with more modest differentiation of glioblastoma from meningi-

oma (AUC, 0.69; 95% CI, 0.47–0.91) and metastasis from meningioma (AUC, 0.65; 95% CI, 0.44–0.87). rCBV was better than PSR in differentiating meningioma from glioblastoma or metastasis. The PSR was better than rCBV in differentiating PCNSL from metastasis. rCBV and PSR performed similarly in differentiating PCNSL from glioblastoma or meningioma.

Glioblastoma and metastasis were poorly differentiated by rCBV (AUC, 0.43; 95% CI, 0.24–0.63) and PSR (AUC, 0.49; 95% CI, 0.28–0.69) but were better distinguished by normalized

baseline SI (AUC, 0.66; 95% CI, 0.47–0.84) with an optimal threshold of 1.27 using the Youden index, which achieved 86% sensitivity and 50% specificity.

DISCUSSION

This study evaluated the utility of PSR for differentiating common contrast-enhancing brain tumors using a DSC-MR imaging protocol designed for rCBV accuracy (preload contrast administration, intermediate FA, low TE).³ Because treatment of glioblastoma multiforme, brain metastasis, and PCNSL differs substantially, a definitive diagnosis at initial imaging may impact short-term patient management, including subsequent diagnostic tests. Similar to results obtained by Mangla et al¹⁰ for PSR-optimized acquisitions (no preload, high FA, intermediate TE), rCBV-optimized PSR differentiates most pair-wise comparisons of glioblastoma, metastasis, PCNSL, and meningioma. However, our results failed to confirm that PSR is strictly better than rCBV in differentiating tumors. Moreover, neither rCBV nor PSR differentiated glioblastoma and metastasis, which is arguably the most difficult distinction in clinical practice. Thus, our results indicate that rCBV-optimized protocols using preload and parameters with reduced T1 sensitivity may suppress the PSR differences previously demonstrated by PSR-optimized protocols without preload.

Diagnosing PCNSL is important because the first-line treatment for PCNSL is chemotherapy, not surgical resection.¹³ We found that, consistent with prior studies,^{10,14} PCNSL has lower

rCBV and higher PSR than glioblastoma and metastases; however, we found that the PSR is not strictly better than rCBV at differentiating PCNSL from other types of tumors. While PSR differentiated PCNSL from metastasis better than rCBV, both parameters achieved similar diagnostic performance when differentiating PCNSL from glioblastoma or meningioma. Even with one-quarter-dose preload, PCNSL signal recovery consistently exceeded baseline, similar to studies without preload. $PSR > 1$ in the setting of elevated rCBV appears to be a particularly simple and effective way to render a prospective, preliminary diagnosis of PCNSL versus other common intra-axial tumors and non-neoplastic pathologies like tumefactive infectious or inflammatory lesions. High PSR exceeding unity is characteristic of PCNSL and reflects the dominance of T1 over T2* effects during the “tail” of the signal-time curve. Although the mechanisms dictating the competition between T1 and T2* effects are complex, tumor vascularity, permeability, cellular features, contrast agent kinetics, pulse sequence parameters, and preload dose all appear to play a role. The unique histologic and physiologic features of PCNSL, such as dense cellularity, small cell size, angiocentric growth pattern, and absence of neoangiogenesis, likely contribute to the characteristically high PSR.¹⁵ By comparison, glioblastoma exhibits greater neoangiogenesis, capillary heterogeneity, and microvascular density.¹⁶ Higher doses of preload may diminish the high PSR of PCNSL, but no studies have evaluated the effect of preload dosing in PCNSL.

We included meningiomas because they can closely resemble dural-based metastases on conventional imaging, and differentiation using DSC-MR imaging would have clinical value. We found that meningiomas have significantly higher rCBV than the other tumors, consistent with a prior case series,¹⁷ primarily owing to the tendency for the meningioma signal-time curve to drop and remain below baseline, resulting in a low PSR. Extra-axial tumors lack a BBB and therefore are expected to have greater contrast extravasation than intra-axial tumors. Contrast-enhancing lesions with an appropriate combination of cell size and density in the absence of a BBB may have postbolus signal-time curves that stay suppressed below the baseline signal, consequently producing artifactually higher rCBV measurements on integration of $\Delta R2^*(t)$. Therefore, it is possible that the reportedly high rCBV for meningioma may reflect low PSR more so than exceptionally high vascular density.

Our study included only intra-axial metastases, and it is unclear whether the rCBV, PSR, and baseline signals of intra-axial metastases are generalizable to dural-based metastases. Extra-axial tumors, for instance, likely have different first-pass kinetics than intra-axial tumors owing to complete absence of the BBB, consequent substantial contrast extravasation and blood pool phase, variable vascularity, and the potential presence of intralesion mineralization. First-pass enhancement may also be more difficult to differentiate from recirculation enhancement in extra-axial tumors. Our results are consistent with 1 study that found significantly higher CBV in 16 meningiomas compared with 6 dural-based metastases,¹⁸ but another study of 12 meningiomas and 8 dural-based metastases found no significant difference in rCBV.¹⁹ Although it is unclear whether preload administration has a substantial impact on CBV estimation in extra-axial lesions

given the substantial degree of contrast agent extravasation, neither of these studies used a preload. Whereas the former used a TE (28 ms) and FA (45°) close to currently accepted optimal values for CBV accuracy,²⁰ the latter did not (8 ms, 7°); this difference could impact CBV estimation. The conclusions of these studies may also differ because of small sample sizes, varying primary tumor types for metastases,²¹ and varying grades for meningiomas.²² We achieved only modest discrimination of metastasis and meningioma using PSR, which was lower for meningiomas than metastases. In light of BBB differences, it is probably best to conclude that if the PSR and CBV of dural-based lesions differ appreciably from those that we found for meningiomas, the lesion is more likely to be a dural-based metastasis. As the signal-time curve becomes more similar to that for meningiomas, with lower PSR and CBV, then the diagnosis is less certain.

Of all pair-wise comparisons, distinguishing a solitary cerebral metastasis from glioblastoma is the most vexing clinical scenario in our experience. We did not observe a significant difference in the rCBV or PSR between glioblastoma and metastasis. These results are consistent with 1 recent study²³ (TE = 80 ms, no preload) but contradict prior no-preload studies (TE = 50 ms, FA = 80°; TE = 54 ms, FA = 35°) that found significantly higher rCBV and PSR in glioblastomas than in metastases.^{10,24} Our use of preload and pulse sequence parameters with greater T2* sensitivity appears to have eliminated these PSR differences. While other studies have found that rCBV in peritumoral nonenhancing FLAIR hyperintensity is significantly greater for glioblastoma than metastasis, we restricted our analysis to contrast-enhancing voxels.^{10,23}

Although rCBV and PSR could not differentiate glioblastoma from metastasis, we found that glioblastoma exhibits significantly higher normalized baseline signal than metastasis. No previous DSC-MR imaging studies have reported differences in baseline signal after preload administration, to our knowledge. Because baseline signal was measured after preload administration, it provides a snapshot of dynamic contrast-enhanced (DCE)-MR imaging and may serve as a proxy for extravascular extracellular volume (V_e) and/or volume transfer constant (k^{trans}). Because metastatic capillaries lack a BBB, greater contrast agent extravasation is expected than in glioblastoma, which possesses a BBB, albeit a heterogeneous, disrupted one.^{25,26} Greater leakage of contrast agent within metastases should increase its distribution within the extravascular extracellular space, which is more restricted in glioblastomas by densely packed capillary buds composing the microvasculature.²⁷ Our imaging protocol appears to uncover these differences in contrast agent extravasation after preload administration, though DSC-MR images were not acquired before preload administration, precluding a comparison of baseline signal before any contrast agent administration. Our results are consistent with a prior DCE-MR imaging study reporting higher k^{trans} in glioblastoma versus metastasis²⁸ and PSR-optimized DSC-MR imaging studies reporting higher PSR in glioblastoma versus metastasis.^{10,24,29} Differences in contrast agent leakage are also supported by a DCE-MR imaging study finding that the SI of glioblastoma and melanoma/hypervascular metastasis remained high after contrast agent administration, whereas the signal of nonmelanoma/hypovascular metastasis decreased.³⁰

Our results support the pursuit of DCE-MR imaging to differentiate glioblastoma and metastasis. DSC-MR imaging paradigms that perform DCE-MR imaging during the administration of the preload dose³¹ or multiecho pulse sequences that acquire DCE-MR imaging data in conjunction with CBV-optimized DSC-MR imaging using a single contrast agent dose³² may provide the opportunity for comprehensive brain tumor analysis with better differentiation of glioblastoma and metastasis.

In our cohort, PCNSL has greater PSR than glioblastoma but similar baseline signal. This discrepancy may be due to histologic differences affecting the degree to which preload controls T1 leakage effects. The high PSR in PCNSL suggests that the dose of preload used in the present study did not adequately control T1-leakage effects. We expect a preload concentration that fully saturates the extravascular space in PCNSL to result in a lower PSR. Thus, it appears that preload dose-dependent decreases in PSR may differ for different types of tumors.

Further investigation is warranted for determining how to best differentiate brain tumors, especially glioblastoma and metastasis. While guidelines exist, there is no consensus on optimal DSC-MR imaging methodology for brain tumors.² Protocol standardization would facilitate comparisons of data among institutions. Given that preload affects PSR, DSC-MR imaging protocols that retain rCBV accuracy without preload may be useful. Such a protocol has recently been shown to provide very accurate rCBV estimates²⁰ but requires use of a low FA (30°) that would likely suppress PSR differences due to reduced T1-weighting. Multiparametric imaging protocols that combine DCE-MR imaging acquisition during preload administration and DSC-MR imaging offer comprehensive signal morphology analysis and may further characterize and differentiate tumors. Additionally, multiecho DSC-MR imaging protocols have been developed that combine simultaneous gradient-echo acquisitions at different TEs to eliminate T1 effects without preload for accurate rCBV estimation, with a high-FA acquisition providing PSR weighting that may help provide tumor differentiation.^{2,32} Single-dose multiecho protocols also enable simultaneous quantification of DCE-MR imaging parameters.³³

While the discrepancies between the results of our study and those of Mangla et al¹⁰ are most likely due to differences in DSC-MR imaging parameters, there are other methodologic differences that may have impacted our comparisons. Mangla et al included patients who had been treated with steroids and patients with presumed metastatic disease without biopsy. In contrast, all of our cases were treatment-naïve and biopsy-proved, so our analysis is less susceptible to treatment effects and selection bias.

There are several limitations to our study. Because this was a retrospective study, we did not control for the elapsed time between preload administration and the DSC-MR imaging acquisition. However, preload incubation time is unlikely to significantly impact our results because previous studies have shown that the enhancement of gliomas and metastases does not significantly decline during the first 25–30 minutes after contrast injection,³⁴ and preload incubation times of 5–10 minutes do not affect rCBV estimates in glioblastomas.⁶ Our study is also limited by the sample size. Because TR, TE, FA, and field strength all affect baseline signal and PSR, we only analyzed our largest cohort of patients

scanned with the same pulse sequence parameters and field strength. We also did not differentiate metastases by primary tumor type, which may be associated with PSR differences.

CONCLUSIONS

With a protocol designed for rCBV accuracy that incorporates preload and intermediate FA, PSR failed to differentiate glioblastoma from metastasis but could differentiate other pair-wise comparisons of glioblastoma, PCNSL, metastasis, and meningioma. This finding differs from those in previous studies in which PSR-optimized DSC-MR imaging (no preload, high-FA) significantly differentiated glioblastoma and metastasis.¹⁰ However, differences in post-preload baseline signal between glioblastoma and metastasis, reflecting tissue-specific competing T1 and T2* leakage effects, motivate pursuit of DCE-MR imaging and no-preload DSC-MR imaging as tools for differentiating glioblastoma and metastasis. Future directions include assessment of tumor differentiation using PSR obtained with a rCBV-accurate DSC-MR imaging protocol without preload and single-dose multiecho protocols that permit simultaneous quantification of DSC-MR imaging and DCE-MR imaging parameters.

Disclosures: Laura C. Bell—RELATED: Grant: National Institutes of Health/National Cancer Institute, R01 CA158079.* Christopher C. Quarles—RELATED: Grant: National Institutes of Health/National Cancer Institute, R01 CA158079.* *Money paid to the institution.

REFERENCES

1. Stadnik TW, Demaerel P, Luytjens RR, et al. **Imaging tutorial: differential diagnosis of bright lesions on diffusion-weighted MR images.** *Radiographics* 2003;23:e7 Medline
2. Welker K, Boxerman J, Kalnin A, et al; American Society of Functional Neuroradiology MR Perfusion Standards and Practice Subcommittee of the ASFN Clinical Practice Committee. **ASFN recommendations for clinical performance of MR dynamic susceptibility contrast perfusion imaging of the brain.** *AJNR Am J Neuroradiol* 2015;36:E41–51 CrossRef Medline
3. Shiroishi MS, Castellazzi G, Boxerman JL, et al. **Principles of T2*-weighted dynamic susceptibility contrast MRI technique in brain tumor imaging.** *J Magn Reson Imaging* 2015;41:296–313 CrossRef Medline
4. Boxerman JL, Schmainda KM, Weisskoff RM. **Relative cerebral blood volume maps corrected for contrast agent extravasation significantly correlate with glioma tumor grade, whereas uncorrected maps do not.** *AJNR Am J Neuroradiol* 2006;27:859–67 Medline
5. Semmineh NB, Xu J, Skinner JT, et al. **Assessing tumor cytoarchitecture using multiecho DSC-MRI derived measures of the transverse relaxivity at tracer equilibrium (TRATE).** *Magn Reson Med* 2015;74:772–84 CrossRef Medline
6. Leu K, Boxerman JL, Ellingson BM. **Effects of MRI protocol parameters, preload injection dose, fractionation strategies, and leakage correction algorithms on the fidelity of dynamic-susceptibility contrast MRI estimates of relative cerebral blood volume in gliomas.** *AJNR Am J Neuroradiol* 2017;38:478–84 CrossRef Medline
7. Boxerman JL, Prah DE, Paulson ES, et al. **The role of preload and leakage correction in gadolinium-based cerebral blood volume estimation determined by comparison with MION as a criterion standard.** *AJNR Am J Neuroradiol* 2012;33:1081–87 CrossRef Medline
8. Bell LC, Hu LS, Stokes AM, et al. **Characterizing the influence of preload dosing on percent signal recovery (PSR) and cerebral blood volume (CBV) measurements in a patient population with high-grade glioma using dynamic susceptibility contrast MRI.** *Tomography* 2017;3:89–95 CrossRef Medline
9. Boxerman JL, Paulson ES, Prah MA, et al. **The effect of pulse se-**

- quence parameters and contrast agent dose on percentage signal recovery in DSC-MRI: implications for clinical applications. *AJNR Am J Neuroradiol* 2013;34:1364–69 CrossRef Medline
10. Mangla R, Kolar B, Zhu T, et al. Percentage signal recovery derived from MR dynamic susceptibility contrast imaging is useful to differentiate common enhancing malignant lesions of the brain. *AJNR Am J Neuroradiol* 2011;32:1004–10 CrossRef Medline
 11. Donahue KM, Krouwer HG, Rand SD, et al. Utility of simultaneously acquired gradient-echo and spin-echo cerebral blood volume and morphology maps in brain tumor patients. *Magn Reson Med* 2000;43:845–53 CrossRef Medline
 12. Altman DG, Royston P. The cost of dichotomising continuous variables. *BMJ* 2006;332:1080 Medline
 13. Han CH, Batchelor TT. Diagnosis and management of primary central nervous system lymphoma. *Cancer* 2017;123:4314–24 CrossRef Medline
 14. Xing Z, You RX, Li J, et al. Differentiation of primary central nervous system lymphomas from high-grade gliomas by rCBV and percentage of signal intensity recovery derived from dynamic susceptibility-weighted contrast-enhanced perfusion MR imaging. *Clin Neuroradiol* 2014;24:329–36 CrossRef Medline
 15. Hartmann M, Heiland S, Harting I, et al. Distinguishing of primary cerebral lymphoma from high-grade glioma with perfusion-weighted magnetic resonance imaging. *Neurosci Lett* 2003;338:119–22 CrossRef Medline
 16. Liao W, Liu Y, Wang X, et al. Differentiation of primary central nervous system lymphoma and high-grade glioma with dynamic susceptibility contrast-enhanced perfusion magnetic resonance imaging. *Acta Radiol* 2009;50:217–25 CrossRef Medline
 17. Zimny A, Sasiadek M. Contribution of perfusion-weighted magnetic resonance imaging in the differentiation of meningiomas and other extra-axial tumors: case reports and literature review. *J Neurooncol* 2011;103:777–83 CrossRef Medline
 18. Kremer S, Grand S, Rémy C, et al. Contribution of dynamic contrast MR imaging to the differentiation between dural metastasis and meningioma. *Neuroradiology* 2004;46:642–48 CrossRef Medline
 19. Lui YW, Malhotra A, Farinhas JM, et al. Dynamic perfusion MRI characteristics of dural metastases and meningiomas: a pilot study characterizing the first-pass wash-in phase beyond relative cerebral blood volume. *AJR Am J Roentgenol* 2011;196:886–90 CrossRef Medline
 20. Semmineh NB, Bell LC, Stokes AM, et al. Optimization of acquisition and analysis methods for clinical dynamic susceptibility contrast MRI using a population-based digital reference object. *AJNR Am J Neuroradiol* 2018;39:1981–88 CrossRef Medline
 21. Kremer S, Grand S, Berger F, et al. Dynamic contrast-enhanced MRI: differentiating melanoma and renal carcinoma metastases from high-grade astrocytomas and other metastases. *Neuroradiology* 2003;45:44–49 CrossRef Medline
 22. Shi R, Jiang T, Si L, et al. Correlations of magnetic resonance, perfusion-weighted imaging parameters and microvessel density in meningioma. *J BUON* 2016;21:709–13 Medline
 23. Neska-Matuszewska M, Bladowska J, Sasiadek M, et al. Differentiation of glioblastoma multiforme, metastases and primary central nervous system lymphomas using multiparametric perfusion and diffusion MR imaging of a tumor core and a peritumoral zone: searching for a practical approach. *PLoS One* 2018;13:e0191341 CrossRef Medline
 24. Cha S, Lupo JM, Chen M-H, et al. Differentiation of glioblastoma multiforme and single brain metastasis by peak height and percentage of signal intensity recovery derived from dynamic susceptibility-weighted contrast-enhanced perfusion MR imaging. *AJNR Am J Neuroradiol* 2007;28:1078–84 CrossRef Medline
 25. Long DM. Capillary ultrastructure in human metastatic brain tumors. *J Neurosurg* 1979;51:53–58 CrossRef Medline
 26. Sarkaria JN, Hu LS, Parney IF, et al. Is the blood-brain barrier really disrupted in all glioblastomas? A critical assessment of existing clinical data. *Neuro Oncol* 2018;20:184–91 CrossRef Medline
 27. Rojiani AM, Dorovini-Zis K. Glomeruloid vascular structures in glioblastoma multiforme: an immunohistochemical and ultrastructural study. *J Neurosurg* 1996;85:1078–84 CrossRef Medline
 28. Zhao J, Yang Z, Luo B, et al. Quantitative evaluation of diffusion and dynamic contrast-enhanced MR in tumor parenchyma and peritumoral area for distinction of brain tumors. *PLoS One* 2015;10:e0138573 CrossRef Medline
 29. Mouthuy N, Cosnard G, Abarca-Quinones J, et al. Multiparametric magnetic resonance imaging to differentiate high-grade gliomas and brain metastases. *J Neuroradiol* 2012;39:301–07 CrossRef Medline
 30. Jung BC, Arevalo-Perez J, Lyo JK, et al. Comparison of glioblastomas and brain metastases using dynamic contrast-enhanced perfusion MRI: comparison of glioblastomas and brain. *J Neuroimaging* 2016;26:240–46 CrossRef Medline
 31. Anzalone N, Castellano A, Cadioli M, et al. Brain gliomas: multicenter standardized assessment of dynamic contrast-enhanced and dynamic susceptibility contrast MR images. *Radiology* 2018;287:933–43 CrossRef Medline
 32. Stokes AM, Skinner JT, Yankeelov T, et al. Assessment of a simplified spin and gradient echo (sSAGE) approach for human brain tumor perfusion imaging. *Magn Reson Imaging* 2016;34:1248–55 CrossRef Medline
 33. Quarles CC, Gore JC, Xu L, et al. Comparison of dual-echo DSC-MRI- and DCE-MRI-derived contrast agent kinetic parameters. *Magn Reson Imaging* 2012;30:944–53 CrossRef Medline
 34. Akeson P, Nordström CH, Holtås S. Time-dependency in brain lesion enhancement with gadodiamide injection. *Acta Radiol* 1997;38:19–24 Medline

Dynamic Contrast-Enhanced MRI in Patients with Brain Metastases Undergoing Laser Interstitial Thermal Therapy: A Pilot Study

J.I. Traylor, D.C.A. Bastos, D. Fuentes, M. Muir, R. Patel, V.A. Kumar, R.J. Stafford, G. Rao, and S.S. Prabhu

ABSTRACT

BACKGROUND AND PURPOSE: Tumor recurrence is difficult to predict in patients receiving laser ablation for intracranial malignancy. We assessed the efficacy of the initial area under the time-to-signal intensity curve at 60 seconds ($iAUC_{60}$) from dynamic contrast-enhanced MR imaging in predicting progression-free survival in patients with brain metastases following laser interstitial thermal therapy.

MATERIALS AND METHODS: The study population was a consecutive series of patients undergoing laser interstitial thermal therapy for brain metastases. Patient demographics including age, sex, tumor histology, and Karnofsky Performance Scale were collected prospectively. Preoperative, postoperative, and 1-month follow-up dynamic contrast-enhanced MRIs were analyzed. Values of $iAUC_{60}$ were computed using a trapezoidal rule applied to the time history of contrast uptake over the first 60 seconds postenhancement. The change in $iAUC_{60}$ ($\Delta iAUC_{60}$) was calculated by taking the difference between the values of $iAUC_{60}$ from 2 time points. Pearson correlation coefficients were calculated between progression-free survival, defined as the time from laser interstitial thermal therapy to tumor recurrence, and $iAUC_{60}$ or $\Delta iAUC_{60}$ values.

RESULTS: Thirty-three cases of laser interstitial thermal therapy for 32 brain metastases in a cohort of 27 patients were prospectively analyzed. A significant relationship was observed between the values of $iAUC_{60}$ from postoperative dynamic contrast-enhanced MR imaging and progression-free survival with Pearson correlation ($P = .03$) and Cox univariate analysis ($P = .01$). The relationship between preoperative and 1-month follow-up dynamic contrast-enhanced MR imaging was not significantly correlated with progression-free survival. Similarly, no statistically significant relationship was observed with $\Delta iAUC_{60}$ and progression-free survival between any time points.

CONCLUSIONS: Progression-free survival is difficult to predict in patients undergoing laser interstitial thermal therapy for brain metastases due to confounding with posttreatment change. $iAUC_{60}$ extracted from postoperative dynamic contrast-enhanced MR imaging shows promise for accurately prognosticating patients following this operative therapy.

ABBREVIATIONS: DCE-MRI = dynamic contrast-enhanced MRI; $\Delta iAUC_{60}$ = change in $iAUC_{60}$; HR = hazard ratio; $iAUC_{60}$ = initial area under the time-to-signal intensity curve at 60 seconds; LITT = laser interstitial thermal therapy; PFS = progression-free survival; RN = radiation necrosis; ROC = receiver operating characteristic

Metastases are the most common underlying cause of intracranial tumor, occurring in approximately 10% of all patients with systemic malignancy.^{1,2} Laser interstitial thermal therapy (LITT) is emerging as a minimally invasive technique for reducing intracranial tumor burden in these patients. The development of real-time temperature feedback with MR thermography has made the intracranial application of LITT possible by minimizing collateral damage to adjacent tissue.³ However, tu-

mor recurrence on the margins of the ablation zone remains a challenge to predict, due to confounding with posttreatment changes.^{4,5} A methodology for predicting recurrence from analysis of post-LITT ablation cavities on advanced MR imaging would be valuable for developing accurate prognoses, guiding future treatment, and illustrating points of LITT technique improvement to optimize ablation and prolong progression-free survival (PFS).

Dynamic contrast-enhanced MR imaging (DCE-MRI), a dynamic T1-weighted perfusion imaging technique, can be used to characterize the vasculature of tissue from which many quantifi-

Received April 22, 2019; accepted after revision June 19.

From the Departments of Neurosurgery (J.I.T., D.C.A.B., M.M., R.P., G.R., S.S.P.), Imaging Physics (D.F., R.J.S.), and Diagnostic Radiology (V.A.K.), The University of Texas MD Anderson Cancer Center, Houston, Texas.

This work was supported, in part, by Monteris Medical.

The funder had no role in study design, data interpretation, or analysis, or manuscript preparation.

Please address correspondence to Sujit S. Prabhu, MD, FRCS, Department of Neurosurgery, The University of Texas MD Anderson Cancer Center, 1515 Holcombe Blvd, Houston, TX 77030; e-mail: sprabhu@mdanderson.org; @jeffreytaylor

<http://dx.doi.org/10.3174/ajnr.A6144>

able physiologic and nonphysiologic variables can be extracted.^{6,7} The initial area under the time-to-signal intensity curve at 60 seconds ($iAUC_{60}$) is one such quantitative parameter that has been evaluated due to ease of implementation and indirect reflection of blood flow and vascular permeability in a tissue ROI.⁶ Recent studies have reported numerous successful applications of $iAUC_{60}$ from treatment-response monitoring in breast cancer to prediction of local recurrence in head and neck cancer.^{8,9} $iAUC_{60}$ has been further applied to aiding complex differential diagnoses in the field of neuro-oncology, particularly in distinguishing radiation necrosis from tumor recurrence in patients undergoing radiation therapy for intracranial tumors.¹⁰⁻¹² This study evaluates the utility of $iAUC_{60}$ from DCE-MR imaging in the prediction of PFS in patients with brain metastases following LITT.

MATERIALS AND METHODS

Study Design and Subjects

This study was performed with approval from our institutional review board with regard to the study of human subjects. Patients who received LITT from May 2016 through August 2017 were enrolled in the study. Inclusion criteria were cerebral metastases from a primary extracranial tumor confirmed by histopathologic analysis. Local recurrence was determined by a neuroradiologist at our institution applying the Response Assessment in Neuro-Oncology Criteria for Brain Metastases (RANO-BM) to follow-up MR imaging at 1-month intervals following LITT (eg, 30 days, 60 days, and so forth).¹³ The time from LITT to follow-up MR imaging at which local recurrence was determined was recorded as PFS. If no local recurrence was observed, the time to last follow-up MR imaging was recorded and the patients were right-censored for PFS analysis. For patients undergoing LITT for >1 lesion, recurrence was defined for each individual lesion. Deep-seated location of the tumor was defined as the location in the white matter or basal ganglia. The following data were extracted from the electronic medical record: age, sex, tumor histology, tumor location, date of LITT procedure, and neurologic status in the form of Karnofsky Performance Scale preoperatively, postoperatively, and at first follow-up.

Operative Technique

All LITT procedures were performed at our institution in an intraoperative MR imaging suite using a Magnetom Espree 1.5T bore (Siemens, Erlangen, Germany) with the NeuroBlate (Monteris Medical, Minneapolis, Minnesota) system. The details for the technical aspects of LITT at our institution have been previously described.¹⁴

Image Analysis

Tumor volume and extent of ablation data were obtained from the iPlan workstation (Brainlab, Munich, Germany) for treatment planning and ablation surveillance. Manual, tridimensional tumor segmentation was completed by a neuroradiologist preoperatively using postcontrast T1-weighted MR imaging. The residual tumor volume was calculated by subtracting the volume of the ablation cavity within the tumor volume using iPlan software.

DCE-MR images were obtained preoperatively and at 1-month follow-up. Immediate postoperative DCE-MRIs were

not initially part of the study protocol. However, an amendment was later made to include imaging at this time point. Thus, there were fewer immediate postoperative DCE-MRIs to analyze than at other time points. ROIs from preoperative images were identified as the entire tumor and manually drawn as masks in 3D Slicer (<https://www.slicer.org/>) using the Editor module.¹⁵ 'Egg-shell' enhancement along the margin of the postablation cavity is a normal finding in the postoperative period on T1-weighted post-contrast MR imaging that does not denote residual or recurrent tumor.¹⁶ Thus, in postoperative and follow-up DCE-MRIs, a sub-volume mask of the brightest, contiguous region of thick enhancement, if present, in the ablation cavity was obtained by 3 separate users (Fig 1). For cases in which a thick region of enhancement in the ablation cavity was not identified, a mask of the entire ablation cavity was obtained instead. A $2 \times 2 \times 1$ voxel control mask was also drawn in the superior sagittal sinus of each case. Using a technique described by Chung et al,¹¹ we extracted $iAUC_{60}$ values by integrating the $iAUC_{60}$ from 0–60 seconds after bolus arrival from intravenous contrast agent administration. $iAUC_{60}$ values were then calculated for each pixel in the ROI mask using a trapezoidal rule. $iAUC_{60}$ values were normalized to the average signal intensity before the bolus arrival. The bolus arrival time was obtained from a manually placed arterial input function on the superior sagittal sinus. The arrival time was calculated as the maximum time derivative in signal intensity. A single bolus arrival time was averaged across the ROI. This method of semiautomatic segmentation of the ROI and automatic $iAUC_{60}$ calculation based on the time to signal intensity is similar to the technique described by Choi et al.¹⁷ The median of the subvolume $iAUC_{60}$ values for postoperative and follow-up DCE-MRIs from the 3 users was then used for further analysis. The change in $iAUC_{60}$ ($\Delta iAUC_{60}$) was also calculated by taking the difference between $iAUC_{60}$ values between pre- and postoperative DCE-MR imaging as well as postoperative and 1-month follow-up imaging.

Statistical Analysis

All statistical analyses were completed in R statistical and computing software (<http://www.r-project.org>) using the *Survival*,¹⁸ *Caret*,¹⁹ and *pROC*²⁰ packages. Scatterplots and survival curves were created in R using the *ggplot2*²¹ and *survminer*²² packages. Patients with no progression on follow-up imaging were right-censored on the basis of the date of last MRI. Cox univariate analysis was used to evaluate the significance of $iAUC_{60}$ from preoperative, postoperative, and 1-month follow-up in predicting PFS and was presented with a level of significance (P value), hazard ratios (HRs), and CI. Correlations between PFS and $iAUC_{60}$ values were assessed with the Pearson correlation coefficient (r) and presented with the level of significance (P value) and CI. Patients without observed local recurrence, either by loss to follow-up or death, were censored for PFS statistical analysis. Cases censored after 100 days were included in correlation analysis (PFS and $iAUC_{60}$). A receiver operating characteristic (ROC) curve was constructed to identify $iAUC_{60}$ thresholds for statistically significant relationships using the Youden Index and was reported with sensitivity and specificity values, area under the ROC curve, and a confusion matrix of prediction values.²³ To construct the ROC curve, we binarized PFS outcomes to local

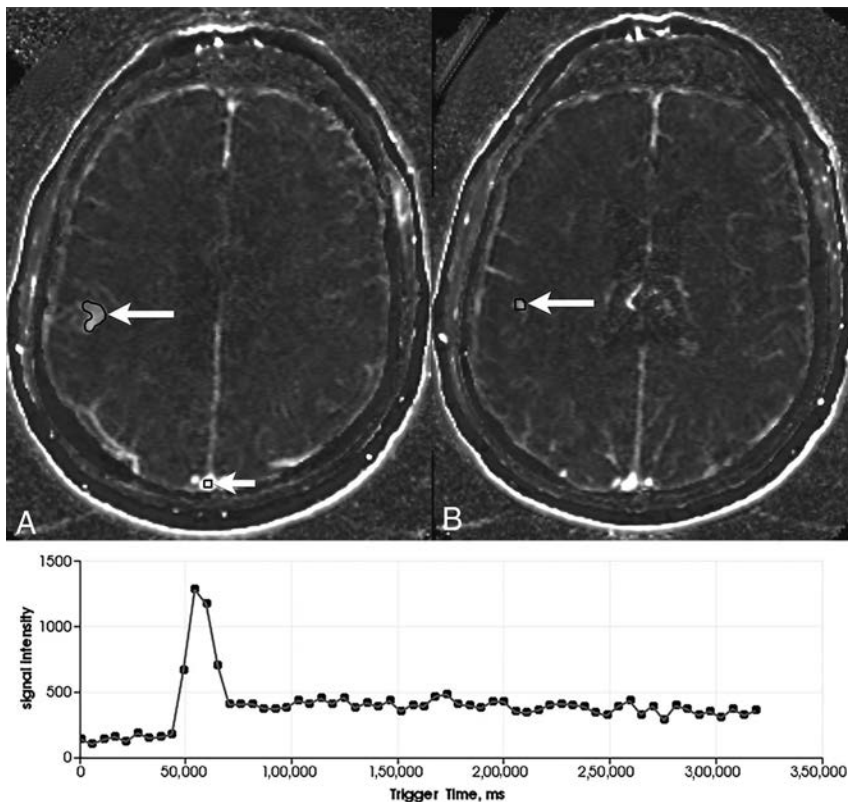


FIG 1. Screenshots from 3D Slicer showing an outline of the masks (white arrows) delineating a metastatic lesion in the right frontal lobe from breast cancer on an axial plane DCE-MRI. (A) shows the metastasis as well as the $2 \times 2 \times 1$ voxel control mask in the superior sagittal sinus, while (B) shows the same lesion mask two slices inferiorly. Also shown is the arterial input function of the contrast history at a single pixel (lower part).

recurrence status at 6 months from LITT therapy. A P value $< .05$ was considered significant. Similarly, CIs were set at 95% confidence.

RESULTS

Patient Demographics

Patient demographics and clinical features are summarized in Table 1. A total of 32 brain metastases of the cohort of 27 patients were analyzed. LITT was used for 2 separate metastases in 4 patients (15%). One patient with 2 intracranial metastases from breast cancer lesions underwent LITT 3 times ($n = 33$), once for a lesion in the posterior fossa and twice for a lesion in the corpus callosum. Deep-seated locations were identified in 6.3% of cases ($n = 1$ corpus callosum, $n = 1$ basal ganglia). Of the 33 total lesions, 51.5% ($n = 17$) were completely ablated during the LITT procedure. Of the 16 remaining lesions, the median volume of the residual tumor was 0.50 cm^3 (range, $0.03\text{--}4.61 \text{ cm}^3$). Regional posttreatment enhancement was observed in 80% ($n = 16$) of the 20 total patients for which immediate postoperative DCE-MR imaging was available. Of the 16 total patients with observed regional enhancement on postoperative DCE-MR imaging, 50% ($n = 8$) were observed to experience local progression. Of the 33 total LITT cases, 30.3% underwent cranial radiation therapy ($n = 8$ stereotactic radiosurgery, $n = 2$ whole-brain radiation therapy) to the lesion due to local progression. The median PFS for the treatment cohort ($n = 33$) was 137 days from LITT (range, 33–

497 days) (Fig 2). Three of the 27 patients (11.1%) were deceased by last follow-up. No post-LITT hemorrhage was observed in any patients during follow-up.

PFS Correlation with $iAUC_{60}$ and $\Delta iAUC_{60}$ from DCE-MR Imaging

Figure 3 compares immediate postoperative DCE-MRIs from 2 patients, 1 with a short PFS (local recurrence observed 86 days from LITT) and 1 with good local control (no local recurrence observed at 329 days from LITT). Preoperative DCE-MR images were available for all 27 patients ($n = 33$ cases of LITT), though only 15 cases were non-censored for correlation analysis. Postoperative DCE-MRIs were only available for 17 ($n = 20$ cases) patients because these were not included in the original protocol, with only 11 cases non-censored for correlation analysis. Furthermore, 1-month follow-up DCE-MR images were available for only 21 patients ($n = 25$ cases) because of loss to follow-up, with 20 noncensored cases available for correlation analysis. No significant linear relationship was observed between preoperative DCE-MR imaging $iAUC_{60}$ and PFS ($r = 0.06$, $n = 15$, $P = .82$; 95% CI, $-0.46\text{--}0.56$). However, a significant

relationship was calculated between $iAUC_{60}$ from postoperative DCE-MR imaging and PFS ($r = -0.64$, $n = 11$, $P = .03$; 95% CI, -0.90 to -0.07) (Fig 4A). A nonsignificant relationship was observed between $iAUC_{60}$ from DCE-MR imaging at 1-month follow-up and PFS ($r = 0.01$, $n = 20$, $P = .96$; 95% CI, $-0.46\text{--}0.48$); however, a clear $iAUC_{60}$ outlier value can be seen on the plot. With this outlier removed, the relationship between DCE-MR imaging at 1-month follow-up and PFS was significant ($r = -0.46$, $n = 19$, $P = .05$; 95% CI, -0.75 to -0.01) (Fig 4B). Analysis of $\Delta iAUC_{60}$ between pre- and immediate postoperative DCE-MR imaging yielded no significant relationship ($r = 0.28$, $n = 11$, $P = .40$; 95% CI, $-0.38\text{--}0.76$). Furthermore, no significant relationship was observed with the $\Delta iAUC_{60}$ values between postoperative imaging and DCE-MR imaging at 1-month follow-up ($r = -0.10$, $n = 10$, $P = .78$; 95% CI, $-0.69\text{--}0.56$) (Fig 4C).

When treated as a continuous variable, $iAUC_{60}$ was not found to be a significant predictor of PFS from preoperative ($P = .27$, HR = 0.66; 95% CI, 0.31–1.37) and 1-month follow-up ($P = .27$, HR = 0.4; 95% CI, 0.13–1.75) DCE-MR images on Cox univariate analysis. Similarly, $\Delta iAUC_{60}$ between postoperative and 1-month follow-up DCE-MR imaging was not associated with PFS ($P = .65$, HR = 1.45; 95% CI, 0.30–7.06). However, $iAUC_{60}$ from postoperative DCE-MR imaging was found to be a significant predictor of PFS on Cox univariate analysis ($P = .01$, HR = 70.99; 95% CI, 2.9–1738.00).

Table 1: Demographics and clinical features

Descriptive	No. (%)
Age groups (per patient, <i>n</i> = 27) (yr)	
50 and younger	3 (11.1)
51–64	12 (44.4)
65–74	9 (33.3)
75 or older	3 (11.1)
Sex (per patient, <i>n</i> = 27)	
Female	16 (59.2)
Male	11 (40.7)
Histology (per patient, <i>n</i> = 27)	
Breast	9
Adenocarcinoma	5
NSCLC	5
RCC	3
Colon	2
Sarcoma	1
SCC	1
Small-cell carcinoma	1
Median KPS (per treatment, <i>n</i> = 33)	
Pre	90
Post	90
1 Month	90
Median PFS (per treatment, <i>n</i> = 33) (days)	137
Deceased (per patient, <i>n</i> = 27)	3 (11.1)
Prior SRS (per treatment, <i>n</i> = 33)	25 (75.8)
Completely ablated (per treatment, <i>n</i> = 33)	17 (51.5)
Posttreatment enhancement on postoperative imaging (<i>n</i> = 20)	16 (80)
Preoperative DCE-MRI available (per treatment, <i>n</i> = 33)	33 (100)
Postoperative DCE-MRI available (per treatment, <i>n</i> = 33)	20 (60.6)
One-month DCE-MRI available (per treatment, <i>n</i> = 33)	25 (75.7)
Local recurrence (per treatment, <i>n</i> = 33)	14 (42.4)
Post-LITT chemotherapy (per treatment, <i>n</i> = 33)	16 (48.5)

Note:—NSCLC indicates non-small-cell lung cancer; RCC, renal cell carcinoma; SCC, squamous cell carcinoma; KPS, Karnofsky performance scale; SRS, stereotactic radiosurgery.

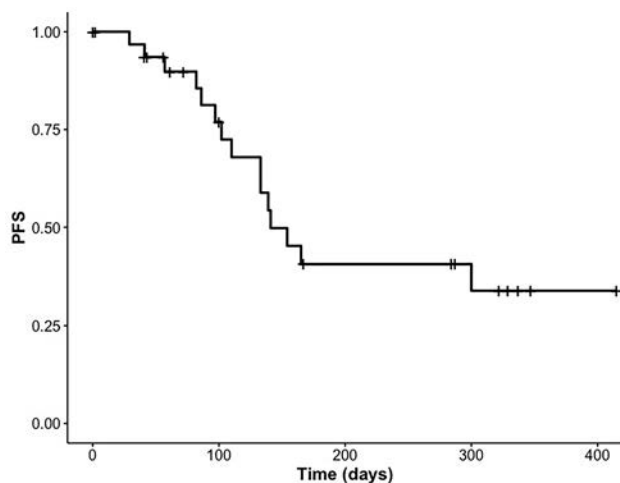


FIG 2. The Kaplan-Meier curve of progression-free survival for all LITT cases (*n* = 33).

An ROC curve was constructed to assess the ability of $iAUC_{60}$ from statistically significant imaging time points (postoperative DCE-MR imaging) to predict 6-month local recurrence status. The area under the ROC curve was calculated as 0.82. The optimal $iAUC_{60}$ value cutoff based on the Youden Index was 1.43. The sensitivity and specificity were 0.75 (95% CI, 0.50–1.00) and 1.00 (95% CI, 0.43–1.00), respectively. The confusion matrix resulting from this ROC analysis can be seen in Table 2.

DISCUSSION

The results of this study suggest a relationship between the $iAUC_{60}$ from DCE-MR imaging and PFS. The association was strongest with $iAUC_{60}$ from imaging obtained immediately post-LITT and establishes a methodology by which subsequent prognostic techniques can be based. Local tissue inflammation, edema, and increased vascular permeability are known characteristics of a local treatment-related response following radiation therapy.²⁴ Although less well-described in patients undergoing LITT, ambiguous contrast enhancement in the postoperative period until follow-up has similarly been known to mimic residual tumor.²⁵ The increased vascular permeability underlying these posttreatment changes is often indistinguishable from tumor recurrence on conventional brain MR imaging, creating a diagnostic and management conundrum in patients with persistent enhancement following definitive brain tumor management. On the basis of clinical DCE-MR imaging applications, we hypothesized that higher $iAUC_{60}$ values would indicate shorter time to local recurrence due to a unique profile of contrast enhancement in tumor tissue

and associated vasculature. The inverse linear relationship seen when plotting postoperative DCE-MR imaging $iAUC_{60}$ values against associated PFS would appear to be consistent with this hypothesis.

Because of early postoperative changes confounding signal intensity, we originally theorized that persistently high $iAUC_{60}$ values after 1 month would consequently be more predictive of eminent disease progression because an underlying posttreatment effect would be less robust. A significant correlation was observed between DCE-MR imaging at 1-month follow-up and PFS, but only after removal of a clear statistical outlier, presenting a potentially confounding variable in this relationship. The $iAUC_{60}$ value for this patient was well above the value of any other in the cohort and may represent some inter-image variability in extracted $iAUC_{60}$ values. Interestingly, no relationship was observed between immediately post-LITT and 1-month follow-up DCE-MR imaging, indicating that another process may be confounding these parameters. Despite these findings, the negative correlation between postoperative and follow-up DCE-MR imaging and $iAUC_{60}$ values would appear to correspond to current evidence suggesting that the extent of ablation predicts PFS in patients with brain metastases.²⁶ Conversely, the weak relationship between the preoperative $iAUC_{60}$ and PFS as well as the $\Delta iAUC_{60}$ between pre- and postoperative DCE-MR imaging is to be expected because the extent of ablation is not taken into account in the preoperative image.

The unique ability to observe vascular changes in tissue has led to the establishment of DCE-MR imaging as a noninvasive method for analyzing blood flow and vessel permeability in ROIs.⁶ Within the field of neuro-oncology, quantification of vascular parameters with DCE-MR imaging has found numerous clinical applications in tumor characterization and diagnosis.²⁷⁻²⁹ Specifically, a number of studies have successfully used DCE-MR imaging to differentiate radiation necrosis (RN) and tumor recurrence.^{27,30-34} The authors of these studies often used quantitative parameters such as volume transfer constant, fractional extravascular extracellular space volume (v_e), reflux rate (k_{ep}), and fractional plasma volume (v_p) to contrast the difference in vasculature between RN and recurrence. Like posttreatment changes, RN presents as persistent enhancement on imaging that can obscure a diagnosis of recurrence on follow-up imaging. However, RN presents a more intuitive application of DCE-MR imaging because there is a stark, quantifiable contrast in the density of vasculature in the 2 disease processes.⁷

Our study applies DCE-MR imaging in the assessment of tumor recurrence from post-LITT treatment change using a simple quantitative parameter ($iAUC_{60}$) that is easier to extract than the aforementioned variables. Specifically, $iAUC_{60}$ has been estab-

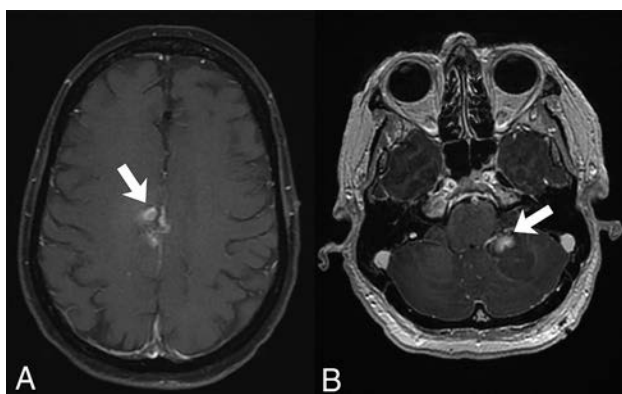


FIG 3. Immediate postoperative T1-weighted postcontrast MRIs showing a region of T1 hyperintensity (white arrows) consistent with treatment change within the ablation zone in a patient with a short PFS (86 days from LITT, $iAUC_{60} = 1.81$) (A) and good long-term control (no recurrence 329 days from LITT, $iAUC_{60} = 1.29$) (B). This patient illustrates that T1-weighted postcontrast MR imaging is not sufficient for distinguishing completely ablated lesions versus partially ablated lesions shortly after thermal ablation and supports the need for DCE-MR imaging in this setting.

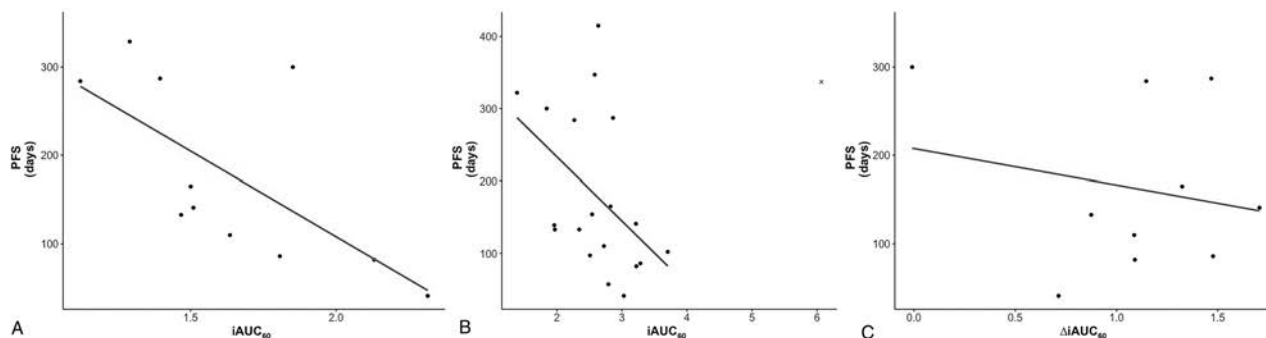


FIG 4. Scatterplot with the line of best fit for $iAUC_{60}$ values from postoperative DCE-MR imaging ($r = -0.64$, $P = .03$) (A) and DCE-MR imaging at 1-month follow-up with the line of best fit drawn with the outlier (marked by x) excluded ($r = -0.46$, $P = .05$) (B). The correlation of PFS and $\Delta iAUC_{60}$ between postoperative and 1-month follow-up DCE-MR imaging is also shown ($r = -0.10$, $P = .78$) (C).

lished as an effective and reproducible measure of tissue perfusion that is easier to calculate than other quantifiable parameters requiring complex model-fitting and additional data on arterial concentration and/or the exchange of contrast between the plasma and extracellular space.^{6,35} Posttreatment change following LITT is a discrete physiologic entity from RN following radiation therapy; the zone of necrosis within the ablation cavity transforms into granulation tissue and ultimately a ring of reactive gliosis with necrotic debris.³⁶ Tissue ablation also has distinct subsequent vascular effects because preservation of the general vascular structure with a potential breakdown in the blood-brain barrier can be observed, similar to known tumoral effects.^{37,38} Because this local tissue reaction to LITT ablation undergoes an angiogenic process similar to that of a recurrent tumor, the application of DCE-MR imaging in this scenario is less straightforward. Nevertheless, our findings suggest some utility in determining early tumor recurrence in these patients, though these results should be confirmed in larger comparative studies investigating additional DCE-MR imaging quantitative parameters (eg, histogram analysis).

Limitations

Although this study benefits from prospective data collection, it is limited by a small sample size. Additionally, a number of subjects were lost to follow-up, and tumor progression was subsequently not observed, further reducing the number of noncensored cases, particularly for the postoperative DCE-MR imaging cohort ($n = 11$). Furthermore, some patients were counted twice in the analysis if both metastatic lesions were treated with LITT. Although this can introduce some confounding in outcome, the separate LITT treatments for different intracranial metastases can be considered discrete samples because they do not affect the associated $iAUC_{60}$ and PFS. Furthermore, the second outcome was censored due to the short follow-up for the patient who received LITT twice

Table 2: Confusion matrix of ROC analysis of postoperative DCE-MRI $iAUC_{60}$ values

Predicted	Reference	
	Short-PFS	Long-PFS
Short-PFS	7	1
Long-PFS	0	3

Note:—Short-PFS indicates time to local recurrence of <6 months; Long-PFS, time to local recurrence of >6 months.

for the same lesion and was thus not considered in the statistical analysis.

The methodology by which we attained the $iAUC_{60}$ may also limit the ability of this parameter to predict PFS and differentiate between posttreatment changes and progression. By simply masking the entire ROI on the DCE-MR imaging, the associated $iAUC_{60}$ can be obscured by variables unique to each patient. For example, a larger tumor area with a smaller region of residual tumor with greater enhancement would have a lower total $iAUC_{60}$ value than a smaller ROI covering posttreatment changes with homogeneous-but-moderate enhancement. Thus, to establish a role for DCE-MR imaging in predicting tumor recurrence post-LITT, larger studies that assess each patient as a discrete sample and compare various methodologies of $iAUC_{60}$ extraction are needed. Furthermore, hemorrhage is an observed phenomenon following LITT ablation that presents as regional enhancement within the ablation cavity.³⁹ The efficacy of $iAUC_{60}$ in differentiating true recurrence from hemorrhagic enhancement was not measured because this complication was not observed in our cohort. Despite these limitations, this pilot study is the first of its kind to demonstrate a significant relationship between PFS and the $iAUC_{60}$ values from immediately postoperative DCE-MRIs and paves the way for additional studies to investigate these methods in predicting local recurrence in patients undergoing LITT for brain metastases.

CONCLUSIONS

Predicting PFS in patients undergoing LITT for brain metastases presents a dilemma in prognosis and subsequent management. $iAUC_{60}$ from DCE-MR imaging is a potential quantifiable parameter for PFS prediction in these patients and can guide subsequent treatment. However, additional studies are warranted to compare $iAUC_{60}$ values from DCE-MR imaging with those from other advanced MR imaging sequences before this technique can be validated for predicting time to local tumor recurrence.

Disclosures: Jeffrey I. Traylor—RELATED: Grant: Monteris Medical.* *Money paid to the institution.

REFERENCES

1. Schouten LJ, Rutten J, Huveneers HA, et al. **Incidence of brain metastases in a cohort of patients with carcinoma of the breast, colon, kidney, and lung and melanoma.** *Cancer* 2002;94:2698–705 CrossRef Medline
2. Lin X, DeAngelis LM. **Treatment of brain metastases.** *J Clin Oncol* 2015;33:3475–84 CrossRef Medline
3. De Poorter J. **Noninvasive MRI thermometry with the proton resonance frequency method: study of susceptibility effects.** *Magn Reson Med* 1995;34:359–67 CrossRef Medline
4. Carpentier A, McNichols RJ, Stafford RJ, et al. **Laser thermal therapy: real-time MRI-guided and computer-controlled procedures for metastatic brain tumors.** *Lasers Surg Med* 2011;43:943–50 CrossRef Medline
5. Patel TR, McHugh BJ, Bi WL, et al. **A comprehensive review of MR imaging changes following radiosurgery to 500 brain metastases.** *AJNR Am J Neuroradiol* 2011;32:1885–92 CrossRef Medline
6. Yankeelov TE, Gore JC. **Dynamic contrast enhanced magnetic resonance imaging in oncology: theory, data acquisition, analysis, and examples.** *Curr Med Imaging Rev* 2009;3:91–107 CrossRef Medline
7. Walker AJ, Ruzevick J, Malayeri AA, et al. **Postradiation imaging changes in the CNS: how can we differentiate between treatment**

- effect and disease progression?** *Future Oncol* 2014;10:1277–97 CrossRef Medline
8. Rieber A, Brambs HJ, Gabelmann A, et al. **Breast MRI for monitoring response of primary breast cancer to neo-adjuvant chemotherapy.** *Eur Radiol* 2002;12:1711–19 CrossRef Medline
9. Choi YJ, Lee JH, Sung YS, et al. **Value of dynamic contrast-enhanced MRI to detect local tumor recurrence in primary head and neck cancer patients.** *Medicine* 2016;95:e3698 CrossRef Medline
10. Narang J, Jain R, Arbab AS, et al. **Differentiating treatment-induced necrosis from recurrent/progressive brain tumor using nonmodel-based semiquantitative indices derived from dynamic contrast-enhanced T1-weighted MR perfusion.** *Neuro Oncol* 2011;13:1037–46 CrossRef Medline
11. Chung WJ, Kim HS, Kim N, et al. **Recurrent glioblastoma: optimum area under the curve method derived from dynamic contrast-enhanced T1-weighted perfusion MR imaging.** *Radiology* 2013;269:561–68 CrossRef Medline
12. Hatzoglou V, Yang TJ, Omuro A, et al. **A prospective trial of dynamic contrast-enhanced MRI perfusion and fluorine-18 FDG PET-CT in differentiating brain tumor progression from radiation injury after cranial irradiation.** *Neuro Oncol* 2016;18:873–80 CrossRef Medline
13. Lin NU, Lee EQ, Aoyama H, et al; Response Assessment in Neuro-Oncology (RANO) group. **Response assessment criteria for brain metastases: proposal from the RANO group.** *Lancet Oncol* 2015;16:e270–78 CrossRef Medline
14. Thomas JG, Rao G, Kew Y, et al. **Laser interstitial thermal therapy for newly diagnosed and recurrent glioblastoma.** *Neurosurg Focus* 2016;41:E12 CrossRef Medline
15. Fedorov A, Beichel R, Kalpathy-Cramer J, et al. **3D Slicer as an image computing platform for the Quantitative Imaging Network.** *Magn Reson Imaging* 2012;30:1323–41 CrossRef Medline
16. Missios S, Bekelis K, Barnett GH. **Renaissance of laser interstitial thermal ablation.** *Neurosurg Focus* 2015;38:E13 CrossRef Medline
17. Choi YS, Lee HJ, Ahn SS, et al. **Primary central nervous system lymphoma and atypical glioblastoma: differentiation using the initial area under the curve derived from dynamic contrast-enhanced MR and the apparent diffusion coefficient.** *Eur Radiol* 2017;27:1344–51 CrossRef Medline
18. Therneau TM, Grambsch PM. *Modeling Survival Data: Extending the Cox Model.* Springer, New York; 2000
19. Kuhn M. **Caret: classification and regression training.** *Astrophysics Source Code Library* 2015. <https://CRAN.R-project.org/package=caret>. Accessed April 21, 2019
20. Robin X, Turck N, Hainard A, et al. **pROC: an open-source package for R and S+ to analyze and compare ROC curves.** *BMC Bioinformatics* 2011. <https://CRAN.R-project.org/package=pROC>;12:77. Accessed April 21, 2019
21. Wickham H. *ggplot2: Create Elegant Data Visualisations Using the Grammar of Graphics.* Springer-Verlag; 2016. <https://CRAN.R-project.org/package=ggplot2>. Accessed April 21, 2019
22. Kassambara A, Kosinski A, Biecek P, et al. **Survminer: drawing survival curves using 'ggplot2'.** 2019. <https://CRAN.R-project.org/package=survminer>. Accessed April 21, 2019
23. Youden WJ. **Index for rating diagnostic tests.** *Cancer* 1950;3:32–35 Medline
24. Hygino da Cruz LC Jr, Rodriguez I, Domingues RC, et al. **Pseudoprogession and pseudoresponse: imaging challenges in the assessment of posttreatment glioma.** *AJNR Am J Neuroradiol* 2011;32:1978–85 CrossRef Medline
25. Elster AD, DiPersio DA. **Cranial postoperative site: assessment with contrast-enhanced MR imaging.** *Radiology* 1990;174:93–98 CrossRef Medline
26. Salehi A, Kamath AA, Leuthardt EC, et al. **Management of intracranial metastatic disease with laser interstitial thermal therapy.** *Front Oncol* 2018;8:499 CrossRef Medline
27. Larsen VA, Simonsen HJ, Law I, et al. **Evaluation of dynamic contrast-enhanced T1-weighted perfusion MRI in the differentiation**

- of tumor recurrence from radiation necrosis. *Neuroradiology* 2013; 55:361–69 CrossRef Medline
28. Hatzoglou V, Tisnado J, Mehta A, et al. **Dynamic contrast-enhanced MRI perfusion for differentiating between melanoma and lung cancer brain metastases.** *Cancer Med* 2017;6:761–67 CrossRef Medline
 29. Choi YS, Ahn SS, Lee HJ, et al. **The initial area under the curve derived from dynamic contrast-enhanced MRI improves prognosis prediction in glioblastoma with unmethylated MGMT promoter.** *AJNR Am J Neuroradiol* 2017;38:1528–35 CrossRef Medline
 30. Giglio P, Gilbert MR. **Cerebral radiation necrosis.** *Neurologist* 2003; 9:180–88 CrossRef Medline
 31. Gasparetto EL, Pawlak MA, Patel SH, et al. **Posttreatment recurrence of malignant brain neoplasm: accuracy of relative cerebral blood volume fraction in discriminating low from high malignant histologic volume fraction.** *Radiology* 2009;250:887–96 CrossRef Medline
 32. Artzi M, Liberman G, Nadav G, et al. **Differentiation between treatment-related changes and progressive disease in patients with high grade brain tumors using support vector machine classification based on DCE MRI.** *J Neurooncol* 2016;127:515–24 CrossRef Medline
 33. Bolcaen J, Descamps B, Acou M, et al. **In vivo DCE-MRI for the discrimination between glioblastoma and radiation necrosis in rats.** *Mol Imaging Biol* 2017;19:857–66 CrossRef Medline
 34. Mitsuya K, Nakasu Y, Horiguchi S, et al. **Perfusion weighted magnetic resonance imaging to distinguish the recurrence of metastatic brain tumors from radiation necrosis after stereotactic radiosurgery.** *J Neurooncol* 2010;99:81–88 CrossRef Medline
 35. Jesberger JA, Rafie N, Duerk JL, et al. **Model-free parameters from dynamic contrast-enhanced-MRI: sensitivity to EES volume fraction and bolus timing.** *J Magn Reson Imaging* 2006;24:586–94 CrossRef Medline
 36. Sharma M, Balasubramanian S, Silva D, et al. **Laser interstitial thermal therapy in the management of brain metastasis and radiation necrosis after radiosurgery: an overview.** *Expert Rev Neurother* 2016; 16:223–32 CrossRef Medline
 37. Schulze PC, Vitzthum HE, Goldammer A, et al. **Laser-induced thermotherapy of neoplastic lesions in the brain—underlying tissue alterations, MRI-monitoring and clinical applicability.** *Acta Neurochir (Wien)* 2004;146:803–12 Medline
 38. Fidler IJ, Yano S, Zhang RD, et al. **The seed and soil hypothesis: vascularisation and brain metastases.** *Lancet Oncol* 2002;3:53–57 CrossRef Medline
 39. Medvid R, Ruiz A, Komotar RJ, et al. **Current applications of MRI-guided laser interstitial thermal therapy in the treatment of brain neoplasms and epilepsy: a radiologic and neurosurgical overview.** *AJNR Am J Neuroradiol* 2015;36:1998–2006 CrossRef Medline

Molecular Subtype Classification in Lower-Grade Glioma with Accelerated DTI

E. Aliotta, H. Nourzadeh, P.P. Batchala, D. Schiff, M.B. Lopes, J.T. Druzgal, S. Mukherjee, and S.H. Patel



ABSTRACT

BACKGROUND AND PURPOSE: Image-based classification of lower-grade glioma molecular subtypes has substantial prognostic value. Diffusion tensor imaging has shown promise in lower-grade glioma subtyping but currently requires lengthy, nonstandard acquisitions. Our goal was to investigate lower-grade glioma classification using a machine learning technique that estimates fractional anisotropy from accelerated diffusion MR imaging scans containing only 3 diffusion-encoding directions.

MATERIALS AND METHODS: Patients with lower-grade gliomas ($n = 41$) (World Health Organization grades II and III) with known *isocitrate dehydrogenase (IDH)* mutation and 1p/19q codeletion status were imaged preoperatively with DTI. Whole-tumor volumes were autodelineated using conventional anatomic MR imaging sequences. In addition to conventional ADC and fractional anisotropy reconstructions, fractional anisotropy estimates were computed from 3-direction DTI subsets using DiffNet, a neural network that directly computes fractional anisotropy from raw DTI data. Differences in whole-tumor ADC, fractional anisotropy, and estimated fractional anisotropy were assessed between *IDH*-wild-type and *IDH*-mutant lower-grade gliomas with and without 1p/19q codeletion. Multivariate classification models were developed using whole-tumor histogram and texture features from ADC, ADC + fractional anisotropy, and ADC + estimated fractional anisotropy to identify the added value provided by fractional anisotropy and estimated fractional anisotropy.

RESULTS: ADC ($P = .008$), fractional anisotropy ($P < .001$), and estimated fractional anisotropy ($P < .001$) significantly differed between *IDH*-wild-type and *IDH*-mutant lower-grade gliomas. ADC ($P < .001$) significantly differed between *IDH*-mutant gliomas with and without codeletion. ADC-only multivariate classification predicted *IDH* mutation status with an area under the curve of 0.81 and codeletion status with an area under the curve of 0.83. Performance improved to area under the curve = 0.90/0.94 for the ADC + fractional anisotropy classification and to area under the curve = 0.89/0.89 for the ADC + estimated fractional anisotropy classification.

CONCLUSIONS: Fractional anisotropy estimates made from accelerated 3-direction DTI scans add value in classifying lower-grade glioma molecular status.

ABBREVIATIONS: AUC = area under the curve; Codel = codeletion; dFA = fractional anisotropy estimates; FA = fractional anisotropy; LGG = lower-grade glioma; MUT = mutated; Noncodel = noncodeleted; WT = wild-type; *IDH* = *isocitrate dehydrogenase*

The classification of diffuse lower-grade gliomas (LGGs) into molecular subtypes as designated by the World Health Organization in 2016 has important prognostic implications. Median survival in LGG is >6 years in the presence of an *isocitrate dehy-*

drogenase (IDH) gene mutation (IDH_{MUT}) but reduces to <2 years in the absence of such a mutation (IDH wild-type [IDH_{WT}]).¹ Among IDH_{MUT} LGGs, the presence of 1p/19q chromosomal codeletion (IDH_{MUT} -Codel) predicts sensitivity to chemoradiation therapy and further improves overall survival compared with 1p/19q noncodeleted LGGs (IDH_{MUT} -Noncodel).^{1,2} Moreover, the impact of surgery appears to differ among the molecular subtypes.^{3,4} Therefore, noninvasive, pre-surgical imaging biomarkers that can reliably predict genomic subtypes are of strong clinical interest.

Diffusion-weighted imaging and diffusion tensor imaging are quantitative MR imaging techniques that probe microstructural tissue characteristics by observing the rate and directionality of restricted water diffusion. Both DWI and DTI have demonstrated sensitivity to *IDH*-mutation and 1p/19q codeletion status in

Received April 16, 2019; accepted after revision July 1.

From the Departments of Radiation Oncology (E.A., H.N.), Radiology (P.P.B., J.T.D., S.M., S.H.P.), Neurology (D.S.), and Pathology (Neuropathology) (M.B.L.), University of Virginia, Charlottesville, Virginia.

Sohil H. Patel was supported by a Radiological Society of North America Research Scholar Grant (RSCH1819).

Please address correspondence to Eric Aliotta, PhD, Radiological Physics, University of Virginia, 1335 Lee St, Box 800375, Charlottesville, VA 22908; e-mail: eric.aliotta@virginia.edu

Indicates article with supplemental on-line tables.

<http://dx.doi.org/10.3174/ajnr.A6162>

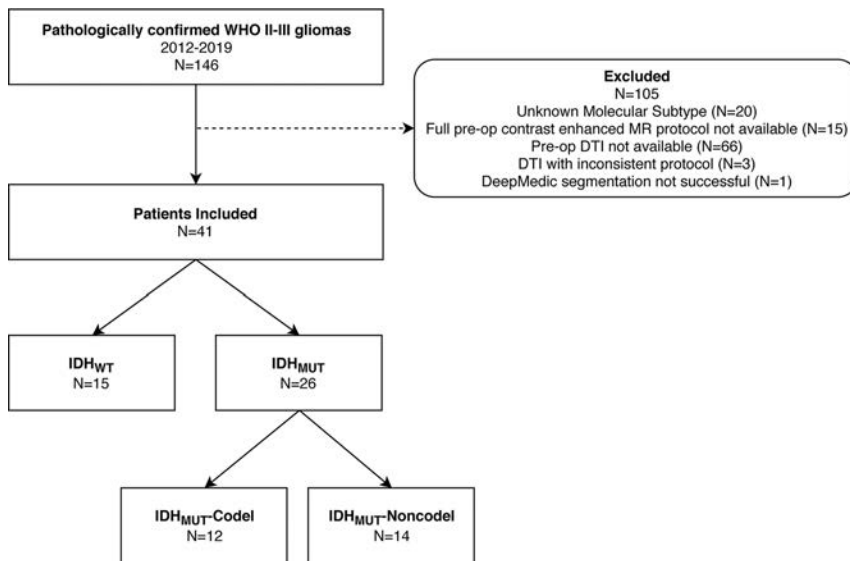


FIG 1. Patient population flow chart.

LGGs via differences in the ADC and/or fractional anisotropy (FA),⁵⁻⁸ which have been attributed to differences in cellularity and tumor proliferation rates among subtypes.⁹ While FA has been shown to provide additional value beyond ADC in LGG subtyping, it currently requires the addition of a DTI scan, which is a more specialized imaging technique than DWI and is not part of most routine clinical protocols. Furthermore, because DTI requires acquisitions with diffusion encoding along many directions (at least 6, typically ≥ 20), its acquisition time is substantially longer than conventional DWI, which only requires diffusion encoding along 3 orthogonal directions. Although MR imaging acceleration techniques such as simultaneous multislice imaging and compressed sensing can greatly accelerate DTI acquisitions,^{10,11} most clinical diffusion MR imaging scans are still DWIs.

A recently developed DTI reconstruction method called DiffNet (<https://github.com/ealiotta/diffnet>) uses machine learning to estimate FA from accelerated scans with as few as 3 diffusion-encoding directions.¹² This means that, in principle with DiffNet, the discriminatory power provided by DTI can be extracted from standard DWI scans. While DiffNet has been shown to provide accurate FA map estimates, it remains to be seen whether these estimates add the same value as conventionally reconstructed FA maps from DTI in LGG molecular subtyping.

The purpose of this study was to determine whether FA values estimated using DiffNet from diffusion MR imaging scans with only 3 diffusion-encoding directions add discriminatory value beyond ADC in LGG molecular subtyping. We evaluated the LGG classification in patients who underwent preoperative DTI scans in addition to standard contrast-enhanced MR imaging brain protocols. Classifications were performed using bootstrapped multinomial linear regressions using whole-tumor histogram and texture features from ADC maps alone, ADC plus FA maps, and ADC-plus-DiffNet estimated FA (dFA) maps.

MATERIALS AND METHODS

Patient Cohort

The local institutional review board approved this retrospective study and provided a waiver of the informed consent requirement. One hundred forty-six patients with pathologically confirmed World Health Organization grade II and III gliomas who were imaged at our institution between 2012 and 2019 were identified. Patients with an unknown molecular subtype ($n = 20$), without full preoperative contrast-enhanced MR imaging examinations ($n = 15$), and without preoperative DTI ($n = 66$) or with preoperative DTI with an inconsistent protocol ($n = 3$) were excluded. One additional patient was excluded from analysis due to an unsuccessful tumor autosegmentation (process described below), leaving a total of 41 patients

($IDH_{WT} = 15$; $IDH_{MUT-Codel} = 12$; $IDH_{MUT-Noncodel} = 14$) who were included in our analysis. This group comprised 26 World Health Organization grade II and 15 World Health Organization grade III tumors and 24 male and 17 female patients with a mean age of 45.9 years (range, 18–76 years). A flow chart describing the study population is shown in Fig 1.

Neuropathology

IDH-mutation and 1p/19 codeletion status were tested for all patients in the molecular pathology laboratory at our institution. Formalin-fixed, paraffin-embedded tissue sections were processed routinely for histologic and immunohistochemical analysis. *IDH* mutation status was tested using immunohistochemistry, in which *IDH1* R132H mutations were detected with H09 antibodies.¹³ In immunohistochemistry cases negative for *IDH1* R132H mutations, *IDH1/2* mutation status was assessed using DNA pyrosequencing as described previously.¹⁴ The 1p/19q codeletion status was determined using dual color fluorescence in situ hybridization¹⁵ ($n = 38$) or chromosomal microarray analysis using the OncoScan (Thermo Fisher Scientific, Waltham, Massachusetts) platform ($n = 3$).

Imaging Protocols

Patients were imaged on either 1.5T ($n = 3$) or 3T scanners ($n = 38$) with pre- and postcontrast T1-weighted scans (TE = 1.9–5.0 ms, TR = 9.5–2300 ms, in-plane resolution = 0.5–1.1 mm, slice thickness = 0.9–1.2 mm) as well as T2-weighted (TE = 82–413 ms, TR = 3200–9000 ms, in-plane resolution = 0.25–1.0 mm, slice thickness = 0.9–5.0 mm) and T2 FLAIR scans (TE = 80–388 ms, TR = 5000–10,000 ms, TI = 2800–2500 ms, in-plane resolution = 0.5–1.0 mm, slice thickness = 0.9–5.0 mm). The DTI protocol included 20 diffusion-encoding directions with $b = 1000$ s/mm² and 1 $b = 0$ reference, 1.7- to 1.9-mm in-plane spatial resolution, 4.0- to 5.0-mm slice thickness with slice-interleaved single-shot EPI (TE = 6–104 ms and TR = 3300–4800 ms). DTI

scans were repeated 2–4 times and averaged off-line to improve the SNR.

Tumor Segmentation

Conventional MR images (T1 pre- and postcontrast, T2, and T2-FLAIR) were coregistered to the reference frame of the T1 postcontrast images. Brain extraction was then performed using the Robust Brain Extraction algorithm (<https://www.nitrc.org/projects/robex>),¹⁶ followed by automatic tumor segmentation using DeepMedic (<https://github.com/Kamnitsask/deepmedic>)¹⁷ as implemented in the Brain Cancer Imaging Phenomics Toolkit (<https://captk.projects.nitrc.org/>).¹⁸ Following autosegmentation, tumor volumes were reviewed for obvious errors or segmentation failures, and clearly spurious regions were removed. The DeepMedic output included specific regions for edema, contrast-enhancing gross tumor, and nonenhancing tumor, but all regions were combined into single, whole-tumor ROIs. These ROIs were then registered onto the lower resolution DTI reference frame.

ADC and FA Reconstruction

ADC and FA values were reconstructed off-line from DTI using conventional linear-least-squares fitting and Eigensystem decomposition¹⁹ at each voxel using custom Matlab code (MathWorks, Natick, Massachusetts).

Subsets containing only 3 diffusion encoding directions were then extracted from the full DTI scans to replicate conventional DWI acquisitions and simulate a scenario in which DTI was not acquired. These directions were selected to maximize orthogonality and thus closely mimic a DWI acquisition. dFA maps were then computed from these undersampled scans by applying the DiffNet neural network at each voxel.¹² DiffNet consists of a multilayer perceptron neural network design with 2 hidden layers and a total of 200 nodes and was previously trained to compute FA values from undersampled DTI signals at individual voxels. DiffNet can estimate FA without a full DTI dataset because it bypasses the intermediary tensor-model-fitting reconstruction step and directly infers FA from raw data. DiffNet was implemented in Python (python.org) and is available for download (github.com/ealiotta/diffnet).

ADC and FA Comparisons

Differences in ADC, FA, and dFA among LGG subgroups were assessed by computing mean whole-tumor values for each parameter and comparing distributions among subgroups using the Student *t* test. Statistical significance was assessed using the Bonferroni correction for multiple comparisons in which *P* values < 0.008 (.05/6) were considered statistically significant.

Histogram Feature Extraction

To assess the full distributions of each DTI parameter, we extracted several histogram features for ADC, FA, and dFA within whole-tumor ROIs. As described elsewhere,⁶ 10th, 25th, 50th, 75th, 90th percentile values, skewness, and kurtosis were computed from ADC, FA, and dFA distributions.

Texture Feature Extraction

Texture analysis of the ADC, FA, and dFA maps was performed using gray level co-occurrence matrices as previously described in this context.⁶ For each map, homogeneity, correlation, energy, and contrast were computed within the whole-tumor ROIs using a Matlab-based radiomic toolbox (<https://github.com/mvallieres/radiomics>) developed by Vallières et al.²⁰ Gray level co-occurrence parameters were computed within each ROI using equal-probability quantization at 8 quantization levels. The number of radiomic features was kept purposely small to avoid false-positive discoveries, given our cohort size.²¹

Multivariate Classification

In total, 12 features (mean, 7 histogram features, and 4 texture features) were compiled for each ADC, FA, and dFA map. To classify *IDH*-mutation and 1p/19q codeletion statuses using all available features, we developed multivariate logistic regression models using imbalance-adjusted bootstrap resampling.^{20,22} Imbalance-adjusted bootstrap resampling permits robust feature selection and generalizable multivariate modeling with a limited dataset by optimizing model parameters on bootstrapped training/testing data subsets while accounting for class imbalances within subsets at each bootstrap repetition.

First, the optimal feature sets were selected from the available histogram and texture features by optimizing classification performance across 50 bootstrapped samples with models containing between 1 and 10 features. With each repetition, patients were randomly divided into training and testing groups with a 60%/40% split, and class imbalances in each group (ie, a differing number of *IDH*_{MUT} versus *IDH*_{WT} or *IDH*_{MUT}-Codel versus *IDH*_{MUT}-Noncodel cases) were corrected by repeating instances from the underrepresented class. Regression models were then generated at each iteration using all combinations of available features to optimize prediction accuracy on the training group. The optimal model order (ie, number of features) was then selected by choosing the simplest model (ie, lowest number of features) for which classification area under the curve (AUC) in the testing group reached a maximum or plateau.

This procedure was repeated using ADC, ADC + FA, and ADC + dFA features for both *IDH*-mutation and 1p/19q codeletion classifications, generating an optimized feature set for each case. Once optimal feature sets were determined for each classification scheme, a final prediction model was generated by computing model coefficients using imbalance-adjusted bootstrap resampling with 1000 repetitions and taking the average regression coefficients across repetitions. This process ensured that the classification model was not overfitting to any specific subset of patients used for training. Model performance was then quantified in terms of AUC, sensitivity, and specificity in the testing group with each bootstrap repetition, generating a distribution of each parameter for each model. Model performance was evaluated according to the mean and standard error of each metric across repetitions.

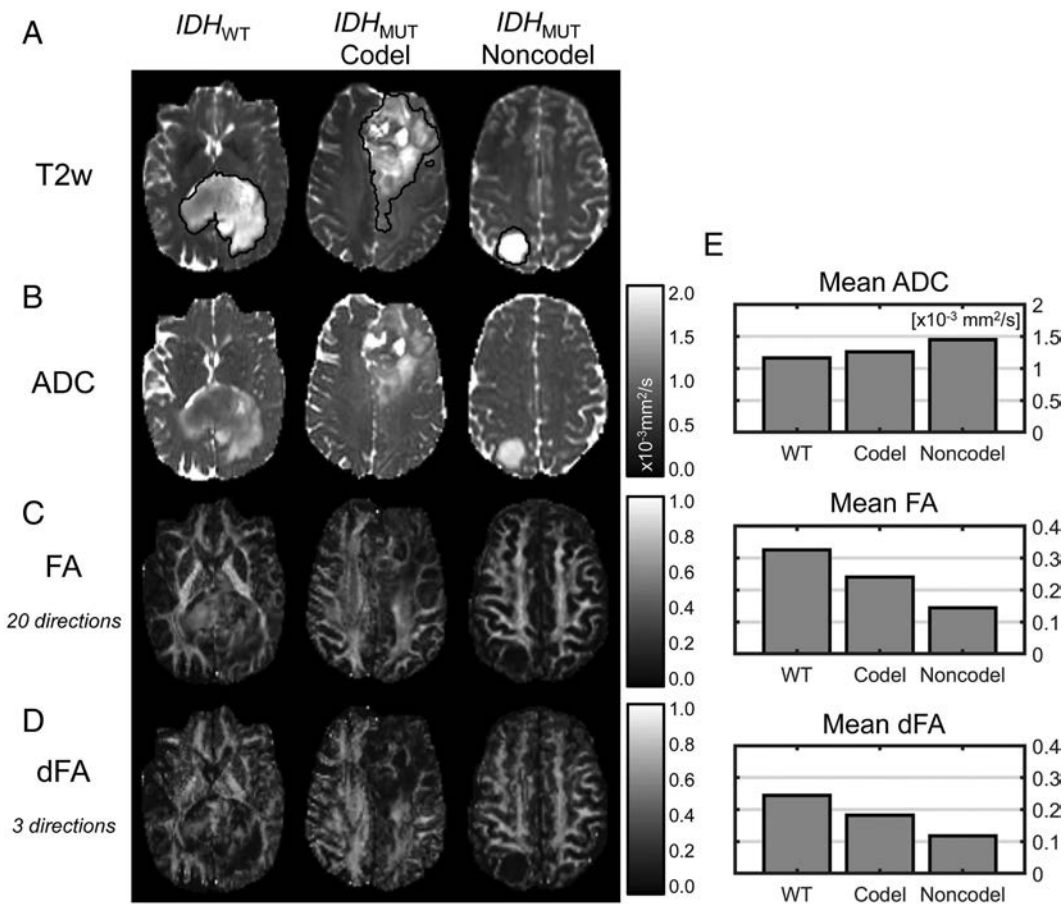


FIG 2. Sample T2-weighted images with tumor segmentations (A), ADC maps (B), FA maps (C), and dFA maps (D) from each LGG molecular subtype as well as mean ADC, FA, and dFA values (E) from these individual cases.

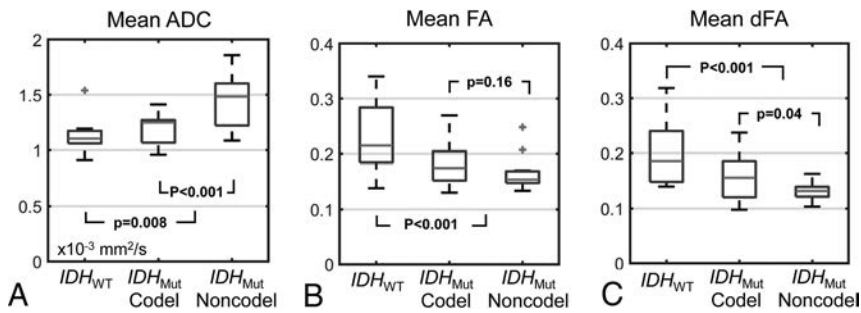


FIG 3. Boxplots showing mean ADC (A), FA (B), and dFA (C) values across LGG subtypes. Central lines indicate median values, box edges indicate 25th and 75th percentiles, and whiskers extend to the full data range, excluding outliers (which are indicated by plus signs). P values < 0.008 indicate statistically significant differences to account for multiple comparisons.

RESULTS

Quantitative Subgroup Differences

Sample ADC, FA, and dFA maps from each LGG subtype are shown in Fig 2, and mean values across patients within each LGG subtype are shown in Fig 3. For IDH_{WT} versus IDH_{MUT} , significant differences were observed in ADC (1.18 ± 0.16 versus $1.36 \pm 0.24 \times 10^{-3} \text{ mm}^2/\text{s}$, $P = .008$), FA (0.22 ± 0.05 versus 0.17 ± 0.04 , $P < .001$), and dFA (0.19 ± 0.05 versus 0.14 ± 0.03 , $P < .001$). For IDH_{MUT} -Codel versus IDH_{MUT} -Noncodel, a significant difference in ADC was observed (1.20 ± 0.14 versus $1.48 \pm 0.23 \times 10^{-3} \text{ mm}^2/\text{s}$, $P < .001$). Insignificant differences were observed in FA and dFA between IDH_{MUT} -Codel and IDH_{MUT} -Noncodel,

though both were slightly higher in the IDH_{MUT} -Codel group (FA: 0.18 ± 0.04 versus 0.16 ± 0.03 , $P = .16$; dFA: 0.16 ± 0.04 versus 0.13 ± 0.01 , $P = .04$). Comparisons among all other histogram and texture features are shown in On-line Tables 1 and 2.

Classification Feature Selection

Optimal feature combinations determined in the imbalance-adjusted bootstrap resampling feature selection process are listed in the Table.

Following feature selection, the ADC-only IDH -mutation status classification

included only 1 histogram feature (75th percentile ADC); the ADC + FA model contained 3 histogram features (2 ADC features and 1 FA feature) and 3 texture features (1 ADC feature and 2 FA features); and the ADC + dFA model included 2 histogram features and 2 texture features (1 ADC and 1 FA feature each).

For 1p/19q codeletion status classification, the ADC-only model used 1 histogram feature (50th percentile ADC), the ADC + FA model used 5 histogram features (3 ADC features and 2 FA features), and the ADC + dFA model used 4 histogram features (2 ADC features and 2 dFA features).

Features selected in the imbalance-adjusted bootstrap resampling process for each classification scheme^a

	Histogram and Texture Features					
	ADC		ADC + FA		ADC + dFA	
	Feature	Weight	Feature	Weight	Feature	Weight
<i>IDH</i> _{WT} vs <i>IDH</i> _{MUT}	ADC 75%	-6.5	ADC 10%	109.4	ADC 10%	40.4
			ADC 90%	-71.4	ADC homogeneity	60.2
			ADC energy	4363.0	dFA energy	-1459.0
			FA 75%	227.5	dFA skewness	-6.45
			FA contrast	24.2		
<i>IDH</i> _{MUT} -Codel vs <i>IDH</i> _{MUT} -Noncodel	ADC 50%	-10.7	FA homogeneity	-346.9	ADC 75%	-62.9
			ADC 50%	-266.8	ADC 10%	40.0
			ADC 25%	306.8	ADC 50%	202.9
			ADC skewness	-17.9	dFA 50%	11.9
			FA 75%	460.9	dFA skewness	11.9
			FA skewness	-141.5		

^a For *IDH*_{WT} vs *IDH*_{MUT}, positive values indicate positive correlations with *IDH*_{WT}. For *IDH*_{MUT}-Codel vs *IDH*_{MUT}-Noncodel, positive values indicate positive correlations with *IDH*_{MUT}-Noncodel. ADC units are in square millimeters/millisecond.

Classification Performance

For *IDH* mutation status classification, the ADC-only model achieved AUC = 0.81 ± 0.03, sensitivity = 0.84 ± 0.06, and specificity = 0.67 ± 0.05. The ADC + FA model achieved AUC = 0.90 ± 0.03, sensitivity = 0.80 ± 0.07, and specificity = 0.80 ± 0.04. The ADC + dFA model achieved AUC = 0.89 ± 0.03, sensitivity = 0.83 ± 0.06, and specificity = 0.77 ± 0.04.

For codeletion status classification, the ADC only model achieved AUC = 0.83 ± 0.03, sensitivity = 0.81 ± 0.06, and specificity = 0.73 ± 0.04. The ADC + FA model achieved AUC = 0.94 ± 0.02, sensitivity = 0.83 ± 0.05, and specificity = 0.84 ± 0.05. The ADC + dFA model achieved AUC = 0.89 ± 0.03, sensitivity = 0.76 ± 0.07, and specificity = 0.79 ± 0.05.

DISCUSSION

FA estimates obtained from 3-direction diffusion MR imaging scans using DiffNet added discriminatory value in classifying LGGs according to both *IDH*-mutation and 1p/19q codeletion statuses in addition to ADC maps alone. Although conventional FA values reconstructed from full DTI data provided marginally better classification performance than dFA, both parameters added to the performance of the ADC-only classification. This feature indicates that DiffNet can aid in LGG classification when only DWI is performed. Because DWI scans are included in most standard MR imaging brain protocols, clinical value can be added in many scenarios without the need for additional DTI scans. It should be noted, however, that DTI is often performed to aid in surgical planning and thus is available in many cases.

Several of our findings regarding conventional DTI analysis for LGG classification are consistent with prior work. For example, prior studies have reported lower ADC^{5,8,23-25} and higher FA^{6,7} values in *IDH*_{WT} LGG compared with *IDH*_{MUT} gliomas. Others have also reported significantly higher ADC^{7,26} and slightly, but nonsignificantly, lower FA values⁷ in *IDH*_{MUT}-Noncodel versus *IDH*_{MUT}-Codel tumors.

Other imaging features have previously been used to classify gliomas into molecular subtypes. These include conventional imaging characteristics based on tumor location,^{27,28} contrast enhancement,^{27,28} margins,^{29,30} T2-FLAIR mismatch,^{31,32} and calcification.³³ Advanced techniques including perfusion MR

imaging,^{5,23,34,35} MR imaging spectroscopy,^{28,36,37} and radiomic texture analysis²² have also demonstrated discriminatory value. These features can potentially be combined with FA and ADC to further improve classification performance. Additional improvements may also be achievable through more sophisticated classification schemes than the logistic regressions used in this work, such as support-vector machines or random forests.

ADC energy had positive regression coefficients in the *IDH*-mutation classification, which indicates that uniform ADC values within the tumor are associated with *IDH*_{WT}. On the other hand, FA homogeneity and dFA energy (both

of which indicate parameter uniformity within the tumor) had negative regression coefficients indicating negative associations with *IDH*_{WT}. These results further indicate that FA and dFA provide complementary information to ADC for LGG classification and agree with prior study results showing higher ADC orderliness and a lack of locally correlated FA values in *IDH*_{WT} tumors.⁶

Our finding that increased ADC skewness is associated with *IDH*_{MUT}-Noncodel tumors is also consistent with prior work.⁶ However, these authors also found FA energy and correlation as a significant predictor of *IDH*_{MUT}-Noncodel. Neither these nor any ADC, FA, or dFA texture features were selected in our final codeletion-status classification models.

Notably, our codeletion-status classification models included FA skewness and dFA skewness but in opposite directions (increased FA skewness was associated with *IDH*_{MUT}-Codel while increased dFA skewness was associated with *IDH*_{MUT}-Noncodel). This is a surprising finding but may be due to a known FA-dependent bias in dFA. It was shown previously that dFA has a negative bias that gets larger as FA values increase,¹² which affects the shape of dFA distributions. This can alter distribution skewness and thus associated relationships with molecular subtypes.

This study has limitations that should be discussed. This is a retrospective, single-institution study with a relatively small sample size, and prospective validation on larger samples is necessary. We have made DiffNet publicly available in hopes of facilitating independent validation of our results at separate institutions. Furthermore, although there is no technical difference between a subsampled DTI dataset containing only 3 diffusion-encoding directions and a conventional DWI scan, prospective analysis including only true DWI data is warranted.

CONCLUSIONS

DiffNet neural network-derived FA estimates based on 3-direction DTI scans improve *IDH*-mutation and 1p/19q codeletion classification in LGGs compared with ADC values alone. The application of the DiffNet neural network to conventional DWI data may improve the prediction of LGG molecular subtypes.

Disclosures: Sohil H. Patel—RELATED: Grant: Radiological Society of North America Research Scholar Grant*; UNRELATED: Other: I provided written expert opinion in a malpractice lawsuit.* *Money paid to the institution.

REFERENCES

1. Brat DJ, Verhaak RG, Aldape KD, et al; Cancer Genome Atlas Research Network. **Comprehensive, integrative genomic analysis of diffuse lower-grade gliomas.** *N Engl J Med* 2015;372:2481–98 CrossRef Medline
2. Jenkins RB, Blair H, Ballman KV, et al. **A t(1;19)(q10;p10) mediates the combined deletions of 1p and 19q and predicts a better prognosis of patients with oligodendroglioma.** *Cancer Res* 2006;66:9852–61 CrossRef Medline
3. Wijnenga MM, French PJ, Dubbink HJ, et al. **The impact of surgery in molecularly defined low-grade glioma: an integrated clinical, radiological, and molecular analysis.** *Neuro Oncol* 2018;20:103–12 CrossRef Medline
4. Kawaguchi T, Sonoda Y, Shibahara I, et al. **Impact of gross total resection in patients with WHO grade III glioma harboring the IDH 1/2 mutation without the 1p/19q co-deletion.** *J Neurooncol* 2016;129:505–14 CrossRef Medline
5. Leu K, Ott GA, Lai A, et al. **Perfusion and diffusion MRI signatures in histologic and genetic subtypes of WHO grade II–III diffuse gliomas.** *J Neurooncol* 2017;134:177–88 CrossRef Medline
6. Park YW, Han K, Ahn SS, et al. **Whole-tumor histogram and texture analyses of DTI for evaluation of IDH1-mutation and 1p/19q-codeletion status in World Health Organization grade II gliomas.** *AJNR Am J Neuroradiol* 2018;39:693–98 CrossRef Medline
7. Xiong J, Tan W, Wen J, et al. **Combination of diffusion tensor imaging and conventional MRI correlates with isocitrate dehydrogenase 1/2 mutations but not 1p/19q genotyping in oligodendroglial tumours.** *Eur Radiol* 2016;26:1705–15 CrossRef Medline
8. Suh CH, Kim HS, Jung SC, et al. **Imaging prediction of isocitrate dehydrogenase (IDH) mutation in patients with glioma: a systemic review and meta-analysis.** *Eur Radiol* 2019;29:745–58 CrossRef Medline
9. Beppu T, Inoue T, Shibata Y, et al. **Fractional anisotropy value by diffusion tensor magnetic resonance imaging as a predictor of cell density and proliferation activity of glioblastomas.** *Surg Neurol* 2005;63:56–61; discussion 61 CrossRef Medline
10. Setsompop K, Gagoski BA, Polimeni JR, et al. **Blipped-controlled aliasing in parallel imaging for simultaneous multislice echo planar imaging with reduced g-factor penalty.** *Magn Reson Med* 2012;67:1210–24 CrossRef Medline
11. Wu Y, Zhu Y, Tang Q, et al. **Accelerated MR diffusion tensor imaging using distributed compressed sensing.** *Magn Reson Med* 2014;71:763–72 CrossRef Medline
12. Aliotta E, Nourzadeh H, Sanders J, et al. **Highly accelerated, model-free diffusion tensor MRI reconstruction using neural networks.** *Med Phys* 2019;46:1581–91 CrossRef Medline
13. Capper D, Weissert S, Bals J, et al. **Characterization of R132H mutation-specific IDH1 antibody binding in brain tumors.** *Brain Pathol* 2010;20:245–54 CrossRef Medline
14. Felsberg J, Wolter M, Seul H, et al. **Rapid and sensitive assessment of the IDH1 and IDH2 mutation status in cerebral gliomas based on DNA pyrosequencing.** *Acta Neuropathol* 2010;119:501–07 CrossRef Medline
15. Riemenschneider MJ, Jeuken JWM, Wesseling P, et al. **Molecular diagnostics of gliomas: state of the art.** *Acta Neuropathol* 2010;120:567–84 CrossRef Medline
16. Iglesias JE, Liu CY, Thompson P, et al. **Robust brain extraction across datasets and comparison with publicly available methods.** *IEEE Trans Med Imaging* 2011;30:1617–34 CrossRef Medline
17. Kamnitsas K, Ledig C, Newcombe VF, et al. **Efficient multi-scale 3D CNN with fully connected CRF for accurate brain lesion segmentation.** *Med Image Anal* 2017;36:61–78 CrossRef Medline
18. Rathore S, Bakas S, Pati S, et al. **Brain Cancer Imaging Phenomics Toolkit (brain-CaPTk): an interactive platform for quantitative analysis of glioblastoma.** In: Crimi A, Bakas S, Kuijff H, et al, eds. *Brainlesion: Glioma, Multiple Sclerosis, Stroke and Traumatic Brain Injuries.* New York: Springer; 2017;10670:133–45 CrossRef
19. Kingsley PB. **Introduction to diffusion tensor imaging mathematics, Part III: tensor calculation, noise, simulations, and optimization.** *Concepts Magn Reson Part A* 2006;28A:155–79 CrossRef
20. Vallières M, Freeman CR, Skamene SR, et al. **A radiomics model from joint FDG-PET and MRI texture features for the prediction of lung metastases in soft-tissue sarcomas of the extremities.** *Phys Med Biol* 2015;60:5471–96 CrossRef Medline
21. Chalkidou A, O’Doherty MJ, Marsden PK. **False discovery rates in PET and CT studies with texture features: a systematic review.** *PLoS One* 2015;10:e0124165 CrossRef Medline
22. Zhou H, Vallières M, Bai HX, et al. **MRI features predict survival and molecular markers in diffuse lower-grade gliomas.** *Neuro Oncol* 2017;19:862–70 CrossRef Medline
23. Xing Z, Yang X, She D, et al. **Noninvasive assessment of IDH mutational status in World Health Organization grade II and III astrocytomas using DWI and DSC-PWI combined with conventional MR imaging.** *AJNR Am J Neuroradiol* 2017;38:1138–44 CrossRef Medline
24. Lee S, Choi SH, Ryou I, et al. **Evaluation of the microenvironmental heterogeneity in high-grade gliomas with IDH1/2 gene mutation using histogram analysis of diffusion-weighted imaging and dynamic-susceptibility contrast perfusion imaging.** *J Neurooncol* 2015;121:141–50 CrossRef Medline
25. Wasserman JK, Nicholas G, Yaworski R, et al. **Radiological and pathological features associated with IDH1–R132H mutation status and early mortality in newly diagnosed anaplastic astrocytic tumours.** *PLoS One* 2015;10:e0123890 CrossRef Medline
26. Fellah S, Caudal D, De Paula AM, et al. **Multimodal MR imaging (diffusion, perfusion, and spectroscopy): is it possible to distinguish oligodendroglial tumor grade and 1p/19q codeletion in the pretherapeutic diagnosis?** *AJNR Am J Neuroradiol* 2013;34:1326–33 CrossRef Medline
27. Lasocki A, Tsui A, Gaillard F, et al. **Reliability of noncontrast-enhancing tumor as a biomarker of IDH1 mutation status in glioblastoma.** *J Clin Neurosci* 2017;39:170–75 CrossRef Medline
28. Nakae S, Murayama K, Sasaki H, et al. **Prediction of genetic subgroups in adult supra tentorial gliomas by pre- and intraoperative parameters.** *J Neurooncol* 2017;131:403–12 CrossRef Medline
29. Qi S, Yu L, Li H, et al. **Isocitrate dehydrogenase mutation is associated with tumor location and magnetic resonance imaging characteristics in astrocytic neoplasms.** *Oncol Lett* 2014;7:1895–902 CrossRef Medline
30. Delfanti RL, Piccioni DE, Handwerker J, et al. **Imaging correlates for the 2016 update on WHO classification of grade II/III gliomas: implications for IDH, 1p/19q and ATRX status.** *J Neurooncol* 2017;135:601–09 CrossRef Medline
31. Patel SH, Poisson LM, Brat DJ, et al. **T2-FLAIR mismatch, an imaging biomarker for IDH and 1p/19q status in lower-grade gliomas: a TCGA/TCIA project.** *Clin Cancer Res* 2017;23:6078–85 CrossRef Medline
32. Broen MP, Smits M, Wijnenga MM, et al. **The T2-FLAIR mismatch sign as an imaging marker for non-enhancing IDH-mutant, 1p/19q-intact lower-grade glioma: a validation study.** *Neuro Oncol* 2018;20:1393–99 CrossRef Medline
33. Saito T, Muragaki Y, Maruyama T, et al. **Calcification on CT is a simple and valuable preoperative indicator of 1p/19q loss of heterozygosity in supratentorial brain tumors that are suspected grade II and III gliomas.** *Brain Tumor Pathol* 2016;33:175–82 CrossRef Medline
34. Tan W, Xiong J, Huang W, et al. **Noninvasively detecting Isocitrate dehydrogenase 1 gene status in astrocytoma by dynamic susceptibility contrast MRI.** *J Magn Reson Imaging* 2017;45:492–99 CrossRef Medline
35. Yamashita K, Hiwatashi A, Togao O, et al. **MR imaging–based analysis of glioblastoma multiforme: estimation of IDH1 mutation status.** *AJNR Am J Neuroradiol* 2016;37:58–65 CrossRef Medline
36. Choi C, Raisanen JM, Ganji SK, et al. **Prospective longitudinal analysis of 2-hydroxyglutarate magnetic resonance spectroscopy identifies broad clinical utility for the management of patients with IDH-mutant glioma.** *J Clin Oncol* 2016;34:4030–39 CrossRef Medline
37. Tietze A, Choi C, Mickey B, et al. **Noninvasive assessment of isocitrate dehydrogenase mutation status in cerebral gliomas by magnetic resonance spectroscopy in a clinical setting.** *J Neurosurg* 2018;128:391–98 CrossRef Medline

Widespread Increased Diffusivity Reveals Early Cortical Degeneration in Huntington Disease

F. Sampedro, S. Martínez-Horta, J. Perez-Perez, A. Horta-Barba, J. Martín-Lahoz, A. Alonso-Solís, I. Corripio, B. Gomez-Anson, and J. Kulisevsky



ABSTRACT

BACKGROUND AND PURPOSE: Huntington disease is a devastating genetic neurodegenerative disorder for which no effective treatment is yet available. Although progressive striatal atrophy is its pathologic hallmark, concomitant cortical deterioration is assumed to occur, but it is poorly characterized. Our objective was to study the loss of cortical integrity and its association with clinical indicators throughout the course of the disease.

MATERIALS AND METHODS: Using a cohort of 39 patients with Huntington disease and 25 controls with available MR imaging (TIWI and DTI), we compared cortical atrophy and intracortical diffusivity across disease stages. Intracortical diffusivity is a DTI-derived metric that has recently been suggested to detect incipient neuronal death because water can diffuse more freely in cortical regions with reduced neural density.

RESULTS: We observed progressive thinning and increasing diffusivity within the cerebral cortex of patients with Huntington disease ($P < .05$, corrected for multiple comparisons). Most important, in the absence of pronounced atrophy, widespread increased diffusivity was already present in individuals with premanifest Huntington disease, correlating, in turn, with clinical and disease-specific progression markers.

CONCLUSIONS: Intracortical diffusivity may be more sensitive than cortical thinning for tracking early neurodegeneration in Huntington disease. Moreover, our findings provide further evidence of an early cortical compromise in Huntington disease, which contributes to our understanding of its clinical phenotype and could have important therapeutic implications.

ABBREVIATIONS: CAG = cytosine-adenine-guanine; CN = healthy controls; Cth = cortical thickness; DBS = disease burden score; earlyHD = early-symptomatic HD; HD = Huntington disease; MD = mean diffusivity; midadvHD = middle-advanced HD; preHD = premanifest HD; SDMT = Symbol Digit Modalities Test; TMT = Trail-Making Test; UHDRS = Unified Huntington's Disease Rating Scale

Huntington disease (HD) is a fatal neurologic disorder with no effective treatment currently available. Inherited in an autosomal-dominant pattern, it is the most prevalent monogenic neurodegenerative disease. A cytosine-adenine-guanine (CAG) triplet repeat expansion in the *huntingtin gene* (*HTT*) drives a pathologic brain aggregation of mutant *huntingtin* protein, which promotes neuronal cell injury and death. Typically around the

fourth decade of life, HD gene mutation carriers experience progressive motor, cognitive, and neuropsychiatric alterations, resulting in a devastating loss of functional independence.¹ Although the pathologic hallmark of HD is a massive loss of the medium spiny neurons of the striatum, the current view of this disorder is that diffuse cortical and subcortical neurodegeneration underlies the clinical picture.²

Characterizing early brain degeneration in HD may prove critical to designing and monitoring novel therapeutic strategies to prevent or delay its clinical onset. Neuroimaging indicators hold great potential in this setting, but their sensitivity and interpretation need further assessment. In this vein, the study of individuals

Received January 29, 2019; accepted after revision July 7.

From the Movement Disorders Unit (F.S., S.M.-H., J.P.-P., A.H.-B., J.M.-L., J.K.), Neurology Department; Neuroradiology, Radiology Department (B.G.-A.); and Psychiatry Department (I.C.), Hospital de la Santa Creu i Sant Pau, Barcelona, Spain; Biomedical Research Institute (F.S., S.M.-H., J.P.-P., A.H.-B., J.M.-L., A.A.-S., I.C., J.K.), Barcelona, Spain; Centro de Investigación en Red-Enfermedades Neurodegenerativas (F.S., S.M.-H., J.P.-P., A.H.-B., J.M.-L., J.K.), Madrid, Spain; Universitat Autònoma de Barcelona (S.M.-H., J.P.-P., J.M.-L., B.G.-A., J.K.), Barcelona, Spain; European Huntington's Disease Network (S.M.-H., J.P.-P., A.H.-B., J.K.), Ulm, Germany; and Centro de Investigación Biomédica en Red-Salud Mental (I.C.), Madrid, Spain.

This study was partially funded by Fondo de Investigaciones Sanitarias (FIS) of the Instituto de Salud Carlos III (ISCIII) and Fondo Europeo de Desarrollo Regional (FEDER), Grant No. PI17/001885.

Please address correspondence to Jaime Kulisevsky, MD, PhD, Movement Disorders Unit, Neurology Department, Hospital de la Santa Creu i Sant Pau, Mas Casanovas 90-08041 Barcelona, Spain; e-mail: jkulisevsky@santpau.cat

Indicates open access to non-subscribers at www.ajnr.org

Indicates article with supplemental on-line tables.

<http://dx.doi.org/10.3174/ajnr.A6168>

with genetically confirmed-but-premanifest HD (preHD) offers a unique opportunity to evaluate the performance of imaging indicators in identifying early neurodegeneration. In contrast to pre-clinical subjects at risk for other neurodegenerative disorders, such as sporadic Alzheimer disease or Parkinson disease, individuals with premanifest HD will inevitably develop clinical symptoms in the upcoming years. Imaging indicators that best identify cortical and subcortical deterioration in subjects with premanifest HD would therefore be good candidates for use in clinical trials to noninvasively monitor early neurodegeneration.

In this context, MR imaging indicators are the best-suited approach to monitor disease progression because of their high-resolution and radiation-free acquisition. However, detecting subtle signs of early cortical deterioration with this technique may be challenging due to a number of technical and conceptual limitations of the most commonly used MR imaging indicators. Atrophy assessment via voxel-based morphometry (VBM) or cortical thickness (Cth), for example, is highly specific, but it may not be sufficiently sensitive to detect early neural loss.³ Second, white matter integrity estimated from diffusion tensor imaging does not directly assess the loss of cortical neurons, which is probably the main mechanism underlying cognitive and neuropsychiatric symptoms in neurodegenerative diseases. Third, clinical interpretation of functional MR imaging measures such as resting-state connectivity is challenging due to the complex nature of imaging indicators and the presence of compensatory mechanisms.

In view of these limitations, imaging markers capable of detecting early loss of neural tissue within the cerebral cortex need to be proposed and validated for the study of neurodegeneration. It was recently suggested that an increase in intracortical mean diffusivity (MD) of water molecules reflects early cortical compromise.^{4,5} Conceptually, an incipient degeneration of cortical neurons that do not yet translate into cortical thinning may be detected through a regional increase of water mobility due to the recent cell death. MD data can be derived from DTI scans, and in contrast to other DTI-derived metrics such as fractional anisotropy, regional MD is an adequate indicator of gray matter integrity due to its isotropic structure.⁴ Moreover, this measure has recently shown higher effect sizes and increased sensitivity in identifying cortical degeneration in other neurodegenerative diseases.⁵

In this work, we characterized intracortical MD and atrophy changes across HD stages. Our main objective was to investigate whether MD abnormalities precede atrophy detection. Our secondary objective was to study the possible associations between these imaging alterations and the patients' motor, cognitive, and neuropsychiatric statuses.

MATERIALS AND METHODS

Participants and Clinical Assessments

We included 39 HD gene-mutation carriers (CAG \geq 39) from the outpatient clinic of the Movement Disorders Unit at Hospital de la Santa Creu i Sant Pau (Barcelona, Spain). Within this HD group, participants were classified as having preHD, early-symptomatic HD (earlyHD), or middle-advanced HD (midadvHD) according to previously defined criteria.⁶⁻⁸ Individuals with a Unified Huntington's Disease Rating Scale (UHDRS) Total

Motor Score of $<$ 5 and a diagnostic confidence level of $<$ 3 were classified as having preHD. Patients showing a Total Motor Score of \geq 5, a diagnostic confidence level of 4, and a Total Functional Capacity Scale score between 11 and 13 were classified as having earlyHD, and those showing a Total Functional Capacity Scale score of $<$ 11 were combined to form a midadvHD group. We also included 25 healthy controls (CN) who had no family history of movement or psychiatric disorders. This CN group had an age distribution similar to that of the preHD group because the imaging comparison between CN and preHD would be key to evaluating the sensitivity of early markers of neurodegeneration.

We recorded demographic, motor, cognitive, neuropsychiatric, and disease-specific indicators for all HD participants. We used the disease burden score (DBS), defined as age \times (CAG 35.5) as an index of the burden of pathology due to lifetime exposure to mutant huntingtin.⁹ In subjects with premanifest HD, the estimated years to clinical onset can be obtained by the formula described in Langbehn et al.¹⁰ Functional capacity, motor symptoms, and global cognitive status were recorded using the UHDRS. We also addressed the severity of apathy, the most prevalent and characteristic neuropsychiatric feature of HD.⁶ Last, we administered the UHDRS cognitive subtest with additional cognitive tasks. We recorded the following set of cognitive indicators, known to be sensitive to HD progression: the Symbol Digit Modalities Test (SDMT), the Stroop Task, the Trail-Making Test (TMT), the F-A-S verbal fluency test, and semantic fluency.¹¹

Neuroimaging Acquisition and Methods

Volumetric MR imaging and DTI were available for all participants. 3D-T1 images were acquired on a 3T Achieva scanner (Philips Healthcare, Best, the Netherlands) using an MPRAGE sequence (TR/TE = 6.74/3.14 ms, flip angle = 8°, FOV = 23 cm, matrix = 256 \times 256, and slice thickness = 1 mm). DTI scans were also obtained using the following acquisition parameters: TR = 10,433 ms, TE = 57 ms, slice thickness = 2 mm, flip angle = 90°, 15 directions, b factor = 800.

For each participant, we quantified cortical thickness and intracortical diffusivity. Cortical thickness analysis was performed using the FreeSurfer 6.0 software package (<http://surfer.nmr.mgh.harvard.edu>). The specific methods used for cortical reconstruction of volumetric images have been fully described elsewhere.¹² Briefly, optimized surface-deformation models following intensity gradients accurately identify white matter and gray matter boundaries in the cerebral cortex, from which cortical thickness is computed at each vertex. On visual inspection, no major surface reconstruction errors were observed in our sample. Mean diffusivity maps were computed from DTI scans and aligned to the associated T1-weighted image using the FreeSurfer module Tracula (<https://surfer.nmr.mgh.harvard.edu/fswiki/FsTutorial/Tracula>).¹³ To study differences in MD across groups, we first used the FreeSurfer's partial volume correction (PVC) tools to account for a possible volume fraction effect (i.e. concomitant atrophy). We then sampled intracortical MD values half-way between the white and pial surfaces of the cortical ribbon, thereby obtaining surface-based vertex-wise MD data along the cerebral cortex. By definition, Cth and intracortical MD can only be measured in cortical regions. In subcortical regions, we also computed

Clinical and demographic information across groups^a

	CN	HD	PreHD	EarlyHD	MidadvHD	P Value
No.	25	39	15	16	8	
Age (yr)	38.6 ± 9.4	47.8 ± 13.6	37.8 ± 10.9	55.0 ± 11.8	52.3 ± 10.4	.004, ^b .81, ^c <.001, ^d .57 ^e
Female sex (%)	36%	69%	80%	56%	75%	.01, .01, .16, .37
Education (yr)	12.1 ± 1.9	13.4 ± 5.7	16.4 ± 3.2	11.1 ± 5.2	12.5 ± 6.5	.24, <.001, .002, .61
CAG length	NA	43.1 ± 2.9	43.1 ± 2.9	42.6 ± 2.9	43.8 ± 2.9	NA, NA, .59, .31
DBS ^f	NA	339.6 ± 105.3	273.3 ± 108.9	364.5 ± 78.2	414.4 ± 78.1	NA, NA, .01, .15
Estimated yr to onset ^g	NA	NA	15.8 ± 7.8	NA	NA	
TFC	NA	11.3 ± 3.0	12.9 ± 0.2	12.1 ± 0.9	6.4 ± 3.5	NA, NA, .004, <.001,
UHDRS-TMS	NA	20.6 ± 20.7	1.4 ± 1.5	23.6 ± 14.2	50.5 ± 8.3	NA, NA, <.001, <.001,
UHDRS-Cogscore	NA	220.6 ± 112.8	323.9 ± 48.4	189.4 ± 66.1	65.8 ± 60.2	NA, NA, <.001, <.001,
Apathy score ^h	NA	4.9 ± 5.3	2.5 ± 3.7	4.6 ± 5.4	9.8 ± 4.7	NA, NA, = .2, .03
FAS	NA	28.5 ± 17.3	43.6 ± 12.4	22.7 ± 12.3	9.7 ± 6.4	NA, NA, <.001, .01
SDMT	NA	35.1 ± 20.1	54.7 ± 8.4	27.7 ± 12.9	9.8 ± 8.1	NA, NA, <.001, .001
Semantic fluency	NA	16.4 ± 7.0	23.0 ± 4.2	14.3 ± 3.5	7.1 ± 3.3	NA, NA, <.001, .001
Stroop Color	NA	51.6 ± 28.9	75.5 ± 20.6	44.3 ± 17.8	16.8 ± 19.5	NA, NA, <.001, .01
Stroop Word	NA	71.9 ± 34.5	99.2 ± 19.1	68.1 ± 21.7	22.0 ± 22.4	NA, NA, <.001, .001
TMT (parts B-A)	NA	-4.6 ± 8.0	0.3 ± 0.7	-3.6 ± 5.1	-17.6 ± 8.5	NA, NA, .008, .004
TMT cognitive flexibility	NA	1.5 ± 1.4	1.1 ± 1.1	2.0 ± 1.4	1.0 ± 1.4	NA, NA, .07, .15

Note:—NA indicates not available; TFC, Total Functional Capacity; TMS, Total Motor Score; Cogscore, Cognitive Score; FAS, F-A-S test of verbal fluency.

^a Values are expressed as mean ± standard deviation.

^b CN vs HD.

^c CN vs preHD.

^d PreHD vs earlyHD.

^e EarlyHD vs midadvHD.

^f DBS = 9.

^g Derived from 10.

^h Derived from 23.

volume information and average MD values in common subcortical structures (caudate, putamen, accumbens, pallidum, amygdala, thalamus, and hippocampus).

Statistical Analyses

We compared clinical, sociodemographic, and scalar subcortical volumetric and MD data across groups using 2-sample *t* test analysis for continuous variables and the χ^2 test for categorical variables. Differences were considered significant using a probability value < .05.

Cortical vertex-wise measures (Cth and MD) were first smoothed using a Gaussian kernel of 10-mm full width at half maximum to increase the signal-to-noise ratio. A generalized linear model was then performed to compare these measures across groups, using age, sex, and education as covariates of no interest. Clusters surviving $P < .05$ and family-wise error correction for multiple comparison by a Monte Carlo simulation with 10,000 repeats were considered significant.

Finally, aiming to investigate the clinical translation of the imaging findings, we computed mean atrophy and MD values at the identified cortical clusters and subcortical regions showing significant differences across groups. Using Pearson correlation coefficients, we then studied the association of these imaging measures with clinical indicators within an exploratory analysis, for which a $P < .05$ was considered significant.

RESULTS

The Table summarizes the demographic, clinical, and neuropsychological characteristics of all participants.

A clinical decay in motor, cognitive, and neuropsychiatric indicators was observed across HD stages. Patients with premanifest HD were younger than those with manifest HD, but differences in genetic burden across HD groups were not significant.

The Figure shows cortical thickness and intracortical MD differences across HD groups with respect to the CN group.

Progressive cortical thinning and increasing diffusivity were observed across HD stages. However, MD alterations were more pronounced and more extensive than atrophic differences in all HD groups. In the preHD group, whereas only 3 relatively small atrophic clusters were shown (left caudal middle frontal, left inferior-parietal, and right inferior-temporal), diffusivity was increased in precentral, rostral middle and superior-frontal, entorhinal, posterior cingulate/precuneus, superior-temporal, insula, bankssts region, and inferior-parietal and postcentral regions. Patients with earlyHD showed widespread cortical thinning and increased MD. The following regions showed cortical thinning with the highest significance ($P < .005$ family-wise error): superior-frontal/temporal-parietal, inferior-temporal/parietal, postcentral, cingulate isthmus, and supramarginal gyrus. In contrast, the most significant increases in MD were found in caudal middle frontal, orbitofrontal, precentral, pericalcarine, cuneus, precuneus, and superior-temporal/-parietal regions. In particular, MD increases in the absence of Cth differences in patients with earlyHD were observed in the following regions: superior-frontal gyri, occipital and entorhinal cortices, and temporal poles. Regarding patients with midadvHD, because atrophy and increased MD were widespread throughout the cerebral cortex, no further explorations were performed.

On-line Table 1 shows volumetric and MD information in common subcortical structures across groups.

Progressive atrophy and increasing diffusivity were observed in most subcortical structures across CN, preHD, earlyHD, and midadvHD groups. While these changes were most pronounced in the striatum, other important structures such as the thalamus, hippocampus, and amygdala were also involved. Similar signifi-

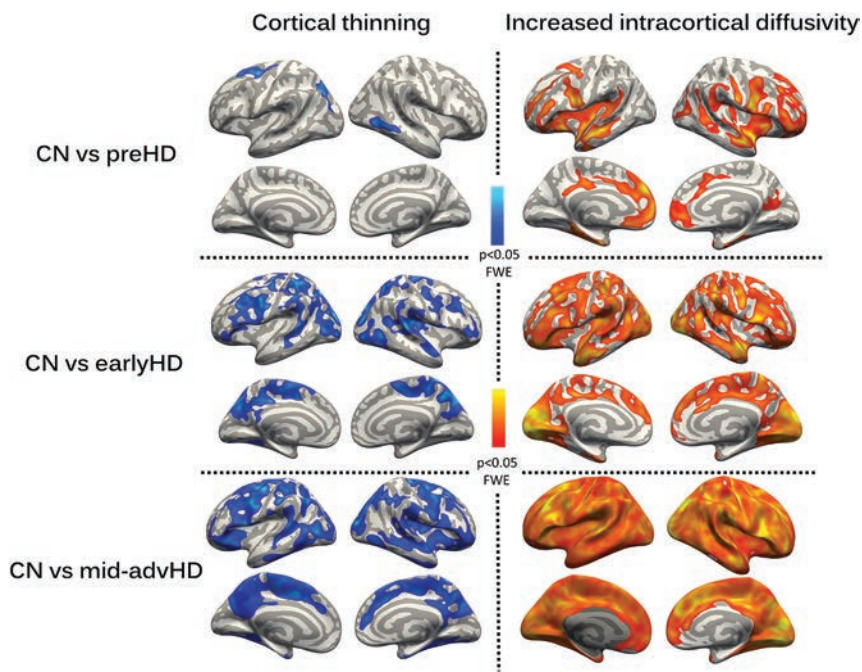


FIGURE. Differences in intracortical MD and cortical thickness across HD stages with respect to CN, using age, sex, and education as covariates of no interest ($P < .05$ family-wise error).

cant differences were found across groups in terms of subcortical volumetric and MD measures. Patients with preHD showed lower subcortical volumes than CN in all the regions considered. They also showed increased MD in all these regions except in the pallidum, left amygdala, right accumbens, and right thalamus. Patients with earlyHD showed lower subcortical volumes than those with preHD except for the left accumbens, bilateral amygdala, and bilateral thalamus and hippocampus; and subcortical diffusivity was increased in the striatum and left thalamus.

Finally, On-line Table 2 illustrates a set of exploratory correlations between imaging indicators and clinical information within the preHD and earlyHD groups. CN and midadvHD were not considered in this analysis due to missing information and massive atrophic and clinical deterioration, respectively. In On-line Table 3, these correlations were controlled for caudate atrophy to identify independent contributions of cortical degeneration to clinical indicators.

Diffusivity abnormalities showed good correlations with pre-clinical indicators of disease progression (DBS, estimated years to onset) and also with motor, cognitive, and neuropsychiatric status. Volumetric and Cth degeneration showed a much lower number of significant associations with clinical indicators, especially within the preHD group. Topographically, clinical-imaging associations were not restricted to frontostriatal territories. Even after controlling for caudate atrophy, significant clinical-imaging correlations were found in a large number of frontotemporo-parieto-occipital clusters and extrastriatal subcortical regions (eg, thalamus, hippocampus).

DISCUSSION

In this work, we characterized cortical microstructural changes across Huntington disease stages using intracortical diffusivity, a promising image-derived indicator of early neurodegeneration

within the cerebral cortex. We found that clinical deterioration in this population concurred with progressive cortical thinning and increases in diffusivity. Additionally, as expected, concomitant subcortical impairment along disease stages was also revealed by both imaging modalities.

Of particular note among our findings was the widespread increase in intracortical diffusivity that was already evidenced in individuals with premanifest HD with respect to the control group, even in regions with preserved cortical thickness. This imaging indicator has been suggested to reflect an incipient neural loss within the cerebral cortex.⁴ Most important, MD values at the identified cortical regions correlated with inherent markers of disease progression (DBS, estimated years to onset) and with motor and cognitive measures. From an imaging perspective, because cortical thinning was not detected in

most of these regions, these results suggest that intracortical MD may outperform Cth at tracking early cortical neurodegeneration in HD. In addition, because both subcortical MD and volumetric information appropriately characterized disease progression in our sample, MD indicators show the potential for use in clinical trials. Furthermore, the fact that we observed a substantial cortical compromise in patients with earlyHD strongly suggests that future neuroimaging studies should look beyond subcortical alterations because analyses only restricted to those regions (such as¹⁴⁻¹⁶) may overlook some important contributions of cortical degeneration in the HD phenotype.

From a clinical point of view, identifying early cortical and subcortical degeneration beyond frontostriatal territories might contribute to a better understanding of clinical manifestations in HD. We observed an association between cognitive performance (UHDRS-Cognitive Score, Stroop, and SDMT) and imaging indicators in key brain regions such as the entorhinal cortex, precuneus, and hippocampus. Most important, the compromise of these key brain regions was previously evidenced in the neuroimaging analyses. These results suggest that even in early disease stages, the ongoing neurodegeneration in HD impacts important brain circuitry beyond frontostriatal areas. In this vein, this early cortical microstructural compromise probably leads to functional connectivity or white matter abnormalities, which have been previously related to clinical manifestations in HD.¹⁷⁻¹⁹ Taken together, our findings reinforce the need to consider HD as a whole-brain neurodegenerative disease even from its early stages, as evidenced by the diffuse cortical damage observed in individuals with premanifest HD. Most interesting, early cortical deterioration may underlie the onset of cognitive and neuropsychiatric symptoms in HD.

From a biologic perspective, a first point to note is that we did not find imaging evidence of neuroinflammation in HD because

no brain region showed a decrease in cortical diffusivity.^{20,21} Nevertheless, the specific pathologic mechanisms responsible for early cortical damage in HD need further assessment. In this context, PET imaging using *mutant huntingtin* tracers could help to disentangle whether this abnormal protein aggregates and damages the cerebral cortex or whether cortical deterioration is driven by a parallel and partially independent pathologic pathway.²²

The main strength of this study is the use of a multimodal surface-based imaging approach that includes PVC-MD assessment, a promising indicator of early cortical degeneration. Additionally, we were able to characterize the clinical-imaging continuum of a well-characterized HD sample.

The study has 2 main limitations, the first of which is the relatively low number of patients and a control group that lacked a detailed cognitive assessment. The second limitation is that cross-sectionality and exploratory clinical-imaging correlations could hinder the interpretation of our results.

CONCLUSIONS

The early widespread increase in diffusivity within the cerebral cortex of patients with HD correlated with clinical indicators of disease progression. Our results provide further evidence of concomitant corticostriatal degeneration in HD, which contributes to our understanding of its phenotype and may have clinical and therapeutic implications.

ACKNOWLEDGMENTS

The authors wish to thank the study team and all the study participants and their families.

Disclosures: Jesus Perez-Perez—RELATED: Grant: Fondo de Investigaciones Sanitarias de España Spanish Government, Carlos III Health Institute. Comments: This study was partially funded by Fondo de Investigaciones Sanitarias de España Spanish Government grant No. PI17/001885*. UNRELATED: Grants/Grants Pending: Fondo de Investigaciones Sanitarias de España Spanish Government, Carlos III Health Institute. Comments: I am the Principal Investigator of grant No. PI17/001885.*Money paid to the institution.

REFERENCES

1. Walker FO. **Huntington's disease.** *Lancet* 2007;369:218–28 CrossRef Medline
2. McColgan P, Tabrizi SJ. **Huntington's disease: a clinical review.** *Eur J Neurol* 2018;25:24–34 CrossRef Medline
3. Haller S, Kekardaki A, Delaloye C, et al. **Combined analysis of grey matter voxel-based morphometry and white matter tract-based spatial statistics in late-life bipolar disorder.** *J Psychiatry Neurosci* 2011;36:391–401 CrossRef Medline
4. Weston PSJ, Simpson IJA, Ryan NS, et al. **Diffusion imaging changes in grey matter in Alzheimer's disease: a potential marker of early neurodegeneration.** *Alzheimers Res Ther* 2015;7:47 CrossRef Medline
5. Illán-Gala I, Montal V, Borrego-Écija S, et al; Catalan Frontotemporal Dementia Initiative (CATFI) and the Frontotemporal Lobar Degeneration Neuroimaging Initiative (FTLDNI). **Cortical microstructure in the behavioural variant of frontotemporal dementia: looking beyond atrophy.** *Brain* 2019;142:1121–33 CrossRef Medline

6. Martinez-Horta S, Perez-Perez J, van Duijn E, et al; Spanish REGISTRY investigators of the European Huntington's Disease Network. **Neuropsychiatric symptoms are very common in premanifest and early stage Huntington's disease.** *Parkinsonism Relat Disord* 2016;25:58–64 CrossRef Medline
7. Tabrizi SJ, Langbehn DR, Leavitt BR, et al; TRACK-HD investigators. **Biological and clinical manifestations of Huntington's disease in the longitudinal TRACK-HD study: cross-sectional analysis of baseline data.** *Lancet Neurol* 2009;8:791–801 CrossRef Medline
8. Shoulson I, Fahn S. **Huntington disease: clinical care and evaluation.** *Neurology* 1979;29:1–3 CrossRef Medline
9. Penney JB Jr, Vonsattel JP, MacDonald ME, et al. **CAG repeat number governs the development rate of pathology in Huntington's disease.** *Ann Neurol* 1997;41:689–92 CrossRef Medline
10. Langbehn DR, Hayden M, Paulsen JS; PREDICT-HD Investigators of the Huntington Study Group. **CAG-repeat length and the age of onset in Huntington disease (HD): a review and validation study of statistical approaches.** *Am J Med Genet B Neuropsychiatr Genet* 2010;153B:397–408 CrossRef Medline
11. Terwindt PW, Hubers AA, Giltay EJ, et al. **Screening for cognitive dysfunction in Huntington's disease with the clock drawing test.** *Int J Geriatr Psychiatry* 2016;31:1013–20 CrossRef Medline
12. Fischl B, Dale AM. **Measuring the thickness of the human cerebral cortex from magnetic resonance images.** *Proc Natl Acad Sci U S A* 2000;97:11050–55 CrossRef Medline
13. Yendiki A, Panneck P, Srinivasan P, et al. **Automated probabilistic reconstruction of white-matter pathways in health and disease using an atlas of the underlying anatomy.** *Front Neuroinform* 2011;5:23 CrossRef Medline
14. Niccolini F, Pagano G, Fusar-Poli P, et al. **Striatal molecular alterations in HD gene carriers: a systematic review and meta-analysis of PET studies.** *J Neurol Neurosurg Psychiatry* 2018;89:185–96 CrossRef Medline
15. Hobbs NZ, Barnes J, Frost C, et al. **Onset and progression of pathologic atrophy in Huntington disease: a longitudinal MR imaging study.** *AJNR Am J Neuroradiol* 2010;31:1036–41 CrossRef Medline
16. Aylward EH, Rosenblatt A, Field K, et al. **Caudate volume as an outcome measure in clinical trials for Huntington's disease: a pilot study.** *Brain Res Bull* 2003;62:137–41 CrossRef Medline
17. Gregory S, Scahill RI, Seunarine KK, et al. **Neuropsychiatry and white matter microstructure in Huntington's disease.** *J Huntingtons Dis* 2015;4:239–49 CrossRef Medline
18. Wolf RC, Sambataro F, Vasic N, et al. **Default-mode network changes in preclinical Huntington's disease.** *Exp Neurol* 2012;237:191–98 CrossRef Medline
19. Klöppel S, Stonnington CM, Petrovic P, et al. **Irritability in pre-clinical Huntington's disease.** *Neuropsychologia* 2010;48:549–57 CrossRef Medline
20. Montal V, Vilaplana E, Alcolea D, et al. **Cortical microstructural changes along the Alzheimer's disease continuum.** *Alzheimers Dement* 2018;14:340–51 CrossRef Medline
21. Gispert JD, Suárez-Calvet M, Monté GC, et al. **Cerebrospinal fluid STREM2 levels are associated with gray matter volume increases and reduced diffusivity in early Alzheimer's disease.** *Alzheimers Dement* 2016;12:1259–72 CrossRef Medline
22. Simmons DA, James ML, Belichenko NP, et al. **TSPO-PET imaging using [18F]PBR06 is a potential translatable biomarker for treatment response in Huntington's disease: preclinical evidence with the p75NTR ligand LM11A-31.** *Hum Mol Genet* 2018;27:2893–912 CrossRef Medline

Usefulness of the Delay Alternating with Nutation for Tailored Excitation Pulse with T1-Weighted Sampling Perfection with Application-Optimized Contrasts Using Different Flip Angle Evolution in the Detection of Cerebral Metastases: Comparison with MPRAGE Imaging

 D. Kim,  Y.J. Heo,  H.W. Jeong,  J.W. Baek,  J.-Y. Han,  J.Y. Lee,  S.-C. Jin, and  H.J. Baek

ABSTRACT

BACKGROUND AND PURPOSE: Contrast-enhanced T1-weighted sampling perfection with application-optimized contrasts by using different flip angle evolution (SPACE) with the delay alternating with nutation for tailored excitation (DANTE) pulse could suppress the blood flow signal and provide a higher contrast-to-noise ratio of enhancing lesion-to-brain parenchyma than the MPRAGE sequence. The purpose of our study was to evaluate the usefulness of SPACE with DANTE compared with MPRAGE for detecting brain metastases.

MATERIALS AND METHODS: Seventy-one patients who underwent contrast-enhanced SPACE with DANTE and MPRAGE sequences and who were suspected of having metastatic lesions were included. Two neuroradiologists determined the number of enhancing lesions, and diagnostic performance was evaluated using figure of merit, sensitivity, positive predictive value, interobserver agreement, and reading time. Contrast-to-noise ratio_{lesion/parenchyma} and contrast-to-noise ratio_{white matter/gray matter} were also assessed.

RESULTS: SPACE with DANTE (observer one, 328; observer two, 324) revealed significantly more small (<5 mm) enhancing lesions than MPRAGE (observer one, 175; observer two, 150) ($P < 0.001$ for observer 1, $P \leq .0001$ for observer 2). Furthermore, SPACE with DANTE showed significantly higher figure of merit and sensitivity and shorter reading time than MPRAGE for both observers. The mean contrast-to-noise ratio_{lesion/parenchyma} of SPACE with DANTE (52.3 ± 43.1) was significantly higher than that of MPRAGE (17.5 ± 19.3) ($P \leq .0001$), but the mean contrast-to-noise ratio_{white matter/gray matter} of SPACE with DANTE (-0.65 ± 1.39) was significantly lower than that of MPRAGE (3.08 ± 1.39) ($P \leq .0001$).

CONCLUSIONS: Compared with MPRAGE, SPACE with DANTE significantly improves the detection of brain metastases.

ABBREVIATIONS: CE = contrast-enhanced; CNR = contrast-to-noise ratio; DANTE = delay alternating with nutation for tailored excitation; FOM = figure of merit; JAFROC = jackknife free-response receiver operating characteristic; SPACE = sampling perfection with application-optimized contrasts by using different flip angle evolution

The incidence and prevalence of brain metastases are increasing due to their early detection using advanced imaging techniques and median survival is increasing because of improved therapies.¹ Accurate diagnosis of brain metastasis before treatment is important because therapeutic planning is dependent on the presence and number of metastatic lesions. Early detection of brain metastases is also important for prognosis because the local control rate is significantly higher for small metastatic lesions

(<10-mm diameter) treated using radiosurgery.^{2,3} Contrast-enhanced (CE) 3D T1-weighted scanning shows higher sensitivity than 2D T1-weighted enhanced scanning for the detection of small brain metastases and has been used more frequently for the evaluation of brain metastases.^{4,5}

The 3D CE T1-weighted images provide submillimeter resolution and are appropriate for the evaluation of small metastases. However, 3D CE gradient-echo images have a limitation that may mimic the normal enhancing vessels as small metastatic lesions, particularly in regions close to the cortices or sulci.⁶ In contrast to 3D gradient-echo images, 3D CE spin-echo images incorporate blood suppression and make it easy to differentiate blood signals from enhanced tumors, particularly for small lesions.⁷⁻⁹ Thus, 3D spin-echo images demonstrate contrast-enhancing lesions more clearly than gradient-echo images, resulting in improved detection.¹⁰

However, sampling perfection with application-optimized contrasts by using different flip angle evolution (SPACE se-

Received February 22, 2019; accepted after revision June 27.

From the Departments of Radiology (D.K., Y.J.H., H.W.J., J.W.B., J.-Y.H.), and Internal Medicine (J.Y.L.), Inje University Busan Paik Hospital, Busan, Korea; Department of Neurosurgery (S.-C.J.), Inje University Haeundae Paik Hospital, Busan, Republic of Korea; and Department of Radiology (H.J.B.), Gyeongsang National University School of Medicine and Gyeongsang National University Changwon Hospital, Changwon, Republic of Korea.

Please address correspondence to Young Jin Heo, MD, Department of Radiology, Inje University Busan Paik Hospital, Bokji-ro 75, Busanjin-Gu, Busan, Republic of Korea, 47392; e-mail: youngjin726@hanmail.net

<http://dx.doi.org/10.3174/ajnr.A6158>

quence; Siemens, Erlangen, Germany) alone is not sufficient for evaluation of enhancing lesions because residual blood signals can occasionally be mistaken for these lesions. Thus, black-blood imaging has been used to nullify the signal of blood flow in the evaluation of brain metastases. A few studies^{9,11,12} using black-blood imaging have shown improved diagnostic performance for the detection of brain metastases due to a higher contrast-to-noise ratio (CNR). A 3D black-blood imaging method, delay alternating with nutation for tailored excitation (DANTE), is an advanced technique. It can suppress the residual blood flow, which is incompletely suppressed by SPACE.¹³ No previous study has used the DANTE preparation pulse in the evaluation of brain metastasis, to our knowledge. We hypothesized that the combination of DANTE preparation and the inherent black-blood effect due to SPACE may be advantageous for the detection of contrast-enhancing lesions in the brain parenchyma. Thus, the purpose of our study was to evaluate the usefulness of SPACE with DANTE in the detection of brain metastases compared with MPRAGE imaging.

MATERIALS AND METHODS

Patient Population

This study was approved by the institutional review board of Inje University Busan Paik Hospital, and the need for informed consent was waived. Between May 2018 and January 2019, three hundred fifty-eight patients with pathologically-proved primary cancer underwent 3D CE T1-weighted MR imaging using the SPACE with DANTE and MPRAGE sequences in the same imaging session for evaluation of brain metastases. The diagnoses of the brain metastases were based on previous and follow-up MR imaging findings determined in consensus by 2 experienced neuroradiologists, one with 19 years and one with 4 years of experience in neuroimaging, who did not participate in image analysis. Brain metastases were determined according to the following criteria: 1) newly occurring enhancing lesions or an increase in size of the existing lesions at follow-up MR imaging or a decrease in size or disappearance after treatment; 2) what appeared as a lesion not being a normal enhancing structure or an artifact; and 3) contrast-enhancing lesions located in the brain parenchyma. Contrast-enhancing lesions that were visualized on only 1 sequence were also evaluated. We considered these as false-positive lesions, and the possible causes were recorded. Patients who exhibited no enhancing lesions ($n = 200$), those who exhibited enhancing lesions but did not undergo follow-up MR imaging ($n = 58$), and those who had leptomeningeal metastasis ($n = 29$) were excluded. Finally, 71 patients with a mean age of 64.3 years (age range, 40–84 years; 46 men and 25 women) were included. The diagnoses of primary tumors were lung cancer ($n = 53$), breast cancer ($n = 8$), colon cancer ($n = 2$), prostate cancer ($n = 2$), renal cell cancer ($n = 1$), gastric cancer ($n = 1$), ovarian cancer ($n = 1$), endometrial cancer ($n = 1$), uterine cervix cancer ($n = 1$), and external auditory canal tumor ($n = 1$); 540 enhancing lesions were designated as brain metastases, and 28 enhancing lesions were detected on either of the two 3D-enhanced sequences. The median interval between the initial and follow-up MR imaging was 115.0 days (range, 26–2061 days).

MR Imaging Protocol

All studies were performed using a 3T MR imaging scanner (Magnetom Skyra; Siemens, Erlangen, Germany) and a 64-channel head coil. After we obtained routine precontrast images using axial fluid-attenuated inversion recovery, T2-weighted, T1-weighted, gradient-echo, 3D SPACE, and 3D MPRAGE images with fat suppression were obtained immediately following intravenous administration of 0.1 mmol/kg body weight of Dotarem (gadoterate meglumine; Guerbet, Aulnay-sous-Bois, France). The scan parameters of postcontrast MR imaging were as follows for SPACE with DANTE imaging: TR, 800 ms; TE, 15 ms; flip angle, variable; fat suppression, Fat-Sat (chemical shift selective suppression); parallel acquisition techniques factor, 2; FOV, 230 × 230; bandwidth, 422 Hz/pixel; matrix, 320 × 320; number of slices, 240; echo spacing, 4.88 ms; voxel size, 0.72 × 0.72 × 0.72 mm; scan time, 5 minutes 54 seconds; DANTE preparation pulse were applied; for MPRAGE imaging: TR, 2200 ms; TE, 3.05 ms; flip angle, 9°; fat suppression, water excitation; parallel acquisition techniques factor, 2; FOV, 230 × 230; bandwidth, 260 Hz/pixel; matrix, 320 × 320; number of slices, 240; echo spacing, 8.8 ms; voxel size, 0.72 × 0.72 × 0.72 mm; flip angle, 9°; scan time, 5 minutes 32 seconds. We obtained sagittal planes covering the whole brain for the SPACE and MPRAGE imaging to reduce the scan time. We performed SPACE with DANTE and MPRAGE sequences in alternative order by random distribution to avoid timing bias, which can increase contrast agent uptake due to the delay after injection. The order of sequences was the following: SPACE with DANTE followed by MPRAGE in 32 patients and MPRAGE followed by SPACE with DANTE in 39 patients.

Image Analysis

Determination of Metastatic Lesions. Two neuroradiologists, one with 5 years of experience and one with 1 year of experience in neuroimaging, independently evaluated the presence of brain metastases using SPACE with DANTE and MPRAGE imaging with a 4-week interval to minimize any learning bias. One observer evaluated SPACE with DANTE followed by MPRAGE, and another observer evaluated MPRAGE followed by SPACE with DANTE. Both observers reported all enhancing lesions in the brain parenchyma, except for the normal anatomic structures or artifacts. The metastatic lesions were classified into 2 groups by lesion size: large (≥ 5 mm) and small (≤ 5 mm). Both observers also reported the level of confidence of metastatic lesions at each location on a rating scale (ranging from a lowest confidence level of 0 to a highest confidence level of 100), and the reading time of each case was recorded.

Evaluation of Image Quality. We evaluated and compared the CNR of lesions with normal parenchyma ($CNR_{\text{lesion/parenchyma}}$) and the CNR of white matter with gray matter ($CNR_{\text{white matter/gray matter}}$) among the SPACE with DANTE and MPRAGE images. For evaluation of $CNR_{\text{lesion/parenchyma}}$, we selected homogeneous, solid enhancing lesions of >5 mm and excluded rimlike enhancing lesions due to the difficulty in drawing the ROI. The CNR of enhancing lesions was calculated according to Kammer et al⁶:

$$CNR_{\text{lesion/parenchyma}} = (SI_{\text{lesion}} - SI_{\text{parenchyma}}) / SD_{\text{parenchyma}}$$

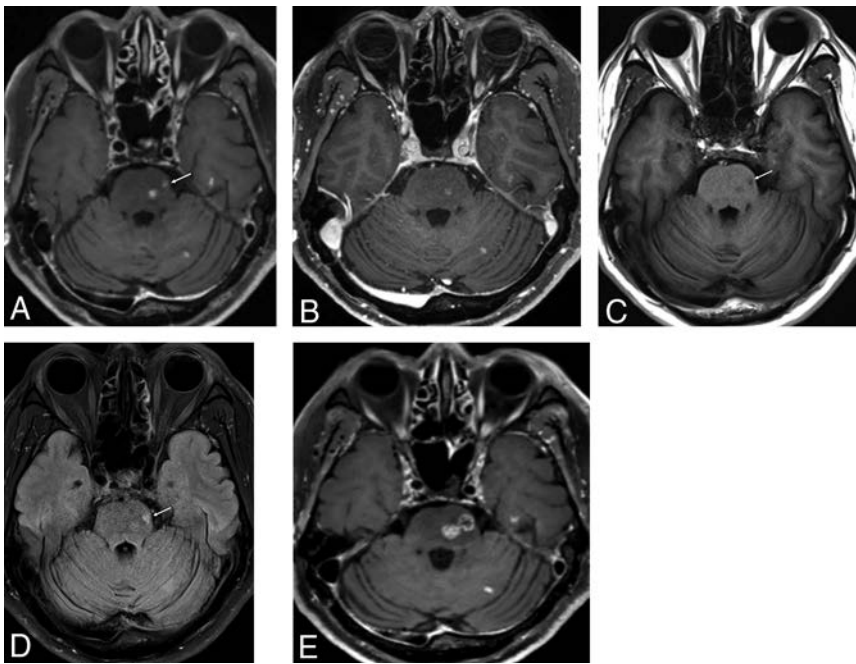


FIG 1. MR images of a 62-year-old male patient with lung cancer. Contrast-enhanced SPACE with DANTE (A) clearly shows a focal enhancing lesion in the left pons (arrow), but this is barely visible in MPRAGE (B). However, this lesion was accompanied by signal changes in the precontrast 2D T1-weighted (C) and FLAIR images (D) and an increase in size on follow-up MR imaging after 3 months (E).

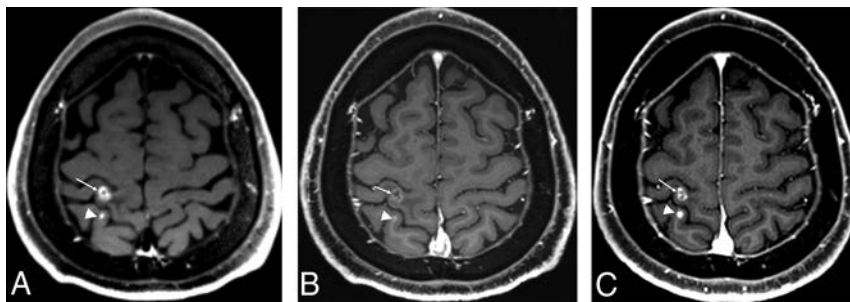


FIG 2. MR images of a 54-year-old male patient with lung cancer. Contrast-enhanced SPACE with DANTE (A) clearly shows two enhancing lesions in the right parietal lobe (arrow and arrowhead). One enhancing lesion is clearly visible (arrow), but the other enhancing lesion at the posterior aspect (arrowhead) is poorly visible on MPRAGE (B). However, this lesion has increased (arrowhead) in size and shows increased enhancement on the follow-up MR imaging 3 months later (C).

We calculated the CNR for differentiating the gray and white matter as follows:

$$\text{CNR}_{\text{white matter/gray matter}} = (\text{SI}_{\text{white matter}} - \text{SI}_{\text{gray matter}}) / \text{SD}_{\text{white matter}}$$

Here, SI denotes the mean signal intensity of the ROI, and SD denotes the standard deviation of noise. To the extent possible, we endeavored to ensure identical size and location while drawing the ROI of each sequence, with side-by-side comparison of the two 3D-enhanced sequences and occasional use of zooming. For determining the SI and SD of the parenchyma, the ROIs were placed in the adjacent parenchyma because of inhomogeneous noise distribution in parallel imaging¹⁴ and included both white matter and gray matter. The ROIs of white matter were placed at the genu of the corpus callosum, and the ROIs of gray matter were placed at the head of the normal caudate nucleus. Every ROI of normal parenchyma, white matter, and gray matter measured

22.73 mm². Every ROI of enhancing lesions was placed at the center of the lesion, to the extent possible, by 1 neuroradiologist (one with 5 years of experience), and the area of the ROI was dependent on lesion size, varying between 3.72 and 22.73 mm².

Statistical Analysis

All statistical analyses were performed using SAS, Version 9.4 (SAS Institute, Cary, North Carolina). The variables are presented as number or mean \pm SD. For evaluation of the diagnostic performance of each observer in each reading session, we used figure of merit (FOM) derived from the jackknife free-response receiver operating characteristic (JAFROC) analysis with method 1 of Chakraborty and Berbaum.^{11,12,15,16} A free software JAFROC analysis package is available at <http://www.devchakraborty.com>. The paired *t* test was used to compare the number of lesions, CNR, and reading time between SPACE with DANTE and MPRAGE. The sensitivity and positive predictive value of different MR images were calculated using a 2-way contingency table. *P* values < .05 were considered statistically significant. Interobserver agreement for each MR image was calculated using κ statistics; 0–0.20, 0.21–0.40, 0.41–0.60, 0.61–0.80, and 0.81–1.00 were regarded as slight, fair, moderate, substantial, and almost perfect agreement, respectively, based on the Landis and Koch method.¹⁷

RESULTS

Diagnostic Performance of the MR Images

SPACE with DANTE (observer one, 328; observer two, 324) revealed significantly more small (<5 mm) enhancing lesions in the brain parenchyma than MPRAGE (observer one, 175; observer two, 150) (*P* = .0006 for observer 1, *P* \leq .0001 for observer 2) (Figs 1 and 2 and Table 1). In the detection of lesions of >5 mm, SPACE with DANTE (observer one, 186; observer two, 188) also revealed more enhancing lesions than MPRAGE (observer one, 168; observer two, 169), but this difference failed to reach statistical significance. Moreover, SPACE with DANTE showed higher sensitivity than MPRAGE for the detection of brain metastases, regardless of the lesion size (Fig 3). Both SPACE with DANTE and MPRAGE showed almost perfect interobserver agreement (κ = 0.99 for SPACE with DANTE and 0.98 for MPRAGE for lesions smaller than 5 mm; κ = 0.99 for SPACE with DANTE and 0.98 for MPRAGE for lesions of >5 mm) for the detection of brain metastases, regardless of lesion size. The FOM of SPACE with

Table 1: Comparison of lesion detectability according to lesion size

	SPACE with DANTE	MPRAGE	P Value
Lesion diameter ≤5 mm			
Observer 1			
No. of lesions ^a	328 (4.39 ± 7.54)	175 (2.96 ± 5.13)	.0006
Sensitivity (%) ^b	87.4	49.4	
PPV (%) ^b	98.1	95.6	
Observer 2			
No. of lesions ^a	324 (4.50 ± 7.52)	150 (2.76 ± 5.20)	<.0001
Sensitivity (%) ^b	86.86	51.14	
PPV (%) ^b	97.8	98.4	
ICC ^c	0.99	0.98	
Lesion diameter >5 mm			
Observer 1			
No. of lesions ^a	186 (2.62 ± 4.51)	168 (2.37 ± 3.52)	.0978
Sensitivity (%) ^b	94.74	85.79	
PPV (%) ^b	96.77	97.02	
Observer 2			
No. of lesions ^a	188 (2.65 ± 4.37)	169 (2.38 ± 3.92)	.0531
Sensitivity (%) ^b	95.26	87.37	
PPV (%) ^b	96.28	98.22	
ICC ^c	0.99	0.98	

Note:—ICC indicates intraclass correlation coefficient; PPV, positive predictive value.

^a Data represent the number (mean). Values were compared using paired *t* tests.

^b Values were calculated using a 2-way contingency table.

^c Values were calculated using κ statistics.

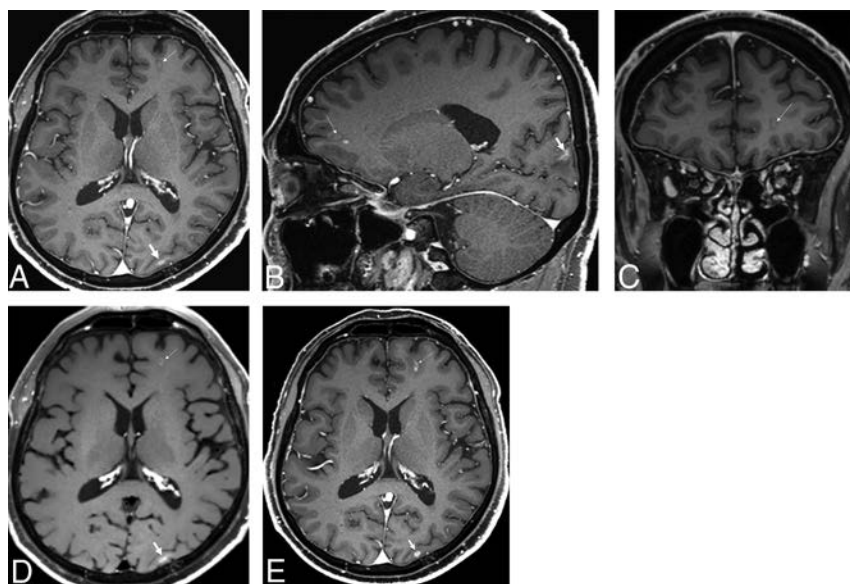


FIG 3. Minute and faint enhancing lesions at the left frontal and occipital lobes were missed by observer 2 (A). A left frontal lesion also shows faint enhancement on sagittal and coronal reconstructed MPRAGE images (B and C). However, these enhancing lesions show more prominent enhancement on SPACE with DANTE (D) and increased size on the follow-up MR imaging (E) 4 months later.

Table 2: Comparison of FOM according to lesion size^a

	SPACE with DANTE	MPRAGE	P Value
Lesion diameter ≤5 mm			
Observer 1			
	0.904	0.698	
Observer 2			
	0.861	0.702	
Mean ± SD	0.882 ± 0.023	0.700 ± 0.038	.0017
Lesion diameter >5 mm			
Observer 1			
	0.957	0.921	
Observer 2			
	0.943	0.928	
Mean ± SD	0.950 ± 0.013	0.925 ± 0.014	.1762

^a Data for observers 1 and 2 are mean value of FOM data compared between SPACE with DANTE and MPRAGE.

DANTE was significantly higher than that of MPRAGE for both observers in the detection of lesions smaller than 5 mm ($P = .0017$) (Table 2). However, the FOM was not significantly different between the 2 sequences in the detection of lesions of >5 mm ($P = .1762$).

SPACE with DANTE revealed more false-positive findings ($n = 18$) due to incomplete vessel suppression ($n = 15$) (Fig 4) and flow-related artifacts ($n = 3$). On MPRAGE ($n = 10$), the causes for the false-positive findings were vascular structures ($n = 9$) and flow-related artifacts ($n = 1$). However, these findings were not significantly different between the two 3D-enhanced MR images. The average reading time of SPACE with DANTE (observer one, 45.4 ± 31.7 seconds; observer two, 53.7 ± 21.5 seconds) was significantly shorter than that of MPRAGE for both observers (observer one, 73.0 ± 54.1 seconds; observer two, 72.0 ± 22.8 seconds) ($P \leq .0001$).

Evaluation of Image Quality

A total of 51 patients who exhibited homogeneous, solid enhancing lesions of >5 mm were evaluated. The mean $CNR_{\text{lesion/parenchyma}}$ of SPACE with DANTE (52.3 ± 43.1) was significantly higher than that of MPRAGE (17.5 ± 19.3) ($P \leq .0001$) (Table 3 and Fig 5). However, the mean $CNR_{\text{white matter/gray matter}}$ of SPACE with DANTE (-0.65 ± 1.39) was significantly lower than that of MPRAGE (3.08 ± 1.39) ($P \leq .0001$).

DISCUSSION

We compared the diagnostic performance of CE 3D-SPACE with DANTE and MPRAGE for detecting brain metastases. The SPACE with DANTE sequences showed significantly higher sensitivity than the MPRAGE sequences, especially for smaller lesions (<5 mm), and they also showed higher interobserver agreement than the MPRAGE sequences. The SPACE with DANTE sequences showed improved arterial and venous blood suppression compared with SPACE alone.^{7,13} Moreover, DANTE can supplement this suppression using the gradient pulse in the phase-encoding direction.^{13,18} It also suppresses the signal due to slow blood flow, which is incompletely suppressed by SPACE.^{13,19} In addition, SPACE generates intravoxel dephasing and helps maintain the black-blood effect that DANTE cannot sustain during the readout period.¹³ These factors may simplify the reading process; thus, the reading time of SPACE

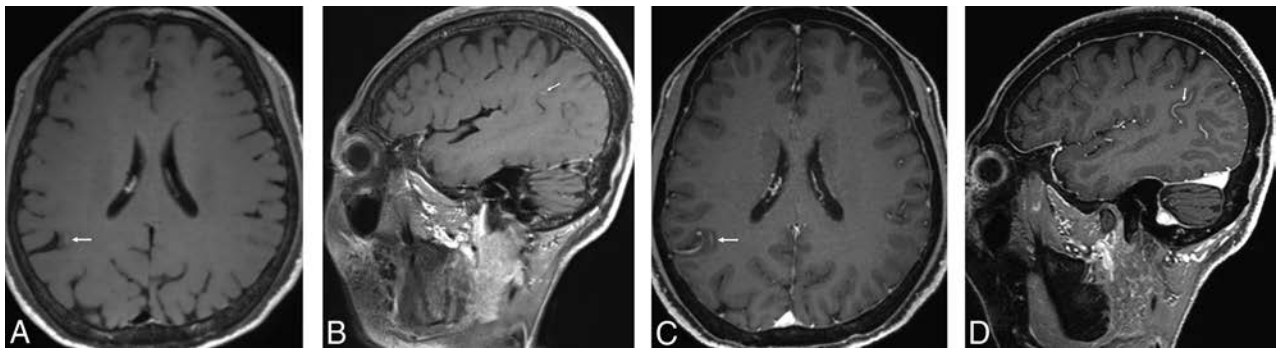


FIG 4. Contrast-enhanced SPACE with DANTE (A and B) shows a focal, linear enhancing lesion in the right parietal lobe. However, we could easily recognize this as a false-positive finding caused by incomplete vessel suppression on MPRAGE images (C and D).

Table 3: CNR_{lesion/parenchyma} and CNR_{white matter/gray matter} of SPACE with DANTE and MPRAGE^a

	SPACE with		P Value
	DANTE	MPRAGE	
CNR (n = 51)			
Lesion/parenchyma	52.3 ± 43.1	17.5 ± 19.3	<.0001
White matter/gray matter	-0.65 ± 1.39	3.08 ± 1.39	<.0001

^a Data are presented as means. Values were calculated using paired t tests.

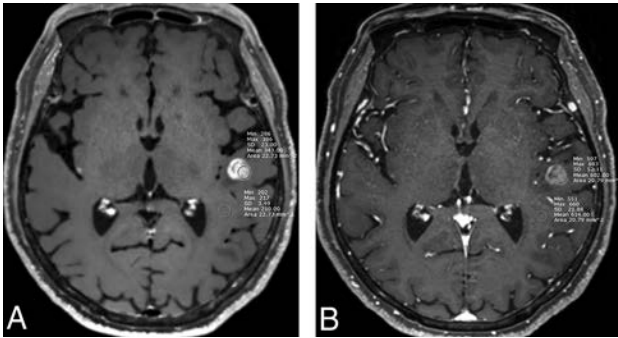


FIG 5. The CNR_{lesion/parenchyma} of SPACE with DANTE (8.62) (A) was higher than that of MPRAGE (3.49) (B).

with DANTE was significantly shorter than that of MPRAGE for both observers.

We measured the CNR of enhancing lesions for both SPACE with DANTE and MPRAGE images using the following formula: $CNR_{lesion/parenchyma} = (SI_{lesion} - SI_{parenchyma}) / SD_{parenchyma}$. Our study showed that the CNR_{lesion/parenchyma} of SPACE with DANTE is higher than that of MPRAGE. This finding is in agreement with those of previous studies,^{6,11,20} which showed lower contrast enhancement of gradient-echo images than of spin-echo images and higher CNR_{lesion/parenchyma} of SPACE images than of MPRAGE images. Previous studies^{4,8,10} have provided several reasons for the better detection of contrast-enhancing lesions using the spin-echo sequence than using the gradient-echo sequence. Previous studies^{10,20,21} suggested that the higher CNR of enhancing metastatic lesions to the normal parenchyma of the spin-echo sequence than of the gradient-echo sequence contributes to the higher detectability of metastatic lesions. Our result that the CNR of SPACE with DANTE is higher than that of MPRAGE is consistent with the findings of previous studies.^{10,20,21} The higher magnetization transfer effect of SPACE than MPRAGE has been suggested as another factor influenc-

ing its higher detection accuracy.^{8,22} A variable flip angle, which might be introduced as off-resonance pulses, induces magnetization transfer effects. It preferentially reduces the signal from the brain parenchyma, especially from white matter, rendering enhancing lesions more outstanding. However, SPACE alone is not sufficient for the evaluation of enhancing lesions because residual blood signal can occasionally be mistaken for enhancing lesions.

Therefore, black-blood modules have been used for evaluation of brain metastases. A few studies⁹ have evaluated the detectability of brain metastasis using 3D CE MR imaging with the black-blood module, but no study has used the DANTE preparation pulse in the evaluation of brain metastasis. A previous study¹⁸ suggested that DANTE preparation is a promising black-blood module that offers a higher signal-to-noise ratio and allows a shorter acquisition time than other types of black-blood modules, such as double inversion recovery or motion-sensitive driven equilibrium preparation modules. Our findings are in agreement with those of Park et al,⁹ who detected significantly more small lesions using the CE 3D black-blood single slab turbo spin-echo sequence than using the CE MPRAGE sequence. They found no significant differences in the detection of larger enhancing lesions (>5 mm), and this finding is in agreement with that of our study.

We could recognize the enhancing lesions more easily using SPACE with DANTE than by using MPRAGE, and the result of our study that SPACE with DANTE required a shorter reading time than MPRAGE for both observers supports this finding. This finding is consistent with those of previous studies that analyzed the reading time.^{11,12} The FOM of SPACE with DANTE was significantly higher than that of MPRAGE for both observers in the detection of lesions of <5 mm in our study. A previous study⁸ reported that SPACE images showed significantly higher diagnostic performance than MPRAGE images, regardless of the observer's experience in neuroradiology. However, Kakeda et al⁴ reported no evident difference in the conspicuity of the enhancing lesions between spin-echo and gradient-echo images in a lesion-by-lesion comparison. This is probably because 3D gradient-echo images and 2D spin-echo images were compared, unlike in our study.

SPACE with DANTE revealed more false-positive lesions than MPRAGE, and 83.3% of these were caused by incomplete

suppression of the blood flow. This finding is consistent with a previous study²³ reported that CE-SPACE showed more false-positive findings than MPRAGE. The variable flip angle of the SPACE sequence imperfectly suppresses the vascular signal and could lead to misinterpretation of the remaining vessels as a metastatic lesion. Furthermore, turbo spin-echo motion-sensitive driven equilibrium¹¹ shows more false-positive lesions than the non-motion-sensitive driven equilibrium sequence due to incomplete blood flow suppression of small peripheral vessels, and these findings hamper interpretation. However, we could easily recognize these structures as false-positive lesions by considering multiplanar reconstruction and MPRAGE images. This method has already been confirmed by a previous study,¹¹ which decreased the false-positive rate and preserved diagnostic performance. Kato et al⁸ also reported several false-positive events, but the causes were different from those identified in our study. None of the venous sinuses or choroid plexuses were misdiagnosed as metastasis in our study.

Our study has several limitations. First, this study was retrospective in design. Second, pathologic confirmation of all metastatic lesions was not possible because patients with multiple brain metastases usually do not undergo an operation. Third, we could not include SPACE without a DANTE pulse due to its limited acquisition time. However, a previous study¹³ has already shown the improved suppression of arterial and venous blood using SPACE with DANTE compared with SPACE. Another study¹¹ using turbo spin-echo motion-sensitive driven equilibrium showed that it achieves better blood vessel suppression than non-turbo spin-echo motion-sensitive driven equilibrium, with a similar CNR. Nevertheless, further studies comparing SPACE without DANTE and SPACE with DANTE are needed and may support our results. Finally, in the present study, the observers were not blinded to the type of MR images because the differentiation of gray and white matter was evidently different between the 2 sequences.

CONCLUSIONS

Using SPACE with DANTE could improve the diagnostic performance for brain metastases; this approach also has almost perfect interobserver agreement. Compared with MPRAGE, SPACE with DANTE significantly improves the detection of brain metastases, particularly of those of <5 mm, without significantly increasing the false-positive rate. This information should be considered in the development of optimal brain tumor imaging protocols.

ACKNOWLEDGMENTS

The authors thank In Seong Kim and Kang Soo Kim (Siemens, South Korea) for the DANTE application optimization.

REFERENCES

- Langer CJ, Mehta MP. **Current management of brain metastases, with a focus on systemic options.** *J Clin Oncol* 2005;23:6207–19 CrossRef Medline
- Chang EL, Hassenbusch SJ 3rd, Shiu AS, et al. **The role of tumor size in the radiosurgical management of patients with ambiguous brain metastases.** *Neurosurgery* 2003;53:272–80; discussion 280–81 CrossRef Medline
- Minniti G, Clarke E, Lanzetta G, et al. **Stereotactic radiosurgery for brain metastases: analysis of outcome and risk of brain radionecrosis.** *Radiat Oncol* 2011;6:48 CrossRef Medline
- Kakeda S, Korogi Y, Hiai Y, et al. **Detection of brain metastasis at 3T: comparison among SE, IR-FSE and 3D-GRE sequences.** *Eur Radiol* 2007;17:2345–51 CrossRef Medline
- Ellingson BM, Bendszus M, Boxerman J, et al; Jumpstarting Brain Tumor Drug Development Coalition Imaging Standardization Steering Committee. **Consensus recommendations for a standardized brain tumor imaging protocol in clinical trials.** *Neuro Oncol* 2015;17:1188–98 CrossRef Medline
- Kammer N, Coppenrath E, Treitl K, et al. **Comparison of contrast-enhanced modified T1-weighted 3D TSE black-blood and 3D MPRAGE sequences for the detection of cerebral metastases and brain tumours.** *Eur Radiol* 2016;26:1818–25 CrossRef Medline
- Suh CH, Jung SC, Kim KW, et al. **The detectability of brain metastases using contrast-enhanced spin-echo or gradient-echo images: a systematic review and meta-analysis.** *J Neurooncol* 2016;129:363–71 CrossRef Medline
- Kato Y, Higano S, Tamura H, et al. **Usefulness of contrast-enhanced T1-weighted sampling perfection with application-optimized contrasts by using different flip angle evolutions in detection of small brain metastasis at 3T MR imaging: comparison with magnetization-prepared rapid acquisition of gradient echo imaging.** *AJNR Am J Neuroradiol* 2009;30:923–29 CrossRef Medline
- Park J, Kim J, Yoo E, et al. **Detection of small metastatic brain tumors: comparison of 3D contrast-enhanced whole-brain black-blood imaging and MP-RAGE imaging.** *Invest Radiol* 2012;47:136–41 CrossRef Medline
- Mugler JP 3rd, Brookeman JR. **Theoretical analysis of gadopentetate dimeglumine enhancement in T1-weighted imaging of the brain: comparison of two-dimensional spin-echo and three-dimensional gradient-echo sequences.** *J Magn Reson Imaging* 1993;3:761–69 CrossRef Medline
- Nagao E, Yoshiura T, Hiwatashi A, et al. **3D turbo spin-echo sequence with motion-sensitized driven-equilibrium preparation for detection of brain metastases on 3T MR imaging.** *AJNR Am J Neuroradiol* 2011;32:664–70 CrossRef Medline
- Kikuchi K, Hiwatashi A, Togao O, et al. **3D MR sequence capable of simultaneous image acquisitions with and without blood vessel suppression: utility in diagnosing brain metastases.** *Eur Radiol* 2015;25:901–10 CrossRef Medline
- Xie Y, Yang Q, Xie G, et al. **Improved black-blood imaging using DANTE-SPACE for simultaneous carotid and intracranial vessel wall evaluation.** *Magn Reson Med* 2016;75:2286–94 CrossRef Medline
- Rand S, Maravilla KR, Schmiedl U. **Lesion enhancement in radio-frequency spoiled gradient-echo imaging: theory, experimental evaluation, and clinical implications.** *AJNR Am J Neuroradiol* 1994;15:27–35 Medline
- Chakraborty DP, Berbaum KS. **Observer studies involving detection and localization: modeling, analysis, and validation.** *Med Phys* 2004;31:2313–30 CrossRef Medline
- Chakraborty DP. **Analysis of location specific observer performance data: validated extensions of the jackknife free-response (JAFROC) method.** *Acad Radiol* 2006;13:1187–93 CrossRef Medline
- Landis JR, Koch GG. **The measurement of observer agreement for categorical data.** *Biometrics* 1977;33:159–74 Medline
- Li L, Chai JT, Biasioli L, et al. **Black-blood multicontrast imaging of carotid arteries with DANTE-prepared 2D and 3D MR imaging.** *Radiology* 2014;273:560–69 CrossRef Medline
- Li L, Miller KL, Jezzard P. **DANTE-prepared pulse trains: a novel approach to motion-sensitized and motion-suppressed quantitative magnetic resonance imaging.** *Magn Reson Med* 2012;68:1423–38 CrossRef Medline
- Chappell PM, Pelc NJ, Foo T, et al. **Comparison of lesion enhancement on spin-echo and gradient-echo images.** *AJNR Am J Neuroradiol* 1994;15:37–44 Medline

21. Komada T, Naganawa S, Ogawa H, et al. **Contrast-enhanced MR imaging of metastatic brain tumor at 3 Tesla: utility of T(1)-weighted SPACE compared with 2D spin echo and 3D gradient echo sequence.** *Magn Reson Med Sci* 2008;7:13–21 CrossRef Medline
22. Constable R, Anderson A, Zhong J, et al. **Factors influencing contrast in fast spin-echo MR imaging.** *Magn Reson Imaging* 1992;10:497–511 CrossRef Medline
23. Kwak HS, Hwang S, Chung GH, et al. **Detection of small brain metastases at 3 T: comparing the diagnostic performances of contrast-enhanced T1-weighted SPACE, MPRAGE, and 2D FLASH imaging.** *Clin Imaging* 2015;39:571–75 CrossRef Medline

Comparison of Unenhanced and Gadolinium-Enhanced Imaging in Multiple Sclerosis: Is Contrast Needed for Routine Follow-Up MRI?

G. Sadigh, A.M. Saindane, A.D. Waldman, N.S. Lava, and R. Hu

ABSTRACT

BACKGROUND AND PURPOSE: Gadolinium enhanced MRI is routinely used for follow-up of patients with multiple sclerosis. Our aim was to evaluate whether enhancing multiple sclerosis lesions on follow-up MR imaging can be detected by visual assessment of unenhanced double inversion recovery and FLAIR sequences.

MATERIALS AND METHODS: A total of 252 consecutive MRIs in 172 adult patients with a known diagnosis of multiple sclerosis were reviewed. The co-presence or absence of associated double inversion recovery and FLAIR signal abnormality within contrast-enhancing lesions was recorded by 3 neuroradiologists. In a subset of patients with prior comparisons, the number of progressive lesions on each of the 3 sequences was assessed.

RESULTS: A total of 34 of 252 MRIs (13%) demonstrated 55 enhancing lesions, of which 52 (95%) had corresponding hyperintensity on double inversion recovery and FLAIR. All lesions were concordant between double inversion recovery and FLAIR, and the 3 enhancing lesions not visible on either sequence were small (<2 mm) and cortical/subcortical ($n = 2$) or periventricular ($n = 1$). A total of 17 (22%) of the 76 MRIs with a prior comparison had imaging evidence of disease progression: Ten (59%) of these showed new lesions on double inversion recovery or FLAIR only, 6 (35%) showed progression on all sequences, and 1 (6%) was detectable only on postcontrast T1, being located in a region of confluent double inversion recovery and FLAIR abnormality.

CONCLUSIONS: There was a high concordance between enhancing lesions and hyperintensity on either double inversion recovery or FLAIR. Serial follow-up using double inversion recovery or FLAIR alone may capture most imaging progression, but isolated enhancing lesions in confluent areas of white matter abnormality could present a pitfall for this approach.

ABBREVIATIONS: CAD = computer-assisted detection; DIR = double inversion recovery; DMT = disease-modifying therapy

Multiple sclerosis affects approximately 727,324 individuals in the United States.¹ Adherence to imaging follow-up is key to obtaining optimal clinical outcomes in patients with MS.² Routine imaging follow-up, in particular, is important to guide therapy.^{3,4} MR imaging is currently the most sensitive available tool for monitoring inflammatory disease activity in patients with MS. Clinical assessments usually underestimate disease activity and burden compared with MRI.³ In addition, concordance between the clinical examination and MR imaging is essential for distinguishing frank relapses from pseudorelapses.

Received May 14, 2019; accepted after revision July 6.

From the Departments of Radiology and Imaging Sciences (G.S., A.M.S., A.D.W., R.H.) and Neurology (N.S.L.), Emory University School of Medicine, Atlanta, Georgia.

Previously presented as an abstract at: Annual Meeting of the American Society of Neuroradiology, May 18–23, 2019; Boston, Massachusetts.

Please address correspondence to Gelareh Sadigh, MD, Department of Radiology and Imaging Sciences, Emory University School of Medicine, 1364 Clifton Rd, Ste BG27, Atlanta, GA 30322; e-mail: gsadigh@emory.edu; @gelarehsadigh

<http://dx.doi.org/10.3174/ajnr.A6179>

Brain MR imaging is recommended before the initiation or modification of disease-modifying therapies (DMTs) and approximately 6 months after a treatment change to allow sufficient time for new therapies to reach their therapeutic potential.³ Continued or worsening disease activity on MR imaging while the patient is on a DMT may prompt a change in therapy because it is indicative of a suboptimal therapeutic response.^{5–7} Additionally, many new lesions, especially those outside the more functionally eloquent regions of the brain, may be clinically silent.³ Therefore, for relapsing forms of MS, a follow-up brain MR imaging should be considered annually for at least the first 2–3 years after starting therapy or switching DMTs. More frequent surveillance may be indicated in clinically aggressive cases or unusual patterns of MR imaging lesions (eg, tumefactive MS).³ Finally, high-risk patients should have surveillance MR imaging performed every 3–6 months to assess progressive multifocal leukoencephalopathy.⁸

In the current routine clinical practice, the follow-up MR imaging for MS is performed by using intravenous gadolinium

contrast. This is mainly due to prior studies reporting higher sensitivity of postcontrast MR imaging in detecting new MS lesions.⁹ However, with higher MR imaging magnet strength and new imaging sequences such as double inversion recovery (DIR), a sequence more sensitive to cortical and infratentorial lesions than FLAIR, this approach needs to be assessed and modified. Recent studies suggest that the use of contrast material at follow-up MR imaging does not change the diagnosis of interval disease progression in patients with MS.¹⁰⁻¹³ Most of these studies have used subtraction¹⁰ or computer-assisted detection (CAD)¹¹ techniques to identify new MS lesions on 3D FLAIR^{10,11} or DIR sequences.¹⁰ This use is especially timely given growing concerns about deposition of free gadolinium in the brain and other organs after using gadolinium-based contrast agents.¹⁴⁻¹⁶ Furthermore, MS commonly affects populations 20–40 years of age¹⁷ with approximately 40 years of life expectancy,¹⁸ which translates into these patients undergoing >40 MR imaging examinations over the course of their disease.

However, the generalizability of the CAD approach is limited because such technologies are not yet widely available in most institutions and can be difficult to incorporate into a routine clinical workflow. In the current study, we sought to evaluate whether enhancing MS lesions on follow-up MR imaging can be detected by visual assessment of unenhanced DIR and FLAIR sequences. This study will provide information on identifying the subgroup of patients with MS who would benefit from gadolinium-enhanced MR follow-up imaging.

MATERIALS AND METHODS

Institutional review board approval and a waiver of informed consent were obtained for this retrospective review. The study was Health Insurance Probability and Accountability Act-compliant.

Study Population

The Radiology Information System data base was searched for consecutive patients older than 18 years of age with a clinical diagnosis of MS who underwent brain MR imaging using the MS protocol at the outpatient radiology clinic of our institution between September 2016 and April 2018. Only patients with an established diagnosis of MS as determined by the medical record and documented by a neurologist were included. Patients with other coexisting conditions involving the central nervous system (stroke, vasculitis, tumor, migraine, epilepsy, and so forth) as determined from the medical record, history of prior neurosurgery, and incomplete or inadequate imaging were excluded. A total of 313 patients were screened, and 280 patients met the initial inclusion criteria, of whom 11 were excluded due to prior neurosurgery, 94 for coexisting conditions, and 3 for incomplete imaging, yielding 172 patients for recruitment.

MR Imaging

All included patients were scanned on the same 3T scanner (Magnetom Skyra; Siemens, Erlangen, Germany) using a dedicated MS MR imaging protocol, which included precontrast volumetric 3D-DIR, axial and sagittal 2D-FLAIR, DWI, gradient recalled-echo, postcontrast T2-weighted fast spin-echo, T1-weighted fast spin-echo, and 3D-MPRAGE sequences. During the study

period, of the 172 patients, 111 had only 1 completed MR imaging examination with adequate image quality, while 48 patients had two, 8 patients had 3, 4 patients had 4, and one patient had 5 completed MR imaging examinations with adequate image quality, resulting in a total of 252 MR imaging examinations. Seventy-six examinations had at least 1 prior comparison included in the study.

For this study, we reviewed volumetric 3D-DIR (sagittal acquisition with 1-mm axial reformat; section thickness, 1.4 mm; FOV, 259 × 259 mm; matrix, 190 × 190; TE, 318 ms; TR, 7500 ms; variable flip angle; echo-train length, 234), axial 2D-T2 FLAIR (axial acquisition; section thickness, 3 mm; FOV, 178 × 220 mm; matrix, 320 × 182; TE, 81 ms; TR, 9000 ms; TI, 2500 ms; flip angle, 150°; echo-train length, 16), and axial volumetric 3D postcontrast T1-weighted MPRAGE (sagittal acquisition, 4–5 minutes after the intravenous administration of 0.1 mmol/kg of gadobenate dimeglumine [MultiHance; Bracco Diagnostics, Princeton, New Jersey] with 1-mm axial reformats; section thickness, 0.9 mm; FOV, 240 × 240 mm; matrix, 256 × 256; TE, 2.32 ms; TR, 1800 ms; flip angle, 8°; echo-train length, 1) sequences. The parameters for all sequences were the same in all patients.

Image Review

All images were anonymized and reviewed on a research DICOM viewer without knowledge of the patients' demographics, clinical symptoms, or treatment. Three board-certified neuroradiologists with 10, 2, and 1 year of experience postfellowship training independently reviewed all 252 examinations. Total lesion burden on 2D-FLAIR and 3D-DIR was classified as mild (<10), moderate (11–20), and severe (>20 or confluent). This decision was made on the basis of the proposed contextual template for MS follow-up MR imaging by Mamlouk et al.¹⁹ The number and locations (cortical/juxtacortical, deep, periventricular, and infratentorial) of enhancing lesions was documented on the basis of 3D postcontrast T1-weighted MPRAGE, and whether these enhancing lesions were detectable on 3D-DIR or 2D-FLAIR by expert visual assessment was determined. For MR imaging examinations with a prior comparison (eg, if the patient had completed >1 examination during the study period), the reviewers also recorded the development of interval new lesions on each of the 3 sequences and whether this new lesion was seen on only 1 sequence or all of them. After the initial independent review, the raters reviewed all discrepant findings and reached a consensus if 2 of 3 raters agreed on a finding.

Statistical Analysis

Continuous variables were reported as median and interquartile range. Categorical variables were reported as numbers and frequencies. Association among categorical variables was computed using the Fisher exact test. Interobserver agreement was evaluated with the interclass correlation coefficient (κ). Statistical analysis was performed using STATA/SE Release 14.2, 2018 (StataCorp, College Station, Texas), with significance defined as $P < .05$.

RESULTS

Patient Demographics

A total of 172 patients were included in the study, 131 (34%) women and 41 (24%) men, with a median age of 42 years

Table 1: The number of examinations categorized by T2 lesion burden and number of enhancing lesions

T2 Lesion Burden	No. of MR Imaging Examinations	No. of MR Imaging Enhancing Lesions					At Least 1
		0	1	2	3	4	
Mild (<10 lesions)	47/252 (19%)	44	3				3/252 (6%)
Moderate (11–20 lesions)	89/252 (35%)	78	7	3		1	11/252 (12%)
Severe (>20 lesions)	116/252 (46%)	99	10	1	4	2	17/252 (15%)
Total	252	221	20	4	4	3	34/252 (13%)

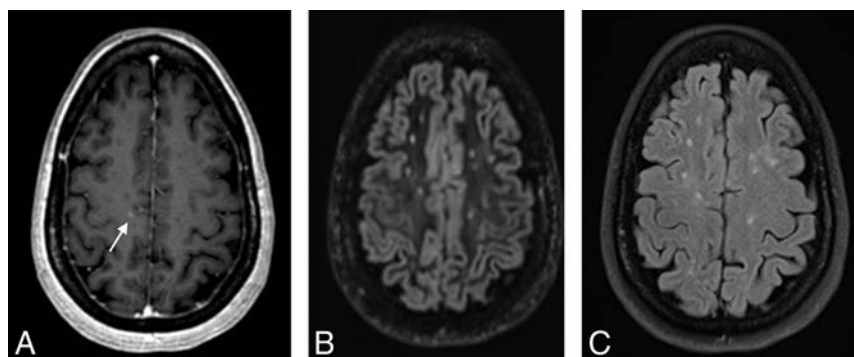


FIG 1. 3D contrast-enhanced T1 MPRAGE (A) demonstrating a faint right frontal subcortical lesion (arrow) not visible on 3D DIR (B) and 2D FLAIR (C).

Table 2: Relationship between new signal abnormality and enhancement in patients with MS with prior comparison MR imaging examinations available

	No Enhancing Lesion	Enhancing Lesion Present	Total
	New DIR/FLAIR	10 (13%)	6 (8%)
Stable DIR/FLAIR	59 (78%)	1 (1%)	60 (79%)
Total	69 (91%)	7 (9%)	76

(interquartile range, 32–50 years). Most patients, 160 (93%), had relapsing-remitting MS at the time of the first included MR imaging in our study, while 5 (3%) had primary-progressive MS, and 7 (4%) had secondary-progressive MS. The median time from initial symptoms to first MR imaging included in the study was 10 years (interquartile range, 4–12 years). The median times from initial symptoms to first MR imaging included in the study were 11, 12, and 12 years for patients with relapsing-remitting, primary-progressive, and secondary-progressive MS, respectively. Most patients (151, 88%) were on DMTs at the time of the first included MR imaging in our study. The 3 most common DMTs were tecfidera ($n=31$), natalizumab (Tysabri) ($n=28$), and glatiramer acetate injection (Copaxone) ($n=24$).

Enhancing Lesions

A total of 47 MRIs (19%) had mild T2 lesion burden, while 89 (35%) and 116 (46%) had moderate and severe T2 lesion burden, respectively (Table 1). A total of 55 enhancing lesions were present on 34 of 252 MRIs (13%). The presence of enhancing lesions was more common in examinations with moderate (12%) and severe (15%) T2 lesion burden than in those with mild (6%) T2

lesion burden (Table 1). Most enhancing lesions, 52 of 55 (95%), were also detectable on 3D-DIR and 2D-FLAIR. All enhancing lesions detectable on 3D-DIR were also detectable on 2D-FLAIR, and vice-versa. The 3 enhancing lesions not visible on both 3D-DIR and 2D-FLAIR sequences were all small (<2 mm), cortical/subcortical ($n=2$) (Fig 1), or periventricular ($n=1$) and occurred in examinations with moderate ($n=2$) or severe lesion burden ($n=1$).

The interobserver agreement (κ) for enhancing lesions also detectable on 3D-DIR and 2D-FLAIR was 0.64, consistent with substantial agreement. However, the κ for enhancing lesions not visible on DIR or FLAIR was 0.10, consistent with only slight agreement.

Progression of Lesions across Time

Seventy-six MRIs had a prior comparison in our study period, with a median interval of 236 days (interquartile range, 191–367 days) between examinations. Of these, a total of 17 (22%) had imaging evidence of progression, defined as new lesions (either on DIR/FLAIR or enhancing) compared with the most immediate prior MR imaging examination (Table 2). The presence of enhancing lesions was associated with new lesions on DIR and FLAIR ($P < .001$). Only one of these MR imaging examinations had a new lesion that was only detectable on postcontrast imaging as a single enhancing lesion in a region of confluent white matter abnormality that did not show interval change on DIR and FLAIR (Fig 2), because the lesion could not be differentiated from confluent periventricular white matter signal abnormality on DIR or FLAIR. Thus, 16 of 17 cases of progression could be detected on the basis of new DIR or FLAIR lesions alone (sensitivity, 94%).

DISCUSSION

In this retrospective review of patients with MS with brain MR imaging examination, our results demonstrate that most enhancing MS lesions (95%) can be identified on DIR and FLAIR sequences obtained using a 3T scanner and when assessed visually without any CAD or subtraction system. There were only 3 small (<2 mm) enhancing lesions without associated signal abnormality on DIR or FLAIR. This result is concordant with Karimian-Jazi et al,¹³ reporting that the enhancing lesions without correlates on FLAIR sequence are significantly smaller than those with correlates. These lesions may represent early breakdown of the blood-brain barrier before development of inflammation or edema.²⁰ However, this likely represents a transient period early in the evolution of new MS lesions, with eventual development of concurrent T2 signal and resolution of

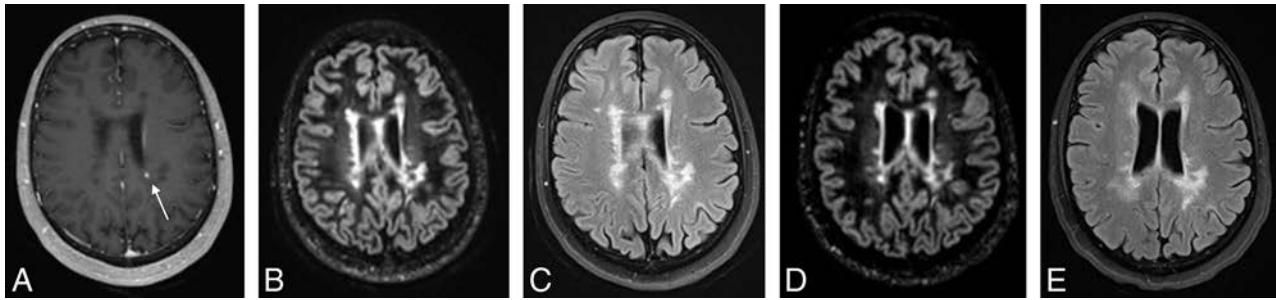


FIG 2. 3D contrast-enhanced T1 MPRAGE (A) demonstrating a left periventricular enhancing lesion (arrow) in a region of confluent white matter lesions that is not detectable as new between the more recent 3D-DIR (B) and 2D-FLAIR (C) and prior 3D-DIR (D) and 2D-FLAIR (E).

enhancement generally within a month.²¹ With imaging follow-up frequency on the order of 6 months to a year, the probability of detecting such lesions is low, and their contribution to the overall evaluation of lesion progression is questionable. Indeed, when we evaluated serial imaging, only 1 of 76 examinations demonstrated lesion progression on the basis of lesion enhancement alone. In that case, the patient did not exhibit new or worsening clinical symptoms, and the patient was maintained on the existing treatment regimen, with clinical stability and resolution of the enhancing lesion on 2 subsequent follow-ups.

Our results are consistent with and augment recent works that used CAD¹¹ and subtraction techniques¹⁰ by showing similar results with standard visual assessment by neuroradiologists. Given the high sensitivity of noncontrast imaging in detecting lesion progression and the lack of a definitive indication to alter clinical management even with a single small enhancing lesion, the cost and benefit of postcontrast MR imaging for routine follow-up of patients with MS should be re-evaluated. Our study is especially important because it evaluates the role of unenhanced DIR and FLAIR using standard visual assessment, which is likely the routine practice in most institutions. Furthermore, it will provide information to identify the subgroup of patients who would benefit from gadolinium-enhanced MR imaging for their follow-up MR imaging. Perhaps, a reasonable approach might be obtaining noncontrast follow-up in clinically stable patients with low-to-moderate lesion burden and reserving contrast-enhanced MR imaging for patients with worsening clinical symptoms or high lesion burden (eg, in which confluent lesions may limit the evaluation of T2 lesion progression). In these 2 scenarios, there is a higher chance that an enhancing lesion may make a difference in clinical management.

Our study is limited by retrospective methodology, small sample size, a short follow-up period, and a lower number of patients with available serial imaging. We intended to include only scans with the relatively recently adopted DIR sequence and to avoid potentially confounding technical factors. Therefore, we included only patients followed on a single 3T scanner at our outpatient clinic, where most of the patients with MS are being scanned. This approach limited the number of prior comparisons we could include and also limits the generalizability of our results to other magnet strengths. However, it is encouraging that other studies using different sequences and scanner types found similar findings. Furthermore, we did not evaluate the enhancing lesions on postcontrast TSE sequences and used only postcontrast

MPRAGE sequences. Finally, although we evaluated the co-presence or absence of enhancing lesions (identified on 3D postcontrast sequences) on both 3D-DIR and 2D-FLAIR sequences and our results were concordant, comparison of a 2D with a 3D sequence is not optimal due to differences in section thickness. It is possible that very small lesions may not be apparent on thick-section 2D-FLAIR images due to volume averaging, though this was not observed in our dataset. With growing evidence that gadolinium is not necessary for the evaluation of lesion progression, the recently revised 2018 Consortium of MS Centers guidelines⁴ states that gadolinium-enhanced MR imaging is now optional for the follow-up of patients with MS to detect subclinical disease activity. We have already seen changes in the ordering pattern of our neurologists in favor of more noncontrast imaging, and a future prospective longitudinal study ideally including multiple institutions comparing the differences in clinical management and outcome of patients followed with the 2 imaging strategies would be helpful.

CONCLUSIONS

Our results add to growing evidence in the literature showing that the evaluation of noncontrast DIR and FLAIR sequences by neuroradiologists can detect most MS lesion progression on follow-up MR imaging examinations without intravenous contrast. Gadolinium-enhanced MR imaging should be considered only in select patients who may benefit from its minimally higher sensitivity and in whom detection of an enhancing lesion would alter management.

Disclosures: Gelareh Sadigh—UNRELATED: Grants/Grants Pending: Radiological Society of North America seed grant and Association of University Radiologists Radiology Research Academic Fellowship. Alex Waldman—UNRELATED: Grants/Grants Pending: Consortium of Multiple Sclerosis Centers Medical Student Research Scholarship (<http://cmscfoundation.org/portfolio/2019-medical-student-research-scholarship/>);* Radiological Society of North America Medical Student Grant (<https://www.rsna.org/en/research/funding-opportunities/research-grants/medical-student-research-grant>); Travel/Accommodations/Meeting Expenses Unrelated to Activities Listed: American Academy of Neurology, Consortium of Multiple Sclerosis Centers, and American Medical Student Association, Comments: American Academy of Neurology Annual Meeting Travel Scholarships in 2018 (\$2000) and 2019 (\$1000), Consortium of Multiple Sclerosis Centers Annual Meeting Travel Scholarship in 2019 (\$2000), American Medical Student Association Leadership Retreat Travel Funding in 2018. Ranliang Hu—UNRELATED: Consulting Fee or Honorarium: Seimens Medical Solutions, Comments: speaker at Dual Energy Workshop; Payment for Lectures Including Service on Speakers Bureau: paid to individual, Comments: Dual Energy Workshop; Payment for Development of Educational Presentations: Siemens, Comments: Dual Energy Workshop.*Money paid to institution.

REFERENCES

1. Wallin MT, Culpepper WJ, Campbell JD, et al. **The prevalence of MS in the United States: a population-based estimate using health claims data.** *Neurology* 2019;92:e1029–40 CrossRef Medline
2. Lizan L, Comellas M, Paz S, et al. **Treatment adherence and other patient-reported outcomes as cost determinants in multiple sclerosis: a review of the literature.** *Patient Prefer Adherence* 2014; 8:1653–64 Medline
3. Traboulsee A, Simon JH, Stone L, et al. **Revised recommendations of the Consortium of MS Centers Task Force for a Standardized MRI Protocol and Clinical Guidelines for the Diagnosis and Follow-Up of Multiple Sclerosis.** *AJNR Am J Neuroradiol* 2016; 37:394–401 CrossRef Medline
4. Consortium of MS Centers MRI Protocol for the Diagnosis and Follow-up of MS and Clinical Guidelines for the Diagnosis and Follow-Up of MS. 2018 revised guidelines. February 2018. https://cdn.ymaws.com/mscare.site-ym.com/resource/collection/9C5F19B9-3489-48B0-A54B-623A1ECE07B/2018MRIGuidelines_booklet_with_final_changes_0522.pdf. Accessed on May 9, 2019.
5. Rudick RA, Lee JC, Simon J, et al. **Significance of T2 lesions in multiple sclerosis: a 13-year longitudinal study.** *Ann Neurol* 2006; 60:236–42 CrossRef Medline
6. Sormani MP, Bonzano L, Roccatagliata L, et al. **Magnetic resonance imaging as a potential surrogate for relapses in multiple sclerosis: a meta-analytic approach.** *Ann Neurol* 2009;65:268–75 CrossRef Medline
7. Prosperini L, Gallo V, Petsas N, et al. **One-year MRI scan predicts clinical response to interferon beta in multiple sclerosis.** *Eur J Neurol* 2009;16:1202–09 CrossRef Medline
8. Wattjes MP, Barkhof F. **Diagnosis of natalizumab-associated progressive multifocal leukoencephalopathy using MRI.** *Curr Opin Neurol* 2014;27:260–70 CrossRef Medline
9. Filippi M, Rovaris M, Bastianello S, et al. **A comparison of the sensitivity of monthly unenhanced and enhanced MRI techniques in detecting new multiple sclerosis lesions.** *J Neurol* 1999;246:97–106 CrossRef Medline
10. Eichinger P, Schon S, Pongratz V, et al. **Accuracy of unenhanced MRI in the detection of new brain lesions in multiple sclerosis.** *Radiology* 2019;291:429–35 CrossRef Medline
11. Mattay RR, Davtayan K, Bilello M, et al. **Do all patients with multiple sclerosis benefit from the use of contrast on serial follow-up MR imaging? A retrospective analysis.** *AJNR Am J Neuroradiol* 2018; 39:2001–06 CrossRef Medline
12. Saindane AM. **Is Gadolinium-based contrast material needed for MRI follow-up of multiple sclerosis?** *Radiology* 2019;291:436–37 CrossRef Medline
13. Karimian-Jazi K, Wildemann B, Diem R, et al. **Gd contrast administration is dispensable in patients with MS without new T2 lesions on follow-up MRI.** *Neurol Neuroimmunol Neuroinflamm* 2018;5: e480 CrossRef Medline
14. Guo BJ, Yang ZL, Zhang LJ. **Gadolinium deposition in brain: current scientific evidence and future perspectives.** *Front Mol Neurosci* 2018;11:335 CrossRef Medline
15. Kang H, Hii M, Le M, et al. **Gadolinium deposition in deep brain structures: relationship with dose and ionization of linear gadolinium-based contrast agents.** *AJNR Am J Neuroradiol* 2018;39:1597–1603 CrossRef Medline
16. Olchoway C, Cebulski K, Łasecki M, et al. **The presence of the gadolinium-based contrast agent depositions in the brain and symptoms of gadolinium neurotoxicity: a systematic review.** *PLoS One* 2017;12:e0171704 CrossRef Medline
17. Krause I, Kern S, Horntrich A, et al. **Employment status in multiple sclerosis: impact of disease-specific and non-disease-specific factors.** *Mult Scler* 2013;19:1792–99 CrossRef Medline
18. Palmer AJ, van der Mei I, Taylor BV, et al. **Modelling the impact of multiple sclerosis on life expectancy, quality-adjusted life years and total lifetime costs: evidence from Australia.** *Mult Scler* 2019 Feb 26. [Epub ahead of print] CrossRef Medline
19. Mamlouk MD, Chang PC, Saket RR. **Contextual radiology reporting: a new approach to neuroradiology structured templates.** *AJNR Am J Neuroradiol* 2018;39:1406–14 CrossRef Medline
20. Kermodé AG, Thompson AJ, Tofts P, et al. **Breakdown of the blood-brain barrier precedes symptoms and other MRI signs of new lesions in multiple sclerosis: pathogenetic and clinical implications.** *Brain* 1990;113:1477–89 CrossRef Medline
21. Harris JO, Frank JA, Patronas N, et al. **Serial gadolinium-enhanced magnetic resonance imaging scans in patients with early, relapsing-remitting multiple sclerosis: implications for clinical trials and natural history.** *Ann Neurol* 1991;29:548–55 CrossRef Medline

Optimal Detection of Subtle Gadolinium Leakage in CSF with Heavily T2-Weighted Fluid-Attenuated Inversion Recovery Imaging

W.M. Freeze, D.N. ter Weele, W.M. Palm, R.W. van Hooren, E.I. Hoff, J.F.A. Jansen, H.I.L. Jacobs, F.R. Verhey, and W.H. Backes



ABSTRACT

SUMMARY: Pericortical enhancement on postcontrast FLAIR images is a marker for subtle leptomeningeal blood-brain barrier leakage. We explored the optimal FLAIR sequence parameters for the detection of low gadolinium concentrations within the CSF. On the basis of phantom experiments and human in vivo data, we showed that detection of subtle pericortical enhancement can be facilitated by using a relatively long TE. Future studies should choose their FLAIR sequence parameters carefully when assessing pericortical enhancement due to subtle blood-brain barrier leakage.

ABBREVIATIONS: BBB = blood-brain barrier; pc = postcontrast

Postcontrast (pc) FLAIR imaging can be applied to visualize leakage of contrast material through the blood-brain barrier (BBB) into the CSF.¹ This technique is becoming increasingly popular because of its superior sensitivity for detecting low gadolinium concentrations in CSF (but not cerebral tissue) compared with pcT1WI.² Another advantage of pcFLAIR imaging over pcT1WI is the suppression of signal from blood containing high gadolinium concentrations, which makes it easier to discern leakage from leptomeningeal vessels. Previous studies have shown contrast agent extravasation in the form of CSF enhancement within the ventricular and/or pericortical space in various neurologic and cardiovascular surgery conditions³⁻⁸ and in cognitively healthy older individuals.² Although the precise clinical relevance

and pathophysiology of pcFLAIR enhancement remains unclear, it has been associated with several adverse conditions, including hemorrhagic transformation after ischemic stroke⁵ and inflammation and reduced cortical thickness in MS.^{3,4}

The conspicuity of pericortical enhancement depends on the specific contrast parameters of the pulse sequence and the time delay from contrast agent administration to pcFLAIR acquisition. Because BBB leakage is very subtle in many disease conditions, low concentrations of leaked contrast agent in the CSF may be missed by the neuroradiologist if the acquisition parameters or postcontrast acquisition timing or both are not tailored to account for BBB leakage. We explored the optimal FLAIR sequence parameters at 3T MR imaging to visualize low gadolinium concentrations within the CSF space using phantom experiments. Subsequently, we compared a regular pcFLAIR sequence with an optimized heavily T2-weighted pcFLAIR sequence. Both FLAIR scans were 3D sequences and were acquired at 2 time points, within a short timeframe after contrast injection and a >1.5-hour delay.

MATERIALS AND METHODS

In Vitro Experiment

We used phantoms with various aqueous gadolinium concentrations mimicking a range of leakage magnitude in CSF and tissue. See our previous publication² and the On-line Appendix for more details.

Participants and MR Imaging Protocol

We prospectively included 6 older individuals who presented with pericortical CSF enhancement in our baseline study, and images were obtained on the same scanner.² There was no overlap be-

Received May 10, 2019; accepted after revision June 19.

From the Department of Psychiatry and Neuropsychology (W.M.F., R.W.v.H., H.I.L.J., F.R.V.), Maastricht University, School for Mental Health and Neuroscience, Alzheimer Centrum Limburg, Maastricht, the Netherlands; Departments of Radiology (D.N.t.W.) and Neurology (E.I.H.), Zuyderland Medical Center Heerlen, Heerlen, the Netherlands; and Department of Radiology and Nuclear Medicine (W.M.F., W.M.P., J.F.A.J., W.H.B.), Maastricht University Medical Center, School for Mental Health and Neuroscience, Maastricht, the Netherlands.

Whitney M. Freeze and David N. ter Weele contributed equally to this work.

This research was supported by Alzheimer Nederland and Stichting 2Bike4Alzheimer (research grant WE-03-2012-40).

Paper previously presented, in part, at: Annual Meeting of NVKF Lustrumcongres, April 4-5, 2019; Woudschoten, the Netherlands.

Please address correspondence to Walter H. Backes, PhD, Department of Radiology & Nuclear Medicine, School for Mental Health and Neuroscience, Maastricht University Medical Center, PO Box 5800, 6202AZ Maastricht, the Netherlands; e-mail: w.backes@mumc.nl

Indicates article with supplemental on-line appendix and table.

Indicates article with supplemental on-line photos.

<http://dx.doi.org/10.3174/ajnr.A6145>

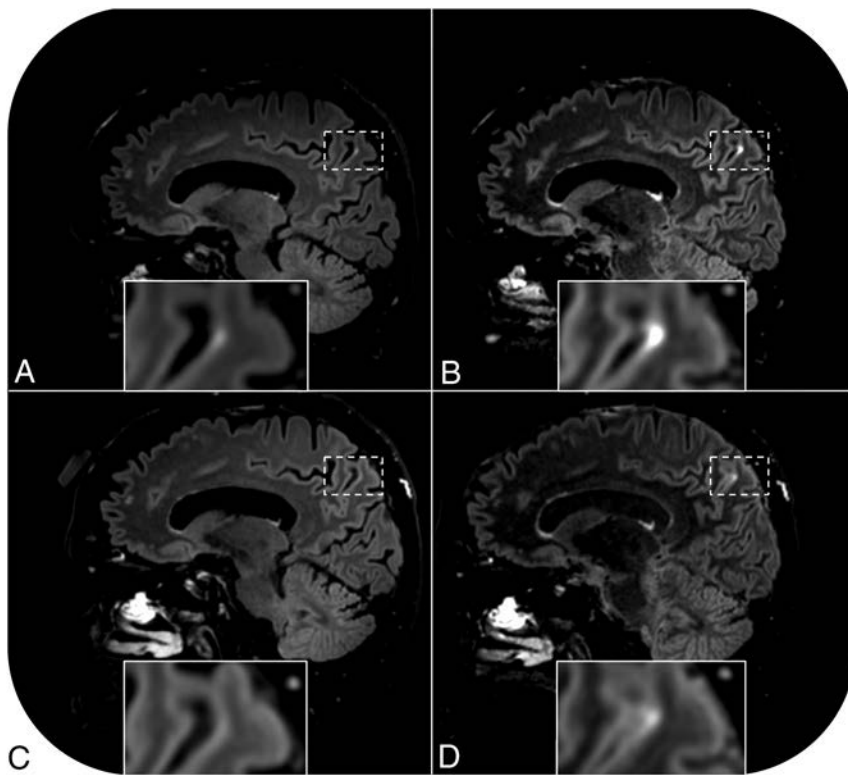


FIGURE. Pericortical enhancement is visible on postcontrast FLAIR images of a 68-year-old cognitively healthy female participant (case 1). Enhancement is apparent on the regular postcontrast FLAIR scan acquired 16 minutes after contrast administration (A) and even more conspicuous on the heavily T2-weighted FLAIR scan acquired immediately thereafter (B). The sequences were repeated 131 minutes after contrast administration. No signal enhancement is visible on the repeat regular postcontrast FLAIR scan (C), but enhancement is still visible on the repeat heavily T2-weighted FLAIR scan (D).

tween the follow-up participants in the baseline study ($n = 3$) and the present work ($n = 6$). During the first scan session, a regular precontrast FLAIR scan was acquired. Subsequently, 16 minutes after intravenous administration of 0.1 mmol/kg of gadobutrol, the regular FLAIR sequence (TR/TE/TI = 4800/290/1650 ms) was repeated, followed by a heavily T2-weighted FLAIR sequence (TR/TE/TI = 4800/500/1650 ms). Both pcFLAIR sequences were repeated in the same order during a second (later) scan session after at least a 1.5-hour delay (range, 100–263 minutes). Additional information on FLAIR sequence details and other MR imaging sequences used to evaluate cerebrovascular damage are described in the On-line Appendix. Informed consent was obtained from all participants before participation. This study was performed in accordance with the local institutional review boards (Zuyderland Medical Center Heerlen and Maastricht University Medical Center) and approved by the medical ethics committee in Maastricht.

Image Analysis

Pericortical enhancement was independently evaluated by 2 raters (the same as in our baseline study)² blinded to clinical data, acquisition time, and scan parameters on all FLAIR scans (including the precontrast FLAIR scans as a negative control). The number of hyperintense foci was counted on each scan. Discrepancies were evaluated by consensus agreement. All images were checked for changes in MR imaging markers of cerebrovascular pathology

compared with baseline by the same experienced neuroradiologist and methods as previously described.²

RESULTS

In Vitro Experiment

The results of our phantom experiments show 2 important concepts that facilitate the detection of low gadolinium concentrations within the CSF, namely the use of relatively long TEs and proper nulling of pure CSF. These concepts as well as the influence of each sequence parameter on the image appearance are further explained in the On-line Appendix and in On-line Figs 1–4.

Neuroradiologic Imaging

The median age of our participants was 73 years (range, 68–84 years), and 4 of 6 were men. All baseline foci of signal enhancement had remained stable with time, and one de novo leakage focus was detected on the regular pcFLAIR images acquired during the first scan session (the total number of pericortical hyperintensities was 9, and in addition, enhancement was observed within an enlarged perivascular space; On-line Table). Pericortical enhancement appeared visually more intense on all heavily T2-weighted pcFLAIR images compared

with the regular pcFLAIR images. In 4 of 6 cases, the enhancing foci ($n = 6$) were visible on all pcFLAIR scans. In 1 case (case 1), a pericortical hyperintensity was visible on all pcFLAIR scans except on the regular pcFLAIR scan that was acquired during the later scan session (Figure). In another case (case 2), two additional foci of enhancement were visible on the heavily T2-weighted FLAIR scan of the first scan session that were not visible on the regular pcFLAIR scan, but all foci had disappeared on both types of pcFLAIR scans that were acquired during the later session (On-line Table). In contrast, widespread signal enhancement within the sulci of another participant (case 3) only became clearly visible on the heavily T2-weighted (but not the regular) pcFLAIR scan in the later scan session (On-line Fig 5). This enhancement resembled the acute lesion-related hyperacute injury marker that has been reported in earlier studies.^{5,6} Most interesting, this case showed a new cerebral microbleed within the thalamus and a region of recent ischemia without cavitation within the basal ganglia that were not present at baseline. No cerebrovascular changes were detected in the other participants compared with baseline, and no enhancement was detected on the precontrast FLAIR images.

DISCUSSION

In the present study, we explored the optimal 3T MR imaging FLAIR sequence parameters to visualize low gadolinium concen-

trations within the CSF space and compared a regular pcFLAIR sequence with a more optimal heavily T2-weighted pcFLAIR sequence acquired at 2 time points after contrast administration. Our results show increased conspicuity of pericortical hyperintensities due to subtle BBB leakage on the heavily T2-weighted pcFLAIR sequence because the strong T2-weighting suppresses the tissue signal, which emphasizes the appearance of CSF enhancement due to contrast agent leakage. In addition, we emphasized the importance of proper nulling of pure CSF, which also facilitates the detection of subtle gadolinium leakage.

Previous studies that assessed BBB leakage of gadolinium-based contrast agents into the CSF with 3T MR imaging used diverse acquisition parameters; these make it difficult to compare the results across various studies, such as the prevalence and number of foci of pericortical enhancement within a specific neurologic disease. Furthermore, previous studies acquired their post-contrast FLAIR scans at varying time points after contrast administration, another factor that influences the appearance of pericortical enhancement. Our results provide guideline acquisition parameters for future studies that are interested in measuring subtle gadolinium leakage in CSF. With regard to acquisition timing, our results show that focal enhancement visible within a short timeframe after contrast administration can disappear at a later time, probably because blood gadolinium concentrations and thereby leakage concentrations decrease with time. However, we also showed 1 patient with neuroradiologic evidence of recent ischemic and hemorrhagic brain lesions who had diffuse gadolinium leakage that only became apparent after a 2-hour delay. Thus, widespread signal enhancement within the sulci in the context of recent or semirecent cerebrovascular damage may become more clearly visible at a later acquisition stage due to delayed and/or cumulative gadolinium leakage, possibly through cerebrovascular clearance pathways.

An obvious limitation of this study is the small sample size and variability in the time delay between the first and second imaging session, which hampers drawing firm conclusions on differences in the number of pericortical leaks that can be detected with either FLAIR sequence. Future studies should explore differences in the number of pericortical leaks that can be detected with either FLAIR sequence further, along with the dynamic mechanisms underlying focal (probably chronic) and widespread (ie, hyperacute injury marker-like, possibly postacute lesion-related) signal enhancement on pcFLAIR images. Most important, pcFLAIR CSF signal enhancement forms a promising biomarker for subtle BBB leakage that can be visually assessed by a neuroradiologist and could be used to monitor and evaluate treatment efficacy in future clinical trials that target cerebrovascular integrity.

CONCLUSIONS

The detection of subtle BBB leakage of gadobutrol into the CSF can be improved by using a heavily T2-weighted pcFLAIR sequence. Future studies that aim to detect low gadolinium concentrations within the CSF should consider the dynamic aspect of the enhancement and choose their FLAIR sequence parameters and acquisition timing carefully.

Disclosures: Whitney M. Freeze—*RELATED: Grant:* Alzheimer Nederland and Stichting 2Bike4Alzheimer, *Comments:* Costs related to data acquisition and part of my (regular) salary were covered by Alzheimer Nederland and Stichting 2Bike4Alzheimer (research grant WE-03-2012-40).* Roy W. van Hooren—*RELATED: Alzheimer Nederland* (research grant WE-03-2012-40), *Comments:* Part of my salary enabling my work for this project was funded by this grant*; *UNRELATED: Employment:* Maastricht University, *Comments:* The rest of my salary was paid by Maastricht University. Heidi I.L. Jacobs—*RELATED: Grant:* Alzheimer Nederland, *Comments:* This research was supported by Alzheimer Nederland (research grant WE-03-2012-40)*; *Support for Travel to Meetings for the Study or Other Purposes:* Alzheimer Nederland, *Comments:* Dr Freeze was supported by Alzheimer Nederland to present this work July 14–18, 2019 at Alzheimer's Association International Conference.* Frans R. Verhey—*UNRELATED: Grants/Grants Pending:* European Commission, *Comments:* Dementia: Intersectorial Strategy for Training and Innovation Network for Current Technology, Marie Curie H2020 Innovative Training Network.* *Money paid to institution.

REFERENCES

1. Köhrmann M, Struffert T, Frenzel T, et al. **The hyperintense acute reperfusion marker on fluid-attenuated inversion recovery magnetic resonance imaging is caused by gadolinium in the cerebrospinal fluid.** *Stroke* 2012;43:259–61 CrossRef Medline
2. Freeze WM, Schnerr RS, Palm WM, et al. **Pericortical enhancement on delayed postgadolinium fluid-attenuated inversion recovery images in normal aging, mild cognitive impairment, and Alzheimer disease.** *AJNR Am J Neuroradiol* 2017;38:1742–47 CrossRef Medline
3. Absinta M, Vuolo L, Rao A, et al. **Gadolinium-based MRI characterization of leptomeningeal inflammation in multiple sclerosis.** *Neurology* 2015;85:18–28 CrossRef Medline
4. Zivadinov R, Ramasamy DP, Vaneckova M, et al. **Leptomeningeal contrast enhancement is associated with progression of cortical atrophy in MS: a retrospective, pilot, observational longitudinal study.** *Mult Scler* 2017;23:1336–45 CrossRef Medline
5. Latour LL, Kang DW, Ezzeddine MA, et al. **Early blood-brain barrier disruption in human focal brain ischemia.** *Ann Neurol* 2004;56:468–77 CrossRef Medline
6. Kidwell CS, Burgess R, Menon R, et al. **Hyperacute injury marker (HARM) in primary hemorrhage: a distinct form of CNS barrier disruption.** *Neurology* 2011;77:1725–28 CrossRef Medline
7. Merino JG, Latour LL, Tso A, et al. **Blood-brain barrier disruption after cardiac surgery.** *AJNR Am J Neuroradiol* 2013;34:518–23 CrossRef Medline
8. Eisele P, Griebel M, Szabo K, et al. **Investigation of leptomeningeal enhancement in MS: a postcontrast FLAIR MRI study.** *Neurology* 2015;84:770–75 CrossRef Medline

Validation of Zero TE–MRA in the Characterization of Cerebrovascular Diseases: A Feasibility Study

S. Shang, J. Ye, W. Dou, X. Luo, J. Qu, Q. Zhu, H. Zhang, and J. Wu



ABSTRACT

BACKGROUND AND PURPOSE: Zero TE–MRA is less sensitive to field heterogeneity, complex flow, and acquisition noise. This study aimed to prospectively validate the feasibility of zero TE–MRA for cerebrovascular diseases assessment, compared with TOF–MRA.

MATERIALS AND METHODS: Seventy patients suspected of having cerebrovascular disorders were recruited. Sound levels were estimated for each MRA subjectively and objectively in different modes. MRA image quality was estimated by 2 neuroradiologists. The degree of stenosis (grades 0–4) and the z-diameter of aneurysms (tiny group ≤ 3 mm and large group > 3 mm) were measured for further quantitative analysis. CTA was used as the criterion standard.

RESULTS: Zero TE–MRA achieved significantly lower subjective perception and objective noise reduction (37.53%). Zero TE–MRA images showed higher signal homogeneity (3.29 ± 0.59 versus 3.04 ± 0.43) and quality of venous signal suppression (3.67 ± 0.47 versus 2.75 ± 0.46). The intermodality agreement was higher for zero TE–MRA than for TOF–MRA (zero TE, 0.90; TOF, 0.81) in the grading of stenosis. Zero TE–MRA had a higher correlation than TOF–MRA (zero TE, 0.84; TOF, 0.74) in the tiny group and a higher consistency with CTA (intraclass correlation coefficient, 0.83; intercept, -0.5084 – -1.1794 ; slope -0.4952 to -0.2093) than TOF–MRA (intraclass correlation coefficient, 0.64; intercept, 0.7000 – 2.6133 ; slope -1.0344 to -0.1923). Zero TE–MRA and TOF–MRA were comparable in the large group. Zero TE–MRA had more accurate details than TOF–MRA of AVM and Moyamoya lesions.

CONCLUSIONS: Compared with TOF–MRA, zero TE–MRA achieved more robust performance in depicting cerebrovascular diseases. Therefore, zero TE–MRA was shown to be a promising MRA technique for further routine application in the clinic in patients with cerebrovascular diseases.

ABBREVIATIONS: ASL = arterial spin-labeling; AVM = arteriovenous malformation; MRA = magnetic resonance angiography; CTA = computed tomography angiography; CE = contrast-enhanced; TOF = time-of-flight; zTE = zero echo time; MIP = maximum intensity projection; VR = volume rendering; MCA = middle cerebral artery; ICA = internal carotid artery

Cerebrovascular diseases are the main causes of ischemic or hemorrhagic incidents within brain tissues and can lead to neurologic deficits or even death. Imaging of the cerebral vasculature plays a pivotal role in the initial diagnosis of cerebrovascular disorders, such as steno-occlusive arterial disease, cerebral an-

eurysm, AVM, and Moyamoya disease, in addition to treatment decisions and follow-up evaluation.^{1,2} Although patients suspected of having cerebrovascular disease are best diagnosed with DSA or CTA due to their superior angiogram quality,^{3,4} these protocols place patients at risk of ionizing radiation and contrast-induced renal insufficiency.

MRA, a noninvasive and radiation-free imaging technique, has been proposed as a promising alternative for vascular disease assessment.⁵ In addition to conventional angiographic techniques, such as TOF–MRA and contrast-enhanced MRA, MRA is also able to use the principles of arterial spin-labeling (ASL) strategies.⁶ ASL–MRA was introduced as a noninvasive approach that uses inflowing blood as an endogenous contrast agent. Recent technical advances in ASL–MRA have dramatically expanded its clinical application. In particular, a newly developed zero TE radial ASL–MRA (zTE–MRA) method that integrates both a continuous ASL strategy and a zTE radial acquisition readout has dem-

Received April 29, 2019; accepted after revision July 2.

From the Department of Radiology (S.S., J.Y., X.L., Q.Z., H.Z., J.W.), Clinical Medical College, Yangzhou University, Yangzhou, Jiangsu, China; and MR Research China (W.D., J.Q.), GE Healthcare, Beijing, China.

This work was supported by a grant from the National Natural Science Foundation of China (NSFC 81571652), “333 Project” of Jiangsu Province (BRA2017154), Science and technology project of Yangzhou (YZ2018059).

Please address correspondence to Jingtao Wu, MD, Department of Radiology, Clinical Medical College, Yangzhou University, No. 98, Nantong West Road, Guangling, Yangzhou 225009, Jiangsu, China; e-mail: wujingtaoctor@126.com

 Indicates open access to non-subscribers at www.ajnr.org

 Indicates article with supplemental on-line photos.

<http://dx.doi.org/10.3174/ajnr.A6173>

Table 1: Parameters of MRA sequences

	TR/TE (ms)	Flip Angle	FOV (cm)	Matrix	Thickness (mm)	Slices	NEX	Bandwidth (kHz)	Slabs	Label Duration (sec)	Coverage	Time (min:sec)
zTE-MRA	862/0.016	3°	15 × 15	166 × 166	1.2	320	1	31.25	—	2	Calvarium-mandible	5:48
TOF-MRA	25/3.4	15°	30 × 24	320 × 256	1.4	256	1	41.67	3	—	Cingulate cortex–mesencephalon	5:08

Note:— indicates no data available; TR, repetition time; TE, echo time; FOV, field of view; NEX, number of excitation.

Table 2: Parameters of CTA sequences

	Collimation	Pitch	FOV (cm)	Gantry Rotation Time (ms)	Thickness (mm)	Slices	Tube Voltage (kV[peak])	Tube Current (mAs)	Dose-Length Product (mGy × cm)	Coverage
CTA	128 × 0.625	0.758	17 × 17	400	0.6	715	100–120	100–450	220–608	Aortic arch–vertex

onstrated potential for the follow-up assessment of coiled aneurysms,^{7–10} highlighting the clinical value of this approach.

However, it remains unclear whether this technique is also useful for the assessment of other cerebrovascular disorders. Meanwhile, the acoustic noise reduction of zTE-MRA has still not been assessed systematically, though this approach was described as silent.^{7–9} To explore this issue, we applied this novel, nonenhanced MRA approach in a clinical population with suspected cerebrovascular diseases. Sound-level assessment and imaging properties were systematically assessed and compared with those obtained using TOF-MRA. In addition, CTA measurements were also performed and used as the criterion standard.

MATERIALS AND METHODS

Patient Cohort

A single-center prospective study was performed with the approval from local institutional review board of Clinical Medical College, Yangzhou University (2017-KY081). Patients suspected of having cerebrovascular disorders were enrolled in this study from May 2017 to February 2018. Cerebrovascular disorders were suspected for the first time by 2 experienced neurologists (Yong Zhen, with 24 years of experience; Long Yu, with 30 years of experience) on the basis of clinical symptoms (eg, dizziness, headache, paralysis, paresthesia, conscious disturbance, dysmnnesia, dementia, and other psychiatric symptoms) and routine head CT examinations (eg, infarction, hemorrhage, encephalatrophy, and other lesions of abnormal density). Written informed consent was obtained from each participant before MR imaging.

The following criteria for patient exclusion were applied in this study: 1) contraindication for MR imaging, including severe claustrophobia, ferromagnetic foreign bodies, or electronic implants; 2) other intracranial lesions, such as tumor or hydrocephalus (traumatic or tumor-related); 3) an acute or subacute window for a vascular event (relatively large acute cerebral infarction or acute cerebral infarction of the brain stem on DWI); 4) additional conditions that could potentially cause severe movement or being uncooperative, such as psychiatric disorders or congenital/acquired deafness; 5) estimated glomerular filtration rate <60 mL/min/1.73 m²; and 6) younger than 18 years of age. Finally, 69 patients (38 men and 31 women; range, 20–83 years of age; mean age, 60.04 ± 13.70 years) were enrolled in this study. One patient had subarachnoid hemorrhage caused by aneurysm and underwent only MRA because of an allergy to iodinated contrast media. The MRA images (On-line Fig 1) were thus used only for image-

quality measurement. Finally, both MRA and CTA were successfully performed in 68 patients.

Image Acquisition

MR imaging measurements (DWI, MRA) were obtained 24 hours before CTA acquisition on a 3T MR imaging scanner (Discovery MR750w; GE Healthcare, Milwaukee, Wisconsin) using a 24-channel head-neck united coil. The corresponding scan parameters and source images are shown in Table 1 and On-line Fig 2.

CTA was acquired on a 64-slice spiral CT scanner (LightSpeed VCT; GE Healthcare) using a contrast medium (iodixanol, Visipaque, 320 mg I/mL; GE Healthcare, Piscataway, New Jersey). The scanning protocol was described in a previously reported study.¹¹ The corresponding scan parameters are shown in Table 2.

Sound Assessment of MRA Measurements

MRAs were performed in random order and separated by a 5-minute interval during scanning.

After each measurement, the patient was asked to rate the sound experience subjectively on a 5-point scale¹²: 0 = no noise, 1 = mild noise, 2 = moderate noise, 3 = loud noise, 4 = very loud noise, and 5 = unacceptable noise/cancellation of MR imaging.

Objective measurements were obtained in an ambient mode (without scanning) and scanning mode using a sound-level meter (Type AS804; Smart Sensor, Guangdong, China) that was placed 1 m from the gantry. Each measurement period lasted for 30 seconds, and measurements were repeated 5 times in different directions.

Image Analysis

The maximum intensity projection (MIP) and volume-rendering (VR) methods were used to reconstruct both MRA and CTA data by a neuroradiologist (Q.Z., with 9 years of experience) using a commercially available dedicated workstation (Advantage Workstation, software Version 4.6; GE Healthcare) We made the following standard projections of MIP and VR: 1) coronal view, 2) lateral view, and 3) the optimal projection used at the lesions.

The corresponding CTA images (source image, MIP, and VR) were independently and blindly evaluated by 2 experienced neuroradiologists (observer C, J.W., with 27 years of experience; observer D, X.L., with 16 years of experience) at separate time points. The corresponding MRA images (source image, MIP, and VR) were independently and blindly evaluated by 2 experienced neuroradiologists (observer A, H.Z., with 25 years of experience; ob-

server B, J.Y., with 20 years of experience)) at separate time points. All images were scored to determine signal homogeneity, lesion conspicuity, quality of venous signal suppression, and diagnostic confidence. A previously reported 4-point scale was applied^{13,14}: 4 = excellent (excellent-quality diagnostic information with a clearly detailed vascular architecture, no artifacts), 3 = good (good-quality diagnostic information with adequate delineation of the vascular architecture, minimal artifacts), 2 = poor (poor-quality diagnostic information with ordinary delineation of the vascular architecture, moderate artifacts), and 1 = not visible (almost no signal of the vascular architecture, severe artifacts). The time interval between the qualitative analyses was 4 weeks. In cases of disagreement, a consensus was established between observers.

Observers were also asked to record additional vascular disease findings based on MRA and CTA images. The measurements were performed on the VR images. For further quantitative analysis, the degree of stenosis was graded according to the standard from NASCET: 0 for <9%, one for <30%, two for 30%–69%, three for 70%–99%, and 4 for 100%. In addition, aneurysms were divided into tiny (≤ 3 mm) and large (> 3 mm) groups according to the long-axis diameters of the lesions as determined on CTA images.

Statistical Analysis

All statistical analyses were performed using SPSS 19.0 software (IBM, Armonk, New York).

The differences in subjective noise-level and image-quality ratings between MRAs were analyzed using Wilcoxon signed rank tests. One-way analysis of variance tests and least significant dif-

ference tests were used to estimate the difference in the objective sound-level measurements between MRAs.

For the stenosis analysis, the Spearman correlation coefficient (r) was used to evaluate the correlation of each MRA to CTA. Weighted κ statistics were used to assess interobserver agreement and intermodality agreement between the results obtained with each MRA and CTA.

The aneurysm measurements obtained on MRA were correlated with those obtained on CTA using a Pearson analysis. Bland-Altman analysis and intraclass correlation coefficients were used to test the consistency of measurements obtained using the MRAs and CTAs. A weighted κ value or an intraclass correlation coefficient higher than 0.81 was interpreted as excellent agreement, while 0.61–0.81 indicated good, 0.41–0.60 indicated moderate, 0.21–0.40 indicated fair, and < 0.21 indicated poor agreement. The 95% confidence interval was calculated. A P value $< .05$ was considered statistically significant.

RESULTS

Patient Cohort

CTA revealed 32 steno-occlusive cases in 26 patients, 31 cerebral aneurysm cases in 22 patients, 11 steno-occlusive cases and 8 cerebral aneurysm cases in 8 patients, 2 patients with AVMS, 3 patients with Moyamoya disease, and 7 patients without evident vascular diseases. The distribution of the steno-occlusive arteries (cases) was as follows: middle cerebral artery (MCA), 18; internal carotid artery (ICA), 10; posterior cerebral artery, 6; anterior cerebral artery, 5; vertebral artery, 2; and basilar artery 2. The distribution of the aneurysms was as follows: posterior communicating artery, 14; anterior communicating artery, 10; ICA, 7; MCA, 4; anterior cerebral artery, 2; posterior inferior cerebellar artery, 1; and vertebral artery, 1. The 2 AVM lesions were located in the left MCA and right ICA (1 each). The 3 Moyamoya lesions were located at the origin of a unilateral MCA.

Sound-Level Assessment

Mean sound-level perception based on subjective sound experience was significantly lower on zTE-MRA than on TOF-MRA (1.36 ± 0.48 versus 4.17 ± 0.75 , $P = .001$). The intensities of sound measured in different modes are shown in Table 3. Noise levels recorded during zTE-MRA scanning were 34.85 dB (37.53%) lower in sound intensity. In addition, there was a slight increase (3.12 dB, 5.68%, $P < .001$) in sound levels over the ambient mode.

Image-Quality Evaluation of zTE- and TOF-MRA

The mean scores for signal homogeneity (3.29 ± 0.59 versus 3.04 ± 0.43 , $P = .03$) and the quality of venous signal suppression (3.67 ± 0.47 versus 2.75 ± 0.46 , $P = .01$) were significantly higher for zTE-MRA than for TOF-MRA. zTE-MRA was comparable with TOF-MRA in lesion conspicuity (3.21 ± 0.51 versus

Table 3: Intensity of sound levels in different modes for zTE-MRA and TOF-MRA

Mode	Sound Level (dB)	F	P
Ambient	54.89 \pm 0.41 ^a	11,824.06	<.001
zTE-MRA	58.01 \pm 0.32 ^{ab}		
TOF-MRA	92.86 \pm 0.64 ^b		

^a A significant difference compared with the TOF-MRA mode.

^b A significant difference compared with the ambient mode.

Table 4: Cross-table of stenosis grade from observers for zTE-MRA (n = 44)^a

zTE-MRA A Grade	zTE-MRA B Grade					Total
	0	1	2	3	4	
0	1	0	0	0	0	1 (2.27%)
1	0	7	3	0	0	10 (22.73%)
2	0	0	14	0	0	14 (31.82%)
3	0	0	4	8	0	12 (27.27%)
4	0	0	0	1	6	7 (15.91%)
Total	1 (2.27%)	7 (15.91%)	21 (47.73%)	9 (20.45%)	6 (13.64%)	44

^a Grading criterion: NASCET. Data represent the number of cases. A and B are observers A and B.

Table 5: Cross-table of stenosis grade from observers for TOF-MRA (n = 44)^a

TOF-MRA A Grade	TOF-MRA B Grade					Total
	0	1	2	3	4	
0	0	0	0	0	0	0 (0.00%)
1	1	9	0	0	0	10 (22.73%)
2	0	1	8	4	0	13 (29.55%)
3	0	0	4	7	0	11 (25.00%)
4	0	0	0	2	8	10 (22.73%)
Total	1 (2.27%)	10 (22.73%)	12 (27.27%)	13 (29.55%)	8 (18.18%)	44

^a Grading criterion: NASCET. Data represent the number of cases. A and B are observers A and B.

3.06 ± 0.45, *P* = .08) and diagnostic confidence (3.23 ± 0.46 versus 3.05 ± 0.44, *P* = .06). Additionally, the peripheral vessels presented on zTE-MRA were less well-defined than on TOF-MRA.

Quantitative Analysis of zTE- and TOF-MRA Images

The interobserver agreement for CTA was excellent (weighted κ , 0.94; 95% CI, 0.90–0.99). CTA revealed eleven (25%) cases with grade 1, thirteen (29.55%) with grade 2, twelve (22.27%) with grade 3, and seven (15.91%) with grade 4. One case (2.27%) was wrongly categorized as grade 1 by TOF-MRA, while zTE-MRA, consistent with CTA, showed that there was no steno-occlusive lesion (On-line Fig 3).

The correlations of the results obtained using each MRA with CTA results were both high (zTE, *r* = 0.94; TOF, *r* = 0.92). There was excellent interobserver agreement for zTE-MRA (weighted κ : 0.92; 95% CI, 0.87–0.98) and TOF-MRA (weighted κ : 0.89; 95% CI, 0.84–0.96). The intermodality agreement between zTE-MRA and CTA was excellent (weighted κ : 0.90; 95% CI, 0.82–0.99), and it was good (weighted κ : 0.81; 95% CI, 0.71–0.92) between TOF-MRA and CTA. These data are shown in Tables 4–6. Some lesions, especially at a critical point between 2 grades, may have been overestimated on TOF-MRA, while on zTE-MRA, the stenosis was equal to that observed on CTA (Fig 1).

All aneurysms (39/39, 100%) were detected by zTE-MRA. On

Table 6: Classification of stenosis grade from observers for zTE-MRA, TOF-MRA, and CTA (n = 44)^a

Stenosis Grade	zTE-MRA	TOF-MRA	CTA
0	1 (2.27%)	0 (0.00%)	1 (2.27%)
1	11 (25.00%)	10 (22.73%)	11 (25.00%)
2	12 (27.27%)	12 (27.27%)	13 (29.55%)
3	11 (25.00%)	11 (25.00%)	10 (22.73%)
4	9 (20.45%)	11 (25.00%)	9 (20.45%)

^a Grading criterion: NASCET. Data represent the number of cases.

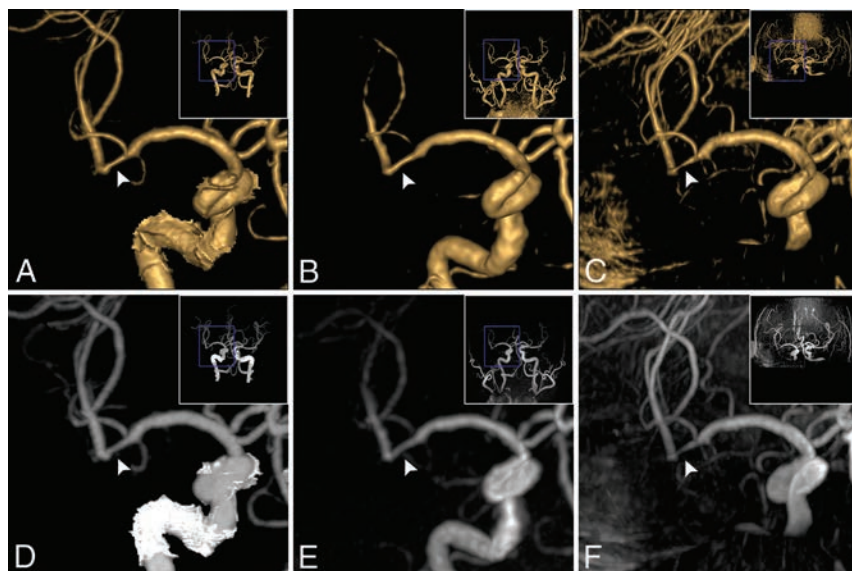


FIG 1. Coronal projection of stenosis in the right MCA M2 segment (a 74-year-old man). A stenosis (34%, grade 2) was observed on VR of CTA (A, white arrowhead) and on VR of zTE-MRA (B, white arrowhead); the stenosis (32%, grade 2) was equal to that on CTA. The stenosis on VR of TOF (C, white arrowhead) was overestimated (72%, grade 3). In correspondence with MIP of CTA (D, white arrowhead), flow signal in the stenosis lesion was homogeneous on MIP of zTE-MRA (E, white arrowhead, score 4) and was heterogeneous on TOF-MRA (F, white arrowhead, score 3).

TOF-MRA, 1 case (2.56%) was missed due to limited coverage. Thus, there were 23 cases (23/38, 60.53%) in the large group and 15 cases (15/38, 39.47%) in the tiny group. The data are shown in Table 7. In the tiny group, according to Bland-Altman analysis, zTE MRA was equal to CTA, whereas TOF-MRA was not. In the large group, according to Bland-Altman analysis, zTE-MRA and TOF-MRA were equal to CTA. In the tiny group, zTE-MRA was more sensitive than TOF-MRA for the depiction of tiny aneurysms (Fig 2). In the large group, zTE-MRA was similar to TOF-MRA in the depiction of large aneurysms (On-line Fig 4).

Because of their distinct characteristics, the 2 patients with AVMs (2/2, 100%) and the 3 with Moyamoya disease (3/3, 100%) were all diagnosed by observers using both MRA sequences. However, zTE-MRA was superior to TOF-MRA with regard to imaging details, such as the depiction of the nidus, draining vein, and venous sinus in AVMs (Fig 3) and stenosed arteries and developed collateral vessels in Moyamoya disease (Fig 4).

DISCUSSION

In this study, by comparing zTE-MRA with TOF-MRA, we demonstrate that zTE-MRA was able to depict cerebrovascular diseases (steno-occlusive arterial disease, cerebral aneurysm, AVM, and Moyamoya disease) with dramatically reduced acoustic noise, higher signal homogeneity, and higher quality of venous signal suppression. Interobserver and intermodality agreement was higher for zTE-MRA than for TOF-MRA for stenosis grading, indicating that zTE-MRA is a robust method for stenosis assessment. In addition, zTE-MRA provided more accuracy with regard to aneurysm-diameter measurement and morphologic assessment, especially in smaller aneurysms. zTE-MRA was superior to TOF-MRA in the identification of lesion details in both AVM and Moyamoya disease, despite the relatively small sample size.

Currently, TOF-MRA is the MR imaging technique conventionally used to depict intracranial arteries. However, there are known major limitations to the use of TOF-MRA for the delineation of cerebrovascular disorders, such as pseudo-occlusions,¹⁵ the inaccurate detection of aneurysms¹⁶ and the nidus and draining veins in AVMs,¹⁷ and collateral vessels in Moyamoya disease.¹⁸ The resultant signal losses are mainly due to saturation secondary to slow flow or phase-dispersion effects caused by turbulent flow,¹⁹ which account for the overestimation or inaccuracy of TOF-MRA observed in our study. In contrast to TOF-MRA, zTE-MRA showed some encouraging characteristics as a nonenhanced MRA approach. Continuous ASL-based angiography was introduced as an endogenous contrast tracer in zTE-MRA to magnetically label inflowing blood, and this placed no constraint on the direction of blood flow.⁶ Thus, zTE-MRA has the potential to visualize slow flow and is independent of flow direction, features especially important for evaluating the

Table 7: Statistical analyses of aneurysms measured on MRA for groups

Group	MRA	Sum	r^a	Intercept (95% CI) ^b	Slope (95% CI) ^b	ICC
Group tiny ^c	zTE	15	0.84	-0.5084-1.1794	-0.4952-0.2093	0.83; 95% CI, 0.57-0.94
	TOF	15	0.74	0.7000-2.6133	-1.0344 to -0.1923	0.64; 95% CI, 0.21-0.86
Group large ^d	zTE	23	0.98	-0.6059-0.2130	-0.02625-0.1200	0.98, 95% CI, 0.97-0.99
	TOF	23	0.95	-1.1571-0.3062	-0.01380-0.2520	0.95, 95% CI, 0.89-0.98

Note:—ICC indicates intraclass correlation coefficient.

^a Pearson correlation coefficient.

^b Intercept and slope are by Bland-Altman analysis.

^c Group tiny ≤ 3 mm.

^d Group large > 3 mm.

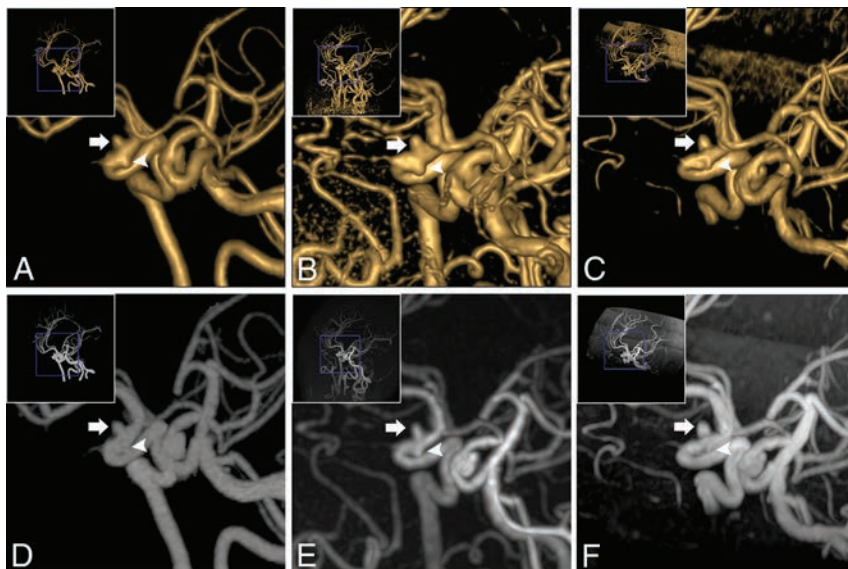


FIG 2. Oblique projection of aneurysms in the right ICA siphon segment (a 63-year-old woman). Two aneurysms were found on VR of CTA (A): The diameters were 3.0×3.2 mm (white arrow) and 2.4×2.1 mm (white arrowhead), respectively. Equal findings were observed on VR of zTE (B, 3.3×3.5 mm, white arrow; $2. \times 2.4$ mm, white arrowhead). On VR of TOF-MRA (C), the large one (3.1×3.4 mm, white arrow) was equal to the one on CTA. However, the tiny one was not evident (1.5×1.4 mm, white arrowhead). Concerning MIP of CTA (D, white arrow and white arrowhead), the same results were observed on MIP of zTE-MRA (E, white arrow and white arrowhead) and TOF-MRA (F, white arrow and white arrowhead).

flow in severe stenosis (grade 3), microaneurysms, and collateral vessels.

Acoustic noise induced by rapid switching of gradient coils during long scan times is still the main drawback that causes patient discomfort and movement.²⁰⁻²² The zTE technique, which uses a sequence solution, attenuates acoustic noise by reducing the slew rate and enabling minimal gradient variations.^{23,24} Alibek et al¹² assessed the noise level and image quality of silent T1-weighted sequences on a clinical 3T MR imaging scanner. However, whether a similar amount of acoustic noise reduction could be achieved using zTE-MRA remains unclear because an extra ASL-based angiography was integrated into this approach. In this study, patients were much more comfortable during zTE-MRA than TOF-MRA, and the reduction in sound intensity between the 2 was comparable with that of a silent T1-weighted sequence. Thus, zTE-MRA would be an acceptable alternative angiography method for these patients.

In addition to acoustic noise attenuation, a zTE inside-out radial acquisition could also minimize the phase dispersion of the labeled blood flow signal in the voxel space, thereby making zTE-MRA insensitive to turbulent flow.^{9,25} The flow signal inside the

large aneurysms was more homogeneous on zTE-MRA than on TOF-MRA in our study, though the correlations with CTA were both high and the consistency with CTA was excellent for the large group.

Susceptibility artifacts, which occur mostly in regions adjacent to the skull base or cavernous sinus, always induce signal loss as a result of air-soft tissue or bone-soft tissue boundary interference.²⁶ Because of its use of a constant gradient and a long readout duration, zTE-MRA is less susceptible to field inhomogeneity and eddy current and can acquire more homogeneous flow signals in vascular lesions, such as stenosis or aneurysms in the ICA siphon segment. Moreover, zTE-MRA is less sensitive than TOF-MRA to motion effects,²⁷ and it therefore minimizes the misregistration and degradation of image quality and achieves improved diagnostic performance.

According to the principles of the ASL strategy used by zTE-MRA, images are acquired via subtraction to yield an angiographic image with nearly zero background.⁷ The efficiency of postprocessing (ie, VR or MIP reconstructions) can be improved with automatic subtraction, whereas the artifacts caused by skull and brain tissue on TOF-MRA must be manually removed. Furthermore, zTE-MRA demonstrated effective background suppression while a search for aneurysms was performed in the setting of subarachnoid hemorrhage in the presence of residual T1-bright blood. An optimal postlabel delay was set,^{6,28} ensuring that the labeled bolus flowed into the target tissue in the imaging region and that the labeled protons lost their signal before entering the veins. Thus, better diagnostic image quality was achieved due to an acceptable signal-to-noise ratio and the elimination of vein contamination. Additionally, zTE-MRA can detect arteriovenous shunting on the basis of this technical feature. In this study, we identified a huge AVM and found that zTE-MRA was capable of revealing its tubular structures, nidus, and draining veins and even a venous sinus.

Contrast-enhanced MRA is another commonly used noninvasive MRA approach performed by administering a T1-shortening paramagnetic contrast medium. Despite the controversy related to its diagnostic accuracy,^{15,16} contrast-enhanced MRA has

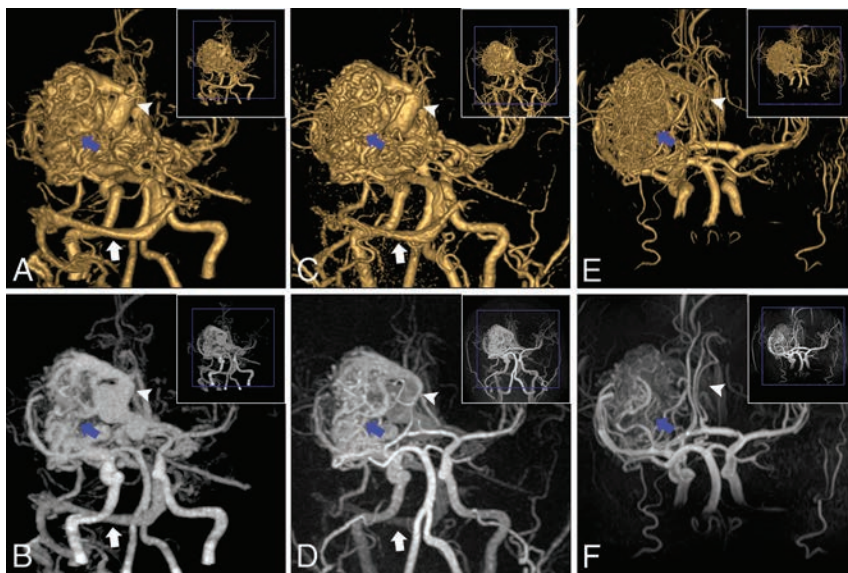


FIG 3. An AVM in the left MCA M1 segment (a 27-year-old man). For the AVM, the nidus (blue arrow), draining vein (white arrowhead), and venous sinus (transverse sinus and sigmoid sinus, white arrow) were clearly depicted on VR and MIP of CTA (A and B) and zTE-MRA (C and D), whereas they were not well-defined (nidus, blue arrow; draining vein, white arrowhead) and were missed (venous sinus) on VR and MIP of TOF-MRA (E and F).

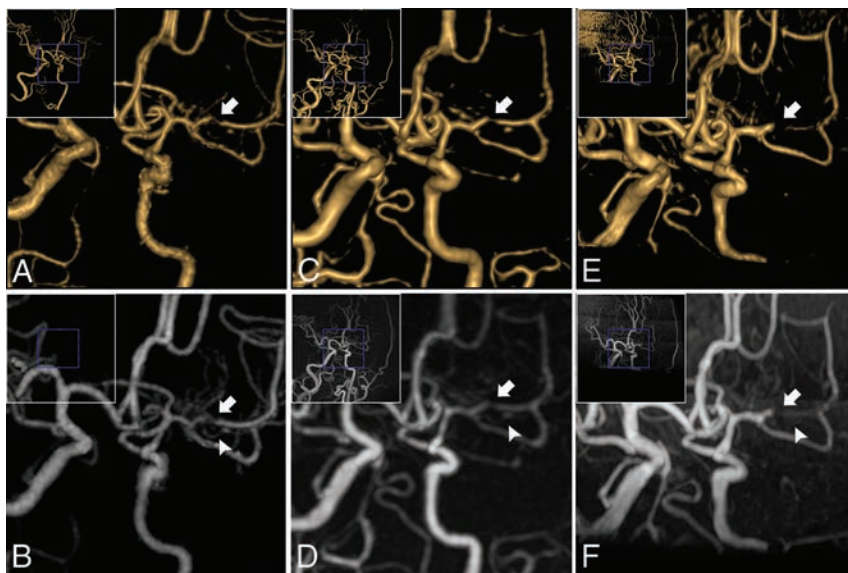


FIG 4. Oblique projection of Moyamoya disease in the left MCA M1 segment (a 43-year-old woman). The stenosed MCA (white arrowhead) and developed collateral vessels (white arrow) were scanned on VR and MIP of CTA (A and B) and zTE-MRA (C and D). A false occlusion in MCA (white arrowhead) and ill-defined collateral vessels (white arrow) were seen on VR and MIP of TOF-MRA (E and F).

demonstrated some superiorities over TOF-MRA, such as it is less vulnerable to blood flow disturbances, has a reduced risk of movement artifacts, and provides large coverage for additional findings, while TOF-MRA also has some advantages over contrast-enhanced MRA in that it requires no exogenous contrast agent and is repeatable and easy to manipulate. Although our results indicate that zTE-MRA integrates these potential aspects beyond the reduction of venous artifacts, these characteristics need to be verified by further research.

In the present study, we demonstrated that zTE-MRA is a robust sequence that maintains both zTE-like and ASL-like charac-

teristics. Several studies⁷⁻¹⁰ have focused on zTE-MRA in the follow-up imaging of various aneurysm embolizations and have revealed that this method achieves higher image quality than is obtained by TOF-MRA. Our study enriches our knowledge of zTE-MRA and highlights the clinical usefulness in evaluating cerebrovascular diseases.

Holdsworth et al²⁴ noted that zTE-MRA is more prone to blurring of the vessel edge because of center-out radial sampling, as shown in Fig 1 and our previous study.¹⁰ Qu et al²⁹ implemented a hybrid ASL strategy in zTE-MRA that led to a clearer depiction of vessels. Therefore, image quality could be further improved by the development of new techniques.

However, some limitations of this study should be recognized. First, because of the high accuracy of CTA and the disadvantages of DSA, CTA was used as the reference in this study. Furthermore, DSA is not generally routinely used for screening cerebrovascular diseases, and it would be very difficult to obtain approval of the ethics committee to evaluate this issue in our patient population. However, DSA would be more accurate if used as the reference. Second, contrast-enhanced MRA was not performed as a comparison method because there is some concern regarding the combined adverse effects of MR imaging and CTA contrast media on renal function. In addition, we aimed to investigate the validation of zTE-MRA in noncontrast MRA sequences. Third, when scan time was compromised, the resolution of peripheral vessels by zTE-MRA seemed to be lower than that achieved by TOF-MRA, though larger coverage was obtained, and cerebrovascular lesions were visualized much better on zTE-MRA. The modification of some parameters would improve the resolution of zTE-MRA in future studies. Fourth, the data obtained for objective sound-level measurements do not reflect the real situation inside the coil, though noise levels were statistically lower during the zTE-MRA scan. More advanced and accurate measurement techniques must be used in future studies.

CONCLUSIONS

In this study, we found that compared with TOF-MRA, zTE-MRA achieved higher image quality and accuracy, provided a more comfortable experience for the patient, and produced results more consistent with those obtained using CTA. Due to its

robust performance, zTE-MRA is demonstrated to be a promising non-contrast-enhanced alternative MRA technique that could be more routinely used in the clinic for patients with cerebrovascular diseases. Future studies should also provide supporting evidence and verification in larger clinical populations for zTE-MRA and should also include additional varieties of diseases.

REFERENCES

- Hollnagel DI, Summers PE, Poulikakos D, et al. **Comparative velocity investigations in cerebral arteries and aneurysms: 3D phase-contrast MR angiography, laser Doppler velocimetry and computational fluid dynamics.** *NMR Biomed* 2009;22:795–808 CrossRef Medline
- Lavina B. **Brain vascular imaging techniques.** *Int J Mol Sci* 2016;18 CrossRef Medline
- Li Q, Lv F, Wei Y, et al. **Automated subtraction CT angiography for visualization of the whole brain vasculature: a feasibility study.** *Acad Radiol* 2013;20:1009–14 CrossRef Medline
- Zhao DL, Wan Y, Wang GK, et al. **Evaluation of image quality in carotid and cerebrovascular disease: a comparative study between subtraction and routine computed tomography angiography.** *Echocardiography* 2016;33:1735–40 CrossRef Medline
- Roth C. **Cerebrovascular diagnostics: imaging** [in German]. *Radiologe* 2012;52:1101–06 CrossRef Medline
- Wu H, Block WF, Turski PA, et al. **Noncontrast-enhanced three-dimensional (3D) intracranial MR angiography using pseudocontinuous arterial spin labeling and accelerated 3D radial acquisition.** *Magn Reson Med* 2013;69:708–15 CrossRef Medline
- Irie R, Suzuki M, Yamamoto M, et al. **Assessing blood flow in an intracranial stent: a feasibility study of MR angiography using a silent scan after stent-assisted coil embolization for anterior circulation aneurysms.** *AJNR Am J Neuroradiol* 2015;36:967–70 CrossRef Medline
- Takano N, Suzuki M, Irie R, et al. **Usefulness of non-contrast-enhanced MR angiography using a silent scan for follow-up after Y-configuration stent-assisted coil embolization for basilar tip aneurysms.** *AJNR Am J Neuroradiol* 2017;38:577–81 CrossRef Medline
- Takano N, Suzuki M, Irie R, et al. **Non-contrast-enhanced silent scan MR angiography of intracranial anterior circulation aneurysms treated with a low-profile visualized intraluminal support device.** *AJNR Am J Neuroradiol* 2017;38:1610–16 CrossRef Medline
- Shang S, Ye J, Luo X, et al. **Follow-up assessment of coiled intracranial aneurysms using zTE MRA as compared with TOF MRA: a preliminary image quality study.** *Eur Radiol* 2017;27:4271–80 CrossRef Medline
- Yang L, Huang X, Duan S. **Clinical application and technique of 64-slice spiral CT subtraction angiography in head and neck.** *Vasa* 2012;41:27–33 CrossRef Medline
- Alibek S, Vogel M, Sun W, et al. **Acoustic noise reduction in MRI using Silent Scan: an initial experience.** *Diagn Interv Radiol* 2014;20:360–63 CrossRef Medline
- Cong F, Zhuo Y, Yu S, et al. **Noncontrast-enhanced time-resolved 4D dynamic intracranial MR angiography at 7T: a feasibility study.** *J Magn Reson Imaging* 2018;48:111–20 CrossRef Medline
- Kim YK, Lin WC, Sung K, et al. **Reducing artifacts during arterial phase of gadoxetate disodium-enhanced MR imaging: dilution method versus reduced injection rate.** *Radiology* 2017;283:429–37 CrossRef Medline
- Boujan T, Neuberger U, Pfaff J, et al. **Value of contrast-enhanced MRA versus time-of-flight MRA in acute ischemic stroke MRI.** *AJNR Am J Neuroradiol* 2018;39:1710–16 CrossRef Medline
- HaiFeng L, YongSheng X, YangQin X, et al. **Diagnostic value of 3D time-of-flight magnetic resonance angiography for detecting intracranial aneurysm: a meta-analysis.** *Neuroradiology* 2017;59:1083–92 CrossRef Medline
- Fujima N, Osanai T, Shimizu Y, et al. **Utility of noncontrast-enhanced time-resolved four-dimensional MR angiography with a vessel-selective technique for intracranial arteriovenous malformations.** *J Magn Reson Imaging* 2016;44:834–45 CrossRef Medline
- Togao O, Hiwatashi A, Obara M, et al. **Acceleration-selective arterial spin-labeling MR angiography used to visualize distal cerebral arteries and collateral vessels in Moyamoya disease.** *Radiology* 2018;286:611–21 CrossRef Medline
- Igase K, Igase M, Matsubara I, et al. **Mismatch between TOF MR angiography and CT angiography of the middle cerebral artery may be a critical sign in cerebrovascular dynamics.** *Yonsei Med J* 2018;59:80–84 CrossRef Medline
- McNulty JP, McNulty S. **Acoustic noise in magnetic resonance imaging: an ongoing issue.** *Radiography* 2009;15:320–26 CrossRef Medline
- Mollasadeghi A, Mehrparvar AH, Atighechi S, et al. **Sensorineural hearing loss after magnetic resonance imaging.** *Case Rep Radiol* 2013;2013:510258 CrossRef Medline
- Munn Z, Jordan Z. **Interventions to reduce anxiety, distress and the need for sedation in adult patients undergoing magnetic resonance imaging: a systematic review.** *Int J Evid Based Healthc* 2013;11:265–74 CrossRef Medline
- Weiger M, Brunner DO, Dietrich BE, et al. **ZTE imaging in humans.** *Magn Reson Med* 2013;70:328–32 CrossRef Medline
- Holdsworth SJ, Macpherson SJ, Yeom KW, et al. **Clinical evaluation of silent T1-weighted MRI and silent MR angiography of the brain.** *AJR Am J Roentgenol* 2018;210:404–11 CrossRef Medline
- Moon JL, Baek HJ, Ryu KH, et al. **A novel non-contrast-enhanced MRA using silent scan for evaluation of brain arteriovenous malformation: a case report and review of literature.** *Medicine (Baltimore)* 2017;96:e8616 CrossRef Medline
- Choi CG, Lee DH, Lee JH, et al. **Detection of intracranial atherosclerotic steno-occlusive disease with 3D time-of-flight magnetic resonance angiography with sensitivity encoding at 3T.** *AJNR Am J Neuroradiol* 2007;28:439–46 Medline
- Weiger M, Wu M, Wurnig MC, et al. **Rapid and robust pulmonary proton ZTE imaging in the mouse.** *NMR Biomed* 2014;27:1129–34 CrossRef Medline
- Dai W, Garcia D, Bazelaire CD, et al. **Continuous flow-driven inversion for arterial spin labeling using pulsed radio frequency and gradient fields.** *Magn Reson Med* 2008;60:1488–97 CrossRef Medline
- Qu J, Wu B, Zhou Z. **Silent magnetic resonance angiography with hybrid arterial spin labeling techniques.** In: *Proceedings of the Annual Meeting of the International Society for Magnetic Resonance in Medicine*, Singapore. May 7–13, 2016

Defining Ischemic Core in Acute Ischemic Stroke Using CT Perfusion: A Multiparametric Bayesian-Based Model

K. Nael, E. Tadayon, D. Wheelwright, A. Metry, J.T. Fifi, S. Tuhirim, R.A. De Leacy, A.H. Doshi, H.L. Chang, and J. Mocco



ABSTRACT

BACKGROUND AND PURPOSE: The Bayesian probabilistic method has shown promising results to offset noise-related variability in perfusion analysis. Using CTP, we aimed to find optimal Bayesian-estimated thresholds based on multiparametric voxel-level models to estimate the ischemic core in patients with acute ischemic stroke.

MATERIALS AND METHODS: Patients with anterior circulation acute ischemic stroke who had baseline CTP and achieved successful recanalization were included. In a subset of patients, multiparametric voxel-based models were constructed between Bayesian-processed CTP maps and follow-up MRIs to identify pretreatment CTP parameters that were predictive of infarction using robust logistic regression. Subsequently CTP-estimated ischemic core volumes from our Bayesian model were compared against routine clinical practice oscillation singular value decomposition–relative cerebral blood flow <30%, and the volumetric accuracy was assessed against final infarct volume.

RESULTS: In the constructed multivariate voxel-based model, 4 variables were identified as independent predictors of infarction: TTP, relative CBF, differential arterial tissue delay, and differential mean transit time. At an optimal cutoff point of 0.109, this model identified infarcted voxels with nearly 80% accuracy. The limits of agreement between CTP-estimated ischemic core and final infarct volume ranged from –25 to 27 mL for the Bayesian model, compared with –61 to 52 mL for oscillation singular value decomposition–relative CBF.

CONCLUSIONS: We established thresholds for the Bayesian model to estimate the ischemic core. The described multiparametric Bayesian-based model improved consistency in CTP estimation of the ischemic core compared with the methodology used in current clinical routine.

ABBREVIATIONS: AIS = acute ischemic stroke; ATD = arterial tissue delay; AUC = area under the curve; diff = differential; oSVD = oscillation singular value decomposition; rCBF = relative CBF

In patients with acute ischemic stroke (AIS), characterization of ischemic core on baseline imaging is essential for proper treatment decision-making.^{1–3} While DWI provides the most accurate estimation of ischemic core,^{4,5} CTP can improve the diagnostic yields of CT-based imaging techniques for delineation of ischemic core to approach those of MR imaging.^{6–8}

Following successful implementation of CTP for improved

treatment selection in patients presenting with large-vessel occlusion and up to 24 hours from the onset,^{9,10} CTP is now included in the latest American Heart Association guidelines for treatment selection in patients with anterior circulation large-vessel occlusion who present beyond 6 hours from the onset of symptoms (class I, level of evidence A).¹¹

As quantitative CTP is gaining momentum for widespread clinical use, neurology and radiology communities need to be aware of its potential pitfalls. One of the disadvantages of CTP is substantial variability and the potential for erroneous estimation of the ischemic core, which may be at least partially related to the inherently noisy nature of CTP datasets.^{12,13} Because an ischemic core volume of >50–70 mL^{14,15} could potentially exclude patients from a life-saving treatment, this pitfall could have important therapeutic and prognostic implications.

Although recent application of quantitative CTP has shown promising results in the supervised and controlled environment of clinical trials, there remains variability and inconsistency in the

Received March 26, 2019; accepted after revision July 7.

From the Department of Radiology (K.N., E.T., A.M., A.H.D.), Neuroimaging Advanced and Exploratory Lab, and Departments of Neurology (D.W., J.F., S.T.), Neurosurgery (J.F., R.A.D.L., J.M.), and Population Health Science and Policy (H.C.), Icahn School of Medicine at Mount Sinai, New York, New York.

Preliminary results of this article previously presented at: International Stroke Conference, February 5–8, 2019; Honolulu, Hawaii. Abstract: WP87.

Please address correspondence to Kambiz Nael, MD, Icahn School of Medicine at Mount Sinai, Department of Radiology, One Gustave L. Levy Place, Box 1234, New York, New York; e-mail: Kambiznael@gmail.com; @kambiznael

Indicates open access to non-subscribers at www.ajnr.org

<http://dx.doi.org/10.3174/ajnr.A6170>

accuracy of quantitative CTP data provided in routine daily practice.^{13,16-20}

The Bayesian method is a robust probabilistic method that minimizes the effects of oscillation and high levels of noise during residue function estimation compared with other deconvolution methods.^{21,22} The advantages of the Bayesian model to provide more accurate estimation of perfusion values and reduction of variability have been shown in experimental phantom studies^{23,24} and also recently in a cohort of patients with AIS.²⁵

In this study we had 2 aims: first, to define the optimal Bayesian-based thresholds for estimation of ischemic core. In particular, we aimed to develop a multiparametric model from our CTP datasets that provides a high degree of accuracy in the estimation of ischemic core in comparison with MR imaging. The second aim was a comparative analysis between the diagnostic accuracy of our Bayesian-based model and routinely used postprocessing methodology to estimate the ischemic core from CTP datasets in patients with AIS.

MATERIALS AND METHODS

Patients

We included consecutive patients with AIS who presented to our institution between January 2016 and July 2018 and had the following inclusion criteria: 1) anterior circulation ischemic stroke with proximal arterial occlusion (carotid or MCA); 2) baseline CTP; 3) successful recanalization defined by TICI \geq 2b via mechanical thrombectomy; and 4) follow-up imaging within 1 week after recanalization to calculate the final infarct volume. We excluded patients who had the following: 1) time from CTP to recanalization of >4 hours; 2) rethrombosis/reocclusion of the recanalized artery on follow-up MRA/CTA; or 3) development of significant intracranial hemorrhage that precluded accurate estimation of infarct volume on follow-up imaging. The study was performed under an approved institutional review board guideline.

CTP Image Acquisition

CTP was performed on 2 CT scanners, a LightSpeed VCT (GE Healthcare, Milwaukee, Wisconsin) and a Somatom Definition (Siemens, Erlangen, Germany). We used the following scan parameters: 100-mm coverage in the z-axis, 80 kV, 150 mA, effective dose = 3.3 mSv, slice thickness = 5 mm, collimation = 64×0.625 mm. Total acquisition time was 60 seconds (30 consecutive spiral acquisitions of 2 seconds each). A total of 50 mL of Isovue-370 (iopamidol; Bracco, Princeton, New Jersey) was injected intravenously followed by a 20-mL saline flush at 5 mL/s.

Image Analysis

CTP data were processed using FDA-approved postprocessing software (Olea Sphere Version 6.0; Olea Medical, La Ciotat, France). First, the arterial input function was detected automatically using a cluster-analysis algorithm.²⁶ This arterial input function was subsequently used by the Bayesian probabilistic method²² to generate the perfusion parametric maps, including TTP, CBF, CBV, arterial tissue delay (ATD), and MTT. Relative

values for CBF and CBV (rCBF, relative CBV) were calculated by dividing the absolute values of each voxel within the infarction mask by the mean value of the contralateral side.

Model Development (Voxel-Based Analysis). The first 19 patients who had pretreatment CTP and postthrombectomy MR imaging were included for model development. For image registration and analysis, the CTP template was first thresholded to 0–180 HU and the brain was extracted from the CTP template using the FSL Brain Extraction Tool ($f = 0.01$) (BET; <https://fsl.fmrib.ox.ac.uk/fsl/fslwiki/BET>). To account for regional differences in perfusion values across brain areas, 5 additional maps were generated (difference maps) by subtracting the mean value of a cube of 27 voxels centered on the voxel exactly on the contralateral hemisphere of each voxel. The contralateral voxel was defined as the voxel on the opposite hemisphere that had a similar Euclidean distance from the center (anterior commissure) on the axial plane.

These differential (diff) maps (TTP_{diff}, rCBF_{diff}, relative CBV_{diff}, ATD_{diff}, and MTT_{diff}) in addition to the 5 primary parametric maps (a total of 10 variables) were included in image-analysis and predictive modeling. Extracted brain from all CTP maps was linearly transformed and registered to brain MR imaging using the FMRIB Linear Image Registration Tool (FLIRT; <https://fsl.fmrib.ox.ac.uk/fsl/fslwiki/FLIRT>) with 9 *df* and a mutual information cost function. All registrations were visually inspected for accuracy.

An infarction mask and 2 noninfarction masks, 1 on the ipsilateral and 1 on the contralateral side of the lesion, were drawn on the MR imaging for each subject by a board-certified neuroradiologist. Coregistered DWI was available to guide and confine the VOI to the region of acute infarction. All CTP voxel values from these 3 masks in each patient were exported for statistical analysis.

Volumetric Analysis. The final output of our Bayesian-based predictive model defined by its logit scores (see Results) was used to calculate the ischemic core volume in the remaining patients ($n = 48$), whose CTP data were not used for model development. The logit scores were programmed into a software developmental kit (Olea Infinite Software Developmental Kit; Olea Medical). The DICOM images of Bayesian-processed CTP maps were exported into this software to calculate the ischemic core volume using the logit scores of our model.

In addition, the CTP-estimated ischemic core volume for each patient was calculated by applying the broadly used threshold methodology (rCBF $<30\%$)⁷ currently applied in clinical practice using an oscillation singular value decomposition (oSVD).²⁷

The volume of final infarction was calculated by applying a volume of interest on the DWI hyperintense region using a voxel-based signal intensity method subsuming the entire region of DWI hyperintensity. When follow-up MR imaging was not available, follow-up CT within 24–48 hours from thrombectomy was used for determination of final infarct volume. In these patients, the infarct (defined as established hypodense regions) was manually delineated by a neuroradiologist with 10 years of experience.

Statistical Analysis

Voxel-level logistic regression models were used to identify pretreatment CTP parameters (5 parametric maps + 5 differential maps) that were predictive of infarction. Voxels from baseline CTP that fell within the MR imaging–defined infarct area were considered true infarction, and all other voxels were considered not infarcted. Because the infarct status among voxels from the same subject may be correlated, the Huber-White standard errors (ie, robust standard errors) were computed to account for the additional source of variability. CTP parameters that were significant at the .15 level in the univariate logistic regression analysis were considered for the multivariable model. A backward-selection

approach was then used to identify significant variables at the .05 level.

The final multiparametric model was assessed using receiver operating characteristic curve analysis. The optimal cutoff point (measured on the logit scale) that identified a voxel as infarct was determined by the Youden index. Summary measures such as sensitivity, specificity, and accuracy were calculated on the basis of the optimal threshold to quantify how well the final model differentiated between infarct and noninfarct voxels.

Finally, the CTP-estimated ischemic core volumes obtained from $\text{oSVD-rCBF} < 30\%$ (that is used in routine practice) and from the multiparametric Bayesian model (optimal logit score) were compared against the final infarct volume using Bland-Altman methods. The optimal volumetric agreement was determined by the smallest mean magnitude (absolute) difference in lesion volume. All statistical analyses were performed at the .05 (2-sided) significance level using SAS 9.4 (SAS Institute, Cary, North Carolina), R 3.1.1 statistical and computing software (<http://www.r-project.org>), and SPSS 17.0 (IBM, Armonk, New York).

Table 1: Voxel-based univariate analysis of infarction and noninfarction voxels^a

Variable	Infarction	Noninfarction	P Value ^b
TTP	32.00 (1.95)	24.30 (1.19)	<.001
rCBF	24.78 (2.81)	48.43 (6.49)	<.001
rCBV	2.81 (0.46)	4.09 (0.56)	.02
ATD	3.58 (0.18)	1.49 (0.16)	<.001
MTT	6.58 (0.58)	5.33 (0.15)	.01
rCBV _{diff}	-25.60 (10.93)	3.20 (1.20)	.02
rCBV _{diff}	-1.15 (0.52)	0.06 (0.06)	.03
TTP _{diff}	8.39 (0.41)	0.25 (0.17)	<.001
ATD _{diff}	2.15 (0.17)	-0.16 (0.06)	<.001
MTT _{diff}	2.19 (0.49)	-0.12 (0.06)	<.001

Note:—rCBV indicates relative CBV.

^a The values are presented as mean (SD). The SDs reported are the Huber-White (robust) standard errors. All units are in seconds, except for rCBF and rCBV, which are unitless.

^b P values are based on a linear regression model with the presence of infarct as the independent variable and imaging parameters as the outcome.

RESULTS

A total of 88 charts were reviewed with 67 patients (40 women, 27 men) available for analysis. Two patients were excluded due to development of a large intracranial hemorrhage. Two patients were excluded because they had rethrombosis of the recanalized MCA on follow-up MRA. Nine patients were excluded because of nondiagnostic CTP (significant motion, $n = 4$), insufficient contrast bolus ($n = 2$), and a truncated arterial input function ($n =$

3). Eight patients were excluded due to having >4 hours of recanalization time from the onset of CTP. The mean age was 69.6 ± 14.4 years. The median stroke severity measured by the NIHSS was 15 (interquartile range, 9–21). A total of 15 (22%) patients had internal carotid artery occlusion, and 52 (78%) had proximal MCA occlusion (M1, $n = 38$; M2, $n = 14$). The mean of time from symptom onset was 8.7 ± 5.2 hours. A total of 25 patients presented <6 hours from the onset, and 42 presented after 6 hours. The median time from CTP to recanalization was 1.8 hours (interquartile range, 1.3–2.7 hours), and from CTP to follow-up imaging used for determination of final infarction, it was 24 hours (interquartile range, 19–31 hours). Final recanalization scores were TICI 2b ($n = 22$, 33%), TICI 2c ($n = 16$, 24%) and TICI 3 ($n = 29$, 43%).

Voxel-Based Analysis

A total of 2,577,261 voxels in 19 patients were included in the voxel-based analysis. All 10 imaging variables were significantly associated with infarction in the univariate analysis (Table 1). The final

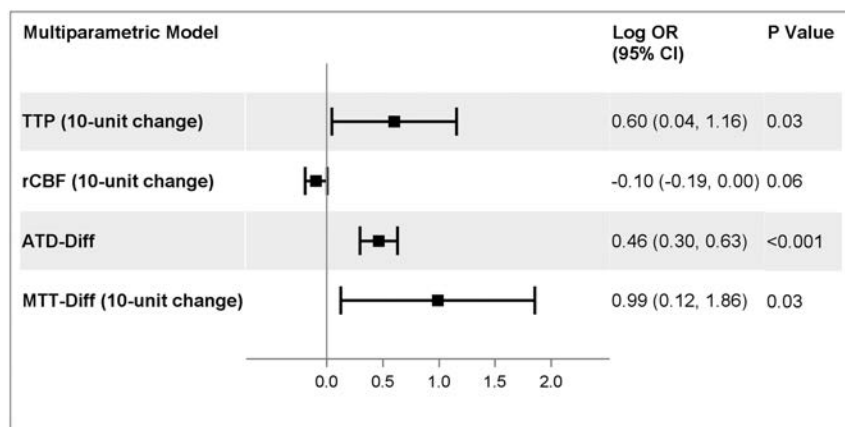


FIG 1. Multiparametric voxel-based model for infarction.

Table 2: Optimal threshold, sensitivity, specificity, and accuracy for TTP, rCBF, ATD_{diff}, MTT_{diff}, and the final model in identifying infarcted voxels

Variable	Threshold	Sensitivity	Specificity	Accuracy	AUC
TTP	28.82 seconds	65.3%	77.9%	76.5%	0.76
rCBF	22.10	60.0%	72.9%	71.5%	0.73
ATD _{diff}	0.87 seconds	68.1%	80.2%	78.9%	0.80
MTT _{diff}	1.38 seconds	56.2%	74.5%	72.5%	0.69
Final model ^a	0.109 ^b	74.2%	80.0%	79.4%	0.84

^a The final model consisted of TTP, rCBF, ATD_{diff}, and MTT_{diff} as the independent variables and the presence of infarct as the outcome.

^b Equation of the final model: $\text{logit}(P) = -3.9170 + 0.0601 \times \text{TTP} - 0.0095 \times \text{rCBF} + 0.4629 \times \text{ATD}_{\text{diff}} + 0.0989 \times \text{MTT}_{\text{diff}}$ where $\text{logit}(P)$ = estimated log odds of infarction for a given voxel. If $\text{logit}(P)$ is greater than the optimal threshold of 0.109, the voxel is classified as infarct.

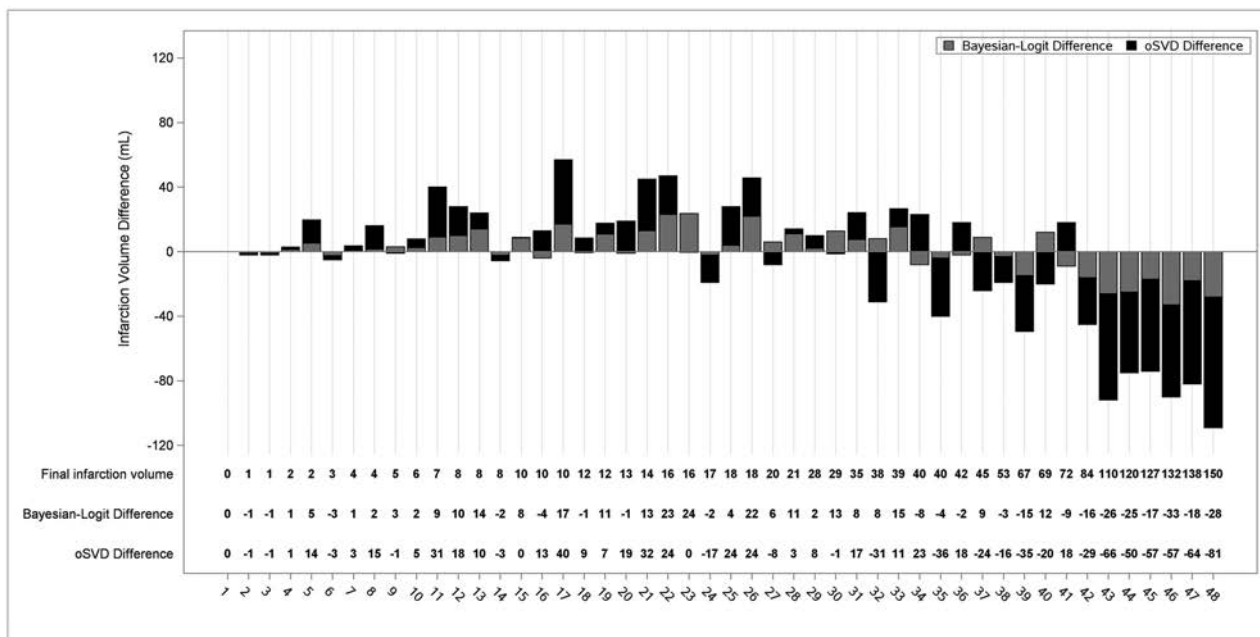


FIG 2. Stacked bar graph visualization of errors in ischemic core volume estimation compared with final infarction volume by Bayesian-logit and oSVD postprocessing. The error values are noticeably greater with oSVD (black bars) compared with Bayesian-logit (gray bars).

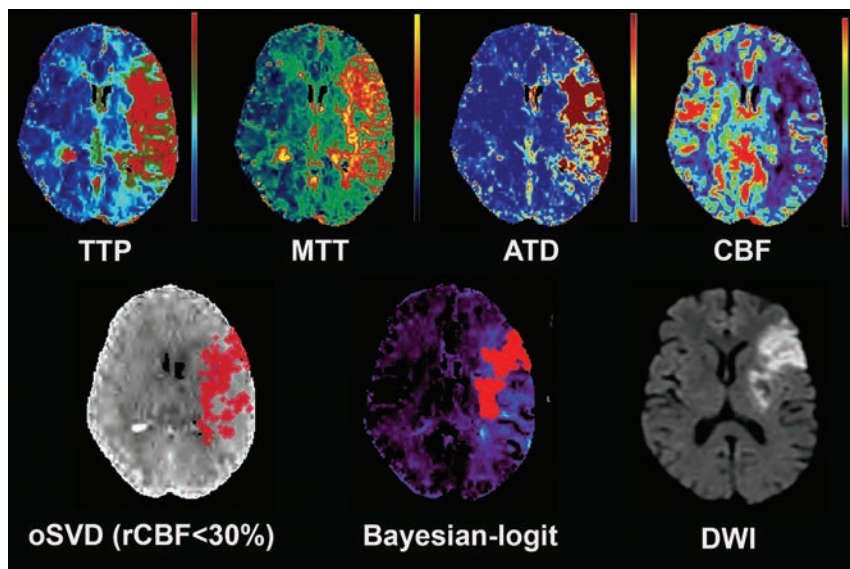


FIG 3. A 74-year-old woman who presented with left M1 occlusion and a baseline NIHSS score of 26. She underwent successful mechanical thrombectomy (TICI 2c). The time from CTP to recanalization was 78 minutes, and the time from CTP to MR imaging was 19 hours. The 4 CTP maps included in our final model are shown. Note that the estimated ischemic core derived from our multiparametric Bayesian-logit model provides more accurate estimation of final infarction on MR imaging in comparison with what is estimated from oSVD-CBF <30% (current clinical practice).

multiparametric model contained 4 variables that remained independent predictors of infarction when evaluated against other imaging parameters. The CTP measures that were associated with an increased log odds of infarction included TTP (10-unit change, log odds ratio, 0.60; 95% CI, 0.04–1.16; $P = .03$), ATD_{diff} (log odds ratio, 0.46; 95% CI, 0.30–0.63; $P < .001$), and MTT_{diff} (10-unit change, log odds ratio, 0.99; 95% CI, 0.12–1.86; $P = .03$). Higher rCBF was protective (10-unit change, log odds ratio, -0.10 ; 95% CI, -0.19 to 0 ; $P = .058$) (Fig 1). The parameters

relative CBV and MTT were highly correlated with rCBF and MTT_{diff} , respectively, and were subsequently removed.

Based on the final model, the optimal cut-point value (ie, optimal logit score) that discriminated infarcted voxels from noninfarcted ones was 0.109. At this threshold, the accuracy of the classification was 79.4%, with a sensitivity of 74.2% and a specificity of 80%. The area under the receiver operating characteristic curve (AUC) was 0.84 (Table 2). Receiver operating characteristic analysis was also performed on the individual components of the final model. The optimal thresholds identified were: TTP, 28.82 seconds (AUC = 0.76); rCBF, 22.1 (AUC = 0.73); ATD_{diff} , 0.87 second (AUC = 0.80); and MTT_{diff} , 1.38 seconds (AUC = 0.69).

Volumetric Analysis

Volumetric analysis was based on 48 patients whose CTP data were not used to develop the voxel-level models. The

mean final infarct volume calculated from the follow-up MR imaging ($n = 40$) and CT ($n = 8$) was 36 mL (± 41). The mean estimated ischemic core volumes were 31 mL (± 24) for oSVD and 37 mL (± 33) for the Bayesian-based logit score.

The means of differences between CTP-estimated ischemic core volume and final infarct volume were -4 mL (95% CI, -13 to 4 mL) for oSVD-CBF <30% and 1 mL (95% CI, -3 to 5 mL) for the Bayesian-based logit score. The individualized error bars for estimation of the final infarct volume between the Bayesian-

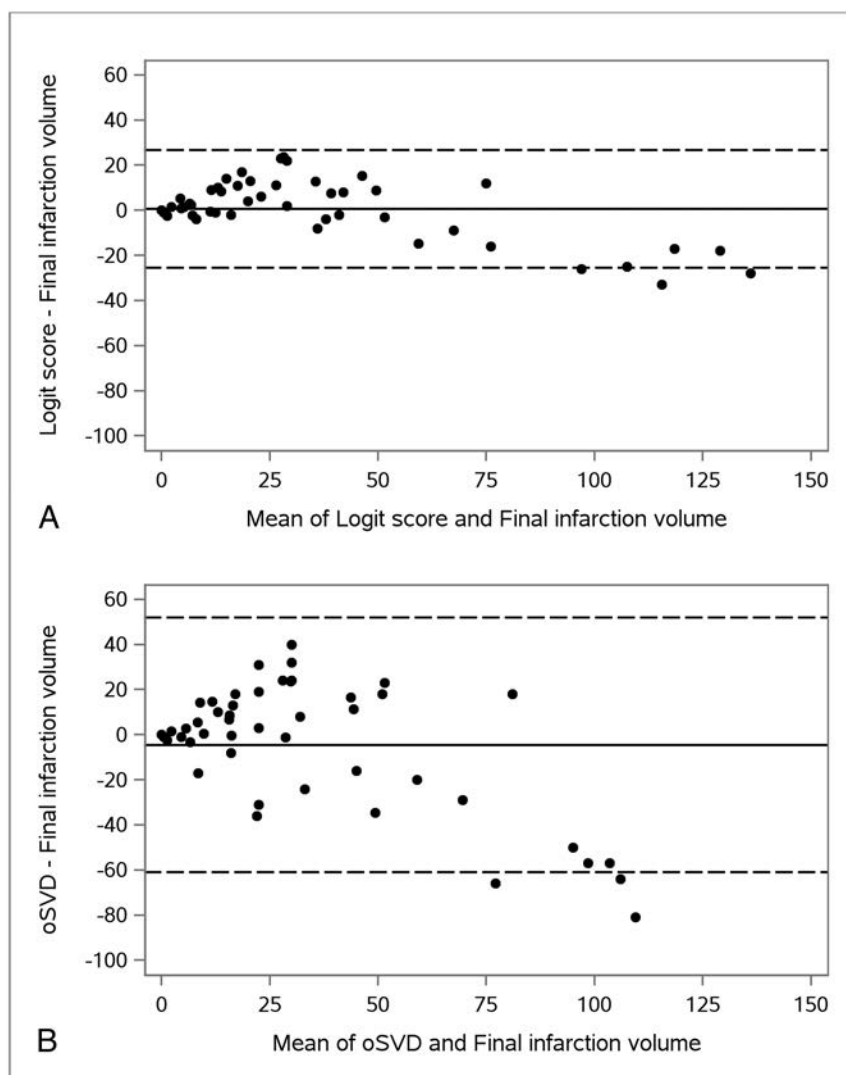


FIG 4. Bland-Altman plots of calculated final infarct volume and estimated ischemic core volume using the Bayesian-based logit score (A) and oSVD-rCBF <30% (B). *Solid lines* represent the mean differences. *Dashed lines* indicate 2 SDs above and below the mean differences. The limits of agreement were -25 to 27 for the Bayesian-based logit score and -61 to 52 for oSVD-CBF <30%.

based approach and the currently used clinical method (oSVD-rCBF <30%) are shown in Fig 2.

Figure 3 shows an example of CTP-estimated ischemic core using oSVD-rCBF and our Bayesian-based logit score in comparison with MR imaging.

Bland-Altman plots for comparison of CTP-estimated ischemic core volume and final infarct volume for each postprocessing method are summarized in Fig 4. The limits of agreement defined as the mean \pm 2 times the SD of the differences were -25 to 27 for the Bayesian-based logit score and -61 to 52 for oSVD-CBF.

DISCUSSION

Although quantitative CTP has been used successfully for treatment selection of patients with AIS in a controlled environment of randomized clinical trials, its day-to-day use may still be challenging due to inconsistencies of the results that are reflected in the literature.^{13,16,17,19,25,28,29}

There are several barriers to effective implementation of CTP in acute stroke care, including differences in CT scanners and hardware, postprocessing methodology such as different software packages, and different deconvolution techniques for quantitative analysis.³⁰⁻³³ One of the potential limitations of quantitative CTP is related to the inherently noisy nature of CTP data, which can affect postprocessing and result in erroneous calculation of the ischemic core. This limitation can become a larger problem when postprocessing is performed by deconvolution via singular value decomposition, a highly noise-sensitive technique,^{34,35} currently used by most commercially available postprocessing software.

The theoretic advantages of the Bayesian method for more accurate estimation of perfusion parameters have been shown in digital phantom and simulation studies.²²⁻²⁴ A recent study in patients with AIS also showed reduced variability in CTP-estimated ischemic core volume by the Bayesian method in comparison with singular value decomposition.²⁵

This study, to our knowledge, is the first to establish optimal thresholds for estimation of ischemic core volume using the Bayesian method. We showed that the most accurate single parameter for estimation of infarction was ATD_{diff} with an overall accuracy of 78.9% (AUC = 0.80). For every 1-second-delay difference within the ischemic territory and contralateral hemisphere, the odds ratio of a voxel being infarcted was 1.59

(95% CI, 1.35–1.88, $P < .001$). Most interesting, the threshold for Bayesian-estimated rCBF was lower than what is used currently for singular value decomposition-based methodology (22.1% versus 30%). This finding confirms the results of a recent study showing that Bayesian-estimated rCBF at the threshold of 30% can result in overestimation of the ischemic core.²⁵ The final multiparametric Bayesian-based model provided the highest diagnostic accuracy in predicting infarction, with an overall accuracy of 79.4% (AUC = 0.84). In this model, if the logit score of a voxel was greater than the optimal threshold of 0.109, the voxel would be classified as an infarct.

One advantage of our multiparametric model is that it uses a combination of time maps in addition to currently used rCBF to provide a more accurate estimation of ischemic core, in particular for patients in whom some degree of reperfusion of the ischemic core is present. Increased blood flow within the ischemic territory is a known phenomenon that increases progressively with time

from onset,³⁶⁻³⁸ with the reported incidence of 16% at 8 hours from the onset of ischemia.³⁶ In the absence of thrombolytic treatment, the restoration of blood flow within the ischemic core might be from reperfusion related to spontaneous recanalization of the occluded artery or via development of collateral flow or from severe reperfusion/luxury perfusion related to blood-brain barrier injury.³⁹⁻⁴¹ Regardless of the underlying mechanism, following reperfusion, blood flow within the ischemic core may return to levels beyond the defined threshold (ie, rCBF <30%), which, in turn, can result in erroneous estimation of the ischemic core volume.

The erroneous estimation of ischemic core due to infarct reperfusion can be best addressed using a combination of parametric maps, including time maps and CBF to provide supplementary information that can best approximate the physiologic status of a given voxel within the ischemic bed. Because more patients with AIS are being treated later during their disease course (up to 24 hours) and because the incidence of spontaneous reperfusion of the infarct increases with time,³⁶ multiparametric models such as ours can provide a more realistic estimation of ischemic core volume over what is estimated through rCBF alone.

Our multiparametric Bayesian-based approach showed great reduction in the variability of the estimated ischemic core. Compared with the calculated final infarct volume, the limits of agreement ranged from -25 to +27 mL for our multiparametric Bayesian-based model compared with -61 to +52 mL for oSVD-rCBF. With reliance on ischemic core volume to include or exclude patients from attempted revascularization treatment,^{14,15} accurate and reliable quantification of ischemic core is of paramount importance outside the controlled and supervised environment of clinical trials if CTP is to be adopted broadly in routine clinical practice. The reduced variability in the estimation of the ischemic core afforded by our multiparametric Bayesian model can play a critical role for the broad acceptance of CTP in clinical practice and to ensure that patient selection for mechanical thrombectomy is optimized.

One of the limitations of our study is that due to the retrospective study design, we did not strictly control the time between CTP and recanalization or the time between CTP and MR imaging acquisitions. Growth of infarction and increased volume are possible between CTP and the scans that were used for final infarct volume calculation. We tried to minimize these confounding factors by including patients with successful recanalization and by excluding patients with time from CTP to recanalization of >4 hours. Another limitation is that we used recanalization of \geq TICI 2b as a cutoff for successful recanalization; however, going forward and with advances in mechanical thrombectomy, \geq TICI 2c may be used as a cutoff for successful outcome. Last, the final imaging study used for determination of final infarct volume in our volumetric analysis was CT in a subset of patients (16%) because they could not undergo MR imaging. Although follow-up CT has been used as an acceptable method for determination of final infarct volume, it is plausible that this can result in inconsistencies in comparison with the more accurate MR imaging.

CONCLUSIONS

We established thresholds for the Bayesian model to estimate ischemic core using CTP. The described multiparametric Bayesian-based model improved consistency in the CTP estimation of ischemic core in comparison with the methodology used in current clinical routine. If its potential is realized in a prospective study, the described model can be used for accurate estimation and reduced variability of CTP-estimated ischemic core for broader acceptance of CTP outside the controlled environment of clinical trials.

Disclosures: Kambiz Nael—UNRELATED: Board Membership: Olea Medical, Comments: Medical Advisory Board. Helena Chang—UNRELATED: Employment: Mount Sinai. J. Mocco—UNRELATED: Consultancy: Imperative Care, Cerebrotech Medical Systems, Viseon, Endostream Medical, Rebound Therapeutics, Vastrax, Comments: consultant/ownership interest; Grants/Grants Pending: Stryker, Penumbra, Medtronic, MicroVention, Comments: research support.

REFERENCES

1. Yoo AJ, Leslie-Mazwi TM, Jovin TG. **Future directions in IAT: better studies, better selection, better timing and better techniques.** *J Neurointerv Surg* 2013;5(Suppl 1):i1-6 CrossRef Medline
2. Tarpley J, Franc D, Tansy AP, et al. **Use of perfusion imaging and other imaging techniques to assess risks/benefits of acute stroke interventions.** *Curr Atheroscler Rep* 2013;15:336 CrossRef Medline
3. Ribo M, Tomasello A, Lemus M, et al. **Maximal admission core lesion compatible with favorable outcome in acute stroke patients undergoing endovascular procedures.** *Stroke* 2015;46:2849-52 CrossRef Medline
4. Jauch EC, Saver JL, Adams HP Jr, et al; American Heart Association Stroke Council, Council on Cardiovascular Nursing, Council on Peripheral Vascular Disease, Council on Clinical Cardiology. **Guidelines for the early management of patients with acute ischemic stroke: a guideline for healthcare professionals from the American Heart Association/American Stroke Association.** *Stroke* 2013;44:870-947 CrossRef Medline
5. Schellinger PD, Bryan RN, Caplan LR, et al; Therapeutics and Technology Assessment Subcommittee of the American Academy of Neurology. **Evidence-based guideline: the role of diffusion and perfusion MRI for the diagnosis of acute ischemic stroke: report of the Therapeutics and Technology Assessment Subcommittee of the American Academy of Neurology.** *Neurology* 2010;75:177-85 CrossRef Medline
6. Kamalian S, Kamalian S, Maas MB, et al. **CT cerebral blood flow maps optimally correlate with admission diffusion-weighted imaging in acute stroke but thresholds vary by postprocessing platform.** *Stroke* 2011;42:1923-28 CrossRef Medline
7. Campbell BC, Christensen S, Levi CR, et al. **Cerebral blood flow is the optimal CT perfusion parameter for assessing infarct core.** *Stroke* 2011;42:3435-40 CrossRef Medline
8. Wintermark M, Flanders AE, Velthuis B, et al. **Perfusion-CT assessment of infarct core and penumbra: receiver operating characteristic curve analysis in 130 patients suspected of acute hemispheric stroke.** *Stroke* 2006;37:979-85 Medline
9. Nogueira RG, Jadhav AP, Haussen DC, et al; DAWN Trial Investigators. **Thrombectomy 6 to 24 hours after stroke with a mismatch between deficit and infarct.** *N Engl J Med* 2018;378:11-21 CrossRef Medline
10. Albers GW, Marks MP, Kemp S, et al; DEFUSE 3 Investigators. **Thrombectomy for stroke at 6 to 16 hours with selection by perfusion imaging.** *N Engl J Med* 2018;378:708-18 CrossRef Medline
11. Powers WJ, Rabinstein AA, Ackerson T, et al; American Heart Association Stroke Council. **2018 Guidelines for the Early Management of Patients with Acute Ischemic Stroke: a Guideline for Healthcare Professionals from the American Heart Association/American Stroke Association.** *Stroke* 2018;49:e46-110 CrossRef Medline

12. González RG. **Current state of acute stroke imaging.** *Stroke* 2013;44:3260–64 CrossRef Medline
13. Schaefer PW, Souza L, Kamalian S, et al. **Limited reliability of computed tomographic perfusion acute infarct volume measurements compared with diffusion-weighted imaging in anterior circulation stroke.** *Stroke* 2015;46:419–24 CrossRef Medline
14. Saver JL, Goyal M, Bonafe A, et al; SWIFT PRIME Investigators. **Stent-retriever thrombectomy after intravenous t-PA vs. t-PA alone in stroke.** *N Engl J Med* 2015;372:2285–95 CrossRef Medline
15. Campbell BC, Mitchell PJ, Kleinig TJ, et al; EXTEND-IA Investigators. **Endovascular therapy for ischemic stroke with perfusion-imaging selection.** *N Engl J Med* 2015;372:1009–18 CrossRef Medline
16. Copen WA, Morais LT, Wu O, et al. **In acute stroke, can CT perfusion-derived cerebral blood volume maps substitute for diffusion-weighted imaging in identifying the ischemic core?** *PLoS One* 2015;10:e0133566 CrossRef Medline
17. Bandera E, Botteri M, Minelli C, et al. **Cerebral blood flow threshold of ischemic penumbra and infarct core in acute ischemic stroke: a systematic review.** *Stroke* 2006;37:1334–39 Medline
18. Turowski B, Schramm P. **An appeal to standardize CT- and MR-perfusion.** *Clin Neuroradiol* 2015;25(Suppl 2):205–10 CrossRef Medline
19. Huisa BN, Neil WP, Schrader R, et al. **Clinical use of computed tomographic perfusion for the diagnosis and prediction of lesion growth in acute ischemic stroke.** *J Stroke Cerebrovasc Dis* 2014;23:114–22 CrossRef Medline
20. Geuskens RR, Borst J, Lucas M, et al; MR CLEAN trial investigators (www.mrclean-trial.org). **Characteristics of misclassified CT perfusion ischemic core in patients with acute ischemic stroke.** *PLoS One* 2015;10:e0141571 CrossRef Medline
21. Mouridsen K, Friston K, Hjort N, et al. **Bayesian estimation of cerebral perfusion using a physiological model of microvasculature.** *Neuroimage* 2006;33:570–79 Medline
22. Bouteliet T, Kudo K, Pautot F, et al. **Bayesian hemodynamic parameter estimation by bolus tracking perfusion weighted imaging.** *IEEE Trans Med Imaging* 2012;31:1381–95 CrossRef Medline
23. Sasaki M, Kudo K, Bouteliet T, et al. **Assessment of the accuracy of a Bayesian estimation algorithm for perfusion CT by using a digital phantom.** *Neuroradiology* 2013;55:1197–203 CrossRef Medline
24. Kudo K, Bouteliet T, Pautot F, et al. **Bayesian analysis of perfusion-weighted imaging to predict infarct volume: comparison with singular value decomposition.** *Magn Reson Med Sci* 2014;13:45–50 CrossRef Medline
25. Sakai Y, Delman BN, Fifi JT, et al. **Estimation of ischemic core volume using computed tomographic perfusion.** *Stroke* 2018;49:2345–52 CrossRef Medline
26. Mouridsen K, Christensen S, Gyldensted L, et al. **Automatic selection of arterial input function using cluster analysis.** *Magn Reson Med* 2006;55:524–31 Medline
27. Wu O, Østergaard L, Weisskoff RM, et al. **Tracer arrival timing-insensitive technique for estimating flow in MR perfusion-weighted imaging using singular value decomposition with a block-circulant deconvolution matrix.** *Magn Reson Med* 2003;50:164–74 Medline
28. Hasan TF, Rabinstein AA, Middlebrooks EH, et al. **Diagnosis and management of acute ischemic stroke.** *Mayo Clin Proc* 2018;93:523–38 CrossRef Medline
29. Xin Y, Han FG. **Diagnostic accuracy of computed tomography perfusion in patients with acute stroke: a meta-analysis.** *J Neurol Sci* 2016;360:125–30 CrossRef Medline
30. Konstas AA, Goldmakher GV, Lee TY, et al. **Theoretic basis and technical implementations of CT perfusion in acute ischemic stroke, Part 1: theoretic basis.** *AJNR Am J Neuroradiol* 2009;30:662–68 CrossRef Medline
31. Bivard A, Levi C, Spratt N, et al. **Perfusion CT in acute stroke: a comprehensive analysis of infarct and penumbra.** *Radiology* 2013;267:543–50 CrossRef Medline
32. Goyal M, Menon BK, Derdeyn CP. **Perfusion imaging in acute ischemic stroke: let us improve the science before changing clinical practice.** *Radiology* 2013;266:16–21 CrossRef Medline
33. Kudo K, Sasaki M, Yamada K, et al. **Differences in CT perfusion maps generated by different commercial software: quantitative analysis by using identical source data of acute stroke patients.** *Radiology* 2010;254:200–09 CrossRef Medline
34. Konstas AA, Goldmakher GV, Lee TY, et al. **Theoretic basis and technical implementations of CT perfusion in acute ischemic stroke, Part 2: technical implementations.** *AJNR Am J Neuroradiol* 2009;30:885–92 CrossRef Medline
35. Fieselmann A, Kowarschik M, Ganguly A, et al. **Deconvolution-based CT and MR brain perfusion measurement: theoretical model revisited and practical implementation details.** *Int J Biomed Imaging* 2011;2011:467563 CrossRef Medline
36. Rubin G, Firlik AD, Levy EI, et al. **Xenon-enhanced computed tomography cerebral blood flow measurements in acute cerebral ischemia: review of 56 cases.** *J Stroke Cerebrovasc Dis* 1999;8:404–11 Medline
37. Hakim AM, Pokrupa RP, Villanueva J, et al. **The effect of spontaneous reperfusion on metabolic function in early human cerebral infarcts.** *Ann Neurol* 1987;21:279–89 Medline
38. Jørgensen HS, Sperling B, Nakayama H, et al. **Spontaneous reperfusion of cerebral infarcts in patients with acute stroke: incidence, time course, and clinical outcome in the Copenhagen Stroke Study.** *Arch Neurol* 1994;51:865–73 Medline
39. Shimosegawa E, Hatazawa J, Inugami A, et al. **Cerebral infarction within six hours of onset: prediction of completed infarction with technetium-99m-HMPAO SPECT.** *J Nucl Med* 1994;35:1097–103 Medline
40. Baron JC, Boussier MG, Comar D, et al. **Noninvasive tomographic study of cerebral blood flow and oxygen metabolism in vivo: potentials, limitations, and clinical applications in cerebral ischemic disorders.** *Eur Neurol* 1981;20:273–84 Medline
41. Lin L, Bivard A, Parsons MW. **Perfusion patterns of ischemic stroke on computed tomography perfusion.** *J Stroke* 2013;15:164–73 CrossRef Medline

Color-Mapping of 4D-CTA for the Detection of Cranial Arteriovenous Shunts

M. Meijs, S.A.H. Pegge, K. Murayama, H.D. Boogaarts, M. Prokop, P.W.A. Willems, R. Manniesing, and F.J.A. Meijer



ABSTRACT

BACKGROUND AND PURPOSE: 4D CT angiography is increasingly used in clinical practice for the assessment of different neurovascular disorders. Optimized processing of 4D-CTA is crucial for diagnostic interpretation because of the large amount of data that is generated. A color-mapping method for 4D-CTA is presented for improved and enhanced visualization of the cerebral vasculature hemodynamics. This method was applied to detect cranial AVFs.

MATERIALS AND METHODS: All patients who underwent both 4D-CTA and DSA in our hospital from 2011 to 2018 for the clinical suspicion of a cranial AVF or carotid cavernous fistula were retrospectively collected. Temporal information in the cerebral vasculature was visualized using a patient-specific color scale. All color-maps were evaluated by 3 observers for the presence or absence of an AVF or carotid cavernous fistula. The presence or absence of cortical venous reflux was evaluated as a secondary outcome measure.

RESULTS: In total, 31 patients were included, 21 patients with and 10 without an AVF. Arterialization of venous structures in AVFs was accurately visualized using color-mapping. There was high sensitivity (86%–100%) and moderate-to-high specificity (70%–100%) for the detection of AVFs on color-mapping 4D-CTA, even without the availability of dynamic subtraction rendering. The diagnostic performance of the 3 observers in the detection of cortical venous reflux was variable (sensitivity, 43%–88%; specificity, 60%–80%).

CONCLUSIONS: Arterialization of venous structures can be visualized using color-mapping of 4D-CTA and proves to be accurate for the detection of cranial AVFs. This finding makes color-mapping a promising visualization technique for assessing temporal hemodynamics in 4D-CTA.

ABBREVIATIONS: CCF = carotid cavernous fistula; TTS = time-to-signal

Four-dimensional CT angiography (4D-CTA) is increasingly used in clinical practice for the assessment of different neurovascular disorders as a noninvasive alternative to invasive DSA.¹ Multiple acquisitions over time enable visualization of the cerebral vasculature hemodynamics. Dynamic acquisition during the passage of a contrast bolus enables accurate detection of arterial-venous shunting, seen as abnormal early contrast enhancement of

a dural sinus or cortical vein, due to an AVM or AVF.^{2–5} The main arterial feeders of AVFs can be identified, and the pathway of venous drainage can be estimated. Compared with DSA, 4D-CTA is less time-consuming, less expensive, and has a lower risk of complications.^{6,7} In addition, 4D-CTA is less sensitive to the timing of the acquisition relative to the contrast bolus injection as opposed to static, single-phase CTA.

The high spatial and temporal resolution of 4D-CTA yields large amounts of data, resulting in a laborious and time-consuming diagnostic evaluation and hampers direct interpretation, even for experienced observers. The challenge of 4D-CTA lies in comprehensively and accurately visualizing the essential parts of the imaging data. For example, in the diagnostic work-up of cranial arteriovenous shunts, a continuous 4D-CTA acquisition with high temporal and spatial resolution is crucial, and hemodynamics is evaluated by creating dynamic CTA subtraction images. The evaluation of dynamic CTA requires an accurate evaluation of multiple individual time points for the detection of arterialized venous structures. In a more sophisticated ap-

Received September 18, 2018; accepted after revision June 25, 2019.

From the Departments of Radiology and Nuclear Medicine (M.M., S.A.H.P., M.P., R.M., F.J.A.M.) and Neurosurgery (H.D.B.), Radboud University Medical Center, Nijmegen, the Netherlands; Department of Radiology (K.M.), Fujita Health University, Toyoake, Japan; and Department of Neurosurgery (P.W.A.W.), University Medical Center Utrecht, Utrecht, the Netherlands.

This work was supported by funding from Canon Medical Systems, Japan, and the Nederlandse Organisatie voor Wetenschappelijk Onderzoek.

Please address correspondence to Midas Meijs, MSc, Departments of Radiology and Nuclear Medicine, Radboud University Medical Center, P.O. Box 9101, NL - 6500 HB, Nijmegen, the Netherlands; e-mail: Midas.Meijs@radboudumc.nl

Indicates open access to non-subscribers at www.ajnr.org

Indicates article with supplemental on-line videos.

<http://dx.doi.org/10.3174/ajnr.A6156>

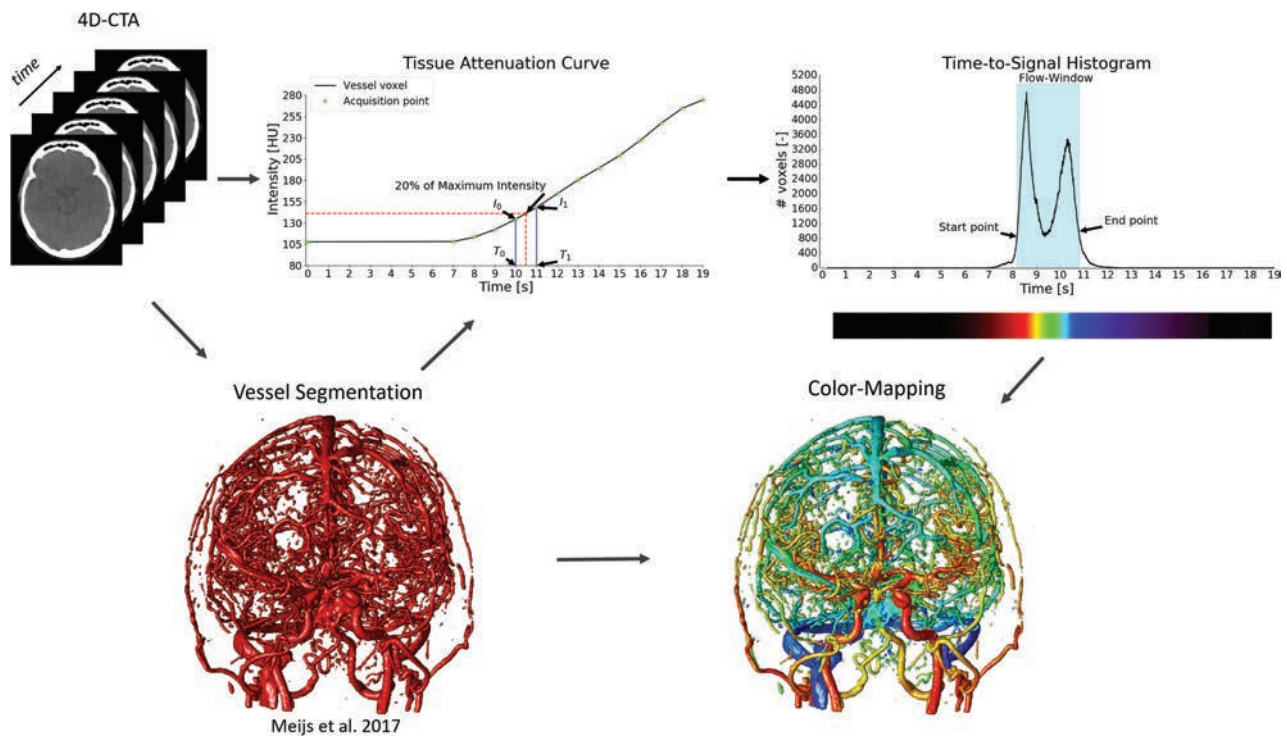


FIG 1. Overview of the proposed method. First, the vessels are segmented in the 4D-CTA acquisitions. Second, time-to-signal is calculated per vessel voxel in the segmentation. Third, the TTS values are aggregated in a histogram, and the start and end of the flow window are determined. Last, a color scale is mapped to the flow window, and the colors are overlaid on the vessel segmentation.

proach for evaluating the vascular morphology on 4D-CTA, the whole 4D dataset can be condensed into a 3D dataset using a temporal maximum intensity projection.⁸ However, this projection has the disadvantage of temporal information being lost.

In this work, a visualization technique for 4D-CTA is proposed that is based on mapping the contrast bolus arrival times in the cerebral vasculature to a color scale. A flow window is adjusted specifically for each patient on the basis of the aggregated temporal information. The method retains temporal (4D) information in a 3D reconstruction. The 4D-CTA color-mapping method was evaluated in an observer study for the detection of cranial AVFs.

MATERIALS AND METHODS

Study Design and Study Population

All patients older than 18 years of age who underwent both 4D-CTA and DSA in our hospital (Radboud University Medical Hospital, Nijmegen) from 2011 to 2018 for the clinical suspicion of a cranial AVF or carotid cavernous fistula (CCF) were retrospectively collected. Patients with a proved AVM (ie, the presence of an intervening nidus) were excluded. The study was approved by the medical ethical committee of our hospital, and informed consent was waived because of the retrospective collection of the study data. The study was conducted in accordance with the ethical standards of the 1964 Declaration of Helsinki and its later amendments.

Data Acquisition

All patients underwent whole-brain 4D-CTA on a 320-detector-row Aquilion ONE CT scanner (Canon Medical Systems, Tokyo,

Japan). The 4D-CTA scanning protocol consisted of a 10- to 12-second continuous acquisition (80 kV, 115 mAs, 0.5-second rotation speed) reconstructed at a temporal resolution of 1 volume per second. A 50-mL contrast agent bolus of iomeprol (300 mg iodine/mL, Iomeron; Bracco, Milan, Italy) was intravenously injected. A test bolus of 15 mL of contrast agent was used for the timing of the acquisition. Image reconstruction was performed with a smooth reconstruction kernel (FC41), resulting in an image matrix of 512×512 with voxel sizes of $0.43 \times 0.43 \times 0.5$ mm. The estimated mean radiation dose for the 4D-CTA examinations was 6.6 mSv (dose-length product, 3176; k-factor, 0.0021).

Color-Mapping

The color-mapping visualization of 4D-CTA consists of 4 steps (Fig 1). First, the vessels are segmented using a random forest classifier using a weighted temporal average and variance as the main image features.⁹ The second step is calculation of the contrast bolus arrival times in the segmented vessels. Gaussian blurring is applied in the temporal direction with $\sigma = 3$ seconds to reduce noise while maintaining spatial resolution. The tissue attenuation curve per voxel describes contrast changes over time in Hounsfield units (HU). For each vessel voxel, a point on this curve is searched where the attenuation reaches a fraction, α , of the maximum signal intensity, corrected for the baseline intensity:

$$1) \quad I_{\text{Threshold}} = I_{\text{min}} + \alpha \times (I_{\text{max}} - I_{\text{min}}).$$

Here, I_{min} and I_{max} are the minimum and maximum intensity in the temporal direction for the current voxel. Depending on the application, α may range from 0 to 1, where 1 resulted in the

temporal maximum intensity projection and the time-to-peak. In our method, the parameter, α , was set to 0.2 for optimal evaluation of contrast bolus arrival times. The TTS is linearly interpolated using $I_{\text{Threshold}}$ and the known acquisition time points as follows:

$$2) \quad TTS = T_0 + \beta \times (T_1 - T_0),$$

With

$$3) \quad \beta = \frac{I_{\text{Threshold}} - I_0}{I_1 - I_0}.$$

Here, T_0 , T_1 , I_0 , and I_1 are the acquisition time points and intensity values around $I_{\text{Threshold}}$, respectively, as shown in the profile intensity curve plot in Fig 1. In the next step, all TTS values of the vessels are aggregated in a histogram that is used to determine a flow window for each patient specifically. The start and end of the flow window are defined as the first and last time points that reach 20% of the maximum peak in the histogram, as illustrated by the TTS histogram in Fig 1. In the final step of the method, a color scale is adjusted around the flow window and overlaid on the vessel segmentation to visualize the arrival times and thus the flow dynamics in the cerebral vasculature.

Diagnostic Evaluation

Three observers, 2 neuroradiologists (F.J.A.M., S.A.H.P.) and a neurosurgeon (H.D.B.) with various levels of experience in reading 4D-CTA, evaluated the color-mapping visualization datasets. The cases were presented to the observers in a random order, and

the observers were blinded to clinical symptoms, DSA, and patient outcome. Initially, only color-mapping processing of 4D-CTA as an overlay on temporal average images of the 4D-CTA was presented to the observers (method 1). In a second step, dynamic subtraction rendering of 4D-CTA was available in addition to color-mapping (method 2).

The primary outcome measure was the detection of cranial AVFs. In case an AVF or CCF was identified, the location, dominant arterial feeders, and the pattern of venous drainage were assessed. The secondary outcome measure was the presence or absence of cortical venous reflux, which is of relevance for grading the dural AVF and for treatment decision-making.¹⁰ The CCFs were graded as either direct type (originating from the internal carotid artery) or indirect type (branches of the external carotid artery serving as arterial feeders).

Reference Standard and Statistical Analysis

DSA was performed in the clinical diagnostic work-up of all cases, was independently evaluated by neurovascular interventionalists, and served as the reference standard for the primary and secondary outcome measures. Measures of diagnostic accuracy for the detection of AVFs on 4D-CTA color-mapping were calculated per observer. Fleiss κ statistics¹¹ was used for assessing agreement for AVF detection among the 3 observers. The Krippendorff statistical test¹² was used for evaluating interobserver agreement on cortical venous reflux (taking possible missing data points into account). SPSS Statistics (Version 25; IBM, Armonk, New York) and Python 3.6 were used for data management and data analyses.

RESULTS

Study Population

A total of 34 patients were included, of whom 3 were excluded due to failure of the vessel segmentation. The failure was the result of heavy distortion due to metal artifacts and poor contrast opacification of the vasculature. The remaining study population consisted of 31 patients, 21 with and 10 without a cranial AVF. The group of AVFs consisted of 18 dural AVFs and 3 CCFs. An overview of the study population demographics and AVF characteristics is provided in Table 1.

Diagnostic Accuracy

The results of the color-mapping evaluation of 4D-CTA per observer are provided in Table 2. Overall, there was high sensitivity (86%–100%) and moderate-to-high specificity (70%–100%) for the detection of cranial AVFs on color-mapping 4D-CTA. For

Table 1: Patient demographics and characteristics of the AVFs

	Cranial AVF Present (n = 21)	Cranial AVF Absent (n = 10)
Sex (male/female)	13:8	3:7
Mean age (SD) (yr)	62 (12)	51 (14)
Presenting with pulsatile tinnitus (No.)	8	7
Mean time to DSA (SD) (day)	49 (68)	179 (205)
Dural AVF location (No.)		
Dural sinus	9	—
Posterior fossa	5	—
Anterior skull base	2	—
Supratentorial convexity	2	—
Dural AVF classification (No.)		
Borden type I	9	—
Borden type II	3	—
Borden type III	6	—
CCF		
Direct type	1	—
Indirect type	2	—

Note: — indicates no data.

Table 2: Diagnostic accuracy of the 3 observers for the detection of cranial AVFs (n = 31), with DSA serving as the reference standard^a

Detection of AVF	Observer 1, Method 1 ^b		Observer 2, Method 1 ^b		Observer 3, Method 1 ^b		Observer 1, Method 2 ^c		Observer 2, Method 2 ^c		Observer 3, Method 2 ^c	
True-positive, true-negative	19	10	21	10	18	7	20	10	21	10	18	7
False-positive, false-negative	0	2	0	0	3	3	0	1	0	0	3	3
Sensitivity (%) (95% CI)	90 (70–99)		100 (81–100)		86 (63–96)		95 (76–100)		100 (81–100)		86 (63–96)	
Specificity (%) (95% CI)	100 (69–100)		100 (66–100)		70 (35–92)		100 (69–100)		100 (66–100)		70 (35–92)	
PPV (%) (95% CI)	100 (80–100)		100 (81–100)		86 (63–96)		100 (80–100)		100 (81–100)		86 (63–96)	
NPV (%) (95% CI)	83 (57–94)		100 (66–100)		70 (35–92)		91 (60–98)		100 (66–100)		70 (35–92)	
Fleiss κ	0.619 (Substantial agreement)						0.661 (Substantial agreement)					

Note: —PPV indicates positive predictive value; NPV, negative predictive value.

^a The Fleiss κ for interobserver agreement is shown per method.

^b Method 1, color-mapping only.

^c Method 2, color-mapping and dynamic subtraction rendering of 4D-CTA.

Table 3: Diagnostic accuracy for the detection of cortical venous reflux on 4D-CTA for the correctly identified AVFs by the 3 observers, with DSA serving as the reference standard^a

Cortical Venous Reflux	Observer 1, Method 1 (n = 16) ^b		Observer 2, Method 1 (n = 18) ^b		Observer 3, Method 1 (n = 15) ^b		Observer 1, Method 2 (n = 17) ^c		Observer 2, Method 2 (n = 18) ^c		Observer 3, Method 2 (n = 15) ^c	
True-positive, true-negative	6	6	7	8	3	5	6	6	7	8	4	5
False-positive, false-negative	3	1	2	1	3	4	4	1	2	1	3	3
Sensitivity (%) (95% CI)	86 (42–100)		88 (47–100)		43 (10–82)		86 (42–100)		88 (47–100)		57 (18–90)	
Specificity (%) (95% CI)	67 (30–93)		80 (44–97)		63 (25–92)		60 (26–88)		80 (44–97)		63 (24–91)	
PPV (%) (95% CI)	67 (43–84)		78 (50–93)		50 (23–78)		60 (40–77)		78 (50–93)		57 (31–80)	
NPV (%) (95% CI)	86 (48–98)		89 (55–98)		56 (35–74)		86 (48–98)		89 (55–98)		63 (32–84)	
Krippendorff α	0.294 (Fair agreement)						0.372 (Fair agreement)					

Note:—PPV indicates positive predictive value; NPV, negative predictive value.

^a The Krippendorff α for interobserver agreement is shown per method.

^b Method 1, color-mapping only.

^c Method 2, color-mapping and dynamic subtraction rendering of 4D-CTA.

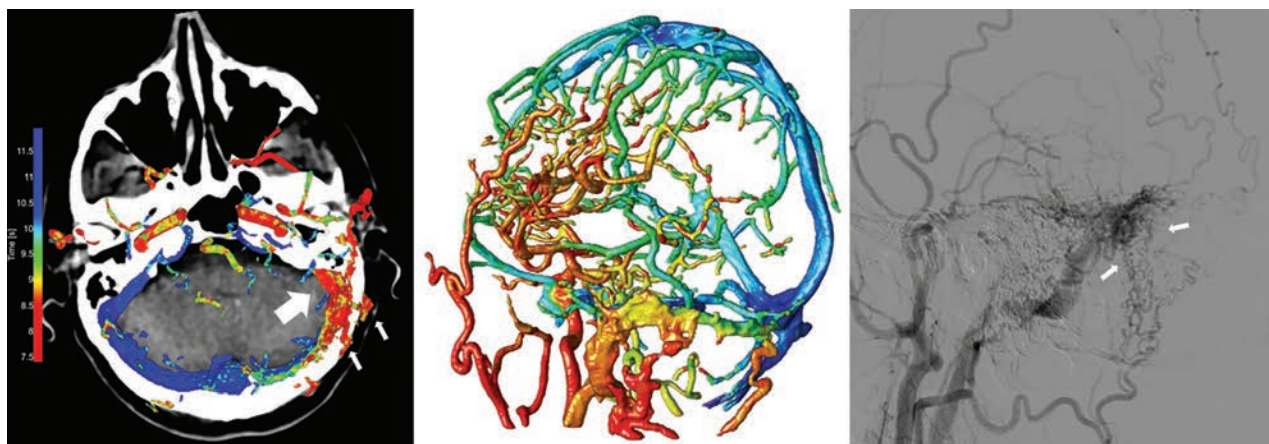


FIG 2. Left image, 4D-CTA color-mapping in a patient with a dural AVF located in the left sigmoid sinus. Early contrast bolus arrival and arterialization of the left sigmoid sinus are depicted in red (*large arrow*). Middle image, 3D rendering of color-mapping. Right image, conventional angiography. Note the occipital artery branches serving as arterial feeders (*small arrows*) with antegrade venous drainage in the jugular vein.

observer 1, two cases were rated false-negative on 4D-CTA color-mapping, of which 1 (a CCF) was detected with additional dynamic subtraction rendering. All AVFs were correctly identified on 4D-CTA color-mapping by observer 2, even before the availability of dynamic subtraction rendering. For observer 3, three cases were read as false-negative and 3 cases were read as false-positive. For observers 2 and 3, there were no changes in the reading before and after the availability of dynamic subtraction rendering. In all cases with a true-positive evaluation of 4D-CTA, there was full agreement with DSA for the location of the AVFs for all observers. The interobserver agreement for the detection of cranial AVFs was substantial (0.619 for method 1 and 0.661 for method 2).

The diagnostic performance in the detection of cortical venous reflux was highly variable among the observers (Table 3), ranging from low-to-high sensitivity (43%–88%) and moderate specificity (60%–80%) for both methods. Only for observer 3 was there a slight increase in sensitivity with the availability of dynamic subtraction rendering because cortical venous reflux was correctly identified in 1 additional case (initial false-negative reading on color-mapping). Regarding the 3 cases with a CCF included in the evaluation, 1 case with an indirect type of CCF was, as mentioned, initially missed on

color-mapping by observer 1 but was detected with the availability of dynamic subtraction rendering. This case was detected by observers 2 and 3 but was misclassified as a direct type by observer 2 and could not be classified by observer 3. The interobserver agreement for the detection of cortical venous reflux was fair (0.294 for method 1 and 0.372 for method 2).

DISCUSSION

We have presented a visualization technique to represent temporal information of the cerebral vasculature in a 4D-CTA acquisition, enabling accurate detection and enhanced visualization of cranial AVFs. The visualization of contrast bolus arrival times using a color scale enables temporal information (4D) to be assessed on a 3D volume without losing information. The 3 observers were able to accurately detect and localize the AVFs using 4D-CTA color-mapping, even without the availability of dynamic subtraction rendering. The difference in the diagnostic performance among the observers is most likely related to the level of experience in reading 4D-CTA studies and is a reflection of clinical practice. Examples of AVFs in different locations as detected on 4D-CTA color-mapping are provided in Figs 2–4.

The detection of cortical venous reflux on 4D-CTA color-mapping, with the availability of dynamic subtraction rendering, proved

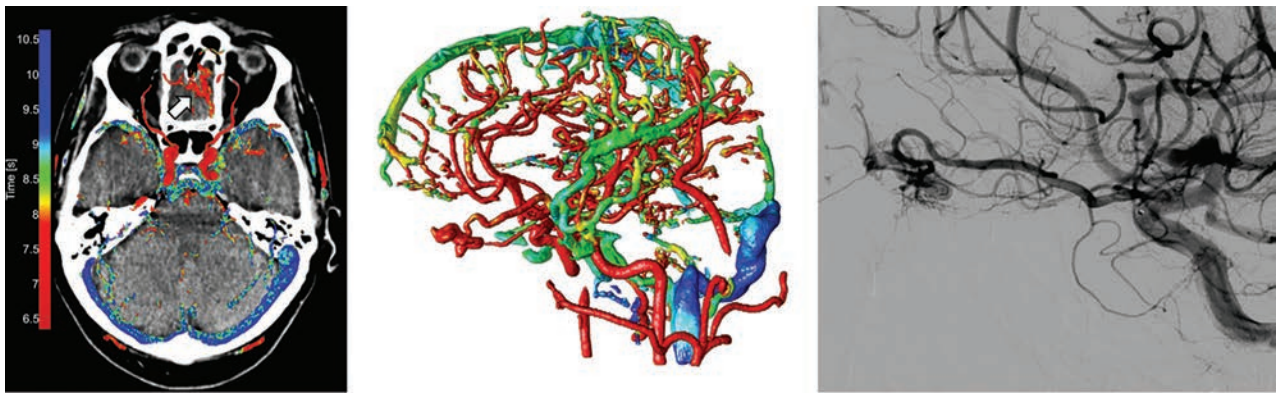


FIG 3. Left image, 4D-CTA color-mapping in a patient with a small dural AVF located at the left anterior skull base. Middle image, 3D rendering of color-mapping. Right image, conventional angiography. Early contrast bolus arrival of the AVF is seen as a prominent red (*arrow*). The ophthalmic artery with ethmoidal branches serving as the arterial feeder and arterIALIZATION of a tortuous cortical draining vein are clearly seen.

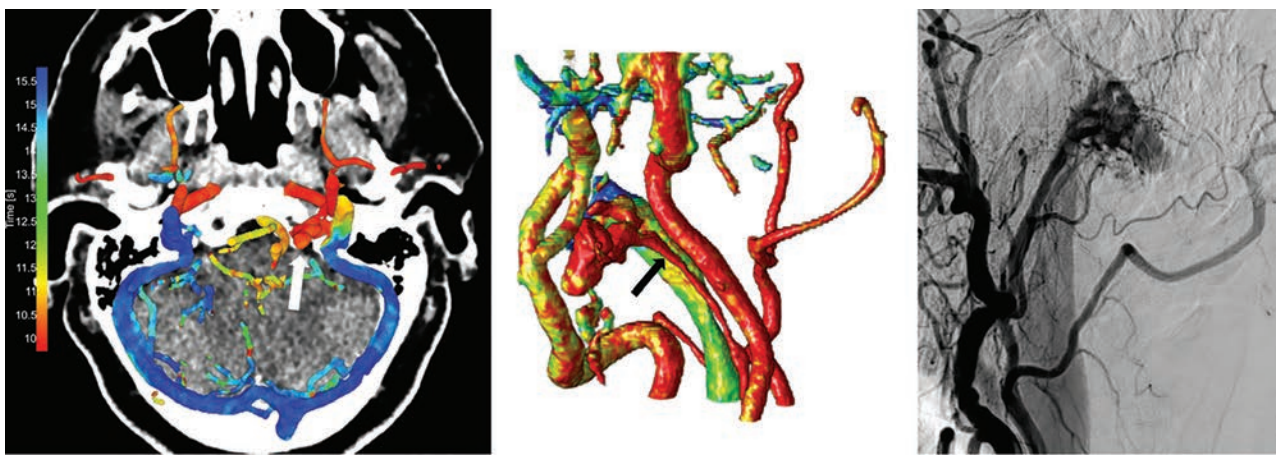


FIG 4. Left image, 4D-CTA color-mapping of 4D-CTA in a patient with a dural AVF located in the left condylar venous plexus (*white arrow*). Middle image, 3D rendering of the color-mapping. Right image, conventional angiography. The ascending pharyngeal artery serves as the feeding artery (*black arrow*), and venous drainage is into the green jugular vein.

challenging. The performance in the detection of cortical venous reflux was probably also related to the observers' experience in reading 4D-CTA because observers 1 and 2 were considerably more experienced in reading 4D-CTA than observer 3. Cortical venous reflux can be depicted on 4D-CTA, as has been reported previously^{1,13}, but there were discrepancies with DSA in a considerable number of cases. Although our study population was scanned with a continuous 4D-CTA volume acquisition, the temporal resolution was set at 1 volume per second based on which color-mapping was applied. A higher temporal resolution would enable targeted color-mapping in a more specific timeframe during the acquisition, which could improve the evaluation of cortical venous reflux.

The cerebral vessel segmentation is an important part of the presented method. It allows the arrival times to be extracted directly from the vascular system, and it reduces the large amount of 4D-CTA data to the essential parts needed for the diagnostic evaluation and visualization of the cerebral vasculature hemodynamics. The accuracy of the color-mapping method is therefore strongly dependent on the quality of the vessel segmentation, which is especially challenging for small-caliber arteries and veins. When combined with vessel labeling, this method could serve as a base for automated detection of AVFs.

Three patients were excluded due to failed color-mapping, which resulted from insufficient vessel segmentation. Although only 3 patients were excluded, it is a relatively large percentage of the small dataset. The vessel segmentation algorithm was primarily developed for a discontinuous 4D-CTA scanning protocol used in acute ischemic stroke.⁹ This feature may cause the vessel-segmentation algorithm to be less equipped to handle image artifacts and suboptimal contrast opacification of the vasculature. A vessel segmentation algorithm optimized for a continuous 4D-CTA scanning protocol might result in a decreased failure rate of the vessel segmentations.

The α factor in the TTS calculation of the presented method defines the threshold for the contrast bolus arrival time in the cerebral vasculature and determines the final visualization. A low α factor is more suited to a detailed distinction in early contrast-arrival times, making it more sensitive for the detection of arterIALIZED venous structures (ie, arteriovenous shunts). In other pathologies such as ischemic stroke, a higher α factor resembles the time-to-peak, which is beneficial for the evaluation of the collateral vessel status, which is an important independent predictor of patient outcome.¹⁴ Preliminary results already showed that the temporal dynamics of collateral flow in the circle of Willis can be

depicted in patients with a unilateral carotid artery occlusion using the presented method.¹⁵ It is expected that color-mapping could also be beneficial for 4D-CTA evaluation of vascular malformations in other organ systems or in the evaluation of cardiovascular pathology. The visualization of arrival times using a color scale has been suggested before in 2D-DSA¹⁶⁻¹⁸ and in 4D-CTA,^{19,20} but none of these methods are adjusted for each patient individually independent from the cerebral blood flow, heart rate, and cardiac output function. The application of a histogram to normalize the arrival times for each patient individually is a novel approach that allows an automatic visualization and comparison among patients with different contrast bolus arrival times. The 20% threshold on the TTS histogram was chosen to ensure the detection of the contrast bolus arrival at a reasonable signal-to-noise ratio. Relevant arrival times in other parts of the vasculature that might be outside the flow window are still visualized as the flow-window servers as anchor points the color scale and no arrival times are masked out.

Our study has some limitations. First, our study population was collected retrospectively with the risk of selection bias. Our findings therefore need validation in a prospective cohort study. Second, dynamic subtraction rendering of 4D-CTA was not independently evaluated from color-mapping because we chose to evaluate color-mapping in a manner similar to that applied in clinical practice in which both color-mapping and dynamic subtraction rendering are available. Our goal was not to repeal dynamic subtraction rendering of 4D-CTA but to provide color-mapping as an initial evaluation tool of 4D-CTA, enabling accurate detection of an AVF, with dynamic subtraction rendering available for further detailed analysis. However, a direct comparison is of added value, which can be evaluated in a future prospective study. Third, the role of 4D-CTA in the diagnostic work-up of AVFs is still under debate, and a direct comparison of the diagnostic accuracy of 4D-CTA with DSA or time-resolved MR angiography is lacking. MR angiography is preferable to 4D-CTA because the patient is not exposed to radiation. On the contrary, 4D-CTA is preferable to dynamic MR angiography because 4D-CTA is much less limited by the trade-off between temporal and spatial resolution.²¹ In addition, the radiation dose of 4D-CTA is currently considerably reduced by advanced noise filtering and registration techniques, though this reduction still strongly depends on the exact scanning protocol. Last, we did not include subjects with intracranial AVMs in our cohort to have a more homogeneous study population. It is expected that AVMs can also be detected with high accuracy using 4D-CTA color-mapping because an AVM is also characterized by AV shunting. Nevertheless, a follow-up study is needed to validate this assumption.

CONCLUSIONS

Arterialization of venous structures is visualized by color-mapping of 4D-CTA and proves to be accurate for the detection of cranial AVFs. This finding makes color-mapping a promising visualization technique for 4D-CTA.

Disclosures: Midas Meijs—RELATED: Grant: Dutch Research Council (Dutch Technology Foundation).* Kazuhiro Murayama—RELATED: Support for Travel to Meetings for the Study or Other Purposes: Canon Medical Systems*; UNRELATED: Comments: Grant-in-Aid for Scientific Research.* Frederick J.A. Meijer—UNRELATED: Board Membership: Editorial Board of *Neuroradiology*; Patents (Planned, Pending or Issued): color-mapping algorithm. Mathias Prokop—UNRELATED: Grants/Grants Pending: Canon Medical Systems, Siemens*; Payment for Lectures Including Service on Speakers Bureaus: Bracco, Bayer, Canon Medical Systems, Siemens.* *Money paid to institution.

REFERENCES

1. Kortman HG, Smit EJ, Oei MT, et al. **4D-CTA in neurovascular disease: a review.** *AJNR Am J Neuroradiol* 2015;36:1026–33 CrossRef Medline
2. Smit EJ, Vonken EJ, Meijer FJ, et al. **Timing-invariant CT angiography derived from CT perfusion imaging in acute stroke: a diagnostic performance study.** *AJNR Am J Neuroradiol* 2015;36:1834–38 CrossRef Medline
3. Campbell BC, Weir L, Desmond PM, et al. **CT perfusion improves diagnostic accuracy and confidence in acute ischaemic stroke.** *J Neurol Neurosurg Psychiatry* 2013;84:613–18 CrossRef Medline
4. Kaschik IN, Kloska SP, Struffert T, et al. **Clot burden and collaterals in anterior circulation stroke: differences between single-phase CTA and multi-phase 4D-CTA.** *Clin Neuroradiol* 2016;2:309–15 CrossRef Medline
5. Willems PW, Taeshineetanakul P, Schenk B, et al. **The use of 4D-CTA in the diagnostic work-up of brain arteriovenous malformations.** *Neuroradiology* 2012;54:123–31 CrossRef Medline
6. Willinsky RA, Taylor SM, TerBrugge K, et al. **Neurologic complications of cerebral angiography: prospective analysis of 2,899 procedures and review of the literature.** *Radiology* 2003;227:522–28 CrossRef Medline
7. Kaufmann TJ, Huston J 3rd, Mandrekar JN, et al. **Complications of diagnostic cerebral angiography: evaluation of 19,826 consecutive patients.** *Radiology* 2007;243:812–19 CrossRef Medline
8. Smit EJ, Vonken EJ, van der Schaaf IC, et al. **Timing-invariant reconstruction for deriving high-quality CT angiographic data from cerebral CT perfusion data.** *Radiology* 2012;263:216–25 CrossRef Medline
9. Meijs M, Patel A, van de Leemput S, et al. **Robust segmentation of the full cerebral vasculature in 4D CT images of suspected stroke patients.** *Sci Rep* 2017;7:15622 CrossRef Medline
10. Borden JA, Wu JK, Shucart WA, et al. **A proposed classification for spinal and cranial dural arteriovenous fistulous malformations and implications for treatment.** *J Neurosurg* 1995;82:166–79 Medline
11. Fleiss JL. **Measuring nominal scale agreement among many raters.** *Psychol Bull* 1971;76:378 CrossRef
12. Krippendorff K. **Agreement and information in the reliability of coding.** *Communication Methods and Measures* 2011;5:93–112 CrossRef
13. Beijer TR, van Dijk EJ, de Vries J, et al. **4D-CT angiography differentiating arteriovenous fistula subtypes.** *Clin Neurol Neurosurg* 2013; 115:1313–16 CrossRef Medline
14. Elijovich L, Goyal N, Mainali S, et al. **CTA collateral score predicts infarct volume and clinical outcome after endovascular therapy for acute ischemic stroke: a retrospective chart review.** *J Neurointerv Surg* 2016;8:559–62 CrossRef Medline
15. Meijs M, de Leeuw FE, Boogaarts HD, et al. **Circle of Willis collateral flow in carotid artery occlusion is depicted by 4D-CTA.** *World Neurosurg* 2018;114:421–26.e1 CrossRef Medline
16. Cover KS, Lagerwaard FJ, van den Berg R, et al. **Color intensity projection of digitally subtracted angiography for the visualization of brain arteriovenous malformations.** *Neurosurgery* 2007;60:511–14; discussion 514–15 CrossRef Medline
17. Strother C, Bender F, Deuerling-Zheng Y, et al. **Parametric color coding of digital subtraction angiography.** *AJNR Am J Neuroradiol* 2010;31:919–24 CrossRef Medline
18. Satow T, Oishi S, Yamada M, et al. **TCT-804 CCC (Color Coded**

- Circulation): a novel technique to determine complicated blood flow patterns. *JACC* 2015;66:B327–28
19. Thierfelder KM, Havla L, Beyer SE, et al. **Color-coded cerebral computed tomographic angiography: implementation of a convolution-based algorithm and first clinical evaluation in patients with acute ischemic stroke.** *Invest Radiol* 2015;50:361–65 CrossRef Medline
 20. Barfett JJ, Fierstra J, Willems PW, et al. **Intravascular functional maps of common neurovascular lesions derived from volumetric 4D CT data.** *Invest Radiol* 2010;45:370–77 CrossRef Medline
 21. Saleh R, Lohan D, Villablanca J, et al. **Assessment of craniospinal arteriovenous malformations at 3T with highly temporally and highly spatially resolved contrast-enhanced MR angiography.** *AJNR Am J Neuroradiol* 2008;29:1024–31 CrossRef Medline

Quantitative and Qualitative Comparison of 4D-DSA with 3D-DSA Using Computational Fluid Dynamics Simulations in Cerebral Aneurysms

S. Lang, P. Hoelter, A.I. Birkhold, M. Schmidt, J. Endres, C. Strother, A. Doerfler, and H. Luecking

ABSTRACT

BACKGROUND AND PURPOSE: 4D-DSA allows time-resolved 3D imaging of the cerebral vasculature. The aim of our study was to evaluate this method in comparison with the current criterion standard 3D-DSA by qualitative and quantitative means using computational fluid dynamics.

MATERIALS AND METHODS: 3D- and 4D-DSA datasets were acquired in patients with cerebral aneurysms. Computational fluid dynamics analysis was performed for all datasets. Using computational fluid dynamics, we compared 4D-DSA with 3D-DSA in terms of both aneurysmal geometry (quantitative: maximum diameter, ostium size [OZ1/OZ2], volume) and hemodynamic parameters (qualitative: flow stability, flow complexity, inflow concentration; quantitative: average/maximum wall shear stress, impingement zone, low-stress zone, intra-aneurysmal pressure, and flow velocity). Qualitative parameters were descriptively analyzed. Correlation coefficients (r , P value) were calculated for quantitative parameters.

RESULTS: 3D- and 4D-DSA datasets of 10 cerebral aneurysms in 10 patients were postprocessed. Evaluation of aneurysmal geometry with 4D-DSA ($r_{\text{maximum diameter}} = 0.98$, $P_{\text{maximum diameter}} < .001$; $r_{\text{OZ1/OZ2}} = 0.98/0.86$, $P_{\text{OZ1/OZ2}} < .001/.002$; $r_{\text{volume}} = 0.98$, $P_{\text{volume}} < .001$) correlated highly with 3D-DSA. Evaluation of qualitative hemodynamic parameters (flow stability, flow complexity, inflow concentration) did show complete accord, and evaluation of quantitative hemodynamic parameters ($r_{\text{average/maximum wall shear stress diastole}} = 0.92/0.88$, $P_{\text{average/maximum wall shear stress diastole}} < .001/.001$; $r_{\text{average/maximum wall shear stress systole}} = 0.94/0.93$, $P_{\text{average/maximum wall shear stress systole}} < .001/.001$; $r_{\text{impingement zone}} = 0.96$, $P_{\text{impingement zone}} < .001$; $r_{\text{low-stress zone}} = 1.00$, $P_{\text{low-stress zone}} = .01$; $r_{\text{pressure diastole}} = 0.84$, $P_{\text{pressure diastole}} = .002$; $r_{\text{pressure systole}} = 0.9$, $P_{\text{pressure systole}} < .001$; $r_{\text{flow velocity diastole}} = 0.95$, $P_{\text{flow velocity diastole}} < .001$; $r_{\text{flow velocity systole}} = 0.93$, $P_{\text{flow velocity systole}} < .001$) did show nearly complete accord between 4D- and 3D-DSA.

CONCLUSIONS: Despite a different injection protocol, 4D-DSA is a reliable basis for computational fluid dynamics analysis of the intracranial vasculature and provides equivalent visualization of aneurysm geometry compared with 3D-DSA.

ABBREVIATIONS: AWSS = average wall shear stress; CFD = computational fluid dynamics; d_{max} = maximum diameter; IZ = impingement zone; LSZ = low-stress zone; MWSS = maximum wall shear stress; OZ = ostium size; r = correlation coefficient; V = flow velocity; WSS = wall shear stress

Due to its accuracy, cerebral angiography consisting of 2D- and 3D-DSA is regarded as the criterion standard for visualization of the cerebral vasculature.^{1,2} Despite the high image qual-

ity of 2D-DSA and the opportunity for 3D visualization of the vasculature using 3D-DSA, both methods have limitations. On the one hand, 2D-DSA offers a dynamic, high-resolution illustration of vessels in selected projections. On the other hand, delineation of anatomic details might be impaired by exclusive use of 2D-DSA.³ Whereas 2D-DSA has overlap of arterial and venous structures, 3D-DSA is limited by its lack of temporal resolution. Hence, especially in complex pathologies, 2D-DSA should be combined with 3D-DSA to improve the validity of cerebral angiography.

Recently a novel method has been implemented⁴ that offers both static and time-resolved 3D volumes (4D-DSA). 4D-DSA has become a reliable method for improved visualization of vascular anatomy that shows excellent agreement with 2D-DSA.⁵⁻⁸ Despite 3D- and 4D-DSA both being based on the rotational ac-

Received April 9, 2019; accepted after revision July 1.

From the Department of Neuroradiology (S.L., P.H., M.S., J.E., A.D., H.L.), University of Erlangen-Nuremberg, Erlangen, Germany; Siemens Healthcare GmbH (A.I.B.), Erlangen, Germany; and Department of Radiology (C.S.), Clinical Sciences Center, University of Wisconsin School of Medicine and Public Health, Madison, Wisconsin.

The Department of Neuroradiology, University of Erlangen-Nuremberg has a research agreement with Siemens Healthcare GmbH, Erlangen, Germany.

Stefan Lang and Philip Hoelter contributed equally to this publication.

Please address correspondence to Stefan Lang, MD, Department of Neuroradiology, University of Erlangen-Nuremberg, Schwabachanlage 6, 91054 Erlangen, Germany; e-mail: Stefan.Lang3@uk-erlangen.de

<http://dx.doi.org/10.3174/ajnr.A6172>

quisitions of mask and fill projection images, there are relevant technical differences between 3D- and 4D-DSA. For realization of time-resolved 3D imaging, a different acquisition protocol is required. Compared with 3D-DSA, 4D-DSA consists of a longer scanning time (4D-DSA = 12 seconds versus 3D-DSA = 5 seconds) and a higher rotational angle (rotational angle 4D-DSA = 260° versus rotational angle 3D-DSA = 200°) to record the in- and outflow of contrast medium. If one took into account that 4D-DSA represents a new and different approach for 3D visualization of vasculature, the question of noninferiority of the static reconstructions of 4D-DSA compared with 3D-DSA comes automatically to the fore. Because of high intra- and interrater inconsistencies due to different windowing, even “simple” measurements of, for example, the height and length of an aneurysm in 2 different datasets, are challenging. Thus, an objective method for comparing both techniques would be desirable.

In this context, computational fluid dynamics (CFD) analysis of cerebral vasculature might be helpful. Despite the controversial discussion on its clinical relevance,⁹ CFD is considered an established method to evaluate intra-aneurysmal hemodynamics.^{10,11} Whereas 3D-DSA is commonly used as a basis for CFD analysis of cerebral aneurysms,^{12,13} there are no data regarding the qualification of 4D-DSA datasets for CFD. Considering that the geometry of the vascular structure has a significant influence on the deduction of flow parameters,¹⁴⁻¹⁷ we concluded that CFD analysis of 1 aneurysm based on both 3D- and 4D-DSA could be useful for the evaluation of the static reconstruction of a 4D-DSA dataset. If one assumes that established flow parameters (eg, wall shear stress and so forth) represent the vascular geometry in aneurysms, CFD might be a suitable method to compare the quality of 3D imaging of 4D-DSA with that of 3D-DSA.

In this article, we present our initial experience with 4D-DSA for the calculation of typical CFD parameters. Our aim was to evaluate 4D-DSA in comparison with 3D-DSA using CFD regarding quantitative and qualitative parameters.

MATERIALS AND METHODS

Patients

Patients with cerebral aneurysms who underwent both a 3D-DSA at the diagnostic stage and a 4D-DSA immediately before the intervention due to optimization of working projections (eg, in case of different head positioning) were included in this study retrospectively.

Data Acquisition and Postprocessing

Angiography (including 3D-DSA and 4D-DSA) was performed using a biplane flat panel detector angiographic system (Artis zee biplane; Siemens, Erlangen, Germany). By standard angiographic methods (via the transfemoral route), a diagnostic catheter (5F) was positioned in the proximal internal carotid artery or in the vertebral artery to obtain standard projections (2D-DSA). Additionally, 3D- and 4D-DSA datasets were acquired using commercially available angiographic applications (12-second syngo Dyna 4D and 5-second DSA; Siemens) as previously described.⁸ The datasets were postprocessed with commercially available software (Dyna 4D; Siemens). According to standardization, we used established reconstruction parameters for both 3D- and 4D-

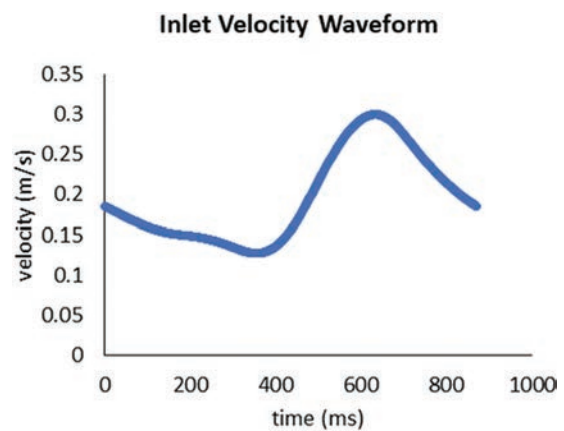


FIG 1. Flow waveform at the inflow representing the inflow conditions used for CFD analysis. A homogeneous velocity profile across the complete inflow cross-section with the velocities given by the inflow curve was applied as inflow boundary conditions. The outflow boundary conditions were defined as zero pressure.

DSA datasets (kernel type: “edge enhanced”; image characteristics: “smooth”; mode of reconstruction: “subtracted”; 512 × 512 image matrix; isotropic voxel size = 0.15 mm). To provide comparability with 3D-DSA, we used the static 3D reconstruction of 4D-DSA exclusively for CFD analysis.

CFD

The simulation was performed on a research prototype (Siemens).¹⁸ Both 3D- and 4D-DSA volumes were cropped to the ROI (ie, the aneurysm and parent vessels). Intensity thresholding was used for segmenting the vessels in the volumetric domain. Threshold values were chosen empirically to obtain comparable vessel diameters and aneurysm volumes. In case of intraluminal contrast inhomogeneities within the processed volume (eg, missing contrast caused by crossflow via a nearby vessel), the segmentation was manually corrected to allow proper flow simulations. First, voxel-based representation was transferred to a mesh representation. Second, inlets and outlets, which describe areas of blood entering and leaving the simulated domain, were specified for vessels proximal and distal to the aneurysm. A homogeneous velocity profile across the complete inflow cross-section with the velocities given by the inflow curve (Fig 1) was applied as a boundary condition for the inlets. Blood entered the simulated domain with an average flow velocity of 0.196 m/s, varying between 0.127 and 0.300 m/s. Zero pressure was defined as outflow boundary conditions. For the hemodynamic simulation itself, the simulated blood was modeled as Newtonian fluid with a viscosity of 0.004 Pa · s and a density of 1000 kg/m³. The heart rate was 69 beats per minute or 0.87 seconds for 1 heart cycle, respectively.

Data Evaluation

All 3D- and 4D-DSA datasets were anonymized and stored in random order. Evaluation of the acquired 3D-DSA and 4D-DSA datasets was performed by 2 experienced neuroradiologists in a consensus reading, blinded to clinical information.

Image Quality

All 3D- and 4D-DSA datasets were evaluated for parameters comprising image and diagnostic quality (eg, movement artifacts).

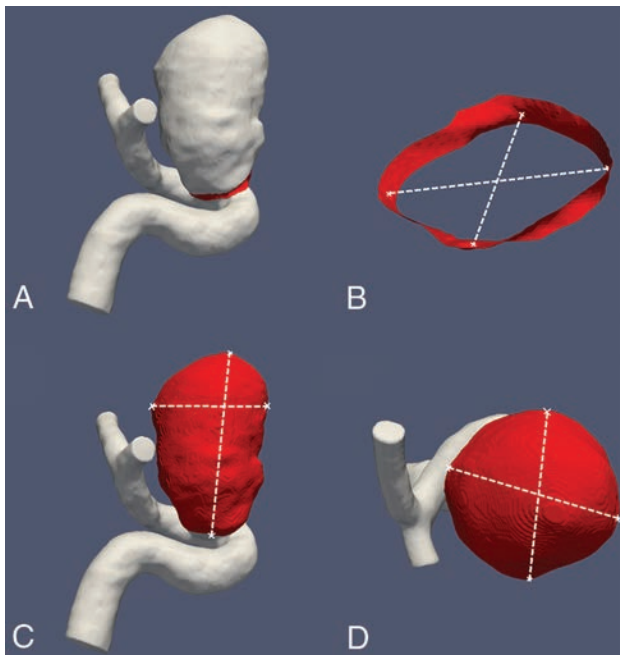


FIG 2. Images exemplarily show measurements of the aneurysmal ostium (A and B) and the aneurysm itself (C and D) for calculation of the ostium size, maximum diameter, and aneurysmal volume.

The quality of the acquired 3D- and 4D-DSA datasets was assessed in a consensus reading using a 5-fold scaled grading system: 4 = excellent (high contrast, no artifacts); 3 = good (high contrast, minimal artifacts, eg, due to movement or metallic implants); 2 = compromised (eg, noticeable movement artifacts and/or reduced homogeneity of the vessel contrast); 1 = heavily compromised (low contrast and/or strong movement artifacts); 0 = not diagnostic (vasculature is not differentiable due to heavy artifacts and/or missing contrast).

Fluid Dynamics Analysis

Geometry, Pressure, and Flow Velocity. Quantitative morphologic aneurysmal parameters comprising maximum diameter (d_{max}) (in millimeters), maximum volume (in cubic millimeters), and ostium size (OZ_1/OZ_2 in millimeters) were analyzed in all 3D- and 4D-DSA datasets (Fig 2). Intra-aneurysmal pressure (P) (in pascals; mean of all elements) and intra-aneurysmal flow velocity (V) (in millimeters/second, mean) during systole and diastole have been additionally analyzed for all 3D- and 4D-DSA datasets.

Hemodynamics. According to Cebal et al,¹⁰ we assessed both 3D- and 4D-DSA datasets regarding the following hemodynamic parameters:

- **Flow complexity:** Intra-aneurysmal flow has been analyzed regarding the configuration of the recirculation zone. Simple flow means a single recirculation zone within the aneurysm. Complex flow patterns are indicated by flow divisions within the aneurysm and feature more recirculation zones.
- **Flow stability:** Intra-aneurysmal flow is regarded as stable if there is no change of the flow pattern during 1 cardiac cycle.
- **Inflow concentration:** Concentrated inflow streams pene-

trate deeply into the aneurysmal sac and are thin in the main flow direction. Diffuse inflow is defined as thick flow streams (compared with the aneurysmal neck) that disperse quickly once they enter the aneurysmal sac.

- **Wall shear stress:** Because WSS is seen as one of the most important parameters regarding the initiation of cerebral aneurysms,¹⁹ average and maximum wall shear stress (AWSS, MWSS) have been analyzed for systole and diastole (in pascals), respectively. Taking different WSS values into account, we specified 2 different zones of the aneurysmal wall.
- **Impingement zone:** The impingement zone (IZ) is considered a region of the aneurysmal sac where the inflow streams impact the aneurysmal wall and change their direction. The area of the impingement zone (in cubic millimeters) has been defined as the area with WSS of $>80\%$ (in pascals) of the maximum WSS and was assessed for both 3D- and 4D-DSA.
- **Low-stress zone:** The low-stress zone (LSZ) is considered an area of the aneurysmal wall where no impact of inflow streams on the aneurysmal wall is detectable. The low-stress zone was defined as the area (in cubic millimeters) with WSS values of <0.4 Pa at the end of the diastole, and it was assessed for both 3D- and 4D-DSA.

Statistical Analysis

All statistical analyses were performed using commercially available software (SPSS Statistics, Version 19; IBM, Armonk, New York). Qualitative parameters (eg, flow complexity, flow stability, inflow concentration, and so forth) were analyzed using descriptive statistics only. Quantitative parameters (ostium size, aneurysmal diameter and volume, intra-aneurysmal pressure, flow velocity, WSS, impingement zone, low-stress zone, and so forth) were tested for normal distribution using the Kolmogorov-Smirnov test. Correlation of quantitative parameters was analyzed by the Spearman rank correlation coefficient (r). A P value $< .05$ was considered statistically significant.

RESULTS

Patients

In total, 10 pairs of 3D-DSA and 4D-DSA datasets were acquired in 10 patients with 1 incidental aneurysm each (6 women and 4 men; mean age, 52.3 ± 8.2 years; age range, 41–78 years). Aneurysm location was in both the anterior and the posterior circulations (ICA = 6, MCA = 2, basilar artery = 2).

Image Quality

Both reviewers completely agreed regarding image quality. All 3D- and all 4D-DSA datasets were rated as diagnostic (3D-DSA: grade 4 = 10; 4D-DSA: grade 4 = 10).

Geometry, Pressure, and Flow Velocity. There was no significant difference regarding geometry between 3D- and 4D-DSA in terms of maximum diameter (d_{max} $_{3D-DSA} = 13.11 \pm 5.7$ mm; d_{max} $_{4D-DSA} = 13.08 \pm 5.51$ mm; $r_{dmax} = 0.988$; $P < .001$), maximum volume (volume $_{3D-DSA} = 721 \pm 848$ mm³; volume $_{4D-DSA} = 698 \pm 813$ mm³; $r_{volume} = 0.976$; $P < .001$), and ostium size ($OZ_{1/3D-DSA} = 5.67 \pm 2.31$ mm, $OZ_{2/3D-DSA} = 5.23 \pm 2.07$ mm; $OZ_{1/4D-DSA} = 5.71 \pm 5.42$ mm, $OZ_{2/4D-DSA} = 5.34 \pm 2.09$ mm;

Table 1: Aneurysmal geometry

Parameter	3D-DSA (Median, IQR)	4D-DSA (Median, IQR)	<i>r</i>
Max. diameter (mm)	11 (9–20)	11 (9–20)	0.988 (<i>P</i> < .001)
Max. volume (mm ³)	356 (161–1196)	381 (159–1065)	0.976 (<i>P</i> < .001)
Ostium size ₁ (mm)	5 (4–7)	5 (4–7)	0.976 (<i>P</i> < .001)
Ostium size ₂ (mm)	5 (4–6)	5 (4–6)	0.857 (<i>P</i> = .002)

Note:—Max. indicates maximum; IQR, interquartile range.

Table 2: Aneurysmal pressure, flow velocity, and hemodynamics

Parameter	3D-DSA (Mean)	4D-DSA (Mean)	<i>r</i>
Intra-aneurysmal pressure _{systole} (Pa)	502.8 ± 242.24	492.2 ± 300.07	0.903 (<i>P</i> < .001)
Intra-aneurysmal pressure _{diastole} (Pa)	189.3 ± 99.13	181.4 ± 114.4	0.842 (<i>P</i> = .002)
Flow velocity _{systole} (mm/s)	80.8 ± 50.94	74.89 ± 48.02	0.930 (<i>P</i> < .001)
Flow velocity _{diastole} (mm/s)	31.61 ± 22.2	29.9 ± 21.45	0.952 (<i>P</i> < .001)
AWSS _{systole} (Pa)	0.933 ± 1.02	0.835 ± 0.853	0.936 (<i>P</i> < .001)
AWSS _{diastole} (Pa)	0.26 ± 0.28	0.24 ± 0.25	0.918 (<i>P</i> < .001)
MWSS _{systole} (Pa)	5.95 ± 1.83	5.63 ± 1.64	0.927 (<i>P</i> < .001)
MWSS _{diastole} (Pa)	1.84 ± 0.73	1.78 ± 0.69	0.879 (<i>P</i> = .001)
IZ (mm ²)	12.4 ± 14.2	8.9 ± 6.81	0.957 (<i>P</i> < .001)
LSZ (mm ²)	254.6 ± 203.55	263.9 ± 199.08	1 (<i>P</i> < .01)

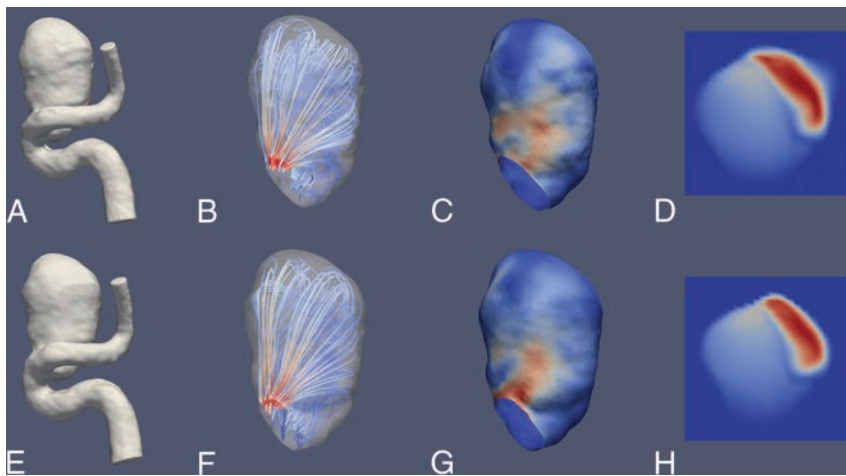


FIG 3. Illustrative case 1. CFD simulations show a saccular aneurysm of the ICA. Upper row (A–D) and lower row (E–H) show reconstruction results derived from a 3D-DSA and a 4D-DSA dataset, respectively. A and E, 3D view of the aneurysm using a volume-rendering technique and demonstrating comparable aneurysmal morphology. B and F, A color-coded visualization of intra-aneurysmal flow using streamlines (red and blue indicate high- and low-velocity magnitudes). The peak velocities show a laminar distribution along the longitudinal axis. C and G, In concordance, note maximum systolic wall shear stress (red and blue indicate high and low WSS) in the corresponding area. D and H, The aneurysmal ostium, the associated flow conditions, and the corresponding areas with high-velocity magnitude (red and blue indicate high- and low-velocity magnitude). Overall, the congruence of hemodynamic characteristics between 3D- and 4D-DSA shows geometric accordance between both techniques.

$r_{OZ1} = 0.976, P < .001; r_{OZ2} = 0.857, P = .002$). There was no significant difference between 3D- and 4D-DSA regarding intra-aneurysmal pressure (systole: $P_{\text{mean } 3\text{D-DSA}} = 502.8 \pm 242.24$ Pa; $P_{\text{mean } 4\text{D-DSA}} = 492.2 \pm 300.07$ Pa; diastole: $P_{\text{mean } 3\text{D-DSA}} = 189.3 \pm 99.13$ Pa; $P_{\text{mean } 4\text{D-DSA}} = 181.4 \pm 114.4$ Pa; $r_{P \text{ systole}} = 0.903, P < .001; r_{P \text{ diastole}} = 0.842, P = .002$). Regarding intra-aneurysmal flow velocity, no significant difference between 3D- and 4D-DSA was detected (systole: $V_{3\text{D-DSA mean}} = 80.8 \pm 50.94$ mm/s; $V_{4\text{D-DSA mean}} = 74.89 \pm 48.02$ mm/s; diastole: $V_{3\text{D-DSA mean}} = 31.61 \pm 22.2$ mm/s; $V_{4\text{D-DSA mean}} = 29.9 \pm 21.45$ mm/s; $r_{V \text{ systole}} = 0.930, P < .001; r_{V \text{ diastole}} = 0.952, P < .001$). See also Tables 1 and 2 for an overview.

Hemodynamics. Qualitative analysis of hemodynamics did not

demonstrate differences between 3D- and 4D-DSA. Assessment of flow complexity (simple 3D-DSA/4D-DSA = 2/2, complex 3D-DSA/4D-DSA = 8/8), flow stability (stable 3D-DSA/4D-DSA = 8/8, unstable 3D-DSA/4D-DSA = 2/2), and inflow concentration (diffuse 3D-DSA/4D-DSA = 4/4, concentrated 3D-DSA/4D-DSA = 6/6) did not show any difference between readers. Analysis of WSS did not provide significant differences between 3D- and 4D-DSA in terms of AWSS (systole: $\text{AWSS}_{3\text{D-DSA}} = 0.933 \pm 1.02$ Pa; $\text{AWSS}_{4\text{D-DSA}} = 0.835 \pm 0.853$ Pa; diastole: $\text{AWSS}_{3\text{D-DSA}} = 0.26 \pm 0.28$ Pa; $\text{AWSS}_{4\text{D-DSA}} = 0.24 \pm 0.25$ Pa; $r_{\text{AWSS systole}} = 0.936; P < .001; r_{\text{AWSS diastole}} = 0.918; P < .001$) and MWSS (systole: $\text{MWSS}_{3\text{D-DSA}} = 5.95 \pm 1.83$ Pa; $\text{MWSS}_{4\text{D-DSA}} = 5.63 \pm 1.64$ Pa; diastole: $\text{MWSS}_{3\text{D-DSA}} = 1.84 \pm 0.73$ Pa; $\text{MWSS}_{4\text{D-DSA}} = 1.78 \pm 0.69$ Pa; $r_{\text{MWSS systole}} = 0.927; P < .001; r_{\text{MWSS diastole}} = 0.879; P = .001$). Calculation of impingement zones ($\text{IZ}_{3\text{D-DSA}} = 12.4 \pm 14.2$ mm²; $\text{IZ}_{4\text{D-DSA}} = 8.9 \pm 6.81$ mm²; $r_{\text{IZ}} = 0.957; P < .001$) and low-stress zones ($\text{LSZ}_{3\text{D-DSA}} = 254.6 \pm 203.55$ mm²; $\text{LSZ}_{4\text{D-DSA}} = 263.9 \pm 199.08$ mm²; $r_{\text{LSZ}} = 1.00; P = .01$) did not show significant differences. See Table 2 for an overview and Figs 3 and 4 for illustrative cases.

DISCUSSION

To date, 2D-DSA (in combination with 3D-DSA) is considered the criterion standard for visualization of the cerebral vasculature. As a novel imaging method, 4D-DSA offers the advantages of both modalities by providing not only time-resolved but also 3D images. Despite the acquisition time of 4D-DSA differing

marginally from that of 3D-DSA (12 versus 5 seconds), total time and effort necessary for postprocessing 4D-DSA volumes are comparable with those of 3D-DSA and do not impair the clinical workflow. On the contrary, 4D-DSA might help reduce the amount of 2D-DSA series (eg, target projections).

Thus, 4D-DSA has the potential to reduce the dose and the amount of contrast medium necessary for cerebral conventional angiography, especially for the diagnostic work-up of complex neurovascular pathologies. Recent literature indicates a high level of reliability of 4D-DSA regarding qualitative parameters,^{5–8} yet knowledge of 4D-DSA regarding quantitative parameters is still limited. Furthermore, injection protocols differ significantly between 3D- and 4D-DSA because time-resolved 4D-DSA datasets

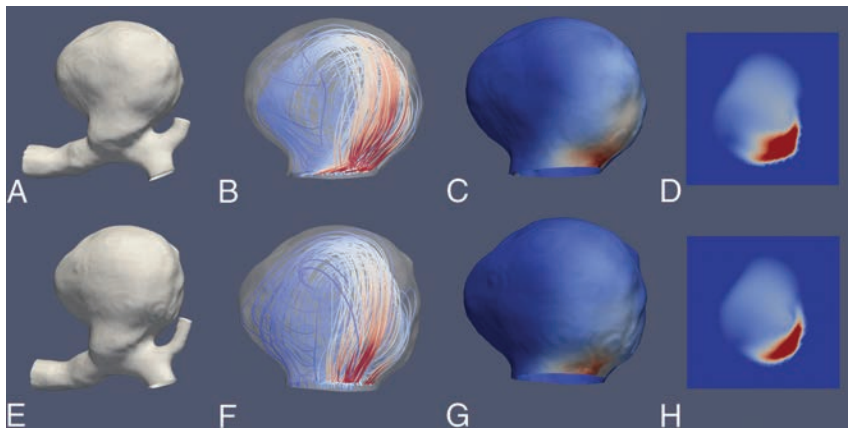


FIG 4. Illustrative case 2. CFD simulations show a large saccular aneurysm of the carotid T. Upper row (A–D) and lower row (E–H) show reconstruction results derived from a 3D-DSA and a 4D-DSA dataset, respectively. A and E, 3D view of the aneurysm using a volume-rendering technique and demonstrating comparable aneurysmal morphology. B and F, Color-coded visualization of intraneurysmal flow using streamlines (red and blue indicate high- and low-velocity magnitudes). The peak velocities show a predominant basal distribution. C and G, In concordance, note maximum systolic wall shear stress (red and blue indicate high and low WSS) in the corresponding area. D and H, Aneurysmal ostium, the associated flow conditions, and the match of areas with high-velocity magnitude (red and blue indicate high- and low-velocity magnitude). Overall, the congruence of hemodynamic characteristics between 3D- and 4D-DSA shows geometric accordance between the techniques.

are acquired using a dynamic injection protocol, whereas 3D-DSA datasets are acquired by continuous injection of contrast medium. Therefore, we analyzed the ability of 4D-DSA to reproduce the vascular geometry in comparison with conventional 3D-DSA. On the one hand, we wanted to evaluate the applicability of 4D-DSA for performing CFD analysis. On the other hand, we wanted to use CFD itself for comparison of 3D- and 4D-DSA datasets with the help of the resulting (qualitative and quantitative) flow parameters.

In our series, all 3D- and 4D-DSA datasets were suitable for CFD analysis. Despite 4D-DSA yielding an insignificant underestimation of hemodynamic parameters compared with 3D-DSA in our series (that might refer to the different injection protocols), our analysis revealed that both qualitative and quantitative CFD parameters showed excellent agreement in the corresponding datasets. Therefore, we conclude that this consistency regarding CFD parameters derives from a consistent representation of aneurysmal geometry and that the dynamic injection protocol for acquisition of 4D-DSA does not influence or compromise the visualization of cerebral vasculature.

There is scant literature comparing the quantitative reliability of 4D-DSA with that of 2D and 3D. A single publication addresses detailed the quantitative accuracy of 4D-DSA in comparison with 2D-DSA: Lang et al⁸ evaluated 4D-DSA in 26 cases of cerebral aneurysms, AVMs, and dural arteriovenous fistulas regarding quantitative and qualitative parameters. Quantitative analysis of injection vessels, aneurysmal size, AVM nidus size, and the diameter of a main feeder of a fistula in 4D-DSA datasets demonstrated excellent agreement with 2D-DSA. Furthermore, qualitative evaluation of 4D-DSA was comparable with that of 2D-DSA. A comparison between 4D-DSA and 3D-DSA was not performed in their series though. Therefore, our data close the gap of knowledge regarding qualification of 4D-DSA for 3D imaging of the

cerebral vasculature. In line with the results of the excellent agreement between 4D- and 2D-DSA, our data demonstrate excellent agreement between 4D- and 3D-DSA.

So far, other authors studying 4D-DSA have focused on qualitative comparisons of 4D-DSA with 3D- and 2D-DSA. In this context, the publication of Sandoval-Garcia et al⁵ aroused our interest in the diagnostic utility of 4D-DSA compared with 2D- and 3D-DSA in the diagnosis of cerebrovascular abnormalities. Their analysis demonstrated in 26 cases of AVMs, dural arteriovenous fistulas, cerebral aneurysms, stenosis, and healthy individuals that the information content of 4D-DSA reconstructions is largely equivalent to that of the combination of 2D- and 3D-DSA. The specific comparison of 4D-DSA with 3D-DSA regarding quantitative parameters was not the object of this publication, yet the authors observed, concordant with our

results, no significant disagreements between 4D-DSA and 2D-/3D-DSA concerning quantitative characteristics (eg, nidus size, aneurysm dimensions, and so forth).

Another publication of Sandoval-Garcia et al⁶ addressed the comparison of 4D-DSA with 2D- and 3D-DSA in the analysis of normal vascular structures in a canine model. The authors assessed, in 15 datasets, the qualification of 4D-DSA for analysis of the cerebral vasculature. The comparison among the 3 modalities was performed exclusively qualitatively though. 4D-DSA was rated superior to 2D- and 3D-DSA, respectively, and was regarded as the preferred method for vascular assessment. The authors did not observe any restriction or inferiority as a consequence of using 4D-DSA, corresponding to our results. Furthermore, the authors concluded that the use of 4D-DSA leads to a reduction in radiation and contrast doses.

Limitations

Although data analysis was successful in all 10 cases, our analysis has several limitations. First, it was limited by the small sample size and the rather mid-to-large size of the included aneurysms. Because the literature has shown the applicability of CFD analysis for small aneurysms as well,¹⁴ we conclude that our results are valid for not only mid-to-large size aneurysms but also small aneurysms. Second, our work covers only 1 type of vascular pathology (cerebral aneurysms) and only datasets acquired by selective injections either via the ICA or the vertebral artery. Comparable with other publications on CFD analyses, missing standardization for postprocessing is a relevant limitation. However, approximations and assumptions regarding blood viscosity and flow conditions are mandatory for CFD.¹⁰ In agreement with the experience of other authors, we could observe a high level of correlation between the hemodynamic patterns in our CFD models, the underlying raw data, and the corresponding 2D-DSA series.²⁰

CONCLUSIONS

Despite a different injection protocol, 4D-DSA is a reliable basis for CFD analysis of the intracranial vasculature and provides equivalent visualization of intracranial aneurysm geometry compared with 3D-DSA.

Disclaimer: The concepts and results presented in this paper are based on research and are not commercially available.

Disclosures: Annette I. Birkhold—UNRELATED: Employment: Siemens. Jürgen Endres—UNRELATED: Consultancy: iSchemaview, Inc; Grant: Bayern Innovativ GmbH Projektträger Bayern-BayMED.* *Money paid to the institution.

REFERENCES

1. Wong SC, Nawawi O, Ramli N, et al. **Benefits of 3D rotational DSA compared with 2D-DSA in the evaluation of intracranial aneurysm.** *Acad Radiol* 2012;19:701–07 CrossRef Medline
2. Geers AJ, Larrabide I, Radaelli AG, et al. **Patient-specific computational hemodynamics of intracranial aneurysms from 3D rotational angiography and CT angiography: an in vivo reproducibility study.** *AJNR Am J Neuroradiol* 2011;32:581–86 CrossRef Medline
3. Hochmuth A, Spetzger U, Schumacher M. **Comparison of three-dimensional rotational angiography with digital subtraction angiography in the assessment of ruptured cerebral aneurysms.** *AJNR Am J Neuroradiol* 2002;23:1199–205 Medline
4. Davis B, Royalty K, Kowarschik M, et al. **4D digital subtraction angiography: implementation and demonstration of feasibility.** *AJNR Am J Neuroradiol* 2013;34:1914–21 CrossRef Medline
5. Sandoval-Garcia C, Yang P, Schubert T, et al. **Comparison of the diagnostic utility of 4D-DSA with conventional 2D- and 3D-DSA in the diagnosis of cerebrovascular abnormalities.** *AJNR Am J Neuroradiol* 2017;38:729–34 CrossRef Medline
6. Sandoval-Garcia C, Royalty K, Aagaard-Kienitz B, et al. **A comparison of 4D-DSA with 2D and 3D-DSA in the analysis of normal vascular structures in a canine model.** *AJNR Am J Neuroradiol* 2015;36:1959–63 CrossRef Medline
7. Lescher S, Gehrisch S, Klein S, et al. **Time-resolved 3D rotational angiography: display of detailed neurovascular anatomy in patients with intracranial vascular malformations.** *J Neurointerv Surg* 2017; 9:887–94 CrossRef Medline
8. Lang S, Gölitz P, Struffert T, et al. **4D-DSA for dynamic visualization of cerebral vasculature: a single-center experience in 26 cases.** *AJNR Am J Neuroradiol* 2017;38:1169–76 CrossRef Medline
9. Kallmes DF. **Point: CFD—computational fluid dynamics or confounding factor dissemination.** *AJNR Am J Neuroradiol* 2012;33: 395–96 CrossRef Medline
10. Cebral JR, Mut F, Weir J, et al. **Association of hemodynamic characteristics and cerebral aneurysm rupture.** *AJNR Am J Neuroradiol* 2011;32:264–70 CrossRef Medline
11. Zeng Z, Kallmes DF, Durka MJ, et al. **Hemodynamics and anatomy of elastase-induced rabbit aneurysm models: similarity to human cerebral aneurysms?** *AJNR Am J Neuroradiol* 2011;32: 595–601 CrossRef Medline
12. Steinman DA, Milner JS, Norley CJ, et al. **Image-based computational simulation of flow dynamics in a giant intracranial aneurysm.** *AJNR Am J Neuroradiol* 2003;24:559–66 Medline
13. Ren Y, Chen GZ, Liu Z, et al. **Reproducibility of image-based computational models of intracranial aneurysm: a comparison between 3D rotational angiography, CT angiography and MR angiography.** *Biomed Eng Online* 2016;15:50 CrossRef Medline
14. Cebral JR, Castro MA, Burgess JE, et al. **Characterization of cerebral aneurysms for assessing risk of rupture by using patient-specific computational hemodynamics models.** *AJNR Am J Neuroradiol* 2005;26:2550–59 Medline
15. Szikora I, Paal G, Ugron A, et al. **Impact of aneurysmal geometry on intraneurysmal flow: a computerized flow simulation study.** *Neuroradiology* 2008;50:411–21 CrossRef Medline
16. Cebral JR, Castro MA, Appanaboyina S, et al. **Efficient pipeline for image-based patient-specific analysis of cerebral aneurysm hemodynamics: technique and sensitivity.** *IEEE Trans Med Imaging* 2005;24:457–67 CrossRef Medline
17. Kono K, Tomura N, Yoshimura R, et al. **Changes in wall shear stress magnitude after aneurysm rupture.** *Acta Neurochir* 2013; 155:1559–63 CrossRef Medline
18. Boegel M, Gehrisch S, Redel T, et al. **Patient-individualized boundary conditions for CFD simulations using time-resolved 3D angiography.** *Int J Comput Assist Radiol Surg.* 2016;11:1061–69 CrossRef Medline
19. Shojima M, Oshima M, Takagi K, et al. **Magnitude and role of wall shear stress on cerebral aneurysm: computational fluid dynamic study of 20 middle cerebral artery aneurysms.** *Stroke* 2004;35: 2500–05 CrossRef Medline
20. Cebral JR, Pergolizzi R Jr, Putman CM. **Computational fluid dynamics modeling of intracranial aneurysms: qualitative comparison with cerebral angiography.** *Acad Radiol* 2007;14:804–13 CrossRef Medline

Analysis of Flow Dynamics and Outcomes of Cerebral Aneurysms Treated with Intracranial Flow-Diverting Devices

J.R. Cebral, B.J. Chung, F. Mut, J. Chudyk, C. Bleise, E. Scrivano, P. Lylyk, R. Kadirvel, and D. Kallmes



ABSTRACT

BACKGROUND AND PURPOSE: Intracranial flow diversion offers a promising treatment option for complex bifurcation aneurysms. The purpose of this study was to compare the flow conditions between successfully occluded and incompletely occluded aneurysms treated with intracranial devices.

MATERIALS AND METHODS: The hemodynamics in 18 completely occluded aneurysms after treatment with intracranial devices was compared against 18 that were incompletely occluded at follow-up. Hemodynamic and geometric parameters were obtained from computational fluid dynamics models constructed from 3D angiographies. Models of the intracranial devices were created and interactively deployed within the vascular models using posttreatment angiography images for guidance. Hemodynamic and geometric variables were compared using the Mann-Whitney test and univariate logistic regression analysis.

RESULTS: Incomplete occlusion was associated with large posttreatment mean aneurysm inflows ($P = .02$) and small reductions in the mean inflow rate ($P = .01$) and inflow concentration index ($P = .03$). Incompletely occluded aneurysms were larger ($P = .002$) and had wider necks ($P = .004$) than completely occluded aneurysms and tended to have more complex flow patterns, though this trend was not significant after adjusting for multiple testing.

CONCLUSIONS: The outcome of cerebral aneurysm treatment with intracranial flow diverters is associated with flow conditions created immediately after device implantation. Flow conditions unfavorable for immediate and complete occlusion seem to be created by improper positioning or orientation of the device. Complete occlusion is more difficult to achieve in larger aneurysms, aneurysms with wider necks, and aneurysms with stronger and more complex flows.

ABBREVIATIONS: AR = aspect ratio; Asize = aneurysm size; AUC = area under the curve; BF = bottleneck factor; corelen = vortex core length; ICI = inflow concentration index; UI = undulation index; NSI = nonsphericity index; Nsize = neck size; Q = mean aneurysm inflow; Qpost = posttreatment aneurysm inflow rate; VE = mean aneurysm velocity; VO = mean vorticity; VOR = volume-to-ostium ratio

Flow diversion (ie, the endoluminal placement of a flow-diverting stent) has become an attractive treatment option for many large and complex aneurysms in which coiling alone tends to have

high rates of recompaction and recanalization.¹ However, these flow-diversion techniques are not free of complications. Problems associated with the treatment of cerebral aneurysms with endoluminal flow diverters include incomplete occlusion or persistent filling of the aneurysm, thromboembolic events, in-stent stenosis or myointimal hyperplasia, delayed aneurysm rupture, and delayed distal hemorrhage.^{2,3} In addition, 2 further concerns are the use of dual-antiplatelet therapy, which increases the chances of other complications, and the treatment of bifurcation aneurysms in which at least 1 of the daughter branches would be jailed by endoluminal devices, which increases the chances of thromboembolic events or vessel occlusions.

Intracranial flow-diverting devices offer the possibility of addressing some of these concerns.⁴⁻⁶ The devices have been developed specifically for bifurcation aneurysms, and most cases do not require the use of dual-antiplatelet therapy as with endoluminal devices. Therefore, they constitute a promising approach for

Received February 27, 2019; accepted after revision July 3.

From the Bioengineering Department (J.R.C., F.M.), Volgenau School of Engineering, George Mason University, Fairfax, Virginia; Department of Mathematical Sciences (B.J.C.), Montclair State University, Montclair, New Jersey; Department of Interventional Neuroradiology (J.C., C.B., E.S., P.L.), Clinica ENERI, Buenos Aires, Argentina; and Department of Interventional Neuroradiology (R.K., D.K.), Mayo Clinic, Rochester, Minnesota.

This work was supported by the National Institutes of Health, grant No. R01 NS076491.

Please address correspondence to Juan R. Cebral, PhD, Bioengineering and Mechanical Engineering Departments, Volgenau School of Engineering, George Mason University, 4400 University Dr, MSN 1J7, Fairfax, VA 22030; e-mail: jcebral@gmu.edu

Indicates open access to non-subscribers at www.ajnr.org

Indicates article with supplemental on-line tables.

Indicates article with supplemental on-line photos.

<http://dx.doi.org/10.3174/ajnr.A6169>

complex bifurcation aneurysms⁷ and an alternative to other techniques such as Y-stent placement and coiling.^{8,9} However, not all aneurysms are immediately occluded after implantation of intrasaccular flow diverters. Thus, the objective of our study was to identify aneurysm and flow characteristics (and their change) associated with subsequent outcome after intrasaccular device implantation (ie, complete or incomplete occlusion). This information is important to understand the reasons underlying failures, pinpoint problematic cases, and enable the prediction of long-term outcomes to improve treatment planning and device selection.

MATERIALS AND METHODS

Data

A total of 42 aneurysms in 39 patients (35 women and 4 men; mean age, 64 years) treated with intrasaccular devices were studied. The aneurysms were imaged with 3D rotational angiography immediately before treatment. 2D-DSA images were acquired immediately before and after implantation of the intrasaccular devices. All aneurysms were treated with the Woven EndoBridge (WEB; Sequent Medical, Aliso Viejo, California) device,⁴ 33 with Dual-Layer (DL), 8 with Single-Layer (SL), and 1 with a Single-Layer Spherical (SLS) devices. Typically, the device size is chosen to be 1 mm larger in diameter compared with the aneurysm width and 1 mm smaller in length than the aneurysm depth (size from the neck to the dome), to allow the device to expand into the aneurysm dome and conform to the aneurysm walls. Of the 42 aneurysms, 6 were discarded because there were no follow-up angiographic studies to evaluate the treatment outcome. Patient, aneurysm, and device characteristics of the remaining 36 aneurysms in 33 patients are summarized in On-line Table 1.

Models

Patient-specific vascular models were constructed from the 3D rotational angiography images using previously developed methods.¹⁰ Unstructured grids composed of tetrahedral elements that fill the lumen of the vascular models were constructed using an advancing front grid generator.¹⁰ Models of the intrasaccular devices were created and interactively placed within the vascular models using DSA image-guidance tools and techniques recently developed.¹¹ Briefly, the vascular model is rendered semitransparent and is superimposed on the DSA image; it is then interactively rotated, zoomed, and translated to make sure it coincides with the vessels visible in the DSA image (ie, both have the same projection). Next, the device is interactively translated and rotated to make the virtual device markers coincide with the actual device markers visible in the DSA image. The process is repeated with different DSA images acquired in different projections (ie, different views) to guide the placement of the 3D virtual device within the vascular model. The process is illustrated with a representative case in On-line Fig 1.

Computational fluid dynamics simulations were performed by numerically solving the Navier-Stokes equations using an in-house finite-element solver.¹² Pulsatile flow conditions were imposed at the inlet boundary by scaling flow waveforms measured in healthy subjects.¹³ To simulate the blood flow after intrasaccular device implantation, we used an immersed boundary method

operating on adaptive unstructured grids.¹⁴ In this approach, the device wires were discretized as a series of overlapping spheres and the mesh elements intersected by the spheres were adaptively refined to resolve the wires. Single-layer devices were modeled as a structure composed of 144 wires of 25 μm in diameter braided at an angle of 80°. Double-layer devices of >8 mm were modeled as an outer layer of 144 wires of 19 μm in diameter and an inner layer of 144 wires of 38 μm in diameter, both braided at an angle of 80°. Double-layer devices <8 mm had 108 wires in each layer instead of 144. Because these devices contain numerous thin wires, the resulting meshes after adaptive refinement were quite large, ranging between 100 and 200 million tetrahedra.

Flow simulations were performed for 2 cardiac cycles, and the results from the second cycle were used to compute a number of flow parameters to quantitatively characterize the aneurysm hemodynamic environment.¹⁵ In particular, these variables characterize the mean aneurysm inflow (Q) and concentration (ICI) of the inflow jet, and the mean aneurysm velocity (VE) and mean vorticity (VO, corelen) of the intra-aneurysmal flow pattern. Similarly, a number of geometric parameters were calculated to characterize the size (aneurysm size [Asize], neck size [Nsize]) and shape (aspect ratio [AR], bottleneck factor [BF], volume-to-osmium ratio [VOR], undulation index [UI], nonsphericity index [NSI]) of the aneurysms.¹⁶ A list of the geometric and hemodynamic variables used and their basic meaning are provided in On-line Table 2. Hemodynamic analysis was performed blinded to aneurysm occlusion outcomes.

Analysis

The outcomes of the treatments were evaluated at follow-up with angiography imaging. Aneurysms were classified into 4 categories: A) no remnant or filling of the aneurysm or device, B) small remnant associated with filling of the proximal recession of the device, C) filling of the proximal compartment of the device (dual-layer only), and D) filling of the distal compartment of the device. Categories A and B were grouped into a “complete” occlusion group, and categories C and D, into an “incomplete” occlusion group. Outcome assessment was performed blinded to the computational fluid dynamics results.

Hemodynamic variables computed for the pretreatment and posttreatment configurations, as well as their percentage change (reduction) from pre- to posttreatment, were compared between the complete and incomplete occlusion groups using the non-parametric Mann-Whitney test. Geometric characteristics of the aneurysms of these 2 groups were similarly compared. Differences were considered significant at $P < .05$ (95% confidence). P values were adjusted for multiple comparisons using the Bonferroni method. For each of the variables with statistically significant differences, univariate logistic regressions were performed, receiver operating characteristic curves were created, and the area under the curve (AUC) was calculated to assess the discriminatory power of each of these variables. Optimal thresholds were computed as the point on the receiver operating characteristic curve closest to the upper-left corner. Multivariate logistic regression analysis was performed with statistically significant variables. All statistical analyses were performed using codes written in R statistical and computing software (<http://www.r-project.org/>).

Table 1: Hemodynamic parameters before treatment, after treatment, and their change (reduction), along with geometric characteristics of aneurysms in the complete and incomplete occlusion groups^a

Variable	Complete (n = 18)		Incomplete (n = 18)		Comparison			
	Mean	SD	Mean	SD	P	P Adjusted	AUC	Threshold
Geometry								
Asize	0.781	0.131	1.060	0.213	<.001 ^b	.002 ^b	0.87	1.04
Nsize	0.502	0.097	0.660	0.132	<.001 ^b	.004 ^b	0.85	0.70
AR	1.335	0.424	1.507	0.352	.11	.85		
BF	1.349	0.215	1.483	0.190	.05	.53		
VOR	0.776	0.390	1.258	0.500	.004 ^b	.06	0.79	1.15
UI	0.124	0.046	0.097	0.052	.09	.77		
NSI	0.190	0.042	0.192	0.030	.71	1.00		
Pre-Tx hemodynamics								
ICI	1.57	0.85	1.72	0.59	.29	1.00		
Q	1.09	0.59	1.67	0.78	.02 ^b	.26	0.74	1.60
VE	14.75	8.87	13.79	7.08	.81	1.00		
VO	405.54	272.72	317.64	196.43	.54	1.00		
Corelen	1.99	0.95	4.47	3.60	.04 ^b	.49	0.71	6.54
Post-Tx hemodynamics								
ICI	1.03	1.13	1.65	1.01	.03 ^b	.37	0.72	2.05
Q	0.61	0.50	1.49	0.96	.001 ^b	.02 ^b	0.82	1.64
VE	3.15	2.90	4.72	4.44	.18	1.00		
VO	130.07	107.78	148.18	128.19	.54	1.00		
Corelen	37.95	41.87	55.34	28.82	.02 ^b	.35	0.73	84.32
Hemodynamic reduction (%)								
ΔICI	46.39	34.55	8.07	32.45	.002 ^b	.03 ^b	0.81	29.17
ΔQ	47.46	28.25	9.93	33.41	<.001 ^b	.01 ^b	0.83	30.10
ΔVE	80.88	11.19	62.90	36.63	.03 ^b	.41	0.72	20.41
ΔVO	67.40	13.96	46.11	44.86	.04 ^b	.49	0.70	-8.83
Δcorelen	-1855.60	1721.87	-2068.93	1965.52	.81	1.00		

Note:—Pre-Tx indicates pretreatment; Post-Tx, posttreatment.

^a Results of univariate analysis between these 2 aneurysm groups.

^b Statistically significant differences ($P < .05$).

RESULTS

Of the 36 aneurysms with follow-up included in the study, 18 were classified into the complete occlusion group and 18 into the incomplete occlusion group. The mean and SD of geometric and hemodynamic variables (and their percentage change) in each aneurysm group are presented in Table 1. The P values of the Mann-Whitney univariate tests and the P values adjusted for multiple testing are provided, and significant differences are indicated by footnote b. The AUC and optimal threshold for the univariate logistic regressions are provided for variables with statistically significant differences between complete and incomplete occlusion groups.

These results indicate that large posttreatment aneurysm inflow rates (Q , $P = .02$) and small reductions in inflow (ΔQ , $P = .01$) and inflow concentration (ΔICI , $P = .03$) from pre- to posttreatment are associated with incomplete occlusion. Pre- and posttreatment flows tended to be more complex (ie, larger vortex corelen length [corelen]) in incompletely occluded aneurysms compared with completely occluded aneurysms, but these differences were not significant when adjusting for multiple testing.

Geometrically, incompletely occluded aneurysms were larger (Asize, $P = .002$) with wider necks (Nsize, $P = .004$) than completely occluded aneurysms. Incompletely occluded aneurysms also tended to have larger volume-to-ostium ratios (ie, larger cavities for similar neck sizes), but this association only reached marginal statistical significance after adjusting for multiple testing (VOR, $P = .06$).

Multivariate statistical logistic regression was performed with the statistically significant variables (Asize, Nsize, posttreatment

aneurysm inflow rate [Qpost], ΔQ , and ΔICI). Stepwise variable selection using the Akaike information criterion retained Asize, Nsize, and Qpost as independent predictors of incomplete occlusion with an AUC = 0.93 and a prediction error of 22% during cross-validation (On-line Fig 2). The linearized model coefficients (measure of the relative importance of the variables) were Asize = 4.58, Nsize = 2.35, Qpost = 3.87.

DISCUSSION

Associations with Incomplete Occlusion

The results of this study indicate that incomplete aneurysm occlusion after treatment with intrasaccular flow diverters is associated with a high persistent inflow rate into the aneurysm immediately after treatment and a small reduction in the inflow rate (and inflow jet concentration) from pre- to posttreatment conditions. These results are not surprising and are consistent with previous studies analyzing the relationship between flow conditions and outcomes of aneurysms treated with endoluminal flow diverters.¹⁷⁻¹⁹ Furthermore, our results suggest that the change in inflow rate (ΔQ) from pre- to posttreatment, and/or the final posttreatment inflow rate could discriminate between incomplete and complete occlusions at follow-up with a predictive power of approximately 82%–83%, as suggested by the corresponding AUCs. Our results also indicate that, in general, it is more difficult to achieve complete occlusions in larger aneurysms, aneurysms with wider necks, and aneurysms with stronger and more complex flows. The multivariate analysis suggests that adding flow information (especially posttreatment inflow rate) improves the

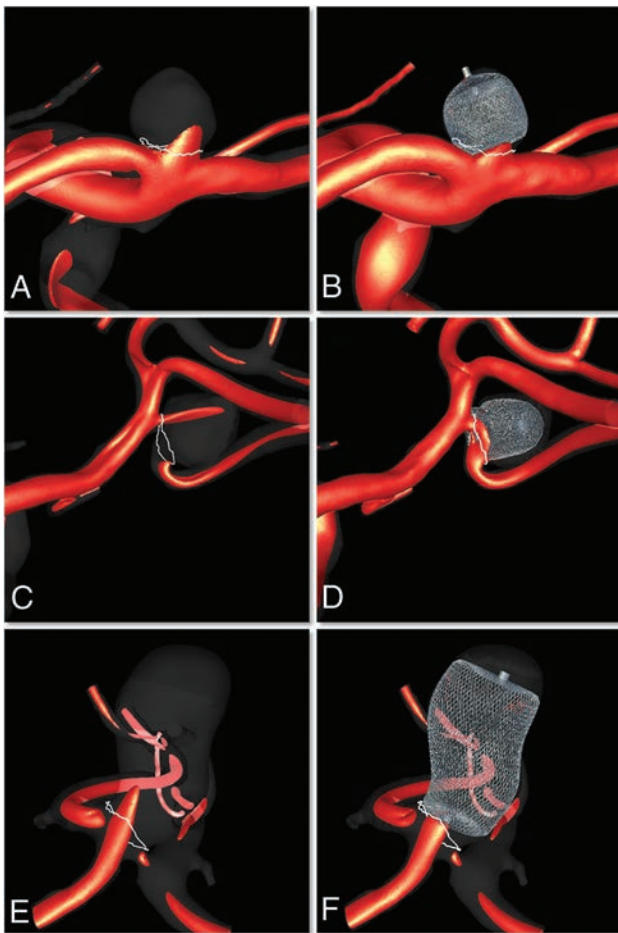


FIG 1. Examples of 3 aneurysms treated with intrasaccular devices that are completely occluded at follow-up. Left column (A, C, and E) shows visualizations of the inflow jet before treatment, and right column (B, D, and F) shows corresponding visualizations immediately after treatment. *Upper row*, ICA bifurcation aneurysm. *Center row*, MCA bifurcation aneurysm. *Lower row*, Anterior communicating artery aneurysm.

assessment of future occlusion based on geometry alone. Furthermore, according to the linearized coefficients of this model, aneurysm size and inflow rate seem to be the most important variables to predict or explain outcomes.

Previous studies have proposed the mean aneurysm flow amplitude ratio, derived from dynamic DSA images, as a predictor of aneurysm occlusion after flow diversion.²⁰ Additionally, a previous study showed that mean aneurysm flow amplitude is related to the VE determined through computational fluid dynamics analysis.²¹ Most interesting, in our study, the reduction in the mean aneurysm flow velocity (ΔVE) tended to be larger in completely occluded aneurysms compared with incompletely occluded aneurysms, but this trend did not achieve statistical significance when adjusting for multiple comparisons. Nevertheless, our univariate logistic regression analysis indicated that ΔVE (and thus perhaps the mean aneurysm flow amplitude ratio) could discriminate between complete and incomplete occlusions with approximately 72% accuracy (AUC = 0.72).

Examples of 3 aneurysms in the complete occlusion group are shown in Fig 1. This figure presents visualizations of the inflow jet before and after treatment. A noticeable reduction in the inflow jet into the aneurysm can be observed in these 3 cases. Similarly,

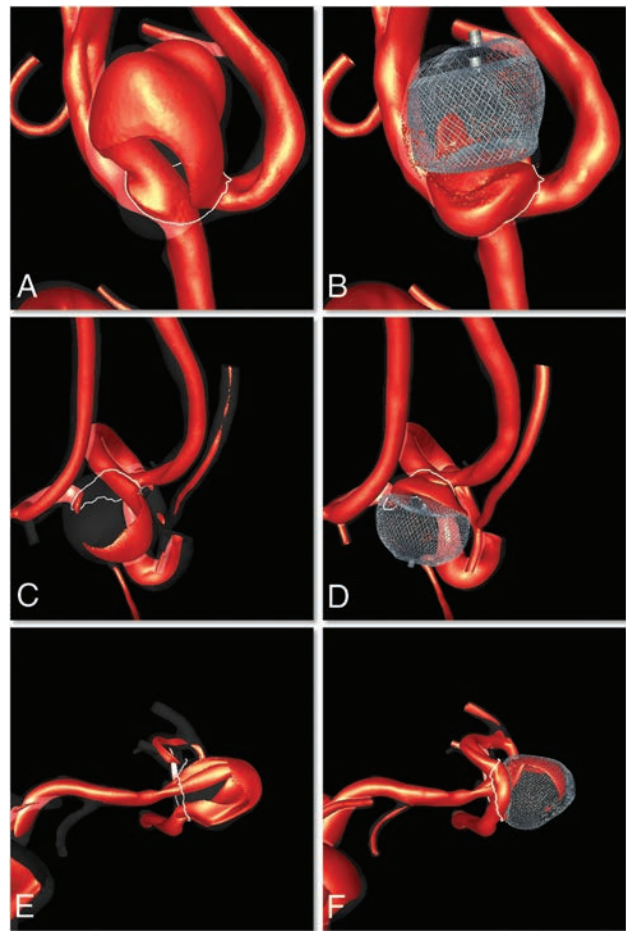


FIG 2. Examples of 3 aneurysms treated with intrasaccular devices that are incompletely occluded at follow-up. Left column (A, C, and E) shows visualizations of the inflow jet before treatment, and right column (B, D, and F) shows corresponding visualizations immediately after treatment. All 3 aneurysms were at the MCA bifurcation.

examples of 3 aneurysms in the incomplete occlusion group are presented in Fig 2. In the first case (upper row), it can be seen that the position of the device is not optimal—that is, the device is not well-apposed to the walls at the aneurysm opening but further into the sac, allowing flow into the aneurysm. In the second case (center row), there seems to be substantial flow into the aneurysm because of suboptimal orientation of the base of the device with respect to the aneurysm opening. In the third case (lower row), though the device seems properly placed, the inflow jet is quite strong and is not sufficiently disrupted by the device. These results seem to be consistent with a previous study of endoluminal flow diversion that indicated that proper sizing of the stent (which produces minimal change in the device cells compared with its reference configuration) is associated with a higher rate of complete aneurysm occlusion.²²

Clinical Implications

Our findings indicate that treatment failure (ie, incomplete occlusion) could result not only because of poor device deployment (which is more common in large aneurysms with wide necks) but also because the devices may not provide sufficient flow disruption, even if appropriately placed, in cases with strong inflow jets.

Therefore, in addition to the aneurysm geometric features that predispose them to failure (size and neck), knowledge of pretreatment flow characteristics (in particular the location and strength of the inflow jet) could help select devices (porosity) and place them optimally to achieve the largest flow disruption possible (lower porosity regions blocking the inflow jet). Additional quantitative knowledge of posttreatment flow conditions could also be used to predict outcomes using statistical models such as the multivariate logistic model presented here. This information is valuable for evaluating the procedure and potentially recommending further steps (eg, deployment of a flow-diverting stent if failure is anticipated). This hemodynamic information could potentially be derived from computational fluid dynamics models, but this step would require significantly reducing the time required for posttreatment computational fluid dynamics simulations. This could be achieved with steady-state simulations (and perhaps reduced vascular models) that can yield mean flow quantities such as the ones presented here in a much shorter time (minutes). Alternatively, flow conditions could be potentially inferred from in vivo measurements such as the mean aneurysm flow amplitude derived from dynamic DSA images (though these techniques would have to be improved for estimating flows in the presence of intrasaccular devices).

Limitations

Patient-specific flow conditions were unavailable; therefore, they were adapted from measurements in healthy subjects. Vessel walls were approximated as rigid, and blood, as a continuous Newtonian fluid. There are uncertainties associated with the exact placement of the virtual devices inside the vascular model. Our interactive image-guided device-placement approach attempted to minimize these uncertainties by reproducing the position and orientation of the device by visually matching the virtual and actual device markers visible in the DSA images from all available viewpoints. Finally, our findings should be further confirmed with larger samples and more aneurysms at different locations.

CONCLUSIONS

The outcomes of cerebral aneurysm treatment with intrasaccular flow-diverting devices are associated with the flow conditions created immediately after implantation of these devices. In particular, a high posttreatment aneurysm inflow rate and a small reduction in the inflow rate (and inflow jet concentration) from pre- to posttreatment conditions are associated with incomplete occlusions. Flow conditions unfavorable for immediate and complete occlusions can be created by improper positioning or orientation of the device. Complete occlusions are more difficult to achieve in larger aneurysms, aneurysms with wider necks, and aneurysms with stronger and more complex flows.

Disclosures: Juan R. Cebral—RELATED: Grant: National Institutes of Health, Comments: research grant*; UNRELATED: Grants/Grants Pending: National Institutes of Health/Philips Healthcare, Comments: research grants.* Fernando Mut—RELATED: Grant: National Institutes of Health.* David Kallmes—RELATED: Grant: Microvention/Sequent Medical, Comments: grant for preclinical research*; UNRELATED: Grants/Grants Pending: Medtronic, NeuroSigma, Neurogami Medical, Comments: support for preclinical research*; Stock/Stock Options: Superior Medical Experts, Comments: Founder. *Money paid to the institution.

REFERENCES

- Pierot L, Biondi A. Endovascular techniques for the management of wide-neck intracranial bifurcation aneurysms: a critical review of the literature. *J Neuroradiol* 2016;43:167–75 CrossRef Medline
- Zhou G, Su M, Yin YL, et al. Complications associated with the use of flow-diverting devices for cerebral aneurysms: a systematic review and meta-analysis. *Neurosurg Focus* 2017;42:E17 CrossRef Medline
- Simgen A, Ley D, Roth C, et al. Evaluation of occurring complications after flow diverter treatment of elastase-induced aneurysm in rabbits using micro-CT and MRI at 9.4 T. *Neuroradiology* 2016;58:987–96 CrossRef Medline
- Ding YH, Lewis DA, Kadirvel R, et al. The Woven EndoBridge: a new aneurysm occlusion device. *AJNR Am J Neuroradiol* 2011;32:607–11 CrossRef Medline
- Pierot L, Liebig T, Sychra V, et al. Intrasaccular flow-disruption treatment of intracranial aneurysms: preliminary results of a multicenter clinical study. *AJNR Am J Neuroradiol* 2012;33:1232–38 CrossRef Medline
- Lubicz B, Mine B, Collignon L, et al. WEB device for endovascular treatment of wide-neck bifurcation aneurysms. *AJNR Am J Neuroradiol* 2013;34:1209–14 CrossRef Medline
- Pierot L, Klisch J, Cognard C, et al. Endovascular WEB flow disruption in middle cerebral artery aneurysms: preliminary feasibility, clinical, and anatomical results in a multicenter study. *Neurosurgery* 2013;73:27–34; discussion 34–35 CrossRef Medline
- Yavuz K, Geyik S, Cekirge S, et al. Double stent-assisted coil embolization treatment for bifurcation aneurysms: immediate treatment results and long-term angiographic outcome. *AJNR Am J Neuroradiol* 2013;34:1778–84 CrossRef Medline
- Cekirge HS, Yavuz K, Geyik S, et al. A novel “Y” stent flow diversion technique for the endovascular treatment of bifurcation aneurysms without endosaccular coiling. *AJNR Am J Neuroradiol* 2011;32:1262–68 CrossRef Medline
- Cebral JR, Castro MA, Appanaboyina S, et al. Efficient pipeline for image-based patient-specific analysis of cerebral aneurysm hemodynamics: technique and sensitivity. *IEEE Trans Med Imaging* 2005;24:457–67 CrossRef Medline
- Mut F, Chung BJ, Chudyk J, et al. Image-based modeling of blood flow in cerebral aneurysms treated with intrasaccular flow diverting devices. *Int J Numer Method Biomed Eng* 2019;35:e3202 CrossRef Medline
- Mut F, Aubry R, Löhner R, et al. Fast numerical solutions of patient-specific blood flows in 3D arterial systems. *Int J Numer Method Biomed Eng* 2010;26:73–85 CrossRef Medline
- Cebral JR, Castro MA, Putman CM, et al. Flow-area relationship in internal carotid and vertebral arteries. *Physiol Meas* 2008;29:585–94 CrossRef Medline
- Appanaboyina S, Mut F, Löhner R, et al. Computational fluid dynamics of stented intracranial aneurysms using adaptive embedded unstructured grids. *International Journal for Numerical Methods in Fluids* 2008;57:457–93 CrossRef
- Mut F, Löhner R, Chien A, et al. Computational hemodynamics framework for the analysis of cerebral aneurysms. *Int J Numer Method Biomed Eng* 2011;27:822–39 CrossRef Medline
- Raghavan ML, Ma B, Harbaugh RE. Quantified aneurysm shape and rupture risk. *J Neurosurg* 2005;102:355–62 CrossRef Medline
- Kulcsár Z, Augsburger L, Reymond P, et al. Flow diversion treatment: intra-aneurysmal blood flow velocity and WSS reduction are parameters to predict aneurysm thrombosis. *Acta Neurochir (Wien)* 2012;154:1827–34 CrossRef Medline
- Cebral JR, Mut F, Raschi M, et al. Analysis of hemodynamics and aneurysm occlusion after flow-diverting treatment in rabbit models. *AJNR Am J Neuroradiol* 2014;35:1567–73 CrossRef Medline
- Paliwal N, Damiano RJ, Davies JM, et al. Association between hemodynamic modifications and clinical outcome of intracranial aneurysms treated using flow diverters. *Proc SPIE Int Soc Opt Eng* 2017;10135 CrossRef Medline

20. Pereira VM, Bonnefous O, Ouared R, et al. **A DSA-based method using contrast-motion estimation for the assessment of the intraneurysmal flow changes induced by flow-diverter stents.** *AJNR Am J Neuroradiol* 2013;34:805–15 CrossRef Medline
21. Cebal JR, Mut F, Chung BJ, et al. **Understanding angiography-based aneurysm flow fields through comparison with computational fluid dynamics.** *AJNR Am J Neuroradiol* 2017;38:1180–86 CrossRef Medline
22. Herbreteau D, Bibi R, Narata AP, et al. **Are anatomic results influenced by WEB shape modification? Analysis in a prospective, single-center series of 39 patients with aneurysms treated with the WEB.** *AJNR Am J Neuroradiol* 2016;37:2280–86 CrossRef Medline

Two-Center Experience in the Endovascular Treatment of Intracranial Aneurysms Using the Woven EndoBridge 17 Device Including Midterm Follow-Up Results: A Retrospective Analysis

C. Maurer, I. König, A. Berlis, W. Weber, and S. Fischer



ABSTRACT

BACKGROUND AND PURPOSE: The Woven EndoBridge device proved its effectiveness in the treatment of ruptured and unruptured intracranial aneurysms as a stand-alone device. Before 2016, Woven EndoBridge deployment required at least a 0.021-inch microcatheter. In 2016, a smaller device, the Woven EndoBridge 17 with finer size increments that used a 0.017-inch microcatheter, was introduced. We retrospectively analyzed our initial and follow-up results with the Woven EndoBridge 17 in ruptured and unruptured aneurysms.

MATERIALS AND METHODS: One hundred twenty-seven intracranial aneurysms in 117 patients were scheduled for treatment with the Woven EndoBridge 17 between June 2017 and February 2019. Twenty-nine aneurysms were ruptured.

RESULTS: Treatment was performed as intended in 124 of 127 cases (97.6%). Additional devices such as stents or coils were used in 12 cases (9.7%). Five thromboembolic complications and 1 hemorrhagic complication were encountered, resulting in clinical deterioration in 2 patients. The overall morbidity and mortality in the entire series have been 1.7% and 0.0% to date, respectively. The follow-up results at 3 and 12 months revealed complete occlusion in 76.1% (70/92) and 78.0% (32/41).

CONCLUSIONS: The Woven EndoBridge 17 device is safe in the treatment of small broad-based aneurysms without the general need for additional devices. The low complication rate and the promising follow-up results underline the value of this technique in a growing range of endovascular treatment options for intracranial aneurysms.

ABBREVIATIONS: AcomA = anterior communicating artery; GCP = good clinical practice

The concept of intra-aneurysmal flow disruption consists of a hemodynamically active implant placed inside the aneurysm sac, which, in combination with an attenuated coverage of the neck area, acts as a scaffold for final neointimal growth, resulting in an intra-aneurysmal thrombosis. Experience with the Woven EndoBridge device (WEB; Sequent Medical, Aliso Viejo, California) as the most established flow disruptor is growing, and its safety and effectiveness in the treatment of ruptured and unruptured aneurysms have been documented in numerous publications including clinical trials.¹⁻⁷ A potential drawback in

treatment with the WEB device consisted of comparatively large microcatheters needed for deployment. In the initial phase, a 0.033- or a 0.027-inch microcatheter was necessary for every WEB device, while in 2015, a modification of the device resulted in the possibility of implanting WEB devices via a 0.021-inch microcatheter. The WEB 17 system, which became available in December 2016, is supposed to facilitate the treatment of small broad-based aneurysms. The possibility of using a 0.017-inch microcatheter might enable the operator to catheterize more distally located lesions and to treat more complex and smaller aneurysms with a potentially lower risk of vessel injury compared with larger catheters. The addition of the WEB 17 system to the pre-existing range of WEB devices, therefore, expands the possibilities and indications for endovascular treatment by intra-aneurysmal flow diversion.

This study is a retrospective evaluation of the immediate and follow-up results of 2 neurovascular centers using the WEB 17 device in the treatment of ruptured and unruptured intracranial aneurysms.

Received April 28, 2019; accepted after revision July 5.

From the Knappschaftskrankenhaus Bochum-Langendreer (I.K., W.W., S.F.), Universitätsklinik, Institut für Diagnostische und Interventionelle Radiologie, Neuroradiologie, Nuklearmedizin, Bochum, Germany; and Klinikum Augsburg (C.M., A.B.), Klinik für Diagnostische Radiologie und Neuroradiologie, Augsburg, Germany.

Please address correspondence to Sebastian Fischer, MD, Knappschaftskrankenhaus Bochum-Langendreer, Universitätsklinik, Institut für Diagnostische und Interventionelle Radiologie, Neuroradiologie, Nuklearmedizin, In der Schornau 23-25, 44892 Bochum, Germany; e-mail: sebif01@googlemail.com

<http://dx.doi.org/10.3174/ajnr.A6177>

MATERIALS AND METHODS

WEB Device

The WEB device is an intra-aneurysmal self-expanding electrothermically detachable implant available in 2 versions, a Single-Layer Sphere (SLS) and a more oblong Single-Layer (SL) configuration. It consists of a braided mesh of platinum-coated nitinol wires that converge at the bottom and the top of the device. A detailed summary of the design and development of the WEB device including its evolutionary steps is given in the literature.^{6,8,9}

The size of the microcatheter needed for delivery of the device depends on the width of the WEB used. While the SL version comes in well-defined width and length sizes, the length of each SLS device is 1.6 mm less than its width. While devices from 4 to 7 mm in width are compatible with a 0.021-inch microcatheter, larger ones need a 0.027-inch (8–9 mm) or a 0.033-inch (10–11 mm) microcatheter. The WEB 17 system is compatible with a 0.017-inch microcatheter and comes in sizes from 3 to 7 mm with 0.5-mm increments between the 3- and 5-mm devices. Devices with sizes from 6 to 7 mm are compatible with both a 0.017- or a 0.021-inch delivery catheter in the SL and SLS configurations. Even though the total number of wires that build the device is less in the WEB 17 compared with the WEB 21 version, the metal coverage at the bottom, as an elementary factor for intra-aneurysmal thrombosis and neointimal growth, is not less (approximately 60% in both versions).^{6,8} The VIA Microcatheter (Sequent Medical) is exclusively designed for the delivery of the WEB device and is therefore available in the mentioned sizes from 0.033 to 0.017 inch. The aneurysms analyzed in the present study were exclusively treated with the WEB 17 system using a VIA 17 microcatheter.

Decision-Making for Treatment with WEB

All cases were discussed in a weekly interdisciplinary conference including neurosurgical, neurologic, and neurointerventional expertise, and the decision for an endovascular treatment was reached by consensus following an “endovascular first” concept at both institutions. The final endovascular treatment strategy was determined by the neurointerventionalist. Clinical and morphologic factors were considered, whereas absolute exclusion criteria for an endovascular approach with the WEB 17 device were a neck width larger than the fundus width referring to an aspect ratio of <1 , an incorporation of a branch into the aneurysmal sac, and an aneurysm size below or above the suitable range for the WEB 17 device given by the manufacturer’s sizing guide (<2.0 to >6.5 mm). Informed consent was obtained at least 24 hours before the procedure. Decision-making in cases of acutely ruptured aneurysms was reached outside the scheduled conference with the responsible neurosurgeon. The treatment results of acute cases were retrospectively analyzed in the following neurovascular conference. Patients in a poor clinical condition following an acute SAH were treated without prior informed consent on the basis of an emergency indication.

Endovascular Procedure: Device Selection

The basic procedural setup with the WEB 17 did not differ from the general institutional standards for any endovascular

aneurysm treatment in both participating centers. The analyzed procedures were performed by 4 neurointerventionalists, each with comprehensive experience in the endovascular treatment of intracranial aneurysms. Procedures were exclusively performed with the patient under general anesthesia on a biplane angiographic system, including the option of rotational angiography (Artis Q; Siemens, Erlangen, Germany). In unruptured aneurysms, a bolus of 5000 IU of heparin was administered, and patients were placed on dual-antiplatelet therapy before the procedure if mandatory to preserve the parent artery with a stent. After termination as intended, patients were kept on 100 mg of acetylsalicylic acid daily for 4–6 weeks. In cases of acutely ruptured aneurysms, the procedure was performed with 5000 IU of heparin without antiplatelet therapy.

Once the target artery was catheterized with an 8F or 6F guiding catheter or a combination of both, the aneurysm was visualized in an appropriate working position free from superimpositions of surrounding arteries. The selection of a WEB device suitable for the aneurysm resulted from calibrated measurements of its height and width in 2 orthogonal projections. The mean value of both determined the selection of the device based of the basic principle of an oversizing of the WEB in width with a compensatory undersizing of its height as described elsewhere.^{6,8} This principle became known as the “+1/–1 rule” before the introduction of the WEB 17 system, indicating an oversizing and undersizing of 1 mm for the appropriate WEB device. The horizontal compression of the device results in a longitudinal extension of 1 mm.¹⁰ The fixed value of 1 mm became improper for very small aneurysms, especially with regard to 0.5-mm increments for WEB 17, meaning that the required extent of oversizing is less in smaller aneurysms. This resulted in a sizing calculator based on an algorithm created by the manufacturer. The size selection of WEB 17 in this study was based on this sizing calculator.

The selected WEB 17 device was then advanced toward the aneurysm with a VIA 17 microcatheter placed in the proximal fundus. The complete unfolding of the device resulted from a gentle withdrawal of the microcatheter in combination with an advancement of the device. Both the microcatheter and the device were finally pushed forward to obtain a stable position inside the aneurysm with a proper apposition to the aneurysmal wall. The device was left undetached for approximately 10 minutes. In cases of malposition or an inadequate size (indicated by contrast filling between the device and the aneurysm wall or an extension toward the parent artery), the device was withdrawn and a larger or smaller device was implanted. In cases of a mild extension of the WEB device inside the parent artery with an anticipated flow disturbance, a self-expanding stent was applied to stabilize the device and to protect the parent artery. This decision was based on the individual interventionalist’s estimation during an observational period of 10 minutes before the final detachment of the device.

Data Analysis and Follow-Up Schedule

Angiographic and clinical data were collected in retrospect and entered in a previously adapted data base. The initial and follow-

up angiographic results were graded on a 5-point scale as suggested by Caroff et al² (no residual flow in the aneurysm/WEB, 1; opacification of the proximal recess of WEB, 2; neck remnant, 3; residual flow inside the WEB, 4; aneurysm remnant, 5).

In the final descriptive analysis, grades 1–2 were summarized as complete occlusion, grades 3 and 4 indicated a neck remnant or flow inside the WEB, and grade 5 represented an aneurysm remnant.

The angiographic follow-up schedule at the 2 centers does not differ from that of interventionally treated aneurysms in general, with examinations planned after 3 and 12 months. The clinical condition of each patient was determined according to the mRS on admission, at discharge, and at each follow-up visit by the responsible neurosurgeon or neurointerventionalist. Patients with a clinical deterioration were analyzed separately with regard to the underlying cause.

Statistical Analysis

The statistical analysis of all variables was performed independently using Excel (Microsoft, Redmond, Washington). Continuous variables were given as the median and range. Independent variables were described as percentages.

Ethics Statement

We declare that all human and animal studies have been approved by the ethics committee of Ruhr Universität, Bochum, Germany. The study was performed in accordance with the ethical standards established in the 1964 Declaration of Helsinki and its later amendments. A separate informed consent from each patient before inclusion in this study was not required due to the retrospective design of the study.

RESULTS

Patients

A total of 117 patients (median age, 53 years; range, 25–81 years) with 127 intracranial aneurysms planned for treatment with the WEB 17 were included at the 2 participating centers during the sample period (June 2017 to February 2019). Of those, 29 aneurysms were acutely ruptured (SAH within 7 days before hospital admission) and the remaining 98 were unruptured.

Aneurysms Treated with WEB 17

One hundred thirteen (88.9%) aneurysms included were located in the anterior circulation, and the remaining 14 (11.1%) were posterior circulation aneurysms. Table 1 summarizes the aneurysm locations in detail.

While 29 aneurysms were acutely ruptured, 91 were found incidentally, 6 were remnants or previously coiled or clipped aneurysms, and 1 was a flow-related aneurysm in a patient with a large arteriovenous malformation. The median width of all aneurysms was 4.0 mm (range, 2.0–6.0 mm) with a median height of 4.0 mm (range, 2.0–7.0 mm) and a median neck size of 3.0 mm (range, 2.0–6.0 mm).

Primary Results

Treatment with the WEB 17 was successful in all except 3 procedures. One was an incidental finding of an aneurysm of the

Table 1: Location of the 127 intracranial aneurysms treated with WEB 17

Location	No.	Ratio (%)
Anterior circulation (<i>n</i> = 113) (88.9%)		
ACA AcomA	33	26.0%
ACA A2	11	8.6%
MCA bif	52	41.0%
MCA M1	2	1.6%
ICA PcomA	10	7.8%
ICA bif	5	4.0%
Posterior circulation (<i>n</i> = 14) (11.1%)		
BA tip	7	5.4%
PCA	1	0.8%
PICA	3	2.4%
Superior cerebellar artery	3	2.4%
		100.0%

Note:—ACA indicates anterior cerebral artery; ACA A2, anterior cerebral artery A2 segment; bif, bifurcation; PcomA, posterior communicating segment; BA tip, basilar artery tip; PCA, posterior cerebral artery.

middle cerebral artery bifurcation in a patient with a previously ruptured aneurysm of the basilar artery treated previously by coiling. The small aneurysm was difficult to catheterize with the VIA 17 microcatheter due to an unfavorable angle, and once a WEB 17 device of 3 mm in width and 2 mm height was deployed, the inferior branch of the middle cerebral artery showed a narrowing. A repositioning of the WEB device ideally with a temporary invagination of the proximal marker to optimize the configuration of the device inside the aneurysm might have been necessary to preserve the parent artery but appeared impossible given the angular anatomy of the parent artery. Therefore, the operator decided to recapture the device. The aneurysm was finally treated by stent-assisted coiling without problems. In the other failed case of an internal carotid artery aneurysm with a tight angulation to the parent artery, the WEB Device (WEB 17-SLS, 4 mm) dislocated into the middle cerebral artery directly after detachment, which was probably related to a combination of improper sizing and an interaction of the microcatheter with the detached device. The device was withdrawn from the middle cerebral artery using an Alligator retrieval device (Medtronic, Dublin, Ireland) without problems, and the aneurysm was finally treated by balloon-assisted coiling. The third case was a residual filling of a large ruptured, previously coiled aneurysm of the anterior communicating artery. Several attempts to place the smallest WEB 17 (SL3-2) failed due to the broad-based morphology, so the aneurysm remnant was finally treated with coils assisted by a remodeling balloon.

Therefore 124 successfully treated aneurysms were analyzed in the study. In 10 cases, the primary selected WEB 17 device was recaptured and a device of a different size was successfully implanted; and in 2 other cases, the final detachment of the WEB was after 2 other devices had to be withdrawn. Criteria to recapture the WEB were an incomplete filling of the aneurysm by the device or an extension of the mesh into the parent artery.

Additional devices such as self-expanding stents or coils were used in 12 (9.7%) cases; this addition was part of the intended treatment strategy in 7 (5.6%) cases (4 cases with stents [LVIS, MicroVention, Tustin, California; and Neuroform Atlas, Stryker

Table 2: Immediate and follow-up results of the aneurysms treated with WEB 17 according to the 5-point scale of Caroff et al^{2,a}

Grade No.	Immediate	Ratio (%)	3-Month Follow-Up	Ratio (%)	12-Month Follow-Up	Ratio (%)
	124	100.0%	92	74.2%	41	33.1%
1	23	18.6%	20.2%	62	67.4%	76.1%
2	2	1.6%		8	8.7%	3
3	2	1.6%	70.9%	11	12.0%	20.7%
4	86	69.4%		8	8.7%	1
5	11	8.8%	8.9%	3	3.2%	3.2%
						2
						4.9%

^a Grade 1: no residual flow in aneurysm/WEB 17; grade 2: opacification of the proximal recess of WEB 17; grade 3: neck remnant; grade 4: residual flow inside the WEB 17; grade 5: aneurysm remnant. Grades 1–2 are summarized as complete occlusion, grades 3 and 4 indicate a neck remnant or flow inside the WEB, and grade 5 represents an aneurysm remnant.

Neurovascular, Kalamazoo, Michigan] to stabilize the device inside the aneurysm and to preserve the parent artery; 3 cases combined with coiling). In the remaining 5 (4.0%) cases, a self-expanding stent was used as a bailout strategy to protect the parent artery. The decision for the additional implantation of a stent was made by the interventionalist as described above.

Angiographic Results

As with extra-aneurysmal flow diverters, an unchanged or at least reduced aneurysm perfusion directly after placement of the WEB device is the typical finding because the process of complete intra-aneurysmal thrombosis and neointimal growth may need up to several months. Nevertheless, some aneurysms occlude promptly after placement of an extra- or intra-aneurysm flow diverter.^{4,11} We found an initial rate of complete aneurysm occlusion in 25 (20.2%) of our 124 cases. This rate changed to 76.1% and 78.0% during the follow-up period of 3 and 12 months (median, 3.6 and 12.3 months; range, 0.2–12.4 and 4.40–24.2 months). Table 2 summarizes the initial and follow-up results according to the 5-point scale of Caroff et al.²

We observed 2 cases of clustering of the WEB device during the follow-up period. One of those was a carotid artery aneurysm (ICA posterior communicating artery), and the other was an anterior communicating artery (AcomA) aneurysm that was retreated by stent-assisted coiling. Two other aneurysms were retreated during the follow-up period due to a remaining perfusion of the neck not covered by the device. The decision for retreatment was made following a discussion in the neurovascular board.

Peri- and Postprocedural Complications

We observed thrombus formation within the parent artery after placement of the WEB 17 in 5 cases. Of those, 3 were successfully treated by an intravenous bolus of 500 mg of acetylsalicylic acid ($n=2$) or a weight-adapted bolus of eptifibatide. There was a spontaneous regression of the thrombus in 1 case. All those were cases of unruptured aneurysms. The last case was a ruptured, irregularly shaped aneurysm of the middle cerebral artery that was treated by a combination of coils and a 4 × 2 mm WEB 17 device placed at the base of the aneurysm. The device dislocated during the detachment process resulting in an occlusion of the inferior branch of the middle cerebral artery followed by a clinically relevant ischemia in the dependent vascular territory. The operator decided against an attempt to reopen the occluded branch with antithrombotic drugs because the patient was scheduled for

the acute evacuation of the intracerebral hematoma caused by the ruptured aneurysm directly after the endovascular intervention.

Another patient with a ruptured MCA bifurcation aneurysm was treated with a 5 × 3 mm WEB 17 device without problems but showed an increasing subarachnoid hemorrhage on the post-interventional CT scans. Although no contrast extravasation was observed peri-interventionally, this case was classified as an intra-procedural or early postinterventional subarachnoid hemorrhage. The patient developed a mild permanent deficit with an ongoing disorder of concentration and a reduction of mental capacity without any focal neurologic deficit (mRS 1), probably related to the described circumstance.

The 2 patients described experienced a clinically relevant deterioration, probably related to the procedure, resulting in a morbidity rate of 1.7% (2/117) and a mortality rate of 0.0%.

DISCUSSION

Our results underline the technical and clinical efficacy of the WEB 17 system in the treatment of ruptured and unruptured intracranial aneurysms, with an acceptable safety profile and convincing complete and adequate occlusion rates of 77.1% and 89.2% after 3 months.

The concept of intra-aneurysmal flow diversion with the WEB device proved its effectiveness in several good clinical practice (GCP) studies and single-center series before the introduction of the WEB 17 system. These GCP studies revealed a midterm adequate occlusion rate of 79.1% and a mortality rate of 1.2%.¹² The recently published 1-year results of the WEB Intrasaccular Therapy (WEB-IT) study with 148 patients treated with the WEB device showed complete and adequate occlusion rates of 58.8% and 84.6%, respectively, with a safety profile comparable with that of the previous GCP studies.¹³ The introduction of the WEB 17 system expanded the indications toward smaller and more distally located aneurysms. The results of the GCP studies (including larger aneurysms partly treated with the older Double-Layer system [WEB-DL]) are therefore not transferrable to the group of aneurysms exclusively treated with the WEB 17 without restriction because smaller aneurysms are generally known for a lower risk of recurrence or reperfusion compared with larger ones.¹⁴ Nevertheless, the occlusion and complication rates found in our series are similar to those of previously published series with the primary versions of the WEB device.^{4,6,10,12,13}

To date, there are only limited series of aneurysms exclusively treated with the WEB 17. Van Rooij et al⁸ analyzed their 46

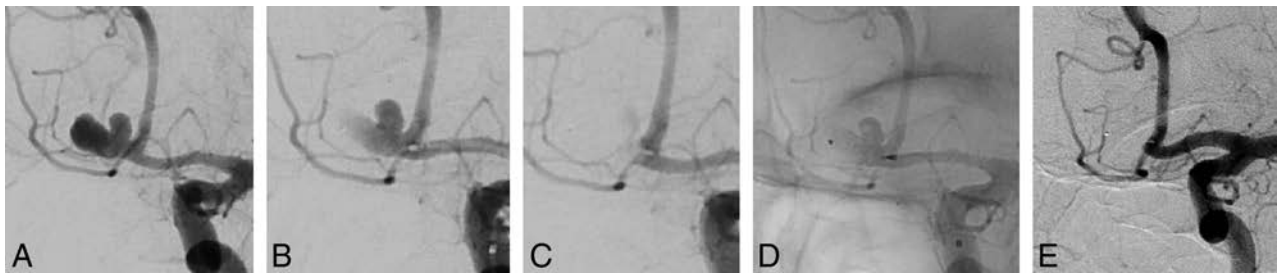


FIGURE. The complete occlusion of an unruptured bilobulated aneurysm of the AcomA in a patient with a history of SAH from another aneurysm. Injection of the left ICA with visualization in left-anterior-oblique view (A), deployment of a 6-mm WEB-SLS in the lower lobule of the aneurysm covering the orifice of the upper lobule (B), progressive thrombosis in both the lower and upper lobules of the aneurysm (C), visualization of the WEB 17 in the lower lobule of the aneurysm (fluoroscopy) (D), and 9-month follow-up angiography with stable and complete occlusion of the aneurysm (E).

aneurysms treated with the WEB 17 system. Of those, 25 were ruptured. They found 2 thromboembolic complications related to the procedure but not the device, and the patients remained without permanent clinical impairment. The complete and adequate occlusion rates at 3 months of 72% and 95% are comparable with the occlusion rates found in our series. Most interesting, there was only 1 case of an aneurysm remnant not sealed by the WEB device directly after placement. We did not analyze the number of cases with remnants or daughter aneurysms not sealed by the device, but in our experience, a complete filling of the entire aneurysm sac is not obligatory as long as the neck area is completely covered by the attenuated bottom of the WEB device, which facilitates a subsequent thrombosis of the entire aneurysm (see the illustrative case in the Figure). This characteristic is helpful, especially in the treatment of acutely ruptured aneurysms because potentially more vulnerable blebs of the aneurysm sac do not need to be catheterized separately.

In another study of 28 unruptured aneurysms treated with the WEB 17, 1 delayed thromboembolic complication was encountered. The complete occlusion rate was 91.7% during the short- and midterm follow-up periods.¹⁵

Besides these convincing angiographic and clinical results, the technical alterations of the WEB 17 allow the treatment of not only smaller aneurysms. With the possibility of introducing the WEB through a 0.017-inch microcatheter, catheterization of more distally located aneurysms with a tight angulation to the parent artery becomes easier compared with the larger VIA microcatheters. There were 8.6% distally located aneurysms of the anterior cerebral artery in our series. The WEB 17 consists of 72–108 wires compared with 144 wires in the previous versions. However, the amount of metal coverage at the bottom of the device, the hemodynamically active section, does not differ among all available sizes of the WEB. The metal coverage of approximately 60% for the WEB 17 is a consequence of a different braiding design compared with the previous versions. The lower amount of material makes it easier to deploy the device in tortuous anatomies with a more stable position of the microcatheter compared with the previous versions. The formability of the WEB 17 seems to be more pronounced, facilitating configuration within the aneurysm sac and allowing a recapture with less traction if necessary. Nevertheless, a triaxial access to the aneurysm increases the

stability during the implantation of the device, especially in tortuous anatomies.

Pierot et al¹⁶ presented a series of aneurysms in “atypical” locations treated with the WEB device, with impressive angiographic and clinical results. “Atypical” in this context means a location or morphology other than a bifurcation as the typical indication for the WEB device. With the WEB 17 being a softer device compared with previous versions, treatment of these atypical (sidewall) locations becomes straightforward. Our series with several aneurysms in atypical locations (A2, ICA posterior communicating artery, PICA) underlines this expansion of indications for WEB 17.

Asnafi et al,⁴ in a systemic review of 15 studies on the WEB device (all performed without the WEB 17), found a 12.0% rate of additional devices used in combination with the WEB. This is in line with the 9.7% in our series, in which additional devices were applied as a bailout strategy in 4.0%. Most interesting, in the series of van Rooij et al⁸ with the WEB 17, all aneurysms were treated without additional devices. This might be the consequence of the high rate of acutely ruptured aneurysms in their series (54%), in which the use of stents with their need for a dual-antiplatelet therapy is unfavorable. This refers to our treatment regimen with the WEB. In cases of unruptured aneurysms, patients were placed on dual-antiplatelet therapy before the procedure with a monotherapy of 100 mg of acetylsalicylic acid prescribed for 4–6 weeks. This concept not only allows a switch to stent-assisted coiling in cases of failure with the WEB but also allows a stent to stabilize the WEB or to preserve the parent artery in cases of doubt.

The design of WEB 17 with a lower number of wires might promote a compaction during the follow-up period with potentially lower occlusion rates compared with the previous version of the device. This relation, based on the WEB 17 being a softer device, remains hypothetical, and we think that with an exact sizing, the rate of compaction will not be different from that with the previous device.

The retreatment rate in our series was 2.4%, which is relevantly lower than the rates of 12.3% and 21.1% reported in other series with the WEB device.^{17,18} One reason can be found in the increasing experience with the WEB device (learning curve), resulting in a more appropriate initial size selection with a lower retreatment rate as described in the literature.^{18,19} Another reason

might be found in the smaller aneurysm size in this series and the comparatively short follow-up period. A comparative analysis of all aneurysms treated with WEB 21 and WEB 17 with longer follow-up data that is currently being conducted at our institution will help to identify the factors influencing a stable long-term occlusion.

Our study has several limitations that are mainly related to the retrospective design. The angiographic results were not analyzed independently. Because the WEB 17 system is a comparatively new device (available in Europe since December 2016), only midterm follow-up results are reported in our series, which impedes a direct comparison with other treatment options for broad-based bifurcation aneurysms. The mismatch of unruptured and ruptured aneurysms makes a statistically exploitable comparison unfeasible.

CONCLUSIONS

The WEB 17 device is safe in the treatment of broad-based aneurysms without the general need for additional devices or dual antiplatelet therapy. The system enlarges the indications toward smaller, otherwise difficult-to-treat, aneurysms. The low complication rate and the promising follow-up results underline the value of this technique in the growing range of endovascular treatment options for intracranial aneurysms. Comparative clinical trials with longer follow-up data will allow a direct comparison with conventional endovascular techniques.

Disclosures: Christoph Maurer—UNRELATED: Grants/Grants Pending: MicroVention and Stryker, Comments: educational grant by MicroVention and Stryker. Ansgar Berlis—RELATED: Consulting Fee or Honorarium: proctoring for MicroVention and Sequent Medical*; UNRELATED: Consultancy: proctoring for Stryker and Medtronic; Payment for Lectures Including Service on Speakers Bureaus: Penumbra*; Other: Clinical Event Committee for phenox. Werner Weber—UNRELATED: Consultancy: Penumbra, MicroVention, Stryker, phenox, Comments: proctoring, lecture, and chair. Sebastian Fischer—UNRELATED: Consultancy: Stryker, phenox, MicroVention, Kaneka Corporation, Comments: speaker honorarium; Payment for Lectures Including Service on Speakers Bureaus: MicroVention, Comments: speaker honorarium. *Money paid to the institution.

REFERENCES

- Pierot L, Spelle L, Molyneux A. **Clinical and anatomical follow-up in patients with aneurysms treated with the WEB device: 1-year follow-up report in the cumulated population of 2 prospective, multicenter series (WEBCAST and French Observatory).** *Neurosurgery* 2016;78:133–41 CrossRef Medline
- Caroff J, Mihalea C, Klich C, et al. **Single-layer WEBS: intrasaccular flow disrupters for aneurysm treatment—feasibility results from a European study.** *AJNR Am J Neuroradiol* 2015;36:1942–46 CrossRef Medline
- Pierot L, Costalat V, Moret J, et al. **Safety and efficacy of aneurysm treatment with WEB: results of the WEBCAST study.** *J Neurosurg* 2016;214:1250–56 CrossRef
- Asnafi S, Rouchaud A, Pierot L, et al. **Efficacy and safety of the Woven EndoBridge (WEB) device for the treatment of intracranial aneurysms: a systematic review and meta-analysis.** *AJNR Am J Neuroradiol* 2016;37:2287–92 CrossRef Medline

- Fiorella D, Molineux A, Coon A, et al. **Demographic, procedural and 30-day safety results from the WEB intra-saccular therapy study (WEB-IT).** *J NeuroInterv Surg* 2017;0:1191–96 CrossRef Medline
- Popielski J, Berlis A, Weber W, et al. **Two-center experience in the endovascular treatment of ruptured and unruptured intracranial aneurysms using the WEB device: a retrospective analysis.** *AJNR Am J Neuroradiol* 2018;39:111–17 CrossRef Medline
- Tau N, Sadeh-Gonik U, Aulagner G, et al. **The Woven EndoBridge (WEB) for endovascular therapy of intracranial aneurysms: update of a systematic review with meta-analysis.** *Clin Neurol Neurosurg* 2018;166:110–15 CrossRef Medline
- van Rooij SB, Peluso JP, Sluzewski M, et al. **The new low-profile WEB 17 system for treatment of intracranial aneurysms: first clinical experience.** *AJNR Am J Neuroradiol* 2018;39:859–63 CrossRef Medline
- Jiang B, Paff M, Colby GP, et al. **Cerebral aneurysm treatment: modern endovascular techniques.** *Stroke Vasc Neurol* 2016;1:93–100 CrossRef Medline
- Lescher S, Du Mesnil de Rochemont R, Berkefeld J. **Woven Endobridge (WEB) device for endovascular treatment of complex unruptured aneurysms: a single center experience.** *Neuroradiology* 2016;58:383–90 CrossRef Medline
- Fischer S, Vajda Z, Aguilar Perez M, et al. **Pipeline embolization device (PED) for neurovascular reconstruction: initial experience in the treatment of 101 intracranial aneurysms and dissections.** *Neuroradiology* 2012;54:369–82 CrossRef Medline
- Pierot L, Moret J, Barreau X, et al. **Safety and efficacy of aneurysm treatment with WEB in the cumulative population of three prospective, multicenter series.** *J Neurointerv Surg* 2018;10:553–56 CrossRef Medline
- Arthur AS, Molyneux A, Coon AL, et al; WEB-IT Study investigators. **The safety and effectiveness of the Woven EndoBridge (WEB) system for the treatment of wide-necked bifurcation aneurysms: final 12-month results of the pivotal WEB Intrasaccular Therapy (WEB-IT) study.** *J Neurointerv Surg* 2019 Apr 16. [Epub ahead of print] CrossRef Medline
- Feng X, Wang L, Guo E, et al. **Progressive occlusion and recanalization after endovascular treatment for 287 unruptured small aneurysms (<5 mm): a single-center 6-year experience.** *World Neurosurg* 2017;103:576–83 CrossRef Medline
- Mihalea C, Caroff J, Pagiola I, et al. **Safety and efficacy of the fifth generation Woven EndoBridge device: technical note.** *J Neurointerv Surg* 2019;0:1–5 CrossRef
- Pierot L, Biondi A, Narata AP, et al. **Should indications for WEB aneurysm treatment be enlarged? Report of a series of 20 patients with aneurysms in “atypical” locations for WEB treatment.** *J Neuroradiol* 2017;44:203–09 CrossRef Medline
- Kabbasch C, Goertz L, Siebert E, et al. **Treatment strategies for recurrent and residual aneurysms after Woven Endobridge implantation.** *J Neurointerv Surg* 2019;11:390–95 CrossRef Medline
- Hagen F, Maurer C, Berlis A. **Endovascular treatment of unruptured MCA bifurcation aneurysms regardless of aneurysm morphology: short- and long-term follow-up.** *AJNR Am J Neuroradiol* 2019;40:503–09 CrossRef Medline
- Behme D, Berlis A, Weber W, et al. **Woven EndoBridge intrasaccular flow disruptor for the treatment of ruptured and unruptured wide-neck cerebral aneurysms: report of 55 cases.** *AJNR Am J Neuroradiol* 2015;36:1501–06 CrossRef Medline

Sentinel Angiographic Signs of Cerebral Hyperperfusion after Angioplasty and Stenting of Intracranial Atherosclerotic Stenosis: A Technical Note

M. Ghuman, A.C.O. Tsang, J.M. Klostranec, and T. Krings



ABSTRACT

SUMMARY: Cerebral hyperperfusion syndrome is a serious complication of endovascular angioplasty and stent placement for long-standing intracranial stenosis, resulting in neurologic dysfunction, seizure, or reperfusion hemorrhage. Rigorous control of blood pressure is commonly used in the perioperative period to prevent cerebral hyperperfusion syndrome, but the optimal blood pressure is often arbitrary. We describe the angiographic features that reflect impaired cerebral autoregulation and microvascular transit abnormality, which may be used to gauge the optimal blood pressure parameters in the immediate postintervention period for prevention of cerebral hyperperfusion syndrome.

ABBREVIATIONS: BP = blood pressure; CHS = cerebral hyperperfusion syndrome; ICAS = intracranial atherosclerosis; ICH = intracranial hemorrhage

Cerebral hyperperfusion syndrome (CHS) is a well-described complication associated with cerebral revascularization after extracranial angioplasty and stent placement.¹ CHS following intracranial angioplasty is less well-studied but is estimated in observational studies to occur in 3.4% of patients with nearly 80% mortality when complicated by intracerebral hemorrhage (ICH).²⁻⁴ This likely contributed to the adverse outcomes in the intervention arm of the Stenting vs Aggressive Medical Management for Preventing Recurrent Stroke in Intracranial Stenosis (SAMMPRIS) trial.⁴⁻⁶

While the exact pathophysiology of CHS is still not fully understood, impaired cerebral autoregulation and cerebral hemodynamic alterations following revascularization are considered the major mechanisms involved.^{4,5} In patients with intracranial atherosclerosis (ICAS), CHS development is associated with poor control of postoperative blood pressure (BP) and impaired collateral circulation.⁴ For extracranial stenosis, other well-known risk

factors include baseline hypertension, carotid stenosis of $\geq 90\%$, and impaired cerebrovascular reserve.⁴⁻⁶ These factors coupled with maximal arteriolar dilation, compromised cerebral autoregulation, and systemic hypertension translate to an increased cerebral perfusion pressure and cerebral hyperperfusion.

Stringent systemic BP control is a widely used prophylactic strategy in the postrevascularization period and has been shown to reduce the incidence of CHS in high-risk individuals.^{7,8} Ideally, quantitative cerebral blood flow should be monitored to guide the hemodynamic management, but continuous and reliable means of measurement are lacking in routine clinical practice.^{4,5,8} This article illustrates the angiographic signs of hyperperfusion immediately after intracranial stent placement and angioplasty, and their utility in titrating individual BP targets in the postoperative period for the prevention of CHS. This method has been used in our center to select patients for aggressive BP control following intervention.

Techniques

We treat patients with symptomatic ICAS when they are refractory to aggressive medical treatment or if the ischemic symptom is secondary to critical hypoperfusion downstream of the ICAS stenosis instead of perforator occlusion or artery-to-artery embolism. Typically, predilation of the stenotic intracranial ICA or MCA segment is followed by delivery of a Wingspan stent system (Stryker, Kalamazoo, Michigan).⁹

Immediately after stent placement, a control angiogram is obtained at the baseline systemic BP. Particular attention is paid to the downstream vascular field for 2 sentinel signs suggestive of maximal arteriolar dilation and disrupted cerebral autoregulation

Received April 26, 2019; accepted after revision June 25.

From the Department of Medical Imaging (M.G.), Sunnybrook Health Sciences Centre, Toronto, Ontario, Canada; Division of Neurosurgery (A.C.O.T.), Department of Surgery, The University of Hong Kong, Hong Kong; and Department of Medical Imaging (A.C.O.T., J.M.K., T.K.), Toronto Western Hospital, Toronto, Ontario, Canada.

Mandeep Ghuman and Anderson Chun On Tsang made equal contributions to the article.

Please address correspondence to Anderson Chun On Tsang, MD, Room 701, Administrative Block, Department of Neurosurgery, Queen Mary Hospital, 102 Pokfulam Rd, Hong Kong; e-mail: acotsang@hku.hk

 Indicates article with supplemental on-line table.

 Indicates article with supplemental on-line photo.

<http://dx.doi.org/10.3174/ajnr.A6149>

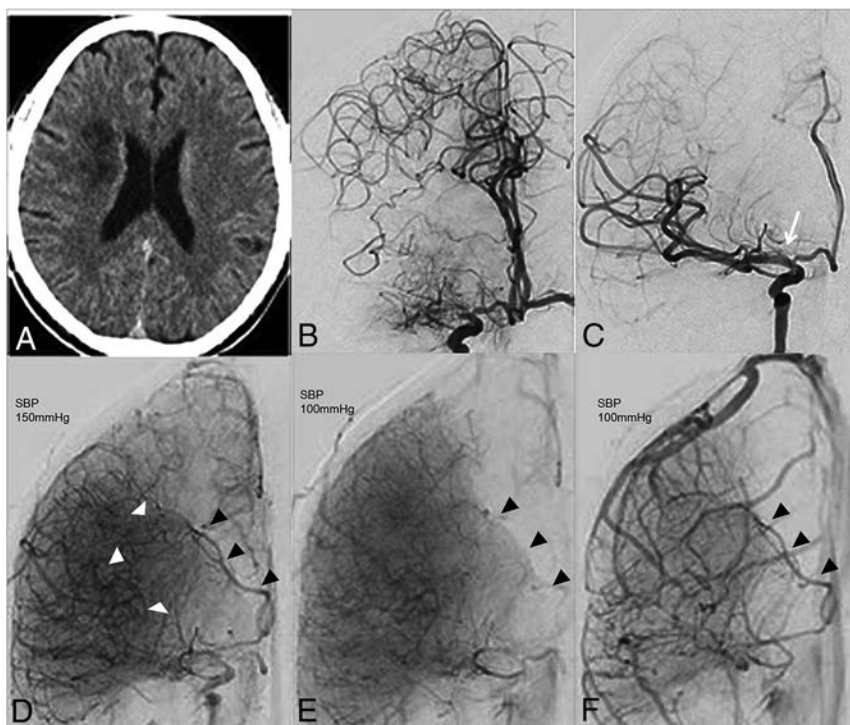


FIGURE. A 66-year-old female patient (patient 1) who presented with left-sided transient ischemic symptoms. *A*, Noncontrast CT of the brain shows hypodensity consistent with previous ischemic infarct in the right corona radiata in the cerebral internal watershed zone. CT angiography and CT perfusion (not shown) revealed high-grade stenosis of right mid-M1 segment of the MCA with corresponding large areas of perfusion mismatch suggestive of salvageable ischemia. *B* and *C*, Pre- and postangioplasty right ICA angiograms demonstrate restoration of the severely compromised lumen of the proximal M1 MCA (*white arrow*), following angioplasty and stent placement. Note the medial shift of the watershed zone after revascularization. *D*, Late arterial phase angiographic image immediately postangioplasty and stent placement at a baseline systolic blood pressure of 158 mm Hg demonstrates early opacification of a vein that drains into the deep venous system (*black arrows*) with prominent capillary blush in the central MCA territory (*white arrowheads*). *E* and *F*, Capillary and venous phase images obtained at a systolic blood pressure of 100 mm Hg depict resolution of early arteriovenous shunting and restoration of homogeneity of the capillary stain, with the filling of the index vein in the normal venous phase. SBP indicates systolic blood pressure.

and thus a risk for hyperperfusion: first, an early draining vein of the treated ischemic territory, defined as early contrast filling of a regular anatomic vein in the late arterial or capillary phase of the angiogram that drains the territory downstream of the treated vessel; second, a prominent capillary blush in the ischemic territory, secondary to abnormal luxurious perfusion of the treated territory in the arterial phase, which becomes denser in the capillary phase compared with the rest of the arterial territory and persists late into the venous phase (Figure and On-line Figure).

In patients with an early draining vein and capillary blush after revascularization, systemic hypotensive therapy is commenced in close collaboration with the neuroanesthesiologist. Control angiograms with the same contrast flow rate (pump injections) are repeated in 10-minute intervals at decreasing BP thresholds (20 mm Hg intervals below baseline) until disappearance of the sentinel signs of hyperperfusion are observed. This BP threshold is then maintained in the first 24 hours postintervention in the neurocritical care unit with the patient being kept intubated and sedated to prevent BP spikes and to better control BP during a 24-hour period. Contralateral angiograms are also obtained to assess the adequacy of perfusion and collateral status, given the

potential for ischemia due to the induced hypotensive state. After 24 hours, patients who exhibit the above sentinel signs of hyperperfusion are awakened and BP control is gradually relaxed while closely monitoring symptoms of CHS such as new or worsening headache and/or change in neurologic function. Patients developing these symptoms would receive a prolonged duration of hypotensive therapy.

Of 14 symptomatic patients with ICAS stenosis treated endovascularly from January 2016 to March 2019, four patients had an early draining vein and/or the capillary blush sign immediately after angioplasty at baseline BP (On-line Table). Individual BP thresholds were titrated using the above-mentioned technique, and continuous hypotensive therapy was maintained with intravenous labetalol infusion for 1–2 days. None of these patients had developed symptoms or complications of CHS at the last clinical follow up, and there were no procedure-related complications. None of the 10 patients in whom no sentinel signs of hyperperfusion were observed developed signs or symptoms of CHS.

DISCUSSION

The present study describes sentinel angiographic signs of cerebral hyperperfusion following revascularization of patients with ICAS stenosis and how these markers are used in our practice in the im-

mediate postangioplasty phase to identify a BP threshold to avoid CHS and its related complications.

We surmise that the occurrence of an early draining vein and capillary blush in the previously ischemic territory is due to the presence of maximally dilated arterioles and capillary bed secondary to long-standing cerebral ischemia. The localized reduction in vascular resistance and hence shortened arterial-venous transit time resulted in an abnormal early draining vein.

At present, there is no description of angiographic features in the literature for assessing the risk for CHS after ICAS revascularization therapy. Our preliminary and observational results suggest that these angiographic signs can serve as sentinel markers of CHS and can be used to optimize the hypotensive therapy BP threshold individually. Moreover, the average time for CHS complication development following extracranial carotid artery angioplasty and stent placement is 12 hours.⁵ Hence, we institute hypotensive therapy for 24 hours after revascularization in patients at risk of CHS. Intraprocedural and postprocedural transcranial Doppler sonography is another technique to monitor for

CHS after extracranial carotid endarterectomy and may be of use in the titration of hypotensive therapy.¹⁰

Angiographic blush and early filling vein were previously described in the setting of acute ischemic stroke following intra-arterial thrombolysis or endovascular thrombectomy and were associated with hemorrhagic transformation.¹¹⁻¹³ In acute ischemic infarct, these signs were thought to be due to hyperemia seen in the early stages of infarction, a so-called “luxury perfusion” state.¹¹⁻¹⁴ It is most conceivable that the early venous filling is secondary to rapid cerebrovascular transit and not true shunting. It is believed that blood flow is accelerated secondary to the marked vasodilation as a result of ischemia.¹² Increased local circulatory rates to maintain perfusion and the opening of precapillary arteriovenous shunts have also been proposed after the initial focal vasodilation effect following infarction.¹¹

Although our patients did not have acute infarction, the distal vessels did not immediately recover to their normal state of reactivity after revascularization but rather continued to be maximally dilated. This resulted in the described imaging findings that we believe may be related to an increased rate of postreperfusion hemorrhage. Future work would be needed to validate this approach in a larger patient cohort and to correlate with long-term clinical outcome.

CONCLUSIONS

In this small study, the angiographic signs of an early draining vein and capillary blush in patients with ICAS stenosis treated with endovascular revascularization were used as sentinel signs to detect cerebral hyperperfusion reflecting the underlying impaired cerebral vascular autoregulation. Progressive reduction of systemic arterial pressure to achieve reversal of these angiographic signs seems to be of clinical use to gauge postangioplasty hypotensive therapy for the prevention of catastrophic complications associated with cerebral hyperperfusion syndrome.

REFERENCES

1. Abou-Chebl A, Yadav JS, Reginelli JP, et al. **Intracranial hemorrhage and hyperperfusion syndrome following carotid artery stenting: risk factors, prevention, and treatment.** *J Am Coll Cardiol* 2004;43:1596–601 CrossRef Medline

2. Meyers PM, Phatouros CC, Higashida RT. **Hyperperfusion syndrome after intracranial angioplasty and stent placement.** *Stroke* 2006;37:2210–11 CrossRef Medline
3. Medel R, Crowley RW, Dumont AS. **Hyperperfusion syndrome following endovascular cerebral revascularization.** *Neurosurg Focus* 2009;26:E4 CrossRef Medline
4. Xu S, Wu P, Shi H, et al. **Hyperperfusion syndrome after stenting for intracranial artery stenosis.** *Cell Biochem Biophys* 2015;71:1537–42 CrossRef Medline
5. Huibers AE, Westerink J, de Vries EE, et al. **Editor’s choice: cerebral hyperperfusion syndrome after carotid artery stenting—a systematic review and meta-analysis.** *Eur J Vasc Endovasc Surg* 2018;56:322–33 CrossRef Medline
6. Chimowitz MI, Lynn MJ, Derdeyn CP, et al; SAMMPRIS Trial Investigators. **Stenting versus aggressive medical therapy for intracranial arterial stenosis.** *N Engl J Med* 2011;365:993–1003 CrossRef Medline
7. Abou-Chebl A, Reginelli J, Bajzer CT, et al. **Intensive treatment of hypertension decreases the risk of hyperperfusion and intracerebral hemorrhage following carotid artery stenting.** *Catheter Cardiovasc Interv* 2007;69:690–96 CrossRef Medline
8. Kim KH, Lee CH, Son YJ, et al. **Post-carotid endarterectomy cerebral hyperperfusion syndrome: is it preventable by strict blood pressure control?** *J Korean Neurosurg Soc* 2013;54:159–63 CrossRef Medline
9. Luo J, Wang T, Peng G, et al. **Endovascular treatment of intracranial atherosclerosis stenosis: current debates and future prospects.** *Front Neurol* 2018;9:666 CrossRef Medline
10. Ogasawara K, Inoue T, Kobayashi M, et al. **Cerebral hyperperfusion following carotid endarterectomy: diagnostic utility of intraoperative transcranial Doppler ultrasonography compared with single-photon emission computed tomography study.** *AJNR Am J Neuroradiol* 2005;26:252–57 Medline
11. Salehi Omran S, Boddu SR, Gusdon AM, et al. **Angiographic blush after mechanical thrombectomy is associated with hemorrhagic transformation of ischemic stroke.** *J Stroke Cerebrovasc Dis* 2018;27:3124–30 CrossRef Medline
12. Ohta H, Nakano S, Yokogami K, et al. **Appearance of early venous filling during intra-arterial reperfusion therapy for acute middle cerebral artery occlusion: a predictive sign for hemorrhagic complications.** *Stroke* 2004;35:893–98 CrossRef Medline
13. Fritzsche D, Reiss-Zimmermann M, Lobsien D, et al. **Arteriovenous shunts and capillary blush as an early sign of basal ganglia infarction after successful mechanical intra-arterial thrombectomy in ischaemic stroke.** *Eur Radiol* 2015;25:3060–65 CrossRef Medline
14. Taveras JM, Gilson JM, Davis DO, et al. **Angiography in cerebral infarction.** *Radiology* 1969;93:549–58 CrossRef Medline

Distal Transradial Access in the Anatomic Snuffbox for Diagnostic Cerebral Angiography

P. Patel, N. Majmundar, I. Bach, V. Dodson, F. Al-Mufti, L. Tomycz, and P. Khandelwal

ABSTRACT

SUMMARY: The aim of this study was to describe the feasibility, technique, and safety of distal transradial access in the anatomic snuffbox for diagnostic cerebral angiography. A retrospective review of diagnostic cerebral angiograms obtained during a 6-month period with distal transradial access was performed. Thirty-four successful procedures were performed via distal transradial access. There were 4 failed attempts. This single-center experience using distal transradial access suggests that this technique is safe and effective.

ABBREVIATIONS: dTRA = distal transradial access; TFA = transfemoral approach; TRA = transradial approach

While the transradial approach (TRA) has been used by cardiologists for coronary angiography since its first reported use in 1989, the TRA has been more recently adopted by neurointerventionalists.¹ At our institution, the transfemoral approach (TFA) was traditionally used for diagnostic cerebral angiograms until last year, when we started using the TRA for diagnostic cerebral angiograms. The benefits of the TRA include reduced access site complications, increased patient comfort, earlier ambulation, and decreased time for postprocedural monitoring. Thus, the TRA was adopted for routine use at our institution for diagnostic cerebral angiography, and the TFA is used when access through the radial artery is difficult. However, the TRA also has its limitations and complications, including radial artery spasm, thrombotic occlusion, hematoma, pseudoaneurysm, arteriovenous fistula, positioning difficulties, the depth of the radial artery in large arms, and compartment syndrome.²

Distal transradial access (dTRA) involves accessing the radial artery immediately above the scaphoid or trapezium bones via the anatomic snuffbox.³ dTRA limits many of the complications of the TRA. Cannulation and sheath placement of the radial artery through the anatomic snuffbox can be performed with the arm in a neutral position, thus foregoing total supination of the wrist and allowing the patient to place the forearm in a more

natural position. Studies of dTRA in interventional cardiology procedures have demonstrated technical and procedural success, markedly reduced access site complications, and decreased rates of radial artery occlusion.^{2,4}

MATERIALS AND METHODS

We performed a retrospective chart review from a prospectively maintained data base of all patients undergoing diagnostic cerebral angiography from October 2018 through March 2019. Two attending physicians and 1 neuroendovascular fellow performed dTRA for the study. All had received formal training either in their fellowship or during a dedicated dTRA training course. This approach was only used for diagnostic cerebral angiography and not for interventional procedures because interventional procedures require larger catheters. Patients who had CT angiography of the head and neck available were studied to assess any anatomic variation before undergoing diagnostic cerebral angiography. Patients were excluded from the study if the caliber of the radial artery was <2 mm, if there was a need for an extensive diagnostic study including the left vertebral artery or thyrocervical trunk, if the radial artery was occluded, if there was evidence of an aberrant subclavian artery or variation of the aortic arch, or due to patient preference. Procedures were performed with a local anesthetic with conscious sedation. Patient demographics, procedural complications, procedural time, and postprocedural care information were collected. Possible major complications included radial artery perforation, pseudoaneurysm formation, or hand ischemia. Possible minor complications included formation of a hematoma or pain at the puncture site. The retrospective study was approved by the Rutgers New Jersey Medical School Institutional Review Board.

Received May 5, 2019; accepted after revision July 1.

From the Departments of Neurosurgery (P.P., N.M., V.D., L.T., P.K.) and Neurology (I.B.), Rutgers New Jersey Medical School, Newark, New Jersey; and Department of Neurology and Neurosurgery (F.A.-M.), Westchester Medical Center, New York Medical College, Valhalla, New York.

Please address correspondence to Priyank Khandelwal, MD, Department of Neurosurgery, Rutgers New Jersey Medical School, 90 Bergen St, Suite 8100, Newark, NJ 07103; e-mail: pk544@njms.rutgers.edu

<http://dx.doi.org/10.3174/ajnr.A6178>



FIG 1. A 5F short vascular sheath in the distal radial artery at the anatomic snuffbox. The hand is secured in a slightly flexed and ulnar-deviated position.

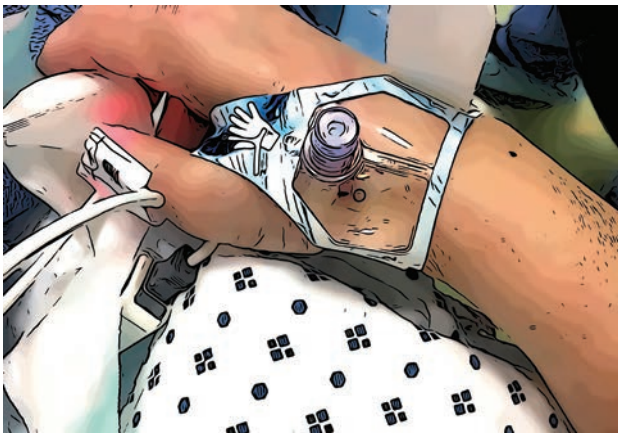


FIG 2. External compression device for closure of the arteriotomy site.

Procedural Technique

Right radial artery diameter was measured in the anatomic snuffbox using sonography in all patients. If the radial artery diameter was <2 mm, a different access site was chosen. The patient's right arm was kept in a midprone position and elevated to the level of the body. The hand was kept slightly flexed and deviated toward the ulna to straighten the radial artery and to bring it to a more superficial plane. Two-to-3 mL of lidocaine (1%) was injected in the skin of the anatomic snuffbox. By means of a 2-cm 21-ga micropuncture needle, the radial artery was punctured with sonographic guidance using a single-wall technique. A 5F Prelude Ideal (Merit Medical, South Jordan, Utah) or a 5F Glidesheath Slender (Terumo, Somerset, New Jersey) vascular sheath was introduced over the wire (Fig 1). Next, 2.5 mg of verapamil and 200 mcg of nitroglycerin were injected intra-arterially after hemodilution. A radial artery roadmap was then obtained. A 5F diagnostic Sim 2 catheter (Terumo) was introduced over a 0.035-inch angled glide wire. The Sim 2 catheter was formed either in the ascending or descending aorta. After we completed the diagnostic cerebral angiography, the sheath was removed. An external compression device was applied over the puncture site to achieve patient hemostasis. We used either a standard TR Band (Terumo)

Demographics

Mean Age (yr)	% Female	Mean No. of Vessels Catheterized	Mean Total Fluoroscopy Time (min)	Mean Fluoroscopy Time per Vessel (min)
54.5 ± 11.5	50%	3.8 ± 1.4	14.4 ± 6.5	3.9 ± 1.4

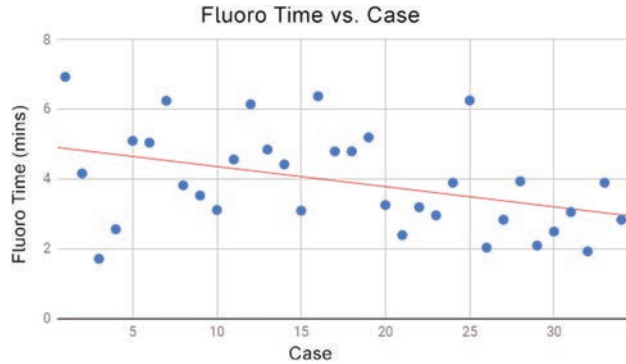


FIG 3. Fluoroscopy time (in minutes) per vessel decreases with increasing operator experience.

after removing the hard plastic from it or the PreludeSync Distal Band (Merit Medical), a dedicated distal radial closure band (Fig 2). Hand perfusion patency was confirmed with continuous pulse oximetry on the right thumb.

RESULTS

A total of 129 cerebral angiograms were obtained during the study period, of which 34 were successfully performed in 31 patients using dTRA. Patients ranged from 33 to 78 years of age (Table). Four patients had failed attempts of dTRA due to severe vasospasm of the radial artery in the proximal segment. In 2 of these patients, conventional TRA was performed after resolution of the spasm. The other 2 patients were converted to TFA. These failures occurred earlier in our transition to dTRA. An average of 3.8 vessels (range, 1-6 vessels) were catheterized per procedure. After successful access, we were able to catheterize all intended vessels. No major complications were recorded. The only reported minor complication was pain of the right wrist in 2 patients, which lasted 1 week. The 12 patients who had previously undergone the TFA reported that they preferred dTRA. Fluoroscopy time per vessel decreased with time, demonstrating that the learning curve associated with this novel procedure can be overcome with experience (Fig 3). While postprocedurally only 2 hours of nursing supervision was required, the average elapsed time between the end of the procedure and discharge was 3 hours 15 minutes due to a variety of patient-related factors and not due to extended monitoring requirements.

DISCUSSION

This retrospective review of dTRA cases found no major complications. While this finding is consistent with those in other studies investigating dTRA, studies that directly compare the complication rates of dTRA and TRA are scarce. It has, however, been demonstrated by Koutouzis et al⁴ that while the

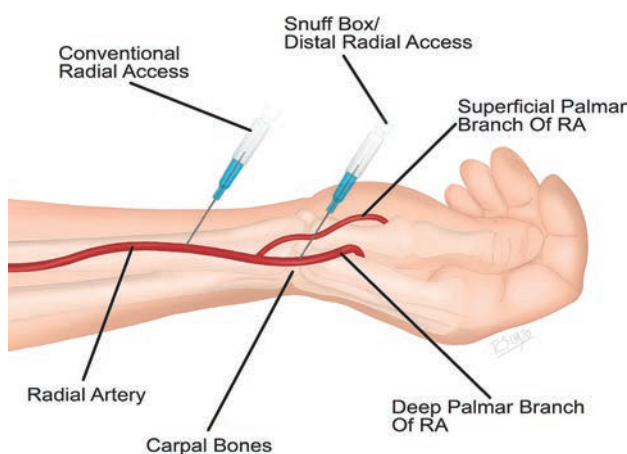


FIG 4. Distal radial artery course through the anatomic snuffbox. Note that the superficial palmar artery branches off before the radial artery enters the anatomic snuffbox.

complication rates of both techniques are similar, dTRA is associated with shorter manual hemostasis. They also, however, found an increased time to cannulation associated with dTRA, highlighting the importance of clinical experience in learning this novel technique.

Radial artery occlusion is a serious concern with the TRA, reported to occur in 1%–10% of coronary procedures.⁵ While radial artery occlusion is generally asymptomatic and rarely affects a patient's quality of life, it can limit future access in that arm. The distal part of the radial artery passes deep through the anatomical snuffbox and continues distally as the deep palmar arch of the hand. Most important, for dTRA, the radial artery is accessed distal to the origin of the superficial palmar branch of the radial artery (Fig 4). This is important in preventing postprocedural hand ischemia because the superficial palmar arch is not at risk of occlusion if the distal radial artery becomes occluded during or after interventional procedures.⁶ With dTRA, any occlusion of the radial artery is distal to the takeoff of the superficial palmar branch of the radial artery. Therefore, if dTRA results in occlusion of the distal radial artery, antegrade blood flow is preserved via the superficial palmar arch.

In our dTRA case series, 4 patients had to be converted to a different access site due to radial artery vasospasm. Overall, the dTRA failure rate has been reported to be around 5.8%.^{2,4,6,7} Spasm is a well-known complication of the TRA and dTRA, though the use of preprocedural sonography to evaluate radial artery diameter can mitigate its risk. The size of the radial artery can be up to 20% smaller in the snuffbox. In addition, the radial artery tends to be smaller in female patients.⁸ Injudicious selection of patients for dTRA may lead to higher conversion rates to different access sites and an increased number of multiple trials before successful cannulation. Sonographic assistance is therefore

highly recommended and is considered mandatory at our institution for any radial approach. Preprocedural radial artery evaluation can limit many access complications that can arise. Experience with the procedure is also important. Training for the dTRA is straightforward. Operators, including neuroendovascular fellows, attended a dedicated dTRA course with hands-on training with manikins and cadavers. As with most procedures, there is a learning curve associated with a new technique. Fluoroscopy time and the number of failed trials decreased with increased experience (Fig 3).

CONCLUSIONS

We demonstrated that the dTRA can provide an alternative approach to conventional radial or transfemoral approaches, with some potential advantages. In our experience, this technique is safe and effective and can potentially reduce procedural costs compared with the more conventional approaches, particularly the TFA. While we did not encounter any major complications, this approach needs to be studied in a larger patient dataset to elucidate its safety and feasibility.

Disclosures: Priyank Khandelwal—UNRELATED: Travel/Accommodations/Meeting Expenses Unrelated to Activities Listed: American College of Cardiology, Comments: \$2000 as a speaker.* Luke Tomycz—RELATED: Consulting Fee or Honorarium: Philips Neuro, Comments: honorarium of \$1500 and flight expenses to participate in meeting in Warsaw in June 2019.* *Money paid to individual.

REFERENCES

1. Snelling BM, Sur S, Shah SS, et al. **Transradial cerebral angiography: techniques and outcomes.** *J Neurointerv Surg* 2018;10:874–81 CrossRef Medline
2. Ziakas A, Koutouzis M, Didagelos M, et al. **Right arm distal transradial (snuffbox) access for coronary catheterization: initial experience.** *Hellenic J Cardiol* 2018 Oct 30. [Epub ahead of print] CrossRef Medline
3. Babunashvili A, Dundua D. **Recanalization and reuse of early occluded radial artery within 6 days after previous transradial diagnostic procedure.** *Cathet Cardiovasc Intervent* 2011;77:530–36 CrossRef Medline
4. Koutouzis M, Kontopodis E, Tassopoulos A, et al. **Distal versus traditional radial approach for coronary angiography.** *Cardiovasc Revasc Med* 2018 Oct 2. [Epub ahead of print] CrossRef Medline
5. Soydan E, Akin M. **Coronary angiography using the left distal radial approach - An alternative site to conventional radial coronary angiography.** *Anatol J Cardiol* 2018;19:243–48 CrossRef Medline
6. McCarthy D, Chen S, Brunet MC, et al. **Distal radial artery access in the anatomical snuffbox for neurointerventions: case report.** *World Neurosurg* 2019;122:355–59 CrossRef Medline
7. Valsecchi O, Vassileva A, Cereda AF, et al. **Early clinical experience with right and left distal transradial access in the anatomical snuffbox in 52 consecutive patients.** *J Invasive Cardiol* 2018;30:218–23
8. Kim Y, Ahn Y, Kim MC, et al. **Gender differences in the distal radial artery diameter for the snuffbox approach.** *Cardiol J* 2018;25:639–41 CrossRef Medline

Non-Contrast-Enhanced Carotid MRA: Clinical Evaluation of a Novel Ungated Radial Quiescent-Interval Slice-Selective MRA at 1.5T

S. Peters, M. Huhndorf, U. Jensen-Kondering, N. Larsen, I. Koktzoglou, R.R. Edelman, J. Graessner, M. Both, O. Jansen, and M. Salehi Ravesh



ABSTRACT

BACKGROUND AND PURPOSE: Non-contrast-enhanced MRA techniques have experienced a renaissance due to the known correlation between the use of gadolinium-based contrast agents and the development of nephrogenic systemic fibrosis and the deposition of gadolinium in some brain regions. The purpose of this study was to assess the diagnostic performance of ungated non-contrast-enhanced radial quiescent-interval slice-selective MRA of the extracranial supra-aortic arteries in comparison with conventional contrast-enhanced MRA in patients with clinical suspicion of carotid stenosis.

MATERIALS AND METHODS: In this prospective study, both MRA pulse sequences were performed in 31 consecutive patients (median age, 68.8 years; 19 men). For the evaluation, the cervical arterial system was divided into 35 segments (right and left side). Three blinded reviewers separately evaluated these segments. An ordinal scoring system was used to assess the image quality of arterial segments and the stenosis grading of carotid arteries.

RESULTS: Overall venous contamination in quiescent-interval slice-selective MRA was rated as “none” by all readers in 84.9% of cases and in 8.1% of cases in contrast-enhanced MRA ($P < .0001$). The visualization quality of arterial segments was considered good to excellent in 40.2% for the quiescent-interval slice-selective MRA and in 52.2% for the contrast-enhanced MRA ($P < .0001$). The diagnostic accuracy of ungated quiescent-interval slice-selective MRA concerning the stenosis grading showed a total sensitivity and specificity of 85.7% and 90.0%, respectively.

CONCLUSIONS: Ungated quiescent-interval slice-selective MRA can be used clinically as an alternative to contrast-enhanced MRA without a significantly different image quality or diagnostic accuracy for the detection of carotid stenosis at 1.5T.

ABBREVIATIONS: CE = contrast-enhanced; QISS = quiescent-interval slice-selective; RF = radiofrequency; CTA = computed tomography angiography; DSA = digital subtracted angiography; DUS = duplex ultrasound; ECG = electro-cardiogram; FLASH = fast low angle shot; FOCI = frequency offset corrected inversion; MRA = magnetic resonance angiography; NASCET = North American Symptomatic Carotid Endarterectomy Trial

Extracranial ICA stenosis is a common disease and a risk factor for an ischemic stroke.¹ Atherosclerosis is the main cause of ICA stenosis.^{2,3} Typical risk factors for atherosclerosis are hypertension, history of smoking, diabetes, obesity, and an elevated low-density cholesterol level.^{4,5} An ICA stenosis can be treated either conservatively, for example with risk-factor control and best medical therapy, or invasively (endarterectomy or stent and angioplasty).^{3,6}

The decision on the preferred method for the treatment of an ICA stenosis depends on several factors. Besides the existence of symptoms, the grade of the stenosis is an important factor.^{3,7} Therefore, determination of the stenosis grade is essential to assess the appropriate treatment.

Duplex sonography, CT angiography, and MR angiography are the non-minimally invasive imaging modalities to evaluate the ICA.⁸ The accuracy of a duplex ultrasound examination of the carotid arteries depends on the experience of the investigator, so a second imaging technique is required in most cases.

Received April 1, 2019; accepted after revision July 4.

From the Department of Radiology and Neuroradiology (S.P., M.H., U.J.-K., N.L., M.B., O.J., M.S.R.), University Medical Center Schleswig-Holstein, Kiel University, Kiel, Germany; Department of Radiology (I.K., R.R.E.), NorthShore University Health System, Evanston, Illinois; University of Chicago Pritzker School of Medicine (I.K.), Chicago, Illinois; Northwestern University Feinberg School of Medicine (R.R.E.), Chicago, Illinois; and Siemens Healthcare (J.G.), Hamburg, Germany.

This work was supported, in part, by the National Institute of Biomedical Imaging and Bioengineering of the National Institutes of Health under award number R01EB027475.

The content is solely the responsibility of the authors and does not necessarily represent the official views of the National Institutes of Health.

Please address correspondence to Mona Salehi Ravesh, MD, Department of Radiology and Neuroradiology, University Medical Center Schleswig-Holstein, Kiel University, Arnold Heller St 3, Bldg 41, 24105 Kiel, Germany; e-mail: Mona.Salehiravesh@uksh.de

Indicates open access to non-subscribers at www.ajnr.org

Indicates article with supplemental on-line appendix.

<http://dx.doi.org/10.3174/ajnr.A6171>

Table 1: Imaging parameters for ungated QISS and CE-MRA sequences

Parameter	Ungated QISS-MRA	CE-MRA
Imaging mode	2D	3D
FLASH TR/TE (ms)	15.0/4.7	3.09/1.2
QISS sequence TR (ms)	1100.8	–
Acquisition matrix (Px)	384 × 384	512 × 512
Acquisition pixel (mm ²)	0.5 × 0.5	0.6 × 0.6
In-plane interpolation	On	On
Slice thickness (mm)	2.0	1.0
No. of slices	128	80
Slice distance factor (%)	–33	20
No. of averages	1	1
Receiver bandwidth (Hz/Px)	303	540
Flip angle	30°	30°
Slice orientation	Tilted transversal to coronal (45° tilt)	Coronal
K-space trajectory	Radial	Cartesian
No. of radial projections	204	–
No. of shots per slice	3	–
Phase oversampling (%)	0	40
Filter	Distortion correction (2D); prescan normalizer	Distortion correction (3D); prescan normalizer
B ₀ shim mode	Heart	Tune-up
Asymmetric echo	Off	On
RF pulse type	Normal	Normal
Gradient mode	Fast	Fast
RF spoiler	On	On
iPAT modus (acceleration factor/No. of reference lines)	–	2/24
Partial Fourier (phase and slice)	–	6th/8th
Venous saturation slab thickness (mm)	100	–
Distance between venous saturation and imaging slab (mm)	10	–
TI (ms)	530	–
Acquisition time (min:sec)	7:03	0:20

Note:—iPAT indicates integrated parallel imaging technique; TI, time from in-plane and venous saturation to the acquisition of central *k*-space (*k_y* = 0); Px, pixel; –, sequence parameter is not available; TR, repetition time; TE, echo time; RF, radiofrequency; Hz, Hertz.

Additionally, extensive calcified plaques of the vessel wall impair accurate assessment of the grade of stenosis, which is difficult due to acoustic shadowing. Contrast-enhanced MRA (CE-MRA) using a gadolinium-based contrast agent is an often used minimally invasive method for grading an ICA stenosis. In patients with renal insufficiency, a gadolinium-based contrast agent should be used with caution.⁹ For these patients, the CE-CTA is not a suitable alternative due to the use of a potentially nephrotoxic iodine contrast medium. Furthermore, the deposition of a gadolinium-based contrast agent in the brain of patients even with good renal function is a subject of ongoing discussions and investigations into using non-CE MR imaging techniques.^{10,11} The above concerns about MR imaging contrast agent safety have spurred new developments in non-CE MR imaging techniques with reliable clinical results.^{12–14} 2D/3D-TOF-MRA is a commonly used non-contrast-enhanced approach for MRA of the extracranial carotid arteries. However, both techniques are time-consuming compared with CE-MRA. The image quality and anatomic coverage provided by TOF-MRA is inferior to that of CE-MRA.^{15,16} Moreover, TOF is more sensitive to respiratory and flow artifacts and has a tendency to overestimate stenoses.¹⁴

Recently, a new technique for non-CE-MRA of the arteries was presented. The so-called quiescent-interval slice-selective (QISS)¹⁷ MRA was first used to examine the peripheral arteries and showed promising results.¹³ Recent advances in the QISS technique facilitate non-CE-MRA of other vessels,¹⁸ in particular the extracranial carotid arteries at 3T.^{19,20} The aim of this study

was to test the feasibility of an ungated radial implementation of QISS-MRA at 1.5T and to assess its diagnostic performance for imaging the extracranial carotid arteries compared with the clinical standard technique of CE-MRA. For simplification, the ungated non-CE radial QISS-MRA is abbreviated as ungated QISS-MRA.

MATERIALS AND METHODS

Patients

Patients who were included in this prospective study had been consecutively referred to our center from May to September 2018 for clinically indicated extracranial MRA of the supra-aortic arteries. The medical history of all patients was reviewed to determine the reason for the clinically requested MR imaging examination of the carotid arteries. The study exclusion criteria were a history of carotid stent placement; renal insufficiency that precluded the administration of a gadolinium-based contrast agent, as indicated by an estimated glomerular filtration rate of <30 mL/min/1.73 m²; other contraindications for gadolinium-based contrast agent; and contraindications for MR imaging.

This study was performed according to the protocol (No. D 508/18) approved by the ethics committee at the university medical center in Kiel in accordance with the ethical standards established in the 1964 Declaration of Helsinki and its later amendments. Our patients gave written informed consent.

Table 2: Evaluation of ungated QISS-MRA versus CE-MRA based on the introduced 3-, 4-, and 5-point scale scoring systems in the section “Image Analysis” using the Wilcoxon signed rank test

Variable ^a	QISS-MRA ^b	CE-MRA ^b	P Value (QISS-MRA vs CE-MRA)
Image quality	2 (1–3)	2 (1–3)	.46
Venous contamination	0 (0–2)	1 (0–3)	<.0001
Global quality of arterial visualization	2 (1–4)	3 (1–4)	<.0001
Stenosis grading			
Right	1 (1–5)	1 (1–5)	.64
Left	1 (1–5)	1 (1–5)	.73
Segmental quality of arterial visualization			
Right side			
Origin of brachiocephalic artery (1)	3 (1–4)	3 (1–4)	<.0001
Origin of CCA (2)	3 (1–4)	3 (1–4)	<.0001
CCA (3)	3 (1–4)	4 (1–4)	.03
Bifurcation of CCA (4)	3 (1–4)	4 (1–4)	.002
ICA-C1 (cervical) (5)	3 (1–4)	4 (1–4)	.011
ECA (superior thyroid artery) (6)	1 (1–3)	2 (1–4)	.007
ECA (lingual artery) (7)	1 (1–3)	2 (1–4)	.0002
ECA (facial artery) (8)	2 (1–3)	2 (1–4)	.0003
ECA (occipital artery) (9)	2 (1–3)	2 (1–4)	.043
ECA (posterior auricular artery) (10)	1 (1–3)	1 (1–4)	.16
ECA (suprafacial temporal artery) (11)	2 (1–3)	2 (1–4)	.002
ECA (maxillary artery) (12)	2 (1–3)	2 (1–4)	.001
ECA (ascending pharyngeal artery) (13)	1 (1–3)	1 (1–4)	.39
Origin of subclavian artery (14)	2 (1–4)	3 (1–4)	<.0001
Origin of vertebral artery (V0) (15)	2 (1–4)	2 (1–4)	.19
V1 (preforaminal) (16)	3 (1–4)	3 (1–4)	.064
V2 (foraminal) (17)	3 (1–4)	3 (1–4)	.51
V3 (atlantic, extradural, or extraspinal) (18)	3 (1–4)	3 (1–4)	.097
Left side			
Origin of CCA (1)	2 (1–4)	3 (1–4)	.0003
CCA (2)	3 (2–4)	4 (1–4)	.01
Bifurcation of CCA (3)	3 (2–4)	4 (1–4)	.008
ICA-C1 (cervical) (4)	3 (1–4)	4 (1–4)	.02
ECA (superior thyroid artery) (5)	2 (1–3)	2 (1–3)	.02
ECA (lingual artery) (6)	1 (1–3)	2 (1–3)	.002
ECA (facial artery) (7)	2 (1–3)	2 (1–4)	<.0001
ECA (occipital artery) (8)	2 (1–4)	2 (1–3)	.34
ECA (posterior auricular artery) (9)	1 (1–3)	1 (1–3)	.98
ECA (suprafacial temporal artery) (10)	2 (1–3)	2 (1–4)	.0003
ECA (maxillary artery) (11)	2 (1–3)	2 (1–4)	.0008
ECA (ascending pharyngeal artery) (12)	1 (1–3)	1 (1–3)	.34
Origin of subclavian artery (13)	2 (1–4)	3 (1–4)	<.0001
Origin of vertebral artery (V0) (14)	2 (1–4)	2 (1–4)	.001
V1 (preforaminal) (15)	3 (1–4)	3 (1–4)	.002
V2 (foraminal) (16)	3 (1–4)	3 (1–4)	.88
V3 (atlantic, extradural, or extraspinal) (17)	3 (1–4)	3 (1–4)	.11

Note:—CCA indicates common carotid artery; ECA, external carotid artery.

^a Numbers in parentheses indicate the arterial segments on the right and left sides.

^b Data are median (minimum-maximum).

Demographic Data of Study Population

Pertinent demographic data (age, weight, body mass index at MR imaging, examination date, and sex) of the study population were recorded.

MRA Imaging

Imaging was performed on a 1.5T MR imaging system (MAGNETOM Aera, XQ gradients, Siemens Healthcare GmbH, Erlangen, Germany) with a maximum gradient strength of 45 mT/m and a maximum slew rate of 200 mT/m/ms. The MR imaging system was operated by the latest software (Syngo, version

E11C, Siemens Healthcare GmbH, Erlangen, Germany). The MR signal was received using a 20-element head coil, a 4-element neck coil, and a 32-element array coil placed on the upper chest (Siemens Healthcare GmbH, Erlangen, Germany).

The ungated QISS-MRA was performed in all subjects without electrocardiogram gating using a 2D single-shot radial FLASH readout. Flow compensation minimized blood flow artifacts.

Breath-hold first-pass CE-MRA was performed after ungated QISS-MRA in all subjects with the administration of 0.1 mmol/kg body weight of gadolinium-based contrast agent (Gadovist, 1.0 mmol/mL, gadobutrol; Bayer Pharma AG, Berlin, Germany) in an antecubital vein at a rate of 2 mL/s. After the CE-MRA examination, the CE-MRA images were subtracted from a native MRA image (mask), which was acquired with the same parameters before contrast agent injection. The imaging parameters for both MRA pulse sequences are summarized in Table 1.

Image Analysis

Three blinded board-certified radiologists (S.P., M.H., U.J.-K.) each with at least 7 years of experience in neuroradiology and MRA, evaluated all MR imaging datasets independently and during separate reading sessions. Source images and rotating MIP images were reviewed. The image analysis was performed on an Impax EE workstation (Agfa-Gevaert, Mortsel, Belgium).

The overall diagnostic quality of MR images was rated using a scoring scale of 1–3 with respect to the arterial signal and the presence of artifacts (including parallel acquisition reconstruction artifacts,

motion artifacts, and/or noise):

- Grade 1: poor image quality, inadequate arterial signal, and/or the presence of a significant amount of artifacts/noise impairing the diagnosis.
- Grade 2: good image quality sufficient for diagnosis, adequate arterial signal, and/or mild-to-moderate amounts of artifacts/noise not interfering with diagnosis.
- Grade 3: Excellent image quality for highly confident diagnosis, good arterial signal, and no-to-minimal amount of artifacts/noise.

Potentially contaminating venous signal was evaluated on a scale of 0–3:

Grade 0: none.

Grade 1: minimal, allowing interpretation with a high degree of diagnostic confidence.

Grade 2: moderate, exceeding acceptable degree and limiting diagnostic confidence.

Grade 3: severe, markedly limiting diagnostic confidence.

The cervical arteries were divided into 35 segments (Table 2). The continuity, visibility, and edge sharpness of these segments were assessed in all subjects. Visualization of each segment was assessed using a scoring scale of 1–4:

Grade 1: nondiagnostic, barely visible lumen rendering of the segment.

Grade 2: fair, ill-defined vessel borders with suboptimal image quality for diagnosis.

Grade 3: good, minor inhomogeneities not influencing vessel delineation.

Grade 4: excellent, sharply defined arterial borders with excellent image quality for highly confident diagnosis.

The image quality of an arterial segment was deemed diagnostic (grade ≥ 3) if the reader was confidently able to visualize the lumen of the structure of the carotid artery in its entirety.

The stenosis grading of the right and left internal carotid arteries was evaluated on the basis of the NASCET trial²² criteria using a scoring scale of 1–5:

Grade 1: 0% normal patency.

Grade 2: <50% stenosis.

Grade 3: 50%–69% stenosis.

Grade 4: $\geq 70\%$ stenosis.

Grade 5: 100% occlusion.

Table 3: Interobserver agreement for the evaluation of QISS-MRA and CE-MRA based on the introduced 3-, 4-, and 5-point scale scoring systems in the “Image Analysis” section^a

Variable	Interobserver Agreement
Image quality	0.54 (0.46–0.62)
Venous contamination	0.86 (0.80–0.91)
Quality of global arterial visualization	
Right side	0.72 (0.70–0.74)
Left side	0.71 (0.69–0.72)
ICA stenosis	
Right side	0.94 (0.89–0.97)
Left side	0.95 (0.90–0.98)

^a Data are agreement (95% CI).

Table 4: Comparison of ungated QISS-MRA and CE-MRA for assessment of the stenosis grade of the extracranial carotid arteries^a

	Right Side ^b			Left Side ^b		
	1	2	3	1	2	3
Sensitivity (%)	66.7 (9.4–99.2)	100.0 (15.8–100.0)	50.0 (1.3–98.7)	100 (39.8–100.0)	83.3 (35.9–99.6)	100.0 (39.8–100.0)
All readers		71.4 (29.0–96.3)			92.9 (66.1–99.8)	
Both sides			85.7 (63.7–97.0)			
Specificity (%)	89.3 (71.8–97.7)	86.2 (68.3–96.1)	89.7 (72.7–97.8)	92.6 (75.7–99.1)	88.0 (68.8–97.5)	96.3 (81.0–99.9)
All readers		87.7 (78.5–93.3)			92.4 (84.2–97.2)	
Both sides			90.0 (84.3–94.2)			

^a Data are sensitivity/specificity (95% CI).

^b Numbers 1, 2, and 3 refer to the readers.

When multiple stenotic lesions occurred in a particular arterial segment, the most stenotic lesion was considered the diagnostic grade and was used in the analysis.

Detailed information about the ungated QISS-MRA and the statistical analysis are available in the On-line Appendix.

RESULTS

Patient Characteristics

Our study population consisted of 31 patients (median age, 65.0 years [range, 27.7–91.4 years]; weight, 79.2 kg [range, 53.4–120.0 kg]; body mass index, 26.3 kg/m² [range, 17.4–37.9 kg/m²]), including 19 male and 12 female subjects. In 21 subjects, the MR imaging was requested due to the suspicion of an arterio-arterial embolic ischemic stroke or a suspected stroke, in 5 cases for exclusion of a severe carotid stenosis before a cardiac or aortic operation, and in 5 cases to exclude a dissection of the cervical arteries after a trauma or after previous dissections.

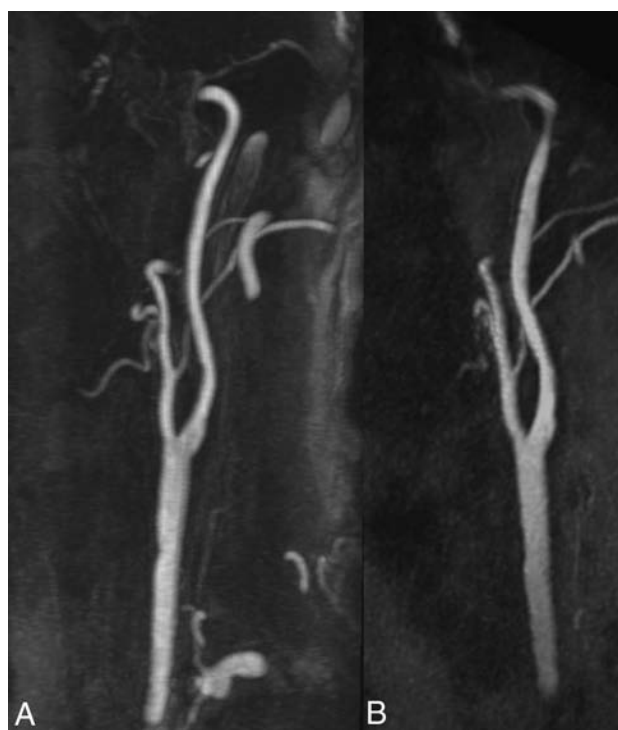


FIG 1. Example of an excellent imaging quality (grade 3) without any venous contamination (grade 0). Maximum intensity projection (MIP) with angulation to the left carotid bifurcation of the CE-MRA (A, slice thickness: 14.5 mm) and the ungated QISS-MRA (B, slice thickness: 14.1 mm) of a 76-year-old patient with clinically suspected infarction of the right hemisphere and suspected stenosis of the right cervical internal carotid artery by sonography (same patient as in Fig 5).

Image Quality

A total of 62 datasets (31 datasets per QISS-MRA and CE-MRA) were evaluated by 3 readers.

For QISS-MRA, reader 1 graded the overall image quality in 6.5% (2/31) as “poor,” in 38.7% (12/31) as “good,” and in 54.8% (17/31) of cases as “excellent”; reader 2 graded 16.1% (5/31) as poor, 71.0% (22/31) as good, and 12.9% (4/31) of cases as excellent; and reader 3 graded 3.2% (1/31) as poor, 93.5% (29/31) as good, and 3.2% (1/31) of cases as excellent.

For CE-MRA, reader 1 graded the overall image quality in 9.7% (3/31) as poor, in 48.4% (15/31) as good, and in 41.9% (13/31) of cases as excellent; reader 2 graded 16.1% (5/31) as poor, 38.7% (12/31) as good, and 45.2% (14/31) of cases as excellent; and reader 3 graded 9.7% (3/31) as poor, 80.6% (25/31) as good, and 9.7% (3/31) of cases as excellent.

Image quality was graded in 23.7% (22/93) of QISS-MRA cases and in 32.3% (27/93) of CE-MRA cases as excellent by all readers. There was no significant difference between the two MRA pulse sequences concerning the image quality (2 median [range, 1–3] versus 2 median [range, 1–3], $P = .46$, Table 2).

Venous Contamination

For QISS-MRA, reader 1 graded the contaminating venous signal in 77.4% (24/31) as “none,” in 19.4% (6/31) as “minimal,” and in 3.2% (1/31) as “moderate”; reader 2 graded 93.5% (29/31) as none, 3.2% (1/31) as minimal, and 3.2% (1/31) as moderate; and reader 3 graded 83.9% (26/31) as none and 16.1% (5/31) as minimal.

For CE-MRA, reader 1 graded the contaminating venous signal in 3.2% (1/31) as none, in 83.4% (26/31) as minimal, in 6.5% (2/31) as moderate, and in 6.5% (2/31) of cases as “severe”; reader 2 graded 12.9% (4/31) as none, 64.5% (20/31) as minimal, 16.1% (5/31) as moderate, and 6.5% (2/31) as severe; and reader 3 graded 9.7% (3/31) as none, 61.3% (19/31) as minimal, 19.4% (6/31) as moderate, and 9.7% (3/31) of cases as severe.

Overall venous contamination was rated as none by all readers in 84.9% (79/93) of QISS-MRA cases and in 8.1% (8/93) of CE-MRA cases (0 [range, 0–2] versus 1 [range, 0–3], $P < .0001$, Table 2).

Visualization of Arterial Segments

A total of 3255 arterial segments (35 arterial segments, 18 on the right side and 17 on the left side) for each patient per QISS-MRA and CE-MRA were evaluated once by all 3 readers.

For QISS-MRA, reader 1 scored 11.2% (121/1085) of segments with grade four, 30.9% (335/1085) with grade three, 29.8% with grade two (323/1085), and 28.2% (306/1085) with grade 1. Reader 2 identified 11.2% (121/1085) of segments with grade four, 30.6% (332/1085) with grade three, 45.0% with grade two (488/1085), and 13.3% (144/1085) with grade 1. Reader 3 graded 11.6% (126/1085) of segments with grade four, 25.2% (273/1085) with grade three, 30.5% with grade 2 (331/1085), and 32.7% (355/1085) with grade 1.

The overall median rating grades of all readers was 2 (range, 1–4).

For CE-MRA, reader 1 identified 22.3% (242/1085) of segments with grade four, 28.1% (305/1085) with grade three, 28.6%

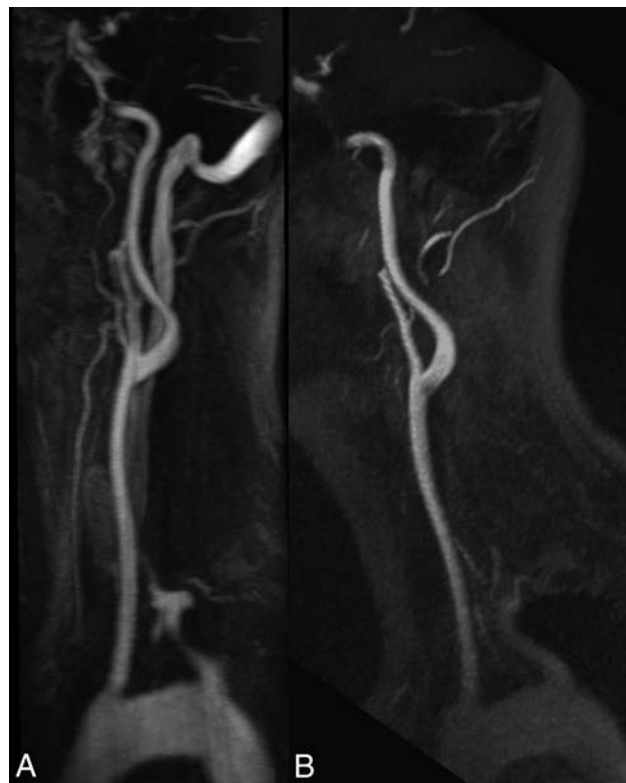


FIG 2. The effect of venous contamination on the image quality. MIP with angulation to the left carotid bifurcation of the CE-MRA (A, slice thickness: 13.9 mm) and the QISS-MRA (B, slice thickness: 13.5 mm) of a 33-year-old patient with suspected cerebral infarction. In the CE-MRA, the bolus is slightly missed, resulting in a severe venous contamination, whereas the QISS-MRA shows no venous signal.

with grade two (310/1085), and 21.0% (228/1085) with grade 1. Reader 2 scored 28.6% (310/1085) of segments with grade four, 36.3% (394/1085) with grade three, 29.0% with grade two (315/1085), and 6.1% (66/1085) with grade 1. Reader 3 graded 16.8% (182/1085) of segments with grade four, 24.6% (267/1085) with grade three, 28.8% with grade two (312/1085), and 29.9% (324/1085) with grade 1.

The overall median rating grades of readers 1 and 2 was 3 (range, 1–4), and of reader 3, it was 2 (range, 1–4).

The visualization quality of arterial segments was considered good to excellent (grade ≥ 3) in 40.2% (1308/3255) for the QISS-MRA and in 52.2% (1700/3255) for the CE-MRA (2 [range, 1–4] versus 3 [range, 1–4], $P < .0001$). A detailed comparison among all arterial segments between both MRA-pulse sequences is shown in Table 2.

There was a strong correlation between the QISS-MRA and CE-MRA sequence concerning the detection of carotid stenosis on both sides ($r = 0.92$, $P < .0001$) with an excellent interobserver agreement of 0.94 for both sides (Table 3).

The interobserver agreement for the QISS-MRA and CE-MRA concerning the image quality was 0.54, contamination with the venous enhancement was 0.86, and visualization of arterial segments on the left and right sides was 0.71.

Detailed information about the evaluation results are available in Tables 2, 3, and 4. Clinical examples are provided in Figs 1–5.

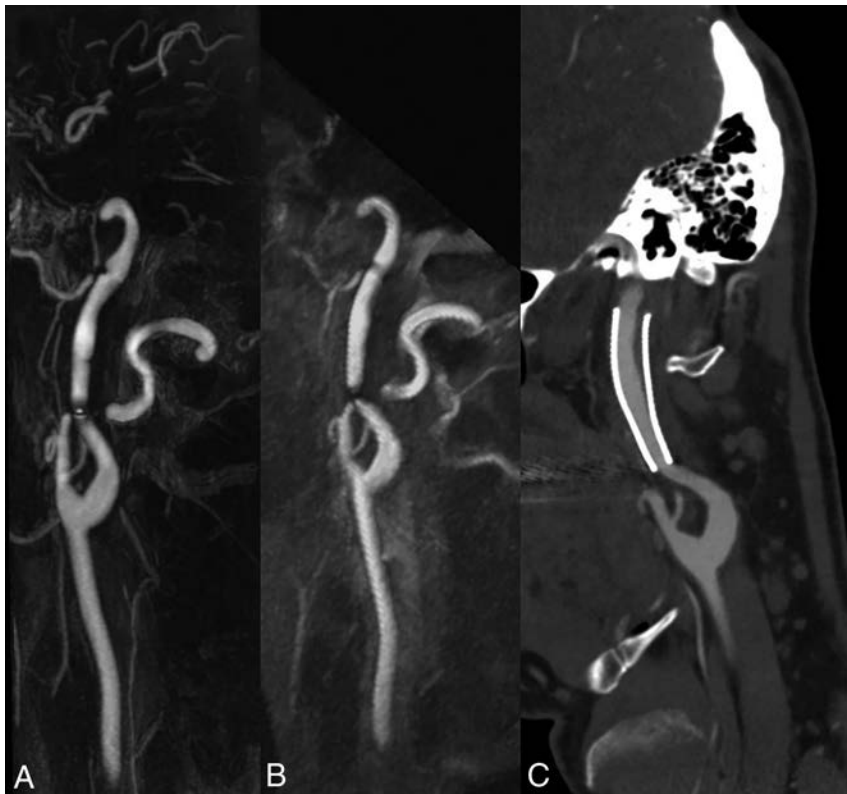


FIG 3. Influence of an implanted stent on the image quality. MIP of the CE-MRA (A, slice thickness: 13.0 mm) and the ungated QISS-MRA (B, slice thickness: 13.0 mm) with angulation to the left internal carotid artery of a 50-year-old patient who was stented 5 years ago due to a carotid artery dissection. The corresponding MIP of a CE-CTA (C, slice thickness: 1.4 mm) was obtained 2 years, and DSA, 1 year after stent placement. In both MRA techniques, there are just slight artifacts at the ends of the stent, and the lumen is well visualized. This patient was not included in this study.

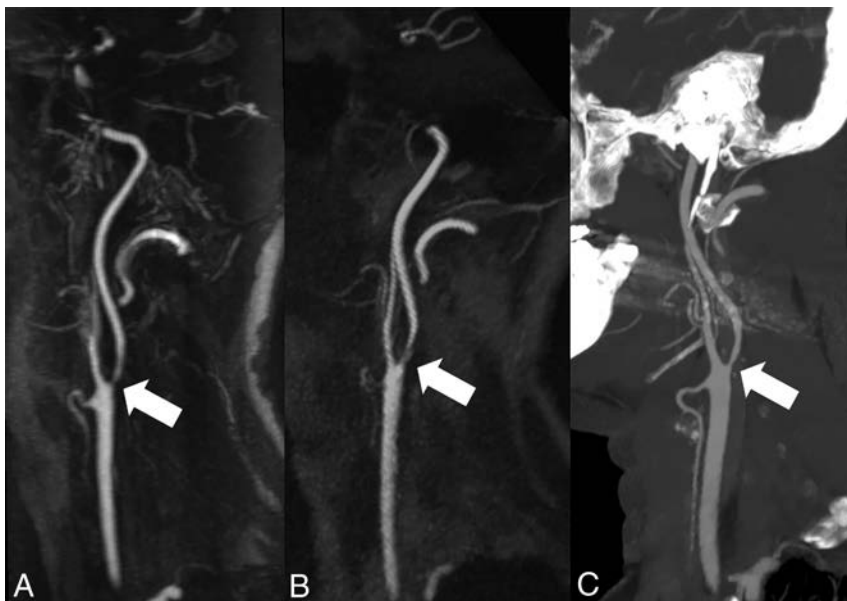


FIG 4. Visualization of internal carotid artery stenosis using CE-MRA and ungated QISS-MRA compared with CE-CTA. MIP with angulation to the left carotid bifurcation of the CE-MRA (A, slice thickness: 13.1 mm), QISS-MRA (B, slice thickness: 13.0 mm), and CE-CTA (C, slice thickness: 13.0 mm) of a 55-year-old patient with confirmed infarction of the left hemisphere and suspected stenosis of the left internal carotid artery using sonography. All 3 techniques verified the diagnosis of carotid stenosis (white arrows).

DISCUSSION

Due to the known correlation between the use of gadolinium-based contrast agents and the development of nephrogenic systemic fibrosis in patients with end-stage renal disease⁹ and also the deposition of gadolinium in some brain regions,¹⁰ non-CE-MRA techniques have experienced a renaissance in research and development and clinical application.^{12,23}

Since the introduction of non-CE QISS-MRA for evaluating the lower extremities in 2010,¹⁷ this technique and its variants have been used and clinically evaluated in a variety of vascular territories. In 2016, Koktzoğlu et al¹⁹ presented the feasibility of a cardiac-gated Cartesian QISS sequence variant for non-CE MRA of the extracranial carotid arteries in 5 healthy volunteers and 5 patients at 3T. The results of QISS were compared with those of 2D-TOF and CE-MRA, and they found that QISS provided better image quality than 2D TOF. Moreover, their initial results suggested that cardiac-gated QISS has potential utility as a non-CE alternative to CE-MRA. A recent retrospective study conducted at 3T has also demonstrated improved image quality of radial QISS with respect to 2D-TOF.²⁰

In our prospective study, for the first time the diagnostic accuracy of ungated QISS-MRA was compared with CE-MRA in patients with suspected extracranial carotid artery stenosis at 1.5T. The main findings of this study are the following: 1) QISS-MRA provides good visualization of the supra-aortic arteries without contrast agent and without cardiac gating; 2) on the basis of the performed segmental evaluation by 3 experienced radiologists, ungated QISS-MRA showed high sensitivity and specificity and a significant correlation with CE-MRA for the detection of carotid artery stenosis; and 3) ungated QISS-MRA is therefore a reliable technique for diagnosing carotid artery stenosis, in particular in patients with contraindications to gadolinium-based contrast agents.

QISS was originally described as a technique that leverages cardiac gating to optimally synchronize the quiescent intervals and readout to rapid systolic and slow diastolic arterial flow, respec-



FIG 5. Visualization of internal carotid artery stenosis using CE-MRA and un gated QISS-MRA compared with invasive DSA. MIP with angulation to the right carotid bifurcation of the CE-MRA (A, slice thickness: 14.0 mm) and the QISS-MRA (B, slice thickness: 13.5 mm) of a 76-year-old patient with clinically suspected infarction of the right hemisphere and suspected stenosis of the cervical internal carotid artery on the right by sonography (same patient as in Fig 1). The corresponding DSA of the right carotid bifurcation (C) before stent angioplasty confirmed the stenosis (white arrows).

tively. However, because most MR imaging protocols for imaging in the head and neck are performed without cardiac or peripheral pulse triggering, it is most convenient from a clinical perspective to image without cardiac synchronization.

In this study, an un gated implementation of the QISS-MRA pulse sequence leveraging radial k -space sampling was used. The consistent arterial contrast obtained using QISS-MRA in this study was predicated on 3 factors: first, the continuous flow found in the brain circulation; second, the combination of a rather lengthy interecho spacing (~ 15 ms) and a low flip angle (30°), which minimized saturation of arterial flow; and third, the use of radial k -space sampling to suppress arterial pulsation artifacts.

The duration of the measurement time using un gated QISS-MRA was fixed to 7 minutes and was independent of patient heart rate and electrocardiogram quality. While the measurement time of CE-MRA on paper is only 20 seconds, the total time to perform CE-MRA is, in fact, longer than that needed for un gated QISS-MRA. This is due to the extra time required for the preparation of patients for contrast agent injection, acquisition of a precontrast dataset as a mask for CE-MRA (~ 20 seconds), and also the post-processing of the CE dataset (~ 30 seconds), which is not needed for the un gated QISS-MRA procedure. The un gated QISS-MRA can be repeated as often as required without problems with venous contamination, for instance for the diagnosis of various arterial abnormalities in head and neck region and also for serial follow-up imaging. Images of the intracranial arteries can also be acquired in addition to the extracranial arteries when the slice-distance factor is set to a value of -20% to -25% instead of

-33% (used in this study), without any extension of measurement time.

As demonstrated in this study, the image quality of un gated QISS-MRA was comparable with that of CE-MRA and was graded as good or excellent in most cases. In some cases, the informative value of the un gated QISS-MRA was even higher due to less venous signal. There was almost no residual venous signal observed in the un gated QISS-MRA. This result indicates sufficient suppression of venous spins by the tracking venous inversion radiofrequency (RF) pulse, despite the use of tilted slices. Compared with axial slices, a possible drawback of tilted slices is the potential for insufficient inflow into vessel segments parallel to the slice direction. A slight reduction of arterial signal intensity was most visible in the aortic arch near the aortic branches. On the basis of our data, however, this reduction of image contrast does not affect the diagnostic accuracy for grading a carotid stenosis. In comparison, some CE-MRA examinations showed severe venous contamination due to mistiming of the

image acquisition with respect to the first pass of the contrast bolus.

The acquisition of a CE-MRA dataset of the extracranial carotid arteries was performed in breath-hold to reduce the image artifacts due to respiratory motion. To avoid possible image artifacts during swallowing, we asked the patients to stop swallowing (eg, for about 20 seconds). In contrast, un gated QISS-MRA could be performed in free breathing. The un gated QISS-MRA pulse sequence is largely insensitive to respiratory motion and arterial pulsation artifacts due to its use of radial k -space sampling, which oversamples the center of the k -space and dilutes the impact of respiratory and flow-related signal fluctuations that occur in a minority of radial views. These physiological signal fluctuations were suppressed with the use of radial k -space sampling so far that there was no residual stripping apparent with un gated QISS-MRA. Meanwhile, the use of an image-based navigator reduced the impact of intermittent swallowing motion artifacts.

All 35 extracranial segments with different shapes, lengths, and diameters were analyzed in our study to show even small, clinically irrelevant differences in imaging quality. The CE-MRA provided slightly better visualization of the small vessels. However, these differences did not influence patient management. Moreover, the clinically relevant findings were also reliably detected by the QISS-MRA.

The results of un gated QISS-MRA correlated strongly with those of CE-MRA concerning the stenosis grading. All 3 neuroradiologists graded the carotid artery stenosis in nearly 90% of seg-

ments (right side, 87.0%; left side, 93.5%) with the same score in ungated QISS-MRA and CE-MRA. In 5 cases, QISS-MRA overestimated the grade of stenosis, and in 1 case, QISS-MRA underestimated it. In 2 cases, the overestimation and in 1 case the underestimation of stenosis grading by QISS-MRA led to a change between grade 1 and 2 (0% to 50% stenosis) without therapeutic relevance.

In 2 cases, the overestimation of stenosis grading by QISS-MRA led to a change between grades 2 and 3. In one of these cases, the stenosis overestimation would have affected patient management due to the presence of symptoms for the right carotid stenosis, but in the other case, this overestimation did not affect the therapy management because the patient did not have the required symptoms on that side.

In the last case, the diagnosis based on the results of QISS-MRA led to an overestimation of the stenosis grade in the right carotid artery from 3 to 4. This change in grading did not affect the therapy management because therapy was indicated due to the symptoms on this side. Discrepancies in stenosis evaluation occur not only between QISS-MRA and CE-MRA but also among different modalities used for the assessment of ICA stenosis such as CE-CT, duplex ultrasound, and DSA. In cases with discrepant results or borderline stenosis grading, we perform conventional angiography prepared for optional stent implantation. Therefore, relevant stenosis will not be missed and will be treated. The diagnostic accuracy of ungated QISS-MRA showed a total sensitivity and specificity of 85.7% and 90.0%, respectively. Furthermore, the evaluation of the ICA stenosis grading revealed an excellent interobserver agreement. These data indicate that ungated QISS-MRA can be potentially used as an alternative to CE-MRA for grading carotid artery stenosis.

The number of patients in our single-center study was relatively small. Potentially, a higher number of patients in a multicenter study is necessary to confirm the diagnostic performance of ungated QISS-MRA across a wider range of clinical indications.

CONCLUSIONS

This study indicates that ungated QISS-MRA is a reliable angiographic technique with significant clinical potential for the visualization of the extracranial carotid arteries and detection of their stenosis at 1.5T. Ungated QISS-MRA is a feasible alternative for patients with contraindications to gadolinium-based contrast agents, especially in high-risk patients with severe renal insufficiency and an irregular cardiac rhythm. Furthermore, ungated QISS-MRA can avoid the timing-related difficulties of CE-MRA.

Disclosures: Sönke Peters—UNRELATED: Employment: University Hospital Schleswig-Holstein. Ulf Jensen-Kondering—UNRELATED: Grants/Grants Pending: grant from the Medical Faculty. Ioannis Koktzoglou—RELATED: Grant: National Institute of Biomedical Imaging and Bioengineering of the National Institutes of Health, Comments: Award No. R01EB027475*; UNRELATED: Other: Siemens, Comments: research support.* Robert R. Edelman—UNRELATED: Grants/Grants Pending: Siemens, Comments: Research support*; Royalties: Siemens, Comments: royalties relating to license for noncontrast MRI. Joachim Graessner—UNRELATED: Employment: Siemens. Olav Jansen—UNRELATED: Consultancy: Route 92 Medical; Payment for Lectures Including Service on Speakers Bureaus: Stryker, Microvention, Bayer Pharma AG. *Money paid to the institution.

REFERENCES

1. Flaherty ML, Kissela B, Khoury JC, et al. **Carotid artery stenosis as a cause of stroke.** *Neuroepidemiology* 2013;40:36–41 CrossRef Medline
2. Boehme AK, Esenwa C, Elkind MS. **Stroke risk factors, genetics, and prevention.** *Circ Res* 2017;120:472–95 CrossRef Medline
3. Padalino DJ, Deshaies EM. **Management of atherosclerotic carotid artery stenosis.** In: Rezzani R, ed. *Carotid Artery Disease: From Bench to Beside and Beyond*. Rijeka: InTech; 2014
4. Hobson RW 2nd, Mackey WC, Ascher E, et al; Society for Vascular Surgery. **Management of atherosclerotic carotid artery disease: clinical practice guidelines of the Society for Vascular Surgery.** *J Vasc Surg* 2008;48:480–86 CrossRef Medline
5. Fishbein MC, Fishbein GA. **Arteriosclerosis: facts and fancy.** *Cardio-vasc Pathol* 2015;24:335–42 CrossRef Medline
6. Wabnitz AM, Turan TN. **Symptomatic carotid artery stenosis: surgery, stenting, or medical therapy?** *Curr Treat Options Cardiovasc Med* 2017;19:62 CrossRef Medline
7. Abbott AL, Paraskevas KI, Kakkos SK, et al. **Systematic review of guidelines for the management of asymptomatic and symptomatic carotid stenosis.** *Stroke* 2015;46:3288–301 CrossRef Medline
8. Adla T, Adlova R. **Multimodality imaging of carotid stenosis.** *Int J Angiol* 2015;24:179–84 CrossRef Medline
9. Grobner T. **Gadolinium: a specific trigger for the development of nephrogenic fibrosing dermopathy and nephrogenic systemic fibrosis?** *Nephrol Dial Transplant* 2006;21:1104–08 CrossRef Medline
10. Kanda T, Ishii K, Kawaguchi H, et al. **High signal intensity in the dentate nucleus and globus pallidus on unenhanced T1-weighted MR images: relationship with increasing cumulative dose of a gadolinium-based contrast material.** *Radiology* 2014;270:834–41 CrossRef Medline
11. Costa AF, van der Pol CB, Maralani PJ, et al. **Gadolinium Deposition in the Brain: A Systematic Review of Existing Guidelines and Policy Statement Issued by the Canadian Association of Radiologists.** *Can Assoc Radiol J* 2018;69:373–82 CrossRef Medline
12. Kramer H, Runge VM, Morelli JN, et al. **Magnetic resonance angiography of the carotid arteries: comparison of unenhanced and contrast enhanced techniques.** *Eur Radiol* 2011;21:1667–76 CrossRef Medline
13. Amin P, Collins JD, Koktzoglou I, et al. **Evaluating peripheral arterial disease with unenhanced quiescent-interval single-shot MR angiography at 3 T.** *AJR Am J Roentgenol* 2014;202:886–93 CrossRef Medline
14. Weber J, Veith P, Jung B, et al. **MR angiography at 3 Tesla to assess proximal internal carotid artery stenoses: contrast-enhanced or 3D time-of-flight MR angiography?** *Clin Neuroradiol* 2015;25:414–18 CrossRef Medline
15. Yucel EK, Anderson CM, Edelman RR, et al. **AHA scientific statement: magnetic resonance angiography—update on applications for extracranial arteries.** *Circulation* 1999;100:2284–301 CrossRef Medline
16. Huston J 3rd, Fain SB, Riederer SJ, et al. **Carotid arteries: maximizing arterial to venous contrast in fluoroscopically triggered contrast-enhanced MR angiography with elliptical centric view ordering.** *Radiology* 1999;211:265–73 CrossRef Medline
17. Edelman RR, Sheehan JJ, Dunkle E, et al. **Quiescent-interval single-shot unenhanced magnetic resonance angiography of peripheral vascular disease: technical considerations and clinical feasibility.** *Magn Reson Med* 2010;63:951–58 CrossRef Medline
18. Edelman RR, Carr M, Koktzoglou I. **Advances in non-contrast quiescent-interval slice-selective (QISS) magnetic resonance angiography.** *Clin Radiol* 2019;74:29–36 CrossRef Medline
19. Koktzoglou I, Murphy IG, Giri S, et al. **Quiescent interval low angle shot magnetic resonance angiography of the extracranial carotid arteries.** *Magn Reson Med* 2016;75:20727–27 CrossRef Medline

20. Koktzoglou I, Aherne EA, Walker MT, et al. **Ungated nonenhanced radial quiescent interval slice-selective (QISS) magnetic resonance angiography of the neck: evaluation of image quality.** *J Magn Reson Imaging* 2019 May 11. [Epub ahead of print] CrossRef Medline
21. ACR Committee on Drugs and Contrast Media. *ACR Manual on Contrast Media*. Version 10.3, 2018: https://www.acr.org/-/media/ACR/Files/Clinical-Resources/Contrast_Media.pdf; 2018. Accessed March 10, 2019
22. **North American Symptomatic Carotid Endarterectomy Trial: methods, patient characteristics, and progress.** *Stroke* 1991;22: 711–20 CrossRef Medline
23. Koktzoglou I, Walker MT, Meyer JR, et al. **Nonenhanced hybridized arterial spin labeled magnetic resonance angiography of the extracranial carotid arteries using a fast low angle shot readout at 3 Tesla.** *J Cardiovasc Magn Reson* 2016;18:18 CrossRef Medline

Carotid Plaque CTA Analysis in Symptomatic Subjects with Bilateral Intraplaque Hemorrhage: A Preliminary Analysis

L. Saba, G. Lanzino, P. Lucatelli, F. Lavra, R. Sanfilippo, R. Montisci, J.S. Suri, and C. Yuan

ABSTRACT

BACKGROUND AND PURPOSE: The presence of IPH is considered the most dangerous feature because it is significantly associated with clinical ipsilateral cerebrovascular events. Our aim was to explore the characterization of plaque with CT in symptomatic subjects with bilateral intraplaque hemorrhage.

MATERIALS AND METHODS: Three-hundred-forty-three consecutive patients with recent anterior circulation ischemic events (<2 weeks) and CT of the carotid arteries (performed within 14 days of the cerebrovascular event) evaluated between June 2012 and September 2017 were analyzed for plaque volume composition to identify all subjects with bilateral intraplaque hemorrhage. Plaque volume was semiautomatically measured, and tissue components were classified according to the attenuation values such as the following: calcified (for values of ≥ 130 HU), mixed (for values of ≥ 60 and < 130 HU), lipid (for values of ≥ 25 and < 60 HU), and intraplaque hemorrhage (for values of < 25 HU). Twenty-one subjects (15 men; mean age, 70 ± 11 years; range, 44–87 years) had bilateral intraplaque hemorrhage and were included in the analysis.

RESULTS: Volume measurement revealed significantly larger plaques on the symptomatic side compared with the asymptomatic one (mean, 28 ± 9 versus 22 ± 8 mm, $P = .007$). Intraplaque hemorrhage volume and percentage were also significantly higher in the plaque ipsilateral to the cerebrovascular event ($P < .001$ and $< .001$, respectively). The volume of other plaque components did not show a statically significant association except for lipid and lipid + intraplaque hemorrhage percentages (23% versus 18% and 11% versus 15%), which were significantly different between the symptomatic and the asymptomatic sides (.016 and .011, respectively). The intraplaque hemorrhage/lipid ratio was higher on the symptomatic side (0.596 versus 0.171, $P = .001$).

CONCLUSIONS: In patients with bilateral intraplaque hemorrhage and recent ischemic symptoms, the plaque ipsilateral to the symptomatic side has significantly larger volume and a higher percentage of intraplaque hemorrhage compared with the contralateral, asymptomatic side.

ABBREVIATIONS: IPH = intraplaque hemorrhage; ROC = receiver operating characteristic

Recent studies of cervical carotid stenosis have shown that the degree of stenosis alone should not be considered the most important parameter to predict the risk of plaque rupture; in-

stead, plaque composition should also be considered in making therapeutic decisions.^{1,2}

Plaque features associated with an increased risk of plaque rupture include the following: intraplaque hemorrhage (IPH), thin or ruptured fibrous cap, the presence and size of the lipid-rich necrotic core, and active plaque inflammation.^{2–5} The presence of IPH is considered the most dangerous feature because it is significantly associated with clinical ipsilateral cerebrovascular events.^{6,7} Most interesting, only a portion of patients with IPH develop clinical cerebrovascular events. Therefore, it is possible that a plaque with IPH associated with ischemic events could have different characteristics compared with a plaque with IPH but no ischemic correlates.⁸ Indeed, a recent study showed that in patients with recent symptoms and bilateral IPH evaluated with MR imaging, the symptomatic side had stronger T1-weighted signals,

Received January 30, 2019; accepted after revision June 28.

From the Department of Radiology (L.S., F.L., R.S., R.M.), Azienda Ospedaliero Universitaria di Cagliari, Monserrato (Cagliari), Italy; Department of Neurologic Surgery (G.L.), Mayo Clinic, Rochester, Minnesota; Department of Radiological, Oncological and Anatomopathological Sciences-Radiology (P.L.), Sapienza University of Rome, Rome, Italy; Diagnostic and Monitoring Division (J.S.S.), Atheropoint, Roseville, California; Department of Electrical Engineering (J.S.S.), University of Idaho, Moscow, Idaho; Center for Biomedical Imaging Research (C.Y.), Department of Biomedical Engineering, Tsinghua University School of Medicine, Beijing, China; and Department of Radiology (C.Y.), University of Washington, Seattle, Washington.

Please address correspondence to Luca Saba, MD, Department of Radiology, Azienda Ospedaliero Universitaria di Cagliari, Polo di Monserrato s.s. 554 Monserrato (Cagliari) 09045, Italy; e-mail: lucasaba@tiscali.it; @lucasabaITA

<http://dx.doi.org/10.3174/ajnr.A6160>

larger necrotic cores, and longer plaques than the asymptomatic side.⁹

MR imaging is currently considered the criterion standard for visualization of IPH.¹⁰ However, recent investigations have suggested that CT can be useful for the detection and quantification of IPH as well.^{11,12} Unlike MR imaging, CT is routinely used in the urgent/emergent evaluation of patients with acute ischemic events, is widely available 24/7, and is more convenient for patients, especially the elderly with acute cerebrovascular syndromes. In this study, we explored plaque characterization in symptomatic subjects with bilateral IPH using CT, and we also aimed to identify plaque composition differences between symptomatic and asymptomatic carotid arteries.

MATERIALS AND METHODS

Study Design and Patient Population

The institutional review board (Azienda Ospedaliero Universitaria di Cagliari) approved this study, and patient consent was waived because of the retrospective nature. Every patient with recent cerebrovascular ischemic events and concomitant CT of the carotid arteries (acquired within 14 days after the cerebrovascular event) was included in this retrospective study. Inclusion criteria were the following:

- 1) Older than 18 years of age.
- 2) Anterior circulation cerebrovascular ischemic events (ischemic stroke, transient ischemic attack, or amaurosis fugax) within the past 2 weeks before the CT of the carotid arteries. To avoid inclusion of subjects with cerebrovascular symptoms due to noncarotid atherosclerotic disease, we classified patients according to the neurologic assessment using the Trial of ORG 10172 in Acute Stroke Treatment (TOAST) criteria.¹³ Individuals with other potential causes of cerebrovascular events such as silent or paroxysmal atrial fibrillation, valvular heart disease, and ventricular endocardial thrombi were excluded.
- 3) The presence of bilateral carotid plaque (focal thickness of ≥ 1.5 mm in the right and left carotid arteries).

By applying these criteria, we screened a total of 343 subjects (289 men, 54 women; mean age, 72 years; age range, 39–86 years) investigated between June 2012 and September 2017 for bilateral IPH. Patient demographics and clinical characteristics were collected by the treating physicians. The degree of stenosis was quantified according to the NASCET criteria.¹⁴

Of the 343 subjects included, 12 (3.49%) had poor image quality. Twenty-one of the 331 remaining patients (6.34%) were identified as having bilateral carotid IPH and were the subject of the present study (Fig 1). Plaque was defined according to the Mannheim consensus¹⁵ as a carotid wall thickness of >1500 μm .

CTA Technique

In all patients, CT of the carotid arteries was performed with a 16–detector row CT system (Brilliance; Philips Healthcare, Best, the Netherlands) according to a standardized protocol. The coverage was from the aortic arch to the carotid siphon with a caudocranial direction, and examinations were performed before and after administration of contrast material. An angiographic

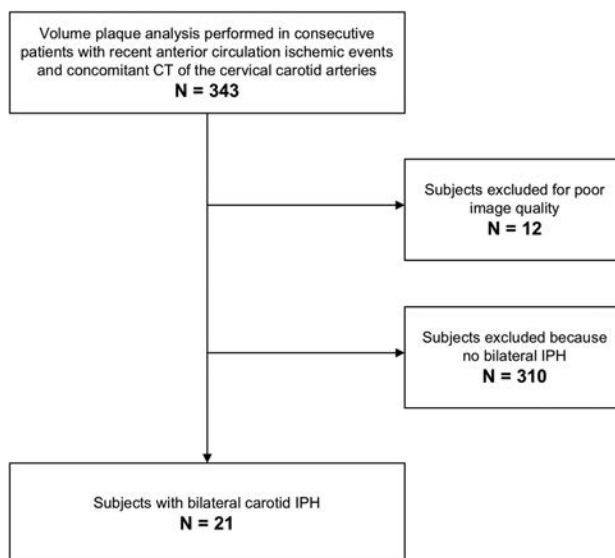


FIG 1. Flow chart.

phase was obtained with the administration of 60–80 mL of pre-warmed contrast medium (iopromide, Ultravist 370; Bayer HealthCare, Berlin, Germany) injected at a flow rate of 4 mL/s. CT technical parameters included the following: slice thickness, 0.6 mm; interval, 0.3 mm; matrix size, 512×512 ; FOV, 14–19 cm. The C-filter algorithm of reconstruction was applied.

IPH and Plaque Analysis Quantification

The volume analysis^{16,17} was performed by 2 experienced radiologists (L.S. and P.L. with 11 and 8 years of experience, respectively, in CT of the supra-aortic vessels) unaware of the patient's symptomatic side, using as window/level settings $W = 850$ and $L = 300$,¹⁸ with a dedicated software (VascuCAP; Elucid Bioimaging, Wenham, Massachusetts) to semiautomatically quantify the volume of the subcomponents.¹⁹ The inner and outer boundaries of the plaque were automatically identified by the software, but each volume was checked manually by the radiologists to avoid mistakes in the segmentations. Special care was used to exclude the presence of thrombus attached to the carotid artery plaque, which was defined according to Eesa et al²⁰ as “an eccentric pedunculated filling defect projecting into the lumen of the vessel.” For the plaque component analysis, the postcontrast scans were considered.

Attenuation values of all voxels within a plaque were measured, and Hounsfield units of each voxel were assumed to represent specific tissue using the thresholds defined by Saba et al¹¹ as calcified (for values of ≥ 130 HU), mixed (for values of ≥ 60 and <130 HU), lipid (for values of ≥ 25 and <60 HU), and IPH (for values of <25 HU) (Fig 2).^{11,17} We also considered a fifth class (attenuation of <60 HU) by considering the fatty component. The percentages of all components were calculated as well as the ratio between IPH/fatty class (with values between 0, if no IPH was present, and 1 if the entire fatty plaque component was due to IPH).

The identification of IPH was the key point of the analysis and was based on the attenuation values of each voxel into the carotid plaque.

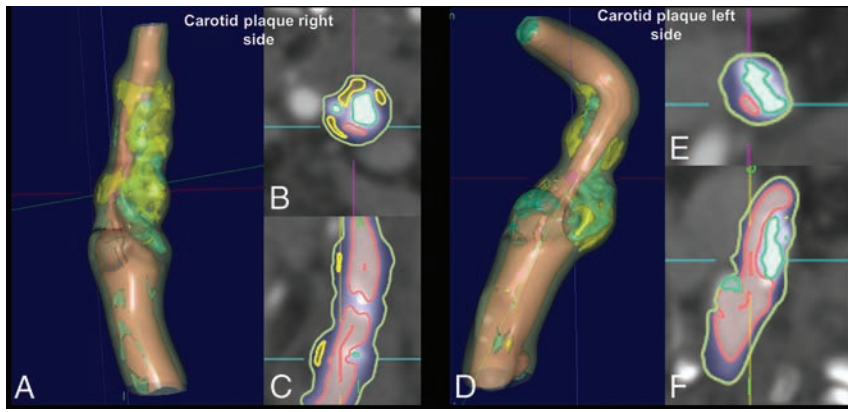


FIG 2. Example of semiautomatic segmentation of the carotid artery plaque of a 63-year-old subject. Both right (A–C) and left (D–F) carotid arteries are shown, and the red lines in the axial (B and E) and coronal planes (C and F) show the IPH components.

Table 1: Clinical characteristics of the 21 subjects with bilateral IPH

	Mean or No. (%)
Age (yr)	70 ± 11
Male sex	15 (71.4%)
Symptomatic side (right)	9 (42.8%)
Smoking	11 (52.4%)
Hypertension	14 (67%)
Hyperlipidemia	13 (61.9%)
Diabetes mellitus	8 (38%)
History of CHD	9 (42.8%)
Family history of CVD	9 (42.8%)

Note:—CHD indicates coronary heart disease; CVD, cardiovascular disease.

Table 2: Wilcoxon analysis^a

	Ipsilateral	Contralateral	P Value
Total plaque Volume (mm ³) ^b	788 (548–941)	689 (551–1189)	.543
IPH	65 (36–161)	15 (12–46)	.001
Fatty	154 (80–279)	141 (91–205)	.375
Lipid	86 (44–115)	103 (62–157)	.095
Mixed	460 (352–555)	424 (313–713)	.339
Calcium	118 (66–206)	119 (99–261)	.182
Percentage			
IPH	15% (6%–19%)	3% (2%–5%)	.001
Fatty	23% (18%–30%)	18% (14%–21%)	.011
Lipid	11% (7%–13%)	15% (10%–16%)	.016
Mixed	57% (52%–63%)	61% (56%–65%)	.312
Calcium	17% (12%–22%)	18% (15%–26%)	.498
IPH/fatty ratio	0.596 (0.344–0.754)	0.171 (0.126–0.1991)	.001

^aWilcoxon Analysis between carotid plaque components and subcomponents between symptomatic and asymptomatic side. Data are expressed in cubic mm.

^bVoxel size is 0.5 mm isotropic.

As explained previously, a semiautomated software was used to identify the tissue components, and the inclusion criteria for the study necessitated the presence of IPH on both sides (therefore, voxels of <25 HU of attenuation). Therefore, to avoid a bias related to the presence of a minimal amount of voxels of < 25 HU (such as the presence of a single voxel with a value < 25 HU), which can be due to simple statistical variability of the tissues, we considered that at least 1% of the voxels of the plaque, should have an attenuation of < 25 HU to serve as a cutoff for the presence of IPH within the plaque.

Bland-Altman plot analysis was performed to calculate the

interobserver agreement in the IPH, fatty, lipid, mixed, and calcified volume calculations.

Statistical Analysis

The normality of each continuous variable group was tested using the Kolmogorov-Smirnov Z-test. Continuous data were described as mean ± SD, and binary variables were summarized as count (percentage). All subjects had bilateral carotid IPH and unilateral ischemic symptoms, so plaques were grouped by whether they were ipsilateral or contralateral to the ischemic symptoms. Because the normality assumption was rejected, differences between

ipsilateral and contralateral IPH + plaques were assessed with the Wilcoxon test for continuous variables. The Pearson ρ correlation analysis was performed to assess the correlation between the degree of stenosis and the plaque volume in symptomatic and asymptomatic IPH. Comparison of the receiver operating characteristic (ROC) area under the curve was performed to test the strength and difference between parameters of IPH ipsilateral and contralateral to the symptoms. A *P* value < .05 indicated statistical significance, and all correlation values were calculated using a 2-tailed significance level. R statistical and computing software (www.r-project.org) was used for statistical analyses.

RESULTS

General Results

Of the 343 patients screened, 21 subjects had bilateral IPH and were included in the analysis. Clinical characteristics of these patients are summarized in Table 1.

The mean time interval between CT and the cerebrovascular event was 4 days (range, 1–12 days). Two of the 21 patients included in this study were also included in a previous publication on a different topic.¹¹

Plaque Morphology

The plaque was significantly longer on the symptomatic side compared with the asymptomatic one (28 ± 9 versus 22 ± 8 mm, *P* = .007). There were no statistically significant differences in the maximum wall thickness (5.6 ± 2.1 versus 5.3 ± 1.9 mm, *P* = .093).

Wilcoxon Analysis

The analysis of IPH as well as plaque characteristics ipsilateral and contralateral to the ischemic events is summarized in Table 2. There was a statistically significant difference in IPH volume and IPH percentage between the 2 sides (*P* values < .001 and < .001, respectively). The volume of other components and percentages did not show a statistically significant difference, except for the lipid and fatty component percentages, which were significantly different between the symptomatic and the asymptomatic sides (respectively, greater in asymptomatic than in symptomatic subjects with *P* values of .016 and .011) (Fig 3). Finally, the IPH/fatty

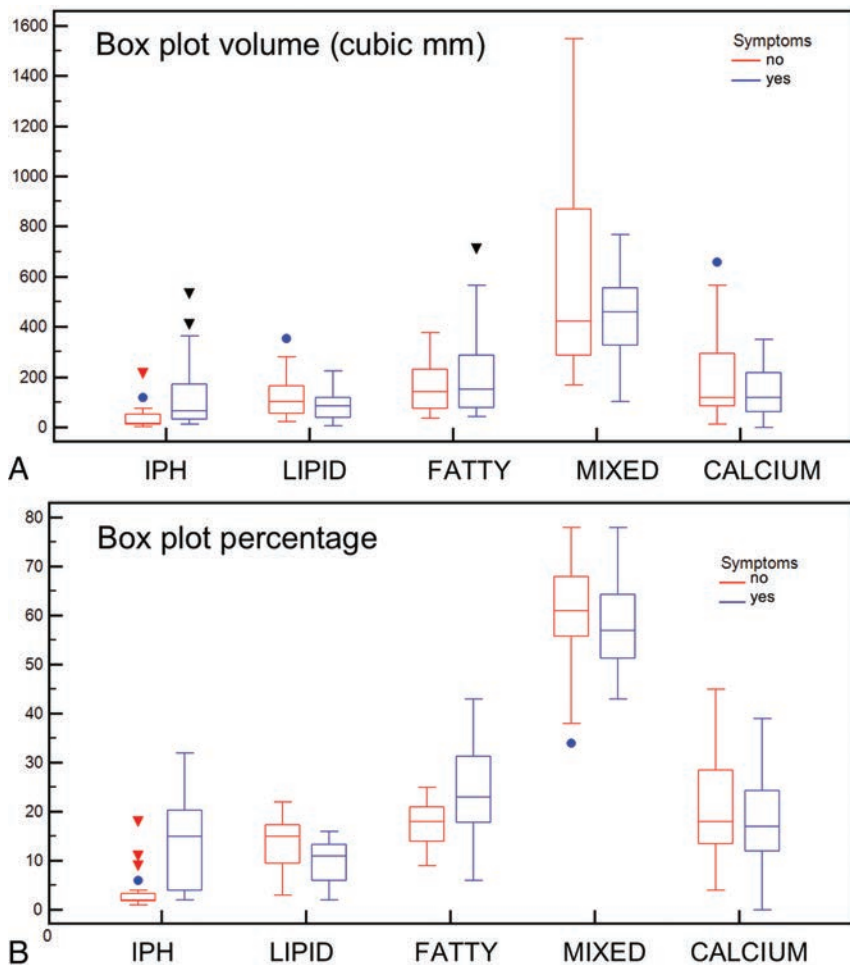


FIG 3. Boxplot analysis of the volume of the plaque components (A) and percentages (B) for symptomatic (blue plots) and asymptomatic (red plots) sides.

ratio also showed a statistically significant difference between the symptomatic and asymptomatic sides (0.596 versus 0.171, P value = .001). Wilcoxon analysis also showed that the degree of stenosis in the symptomatic plaque was not ($P = .728$) higher (49%; interquartile range, 38%–65%) than the contralateral, asymptomatic plaque (47%; interquartile range, 37%–59%).

Pearson ρ Correlation Analysis

The Pearson ρ correlation analysis showed that for both symptomatic and asymptomatic IPH plaques, there was a strong correlation between the degree of stenosis and plaque volume (ρ value = 0.77, P value = .001; and ρ value = 0.76, P value = .001, respectively). However, by analyzing the relationship between the degree of stenosis and IPH volume in asymptomatic plaque, we found no correlation (ρ value = 0.326, P value = .1487), whereas a strong correlation was found in symptomatic subjects between IPH volume and the degree of stenosis (ρ value = 0.642, P value = .002) (Fig 4).

ROC Curve Analysis

For each parameter (subcomponent volume and percentage), the ROC curve versus the presence of symptoms was calculated to test their impact. ROC curves are given in Fig 5. In Table 3 the area

under the curve (AUC), standard error, SD, and P values are summarized.

Interobserver Analysis

The Bland-Altman plot analysis is shown in Fig 6, and there are very good values of interobserver agreement for the total plaque volume (average difference, 8.3 mm³; 95% CI, -76.6–93.1 mm³) and subcomponents, in particular for the lipid (average difference, 1.6 mm³; 95% CI, -25.7–22.5 mm³) and IPH (average difference, 1.6 mm³; 95% CI, -12.1–8.9 mm³) values.

DISCUSSION

Previous studies have demonstrated that IPH is related to the occurrence of cerebrovascular events,^{6,7} yet not all plaques with IPH are associated with stroke/TIA.^{9,21,22} The occurrence and progression of IPH causes carotid plaque rupture in some cases, while in other subjects, there is an evolution of IPH to lipid core and inflammation without plaque rupture.^{23,24} Therefore, the mere presence of IPH alone does not explain plaque rupture and subsequent cerebrovascular events, but one can hypothesize that the specific IPH configuration and not its presence alone leads to plaque rupture.

In this study of patients with recent unilateral symptoms but bilateral IPH, we found that IPH volume and overall IPH percentage ipsilateral to the presenting cerebrovascular event are statistically higher than on the contralateral side. There was no difference between the 2 sides in the volume of other components. These results suggest that IPH occurs on the symptomatic side in larger amounts, and this feature could be the cumulative result of multiple hemorrhagic episodes. In this respect, previous studies using MR imaging have demonstrated that IPH can persist for years.^{25,26} Furthermore, it is also possible that after the acute/subacute phase, there is an evolution of the IPH toward the lipid-rich necrotic core because some authors have hypothesized that IPH could be a precursor of the lipid core.⁶

The lipid and fatty tissue percentages also showed a statistically significant difference between the symptomatic and asymptomatic sides. CT volumetric analysis of carotid plaque offers an important quantitative tool because of the possibility of computing the number of voxels with specific attenuation values and deriving tissue composition. The classification by de Weert et al¹⁷ showed that 60 HU is the optimal cutoff point to differentiate lipid from fibrous tissue. However, it is well-known that even though both lipid-rich necrotic core and IPH are associated with an increased occurrence of cerebrovascular events, the presence of IPH is much

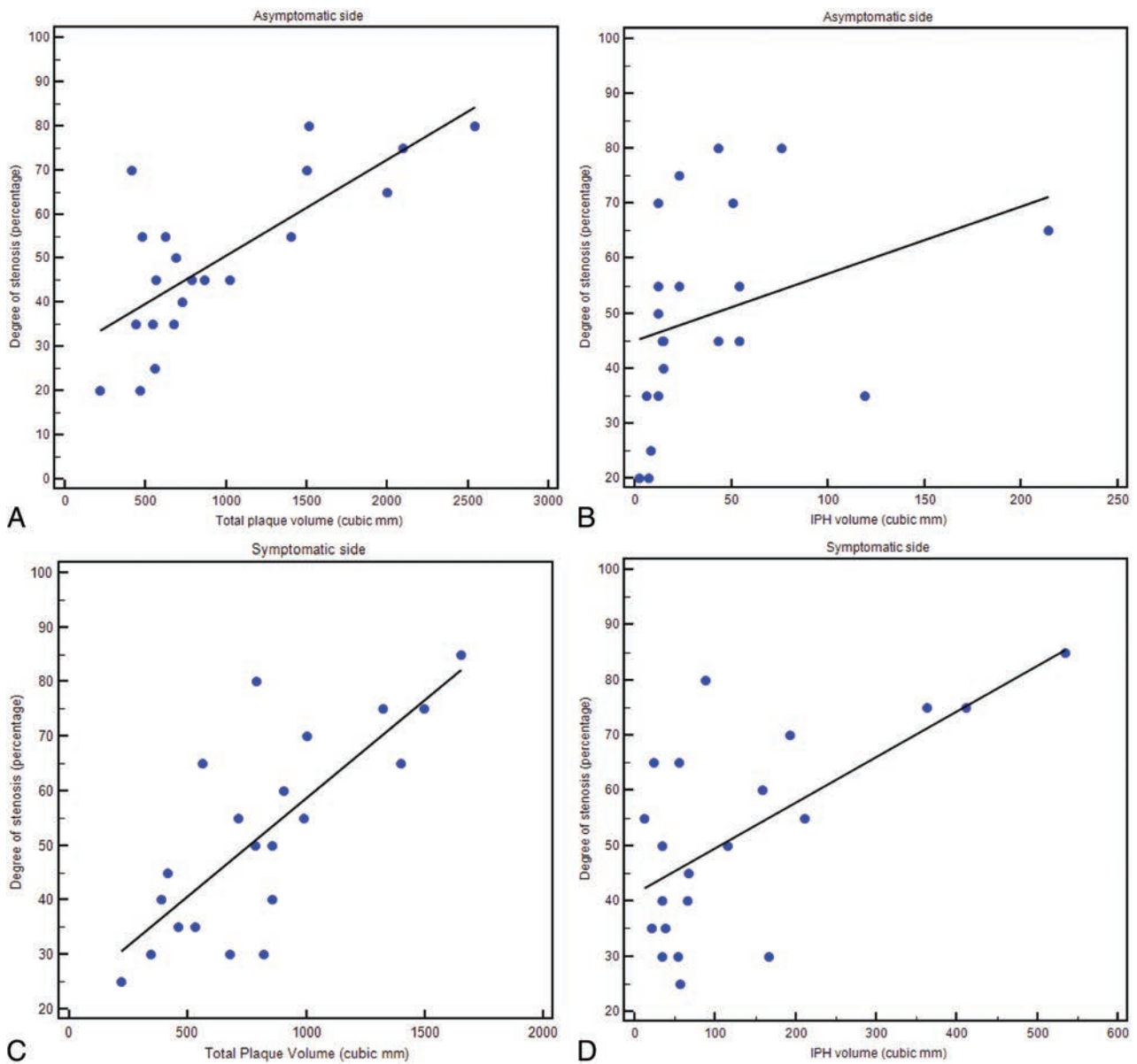


FIG 4. Regression analysis diagrams between total plaque and IPH volume on asymptomatic sides (A and B, respectively) and between total plaque and IPH volume on symptomatic sides (C and D, respectively).

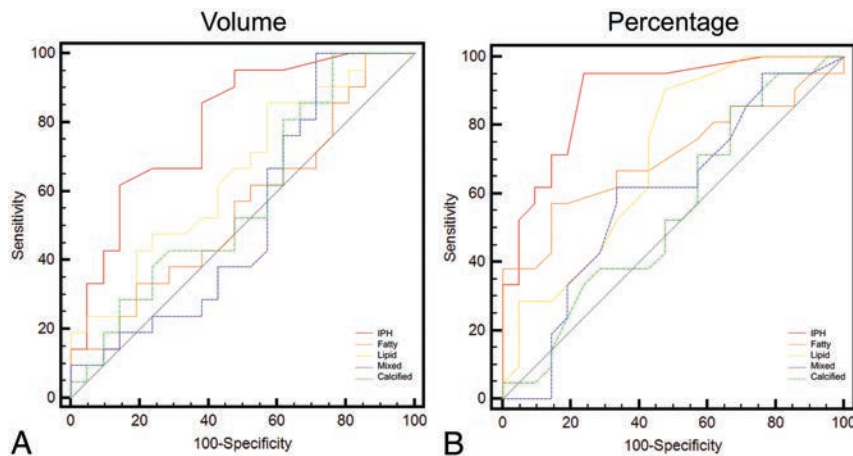


FIG 5. ROC curve analysis of the volume of the plaque components (A) and percentages (B) versus the presence of symptoms.

more important in increasing the risk of these events. Therefore, its identification on CT using a threshold of 25 HU¹¹ represents an important step, and the results of our study suggest that the presence of symptoms is not so much related to the difference in the volume of lipid components but rather to the degree of IPH.

A useful parameter in the assessment of plaque vulnerability is not only the absolute volume of plaque components but their relative percentages. We found that if we consider percentages, a significant difference between symptomatic and asymptomatic plaque is seen not

Table 3: ROC curve analysis

	AUC	SE	95% CI	P Value
Percentage				
IPH (<25 HU)	0.889	0.0506	0.754–0.965	.001
Fatty	0.707	0.0832	0.547–0.837	.013
Lipid	0.71	0.0819	0.549–0.839	.01
Mixed	0.595	0.091	0.433–0.744	.295
Calcium	0.551	0.0915	0.390–0.705	.577
Volume				
IPH (<25 HU)	0.796	0.0695	0.643–0.904	.001
Fatty	0.553	0.091	0.392–0.707	.558
Lipid	0.651	0.0857	0.488–0.791	.077
Mixed	0.529	0.0944	0.370–0.685	.755
Calcium	0.582	0.0907	0.420–0.732	.368
IPH/fatty ratio	0.582	0.0907	0.420–0.732	.368

Note:—AUC indicates area under the curve; SE, standard error.

only for IPH but also for the lipid and fatty components. In particular, the percentage of the lipid component is significantly higher in asymptomatic plaques, whereas the fatty component is higher in symptomatic ones. These observations suggest that not only the total volume of plaque components but rather their unbalanced percentages could induce plaque vulnerability. Previous studies exploring the role of biomechanical properties of the atherosclerotic arterial plaque and their effect in plaque destabilization support this notion.^{27,28}

In our study, the IPH/lipid ratio was also significantly different between symptomatic and asymptomatic sides (0.596 versus 0.171; $P = .001$). This observation could support the hypothesis that IPH can have a role in the formation and progression of the lipid-rich necrotic core.²⁴ Of note, Wilcoxon analysis also showed that the symptomatic plaque was not ($P = .728$) associated with a higher degree of stenosis than the contralateral plaque (49% versus 47%); this finding further supports the emerging notion that plaque composition and not only degree of stenosis play a role in symptoms onset.

Pearson ρ correlation analysis showed that for both symptomatic and asymptomatic plaques with IPH, there is a strong correlation between the degree of stenosis and the total plaque volume (ρ value = 0.771, P value = .0001; and ρ value = .757, P value = .0001, respectively). However, by analyzing the relationship between the degree of stenosis and IPH volume in asymptomatic plaque, we found no correlation (ρ value = 0.326, P value = .1487), whereas a strong correlation was found in symptomatic subjects between IPH volume and the degree of stenosis (ρ value = 0.642, P value = .0017). This difference could be explained by a different carotid plaque remodelling occurring in the acute phase compared with the nonacute phase due to the fast spatial increase determined by the IPH: Sun et al²⁵ showed that symptomatic advanced atherosclerotic carotid plaques have a higher tendency toward inward remodelling. Similarly, Takaya et al²⁶ found that lesions with IPH at baseline had a greater increase in wall volume and a reduction in lumen volume compared with arteries without IPH.

For each parameter (subcomponent volume and percentage), the ROC curve versus the presence of symptoms was calculated to test its impact (Fig 5). The agreement (Fig 6) between observers was very good for the total plaque volume and subcomponents. In

particular, almost similar values of volume were found for the IPH and lipid components, whereas some differences were present in the calcium volume, but this could be explained because the calcium volume is, as an average value, the largest component of the plaque.

Currently, among all available imaging techniques, MR imaging is considered the best technique for the detection of IPH because the appearance of IPH depends on the oxidative state of hemoglobin and is easily detected with common MR imaging.^{2,10,12} A recent investigation performed using MR imaging showed that in symptomatic patients with bilateral IPH, the symptomatic side had a stronger T1-weighted signal than the asymptomatic side.⁹ The effects determined by the volume of the carotid plaque and carotid plaque subcomponents remain to be explored because of the limited ability of MR imaging to adequately calculate the volume of these tissues. The use of CT for the detection and characterization of IPH is still debated because this technique shows nondefinitive results and only 3 studies with relatively few patients have been published with this technique.^{11,29,30} However, other studies suggest that by using CT, it is possible to analyze, with very good detail, the volume of different plaque components.^{19,31} The observation that plaque composition and IPH can be analyzed with CT has very important practical consequences in clinical practice. Unlike MR imaging, CT is routinely used in the urgent/emergent evaluation of patients with acute ischemic events, it is widely available 24/7, and is more convenient for patients, especially the elderly with acute cerebrovascular syndromes because in such cases, good quality MR images are challenging to obtain because of patient movement, discomfort, and lack of cooperation.

Our study has limitations. The cohort analyzed is relatively small ($n = 21$). However, the occurrence of bilateral plaques with IPH in a patient with unilateral symptoms is a relatively uncommon event. Nevertheless, it was important to analyze this specific population because the contralateral (to the symptoms) side functions as an internal control and the ability to analyze plaque differences in the same patients removes many of the variables associated with the use of other types of controls. To include only subjects with bilateral IPH, we introduced an arbitrary threshold to avoid inclusion of subjects with a minimal presence of Hounsfield voxels (eg, only 1 voxel) with a value of <25 HU (ie, a threshold of 1% minimum of the plaque should have <25-HU voxels to be accepted as plaque with IPH). We recognize that this may be arbitrary and may potentially introduce a bias because a small amount of IPH may have been a priori excluded. Moreover, it is possible that some patients with IPH could be excluded because of blooming artifacts due to a cluster of calcium within the plaque.

In this study, there was no histopathologic comparison. Therefore, when we consider IPH, lipid, fatty, mixed, and calcified tissues, the classification is only based on the attenuation values of the tissues. This could be a source of bias (common to any study using CT) because the same type of tissue, even if the same energy levels are applied (as in the current study), could have subtle differences in the Hounsfield attenuation due to body hab-

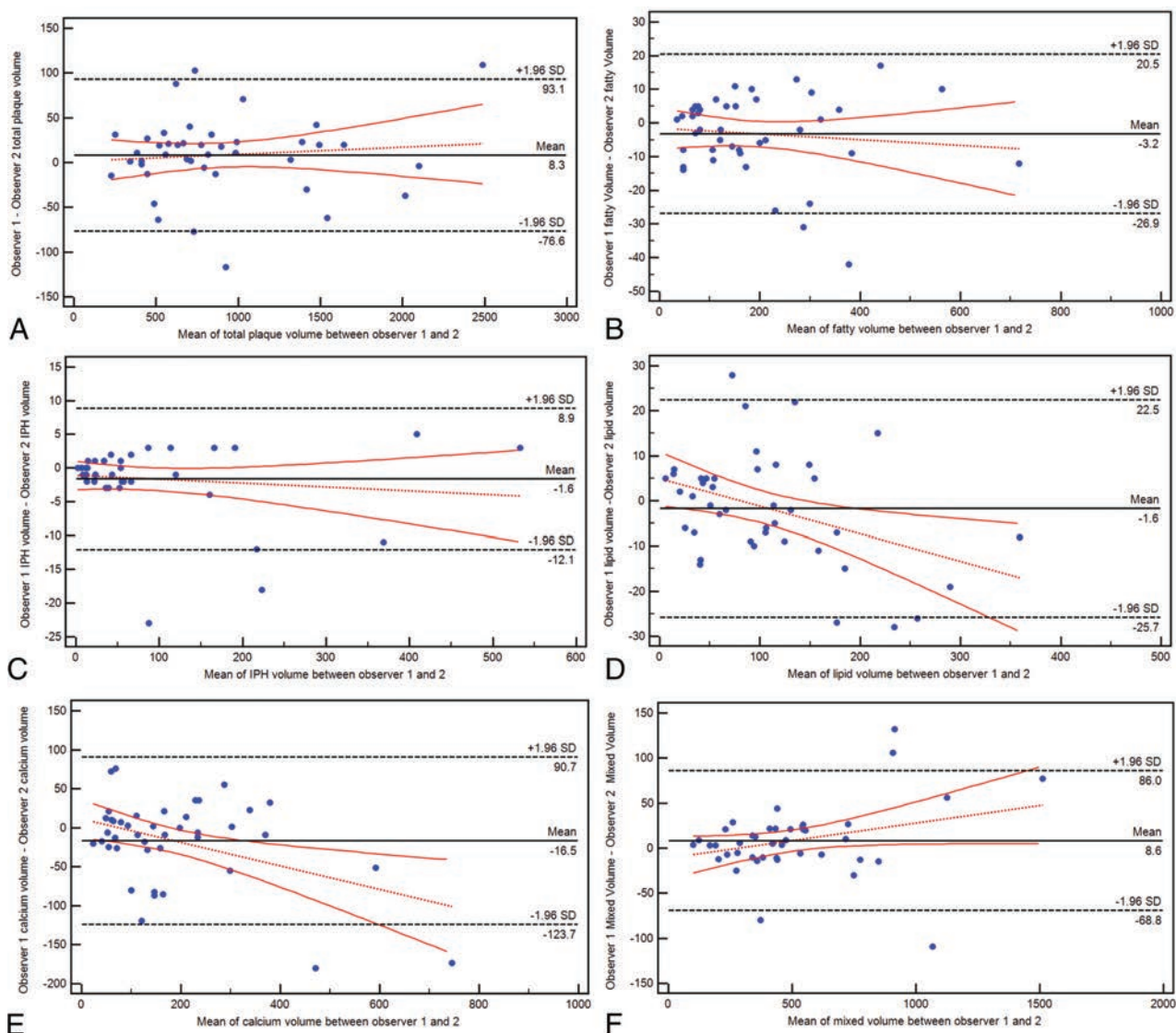


FIG 6. Bland-Altman plot analysis for the interobserver agreement in total volume (A) and fatty (B), IPH (C), lipid (D), calcified (E), and mixed (F) tissue.

itus (such as body mass index, size of the neck, and so forth); also in this case, this is a general limitation of CT when attenuation values are considered but which could affect, in some degree, the measurements and tissue classification. Another limit is that IPH (or a portion of the IPH) denser than 25 HU would be excluded from the analysis by determining a bias. In the study by Saba et al,¹¹ it was demonstrated that in some cases, the IPH could have an attenuation of >25 HU. However, this would introduce only a minor bias because it has been demonstrated that most IPH shows values of <25 HU.

CONCLUSIONS

We have found that in symptomatic subjects with bilateral IPH on CT, the plaque ipsilateral to the symptomatic side has a significantly larger volume and a higher percentage of IPH compared with the contralateral side. In symptomatic plaques, the IPH component is increased compared with the lipid one. These observations have important practical ramifications in the acute evaluation of these patients.

Disclosures: Giuseppe Lanzino—UNRELATED: Board Membership: Superior Medical Editing; Other: Marblehead, Comments: shareholder, shares directly purchased. Chun Yuan—UNRELATED: Grants/Grants Pending: Philips Healthcare.* *Money paid to the institution.

REFERENCES

- Donnan GA, Fisher M, Macleod M, et al. **Stroke.** *Lancet* 2008;371:1612–23 CrossRef Medline
- Saba L, Yuan C, Hatsukami TS, et al; Vessel Wall Imaging Study Group of the American Society of Neuroradiology. **Carotid Artery Wall Imaging: Perspective and Guidelines from the ASNR Vessel Wall Imaging Study Group and Expert Consensus Recommendations of the American Society of Neuroradiology.** *AJNR Am J Neuroradiol* 2018;39:E9–31 CrossRef Medline
- Tang D, Yang C, Huang S, et al. **Cap inflammation leads to higher plaque cap strain and lower cap stress: an MRI-PET/CT-based FSI modeling approach.** *J Biomech* 2017;50:121–29 CrossRef Medline
- DeMarco JK, Huston J 3rd. **Imaging of high-risk carotid artery plaques: current status and future directions.** *Neurosurg Focus* 2014;36:E1 CrossRef Medline
- Millon A, Mathevet JL, Boussel L, et al. **High-resolution magnetic**

- resonance imaging of carotid atherosclerosis identifies vulnerable carotid plaques. *J Vasc Surg* 2013;57:1046–51.e2 CrossRef Medline
6. Hatsukami TS, Yuan C. MRI in the early identification and classification of high-risk atherosclerotic carotid plaques. *Imaging Med* 2010;2:63–75 CrossRef Medline
 7. Demarco JK, Ota H, Underhill HR, et al. MR carotid plaque imaging and contrast-enhanced MR angiography identifies lesions associated with recent ipsilateral thromboembolic symptoms: an in vivo study at 3T. *AJNR Am J Neuroradiol* 2010;31:1395–402 CrossRef Medline
 8. Michel JB, Martin-Ventura JL, Nicoletti A, et al. Pathology of human plaque vulnerability: mechanisms and consequences of intraplaque haemorrhages. *Atherosclerosis* 2014;234:311–19 CrossRef Medline
 9. Wang X, Sun J, Zhao X, et al; CARE-II study investigators. Ipsilateral plaques display higher T1 signals than contralateral plaques in recently symptomatic patients with bilateral carotid intraplaque hemorrhage. *Atherosclerosis* 2017;257:78–85 CrossRef Medline
 10. Brinjikji W, Huston J 3rd, Rabinstein AA, et al. Contemporary carotid imaging: from degree of stenosis to plaque vulnerability. *J Neurosurg* 2016;124:27–42 CrossRef Medline
 11. Saba L, Francone M, Bassareo PP, et al. CT attenuation analysis of carotid intraplaque hemorrhage. *AJNR Am J Neuroradiol* 2018;39:131–37 CrossRef Medline
 12. Saba L, Anzidei M, Sanfilippo R, et al. Imaging of the carotid artery. *Atherosclerosis* 2012;220:294–309 CrossRef Medline
 13. Adams HP Jr, Bendixen BH, Kappelle LJ, et al. Classification of subtype of acute ischemic stroke: definitions for use in a multicenter clinical trial—TOAST. Trial of Org 10172 in Acute Stroke Treatment. *Stroke* 1993;24:35–41 CrossRef Medline
 14. Pelz DM, Fox AJ, Eliasziw M, et al. Stenosis of the carotid bifurcation: subjective assessment compared with strict measurement guidelines. *Can Assoc Radiol J* 1993;44:247–52 Medline
 15. Touboul PJ, Hennerici MG, Meairs S, et al. Mannheim carotid intima-media thickness and plaque consensus (2004–2006–2011): an update on behalf of the advisory board of the 3rd, 4th and 5th watching the risk symposia, at the 13th, 15th and 20th European Stroke Conferences, Mannheim, Germany, 2004, Brussels, Belgium, 2006, and Hamburg, Germany, 2011. *Cerebrovasc Dis* 2012;34:290–96 CrossRef Medline
 16. Saba L, Raz E, Grassi R, et al. Association between the volume of carotid artery plaque and its subcomponents and the volume of white matter lesions in patients selected for endarterectomy. *AJR Am J Roentgenol* 2013;201:W747–52 CrossRef Medline
 17. de Weert TT, Ouhlous M, Zondervan PE, et al. In vitro characterization of atherosclerotic carotid plaque with multidetector computed tomography and histopathological correlation. *Eur Radiol* 2005;15:1906–14 CrossRef Medline
 18. Saba L, Mallarin G. Window settings for the study of calcified carotid plaques with multidetector CT angiography. *AJNR Am J Neuroradiol* 2009;30:1445–50 CrossRef Medline
 19. Sheahan M, Ma X, Paik D, et al. Atherosclerotic plaque tissue: non-invasive quantitative assessment of characteristics with software-aided measurements from conventional CT angiography. *Radiology* 2018;286:622–31 CrossRef Medline
 20. Eesa M, Hill MD, Al-Khathaami A, et al. Role of CT angiographic plaque morphologic characteristics in addition to stenosis in predicting the symptomatic side in carotid artery disease. *AJNR Am J Neuroradiol* 2010;31:1254–60 CrossRef Medline
 21. Treiman GS, McNally JS, Kim SE, et al. Correlation of carotid intraplaque hemorrhage and stroke using 1.5 T and 3 T MRI. *Magn Reson Insights* 2015;8(Suppl 1):1–8 CrossRef Medline
 22. Saba L, Saam T, Jäger HR, et al. Imaging biomarkers of vulnerable carotid plaques for stroke risk prediction and their potential clinical implications. *Lancet Neurol* 2019;18:559–72 CrossRef Medline
 23. Sun J, Balu N, Hippe DS, et al. Subclinical carotid atherosclerosis: short-term natural history of lipid-rich necrotic core—a multicenter study with MR imaging. *Radiology* 2013;268:61–68 CrossRef Medline
 24. Underhill HR, Hatsukami TS, Fayad ZA, et al. MRI of carotid atherosclerosis: clinical implications and future directions. *Nat Rev Cardiol* 2010;7:165–73 CrossRef Medline
 25. Sun J, Underhill HR, Hippe DS, et al. Sustained acceleration in carotid atherosclerotic plaque progression with intraplaque hemorrhage: a long-term time course study. *JACC Cardiovasc Imaging* 2012;5:798–804 CrossRef Medline
 26. Takaya N, Yuan C, Chu BC, et al. Presence of intraplaque hemorrhage stimulates progression of carotid atherosclerotic plaques: a high-resolution magnetic resonance imaging study. *Circulation* 2005;111:2768–75 CrossRef Medline
 27. Gao H, Long Q. Effects of varied lipid core volume and fibrous cap thickness on stress distribution in carotid arterial plaques. *J Biomech* 2008;41:3053–59 CrossRef Medline
 28. Tang D, Yang C, Kobayashi S, et al. Effect of a lipid pool on stress/strain distributions in stenotic arteries: 3-D fluid-structure interactions (FSI) models. *J Biomech Eng* 2004;126:363–70 CrossRef Medline
 29. Ajduk M, Pavić L, Bulimbasić S, et al. Multidetector-row computed tomography in evaluation of atherosclerotic carotid plaques complicated with intraplaque hemorrhage. *Ann Vasc Surg* 2009;23:186–93 CrossRef Medline
 30. Wintermark M, Jawadi SS, Rapp JH, et al. High-resolution CT imaging of carotid artery atherosclerotic plaques. *AJNR Am J Neuroradiol* 2008;29:875–82 CrossRef Medline
 31. Zhu G, Li Y, Ding V, et al. Semiautomated characterization of carotid artery plaque features from computed tomography angiography to predict atherosclerotic cardiovascular disease risk score. *J Comput Assist Tomogr* 2019;43:452–59 CrossRef Medline

Improved Assessment of Middle Ear Recurrent Cholesteatomas Using a Fusion of Conventional CT and Non-EPI-DWI MRI

F. Felici, U. Scemama, D. Bendahan, J.-P. Lavielle, G. Moulin, C. Chagnaud, M. Montava, and A. Varoquaux

ABSTRACT

BACKGROUND AND PURPOSE: Recurrent middle ear cholesteatomas are commonly preoperatively assessed using MR imaging (non-EPI-DWI) and CT. Both modalities are used with the aim of distinguishing scar tissue from cholesteatoma and determining the extent of bone erosions. Inflammation and scar tissue associated with the lesions might hamper a proper delineation of the corresponding extensions on CT images. Using surgical findings as the criterion standard, we assessed the recurrent middle ear cholesteatoma extent using either uncoregistered or fused CT–MR imaging datasets and determined the corresponding accuracy and repeatability.

MATERIALS AND METHODS: Twenty consecutive patients with suspected recurrent middle ear cholesteatoma and preoperative CT–MR imaging datasets were prospectively included. A double-blind assessment and coregistration of the recurrent middle ear cholesteatoma extent and manual delineation of 18 presumed recurrent middle ear cholesteatomas were performed by 2 radiologists and compared with the criterion standard. “Reliability score” was defined to qualify radiologists’ confidence. For each volume, segmentation repeatability was assessed on the basis of intraclass correlation coefficient and overlap indices.

RESULTS: For the whole set of patients, recurrent middle ear cholesteatoma was further supported by surgical results. Two lesions were excluded from the analysis, given that MR imaging did not show a restricted diffusion. Lesions were accurately localized using the fused datasets, whereas significantly fewer lesions (85%) were correctly localized using uncoregistered images. Reliability scores were larger for fused datasets. Segmentation repeatability showed an almost perfect intraclass correlation coefficient regarding volumes, while overlaps were significantly lower in uncoregistered (52%) compared with fused (60%, $P < .001$) datasets.

CONCLUSIONS: The use of coregistered CT–MR images significantly improved the assessment of recurrent middle ear cholesteatoma with a greater accuracy and better reliability and repeatability.

ABBREVIATIONS: FD = fused dataset; ICC = intraclass correlation coefficient; JI = Jaccard index; MEC = middle ear cholesteatoma; rMEC = recurrent MEC; ROC = receiver operating characteristic; UD = uncoregistered dataset; VIBE = volumetric interpolated brain examination

Recurrent middle ear cholesteatoma (rMEC) is a destructive and expanding lesion¹ that can recur after a seemingly complete surgical resection. The frequency of rMEC ranges from 5% to 15% and can reach up to 61%² after an initial operation, particularly with canal wall up techniques. Potential clinical consequences are similar to those resulting from a primary lesion—that is, hearing loss, meningitis, brain abscess, and labyrinthitis. However, the clinical presentation of rMEC differs from that of middle

ear cholesteatoma (MEC) regarding otoscopic assessments. A high rate of false-negative results has been reported, so an additional surgical procedure has often been performed as a diagnostic confirmation.^{3,4} CT is commonly used to assess rMEC, plan revision surgery, and choose middle ear repair strategies.⁵ Endoscopic (transmastoid or transcanal) or microscopic (canal wall up/down) procedures have been used.⁶

In the past decade, MR imaging and, more particularly, DWI have been proposed as an alternative to the additional surgical procedure.⁷ Restricted diffusion in lesions of the middle ear cavity has been reported as a sensitive index of rMEC and false-negative results—that is, missed lesions have been related to small volume or mural cholesteatomas and susceptibility artifacts. Assessment of rMEC using non-EPI-DWI would be more accurate with the ability to detect 3-mm rMEC lesions.^{7,8}

High-resolution CT has been considered so far as the imaging technique of choice for the evaluation of bone tissue changes oc-

Received February 27, 2019; accepted after revision June 17.

From the Department of Medical Imaging (F.F., U.S., G.M., C.C., A.V.), La Conception University Hospital, Department of Otorhinolaryngology–Head and Neck Surgery (J.-P.L., M.M.), North Hospital, and CNRS, CRMBM–CEMEREM UMR 7339, 13385 (D.B., A.V.) and UMRT 24 IFSTTAR (J.-P.L., M.M.), Aix-Marseille University, Marseille, France.

Please address correspondence to Arthur Varoquaux, MD, Service de Radiologie de l’Hôpital la Conception, 147 Boulevard Baille, 13005 Marseille, France; e-mail: Arthur.VAROQUAUX@ap-hm.fr

<http://dx.doi.org/10.3174/ajnr.A6141>

Table 1: MR acquisition data

	T1WI	T2WI	SE DWI	3D-T1 VIBE
TR (ms)	610	4460	2000	9.19
TE (ms)	14	95	105	3.34
FOV (mm)	150 × 150	166 × 129	220 × 220	172 × 200
NEX	2	2	8	2
Slice thickness (mm)	2	2	3	0.7
Acquisition time (min:sec)	2:11	2	3:12	3:23
Matrix size	358 × 512	344 × 384	144 × 192	213 × 288
B-values			$b=1000$	

Note:—SE indicates spin-echo.

curring in rMEC. Erosions of ossicles and the facial nerve canal, labyrinthine system, or tympanic tegmen have been described.⁹ However, high-resolution CT assessment of rMEC can be challenged by multiple factors such as postoperative scarring and fluid and cholesterol granulomas around the lesion.

Most interesting, it has been recently suggested that surgical planning of rMEC could be improved when using information from coregistered MR and CT images.¹⁰ The corresponding usefulness has not been assessed for rMEC. The main aim of the present study was to assess the added value of DWI–CT fusion for the local assessment of rMEC in a clinical workflow. Volumes of lesions were quantified on fused and unfused datasets and compared using intraclass coefficients and similarity indices.

MATERIALS AND METHODS

Research Design

This monocentric prospective study was approved by the institutional ethics committee (2015–27/RCAPHM15_0223), performed with Commission Nationale de l’informatique et des Libertés (CNIL) authorization (1879159-v0), and identified under ClinicalTrials.gov as NCT02903550.

Patients

Between August 2015 and August 2016, twenty consecutive patients (7 women and 13 men; mean age, 41.2 years) were prospectively enrolled before an rMEC operation. Each patient had a history of histologically proved MEC and had an initial operation at least a year before the inclusion. Each patient had a presumed rMEC based on the combined analysis of otoscopy, CT, and MR imaging. Patients were included once they provided written informed consent. Exclusion criteria were middle ear infection, gadolinium allergy, pregnancy, non-MR imaging-compatible implants or devices, surgical contraindications, or refusal to participate.

Imaging Protocol

MR imaging acquisitions were performed at 1.5T (Magnetom Amira; Siemens, Erlangen, Germany). Patients lay supine while their head was placed in a standard 16-channel head and neck phased array coil. High-resolution T1WI, T2WI, and non-EPI-DWI were acquired in the coronal and axial planes (Table 1). A 3D volumetric interpolated brain examination (VIBE) T1WI dataset was acquired after gadoterate meglumine injection (0.1 mmol/kg, Dotarem; Guerbet, Aulnay-sous-Bois, France).

CT was performed using an 80-channel × 0.5 mm multidetector scanner (Aquilion PRIME; Canon Medical, Tokyo, Japan). A single acquisition was performed using routine temporal bone

protocols (collimation = 0.5×4 mm, 135 kV[peak], 200 mAs, resolution time = 0.75 ms, pitch = 0.75 [detail], acquisition FOV = 150 mm [super small], reconstruction FOV = 80 mm). Images were reconstructed in axial, coronal, and sagittal planes (0.5×0.5 mm).

Image Analysis

Both MR and CT images were analyzed using OsiriX Imaging Software (<http://www.osirix-viewer.com>) by 2 experts (A.V. with 16 years’ experience and F.F. with 4 years’ experience) who were blinded to the patient’s clinical status. Observers performed the image assessment and coregistration independently. rMEC lesions were assessed in 18 middle ear areas using a 5-point Likert scale as follows: 1 = no invasion, 2 = unlikely invasion, 3 = unclear invasion, 4 = highly probable invasion, and 5 = obvious invasion; 22 anatomic locations (Table 2) were predefined by the surgical team.

To assess the reproducibility of the manual delineation of the lesions, each expert manually segmented each lesion twice at different times on CT images. The corresponding volumes (vol 1 and vol 2) were quantified using the OsiriX “ROI volume” tool. Lesion segmentation was initially performed on the unfused datasets (uncoregistered dataset [UD]). Then, a rigid coregistration was performed between the 3D-VIBE-T1WI and CT datasets using the OsiriX plugin “Fusion tool.” The ipsi- and contralateral geniculate ganglion and ipsilateral stylomastoid foramen were used as specific landmarks. Fusion quality was defined on the basis of a 4-point quality scale using the distance between the corresponding landmarks with 1, 2, 3, and 4 referring to a distance of 0, <1 mm, between 1 and 2 mm, and >2 mm, respectively. The $b=1000$ non-EPI-DWI was resliced to the coregistered 3D-VIBE-T2WI and then fused to the CT dataset.

The fused dataset (FD) was analyzed 6 weeks later using the same paradigm and the same predefined anatomic locations. The corresponding volumes were referred as vol 3 and vol 4 for observer 1 and 2, respectively.

Surgical Criterion Standard

Surgical findings were considered as the criterion standard for lesion assessment. Using a Likert scale, we defined findings as negative for scores 1 and 2 and as positive for scores 4 and 5 (Table 2, “UD Exact,” “FD Exact”). In addition, a reliability score was computed as follows: 100% for Likert scores 1 and five; 50% for Likert scores 2 and four; 0% for Likert score 3.

Test–Retest Repeatability

To assess the coregistration process and segmentation repeatability, we performed test-retest for volume measurement. The corresponding intraclass coefficients (ICC) for paired measurements (vol 1 to vol 4) and the overlap between manually segmented volumes of interest were computed. Overlap was quantitatively assessed on a voxel basis using the Jaccard index (JI)¹¹:

$$JI = (VOI_a \cap VOI_b) / (VOI_a \cup VOI_b),$$

Table 2: rMEC surgical location findings and MR imaging correspondence

Anatomic Location	No. ^a	PREV	UD Exact	FD Exact	UD Reliab	FD Reliab
Epitympanic recess	18	83%	94%	100%	83%	97%
Posterior epitympanic recess	18	78%	100%	100%	92%	100%
Aditus of mastoid antrum	18	72%	72%	100%	72%	94%
Tegmen antri	18	67%	67%	100%	64%	97%
Anterior epitympanic recess	18	67%	67%	100%	83%	83%
Tegmen tympani	18	61%	83%	100%	81%	94%
Mastoidectomy cavity	18	56%	78%	100%	89%	94%
Facial nerve: tympanic segment	18	44%	67%	100%	64%	89%
Promontory of tympanic cavity	18	33%	94%	100%	86%	97%
Oval window/stapes	18	33%	83%	100%	83%	97%
Mesotympanum	18	28%	72%	100%	69%	100%
Vestibule	18	22%	78%	100%	97%	89%
Facial nerve: second genu	18	22%	83%	100%	81%	97%
Sinus tympani	18	17%	83%	94%	86%	97%
Eustachian tube	18	11%	89%	100%	86%	100%
Dura mater	18	11%	89%	100%	94%	94%
Round window	18	6%	83%	100%	78%	100%
Carotid canal	18	6%	94%	100%	94%	97%
Facial nerve: geniculum	18	6%	89%	100%	83%	97%
Cochlea	18	0%	100%	100%	100%	100%
Temporal lobe	18	0%	100%	100%	97%	100%
Facial nerve: mastoid segment	18	0%	100%	100%	94%	100%

Note:—PREV indicates surgical prevalence; Exact, correctly identified and correctly rejected findings (ie, true-positive + true-negative considering surgical findings as the criterion standard); Reliab, reliability score.
^a Number of lesions.

Table 3: Patient data

	Mean	Range	(%)
No. of patients	20		
Mean age (yr)	41.2	(11.1–70.9)	
Female/male (%)	35/65		
Surgery			
No. of previous interventions	2.9	(1–8)	
Right/left (%)	55/45		
Time to recurrence (mo)	70.6	(9–430)	
MRI to surgery (mo)	2.1	(0–10)	
MRI			
True-positive in DWI	18		90%
False-negative in DWI	2		10%
Fusion quality			
Good	9		50%
Perfect	9		50%

with VOI_a and VOI_b being volumes manually segmented in fused datasets.

ICC values were qualified according to Landis and Koch.¹⁵ The ICC precision of estimates was defined as previously described using the relative 95% confidence interval.¹⁶

Statistical Analyses

The whole set of tests was performed with R statistical and computing software, Version 3.2.0 (<http://www.r-project.org/>), and a *P* value < .05 was considered statistically significant.

Quantitative variables are presented as means ± SDs, while categorical variables are presented as frequencies. Paired Mann-Whitney *U* tests were used to compare exact finding rates, reliability scores, volumes, and segmentation overlap indices computed in UD and FD.

Areas under the receiver operating characteristic (ROC) curve measurements were used to quantify the ability to locate rMEC. The DeLong test¹² was used to compare the areas under the curve of the paired ROC curves with the package pROC version 1.14.0

for R. For quantitative variables, the Youden method¹³ was used to determine the thresholds of the ROC curves.

Single-measure ICCs were calculated using the 2-way random ANOVA on average measures (ICC ranges, 0.00–1.00, with values closer to 1.00 representing better reproducibility).¹⁴ Interpretation of the ICC was categorized according to Landis and Koch.¹⁵ The precision of ICC estimates was defined as previously described using the 95% CI.¹⁶

RESULTS

rMEC Assessment

Among the 20 rMECs, in the 20 patients included in the study, 2 rMEC lesions (11 and 12 mm, respectively) were excluded (Table 3). The corresponding absence of a *b*=1000 signal on DWI was considered a false-negative finding. A total of 18 lesions were analyzed (Table 2) with respect to 22 anatomic locations (*n* = 396). Fusion was qualified as “perfect” in 9 lesions (50%) and as “good” (<1 mm) for the remainder.

The anatomic distribution of lesions is detailed in Table 2. The epitympanic recess was the usual rMEC site. The frequency of exact findings amounted to 84.8% ± 11.2% using UD and was significantly larger (99.7% ± 11.8%, *P* < 0.01) using FD. Similarly, the reliability score significantly rose from 84.5% ± 10.3% to 96.2% ± 4.3% (*P* < 0.01) using UD and FD, respectively (Table 2). The area under the curve value was 0.93 using UD and significantly increased to 0.99 (*P* < 0.01) using FD (Table 4).

Segmentation Reproducibility

Mean lesion volume was 0.36 ± 0.42 mL and ranged from 0.01 to 1.73 mL. Inter- and intraobserver volume calculation variability was almost perfect, with the ICC ranging from 0.86 to 0.95 (*P* < .001, Table 5). The highest ICC (95%) and the best precision (6%) were obtained for the interobserver measurements performed on FD. Intraobserver segmentation overlap (JI) was different between observer 1 (55% ± 23%) and observer 2 (45% ± 27%; *P* < 0.01). A larger interobserver segmentation overlap (60% ± 28%) was measured for FD compared with UD (52% ± 22%, *P* < 0.01).

DISCUSSION

The present results suggest that a better rMEC assessment could be achieved when CT and MR imaging datasets are coregistered and fused. On that basis, both imaging modalities should be considered before an operation.

These results further support and extend those from previous reports that demonstrated the usefulness of FD in the local evaluation of MEC.^{10,17–19} Accordingly, from a comparative analysis between CT alone and FD, a few studies have suggested that MEC would be better assessed using FD.^{10,17,19} This result has been further confirmed from a comparative analysis between DWI alone and FD.^{17–19} The superiority of the FD-based rMEC assess-

Table 4: Clinical performance of rMEC local assessment

DWI-CT	No. ^a	PREV	AUC	AUC CI	Se	Sp	PPV	NPV	P Value ^b
UD	396	33%	0.93	0.90–0.96	80%	96%	88%	92%	
FD	396	33%	0.99	0.99–1.00	100%	100%	99%	100%	<.001

Note:—PREV indicates prevalence of positive surgical findings; AUC, area under the ROC curve; Se, sensitivity; Sp, specificity; PPV, positive predictive value; NPV, negative predictive value.

^a Number of observations (22 locations in 18 lesions).

^b Statistical significance using DeLong tests.

Table 5: Segmentation reproducibility on volume measurements

	ICC	ICC-CI	Preci	Interpret	P Value ^a
Obs1 (vol 1–vol 3)	0.93	0.82–0.97	8%	Almost perfect	<.001
Obs2 (vol 2–vol 4)	0.86	0.67–0.95	14%	Almost perfect	<.001
Unfused (vol 1–vol 2)	0.91	0.78–0.97	10%	Almost perfect	<.001
Fused (vol 3–vol 4)	0.95	0.88–0.99	6%	Almost perfect	<.001

Note:—Preci indicates precision of ICC estimate; Interpret, interpretation of ICC; Obs, observer; vol, volume.

^a Statistical significance using an ANOVA model for ICC.

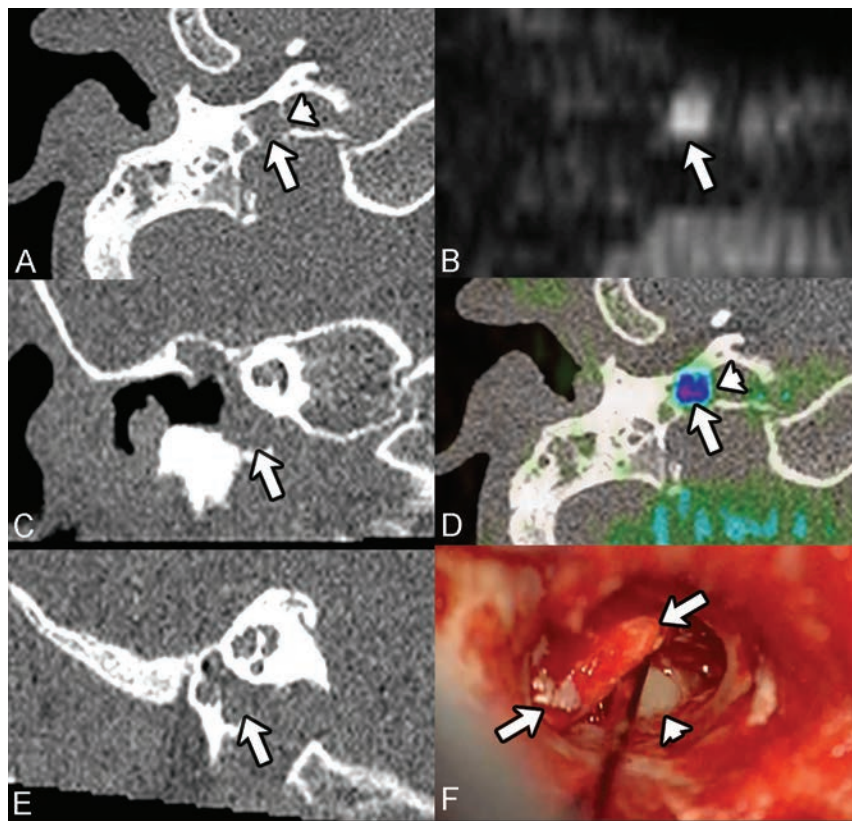


FIGURE. Example of rMEC leading to a carotid canal erosion. Recurrent middle ear cholesteatoma (axial $b=1000$ non-EPI MR imaging, *B*, arrow) probably located (rated Likert 4) in the hypotympanum, on uncoregistered dataset (*A*, *B*, *C*, *E*, arrows). The hypotympanum location is clear (rated Likert 5), considering that the fused dataset ($b=1000$ /CT in axial plane, *D*, arrow) and the vertical carotid canal lysis (*A* and *D*, arrowheads) can be seen. The perioperative surgical findings (*F*) confirmed the hypotympanum rMEC location (arrows) and the carotid canal lysis (arrowhead). In that case, the presurgical image fusion allowed the surgeon to adapt his approach, thus lowering the surgical risks.

ment that we describe in the present study could partly be due to a careful patient selection based on the DWI results, the number of patients, and the number of locations. DWI is an imaging technique that can clearly distinguish cholesteatoma from postsurgical abnormalities such as scars.

In our study, only patients with rMEC were included, and untreated patients were excluded so that the postoperative scar tissue could be addressed. On the contrary, in studies in which

untreated patients have been included, this issue could not be addressed,^{10,17,18} and the advantage of the FD-based assessment could not have been properly investigated. The number of patients with rMEC included in the present study ($n = 20$) was larger compared with other studies in which 2–16 patients were included.^{10,17–19} The number of locations could have also been a central methodologic factor. While 4–6 locations have been assessed in previous studies, the 22 locations assessed in the present study likely led to a reduced α risk. In addition, given that each location has been analyzed in each patient, no missing data had to be considered, and cluster analysis was not considered. The increase of exact location findings was most striking in the tegmen antri, anterior epitympanic recess, tympanic segment of the facial nerve, and mesotympanum. These locations have been reported as frequently occurring.¹⁹

As previously described, the 5-point Likert scale was used to count exact findings, calculate the reliability score, and compare ROC curves.²⁰ Such a scale has been used in a large number of radiologic studies.²¹ As an example of the clinical added value of the FD-based rMEC assessment, the carotid canal was affected in one of the patients, and this was missed using the UD, whereas it was identified using FD (Figure). In this particular case, the proper location had an impact on the surgical procedure and the middle ear repair strategy.

The improved segmentation reproducibility using FD is further supportive of this added value. Scarce data are available in previous studies regarding this

particular issue. ICC values regarding computed volumes illustrated an almost perfect agreement for each segmentation. Although no criterion standard measurements were available for volumes, our analysis disclosed reproducible volume measurements based on CT and $b=1000$ findings. The superior reproducibility of the FD-based assessment was statistically demonstrated using the JI, which has been largely used for volume delineation.¹¹ The JI ranged between 31% and 74%, thereby indicating a poor-

to-high overlap between volumes of interest. One has to keep in mind that the JI assessed both segmentation and coregistration processes, given that each observer performed his own fusion process.

During the past decade, non-EPI-DWI has significantly improved the handling of MEC both in terms of diagnosis and postoperative survey strategy.^{17,22} As recently reported, non-EPI-DWI is less sensitive to susceptibility artifacts and can provide a high signal-to-noise ratio so that high sensitivity (90%) and specificity (94%) can be achieved.⁷ In the present study, 2 lesions of 20 were freely diffusive, leading to a sensitivity of 90%, in agreement with a recent meta-analysis report.⁷ The 100% specificity reported in the present study is likely due to particular attention paid to excluding patients with middle ear infection. False-positive findings can be found due to water restriction in infected areas as described in mastoid abscess.²³

The choice of the non-EPI-DWI technique in the field of rMEC investigations is still a matter of debate. We chose to use TSE-DWI, considering the recognized low artifacts on the skull base and signal homogeneity.²⁴ HASTE-DWI has been noted for the shorter acquisition time,⁷ but information regarding artifacts and contrast-to-noise ratio are missing. The usual slice thickness used for non-EPI-DWI sequences ranges from 2 to 4 mm. The recently developed isotropic 1.5-mm slice thickness non-EPI-DWI at 3T can be considered a major advantage offering 3.4-mm³ voxel volumes.¹⁰ Such a turbo-field echo with diffusion-sensitized driven-equilibrium recall should be considered in the future for high-resolution MR imaging–CT fusion.¹⁰

Registration Process

Registration and fusion processes were performed in a 10-minute clinical workflow using freeware as previously suggested.^{10,17–19} Because the skull base is a nondeformable structure, a rigid coregistration was used for the merging process of high-resolution cross-sectional imaging datasets. To limit observer subjectivity, we did not directly merge DWI and CT scans using a manual fine-tuning. We chose a multistep process involving the selection of 3 invariable landmarks on the 3D-T1 VIBE MR imaging and CT datasets and a reslicing of the $b=1000$ stack on the 3D-T1 VIBE MR imaging dataset. On that basis, 50% of the fusions were qualified as perfect and the remainder as good (< 1 mm), which can still be considered clinically valuable. Imperfect fusion quality could be accounted for by patient motion between the 2 acquisitions. Another accounting factor could be related to the variation between the CT scan isomorphism and the MR imaging matrix diffeomorphism, which depends on magnetic susceptibility. Diffeomorphic artifacts are expected to be larger using ultrafast gradient-echo sequences such as VIBE compared with spin-echo ($b=1000$) sequences. These artifacts could lead to minor voxel mismatch between MR imaging and CT datasets. The use of the recently developed spin-echo 3D sequence (sampling perfection with application-optimized contrasts using different flip angle evolution, SPACE; Siemens) might be an interesting alternative to reduce these artifacts.²⁵ In the present cohort, although 2 patients exhibited rMEC lesions as round pearls in an aerated mastoidectomy cavity, the fusion process was qualified as perfect. Other postprocessing techniques could be used in the future with the

aim of a fully automatic fusion, which should reduce processing time and manual registration bias.²⁶

Clinical Implications for Patients

The present results disclose and further support the idea that fusion of coregistered images can improve rMEC assessment and help in guiding the surgical procedure. Preoperative surgical approaches and specific surgical risks can be expected to be better evaluated, so new developments in endoscopic ear surgery could be expected as part of a safe surgical approach.²⁷ The exact location of rMEC extensions is of high interest because it should allow minimally invasive surgical procedures without any transmastoid surgery conversion during MEC removal.⁶

CONCLUSIONS

Image fusion between coregistered conventional non-EPI-DWI and temporal bone CT significantly improved the local assessment of recurrent cholesteatoma. Further supportive of this additional value, lesion segmentation between and within observer was improved. The impact on operation duration and postoperative complications should be evaluated in future studies.

ACKNOWLEDGMENTS

We acknowledge Yasmina Chaibi (Olea Medical, La Ciotat, France) for her help in data analysis, Professor Richard Nicollas and Dr Brigitte Bourliere for their involvement in patient inclusion, and Professor Jean Gaudard for a thorough review of the statistical section.

REFERENCES

1. Olszewska E, Wagner M, Bernal-Sprekelsen M, et al. **Etiopathogenesis of cholesteatoma.** *Eur Arch Otorhinolaryngol* 2004;261:6–24 CrossRef Medline
2. Kerckhoffs KG, Kommer MB, van Strien TH, et al. **The disease recurrence rate after the canal wall up or canal wall down technique in adults.** *Laryngoscope* 2016;126:980–87 CrossRef Medline
3. Crowson MG, Ramprasad VH, Chapurin N, et al. **Cost analysis and outcomes of a second-look tympanoplasty-mastoidectomy strategy for cholesteatoma.** *Laryngoscope* 2016;126:2574–79 CrossRef Medline
4. Vanden Abeele D, Coen E, Parizel PM, et al. **Can MRI replace a second look operation in cholesteatoma surgery?** *Acta Otolaryngol* 1999;119:555–61 CrossRef Medline
5. Bennett M, Wanna G, Francis D, et al. **Clinical and cost utility of an intraoperative endoscopic second look in cholesteatoma surgery.** *Laryngoscope* 2018;128:2867–71 CrossRef Medline
6. Abdul-Aziz D, Kozin ED, Lin BM, et al. **Temporal bone computed tomography findings associated with feasibility of endoscopic ear surgery.** *Am J Otolaryngol* 2017;38:698–703 CrossRef Medline
7. Muzaffar J, Metcalfe C, Colley S, et al. **Diffusion-weighted magnetic resonance imaging for residual and recurrent cholesteatoma: a systematic review and meta-analysis.** *Clin Otolaryngol* 2017;42:536–43 CrossRef Medline
8. De Foer B, Vercruyse JP, Bernaerts A, et al. **Middle ear cholesteatoma: non-echo-planar diffusion-weighted MR imaging versus delayed gadolinium-enhanced T1-weighted MR imaging—value in detection.** *Radiology* 2010;255:866–72 CrossRef Medline
9. Baráth K, Huber AM, Stämpfli P, et al. **Neuroradiology of cholesteatomas.** *AJNR Am J Neuroradiol* 2011;32:221–29 CrossRef Medline
10. Yamashita K, Hiwatashi A, Togao O, et al. **High-resolution three-dimensional diffusion-weighted MRI/CT image data fusion for cholesteatoma surgical planning: a feasibility study.** *Eur Arch Otorhinolaryngol* 2015;272:3821–24 CrossRef Medline

11. Hanna GG, Hounsell AR, O'Sullivan JM. **Geometrical analysis of radiotherapy target volume delineation: a systematic review of reported comparison methods.** *Clin Oncol (R Coll Radiol)* 2010;22:515–25 CrossRef Medline
12. DeLong ER, DeLong DM, Clarke-Pearson DL. **Comparing the areas under two or more correlated receiver operating characteristic curves: a nonparametric approach.** *Biometrics* 1988;44:837–45 CrossRef Medline
13. Fluss R, Faraggi D, Reiser B. **Estimation of the Youden Index and its associated cutoff point.** *Biom J* 2005;47:458–72 CrossRef Medline
14. Donner A, Koval JJ. **The estimation of intraclass correlation in the analysis of family data.** *Biometrics* 1980;36:19–25 Medline
15. Landis JR, Koch GG. **The measurement of observer agreement for categorical data.** *Biometrics* 1977;33:159–74 CrossRef Medline
16. Varoquaux A, Rager O, Lovblad K-O, et al. **Functional imaging of head and neck squamous cell carcinoma with diffusion-weighted MRI and FDG PET/CT: quantitative analysis of ADC and SUV.** *Eur J Nucl Med Mol Imaging* 2013;40:842–52 CrossRef Medline
17. Locketz GD, Li PM, Fischbein NJ, et al. **Fusion of computed tomography and PROPELLER diffusion-weighted magnetic resonance imaging for the detection and localization of middle ear cholesteatoma.** *JAMA Otolaryngol Neck Surg* 2016;142:947–53 CrossRef Medline
18. Campos A, Mata F, Rebol R, et al. **Computed tomography and magnetic resonance fusion imaging in cholesteatoma preoperative assessment.** *Eur Arch Otorhinolaryngol* 2017;274:1405–11 CrossRef Medline
19. Plouin-Gaudon I, Bossard D, Ayari-Khalfallah S, et al. **Fusion of MRIs and CT scans for surgical treatment of cholesteatoma of the middle ear in children.** *Arch Otolaryngol Neck Surg* 2010;136:878–83 CrossRef Medline
20. Desmots F, Fakhry N, Mancini J, et al. **Shear wave elastography in head and neck lymph node assessment: image quality and diagnostic impact compared with B-mode and Doppler ultrasonography.** *Ultrasound Med Biol* 2016;42:387–98 CrossRef Medline
21. Rosenkrantz AB, Kim S, Lim RP, et al. **Prostate cancer localization using multiparametric MR imaging: comparison of Prostate Imaging Reporting and Data System (PI-RADS) and Likert scales.** *Radiology* 2013;269:482–92 CrossRef Medline
22. Migirov L, Greenberg G, Eyal A, et al. **Imaging prior to endoscopic ear surgery: clinical note.** *Isr Med Assoc J* 2014;16:191–93 Medline
23. Thiriart S, Riehm S, Kremer S, et al. **Apparent diffusion coefficient values of middle ear cholesteatoma differ from abscess and cholesteatoma admixed infection.** *AJNR Am J Neuroradiol* 2009;30:1123–26 CrossRef Medline
24. Dubrulle F, Souillard R, Chechin D, et al. **Diffusion-weighted MR imaging sequence in the detection of postoperative recurrent cholesteatoma.** *Radiology* 2006;238:604–10 CrossRef Medline
25. Lichy MP, Wietek BM, Mugler JP, et al. **Magnetic resonance imaging of the body trunk using a single-slab, 3-dimensional, T2-weighted turbo-spin-echo sequence with high sampling efficiency (SPACE) for high spatial resolution imaging: initial clinical experiences.** *Invest Radiol* 2005;40:754–60 CrossRef Medline
26. Casselman JW, Gieraerts K, Volders D, et al. **Cone beam CT: non-dental applications.** *JBR-BTR* 2013;96:333–53 Medline
27. Bernardeschi D, Lahlou G, De Seta D, et al. **3D endoscopic ear surgery: a clinical pilot study.** *Eur Arch Otorhinolaryngol* 2018;275:379–84 CrossRef Medline

A Persistent Foramen of Huschke: A Small Road to Misery in Necrotizing External Otitis

W.L. van der Meer, M. van Tilburg, C. Mitea, and A.A. Postma

ABSTRACT

BACKGROUND AND PURPOSE: Necrotizing external otitis is a serious complication of external otitis with different spreading patterns. A persistent foramen of Huschke is a dehiscence located antero-inferior in the osseous external ear canal and posterior-medial to the temporomandibular joint. This dehiscence can facilitate extension of infection in an anterior pattern next to classic spread along the fissures of Santorini. The aim of this study was to define the prevalence and size of a persistent foramen of Huschke in patients with necrotizing external otitis.

MATERIALS AND METHODS: We retrospectively examined 78 CT temporal bone studies (39 patients with necrotizing external otitis, 39 control subjects). The side and presence of the foramen were noted, and its prevalence was calculated. The maximal width of the foramen of Huschke was measured in the axial plane and classified as subtle, mild, moderate, or extensive.

RESULTS: A persistent foramen of Huschke was present in 21 patients (26 ears) and 7 control subjects (9 ears). Prevalence was 50% (20/40) and 11.5% (9/78) in affected ears of patients with necrotizing external otitis and control subjects, respectively. Almost all affected ears showed an anterior distribution pattern of necrotizing external otitis. The extensive dehiscence was most common in affected ears.

CONCLUSIONS: An anterior necrotizing external otitis spreading pattern is associated with the presence and increased size of a persistent foramen of Huschke. These findings facilitate the theory that a persistent foramen of Huschke is an additional risk factor for the development of necrotizing external otitis.

ABBREVIATIONS: EAC = external auditory canal; NEO = necrotizing external otitis; TMJ = temporomandibular joint

Necrotizing external otitis (NEO) is a rare-but-serious complication when a persistent external otitis, most commonly caused by the bacteria *Pseudomonas aeruginosa*¹, fails to resolve. The infection can spread via fascial planes to surrounding soft tissues and bone structures. In severe cases, the infection affects intracranial structures and cranial nerves with persistent impairment after treatment.² Patients at risk for NEO most often are elderly with diabetes and/or are immunocompromised, and NEO can have a mortality rate up to 15%.³ Hence, early recognition and tailored treatment with intravenous antibiotics could have a substantial impact on morbidity and mortality.

NEO can be categorized according to an anterior, posterior, medial, or an intracranial spreading pattern or a combination of these aforementioned categories.^{4,5} The classification depends on the affected soft-tissue compartments and bone structures.⁵ In an anterior spreading pattern, the temporomandibular joint (TMJ), masticator space, parotid gland, or surrounding fat planes are involved (Figs 1 and 2). The posterior spreading pattern affects the mastoid process, and the medial spreading pattern affects the sphenoid, clivus, nasopharyngeal or pharyngeal muscles/fat, and cranial nerves IX, X, and XI. The intracranial pattern shows involvement of the jugular fossa, jugular vein, sigmoid sinus, and dura.

The spread of NEO from the external ear canal to its surrounding structures is thought to occur via the fissures of Santorini, also known as the incisurae cartilaginis meatus acustici, by extending through these osteocartilaginous or cartilaginous junctions of the external ear canal, spreading through fascial planes and blood vessels to surrounding compartments (Fig 3). Thus, early changes in NEO can be subtle and therefore easily overlooked. One of the early subtle findings is infiltration of the

Received February 20, 2019; accepted after revision June 30.

From the Departments of Radiology and Nuclear Medicine (W.L.v.d.M., C.M., A.A.P.) and Otorhinolaryngology and Head and Neck Surgery (M.v.T.), Maastricht University Medical Center, Maastricht, the Netherlands; and School for Mental Health and Neuroscience (A.A.P.), Maastricht University, Maastricht, the Netherlands.

Please address correspondence to W.L. van der Meer, MD, Department of Radiology and Nuclear Medicine, Maastricht University Medical Center, P. Debyelaan 25, 6229 HX Maastricht, the Netherlands; e-mail: lieke.vander.meer@mumc.nl

<http://dx.doi.org/10.3174/ajnr.A6161>

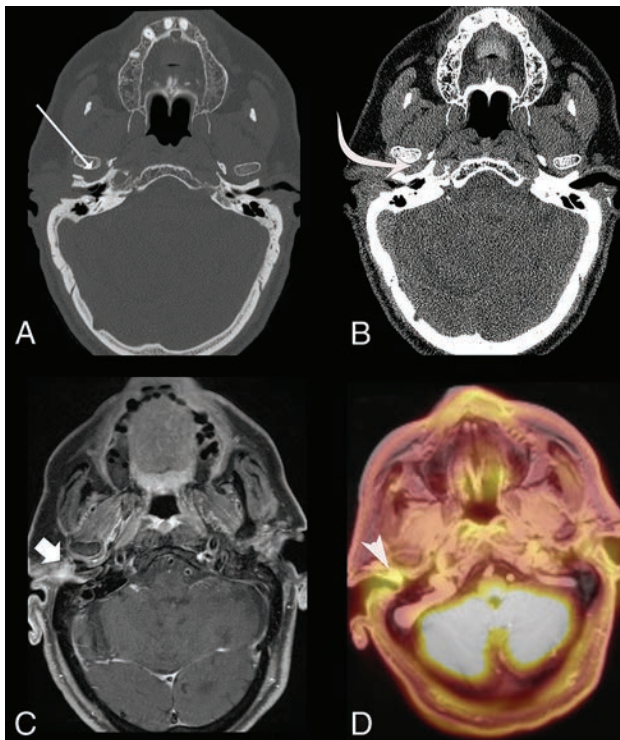


FIG 1. A 79-year-old man with type II diabetes presented with a painful right ear and pain during mastication. CT shows an increased distance of the TMJ (A, *white arrow*) and infiltration of the retrocondylar fat pad and surrounding fat planes (B, *curved arrow*). The contrast-enhanced T1-weighted MR imaging shows enhancement of the retrocondylar fat pad (C, *broad arrow*), with increased FDG accumulation on PET/MR imaging (D, *arrowhead*). The biopsy of the external ear canal was positive for *P Aeruginosa*.

retrocondylar fat pad, which is part of the NEO anterior spreading pattern.⁶ Some patients with NEO have a variant anatomic structure called a persistent foramen of Huschke (foramen tympanicum), a dehiscence located antero-inferior to the osseous external auditory canal (EAC) and posterior-medial to the temporomandibular joint (Fig 3). The foramen of Huschke has been described in relation to EAC salivary fistulas, TMJ herniation, the facilitation of tumor spread, and drainage of odontogenic abscesses in the EAC.⁷⁻¹⁰

The infectious spread from the TMJ to the EAC via the foramen of Huschke may also occur the other way around. A persistent foramen of Huschke can also pose an alternative route for NEO, which will put the TMJ, masticator space, and parotid gland at risk. Identifying this anatomic variation in patients with NEO may help recognize NEO and its extension in early stages of disease, thus preventing consecutive spread to its surrounding tissues, aiding a positive outcome in morbidity and mortality. The goal of this study was to assess the prevalence and size of a persistent foramen of Huschke in patients with NEO and thereby determine its value for routine assessment.

MATERIALS AND METHODS

A PACS survey was conducted with the key words “skull base osteomyelitis,” “necrotizing external otitis,” and “malignant external otitis.” In total, 39 patients diagnosed with NEO on temporal bone high-resolution CT scans in 2005–2018 were retrospec-

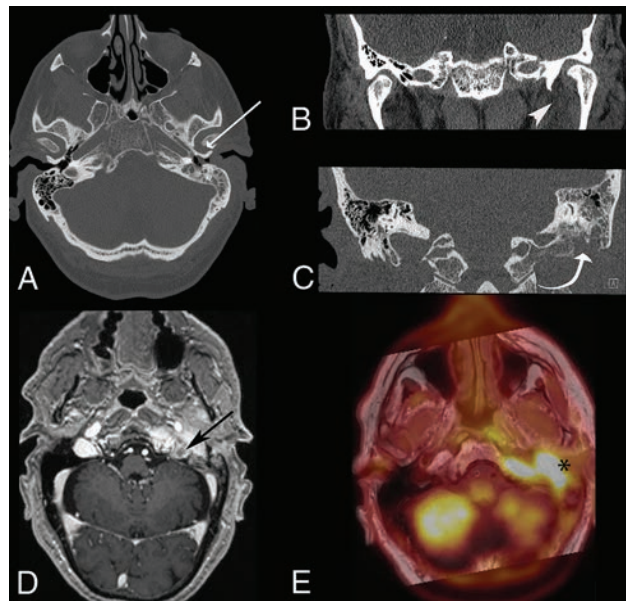


FIG 2. A 76-year-old man without a medical history presented with a painful ear and otorrhea. CT shows an increased distance of the TMJ (A, *white arrow*), obliteration of subtemporal fat lines, and a retrocondylar fat pad sign (B, *arrowhead*), as well as osseous destruction of the mastoid (C, *white curved arrow*). Contrast-enhanced T1-weighted image 2 weeks after diagnosis demonstrates progression of NEO with an anterior, medial, and intracranial spreading pattern complicated by a thrombus in the left jugular vein (D, *black arrow*) with increased FDG accumulation on PET/MR imaging (E, *asterisk*). History revealed non-compliance with antibiotic treatment. Biopsy of the external ear canal was positive for *P Aeruginosa*.

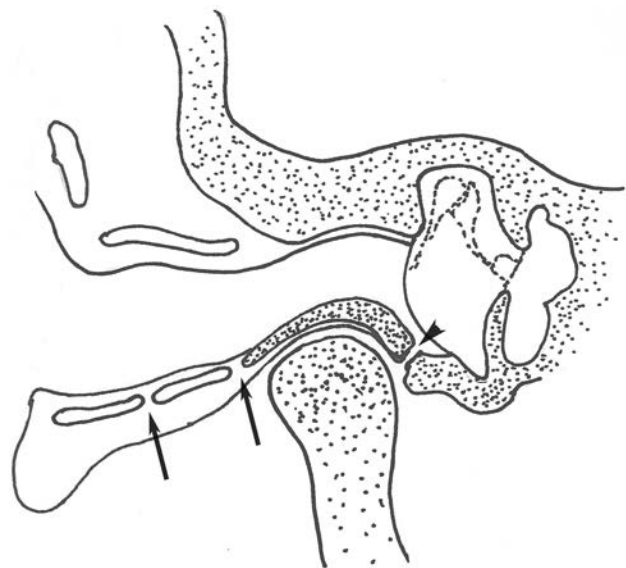


FIG 3. Coronal illustration of the location of the fissures of Santorini and the foramen of Huschke. The fissures of Santorini extend through the osteocartilaginous or cartilaginous junctions of the EAC (arrows). The foramen of Huschke (arrowhead) is located anterior-inferior to the EAC and posterior-medial to the temporomandibular joint.

tively included. All cases of NEO were confirmed by the Ear, Nose, and Throat Department in combination with EAC biopsy results positive for microbiological organisms associated with NEO. Most patients underwent MR imaging, which confirmed the diagnosis of NEO. Scans were assessed for the type of spreading

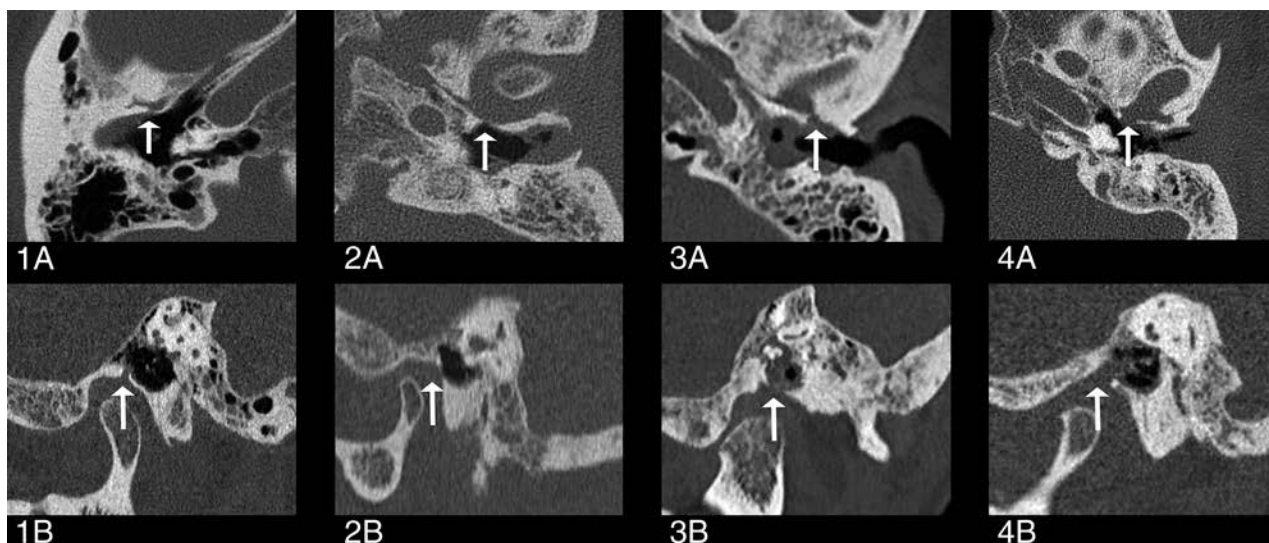


FIG 4. Temporal bone axial and sagittal views of patients with NEO with a persistent foramen of Huschke. The views show a subtle (1A and 1B), mild (2A and 2B), moderate (3A and 3B), and extensive dehiscence (4A and 4B) as indicated by the white arrows.

Table 1: Demographics for patients with NEO and controls^a

Age range (Mean) (yr)	NEO (n = 39)		Controls (n = 39)	
	Women (n = 11)	Men (n = 28)	Women (n = 11)	Men (n = 28)
50–59	1 (51)	2 (50)	1 (59)	2 (56)
60–69	2 (63)	9 (66)	2 (63)	9 (65)
70–79	3 (78)	6 (78)	3 (74)	6 (74)
80 or older	5 (87)	11 (86)	5 (84)	11 (84)

^a Data are number of patients per age range.

pattern and the existence of a persistent foramen of Huschke on the first available CT of the temporal bone during the disease process. CT scans of the temporal bone in the control group with non-NEO or noninflammatory pathology (eg, hearing loss) were matched for age and sex. Control scans with former destruction of the skull (eg, severe cholesteatoma, radiation therapy, or severe otitis media) were excluded. NEO spreading patterns and the presence and/or absence of a foramen of Huschke were scored. The size of the persistent foramen of Huschke was measured as the maximum width in the axial plane and classified as subtle (<0.5 mm), mild (0.5–1.0 mm), moderate (1.0–1.5 mm), or extensive (>1.5 mm) dehiscence (Fig 4). Interpretation and scoring were performed by a radiologist-in-training and a senior head and neck radiologist with >10 years' experience. Scoring discrepancies were solved via consensus. Statistical analyses were performed with SPSS, Version 25 (IBM, Armonk, New York). Frequency and Pearson χ^2 tests were performed with significance levels set at $P < .05$.

RESULTS

Foramen of Huschke

Seventy-eight temporal bone CT studies were performed on 56 male and 22 female subjects with an overall mean age of 74.9 ± 10.8 years (Table 1). A persistent foramen of Huschke was present in 28/78 patients (36%), 21/39 patients with NEO and 7/39 control subjects ($\chi^2 = P < .05$). A persistent foramen of Huschke occurred most often unilaterally and was bilateral in 5 of the 21

Table 2: Prevalence of the foramen of Huschke in patients with NEO and controls

Foramen of Huschke	NEO (n = 39)		Controls (n = 39)		$P < .05$
	No.	Percentage	No.	Percentage	
Absent	18	46%	32	82%	.002 ^a
Present	21	54%	7	18%	.002 ^a
Unilateral	16	41%	5	13%	—
Bilateral	5	13%	2	5%	—
Total	39	100%	39	100%	

Note: — indicates data is not available.

^a Significant.

Table 3: Location of the foramen of Huschke in patients with NEO and controls

Location	Foramen of Huschke			
	Present		Absent	
	No.	Percentage	No.	Percentage
NEO				
Left ear	16	41%	23	59%
Right ear	10	26%	29	74%
Controls				
Left ear	3	8%	36	92%
Right ear	6	15%	33	85%

patients with NEO and 2 of the control subjects, approximately a bilateral occurrence of 25% in both groups (Table 2). In our cohort, no preference for a left or right ear was found (Table 3).

The size of the foramen of Huschke in patients with NEO varied from subtle to extensive. The size was subtle in 6/26, mild in 2/26, moderate in 7/26, and extensive in 11/26 patients. In the latter, 10/11 extensive cases were seen in the affected NEO side (Table 4).

A persistent foramen of Huschke was present in 9 ears (11.5%) of control subjects, of which 2 were bilateral (Table 2). The width of the foramen could be classified as subtle in 6/9, mild in 1/9, and extensive in 2/9 (Table 4). The mean foramen size of the patients with NEO was 2.9 mm in the axial plane (range, 0.2–14.9 mm) versus 1.0 mm (range, 0.2–3.3 mm) in control subjects.

Table 4: Size of the persistent foramen of Huschke specified in controls and patients with NEO

Foramen Size	NEO			Total Control Ears (n = 78)
	Nonaffected Side/Ears (n = 38)	Affected NEO Ears (n = 40)	NEO Total Ears (n = 78)	
Subtle (<0.5 mm)	4	2	6	6
Mild (0.5–1.0 mm)	0	2	2	1
Moderate (1.0–1.5 mm)	1	6	7	0
Extensive (>1.5 mm)	1	10	11	2
Total	6	20	26	9

NEO

Bilateral NEO was present in 1/39; and unilateral NEO, in 38/39 (97%) patients, with a total of 40 affected ears. The anterior spreading pattern was present in all except 1 patient. Twelve patients with NEO showed an anterior spreading pattern in combination with a posterior, medial, or intracranial pattern. A persistent foramen of Huschke was present in 26 ears of patients with NEO, 5 of which showed bilateral foramina (Table 2); 50% (20/40) of NEO-affected ears showed a persistent foramen of Huschke in comparison with 15.8% (6/38) of the unaffected ears (Table 4).

DISCUSSION

The tympanic membrane develops from a tympanic ring with 4 different ossification centers that fuse with the temporal bone.^{11,12} The process of ossification starts at 9 weeks in utero with fusion of the tympanic ring taking up to 5 years.^{11,12} An incomplete medial fusion of the tympanic ring causes a dehiscence located antero-inferior to the osseous external ear canal and posterior-medial to the temporomandibular joint, an anatomic variation also known as a persistent foramen of Huschke.

Several symptoms have been described in relation to a persistent foramen of Huschke. Patients can describe clear discharge often in relation to mastication caused by synovial fluid transport through a fistula between the EAC and the TMJ space.^{7,8} A more prominent dehiscence can cause ear pain or a clicking sensation during mastication because the TMJ retrodiscal or discal tissue protrudes within the EAC.^{13–15} The protrusion of soft tissue into the EAC through the foramen of Huschke can mimic a mass lesion in the EAC. The difference between TMJ soft-tissue herniation and mass lesions can be made with EAC inspection with the patient with an opened mouth because protruded TMJ tissue will retract in this position.^{13,14} As previously mentioned, the foramen of Huschke has been described in relation to infectious or tumorous spread from the TMJ to the EAC.^{9,10} The expansion of the external otitis through the foramen of Huschke to the TMJ was first suggested in 1992, showing discharge in the TMJ without osseous destruction, which can be regarded as one of the earliest stages in NEO.¹⁶

The classic theory of necrotizing external otitis concerns the fissures of Santorini. External otitis can progress via the fissures of Santorini or a temporal bone dehiscence to developing NEO. The relation of the fissures of Santorini as an anterior spreading route for NEO is often suggested, but the fissures are not visible on current imaging techniques due to the fissures of Santorini location and subtle nature. Fistula discharge attributed to the fissures of Santorini often shows positive biochemical results for amylase,

indicating a connection with the parotid gland.⁷ In the case of NEO, one would expect soft-tissue changes of the parotid gland to precede TMJ changes because the osteocartilaginous junction lies more lateral in the EAC. However, of the 38 patients included in our study with an anterior spreading pattern, 11 showed involvement of the parotid space and 34 showed involvement of the TMJ, favoring an infectious spreading via the persistent foramen of Huschke instead or in association with the fissures of Santorini. Thus, an anatomic variation can also be an additional risk factor for progression to NEO.

The prevalence of a persistent foramen of Huschke in the literature ranges from 4.6% to 20%, with a higher prevalence for women and the left ear.^{17–20} The prevalence in the control subjects and unaffected ears in our study is in line with these numbers; however, we did not find a left-sided predominance. We did not investigate a sex difference because the control subjects were sex-matched with the patient group. The prevalence of a persistent foramen in our patient group was 50% in NEO-affected ears; therefore, the prevalence in the diseased ears is far higher than in the healthy population.

Our results support the theory that the foramen of Huschke is a contributing risk factor in the development of necrotizing external otitis because the prevalence of 50% in patients with NEO lies well above the described incidence of 4.6%–38% in overall imaging and cadaver studies.^{11,12,21} The prevalence of a persistent foramen of Huschke has not been investigated in patients with NEO before, to our knowledge. Yeheskeli et al²² investigated the role of involvement of the TMJ in necrotizing external otitis and found that involvement of the TMJ served as a positive clinical factor. The prevalence of TMJ involvement in their study was comparable with the prevalence of the foramen of Huschke; however, the authors did not study the foramen prevalence.²² Our results show that patients with NEO, in addition to a foramen prevalence of 50% at the affected side, often show an extensive dehiscence (>1.5 mm) in contrast to the control group and unaffected ears.

It is difficult to discern whether the dehiscence in patients with NEO is the result of incomplete fusion of the tympanic ring or due to (primary or secondary) bone erosion from the underlying infectious process. Possible erosive changes can therefore skew the trend to a more severe classification. However, an extensive dehiscence was a finding not only in patients with NEO, it was also present in 2/9 control patients. True differentiation between primary bone erosion or incomplete fusion for patients with NEO can only be realized when comparing a respective patient's NEO scan with a preexistent non-NEO afflicted temporal bone scan. The reviewed CT scans were often the first imaging study of the temporal bone. Therefore, the difference between incomplete fusion or bone erosion could not be further distinguished.

One could regard the sample size as a limitation in this study; however, past studies dealt with a corresponding sample size due to the rare nature of NEO. This study with 39 cases of NEO lies well above the average case number per NEO series (22 cases) as reported by a NEO systematic review study.²³ Due to the rare nature of the disease, a prospective study was not feasible to perform in a single center; therefore, we opted for a retrospective cohort design.

The foramen of Huschke has a specified location but not a specified size; therefore, the region should be intensively studied so as not to miss subtle foramina. Cadaver studies showed a variation of the foramen width in the range of 1–5 mm.¹¹ High-resolution CT with a voxel size of 0.25 mm³ can even detect smaller foramina ranging from 0.2 mm.¹⁹ The included CT petrosal scans in our studies were obtained between 2005 and 2018, during which the CT technique, among other parameters, showed a great increase in spatial resolution. The slice thickness used in our study is heterogeneous, ranging from 0.4 to 1 mm, thus leading to a possible underestimation of subtle foramina of Huschke in some patients with NEO. This was not a problem in the current study because the prevalence of the foramen of Huschke in the control group and unaffected ears is in line with literature. Prevalence in the affected NEO ears could potentially be higher.

We demonstrated in our study that the prevalence of a persistent foramen of Huschke is higher in patients with skull base involvement in necrotizing external otitis compared with the healthy population, suggesting a role in the pathophysiology of NEO. Identification of a persistent foramen of Huschke at imaging can help in early identification of an anterior spreading pattern in NEO.

CONCLUSIONS

An anterior spreading pattern from a necrotizing external otitis is associated with the presence and increased size of a persistent foramen of Huschke. These findings suggest a role for the persistent foramen of Huschke next to the fissures of Santorini. Careful inspection in necrotizing external otitis in the region of the foramen of Huschke could identify anterior spread to the skull base in an early stage, aiding in improved patient care and outcome.

Disclosures: W.L. van der Meer—UNRELATED: Employment: Radiology Resident at Maastricht Medical University Center since November 2016. Mark van Tilburg—UNRELATED: Employment: Ear, Nose, and Throat resident.

REFERENCES

- Rubin Grandis J, Branstetter BF 4th, Yu VL. **The changing face of malignant (necrotizing) external otitis: clinical, radiological, and anatomic correlations.** *Lancet Infect Dis* 2004;4:34–39 CrossRef Medline
- Soudry E, Hamzany Y, Preis M, et al. **Malignant external otitis: analysis of severe cases.** *Otolaryngol Head Neck Surg* 2011;144:758–62 CrossRef Medline
- Glikson E, Sagiv D, Wolf M, et al. **Necrotizing otitis externa: diagnosis, treatment, and outcome in a case series.** *Diagn Microbiol Infect Dis* 2017;87:74–78 CrossRef Medline
- Kwon B, Han M, Oh S, et al. **MRI findings and spreading patterns of necrotizing external otitis: is a poor outcome predictable?** *Clin Radiol* 2006;61:495–504 CrossRef Medline
- van Kroonenburgh A, van der Meer W, Bothof R, et al. **Advanced imaging techniques in skull base osteomyelitis due to malignant otitis externa.** *Curr Radiol Rep* 2018;6:1–14 CrossRef Medline
- Lee J, Song, J, Oh S, et al. **Prognostic value of extension patterns on follow-up magnetic resonance imaging in patients with necrotizing otitis externa.** *Arch Otolaryngol Head Neck Surg* 2011;137:688–93 CrossRef Medline
- Rana K, Rathore P, Raj A, et al. **Bilateral spontaneous salivary otorrhea: case report and a review of the literature.** *Int J Pediatr Otorhinolaryngol* 2015;79:1774–77 CrossRef Medline
- Ajduk J, Ries M, Vagic D, et al. **Temporomandibular joint fistula into the external ear canal.** *J Laryngol Otol* 2012;126:837–39 CrossRef Medline
- Jaber S, Rudic M, Keogh I. **Pleomorphic adenoma of the external auditory canal: a rare presentation.** *Case Rep Otolaryngol* 2015;2015:696531 CrossRef Medline
- Pepato A, Yamaji M, Sverzut C, et al. **Lower third molar infection with purulent discharge through the external auditory meatus: case report and review of literature.** *Int J Oral Maxillofac Surg* 2012;41:380–83 CrossRef Medline
- Bhanu PS, Sankar KD. **Incidence of foramen of Huschke in South Andhra population of India.** *J Clin Diagn Res* 2016;10:1–3 CrossRef Medline
- Lacout A, Marsot-Dupuch K, Smoker W, et al. **Foramen tympanicum, or foramen of Huschke: pathologic cases and anatomic CT study.** *AJNR Am J Neuroradiol* 2005;26:1317–23 Medline
- Kim T, Lee S, Kim S, et al. **A case of spontaneous temporomandibular joint herniation into the external auditory canal with clicking sound.** *Korean J Audiol* 2013;17:90–93 CrossRef Medline
- Burlak K, So T, Maclaurin W, et al. **Foramen tympanicum with symptomatic temporomandibular joint herniation.** *Radiol Case Rep* 2018;13:822–24 CrossRef Medline
- Heffez L, Anderson D, Mafee M. **Developmental defects of the tympanic plate: case reports and review of the literature.** *J Oral Maxillofac Surg* 1989;47:1336–40 CrossRef Medline
- Dingle A. **Fistula between the external auditory canal and the temporomandibular joint: a rare complication of otitis externa.** *J Laryngol Otol* 1992;106:994–95 CrossRef Medline
- Tozoglul U, Caglayan F, Harorli A. **Foramen tympanicum or foramen of Huschke: anatomical cone beam CT study.** *Dentomaxillofac Radiol* 2012;41:294–97 CrossRef Medline
- Pekala J, Pekala P, Satapathy B, et al. **Incidence of foramen Tympanicum (of Huschke): comparing cadaveric and radiologic studies.** *J Craniofac Surg* 2018;29:2348–52 CrossRef Medline
- Deniz Y, Geduk G, Zengin A. **Examination of foramen tympanicum: an anatomical study using cone-beam computed tomography.** *Folia Morphol (Warsz)* 2018;77:335–39 CrossRef Medline
- Hashimoto T, Ojiri H, Kawai Y. **The foramen of Huschke: age and gender specific features after childhood.** *Int J Oral Maxillofac Surg* 2011;40:743–46 CrossRef Medline
- Akbulut N, Kursun S, Aksoy S, et al. **Evaluation of foramen Tympanicum using cone-beam computed tomography in orthodontic malocclusions.** *J Craniofac Surg* 2014;25:105–09 CrossRef Medline
- Yehekeli E, Eta R, Gavriel H, et al. **Temporomandibular joint involvement as a positive clinical prognostic factor in necrotizing external otitis.** *J Laryngol Otol* 2016;130:435–39 CrossRef Medline
- Mahdyouun P, Pulcini C, Gahide I, et al. **Necrotizing otitis externa: a systematic review.** *Otol Neurotol* 2013;34:620–29 CrossRef Medline

Subretinal and Retrolaminar Migration of Intraocular Silicone Oil Detected on CT

M. Abdalkader, K. Takumi, M.N. Chapman, G.D. Barest, C. Peeler, and O. Sakai



ABSTRACT

BACKGROUND AND PURPOSE: Intraocular silicone oil injection has been used to treat complicated retinal detachments, and recently its retrolaminar and intracranial migration has been reported. The purpose of this study was to document the prevalence of posterior migration of intraocular silicone oil on head CT and describe the clinical and radiologic findings.

MATERIALS AND METHODS: This retrospective study included 57 patients with intraocular silicone oil injection who underwent unenhanced head CT between November 2008 and July 2018. All images were visually evaluated for subretinal and retrolaminar migration of intraocular silicone oil involving the anterior visual pathway (optic nerve, optic chiasm, and optic tract) and the ventricular system. Attenuation values of those structures were measured and compared with those of the contralateral or adjacent normal structures.

RESULTS: We detected subretinal and retrolaminar silicone oil migration in 7 of the 57 patients (12%), noting silicone oil at the optic nerve head ($n = 2$), retrolaminar optic nerve ($n = 5$), optic chiasm ($n = 3$), optic tract ($n = 3$), and in the lateral ventricles ($n = 1$). Attenuation values of the structures with silicone oil migration were significantly higher than those of the control regions (optic nerve head, 69.2 ± 12.4 vs 29.8 ± 10.2 HU, $P < .001$; retrolaminar optic nerve, 59.9 ± 11.6 vs 30.9 ± 8.6 HU, $P < .001$; optic chiasm, 74.2 ± 11.0 vs 25.6 ± 6.9 HU, $P < .001$; optic tract, 70.1 ± 4.7 vs 28.7 ± 7.2 HU, $P < .001$). No significant ophthalmic or neurologic complications were documented in the patients with silicone oil migration.

CONCLUSIONS: Subretinal and retrolaminar migration of intraocular silicone oil is common. Although there were no apparent complications associated with silicone oil migration, the radiologist and clinician should be aware of this phenomenon.

ABBREVIATION: SiO = silicone oil

Retinal detachment is a serious medical condition that may lead to blindness if not adequately treated.¹ Intraocular silicone oil (SiO) injection following vitrectomy is commonly used as an endotamponade technique to repair complex retinal detachments.² Although considered relatively safe, the use of intraocular SiO is not without complications. The development of glaucoma, cataracts, and keratopathy is a known complication resulting from the diffusion of SiO from the vitreous cavity into adjacent structures.^{3,4}

Retrolaminar SiO migration is a lesser known complication of intraocular SiO injections, occurring when the SiO diffuses posteriorly into the optic apparatus (optic nerve, chiasm, and tract) and potentially into the subarachnoid space and ventricular system.⁵⁻⁷ Vision loss due to optic neuropathy has been reported as a consequence of this posterior migration.⁸ Although several histologic and immunohistopathologic studies have demonstrated SiO migration in the ophthalmologic literature,^{6,9} data about the prevalence and/or radiologic findings of SiO migration are limited.^{5,10-21}

The purpose of this study was to document the prevalence of retrolaminar migration of intraocular SiO on head CT and describe the clinical and radiologic findings.

MATERIALS AND METHODS

Patients

The institutional review board approved this retrospective study. The requirement to obtain written informed consent was waived. Patients with SiO injection treatment who underwent head CT from November 2008 to July 2018 were searched through the

Received February 27, 2019; accepted after revision July 8.

From the Departments of Radiology (M.A., K.T., M.N.C., G.D.B., O.S.), Ophthalmology (C.P.), Neurology (C.P.), Otolaryngology–Head and Neck Surgery (O.S.), and Radiation Oncology (O.S.), Boston Medical Center, Boston University School of Medicine, Boston, Massachusetts.

Paper previously presented, in part, as an oral presentation at: Annual Meeting of the American Society of Neuroradiology and the Foundation of the ASNR Symposium, April 22–27, 2017, Long Beach, California.

Please address correspondence to Osamu Sakai, MD, PhD, Department of Radiology, Boston Medical Center, Boston University School of Medicine, FGH Building, 3rd Floor, 820 Harrison Ave, Boston, MA 02118; e-mail: osamu.sakai@bmc.org



Indicates article with supplemental on-line table.

<http://dx.doi.org/10.3174/ajnr.A6176>

Table 1: Comparisons of clinical features between cases positive and negative for silicone oil migration

Clinical Characteristics	Cases Positive for Migration (n = 7)	Cases Negative for Migration (n = 50)	P	Total (n = 57)
Age (mean) (yr)	56.1 ± 16.6	57.5 ± 18.6	.942 ^a	57.3 ± 18.3
Sex (male/female)	3:4	28:22	.691 ^b	31:26
Indication for silicone oil injection treatment	Diabetic retinal detachment: 4 Trauma: 1 Cytomegalovirus retinitis: 1 Advanced glaucoma: 1	Diabetic retinal detachment: 30 Trauma: 3 Cytomegalovirus retinitis: 2 Advanced glaucoma: 1 Postoperative hemorrhage: 1 Congenital infection: 1 Unknown: 12		Diabetic retinal detachment: 34 Trauma: 4 Cytomegalovirus retinitis: 3 Advanced glaucoma: 2 Postoperative hemorrhage: 1 Congenital infection: 1 Unknown: 12
Interval between silicone injection treatment and CT examination (mean) (mo)	45.8 ± 41.8	37.4 ± 31.7	.779 ^a	39.2 ± 33.5
Intraocular pressure (mean) (mmHg)	23.6 ± 21.4	15.2 ± 5.2	.291 ^a	16.8 ± 10.5

^a Mann-Whitney U test.^b Fisher exact test.

Radiology Information System of our department using a keyword “silicone.” The start date of the study was set as November 2008 when we started including thin-section (1.25 mm) images in our routine unenhanced head CT protocol. Patients who did not have 1.25-mm images were excluded from the study. Patients with severe motion artifacts were also excluded. The electronic medical records were evaluated for patient demographics, relevant medical history, indication of SiO injection treatment, indication for CT examinations, interval between SiO injection treatment and CT examination, ophthalmic examination findings, and intraocular pressure (millimeters of mercury) (Table 1 and On-line Table).

CT Imaging Techniques

All unenhanced head CT examinations were axially acquired at 5- and 1.25-mm section thickness using 64-detector row CT scanners (LightSpeed VCT; GE Healthcare, Milwaukee, Wisconsin) with soft-tissue and bone algorithm reconstructions per our institutional clinical protocol. Axial soft-tissue algorithm-reconstructed 1.25-mm images were used for analysis.

Qualitative Imaging Analysis

All images were visually evaluated for subretinal and retrolaminar migration of SiO, which was defined as areas of increased attenuation of ≥1 component of the visual tract (optic nerve head, retrolaminar optic nerve, optic chiasm, and optic tract) or within the ventricular system. Posterior migration of silicone was assessed by 2 radiologists (M.A. and K.T., with 3 and 17 years of experience in head and neck radiology, respectively) who independently reviewed the CT images; any discrepancies between the 2 radiologists were resolved during a third analysis session in which a decision was reached by consultation with a third radiologist (O.S., with 25 years of experience in head and neck radiology).

Quantitative Imaging Analysis

Attenuation values of the intraocular SiO and the visually identified regions in the visual pathway and ventricles were measured in Hounsfield units. We placed single, as-large-as-

possible, freeform ROIs within each region on the image with the largest cross-sectional area, avoiding partial volume effects. The attenuation value of the optic nerve was measured at the midportion of the intraorbital segment. Care was taken not to include calcification, partial volume effects, or artifacts within the ROIs. The difference between each region and its contralateral side was calculated as the absolute difference in the attenuation value. When measuring the optic chiasm or bilateral lesions, comparison with an adjacent normal structure was performed instead.

Statistical Analysis

We compared the clinical information, ophthalmologic findings, and CT features between cases positive and negative for migration. The Fisher exact test was used to compare sex, age, the interval between SiO injection and CT examination, intraocular pressure, and attenuation values were compared using the Mann-Whitney U test. All data for continuous variables are presented as mean ± SD. A P value < .05 was significant in all analyses. All statistical analyses were performed using SPSS, Version 23.0 (IBM, Armonk, New York).

RESULTS

Patients

Fifty-eight patients with a history of intraocular SiO injection who underwent unenhanced head CT examinations for various clinical indications between November 2009 and July 2018 were identified. Among these, 1 patient who did not have 1.25-mm images was excluded. Ultimately, 57 patients (31 men and 26 women; mean age, 57 years; range, 18–87 years) with intraocular SiO injection were included in this study. Nineteen patients were treated with intraocular SiO injection on the right side, and 34 patients, on the left side; 4 patients were treated on both sides.

Clinical, Ophthalmic, and Radiologic Characteristics of Posterior Migration of Intraocular Silicone Oil

The clinical and CT imaging features of SiO migration cases are summarized in the On-line Table. Posterior migration of

intraocular SiO was identified in 7 of the 57 patients (12.3%) (4 men and 3 women; mean age, 56 years; range, 23–71 years) with 7 eyes of the 61 SiO-treated eyes (11.5%), with SiO at the optic nerve head ($n=2$), retrolaminar optic nerve ($n=5$), optic chiasm ($n=3$), optic tract ($n=3$), and in the lateral ventricles ($n=1$). Two patients had migration to 3 locations each (optic nerve, optic chiasm, and optic tract), and 1 patient, to 4 locations (optic nerve, optic chiasm, optic tract, and lateral ventricles). Representative cases of retrolaminar SiO migration are shown in Figs 1–3.



FIG 1. Subretinal silicone oil migration (case 2). Axial CT image obtained 1 week following right intraocular silicone oil injection demonstrates a punctate region of increased attenuation at the optic nerve head (arrow).

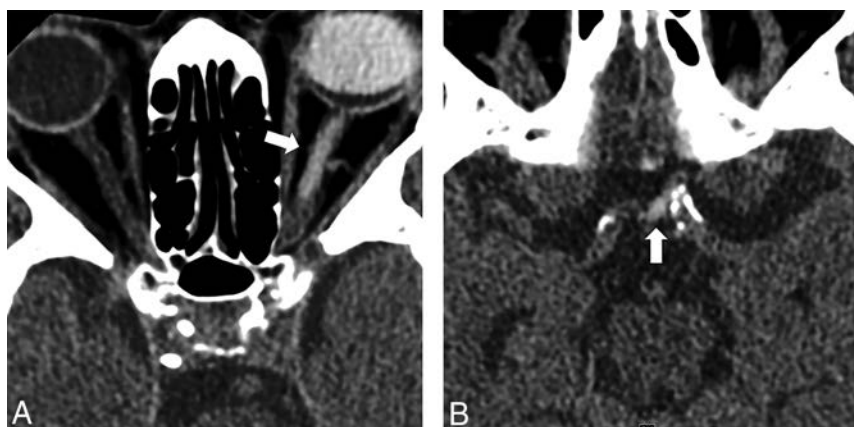


FIG 2. Retrolaminar silicone oil migration at the level of the retrolaminar optic nerve and optic chiasm (case 6). A and B, Axial CT images 1 year after left intraocular silicone oil injection demonstrate abnormal increased attenuation of the intraorbital segment of the left optic nerve (A, arrow) and nodular increased attenuation at the optic chiasm (B, arrow).

Comparison of Clinical Findings between Cases Positive and Negative for Migration

Clinical characteristics in cases positive and negative for migration are summarized in Table 1.

We had recorded vision for 34 of the 57 patients in the cohort (4/7 patients positive for SiO migration and 30/50 negative for SiO migration). For the cases positive for SiO migration, 1 patient had 20/400 vision, 1 had finger-counting vision, and 4 had no light perception vision. For the SiO cases negative for migration, 3 patients had 20/400 vision, 3 had finger-counting vision, 5 had hand motion vision, 8 had light perception vision, and 11 had no light perception vision. On the basis of the available acuity data, there did not appear to be a difference between the cohorts positive and negative for SiO migration ($P=.517$). The best-corrected acuity in both groups ranged from 20/400 to no light perception vision.

There was no significant difference in age and sex between cases positive and negative for migration ($P=.942$, $.691$, respectively). The interval between silicone injection treatment and CT examination was not significantly different between cases positive and negative for migration (45.8 ± 41.8 versus 37.4 ± 31.7 months, $P=.779$). Retrolaminar SiO migration was present as early as 1 week and as late as 4 years after injection. Intraocular pressure elevation had been documented in 3 patients with SiO migration. Intraocular pressure on the side of silicone injection treatment showed no significant difference between cases positive ($n=5$) and negative for migration ($n=20$) (23.6 ± 21.4 versus 15.2 ± 5.2 mm Hg, $P=.291$).

Quantitative CT Analyses

The attenuation value of intraocular SiO was 91.5 ± 12.5 HU, with no significant difference between cases positive and negative for migration (94.1 ± 2.2 versus 91.1 ± 13.3 HU, $P=.228$). Attenuation values of the normal structures were not significantly different between the silicone injection side and the contralateral side (optic nerve head, 30.6 ± 13.8 versus 31.4 ± 9.5 HU, $P=.173$; retrolaminar optic nerve, 34.4 ± 12.9 versus 30.4 ± 7.6 HU, $P=.206$; optic tract, 31.5 ± 11.5 versus 27.9 ± 7.1 HU, $P=.108$; whole region 32.2 ± 12.8 versus 30.0 ± 8.2 HU, $P=.717$). Attenuation values of the regions with SiO migration were significantly higher than those in the control regions (optic nerve head, 69.2 ± 12.4 versus 29.8 ± 10.2 HU, $P<.001$; retrolaminar optic nerve, 59.9 ± 11.6 versus 30.9 ± 8.6 HU, $P<.001$; optic chiasm, 74.2 ± 11.0 versus 25.6 ± 6.9 HU, $P<.001$; optic tract, 70.1 ± 4.7 versus 28.7 ± 7.2 HU, $P<.001$; whole region, 67.0 ± 10.9 versus 29.2 ± 8.6 HU, $P<.001$) (Table 2). One case showed high attenuation in both lateral ventricles (right side, 80.1 HU; left side, 78.8 HU) (Fig 3).

DISCUSSION

Intraocular SiO injection is widely used in the management of complex retinal



FIG 3. Retrolaminar silicone oil migration to the retrolaminar optic nerve and optic chiasm and within the lateral ventricles (case 4). Axial CT images 6 years after left intraocular silicone oil injection demonstrate tubular increased attenuation of the intraorbital segment of the left optic nerve (A, arrow), nodular hyperattenuation in the optic chiasm/optic tract (B, arrow), and biconvex hyperattenuation in the nondependent regions of the frontal horns of the lateral ventricles (C, arrows).

Table 2: Comparisons of attenuation values in the visual tract structures between silicone oil migration lesions and normal regions^a

Structures (Lesion: Normal)	Silicone Oil Migration Lesion	Normal Region	<i>p</i> ^b
Optic head (2:112)	69.2 ± 12.4	29.8 ± 10.2	<.001
Optic nerve (5:119)	59.9 ± 11.6	30.9 ± 8.6	<.001
Optic chiasm (3:53)	74.2 ± 11.0	25.6 ± 6.9	<.001
Optic tract (3:109)	70.1 ± 4.7	28.7 ± 7.2	<.001

^a Data are presented as means. Attenuation values are in Hounsfield units.

^b Mann-Whitney *U* test.

detachments and is considered relatively safe and effective in vitreoretinal surgery.^{2,22,23} Despite its relatively safe profile, SiO may diffuse into various ocular and extraocular tissues, resulting in complications such as glaucoma, keratopathy, and cataract formation.^{3,4} It may also diffuse posteriorly into the subretinal space, optic nerve, optic chiasm, subarachnoid spaces, and potentially the ventricular system. This phenomenon, first described by Ni et al, in 1983,⁶ is known as subretinal or retrolaminar migration of intraocular SiO. The term “retrolaminar” refers to the migration of silicone droplets past the lamina cribrosa, the main structural element where the retinal ganglion cell axons and the central retinal vein and artery enter or exit the eye.²⁴ Although many case reports have described retrolaminar SiO migration, no radiologic studies addressing the frequency or the radiologic features of this phenomenon were found. We believe this is the first study to show the frequency of retrolaminar SiO migration on CT images along with clinical correlation. In this study, migration was detected in 12% of patients, which is comparable with histopathologic studies performed on enucleated eyes with silicone injection (11%–24%).^{9,25,26} Migration of SiO was noted at the optic nerve head, retrolaminar optic nerve, optic chiasm, optic tract, and in the lateral ventricles, and those findings were confirmed by quantitative analyses.

Retrolaminar SiO migration is believed to be a benign phenomenon usually detected incidentally on cross-sectional imaging.⁵ However, visual symptoms have been reported and are thought to be related to silicone-induced optic neuropathy secondary to macrophage infiltration.^{9,26,27} In our series, no

significant neuro-ophthalmologic or neurologic complications related to SiO migration have been documented in the medical records.

The exact mechanism of SiO migration remains uncertain. The role of elevated intraocular pressure in SiO migration was first described by Shields in 1989.⁵ However, not all of our cases or all the published cases were associated with pre-existing elevated intraocular pressure.²⁸ Intraocular pressure at the side of SiO injection treatment in cases positive for migration was slightly higher than that in cases negative for it in our results, though the difference was not statistically significant.

More recent studies suggest that SiO may infiltrate or diffuse directly into the retinal layers and then into the optic nerve by infiltrating along the retinal nerve fibers through the lamina cribrosa. In 2006, Kuhn et al²⁹ proposed that optic pits (congenital abnormalities of the optic nerve head) may serve as an entry point for the retrolaminar migration of SiO. This infiltration may be facilitated by increased intraocular pressure.⁵ The entry of SiO into the subarachnoid space and then the ventricular system may be explained by the passage of the SiO droplets directly from the vitreous space or from the optic nerve into the perioptic subarachnoid spaces through the perivascular spaces of the central retinal vessels where they pierce the optic nerve.^{5,8,15} The diffusion of SiO into the ventricular system is less frequently encountered than into the optic nerve. Boren et al⁵ found 15 case reports of intraventricular SiO.

Silicone oil is usually reported as hyperattenuating on CT images with attenuation ranging between 60 and 140 HU, depending on the viscosity and the location of the SiO.^{10,30} Our qualitative results, supported by quantitative analysis, showed that attenuation values of the regions with SiO migration were significantly higher than those in control regions. At the optic chiasm, only ipsilateral nodular high attenuation was detected. Within the ventricular system, the SiO characteristically floats in nondependent locations because of its lower specific gravity relative to CSF. On MR imaging, SiO has been reported to be hyperintense relative to CSF or contralateral normal vitreous on T1-weighted images. MR imaging may detect SiO droplets as small as 1 mm.^{3,31}

Radiologists should be aware of the occurrence of SiO migration, though it is relatively rare and often without clinical symptoms. Knowledge of the appearance and common locations on CT is important to avoid misdiagnosis of subarachnoid or intraventricular hemorrhage or tumor.

Our study has several limitations. Because posterior migration of SiO is relatively rare, the number of cases positive for migration was small, limiting the statistical power and accuracy of the prevalence. Second, this was a retrospective study that may have been subject to selection bias. Determination of the timing of and chronologic changes in migration was not possible for many patients because imaging follow-up after intraocular injection or after identifying migration is not routinely performed. A detailed ophthalmologic examination including intraocular pressure was not available in all cases, and none had histopathologic confirmation.

CONCLUSIONS

Retrolaminar migration of intraocular SiO is a common phenomenon. Radiologists should be aware of its occurrence and familiar with its imaging characteristics and patterns of migration to prevent misdiagnosis.

Disclosures: Margaret M. Chapman—UNRELATED: Consultancy: Boston Imaging Core Lab. Glenn D. Barest—UNRELATED: Consultancy: Boston Imaging Core Lab. Osamu Sakai—UNRELATED: Consultancy: Boston Imaging Core Lab.

REFERENCES

1. Rothova A, Suttorp-van Schulten MS, Frits Treffers W, et al. **Causes and frequency of blindness in patients with intraocular inflammatory disease.** *Br J Ophthalmol* 1996;80:332-36 CrossRef Medline
2. Cockerham WD, Schepens CL, Freeman HM. **Silicone injection in retinal detachment.** *Arch Ophthalmol* 1970;83:704-12 CrossRef Medline
3. Federman JL, Schubert HD. **Complications associated with the use of silicone oil in 150 eyes after retina-vitreous surgery.** *Ophthalmology* 1988;95:870-76 CrossRef Medline
4. Riedel KG, Gabel VP, Neubauer L, et al. **Intravitreal silicone oil injection: complications and treatment of 415 consecutive patients.** *Graefes Arch Clin Exp Ophthalmol* 1990;28:19-23 CrossRef Medline
5. Boren RA, Cloy CD, Gupta AS, et al. **Retrolaminar migration of intraocular silicone oil.** *J Neuroophthalmol* 2016;36:439-47 CrossRef Medline
6. Ni C, Wang WJ, Albert DM, et al. **Intravitreal silicone injection: histopathologic findings in a human eye after 12 years.** *Arch Ophthalmol* 1983;101:1399-1401 CrossRef Medline
7. Filippidis AS, Conroy TJ, Maragos GA, et al. **Intraocular silicone oil migration into the ventricles resembling intraventricular hemorrhage: case report and review of the literature.** *World Neurosurg* 2017;102:695.e7-95.e10 CrossRef Medline
8. Papp A, Kiss EB, Timár O, et al. **Long-term exposure of the rabbit eye to silicone oil causes optic nerve atrophy.** *Brain Res Bull* 2007;74:130-33 CrossRef Medline
9. Wickham L, Asaria RH, Alexander R, et al. **Immunopathology of intraocular silicone oil: enucleated eyes.** *Br J Ophthalmol* 2007;91:253-57 CrossRef Medline
10. Mathews VP, Elster AD, Barker PB, et al. **Intraocular silicone oil: in vitro and in vivo MR and CT characteristics.** *AJNR Am J Neuroradiol* 1994;15:343-47
11. Chiao D, Ksendzovsky A, Buell T, et al. **Intraventricular migration of silicone oil: a mimic of traumatic and neoplastic pathology.** *J Clin Neurosci* 2015;22:1205-07 CrossRef Medline
12. Mathis S, Boissonnot M, Tasu JP, et al. **Intraventricular silicone oil: a case report.** *Medicine (Baltimore)* 2016;95:e2359 CrossRef Medline
13. Chang CC, Chang HS, Toh CH. **Intraventricular silicone oil.** *J Neurosurg* 2013;118:1127-29 CrossRef Medline
14. Fangtian D, Rongping D, Lin Z, et al. **Migration of intraocular silicone into the cerebral ventricles.** *Am J Ophthalmol* 2005;140:156-58 CrossRef Medline
15. Eller AW, Friberg TR, Mah F. **Migration of silicone oil into the brain: a complication of intraocular silicone oil for retinal tamponade.** *Am J Ophthalmol* 2000;129:685-88 CrossRef Medline
16. Mayl JJ, Flores MA, Stelzer JW, et al. **Recognizing intraventricular silicone.** *Emerg Radiol* 2018;25:215-18 CrossRef Medline
17. Bobba S, Fox OJK, Lee MB, et al. **Contiguous silicone oil migration from the vitreous cavity to the optic tract.** *J Neuroophthalmol* 2017;37:464-65 CrossRef Medline
18. Gnanalingham J, McCreary R, Charles S, et al. **Migration of intraocular silicone oil into brain.** *BMJ Case Rep* 2017;2017 CrossRef Medline
19. Ascaso FJ, Grzybowski A. **Subarachnoidal migration of intraocular silicone oil.** *Acta Neurochir (Wien)* 2017;159:807 CrossRef Medline
20. Cebula H, Kremer S, Chibbaro S, et al. **Subarachnoidal migration of intraocular silicone oil.** *Acta Neurochir (Wien)* 2017;159:347-48 CrossRef Medline
21. Potts MB, Wu AC, Rusinak DJ, et al. **Seeing floaters: a case report and literature review of intraventricular migration of silicone oil tamponade material for retinal detachment.** *World Neurosurg* 2018;115:201-05 CrossRef Medline
22. Watzke RC. **Silicone retinopathy for retinal detachment: a long-term clinical evaluation.** *Arch Ophthalmol* 1967;77:185-96 CrossRef Medline
23. Azen SP, Scott IU, Flynn HW Jr, et al. **Silicone oil in the repair of complex retinal detachments: a prospective observational multicenter study.** *Ophthalmology* 1998;105:1587-97 CrossRef Medline
24. Jonas JB, Berenshtein E, Holbach L. **Anatomic relationship between lamina cribrosa, intraocular space, and cerebrospinal fluid space.** *Invest Ophthalmol Vis Sci* 2003;44:5189-95 CrossRef Medline
25. Biswas J, Verma A, Davda MD, et al. **Intraocular tissue migration of silicone oil after silicone oil tamponade: a histopathological study of enucleated silicone oil-filled eyes.** *Indian J Ophthalmol* 2008;56:425-28 CrossRef Medline
26. Budde M, Cursiefen C, Holbach LM, et al. **Silicone oil-associated optic nerve degeneration.** *Am J Ophthalmol* 2001;131:392-94 CrossRef Medline
27. Mukai N, Lee PF, Schepens CL. **Intravitreal injection of silicone: an experimental study, II: histochemistry and electron microscopy.** *Ann Ophthalmol* 1972;4:273-87 Medline
28. Knecht P, Groscurth P, Ziegler U, et al. **Is silicone oil optic neuropathy caused by high intraocular pressure alone? A semi-biological model.** *Br J Ophthalmol* 2007;91:1293-95 CrossRef Medline
29. Kuhn F, Kover F, Szabo I, et al. **Intracranial migration of silicone oil from an eye with optic pit.** *Graefes Arch Clin Exp Ophthalmol* 2006;244:1360-62 CrossRef Medline
30. Hruby PM, Poley PR, Terp PA, et al. **Headaches secondary to intraventricular silicone oil successfully managed with ventriculoperitoneal shunt.** *Retin Cases Brief Rep* 2013;7:288-90 CrossRef Medline
31. Kiilgaard JF, Milea D, Løgager V, et al. **Cerebral migration of intraocular silicone oil: an MRI study.** *Acta Ophthalmol* 2011;89:522-25 CrossRef Medline

Zero TE MRI for Craniofacial Bone Imaging

A. Lu, K.R. Gorny, and M.-L. Ho



ABSTRACT

SUMMARY: Zero TE MR imaging is a novel technique that achieves a near-zero time interval between radiofrequency excitation and data acquisition, enabling visualization of short-T2 materials such as cortical bone. Zero TE offers a promising radiation-free alternative to CT with rapid, high-resolution, silent, and artifact-resistant imaging, as well as the potential for “pseudoCT” reconstructions. In this report, we will discuss our preliminary experience with zero TE, including technical principles and a clinical case series demonstrating emerging applications in neuroradiology.

ABBREVIATIONS: RF = radiofrequency; SAR = specific absorption rate; ZTE = zero TE

Children in the United States undergo >5 million diagnostic CT examinations per year. For certain indications (eg, acute screening and cortical bone assessment), CT remains a first-line technique. However, adverse effects from radiation are of great concern and include both deterministic (developmental disruption, skin damage, cataracts, sterility, radiation sickness) and stochastic effects (cancer, hereditary defects, growth impairment). These effects are magnified in children due to the increased sensitivity of developing tissues/organs, predisposing conditions that increase susceptibility, and greater cumulative lifetime risk of radiation exposure.¹ Concerns regarding the adverse effects of radiation in the pediatric population have prompted the “Image Gently” campaign.²

Received March 6, 2019; accepted after revision July 8.

From the Department of Radiology, Nationwide Children’s Hospital (M.-L.H.), The Ohio State University College of Medicine, Columbus, Ohio; and Department of Medical Physics (A.L., K.R.G.), Mayo Clinic, Rochester, Minnesota.

This work was supported by a Siemens/Radiological Society of North America Scholar Grant, a Society for Pediatric Radiology Pilot Award, and an American Society of Head and Neck Radiology William N. Hanafee Research Grant.

Poster previously presented at: Annual Meeting of the International Society for Magnetic Resonance in Medicine, April 22-27, 2017; Honolulu, Hawaii. Work was pertinent to the article, but not representing the majority of content.

Improved Delineation of Air-Bone Interface in In-Vivo High-Resolution Bright Bone ZTE MRI at 3T. Electronic exhibit previously presented at: Annual Meeting of the Radiological Society of North America, November 25-30, 2018; Chicago, Illinois. Improved Imaging of Craniosynostosis with Cinematic Rendering and ZTE MRI.

Please address correspondence to Mai-Lan Ho, MD, Department of Radiology, Nationwide Children’s Hospital, The Ohio State University College of Medicine, Columbus, OH, 700 Children’s Dr, ED4, Columbus, OH 43205; e-mail: mailanho@gmail.com

Indicates article with supplemental on-line photos.

<http://dx.doi.org/10.3174/ajnr.A6175>

Zero TE (ZTE) MR imaging has recently emerged as a promising alternative technique that achieves a near-zero time interval between the end of the radiofrequency (RF) excitation and the start of data acquisition. Unlike the conventional RF pulse sequences, the ZTE sequence begins a readout period immediately after the RF pulse, enabling visualization of short-T2 materials (ie, on the order of ≤ 1 ms) such as cortical bone (On-line Fig 1).³⁻⁶ The ZTE sequence is rapid, high-resolution, silent, and resilient to artifacts caused by motion and B_0 inhomogeneity—characteristics that are well-suited to pediatric use.⁷⁻⁹ Raw images demonstrate relative signal void compared with surrounding soft tissues, colloquially known as a “black-bone” display. There is computational potential for “bright-bone” reconstructions that are visually analogous to CT (Figure).^{10,11} Prior work has demonstrated the promise of ZTE and its related techniques, ultrashort-TE and gradient-echo MR imaging, in bone imaging applications, including craniofacial, temporal bone, jaw, and spine.¹²⁻¹⁷ Small clinical case series and ex vivo studies have partially validated ZTE for cranial vault, trauma, and bone microstructural imaging.^{18,19} With ongoing MR imaging technical advances enabling ever-faster scan times and higher contrast/spatial resolution, there is a potential for this single technique to provide comprehensive imaging assessment for patients, a “one-stop shop.” In this report, we discuss our initial experience with ZTE and provide multiple examples demonstrating the diagnostic utility of the sequence for craniofacial bone imaging.

MATERIALS AND METHODS

Technical Considerations

In ZTE, readout gradients are turned on before the RF pulse so that data acquisition can begin immediately after excitation. This

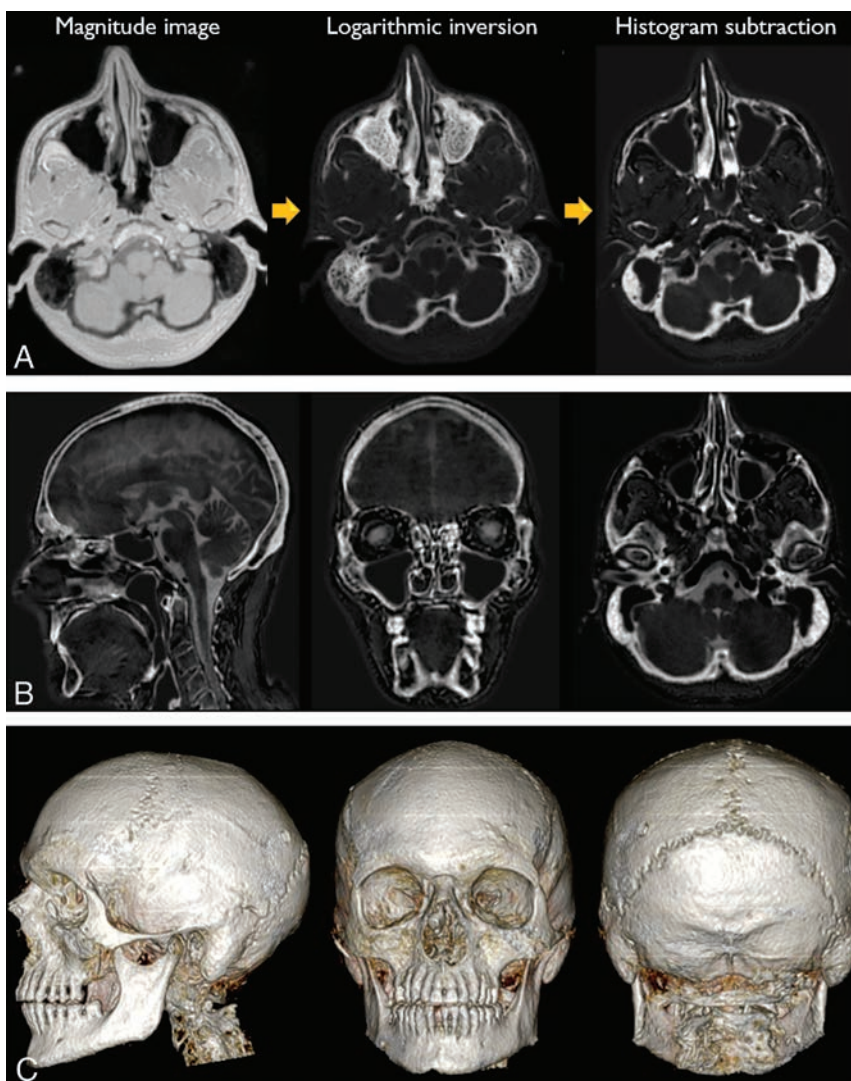


FIGURE. ZTE image display. *A*, Raw magnitude black-bone images underwent signal intensity correction on a section-by-section basis with normalization to mean soft-tissue signal. Multi-resolution ROI-based correction was then applied to account for residual signal intensity variations. Logarithmic inversion of the intensity-corrected data yielded bright-bone images. Histogram subtraction was used to identify and mask the peak signal of air, thus generating the final pseudoCT image. *B*, Sample sagittal, coronal, and axial reformats of pseudoCT reconstruction. *C*, 3D volume-renderings were generated at a separate workstation.

requires high-performance coils with rapid transmit/receive switching capabilities and uses center-out k -space encoding. With ZTE, the readout gradient is already on during the RF pulse, precluding conventional section/slab selection. This necessitates a high-bandwidth excitation with a short-duration hard pulse to ensure that the excitation is as homogeneous and as consistent as possible across the entire FOV from repetition to repetition. The RF excitation is immediately followed by a 3D data acquisition. Gradients are used continuously and modulated between repetitions to sample data along radial trajectories in k -space, rather than being rapidly turned on and off. This process minimizes mechanical vibration and enables a virtually silent technique. Fully sampling the k -space with radial trajectories requires significantly more repetitions (TRs) than an equivalent 3D Cartesian

acquisition. Reduction of total scan time is achieved with the use of short TRs and small flip angles for quasi-steady-state magnetization. Most scan time is targeted toward data acquisition, with minimal dead time occurring during the RF pulse and a single gradient step (On-line Fig 1).³⁻⁶ This feature permits rapid isotropic scanning with high resistance to artifacts, including susceptibility and motion. The technique uses lower changes in amplitude over time (dB/dt) than conventional sequences; low flip angles and built-in scanner safety measures counter the short RF pulse duration that would otherwise raise concern for a high specific absorption rate (SAR).⁹

Patient Indications

Imaging examinations (CT and MR imaging) were ordered by referring physicians for various diagnostic indications, including craniostylosis, trauma, head and neck cancer, radiation therapy, and surgical planning and follow-up. Sedation or anesthesia or both were used for imaging only when deemed medically necessary by the referring clinician. In patients undergoing MR imaging, ZTE images of the whole head were acquired using FDA-approved product hardware (8-channel brain coil array; GE Healthcare, Milwaukee, Wisconsin) and software (Silenz; GE Healthcare).^{7,8} Imaging was preferentially performed at 3T (Discovery MR750w, DV 26.0 software; GE Healthcare), except for patients with MR imaging-conditional devices necessitating imaging at 1.5T (Optima MR450w, DV 26.0 software; GE Healthcare). The ZTE sequence had the

following parameters: 3D imaging mode with sagittal acquisition; TE = 0.016 ms, FOV = 18 × 18 cm, readout matrix = 180 × 180 × 180, section thickness = 1 mm, NEX = 1, receiver bandwidth = 31.25 kHz, flip angle = 2°. These yielded whole-head coverage at a 1-mm isotropic voxel size. Sequence scan time was 2 minutes at 3T and 2 minutes 30 seconds at 1.5T. Two separate data acquisitions were obtained in each patient, for a total imaging time of 4–5 minutes. We used 2 relatively short acquisitions rather than a single acquisition with a higher number of averages to reduce the overall impact of patient motion. All SAR measurements were confirmed to be within FDA safety limits based on predetermined scanner settings. The institutional review board at Mayo Clinic approved retrospective review and analysis of CT and MR images.

Image Postprocessing

By means of a novel technique developed at our institution, source images underwent postprocessing using an off-line Matlab code (MathWorks, Natick, Massachusetts) to improve bone-air differentiation and generate “bright-bone” reconstructions visually analogous to CT.²⁰ For most patients, both ZTE acquisitions were averaged to achieve better SNR after rigid body registration. In cases where 1 ZTE acquisition was visibly distorted by motion and the other was not, only the acquisition with less motion was used for postprocessing, albeit with a lower total SNR. Raw magnitude images underwent signal intensity correction on a section-by-section basis, with normalization to mean soft-tissue signal within each section. Multiresolution ROI-based intensity correction was then applied to account for residual signal intensity variations and thus reduce overall image noise.²¹ Logarithmic inversion of the intensity-corrected data yielded preliminary bright-bone images, but without optimal bone-air delineation. An intensity histogram was generated and an intensity mask was selected to remove the peak signal of air, generating the final pseudoCT image and enabling generation of 3D volume-renderings at a separate workstation (Fig 1).

Case Series

Fourteen patients (2 months to 17 years of age) were successfully imaged. The following examples demonstrate that ZTE was qualitatively comparable with CT for pre- and postoperative assessment of bony abnormalities of the skull, face, and craniocervical junction. The additional value of MR imaging was provided for brain parenchymal and soft-tissue characterization in multiple instances.

Patient 1 was a 3-month-old boy with left anterior plagiocephaly. CT and ZTE comparably demonstrated premature fusion of the left coronal suture with associated calvarial flattening and harlequin eye deformity. The remaining cranial sutures were confirmed to be patent (On-line Fig 2).

Patient 2 was a 7-month-old girl with Apert syndrome. CT and ZTE both demonstrated multisuture craniosynostosis with turribrachycephaly. Gyral remodeling of the inner table (“copper beaten” appearance) was appreciated on both modalities and reflective of increased intracranial pressure. Intracranial malformations were more fully depicted on MR imaging (On-line Fig 3).

Patient 3 was a 2-year-old girl with achondroplasia. CT and ZTE both demonstrated the characteristic J-shaped sella and foramen magnum stenosis. Intracranial abnormalities were more completely imaged on MR imaging (On-line Fig 4).

Patient 4 was a 6-year-old boy with Saethre-Chotzen syndrome. MR imaging was degraded by severe patient motion. Nevertheless, CT and ZTE both demonstrated craniocervical segmentation abnormality with anterior homeotic transformation and basilar impression (On-line Fig 5).

Patient 5 was a 7-month-old boy with hydrocephalus postshunting with worsening posterior plagiocephaly. MR imaging was performed at 1.5T for the patient’s MR imaging-compatible Strata shunt (Medtronic, Minneapolis, Minnesota). CT and ZTE both demonstrated the course of the shunt catheter. There was

secondary flattening of the right parietal calvaria subjacent to the shunt valve, without synostosis. No appreciable difference in diagnostic image quality was observed on the 1.5T scan. Brain abnormalities were more completely characterized on MR imaging than on CT (On-line Fig 6).

Patient 6 was a 15-month-old girl with Shprintzen-Goldberg syndrome postshunting. MR imaging was performed at 1.5T for the patient’s MR imaging-compatible Strata shunt. CT and ZTE both imaged the entirety of the shunt catheter. Multiple craniofacial anomalies were imaged, including pancriosynostosis, severe turribrachycephaly, copper beaten skull, midface hypoplasia, exorbitism, and basilar impression. No appreciable difference in diagnostic image quality was observed on the 1.5T scan. Intracranial malformations were better evaluated on MR imaging than on CT (On-line Fig 7).

Patient 7 was a 7-month-old boy with atraumatic head deformity. CT and ZTE revealed a Galassi type III arachnoid cyst with associated calvarial remodeling and intracranial midline shift (On-line Fig 8).

Patient 8 was a 1-year-old boy with a remote history of a fall and worsening head deformity. CT and ZTE equivalently demonstrated a leptomeningeal cyst or growing fracture of the right parietal calvaria with underlying parenchymal encephalomalacia. This presumably represented expansion of a remote skull fracture with dural injury and chronic CSF pulsations (On-line Fig 9).

Patient 9 was an 8-year-old boy with chronic epilepsy on anticonvulsants. CT and ZTE equivalently demonstrated diffuse hyperostosis with normal sutural, sinonasal, and temporal bone anatomy for his age. Brain abnormalities were better depicted on MR imaging (On-line Fig 10).

Patient 10 was a 2-month-old girl with breathing difficulties. CT and ZTE both showed bilateral choanal stenosis with inward bowing of the posterior nasal walls. Brain abnormalities were more readily evaluated on MR imaging (On-line Fig 11).

Patient 11 was a 17-year-old girl with neurofibromatosis type 1. MR imaging demonstrated orbitotemporal neurofibromatosis with left proptosis and transspatial plexiform neurofibroma. ZTE confirmed characteristic bone remodeling with expansion of the left bony orbit and sphenoid wing dysplasia. Soft-tissue findings were better depicted on MR imaging (On-line Fig 12).

Patient 12 was an 11-year-old girl with right facial pain and swelling. CT and ZTE both depicted erosion of the right pterygoid plate secondary to a right masticator space mass, biopsied as alveolar rhabdomyosarcoma. Additional soft-tissue detail was obtained using MR imaging (On-line Fig 13).

Patient 13 was a 6-year-old boy post-calvarial reconstruction with a polyether etherketone implant. CT and ZTE comparably showed the morphology of the cranioplasty and fixating hardware, with minimal image artifacts (On-line Fig 14).

Patient 14 was a 9-year-old girl with facial trauma due to a motor vehicle collision. Preoperative CT demonstrated a mildly displaced left zygomaticomaxillary fracture. Following surgical fixation, ZTE was performed and confirmed anatomic realignment of fracture fragments by fixating hardware, with minimal image artifacts (On-line Fig 15).

DISCUSSION

Zero TE is the newest in a series of short-TE approaches, including gradient-echo and ultrashort-echo techniques, that can successfully image short-T2 structures including cortical bone, meninges, cartilage, tendons, ligaments, calcium, airway, and lungs.³⁻⁶ Additional intrinsic sequence properties include rapid imaging times, silent scanning, high-resolution isotropic datasets, and resistance to artifacts.⁷⁻⁹ The applicability of ZTE for bone imaging has been successfully demonstrated in small clinical case series and ex vivo studies of the cranial vault, face, jaw, and spine.¹²⁻¹⁹ Because MR imaging already provides superior soft-tissue detail, the addition of a ZTE bone sequence would enable highly efficient and radiation-free evaluation in several pediatric neuroimaging, head/neck imaging, and musculoskeletal imaging scenarios. Inversion recovery techniques can also yield T1-weighted ZTE images useful for assessing brain and spinal cord myelination, tumor and pituitary imaging, vessels, and airway.²²⁻²⁴ Additional potential applications include 3D modeling and printing, metal artifact reduction, fetal imaging, PET/MRI attenuation correction, radiation therapy planning, and interventional guidance.²⁵⁻²⁹

The limitations to wider implementation of ZTE are multifactorial and include physician awareness, scanner and hardware compatibility, vendor sequence availability, clinical workflow, and image postprocessing and analysis. Currently, there is a major knowledge gap regarding the diagnostic parallels between ZTE and CT. Our preliminary data illustrate that the 2 modalities provide qualitatively similar bone detail across a wide variety of neuroimaging pathologies, without any cases of diagnostic discordance. To definitively evaluate the clinical utility of ZTE, we are currently conducting a well-powered and controlled clinical trial to quantitatively evaluate the comparative effectiveness of these 2 modalities. Our hypothesis is that ZTE is equivalent to CT for neuroanatomic landmark visualization across the life span, enables imaging diagnosis across a variety of pathologies, and permits effective anatomic modeling and interventional planning. In addition, we are investigating improved techniques for pseudoCT and 3D reconstructions to facilitate diagnosis. Current vendor-available automated algorithms do not consistently correct for the variable intensities of developing bone, cartilage, soft tissues, and airway secretions, creating diagnostic challenges in the pediatric population. At present, we are working on a semiautomated postprocessing technique²⁰ and investigating machine learning approaches to generate improved pseudoCT images.^{29,30}

CONCLUSIONS

ZTE is a promising technique for radiation-free bone imaging with rapid, high-resolution, silent, and artifact-resistant properties. Although larger studies will be needed, our preliminary experience demonstrates the diagnostic utility and clinical applications of this technique for radiation-free bone imaging.

ACKNOWLEDGMENTS

The authors wish to thank Uldis Bite, MD, and Samir Mardini, MD, for their clinical support of this work; and Norbert G. Campeau, MD, for assistance with On-Line Figure 2E.

Disclosures: Mai-Lan Ho—*RELATED: Grant:* Radiological Society of North America, Society for Pediatric Radiology, American Society of Head and Neck Radiology, *Comments:* Principal Investigator on research grants*; *UNRELATED: Payment for Lectures Including Service on Speakers Bureaus:* American Roentgen Ray Society, *Comments:* honoraria for lectures; *Royalties:* McGraw-Hill, *Comments:* book royalties. *Money paid to the institution.

REFERENCES

1. Risk of ionizing radiation exposure to children: a subject review. *American Academy of Pediatrics—Committee on Environmental Health. Pediatrics* 1998;101(4 Pt 1):717–19 Medline
2. Frush DP, Goske MJ. Image gently: toward optimizing the practice of pediatric CT through resources and dialogue. *Pediatr Radiology* 2015;45:471–75 CrossRef Medline
3. Weiger M, Pruessmann KP, Hennel F. MRI with zero echo time: hard versus sweep pulse excitation. *Magn Reson Med* 2011;66:379–89 CrossRef Medline
4. Schieban K, Weiger M, Hennel F, et al. ZTE imaging with enhanced flip angle using modulated excitation. *Magn Reson Med* 2015; 74:684–93 CrossRef Medline
5. Weiger M, Wu M, Wurnig MC, et al. ZTE imaging with long-T2 suppression. *NMR Biomed* 2015;28:247–54 CrossRef Medline
6. Froidaveaux R, Weiger M, Brunner DO, et al. Filling the dead-time gap in zero echo time MRI: principles compared. *Magn Reson Med* 2018;79:2036–45 CrossRef Medline
7. Alibek S, Vogel M, Sun W, et al. Acoustic noise reduction in MRI using Silent Scan: an initial experience. *Diagn Interv Radiology* 2014;20:360–63 CrossRef Medline
8. Ognard J, Burdin V, Ragoubi Hor R, et al. “Bones in Silenz”: a new T1-weighted SILENZ sequence evaluating the bone in MRI. *Diagn Interv Imaging* 2015;96:973–75 CrossRef Medline
9. Tiberi G, Costagli M, Biagi L, et al. SAR prediction in adults and children by combining measured B1+ maps and simulations at 7.0 Tesla. *J Magn Reson Imaging* 2016;44:1048–55 CrossRef Medline
10. Zheng W, Kim JP, Kadbi M, et al. Magnetic resonance-based automatic air segmentation for generation of synthetic computed tomography scans in the head region. *Int J Radiat Oncol Biol Phys* 2015;93:497–506 CrossRef
11. Delso G, Wiesinger F, Sacolick LI, et al. Clinical evaluation of zero-echo-time MR imaging for the segmentation of the skull. *J Nucl Med* 2015;56:417–22 CrossRef Medline
12. Eley KA, Watt-Smith SR, Sheerin F, et al. “Black Bone” MRI: a potential alternative to CT with three-dimensional reconstruction of the craniofacial skeleton in the diagnosis of craniosynostosis. *Eur Radiol* 2014;24:2417–26 CrossRef
13. Eley KA, Watt-Smith SR, Golding SJ. “Black bone” MRI: a potential alternative to CT when imaging the head and neck: report of eight clinical cases and review of the Oxford experience. *BJR* 2012; 85:1457–64 CrossRef
14. Naganawa S, Nakane T, Kawai H, et al. Visualization of middle ear ossicles in elder subjects with ultra-short echo time MR imaging. *Magn Reson Med Sci* 2017;16:93–97 CrossRef Medline
15. Kobayashi N, Goerke U, Wang L, et al. Gradient-modulated PETRA MRI. *Tomography* 2015;1:85–90 CrossRef Medline
16. Hövener JB, Zwick S, Leupold J, et al. Dental MRI: imaging of soft and solid components without ionizing radiation. *J Magn Reson Imaging* 2012;36:841–46 CrossRef Medline
17. Koo TK, Kwok WE. A non-ionizing technique for three-dimensional measurement of the lumbar spine. *J Biomech* 2016;49:4073–79 CrossRef
18. Dremmen MHG, Wagner MW, Bosemani T, et al. Does the addition of a “black bone” sequence to a fast multisequence trauma MR protocol allow MRI to replace CT after traumatic brain injury in children? *AJNR Am J Neuroradiol* 2017;38:2187–92 CrossRef Medline

19. Weiger M, Stampanoni M, Pruessmann KP. **Direct depiction of bone microstructure using MRI with zero echo time.** *Bone* 2013;54:44–47 CrossRef Medline
20. Lu A, Gorny KR, Ho ML, et al. **Improved delineation of air-bone interface in in-vivo high-resolution bright bone ZTE MRI at 3T.** In: *Proceedings of the Annual Meeting of the International Society for Magnetic Resonance in Medicine.* Honolulu, Hawaii. April 22-27, 2017 P5109
21. Wehrli FW. **Magnetic resonance of calcified tissues.** *J Magn Reson* 2013;229:35–48 CrossRef Medline
22. Weiger M, Brunner DO, Dietrich BE, et al. **ZTE imaging in humans.** *Magn Reson Med* 2013;70:328–32 CrossRef Medline
23. Holdsworth SJ, Macpherson SJ, Yeom KW, et al. **Clinical evaluation of silent T1-weighted MRI and silent MR angiography of the brain.** *AJR Am J Roentgenol* 2018;210:404–11 CrossRef Medline.
24. Niwa T, Nozawa K, Aida N. **Visualization of the airway in infants with MRI using pointwise encoding time reduction with radial acquisition (PETRA).** *J Magn Reson Imaging* 2017;45:839–44 CrossRef Medline
25. Eley KA, Watt-Smith SR, Golding SJ. **“Black Bone” MRI: a novel imaging technique for 3D printing.** *Dentomaxillofac Radiol* 2017; 46:20160407 CrossRef
26. Hilgenfeld T, Prager M, Heil A, et al. **PETRA, MSVAT-SPACE and SEMAC sequences for metal artefact reduction in dental MR imaging.** *Eur Radiol* 2017;27:5104–12 CrossRef
27. Robinson AJ, Blaser S, Vladimirov A, et al. **Foetal “black bone” MRI: utility in assessment of the foetal spine.** *Br J Radiology* 2015;88:20140496 CrossRef Medline
28. Himes NC, Chansakul T, Lee TC. **Magnetic resonance imaging-guided spine interventions.** *Magn Reson Imaging Clin N Am* 2015;23:523–32 CrossRef
29. Wiesinger F, Bylund M, Yang J, et al. **Zero TE-based pseudo-CT image conversion in the head and its application in PET/MR attenuation correction and MR-guided radiation therapy planning.** *Magn Reson Med* 2018;80:1440–51 CrossRef
30. Dinkla AM, Wolterink JM, Maspero M, et al. **MR-only brain radiation therapy: dosimetric evaluation of synthetic CTs generated by a dilated convolutional neural network.** *Int J Radiat Oncol Biol Phys* 2018;102:801–12 CrossRef

Global and Regional Changes in Cortical Development Assessed by MRI in Fetuses with Isolated Nonsevere Ventriculomegaly Correlate with Neonatal Neurobehavior

 N. Hahner,  O.M. Benkarim,  M. Aertsen,  M. Perez-Cruz,  G. Piella,  G. Sanroma,  N. Bargallo,  J. Deprest,  M.A. Gonzalez Ballester,  E. Gratacos, and  E. Eixarch



ABSTRACT

BACKGROUND AND PURPOSE: Fetuses with isolated nonsevere ventriculomegaly (INSVM) are at risk of presenting neurodevelopmental delay. However, the currently used clinical parameters are insufficient to select cases with high risk and determine whether subtle changes in brain development are present and might be a risk factor. The aim of this study was to perform a comprehensive evaluation of cortical development in INSVM by magnetic resonance (MR) imaging and assess its association with neonatal neurobehavior.

MATERIALS AND METHODS: Thirty-two INSVM fetuses and 29 healthy controls between 26–28 weeks of gestation were evaluated using MR imaging. We compared sulci and fissure depth, cortical maturation grading of specific areas and sulci and volumes of different brain regions obtained from 3D brain reconstruction of cases and controls. Neonatal outcome was assessed by using the Neonatal Behavioral Assessment Scale at a mean of 4 ± 2 weeks after birth.

RESULTS: Fetuses with INSVM showed less profound and underdeveloped sulcation, including the Sylvian fissure (mean depth: controls 16.8 ± 1.9 mm, versus INSVM 16.0 ± 1.6 mm; $P = .01$), and reduced global cortical grading (mean score: controls 42.9 ± 10.2 mm, versus INSVM: 37.8 ± 9.9 mm; $P = .01$). Fetuses with isolated nonsevere ventriculomegaly showed a mean global increase of gray matter volume (controls, $276.8 \pm 46.0 \times 10 \text{ mm}^3$, versus INSVM $277.5 \pm 49.3 \times 10 \text{ mm}^3$, $P = .01$), but decreased mean cortical volume in the frontal lobe (left: controls, $53.2 \pm 8.8 \times 10 \text{ mm}^3$, versus INSVM $52.4 \pm 5.4 \times 10 \text{ mm}^3$; $P < .01$). Sulcal depth and brain volumes were significantly associated with the Neonatal Behavioral Assessment Scale severity ($P = .005$, Nagelkerke $R^2 = 0.732$).

CONCLUSIONS: INSVM fetuses showed differences in cortical development, including regions far from the lateral ventricles, that are associated with neonatal neurobehavior. These results suggest the possible use of these parameters to identify cases at higher risk of altered neurodevelopment.

ABBREVIATIONS: INSVM = isolated nonsevere ventriculomegaly; NBAS = Neonatal Behavioral Assessment Scale; VM = ventriculomegaly

Fetal ventriculomegaly (VM) is defined as an enlargement of 1 or both lateral ventricles of ≥ 10 mm measured by sonography.¹ VM is the most common brain anomaly, occurring in

around 1% of pregnancies.² In the absence of additional abnormalities such as aneuploidy, malformation or infections, which are found in approximately 50% of cases, VM is considered as

Received May 13, 2019; accepted June 28.

From the Fetal i + D Fetal Medicine Research Center (N.H., M.P.-C., E.G., E.E.), BCNatal–Barcelona Center for Maternal-Fetal and Neonatal Medicine (Hospital Clínic and Hospital Sant Joan de Déu), Institut Clínic de Ginecologia, Obstetrícia i Neonatologia, Institut d'Investigacions Biomèdiques August Pi i Sunyer, Universitat de Barcelona, Barcelona, Spain; Centre for Biomedical Research on Rare Diseases (E.G., E.E.), Barcelona, Spain; Magnetic Resonance Image Core Facility (N.B.), Institut d'Investigacions Biomèdiques August Pi i Sunyer, Barcelona, Spain; Department of Radiology (N.B.), Centre de Diagnòstic per la Imatge, Hospital Clínic, Barcelona, Spain; BCN MedTech (O.M.B., G.P., G.S., M.A.G.B.), Universitat Pompeu Fabra, Barcelona, Spain; ICREA (M.A.G.B.), Barcelona, Spain; Departments of Radiology (M.A.) and Obstetrics (J.D.), UZ Leuven, Leuven, Belgium; and Institute for Women's Health (J.D.), University College London, London, UK.

The research leading to these results was partially funded by the Erasmus + Programme of the European Union (Framework Agreement No. 2013-0040), Instituto de Salud Carlos III (PI16/00861) integrados en el Plan Nacional de I + D + I y cofinanciados por el ISCIII-Subdirección General de Evaluación y el Fondo Europeo de Desarrollo Regional "Una manera de hacer Europa." CERCA Programme/Generalitat de Catalunya, "la Caixa" Foundation (LCF/PR/GNI4/10270005), AGAUR 2017 SGR grant No. 1531, and The Cerebra Foundation for the Brain-Injured Child, Carmarthen, Wales.

The publication reflects only the views of the authors, and the Commissions holder of the grants cannot be held responsible for any use that may be made of the information contained therein.

Paper previously presented orally at: Ultrasound Meets Magnetic Resonance, September 28–29, 2018, Paris, France; and The Fetal Medicine Foundation World Congress, June 24–28, 2018, Athens, Greece: Regional Differences of Cortical Grey Matter Development in Fetuses with Isolated Non-Severe Ventriculomegaly, Hahner N, Benkarim O, Piella G, Sanroma G, Bargallo N, Gonzalez Ballester MA, Gratacos E, Eixarch E; Poster presentation at: International Society of Ultrasound in Obstetrics and Gynecology Congress, September 16–17, 2017, Vienna, Austria: Differential Cortical Development in Fetuses with Isolated Non-Severe Ventriculomegaly Assessed by MRI, Hahner N, Puerto B, Perez-Cruz M, Gratacos E, Eixarch E. Please address correspondence to Eduard Gratacos, MD, BCNatal–Barcelona Center for Maternal-Fetal and Neonatal Medicine, Sabino de Arana 1, 08028 Barcelona, Spain; e-mail: gratacos@clinic.cat

 Indicates open access to non-subscribers at www.ajnr.org

 Indicates article with supplemental on-line table.

 Indicates article with supplemental on-line photos.

<http://dx.doi.org/10.3174/ajnr.A6165>

isolated, and is, therefore, related to a good prognosis.³ However, even cases with isolated mild VM have a higher risk of abnormal neurodevelopment compared with the healthy population.³ Indeed, about 11% of VM cases present neurobehavioral problems, including motor⁴ and language dysfunction,⁵ cognitive delay,^{4,6} and psychiatric disorders.⁷⁻⁹ Ventricular width¹⁰ and progression of the VM¹¹ are predictive factors of adverse outcomes. Nevertheless, these parameters cannot discriminate cases that will present neurodevelopmental impairment. Thus, early identification of individuals at high risk of abnormal neurodevelopment is crucial in order to ensure the implementation of early therapeutic interventions.

There is some evidence demonstrating altered brain development in VM in the prenatal and postnatal periods. Advanced magnetic resonance (MR) imaging modalities have been used to demonstrate global changes in brain structure such as altered white matter microstructure in neonates¹² and increased gray matter volumes in fetuses,¹³ neonates,¹² and children.¹⁴ Evaluation of cortical development by advanced sonography has demonstrated an inverse relation between calcarine and ventricular size,¹⁵ with depth being an independent marker of later progression.¹⁵ Recently, underdeveloped cortical maturation has been described in fetuses with isolated nonsevere VM (INSVM), including the mesial area and the Sylvian fissure, which are regions in which the effect of ventricular dilation is unlikely.¹⁶ Sonography is the most commonly used imaging tool in fetal medicine; however, it has important limitations in the evaluation of several brain regions, such as the fetal skull shadow which impedes the study of some cortical regions, especially the proximal hemisphere. On the contrary, MR imaging allows complete visualization of both hemispheres, and cortical maturation of the entire brain can be assessed.

The objective of this study was to perform a comprehensive assessment of cortical maturation by MR imaging, including sulci depth, cortical grading, and volume, and to evaluate the association with neonatal neurobehavior.

MATERIALS AND METHODS

Subjects

A prospective case-control study was performed in BCNatal (Hospital Clínic and Hospital Sant Joan de Déu) in Barcelona from 2014 to 2016. The Ethics Committee of our center approved the study protocol (HCB/2014/0484), and all patients and healthy volunteers gave written informed consent.

Nonsevere VM was defined as an atrial width between 10.0 and 14.9 mm at sonographic examination. Progression or regression was defined as a change of lateral ventricular width ≥ 2 mm. Atrial width was assessed by measuring the distance between the inner border of both lateral walls at the height of the glomus and the parieto-occipital sulcus in the axial transventricular plane.¹⁷ Gestational age was dated using the first trimester crown rump length measurement. All patients with an abnormal karyotype or microarray findings, infections, other structural abnormalities associated with higher risk of abnormal neurodevelopment or acquired ventriculomegaly were excluded. The control group was made up of pregnant volunteers with healthy and normally grow-

ing fetuses of singleton pregnancies and were prospectively enrolled specifically for research purposes of this study.

MR Imaging Acquisition

MR imaging was performed at 26.0 to 28.6 gestational weeks. All images were obtained with a 1.5T MR imaging (Magnetom Aera syngo MR D13; Siemens, Erlangen, Germany) using an 8-channel body coil without fetal sedation and following the American College of Radiology guidelines for pregnancy and lactation.⁸ The acquisition used for sulcal depth measurements and grading consisted in single-shot, fast spin-echo T2-weighted sequence (TR = 1000 ms, TE = 137 ms, slice thickness = 3.5 mm, no gap, FOV = 300 × 225 mm, voxel size = 1.17 × 1.17 × 3.5 mm, matrix = 256 × 192, flip angle = 135°, acquisition time = 32 s) acquired in the 3 orthogonal planes of the fetal head. For volumetric analyses, additional images of 4 axial, 2 coronal, and 2 sagittal single-shot fast spin-echo sequences (TR = 1500 ms, TE = 82 ms, slice thickness = 2.5 mm, no gap, voxel size = 1.09 × 1.09 × 2.5 mm, FOV = 280 × 225 mm, matrix = 256 × 256 mm, flip angle = 121°, acquisition time = 47 s) were obtained for later reconstruction. The sequences were repeated when the attending fetal medicine specialist (N.H.) observed insufficient image quality. All clinical images were reviewed by a specialized radiologist (N.B.) to exclude any additional abnormality of the central nervous system.

MR Imaging Analysis

Sulcal Depth. Sulcal measurement was performed off-line using Analyze 9.0 software (AnalyzeDirect, Overland Park, Kansas) for T2-weighted sequences with a 3.5-mm slice thickness. First, laterality was assessed by the fetus's position in utero, and both hemispheres were evaluated. Selection of anatomic planes for 2D measurements was assessed according to sonography guidelines.¹⁷ Sulci were measured using previously described methodology.^{18,19} The measurements were normalized by biparietal diameter (BPD) and multiplied by 100. A midline was drawn for each plane from the frontal towards the occipital skull projecting the interhemispheric fissure in axial views, and from cranial to caudal to highlight the fissure in coronal views. Sulcal and fissure depth was obtained as previously reported¹⁸ by drawing a perpendicular line from the midline toward the border of the specific sulcus as shown in Fig 1A–D.

Cortical Grading. Cortical areas and sulci were graded according to previously described methodology.²⁰ The grading scheme scores all main cortical areas (frontal, parietal, temporal, occipital, and mesial cortical area), sulci (parieto-occipital, superior temporal, central, calcarine, and cingulate sulci), and the Sylvian fissure in a scale from 0 (no maturation) to 5 (maximum degree of maturation) (Fig 1E–L). Subsequently, the scores of all the areas and sulci on each side were considered to calculate the hemispheric and total brain grading scores.

Cortical Volumes. To perform volumetric analyses of the cortex, the fetal brain was first located and extracted from the previously mentioned image stacks using an automatic approach proposed by Keraudren et al.²¹ Then, high-resolution 3D volume reconstruction with a super-resolution of 0.75 × 0.75 × 0.75 mm was obtained according to the method of Kuklisova-Murgasova et al.²²

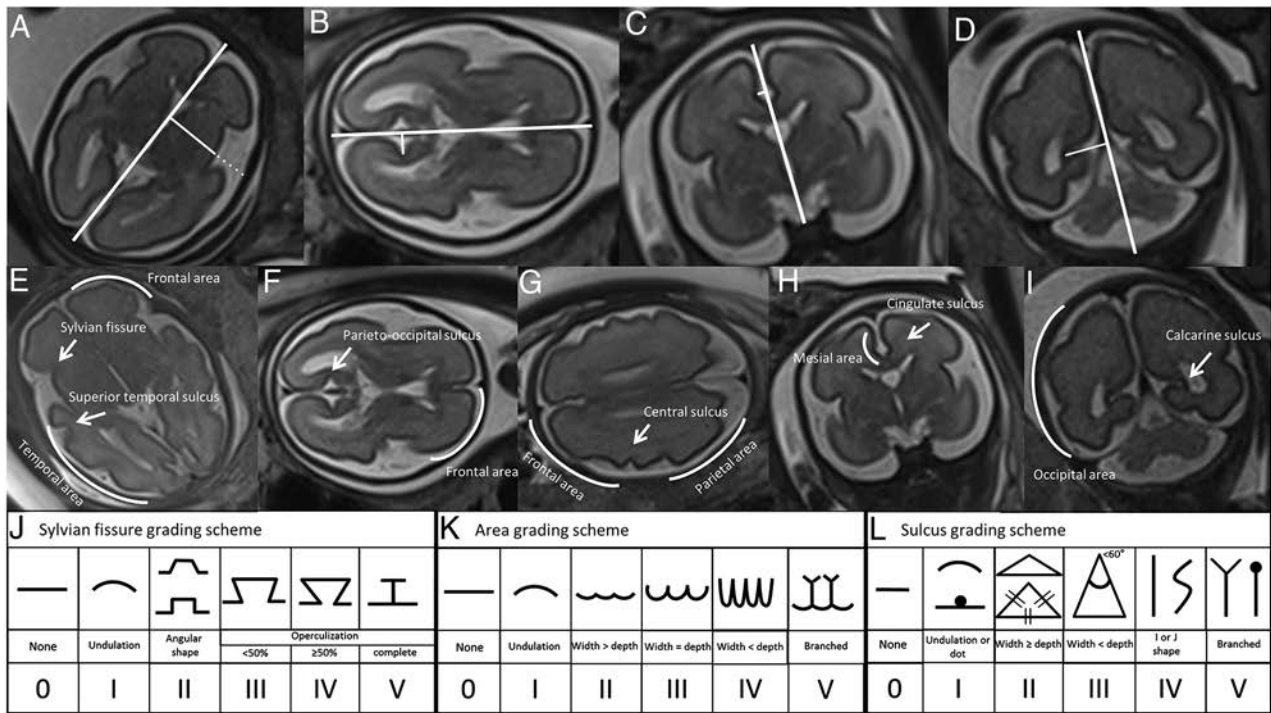


FIG 1. Assessment of sulcal depth and cortical grading. Sulcal depth: The *bold white interhemispheric line* is used as reference for all the measurements and the *thin white line* shows the measurement of the sulcus of interest, including the insula and Sylvian fissure (*dotted line*) in the axial transthalamic plane (A), parieto-occipital sulcus in the axial transventricular plane (B), cingulate sulcus in the coronal transthalamic view (C), and the calcarine sulcus in the coronal transcerebellar plane (D). Cortical grading: *Curved lines* indicate the areas, and *arrows* point out the sulci of interest. In the transthalamic plane frontal and temporal area (E), the Sylvian fissure and superior temporal sulcus were evaluated. In the transventricular plane (F), the parieto-occipital sulcus and frontal area were assessed, and in the plane superior to it (G), the central sulcus and frontal and parietal areas were assessed. The mesial area and cingulate sulcus were evaluated in the coronal transthalamic plane (H), and the calcarine sulcus was assessed in the coronal transcerebellar plane (I). Scheme: grading scale for Sylvian fissure (J), cortical areas (K) and sulci (L) by Pistorius et al.²⁰

Brain tissue was automatically segmented from these reconstructed volumes into white matter, cortex, cerebrospinal fluid (CSF), ventricles, cerebellum, and brainstem. This was done using an ensemble method reported by Sanroma et al,²³ which combines 2 base approaches. All segmentations were further revised and manually corrected if necessary by 2 experts (N.H. and E.E.).

Taking into account that volumetric analyses of the cortex were the focus of the study, the cortex was parcellated into 16 regions along the cortical surface.²⁴ Figure 2 and On-line Figure 1 show the steps from fetal head extraction to parcellation.

Neonatal Neurobehavior

Neonatal neurobehavior was assessed at a mean of 4 ± 2 weeks after birth using the Neonatal Behavioral Assessment Scale (NBAS) developed by Brazelton and Nugent.²⁵ This test evaluates the capacity of neonates to interact with the environment and provides information about brain maturation.²⁶ The 2 observers who performed the test were accredited by the Brazelton Institute (Harvard Medical School, Boston, Massachusetts) and blinded to the identification of cases and controls. The evaluation was made in a small, quiet, semidark, warm room with at least 1 parent present. The scale consists of 35 items, rated from 1 to 9 points, and, are summarized into 6 clusters (habituation, motor system, social-interactive, range of states, regulation of states, and autonomic stability). Cluster scores were transformed into z scores according to a standard population²⁷ and were defined as abnor-

mal if the z score was below -1 . The NBAS severity score was defined as the number of abnormal NBAS clusters in each subject.

Statistical Analyses

Data analyses were performed using SPSS, Version 22.0 for Windows (IBM, Armonk, New York). Normality was tested using the Shapiro-Wilk test. The Student's *t* test for independent samples and the Pearson χ^2 test were used to compare quantitative and qualitative data between those with INSVM and controls. For quantitative variables, a general linear model was carried out, and for categorical variables, ordinal regression was used. To correct for head size, we adjusted sulcal depth by biparietal diameter and volumetric analyses by supratentorial volume. Prenatal data were additionally adjusted by sex and gestational age at MR imaging. Neonatal neurobehavior data were adjusted for sex, breastfeeding, socioeconomic status, gestational age at neonatal examination, and days of neonatal adaptation. The association between prenatal parameters and the NBAS severity score was assessed by ordinal regression.

To assess the reproducibility of cortical grading and sulcal depth using MR imaging, a second observer (M.A.) blinded to the measurements of the first observer applied the same methodology in 20 fetuses using MeVisLab software (MeVis Medical Solutions, Bremen, Germany). Complete MR imaging sequences of each fetus were given to the second observer to select the appropriate images to measure. The

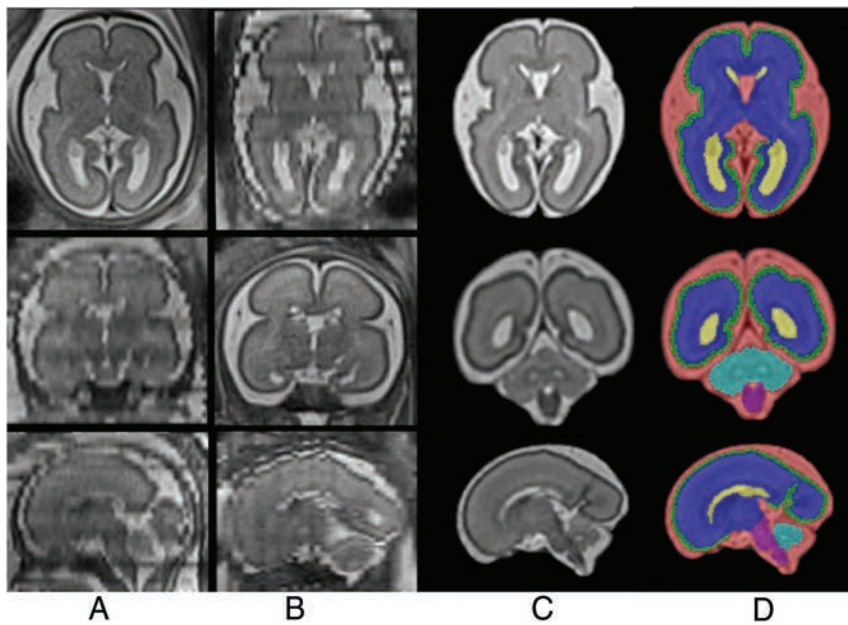


FIG 2. Steps of fetal brain MR imaging reconstruction and tissue segmentation. Columns A and B, The raw stacks, including the image obtained as a reference (Column A, axial, and Column B, coronal) and the orthogonal views (note the low quality of these images). Column C, The 3 orthogonal planes of the final reconstruction. Column D, The segmentation into cortical gray matter (green), white matter (blue), lateral ventricles (yellow), CSF outside the ventricles (red), cerebellum (turquoise), and brain stem (purple).

interclass correlation coefficient was calculated using a 2-way random effect model with absolute agreement.

RESULTS

Subjects

Thirty-three cases of nonsevere VM diagnosed before 28 weeks of gestation were included in our cohort. In 1 case, microarray identified a 16p11.2 duplication is associated with a higher risk of neurodevelopmental disorders and this case was excluded from the cohort. All other fetuses with VM had normal karyotype ($n = 17$) or micro-array ($n = 13$) findings determined by amniocentesis. In 2 cases, parents refused to perform amniocentesis, and a normal microarray findings were obtained in a genetic study using saliva sampling in the postnatal period. Infection was excluded by negative polymerase chain reaction findings in amniotic liquid in 30 cases and in the remaining ones by maternal serologic screening. The control group included 32 healthy fetuses with normal growth. Of these, 2 mothers finally could not attend the MR imaging appointment, and 1 acquisition had to be excluded due to bad image quality, resulting in a final sample size of 32 fetuses with INSVM and 29 controls. The demographic characteristics of the study groups are presented in Table 1.

MR Imaging Data

Sulcal depth measurement and cortical grading evaluation was performed in 98.4% of examinations; only 1 control subject had insufficient image quality and was not considered for final analyses. 3D reconstructions and volumetric analyses were performed in 78.7% of the fetuses.

Sulcal Depth. Table 2 shows the comparison of the measurements of the INSVM fetuses and the controls. As expected, fetuses

with INSVM showed significantly less profound parieto-occipital and calcarine sulci in both hemispheres compared with controls. In addition to these differences in sulci near the ventricles, those with INSVM showed increased insula depths in both hemispheres and a less profound Sylvian fissures in the right hemisphere. No significant differences were found in the cingulate sulcus at this gestational age.

When only bilateral cases were considered, differences were maintained and changes in the Sylvian fissure mean measurement were also observed in the left hemisphere (left: controls, 16.7 ± 1.6 mm, versus INSVM, 15.3 ± 2.3 mm; $P = .02$; right: controls, 16.8 ± 1.9 mm, versus INSVM, 15.5 ± 2.0 mm; $P = .06$).

Cortical Grading. In general, fetuses with INSVM had lower cortical grading scores compared with the control group. Parieto-occipital and calcarine sulci showed delayed grading in both hemispheres (left parieto-occipital sulcus grading, ≥ 3 : controls, 37.9%, versus INSVM, 15.2%, $P = .03$; right: controls, 58.6%, versus INSVM, 30.6%; $P = .02$) (left calcarine sulcus grading, ≥ 4 : controls, 55.1%, versus INSVM, 24.2%; $P = < .01$; right: controls, 65.5%, versus INSVM, 27.3%; $P = < .01$). Furthermore, significantly altered maturation in the left superior temporal sulcus showed (grading, ≥ 2 : controls, 55.2%, versus INSVM, 27.7%; $P = .04$). In the subgroups of fetuses with bilateral INSVM, we identified more marked differences compared with unilateral cases, with significant delay in the right parietal (grading, ≥ 2 : controls, 65.5%, versus INSVM, 18.2%; $P = .03$) and occipital areas (grading, ≥ 2 : controls, 62.0%, versus INSVM, 9.1%; $P = .2$). Finally, considering the sulcation pattern of the whole hemisphere, a significant difference was observed in fetuses with INSVM on both the right and left compared to the control group (Table 2).

Interobserver Agreement. Overall, cortical development assessment showed a good interobserver reproducibility with an interclass correlation coefficient of 0.962 (95% CI, 0.950–0.971) for depth measurements and 0.759 (95% CI, 0.717–0.796) for cortical grading.

Cortical Volumes. Volumetric analyses of 3D reconstructed MR imaging showed, generally greater brain tissue volumes (supratentorial, cortex, white matter, lateral ventricle), with significant differences in cortical and ventricular volumes in the INSVM group (Fig 3). Indeed, as shown in On-line Figure 2, ventricular volume was positively correlated with brain tissue volumes. Regional evaluation identified a significantly lower mean cortical volume in both frontal lobes in the INSVM compared with the control group (left: controls, $53.2 \pm 8.8 \times 10$ mm³, versus INSVM, $52.4 \pm 5.4 \times 10$ mm³; $P = < .01$; right: controls, $52.8 \pm 9.5 \times 10$ mm³, versus INSVM, $51.0 \pm 9.9 \times 10$ mm³; $P = < .01$) and greater volumes of the posterior part of the cingulate gyri in

Table 1: Clinical characteristics of the study groups^a

	Controls (n = 29)	INSVM (n = 32)	P
Maternal age (yr)	33.7 ± 4.2	32.4 ± 5.5	.32
Birth weight (g)	3414 ± 517	3406 ± 553	.96
Gestational age at birth (wk)	39.8 ± 0.9	39.8 ± 1.2	.81
Gestational age at MRI (wk)	27.7 ± 0.9	27.7 ± 0.9	.91
Lateral ventricular width ^a	4.6 ± 1.4	10.6 ± 1.1	<.01 ^b
Fetus sex			.02 ^d
Male	58.6% (17)	87.5% (28)	
Female	41.4% (12)	12.5% (4)	
Laterality of ventriculomegaly			
Bilateral	—	34.4% (11)	
Unilateral left	—	34.4% (11)	
Unilateral right	—	31.2% (10)	
Evolution of lateral ventricular width ^c			
Regressive	—	25% (8)	
Stable	—	75% (24)	
Progressive	—	0% (0)	
Classification according to atrial width			
Mild (10.0–11.9 mm)	—	84.3% (27)	
Moderate (12.0–13.9 mm)	—	16.7% (5)	

Note:— indicates that these characteristics do not apply for the control group.

^a Comparison of clinical characteristics between the control and case cohort. Results are expressed as means or percentage and number of subjects as appropriate.

^b Measurement of the more dilated lateral ventricle by ultrasound at diagnosis.

^c Evolution of lateral ventricular width until term of pregnancy.

^d Significant ($\leq .05$).

Table 2: Sulcal depth and grading scores of the study groups^a

Variable	Controls (n = 29)	INSVM (n = 32)	P
Left hemisphere depths			
Insula	29.4 ± 1.5	29.7 ± 1.8	.03 ^b
Sylvian fissure	16.7 ± 1.6	17.2 ± 2.4	.15
Parieto-occipital sulcus	10.2 ± 2.3	8.1 ± 2.6	<.01 ^b
Cingulate sulcus	3.8 ± 1.3	4.3 ± 2.5	.29
Calcarine sulcus	12.5 ± 2.7	10.9 ± 2.1	<.01 ^b
Right hemisphere depths			
Insula	29.6 ± 1.4	29.7 ± 1.7	.04 ^b
Sylvian fissure	16.8 ± 1.9	16.0 ± 1.6	.01 ^b
Parieto-occipital sulcus	11.1 ± 2.4	9.0 ± 2.8	<.01 ^b
Cingulate sulcus	3.6 ± 1.1	4.0 ± 1.5	.33
Calcarine sulcus	13.5 ± 2.2	11.8 ± 4.8	<.02 ^b
Sum of grading scores			
Left hemisphere	21.1 ± 5.3	18.2 ± 5.1	.01 ^b
Right hemisphere	21.8 ± 5.1	19.6 ± 5.3	.03 ^b
Total cortex	42.9 ± 10.2	37.8 ± 9.9	.01 ^b

^a Comparison of sulcal depth measurements between the control and case cohort. Depth measurements (in millimeters) were normalized by BPD and multiplied by 100. Results are expressed as means. P values were adjusted by gestational age at examination and sex.

^b Values $\leq .05$.

both hemispheres (left: controls, $1.5 \pm 0.2 \times 10^3 \text{ mm}^3$, versus INSVM, $1.7 \pm 0.4 \times 10^3 \text{ mm}^3$; $P = .01$; right, $1.6 \pm 0.2 \times 10^3 \text{ mm}^3$, versus INSVM, $1.9 \pm 0.4 \times 10^3 \text{ mm}^3$; $P = .03$). In addition, fetuses with INSVM had a decreased mean volume in the anterior part of the gyri parahippocampalis and ambiens of the left hemisphere (controls, $3.4 \pm 0.5 \times 10^3 \text{ mm}^3$ versus $3.3 \pm 0.5 \times 10^3 \text{ mm}^3$; $P = .04$). On-line Table 1 shows all the data collected in the regional cortical volume analysis.

Neonatal Neurobehavior

The NBAS could be performed in only 24 fetuses with INSVM and 24 controls (75% and 82.8%, respectively) because parents could not be contacted or refused to participate. Routine neonatal clin-

ical examination findings were normal in all controls. The mean age at NBAS did not significantly differ between the two groups (controls, 44.5 ± 2.1 postmenstrual weeks, versus INSVM, 44.6 ± 2.9 postmenstrual weeks; $P = .94$).

The habituation cluster was only completed in 37.5% of cases ($n = 9$) and was not considered for the analysis. After we adjusted for confounding variables, no significant differences were found between groups. A tendency of weaker performance in the case group was observed in the motor cluster (mean z scores: controls, 0.74 ± 0.71 , versus INSVM 0.32 ± 0.86 ; $P = .644$) and the range of state clusters (mean z scores: controls, -0.19 ± 1.54 , versus INSVM -0.32 ± 1.41 ; $P = .924$), whereas slightly higher values were observed in the social-interactive cluster (mean z scores: controls, 0.71 ± 0.67 , versus INSVM 0.78 ± 0.65 ; $P = .091$).

To explore the association between prenatal parameters and neonatal neurobehavior, we performed ordinal regression of the NBAS severity score (dependent variable) with main clinical data (study group, atrial diameter, bilateral dilation), yielding a nonsignificant model ($P = .768$, $\chi^2 = 1.826$, Nagelkerke $R^2 = 0.032$, $df = 4$). The addition of sulcal depth (insula, Sylvian fissure, and parieto-occipital, calcarine, and cingulate sulci) resulted in a nonsignificant model ($P = .115$, $\chi^2 = 20.508$, Nagelkerke $R^2 = 0.308$, $df = 14$) but increased the explanation of variability between controls and cases from 2.6% to 38.9%. Finally, the addition of volumetric cortical data (total supratentorial volume (STV), total GM, left and right frontal lobes, left and right posterior part of the cingulate gyrus, left anterior part of the gyri parahippocampalis and ambiens), result in a statistically significant model ($P = .005$, $\chi^2 = 41.590$, Nagelkerke $R^2 = 0.732$, $df = 21$), showing a significant association of prenatal cortical parameters with the severity of abnormal neurobehavioral outcomes, providing significant additional information to the main clinical characteristics.

DISCUSSION

To the best of our knowledge, this is the first study to describe global and regional differences in cortical development assessed by MR imaging in fetuses with true INSVM and their correlation with neonatal neurobehavior. These differences were not only limited to regions adjacent to the lateral ventricles but also in-

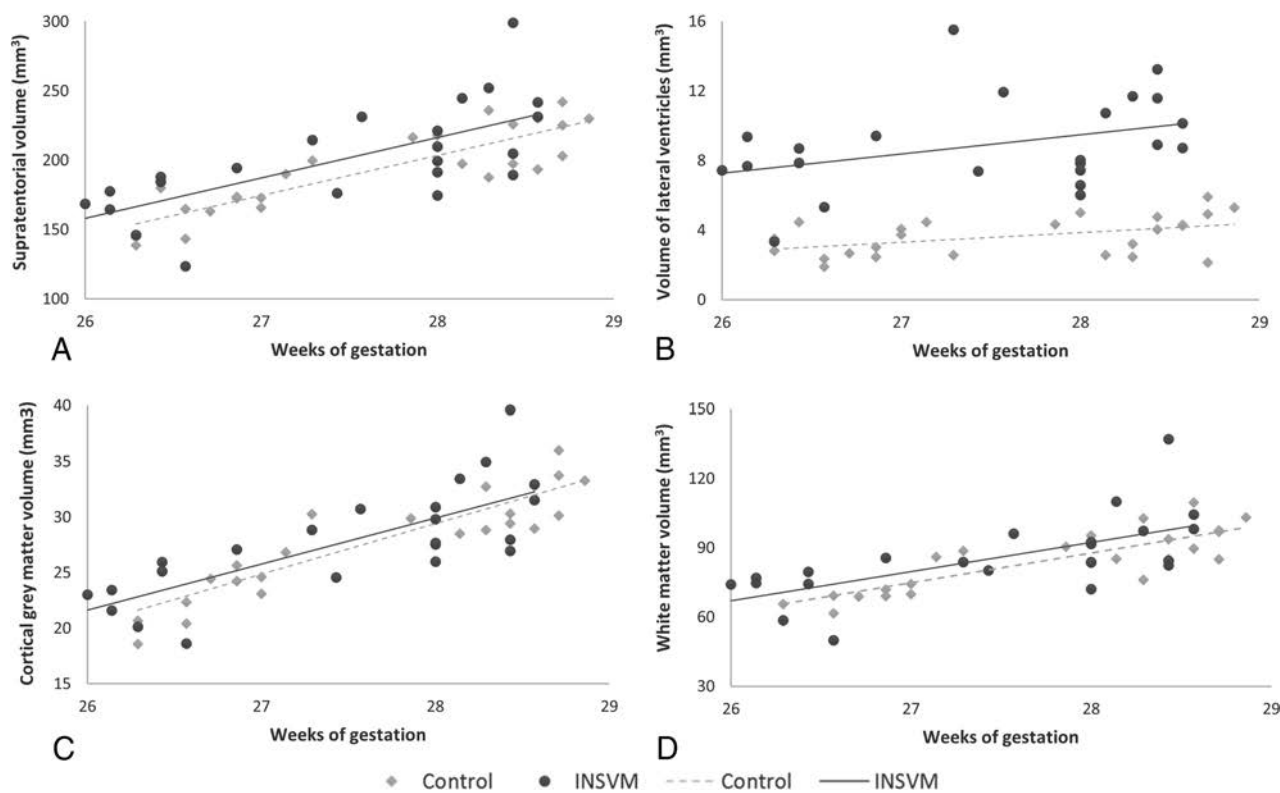


FIG 3. Brain tissue volumes in study groups. Cerebral tissue volumes including both hemispheres in INSVM (circles) and control (rhombuses) cohorts. A, Supratentorial volumes. B, Volumes of the lateral ventricles. C, Cortical gray matter volumes. D, White matter volumes. Volume measures are in cubic millimeters.

cluded the Sylvian fissure, cingulate gyrus, and the frontal, temporal and occipital regions.

Our results are in line with previous data showing significant differences in development of the parieto-occipital and calcarine sulci¹⁵ and the Sylvian fissure and insula using sonography.¹⁶ It should be noted that the Sylvian fissure and insula are involved in speech and language processing and influence pathways of cognition and emotion,^{28,29} 2 functions that have been described as being altered in VM.^{4,6} Nevertheless, this study adds valuable information providing a comprehensive evaluation of global and regional cortical development using different features of prenatal MR imaging, including sulcal depth, grading, and cortical volumes. Global cortical grading was significantly lower in INSVM in both hemispheres, reflecting a general delayed brain development in these fetuses. Additionally, changes in several regions were found, which might explain neurodevelopmental problems presented by a subgroup of patients with INSVM. Among these regions, fetuses with INSVM presented significantly underdeveloped temporal sulcation. Indeed, this region is a key structure in language function and takes part in processing social cognition, which plays a role in subtypes of autism.³⁰ Most interesting, bilateral cases presented widespread changes with delayed development in parietal, temporal, and occipital areas, the Sylvian fissure, and superior temporal sulci, which may reflect a more severe condition.

Several studies in the pre- and postnatal periods have demonstrated greater cortical volumes in mild fetal VM¹²⁻¹⁴ and our data confirm these findings, with a significant increase in cortical gray matter volume. It has been suggested that greater cortical volume

is related to increased surface area along the enlarged ventricular wall, which may result in a larger number of progenitor neurons,¹⁴ or be due to the lack of regular apoptosis in the developing brain.¹³ Regional analysis showed that this enlargement was present in most regions, reaching significance in the posterior part of the cingulate gyrus and the anterior part of the gyri parahippocampalis and ambiens. On the other hand, decreased cortical volumes were found in the frontal lobe of both hemispheres. The frontal lobe is composed of several cytoarchitectural subregions, among them, the superior and medial frontal gyri, which are involved in specific functions such as cognition-related processing and are part of the default network, which is essential for normal cognition and self-referential processing.³¹ Most interesting, these frontal regions with reduced cortical volume are highly connected to the cingulate cortex, showing greater volumes. We hypothesize that these volumetric changes might reflect cytoarchitectonic changes, which could imply changes in interaction and functionality.

The prognosis for INSVM is considered good in around 90% of the cases.³ However, within this pooled risk, there is a wide range of abnormal outcomes from 0%³² to 36%.³³ We failed to demonstrate statistically significant differences in neonatal neurobehavior, but INSVM cases showed weaker performance in the motor and range of state clusters. Nonetheless, we found a significant association between cortical development parameters and NBAS results, explaining more than 70% of the variation in neurodevelopment in INSVM. Previous data have demonstrated the correlation between cortical devel-

opment and later a neurobehavior in fetuses with congenital heart disease³⁴ and fetal growth restriction.³⁵

We acknowledge that this study has some limitations and strengths that should be discussed. First, although MR imaging is not affected by a fetal skull shadow, it has less spatial resolution than high-frequency transvaginal sonography; making tissue borders slightly blurred and less clear compared with sonography, this may have interfered in those sulci in the initial stage of development, such as the cingulate sulci. This finding could also explain the lower interclass correlation coefficient we obtained for the mesial area and cingulate sulcus and the absence of differences in this region. Second, the use of automatic quantification for cortical volumes could be influenced by segmentation of cortical tissue. To overcome this, we reviewed all images and corrected them manually if necessary. And finally, the lack of statistical differences in neurodevelopmental tests between these 2 study groups could be explained by the sample size and the fact that INSVM is a nonhomogeneous population in which only part of the group has abnormal neurodevelopment; therefore, differences between controls and fetuses with INSVM could be weaker. Although in the neonatal stage many neurodevelopmental functions can still not be assessed, several studies have highlighted evidence that neonatal behavioral skills are linked to later neurocognitive development.²⁶

Considering strengths, this is the first study performing a comprehensive assessment of cortical development in a well-selected cohort of INSVM, including 3 different and complementary techniques to quantify cortical development by MR imaging. The methodologies applied are able to identify subtle changes that might not be detected in a standard clinical evaluation and, additionally, provide objective and quantitative data that can be used to develop biomarkers. Moreover, the use of MR imaging allows adequate visualization of both hemispheres, which is commonly limited when performing sonography. Finally, all cases included in this study were strictly selected, ruling out the genetic anomalies and/or fetal infection, resulting in a unique cohort of true INSVM, preventing the inclusion of conditions that could potentially involve brain alterations and bias our results.

From a clinical point of view, the results of this study provide new data suggesting that detailed evaluation of cortical development in INSVM could add predictive value to identify the cases at higher risk of presenting altered neurodevelopment. This finding is of great interest because in our cohort, clinical prognostic markers, including ventricular width and volume and their evolution, were not associated with neonatal neurobehavior. In addition, evaluation of sulcal depth and grading by MR imaging is feasible in clinical settings, and although our results are far from achieving individual prediction, they do provide seminal evidence to continue investigating the use of cortical parameters as imaging biomarkers.

CONCLUSIONS

This is a pioneering study that describes differences of cortical development assessed by MR imaging in fetuses with INSVM that are correlated with neonatal neurobehavior. These results provide the opportunity to explore the utility of these parameters to iden-

tify cases of INSVM at higher risk of presenting altered neurodevelopment and who could therefore, benefit from early intervention. Further studies are needed to explore whether cortical development is also correlated with neurodevelopment later in life.

ACKNOWLEDGMENTS

We thank Magnetic Resonance Imaging Core Facility of the Institut d'Investigacions Biomediques August Pi i Sunyer for their technical help.

Disclosures: Nadine Hahner—*RELATED: Grant:* Agència de Gestió d'Ajuts Universitaris i de Recerca, SGR grant No. 1531; CERCA Programme Generalitat de Catalunya; The Cerebra Foundation for the Brain-Injured Child, Carmarthen Wales; European Commission Education, Audiovisual and Culture Executive Agency, 2013-0040; Ministerio de Economía y Competitividad—Instituto de Salud Carlos III, PI16/00861; "La Caixa" Foundation, LCF/PR/GNI4/10270005*; *Support for Travel to Meetings for the Study or Other Purposes:* European Commission Education, Audiovisual and Culture Executive Agency, 2013-0040.* Jan Deprest—*RELATED: Grant:* European Commission Education, Audiovisual and Culture Executive Agency, 2013-0040; *UNRELATED: Board Membership:* Editorial Board of *Gynaecological Surgery*.* Eduard Gratacos—*RELATED: Grant:* Agència de Gestió d'Ajuts Universitaris i de Recerca, SGR grant No. 1531; CERCA Programme Generalitat de Catalunya; The Cerebra Foundation for the Brain-Injured Child, Carmarthen, Wales; European Commission Education, Audiovisual and Culture Executive Agency, 2013-0040; Ministerio de Economía y Competitividad—Instituto de Salud Carlos III, PI16/00861; "La Caixa" Foundation, LCF/PR/GNI4/10270005.* *Money paid to institution.

REFERENCES

1. Cardoza JD, Goldstein RB, Filly RA. **Exclusion of fetal ventriculomegaly with a single measurement: the width of the lateral ventricular atrium.** *Radiology* 1988;169:711–14 CrossRef Medline
2. Salomon LJ, Bernard JP, Ville Y. **Reference ranges for fetal ventricular width: a non-normal approach.** *Ultrasound Obstet Gynecol* 2007;30:61–66 CrossRef Medline
3. Melchiorre K, Bhide A, Gika AD, et al. **Counseling in isolated mild fetal ventriculomegaly.** *Ultrasound Obstet Gynecol* 2009;34:212–24 CrossRef Medline
4. Leitner Y, Stolar O, Rotstein M, et al. **The neurocognitive outcome of mild isolated fetal ventriculomegaly verified by prenatal magnetic resonance imaging.** *Am J Obstet Gynecol* 2009;201:215.e1–6 CrossRef Medline
5. Ouahba J, Luton D, Vuillard E, et al. **Prenatal isolated mild ventriculomegaly: outcome in 167 cases.** *BJOG* 2006;113:1072–79 CrossRef Medline
6. Sadan S, Malinger G, Schweiger A, et al. **Neuropsychological outcome of children with asymmetric ventricles or unilateral mild ventriculomegaly identified in utero.** *BJOG* 2007;114:596–602 CrossRef Medline
7. Gilmore JH, van Tol J, Kliewer MA, et al. **Mild ventriculomegaly detected in utero with ultrasound: clinical associations and implications for schizophrenia.** *Schizophr Res* 1998;33:133–40 CrossRef Medline
8. Tremblay E, Therasse E, Thomassin-Naggara I, et al. **Quality initiatives: guidelines for use of medical imaging during pregnancy and lactation.** *RadioGraphics* 2012;32:897–911 CrossRef Medline
9. Lyoo IK, Noam GG, Lee CK, et al. **The corpus callosum and lateral ventricles in children with attention-deficit hyperactivity disorder: a brain magnetic resonance imaging study.** *Biol Psychiatry* 1996;40:1060–63 CrossRef Medline
10. Vergani P, Locatelli A, Strobelt N, et al. **Clinical outcome of mild fetal ventriculomegaly.** *Am J Obstet Gynecol* 1998;178:218–22 CrossRef Medline
11. Gaglioti P, Danelon D, Bontempo S, et al. **Fetal cerebral ventriculomegaly: outcome in 176 cases.** *Ultrasound Obstet Gynecol* 2005;25:372–77 CrossRef Medline
12. Lockwood Estrin G, Kyriakopoulou V, Makropoulos A, et al. **Altered**

- white matter and cortical structure in neonates with antenatally diagnosed isolated ventriculomegaly. *Neuroimage Clin* 2016;11:139–48 CrossRef Medline
13. Kyriakopoulou V, Vatansever D, Elkommos S, et al. **Cortical overgrowth in fetuses with isolated ventriculomegaly.** *Cereb Cortex* 2014;24:2141–50 CrossRef Medline
 14. Lyall AE, Woolson S, Wolfe HM, et al. **Prenatal isolated mild ventriculomegaly is associated with persistent ventricle enlargement at ages 1 and 2.** *Early Hum Dev* 2012;88:691–98 CrossRef Medline
 15. Miguelote RF, Vides B, Santos RF, et al. **Cortical maturation in fetuses referred for ‘isolated’ mild ventriculomegaly: a longitudinal ultrasound assessment.** *Prenat Diagn* 2012;32:1273–81 CrossRef Medline
 16. Hahner N, Puerto B, Perez-Cruz M, et al. **Altered cortical development in fetuses with isolated nonsevere ventriculomegaly assessed by neurosonography.** *Prenat Diagn* 2018;38:365–75 CrossRef Medline
 17. International Society of Ultrasound in Obstetrics & Gynecology Education Committee. **Sonographic examination of the fetal central nervous system: guidelines for performing the ‘basic examination’ and the ‘fetal neurosonogram.’** *Ultrasound Obstet Gynecol* 2007;29:109–16 CrossRef Medline
 18. Egaña-Ugrinovic G, Sanz-Cortes M, Figueras F, et al. **Differences in cortical development assessed by fetal MRI in late-onset intrauterine growth restriction.** *Am J Obstet Gynecol* 2013;209:126.e1–8 CrossRef Medline
 19. Alonso I, Borenstein M, Grant G, et al. **Depth of brain fissures in normal fetuses by prenatal ultrasound between 19 and 30 weeks of gestation.** *Ultrasound Obstet Gynecol* 2010;36:693–99 CrossRef Medline
 20. Pistorius LR, Stoutenbeek P, Groenendaal F, et al. **Grade and symmetry of normal fetal cortical development: a longitudinal two- and three-dimensional ultrasound study.** *Ultrasound Obstet Gynecol* 2010;36:700–08 CrossRef Medline
 21. Keraudren K, Kuklisova-Murgasova M, Kyriakopoulou V, et al. **Automated fetal brain segmentation from 2D MRI slices for motion correction.** *Neuroimage* 2014;101:633–43 CrossRef Medline
 22. Kuklisova-Murgasova M, Quaghebeur G, Rutherford MA, et al. **Reconstruction of fetal brain MRI with intensity matching and complete outlier removal.** *Med Image Anal* 2012;16:1550–64 CrossRef Medline
 23. Sanroma G, Benkarim OM, Piella G, et al. **Building an ensemble of complementary segmentation methods by exploiting probabilistic estimates.** In: *Proceedings of the International Workshop on Machine Learning in Medical Imaging*, Athens, Greece. October 17, 2016; Vol 10019 LNCS.;27–35
 24. Benkarim OM, Hahner N, Piella G, et al. **Cortical folding alterations in fetuses with isolated non-severe ventriculomegaly.** *Neuroimage Clin* 2018;18:103–14 CrossRef Medline
 25. Brazelton TB, Nugent JK. *Neonatal Behavioral Assessment Scale*. London: McKeith Press; 1995
 26. Canals J, Hernández-Martínez C, Esparó G, et al. **Neonatal Behavioral Assessment Scale as a predictor of cognitive development and IQ in full-term infants: a 6-year longitudinal study.** *Acta Paediatr* 2011;100:1331–37 CrossRef Medline
 27. Boatella-Costa E, Costas-Moragas C, Botet-Mussons F, et al. **Behavioral gender differences in the neonatal period according to the Brazelton scale.** *Early Hum Dev* 2007;83:91–97 CrossRef Medline
 28. Gasquoine PG. **Contributions of the insula to cognition and emotion.** *Neuropsychol Rev* 2014;24:77–87 CrossRef Medline
 29. Peschke C, Ziegler W, Eisenberger J, et al. **Phonological manipulation between speech perception and production activates a parietofrontal circuit.** *Neuroimage* 2012;59:788–99 CrossRef Medline
 30. Bigler ED, Mortensen S, Neeley ES, et al. **Superior temporal gyrus, language function, and autism.** *Dev Neuropsychol* 2007;31:217–38 CrossRef Medline
 31. Li W, Qin W, Liu H, et al. **Subregions of the human superior frontal gyrus and their connections.** *Neuroimage* 2013;78:46–58 CrossRef Medline
 32. Signorelli M, Tiberti A, Valseriati D, et al. **Width of the fetal lateral ventricular atrium between 10 and 12 mm: a simple variation of the norm?** *Ultrasound Obstet Gynecol* 2004;23:14–18 CrossRef Medline
 33. Bloom SL, Bloom DD, DellaNebbia C, et al. **The developmental outcome of children with antenatal mild isolated ventriculomegaly.** *Obstet Gynecol* 1997;90:93–97 CrossRef Medline
 34. Masoller N, Sanz-Cortés M, Crispi F, et al. **Mid-gestation brain Doppler and head biometry in fetuses with congenital heart disease predict abnormal brain development at birth.** *Ultrasound Obstet Gynecol* 2016;47:65–73 CrossRef Medline
 35. Egaña-Ugrinovic G, Sanz-Cortes M, Figueras F, et al. **Fetal MRI insular cortical morphometry and its association with neurobehavior in late-onset small-for-gestational-age fetuses.** *Ultrasound Obstet Gynecol* 2014;44:322–29 CrossRef Medline

Diffusion-Weighted MR Imaging in a Prospective Cohort of Children with Cerebral Malaria Offers Insights into Pathophysiology and Prognosis

S.M. Moghaddam, G.L. Birbeck, T.E. Taylor, K.B. Seydel, S.D. Kampondeni, and M.J. Potchen



ABSTRACT

BACKGROUND AND PURPOSE: Validation of diffusion-weighted images obtained on 0.35T MR imaging in Malawi has facilitated meaningful review of previously unreported findings in cerebral malaria. Malawian children with acute cerebral malaria demonstrated restricted diffusion on brain MR imaging, including an unusual pattern of restriction isolated to the subcortical white matter. We describe the patterns of diffusion restriction in cerebral malaria and further evaluate risk factors for and outcomes associated with an isolated subcortical white matter diffusion restriction.

MATERIALS AND METHODS: Between 2009 and 2014, comatose Malawian children admitted to the hospital with cerebral malaria underwent admission brain MR imaging. Imaging data were compiled via NeuroInterp, a RedCap data base. Clinical information obtained included coma score, serum studies, and coma duration. Electroencephalograms were obtained between 2009 and 2011. Outcomes captured included death, neurologic sequelae, or full recovery.

RESULTS: One hundred ninety-four/269 (72.1%) children with cerebral malaria demonstrated at least 1 area of diffusion restriction. The most common pattern was bilateral subcortical white matter involvement (41.6%), followed by corpus callosum (37.5%), deep gray matter (36.8%), cortical gray matter (17.8%), and posterior fossa (8.9%) involvement. Sixty-one (22.7%) demonstrated isolated subcortical white matter diffusion restriction. These children had lower whole-blood lactate levels (OR, 0.9; 95% CI, 0.85–0.98), were less likely to require anticonvulsants (OR, 0.6; 95% CI, 0.30–0.98), had higher average electroencephalogram voltage (OR, 1.01; 95% CI, 1.00–1.02), were less likely to die (OR, 0.09; 95% CI, 0.01–0.67), and were more likely to recover without neurologic sequelae (OR, 3.7; 95% CI, 1.5–9.1).

CONCLUSIONS: Restricted diffusion is common in pediatric cerebral malaria. Isolated subcortical white matter diffusion restriction is a unique imaging pattern associated with less severe disease and a good prognosis for full recovery. The underlying pathophysiology may be related to selective white matter vulnerability.

ABBREVIATIONS: CM = cerebral malaria; IWMDR = isolated subcortical white matter diffusion restriction; EEG = electroencephalogram

Malaria remains a common burdensome disease with 219 million new infections and 435,000 deaths in 2017.¹ Pediatric cerebral malaria (CM), the most severe form of the disease, maintains a fatality rate of 15%–25% with long-term neurologic disability in 35%–45% of survivors despite treatment with anti-

malarials that clear parasitemia within hours.² Postmortem studies have shown that CM has diverse pathologic findings, highlighting the complex nature of the host/parasite interaction.^{3,4} MR imaging studies have shown a wide range of findings,⁵ further underscoring the complex nature of this disease. Past use of imaging has helped illuminate pathophysiologic mechanisms driving morbidity and mortality of CM, showing that brain swelling on initial MR imaging predicts death⁶ and demonstrating regions of focal brain atrophy on CT in survivors with epilepsy that correspond to the epileptic foci.⁷

Our group has previously reported the various patterns of MR imaging findings in CM and discussed their implications in terms

Received April 4, 2019; accepted after revision June 28.

From the Department of Imaging Sciences (S.M.M., M.J.P.), and Department of Neurology, Department of Public Health, Center for Experimental Therapeutics (G.L.B.), University of Rochester, Rochester, New York; Department of Osteopathic Medical Specialties (T.E.T., K.B.S.), Michigan State University, East Lansing, Michigan; and Queen Elizabeth Central Hospital (S.D.K.), University of Malawi College of Medicine, Blantyre, Malawi.

This work was supported by the Harry W. Fischer Research Fund, University of Rochester Medical Center Department of Imaging Sciences. Partial funding was provided by the National Institutes of Health: The CHASE Study, NIHROINS094037.

Paper previously presented at: American Society of Neuroradiology Annual Meeting and the Foundation of the ASNR Symposium, May 18–23, 2019; Boston, Massachusetts.

Please address correspondence to Sarah Mohajeri Moghaddam, MD, MPH, Imaging Sciences, 601 Elmwood Ave, Box 648, Rochester, NY 14642; e-mail: sarahmohajeri29@gmail.com

Indicates open access to non-subscribers at www.ajnr.org

<http://dx.doi.org/10.3174/ajnr.A6159>

of the underlying pathophysiologic processes involved in CM.^{5,6,8} The most commonly observed patterns of structural abnormality on CM brain MR imaging include diffuse brain swelling and distinct patterns of abnormalities on T2 in the basal ganglia, cerebral cortex, and white matter.⁵ The initial reports did not include DWI findings due to limitations of the 0.35T technology in our Malawi-based study site. Through additional sequence acquisition and postprocessing, we have now validated the DWI data from the Malawi MR imaging.⁹ Therefore, this report details the DWI findings in this large cohort of children with pediatric CM.

DWI is a mainstay of neurologic imaging and should offer important insights into diseases in resource-limited tropical settings that are only now benefiting from access to advanced imaging technology. DWI signal changes reflect edematous changes in the brain parenchyma from cytotoxic edema. One mechanism of cytotoxic edema is transsynaptic injury, which is thought to be caused by excitotoxic amines released through a number of pathophysiologic mechanisms.¹⁰ Receptors associated with excitotoxic mechanisms are distributed throughout the brain, in both gray and white matter.¹¹ Resultant DWI changes from this mechanism occur in astrocytes, oligodendrocytes, the myelin sheath, and axons, leading to intramyelinic cytotoxic edema. Low ADC values are generally thought to represent areas of cell death. However, cytotoxic edema is a premonitory state, and in some circumstances, reversibility is possible.¹² This is exemplified by recent work in stroke imaging, which has found, with great accuracy, differences in ADC values between infarcted white matter and penumbra with a reversible potential after tissue plasminogen activator administration.¹³

Diffusion-weighted sequences are commonly used to evaluate ischemic stroke and neoplasms. However, diffusion restriction is seen in a number of other conditions and provides insight into their pathophysiology. These conditions include hypoxic-ischemic encephalopathy,¹⁴ diffuse axonal injury,¹⁵ and toxic¹⁶ or metabolic¹⁷ leukoencephalopathy. Diffusion restriction reversibility has been described in several conditions—most commonly involving the white matter. Examples of conditions in which there can be reversible white matter–restricted diffusion include demyelinating disease,¹⁸ heroin-induced encephalopathy,¹⁹ postictal state,²⁰ hypoglycemia,²¹ and vigabatrin-associated vacuolar myelinopathy.²²

Among children admitted to the pediatric research ward with CM in Blantyre during several years, we observed various patterns of diffusion restriction, including the unusual finding of isolated subcortical white matter diffusion restriction (IWMDR) in a substantial minority (22.7%) of children with CM. Given the unique nature of this pattern of diffusion restriction and the limitations in our present understanding of coma etiology in children with CM, in addition to descriptively reporting the DWI findings from the pediatric CM cohort, we further evaluated risk factors for and outcomes associated with white matter–restricted diffusion in pediatric CM.

MATERIALS AND METHODS

Children admitted to the pediatric research ward of Queen Elizabeth Central Hospital between 2009 and 2014 who met the World Health Organization definition of CM and demonstrated malarial

retinopathy^{23,24} were eligible for inclusion in the study. When possible, initial imaging was performed within 12 hours of admission. Children who died or regained consciousness before imaging could be performed and those whose parents did not consent to enrollment in the study were excluded. Standard clinical care including emergent antimalarial treatment was provided according to ward protocols in all cases.²⁵

The appropriate local and United States research ethics committees approved this work. Demographic, clinical, electroencephalogram (EEG), and imaging data were prospectively collected. Clinical variables included temperature, Blantyre coma scale score⁶ at admission, platelet count, whole-blood lactate level, white blood cell and glucose levels, systolic blood pressure, HIV status, seizures before admission, histidine-rich protein levels—a marker of parasite burden,²⁶ the presence/absence of clinical seizures, and overall coma duration. Coma duration was imputed for those who died to be 2 SDs above the mean coma duration in the survivors. Outcomes captured included death, neurologic sequelae at discharge, or intact survival. Admission EEGs were obtained between 2009 and 2011.⁶ EEG characteristics included average and maximal voltage, dominant rhythm frequency, sleep architecture, variability, reactivity, presence and location of slowing, and presence of asymmetry.

Two fellowship-trained radiologists, one trained in MR imaging with 13 years of experience and the other trained in neuroradiology with 16 years of experience, blinded to patient outcomes interpreted all MR imaging. Data were compiled into a searchable RedCap data base developed for this project called “NeuroInterp.”²⁷ Among imaging data collected were the presence or absence of DWI findings in various anatomic locations. DWI sequences were acquired via standard protocol, previously validated on this 0.35T Signa Ovation Excite MR imaging scanner (GE Healthcare, Milwaukee, Wisconsin).⁹ Abnormal findings on DWI were described as being present versus absent; if findings were present, we indicated the predominant location involved, including involvement of the subcortical white matter, cortical gray matter, globus pallidus, putamen, caudate, corpus callosum, and/or posterior fossa. The radiologists provided independent interpretations with discrepancies addressed by consensus review.

A case definition of IWMDR was developed using NeuroInterp-derived data. Cases included those that demonstrated subcortical diffusion restriction, excluding those with concurrent basal ganglia and cortical diffusion restriction.²⁸ Of note, occasional abnormal findings on DWI were also seen in the corpus callosum and posterior fossa in this subgroup.

Statistical analysis was conducted using Epi Info, Version 7.2 (<https://www.cdc.gov/epiinfo/index.html>). Statistical associations for categorical clinical, and outcome variables were determined using Pearson χ^2 tests. Statistical differences in continuous variables were determined using Student *t* and ANOVA tests. Univariate logistic regression models were used to estimate relevant correlation coefficients, which are reported as odds ratios. A *P* value < .05 was considered significant.

RESULTS

A total of 269 consecutive pediatric patients with CM meeting the inclusion criteria were imaged on the 0.35T Signa Ovation Excite

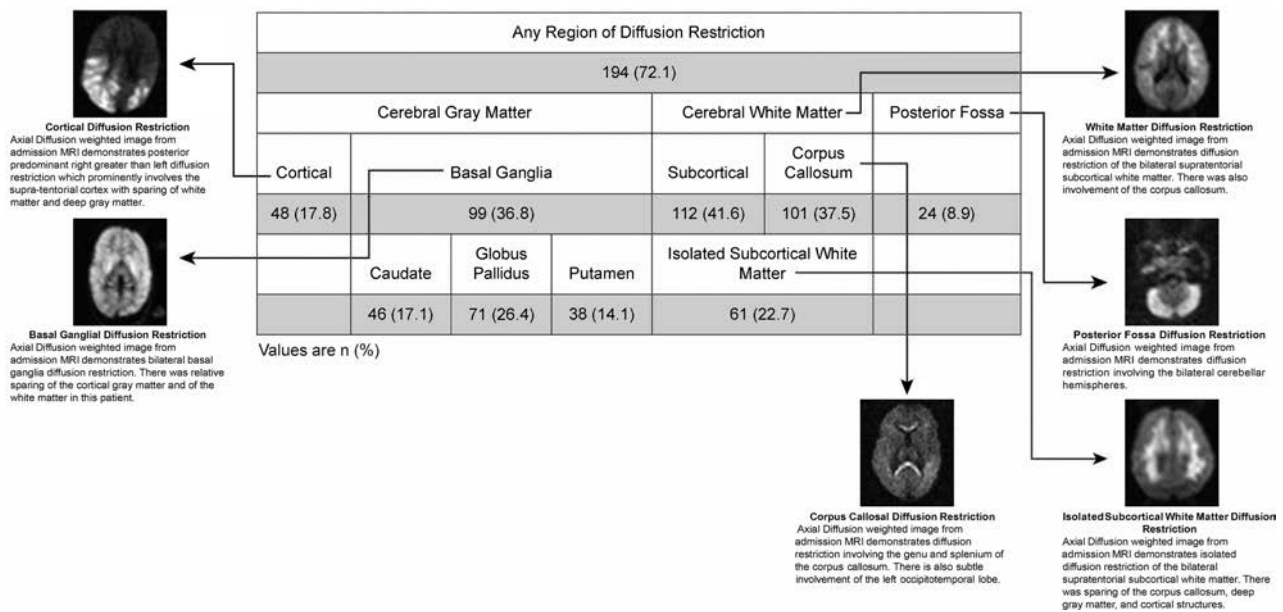


FIG 1. Patterns of diffusion restriction on admission MR imaging in children with retinopathy-positive cerebral malaria. Numbers in each category are reported as No. (%). Examples of each observed pattern are illustrated with accompanying description.

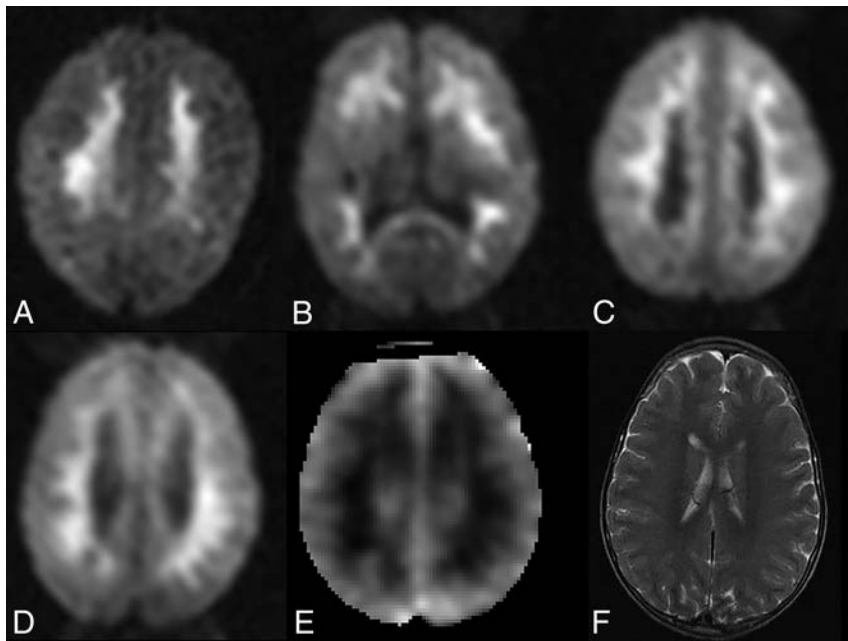


FIG 2. IWMDR on initial brain MR imaging in children with cerebral malaria. A–C, Axial diffusion-weighted images in 3 different comatose children with acute cerebral malaria. There are confluent regions of diffusion restriction in the subcortical white matter without involvement of the cortex or deep gray matter. D–F, Axial DWI in a different patient demonstrates a similar pattern of white matter hyperintensity on diffusion-weighted images, with corresponding hypointensity on ADC maps, consistent with true diffusion restriction. Axial T2-weighted image demonstrates subtle regions of corresponding T2 hyperintensity.

MR imaging scanner between 2009 and 2014. The mean age was 51.4 months. One hundred ninety-four/269 (72.1%) demonstrated at least 1 area of diffusion restriction. Patterns of gray matter involvement included the cortex in 48/269 (17.8%) and the basal ganglia in 99/269 (36.8%) children. Basal ganglia involvement was most commonly seen in the globus pallidus (71/269, 26.4%). White matter involvement was predominantly bilateral and subcortical (112/269, 41.6%) and/or corpus callosal (101/

269, 37.5%). Diffusion restriction was less commonly observed in the posterior fossa (24/269, 8.9%) (Fig 1).

Sixty-one (22.7%) children with CM demonstrated the unusual pattern of IWMDR (Fig 2). IWMDR occurred exclusively in the subcortical regions with no periventricular involvement. Children with IWMDR had significantly lower whole-blood lactate levels (mean, 5.4 versus 6.9 mmol/L; OR, 0.9; 95% CI 0.85–0.98). They were also less likely to require anticonvulsant medication on admission and have clinical seizures (57% versus 71%; OR, 0.6; 95% CI, 0.30–0.98). There was no significant difference between the groups in terms of admission temperature and Blantyre coma scale score, platelet count, white blood cell count, serum glucose levels, systolic blood pressure, HIV status, seizures before admission, and histidine-rich protein levels.

A total of 155/269 children had admission EEGs, of which 36 (23%) demonstrated IWMDR. The average EEG voltage was significantly higher in the

IWMDR group (128.9 versus 104.5 μ V; OR, 1.01; 95% CI, 1.00–1.02). Higher average voltage was associated with survival in prior studies on Malawian children with CM^{6,29} and in a pooled Malawian and Ugandan CM population.²⁹

Although additional EEG variables did not reach statistical significance, likely due to the small sample size³⁰ with IWMDR, there were additional EEG trends within this group that previously conferred favorable outcomes.²⁹ These include a higher

Table 1: Clinical characteristics and outcomes associated with IWMDR in children with cerebral malaria^a

	IWMDR+	IWMDR-	OR	95% CI	P Value
Clinical characteristics					
Admission temperature (°C)	38.9 ± 1.1	38.8 ± 1.2	1.11	0.87–1.42	.40
Plasma lactic acid levels (mmol/L)	5.4 ± 3.6	6.9 ± 4.5	0.91	0.85–0.98	.02
Systolic blood pressure (mm Hg)	41.2 ± 214.7	74.9 ± 137.6	1.00	0.99–1.00	.14
HIV status	5 (9.6%)	32 (16.3%)	0.55	0.20–1.48	.23
Reported preadmission seizure	53 (89.8%)	171 (83.0%)	1.80	0.72–4.52	.21
Plasma glucose level (mmol/L)	6.4 ± 2.1	6.7 ± 3.6	0.97	0.89–1.06	.49
Plasma HRP-II levels	10.2 ± 10.2	10.8 ± 10.1	0.99	0.96–1.02	.67
Received anticonvulsant at admission	35 (57.4%)	148 (71.2%)	0.55	0.30–0.98	.04
Admission Blantyre coma scale score	1.4 ± 0.6	1.3 ± 0.6	1.44	0.90–2.31	.13
Admission white blood cell count × 10 ⁻⁹ /L	10.5 ± 7.9	11.3 ± 7.9	0.98	0.95–1.03	.51
Platelet count × 10 ⁻⁹ /L	56 ± 60	59 ± 64	1.00	1.00–1.00	.81
EEG characteristics					
Average voltage (μV)	128.9 ± 50.7	104.5 ± 53.5	1.01	1.00–1.02	.02
Maximum voltage (μV)	251.1 ± 75.8	219.4 ± 88.5	1.00	0.99–1.01	.06
Sleep architecture	20 (55.6%)	66 (55.5%)	1.00	0.47–2.13	.99
Dominant rhythm frequency (Hz)	2.3 ± 0.9	2.4 ± 1.7	NA	NA	.56
Variability	24 (66.7%)	69 (58.0%)	1.45	0.66–3.17	.35
Reactivity	20 (58.8%)	45 (40.5%)	2.10	0.96–4.58	.06
General slowing	35 (97.2%)	105 (90.5%)	3.67	0.46–29.4	.22
Paradoxical reactivity	10 (50%)	17 (37.0%)	1.70	0.59–4.93	.32
Asymmetry	7 (19.4%)	34 (28.8%)	0.60	0.24–1.49	.27
Outcomes					
Overall coma duration (hrs)	47.5 ± 25.3	74.8 ± 43.9	0.98	0.97–0.99	<.001
Full recovery	55 (90.2%)	148 (71.2%)	3.70	1.50–9.10	.004
Survival with sequelae	5 (8.2%)	27 (13.0%)	0.60	0.22–1.63	.32
Death	1 (1.6%)	33 (15.9%)	0.09	0.01–0.67	.02

Note:—HRP-II indicates histidine-rich protein, a marker of parasite burden; IWMDR+, subjects with purely subcortical white matter abnormalities, excluding those with cortical DWI abnormalities and those with basal ganglia DWI abnormalities; IWMDR-, those who did not meet criteria for IWMDR+; NA, not applicable.

^a Values are No. (%) or means.

maximum EEG voltage (251.1 versus 219.4 μV) and more likelihood of demonstrating retained reactivity (58.8% versus 40.5%) and nonfocal slowing (97.2% versus 90.5%). There were no differences in dominant rhythm frequency, presence of sleep architecture, variability, or asymmetry.

In terms of outcomes, IWMDR was associated with a shorter period of coma and improved outcome at discharge. Only one (1.6%) of those with IWMDR died versus 33 (15.9%) of those without the finding (OR, 0.09; 95% CI, 0.01–0.67). Of those who survived, 55 (90%) fully recovered without evidence of neurologic sequelae at discharge (90% versus 71%; OR, 3.7; 95% CI 1.5–9.1) (Table 1).

DISCUSSION

In the largest series of pediatric cases of CM imaged to date, restricted diffusion was frequently seen, and the finding of isolated restricted diffusion of the subcortical white matter, an MR imaging finding not often seen with other conditions, was remarkably common and was associated with less severe disease clinically and better outcomes. White matter diffusion restriction was associated with lower lactate levels and a lower odds of clinical seizure—2 established predictors of disease severity supporting these patients having a less severe disease state.³¹ The preceding finding may underscore the concept of “selective vulnerability,” wherein white matter–restricted diffusion changes can be seen without cortical or deep gray matter involvement because the white matter is more susceptible to various transient deleterious physiologic changes.¹⁴ In cases of CM coma with good outcome, isolated white matter dysfunction related to selective and revers-

ible white matter vulnerability may explain the previously inexplicable nature of this rapidly reversible coma.

Although uncommon in other settings, isolated white matter transient restricted diffusion has been described in several other disease states (Table 2). Acute toxic leukoencephalopathy, which occurs as a result of various drug or environmental exposures, shows symmetric areas of T2 hyperintensity in the periventricular white matter, often with associated diffusion restriction, and the findings are frequently reversible if toxic exposure is removed and follow-up imaging is performed.^{16,32} Acute toxic leukoencephalopathy–associated isolated white matter–restricted diffusion is thought to arise from intramyelinic cytotoxic edema and resultant myelin vacuolization, capillary endothelial injury inducing cytotoxicity, and/or direct toxic demyelination.¹⁶ Endothelial injury is a central pathophysiologic mechanism in CM. A substantial number of children in our cohort (61/269, 22.7%) demonstrated diffuse subcortical white matter involvement, similar to the typical appearance of acute toxic leukoencephalopathy though with a distribution in the subcortical regions. A recent large-scale study of Malawian children with CM found extensive alterations in blood metabolites during CM compared with levels during convalescence,³³ implicating circulating metabolites possibly playing some role in the overall pathogenesis.

Reversible diffusion restriction is also described in acute severe hypoglycemia, in which restricted diffusion most commonly involves the internal capsule, centrum semiovale, and cerebral cortex and is commonly reversible with appropriate timely treatment.^{21,30,34,35} In hypoglycemia, the pathophysiology of diffusion

Table 2: Conditions with reversible/transient white matter diffusion restriction and their pathophysiology

Condition	Proposed Pathophysiology	Relevance to Cerebral Malaria
Acute toxic leukoencephalopathy	Intramyelinic edema, myelin vacuolization Capillary endothelial injury Direct toxic demyelination ¹⁶	Endothelial injury is a pathophysiologic mechanism in CM ³⁸
Hypoglycemia	Energy failure leading to excitatory edema ²¹	Hypoglycemia is a frequent complication in children with severe falciform malaria ³⁹ ; local/focal hypoglycemia may occur due to sludging even in the absence of systemic hypoglycemia
Peri-/postictal state	Increased metabolic demand leading to energy failure and resultant cytotoxic and vasogenic edema ⁴⁰	Seizures, often recurrent, are a frequent manifestation of CM and associated with worse outcome ²⁹
Penumbra of ischemic infarct	Early white matter ischemic injury with axonal swelling and intramyelinic edema ¹³	Sequestration in postcapillary venules of the brain and venous congestion are central to CM pathogenesis ²⁵
Demyelination	Immune-mediated perivenular inflammation and demyelination ⁴¹	Vascular inflammatory markers are associated with CM, and perivenular inflammation is thought to contribute to CM pathogenesis ³⁸

restriction is not definitively understood but is thought to be related to transmembrane pump energy failure leading to cytotoxic edema and/or excitatory edema. The latter is thought to be responsible for those with predominantly white matter involvement, whose outcomes tend to be more favorable. Our study also showed this finding to be related to favorable CM outcomes with a fatality rate of 0.7% versus 12.6% in the sample overall. Although systemic hypoglycemia is rapidly addressed on admission and would not have been present at the time of imaging, focal metabolic energy failure due to vascular sludging, hyperpyrexia, seizures, and other drivers of high-energy demand ubiquitous in CM could be anticipated and could be reversible with optimal care. Glutamate levels are significantly lower during the acute phase of pediatric CM,³³ supporting the supposition that energy failure could play a role in diffusion restriction.

Hyperthermia has been shown to increase the excitatory amino acids glutamate and aspartate as well as inhibitory amino acids gamma-aminobutyric acid and glycine in the brain. Significant reduction in cerebral blood flow, edema formation, and cell injuries is evident.³⁶ While we did not find a direct relationship between white matter DWI changes and temperature, the temperature at the time of the MR imaging was not specifically noted and markedly elevated temperatures of >39°C during the acute phase are a hallmark of this disease. Therefore, the absence of an association may be related to the temporal nature of our data collection. These changes lead to excitatory edema rather than frank cytotoxic edema. Review of postmortem specimens from prior studies on Malawian children with cerebral malaria has failed to demonstrate intramyelinic edema,⁴ and an excitatory edema state is more likely present, which could lead to findings of restricted diffusion. The presence of excitatory edema would also help explain another unusual finding in cerebral malaria, in which there is an acute onset of coma, which generally resolves with a short duration.

Mechanisms involved in early cytotoxic edema in infarct penumbra^{12,13} are also of particular interest in CM. The current understanding of the pathophysiology of CM predominantly involves the presence of microvascular sequestration. Postmortem studies have demonstrated the presence of sequestration within the postcapillary venules of the brain.²⁵ Cerebral white matter is

highly vulnerable to the effects of focal ischemia. Pathologic changes in oligodendrocytes and myelinated axons appear early and seem to be concomitant with, but independent of, neuronal perikaryal injury.³⁷ Microvascular occlusion may lead to venous congestion and regional hypoperfusion, with the downstream sequelae of excitatory edema in underperfused regions of the brain. This phenomenon could be transient if the patient is treated before progression to cell death occurs.

CONCLUSIONS

Isolated restricted white matter diffusion is common in pediatric CM and is associated with less severe disease and better outcomes compared with patients who do not demonstrate this finding. The underlying pathophysiology of this finding is not thoroughly understood and may result from the selective vulnerability of white matter to several potentially reversible deleterious pathophysiologic changes that occur in patients with CM. IWMDR may represent a marker for a better prognosis. In CM, low ADC values occur in the absence of cytotoxic edema. Other etiologies for fluid redistribution resulting in restricted water motion, such as excitatory edema, should be considered.

Disclosures: Gretchen L. Birbeck—UNRELATED: Board Membership: Fogarty International Center Advisory Board and the American Neurological Association; *Consultancy*: GlaxoSmithKline, *Comments*: related to neuropsychiatric effects of antimalarial drugs; *Grants/Grants Pending*: National Institutes of Health. Karl B. Seydel—UNRELATED: *Employment*: Blantyre Malaria Project. Michael J. Potchen—RELATED: *Grant*: National Institutes of Health*; UNRELATED: *Expert Testimony*: expert witness in medical legal cases; *Grants/Grants Pending*: National Institutes of Health and Radiological Society of North America.* Terrie E. Taylor—RELATED: *Grant*: National Institutes of Health*; UNRELATED: *Board Membership*: Novartis Institute for Tropical Diseases; *Employment*: Michigan State University*; *Grants/Grants Pending*: National Institutes of Health*; *Payment for Lectures Including Service on Speakers Bureaus*: Novartis Institute for Tropical Diseases. *Money paid to the institution.

REFERENCES

- World Health Organization. World malaria report 2018. License: CC BY-NC-SA 3.0 IGO. https://www.who.int/malaria/publications/world_malaria_report/en/. Accessed April 10, 2019
- Lopera-Mesa TM, Doumbia S, Chiang S, et al. **Plasmodium falciparum clearance rates in response to artesunate in Malian children with malaria: effect of acquired immunity.** *J Infect Dis* 2013;207:1655–63 CrossRef Medline

3. Milner DA Jr. **Rethinking cerebral malaria pathology.** *Curr Opin Infect Dis* 2010;23:456–63 CrossRef Medline
4. Dorovini-Zis K, Schmidt K, Huynh H, et al. **The neuropathology of fatal cerebral malaria in Malawian children.** *Am J Pathol* 2011;178:2146–58 CrossRef Medline
5. Potchen MJ, Kampondeni SD, Seydel KB, et al. **Acute brain MRI findings in 120 Malawian children with cerebral malaria: new insights into an ancient disease.** *AJNR Am J Neuroradiol* 2012;33:1740–46 CrossRef Medline
6. Seydel KB, Kampondeni SD, Valim C, et al. **Brain swelling and death in children with cerebral malaria.** *N Engl J Med* 2015;372:1126–37 CrossRef Medline
7. Kampondeni SD, Potchen MJ, Beare NA, et al. **MRI findings in a cohort of brain injured survivors of pediatric cerebral malaria.** *Am J Trop Med Hyg* 2013;88:542–46 CrossRef Medline
8. Postels DG, Li C, Birbeck GL, et al. **Brain MRI of children with retinopathy-negative cerebral malaria.** *Am J Trop Med Hyg* 2014;91:943–49 CrossRef Medline
9. Zhuang Y, Potchen MJ, Kampondeni SD, et al. **Validation of diffusion measurements obtained on a 0.35T MR in Malawi: important insights for radiologists in low income settings with low field MRI.** *Magn Reson Imaging* 2018;45:120–28 CrossRef Medline
10. Moritani T, Smoker WR, Sato Y, et al. **Diffusion-weighted imaging of acute excitotoxic brain injury.** *AJNR Am J Neuroradiol* 2005;26:216–28 Medline
11. Hassel B, Bolding KA, Narvesen C, et al. **Glutamate transport, glutamine synthetase and phosphate-activated glutaminase in rat CNS white matter: a quantitative study.** *J Neurochem* 2003;87:230–37 CrossRef Medline
12. Liang D, Bhatta S, Gerzanich V, et al. **Cytotoxic edema: mechanisms of pathological cell swelling.** *Neurosurg Focus* 2007;22:E2 Medline
13. Sato A, Shimizu Y, Koyama J, et al. **A new threshold of apparent diffusion coefficient values in white matter after successful tissue plasminogen activator treatment for acute brain ischemia.** *J Neuro-radiol* 2017;44:223–26 CrossRef Medline
14. Chalela JA, Wolf RL, Maldjian JA, et al. **MRI identification of early white matter injury in anoxic-ischemic encephalopathy.** *Neurology* 2001;56:481–85 CrossRef Medline
15. Zheng WB, Liu GR, Li LP, et al. **Prediction of recovery from a post-traumatic coma state by diffusion-weighted imaging (DWI) in patients with diffuse axonal injury.** *Neuroradiology* 2007;49:271–79 CrossRef Medline
16. McKinney AM, Kieffer SA, Paylor RT, et al. **Acute toxic leukoencephalopathy: potential for reversibility clinically and on MRI with diffusion-weighted and FLAIR imaging.** *AJR Am J Roentgenol* 2009;193:192–206 CrossRef Medline
17. Maheen Anwar SS, Mubarak F, Sajjad Z, et al. **5-FU induced acute toxic leukoencephalopathy: early recognition and reversibility on DWI-MRI.** *J Coll Physicians Surg Pak* 2014;24(Suppl 1):S8–10 CrossRef Medline
18. Koelman DL, Benkeser DC, Klein JP, et al. **Acute disseminated encephalomyelitis: prognostic value of early follow-up brain MRI.** *J Neurol* 2017;264:1754–62 CrossRef Medline
19. Barnett MH, Miller LA, Reddel SW, et al. **Reversible delayed leukoencephalopathy following intravenous heroin overdose.** *J Clin Neurosci* 2001;8:165–67 CrossRef Medline
20. Cianfoni A, Caulo M, Cerase A, et al. **Seizure-induced brain lesions: a wide spectrum of variably reversible MRI abnormalities.** *Eur J Radiol* 2013;82:1964–72 CrossRef Medline
21. Kang EG, Jeon SJ, Choi SS, et al. **Diffusion MR imaging of hypoglycemic encephalopathy.** *AJNR Am J Neuroradiol* 2010;31:559–64 CrossRef Medline
22. Pearl PL, Vezina LG, Saneto RP, et al. **Cerebral MRI abnormalities associated with vigabatrin therapy.** *Epilepsia* 2009;50:184–94 CrossRef Medline
23. Newton CR, Chokwe T, Schellenberg JA, et al. **Coma scales for children with severe falciparum malaria.** *Trans R Soc Trop Med Hyg* 1997;91:161–65 CrossRef Medline
24. Molyneux ME, Taylor TE, Wirima JJ, et al. **Clinical features and prognostic indicators in paediatric cerebral malaria: a study of 131 comatose Malawian children.** *Q J Med* 1989;71:441–59 Medline
25. Taylor TE, Molyneux ME. **The pathogenesis of pediatric cerebral malaria: eye exams, autopsies, and neuroimaging.** *Ann NY Acad Sci* 2015;1342:44–52 CrossRef Medline
26. Dondorp AM, Desakorn V, Pongtavornpinyo W, et al. **Estimation of the total parasite biomass in acute falciparum malaria from plasma PfHRP2.** *PLoS Med* 2005;2:e204 CrossRef Medline
27. Potchen MJ, Kampondeni SD, Ibrahim K, et al. **NeuroInterp: a method for facilitating neuroimaging research on cerebral malaria.** *Neurology* 2013;81:585–88 CrossRef Medline
28. Helenius J, Soinne L, Perkiö J, et al. **Diffusion-weighted MR imaging in normal human brains in various age groups.** *AJNR Am J Neuroradiol* 2002;23:194–99 Medline
29. Postels DG, Wu X, Li C, et al. **Admission EEG findings in diverse paediatric cerebral malaria populations predict outcomes.** *Malar J* 2018;17:208 CrossRef Medline
30. Aoki T, Sato T, Hasegawa K, et al. **Reversible hyperintensity lesion on diffusion-weighted MRI in hypoglycemic coma.** *Neurology* 2004;63:392–93 CrossRef Medline
31. Idro R, Marsh K, John CC, et al. **Cerebral malaria: mechanisms of brain injury and strategies for improved neurocognitive outcome.** *Pediatr Res* 2010;68:267–74 CrossRef Medline
32. Rimkus Cde M, Andrade CS, Leite Cda C, et al. **Toxic leukoencephalopathies, including drug, medication, environmental, and radiation-induced encephalopathic syndromes.** *Semin Ultrasound CT MR* 2014;35:97–117 CrossRef Medline
33. Gupta S, Seydel K, Miranda-Roman MA, et al. **Extensive alterations of blood metabolites in pediatric cerebral malaria.** *PLoS One* 2017;12:e0175686 CrossRef Medline
34. Terakawa Y, Tsuyuguchi N, Nunomura K, et al. **Reversible diffusion-weighted imaging changes in the splenium of the corpus callosum and internal capsule associated with hypoglycemia: case report.** *Neurol Med Chir (Tokyo)* 2007;47:486–88 CrossRef Medline
35. Schmidt P, Böttcher J, Ragoschke-Schumm A, et al. **Diffusion-weighted imaging of hyperacute cerebral hypoglycemia.** *AJNR Am J Neuroradiol* 2011;32:1321–27 CrossRef Medline
36. Sharma HS. **Methods to produce brain hyperthermia.** *Current Protocols in Toxicology*; 2005;23:11.14.1–11.14.26
37. Pantoni L, Garcia JH, Gutierrez JA. **Cerebral white matter is highly vulnerable to ischemia.** *Stroke* 1996;27:1641–46; discussion 1647 CrossRef Medline
38. Conroy AL, Phiri H, Hawkes M, et al. **Endothelium-based biomarkers are associated with cerebral malaria in Malawian children: a retrospective case-control study.** *PLoS One* 2010;5:e15291 CrossRef Medline
39. Taylor TE, Molyneux ME, Wirima JJ, et al. **Blood glucose levels in Malawian children before and during the administration of intravenous quinine for severe falciparum malaria.** *N Engl J Med* 1988;319:1040–47 CrossRef Medline
40. Xiang T, Li G, Liang Y, et al. **A wide spectrum of variably periictal MRI abnormalities induced by a single or a cluster of seizures.** *J Neurol Sci* 2014;343:167–72 CrossRef Medline
41. Love S. **Demyelinating diseases.** *J Clin Pathol* 2006;59:1151–59 CrossRef Medline

Optimizing the Detection of Subtle Insular Lesions on MRI When Insular Epilepsy Is Suspected

J. Blustajn, S. Krystal, D. Taussig, S. Ferrand-Sorbets, G. Dorfmueller, and M. Fohlen

ABSTRACT

SUMMARY: Insular epilepsy is underdiagnosed and accounts for a number of failed operations. Identifying insular target lesions on MR imaging can help guide intracranial electroencephalography and improve the outcome of surgery. In this study, we present a novel method of exploring the insular region for subtle lesions on 3D MR imaging by MPR postprocessing of slices in oblique reference planes. Using this method, we retrospectively reviewed presurgical MRIs that were initially considered to have normal findings in 7 pediatric patients with intractable insular epilepsy. Insular epilepsy was confirmed in these patients on stereo-electroencephalography and histopathology. The MPR postprocessing method we describe helped detect subtle insular lesions in all 7 patients.

ABBREVIATIONS: FCD = focal cortical dysplasia; SEEG = stereo-electroencephalography

Refractory epilepsy of the insula is one of the most challenging forms of epilepsy to diagnose and treat for a number of reasons. Due to the position of the insula situated at the crossroads of several lobes, the clinical semiology of insular seizures often orients toward a frontal, parietal, or temporal lobe origin.¹ Furthermore, because the insula is covered by the opercular folds, its electrical activity is partly shielded from scalp electroencephalography. Several authors have shown that the ictal discharge in insular seizures could mimic frontal, temporal, central, or parietal seizure-onset zones, misleading the diagnosis.¹⁻³

When insular epilepsy is suspected, stereo-electroencephalography (SEEG) is often required to accurately locate the ictal onset zone.^{1,4} The proper positioning of these intracranial electrodes depends on the ability of MR imaging to define a target lesion. When MR imaging is unable to define a lesion, the chances of a successful operation are significantly reduced.

Because the insula covers a small surface area of the brain and its cortex forms discrete gyri oriented in an oblique sagittal plane, it may be difficult to identify its architecture and its limits on MR imaging viewed in standard orthogonal planes (sagittal, axial, and coronal).

In this retrospective study of 7 pediatric patients who under-

went an operation for refractory insular epilepsy, we show how MPR postprocessing of high-resolution 3D-T1WI and 3D-T2WI can help identify subtle insular lesions that were initially missed on presurgical MR imaging but were subsequently identified on SEEG and histopathology.

METHODOLOGY

Local regional ethics approval was obtained for this retrospective study.

Case Selection

Of the 293 patients who had undergone focal resection for refractory epilepsy in our institution between January 2009 and December 2016, we selected those with insular epilepsy on the basis of SEEG results (30 patients; 10%). Of these patients, we excluded those MRIs positive for insular lesions (11 patients). Among the remaining cases, apparently “nonlesional,” we excluded those whose presurgical MRIs were performed with insufficient resolution (maximum voxel size of 1 mm³) (12 patients).

Seven patients were retained in our study, 4 boys and 3 girls with a mean age at the time of presurgical MR imaging of 8.6 years (range, 3–14.7 years).

Imaging Acquisition and Analysis

MR imaging was performed on a 3T Ingenia scanner (Philips Healthcare, Best, the Netherlands) using a 32-channel head coil. All of the scans were obtained with the patient under general anesthesia, as is routine in our institution for children younger than 7 years of age or for patients with difficulty in remaining calm for the duration of the examination.

Received April 3, 2019; accepted after revision June 17.

From the Diagnostic Neuroradiology Department (J.B., S.K.) and Pediatric Neurosurgery Department (D.T., S.F.-S., G.D., M.F.), Rothschild Foundation Hospital, Paris, France.

Please address correspondence to Martine Fohlen, MD, Pediatric Neurosurgery Department, Fondation Adolphe de Rothschild, 29 rue Manin, 75019, Paris, France; e-mail: mfohlen@for.paris; @FondARothschild

<http://dx.doi.org/10.3174/ajnr.A6143>

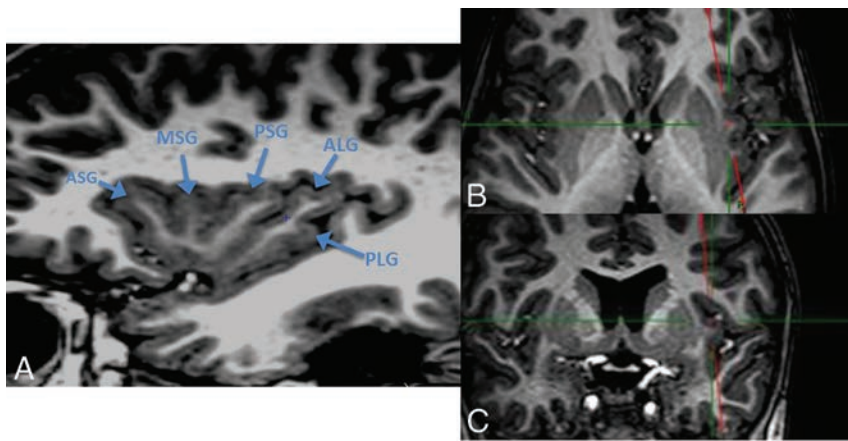


FIG 1. 3D-T1-weighted sequence with MPR processing showing the common gyral pattern of the insula: reference view to analyze the insula. *A*, T1WI oblique sagittal view, parallel to the base of the insula, anterior lobule. ASG indicates anterior short gyrus; MSG, middle short gyrus; PSG, posterior short gyrus. Posterior lobule: ALG indicates anterior long gyrus; PLG, posterior long gyrus, which appears classically shorter than the ALG. *B*, T1WI axial view shows the oblique cut plane parallel to the base of the insula. *C*, T1WI coronal view shows the oblique cut plane parallel to the base of the insula.

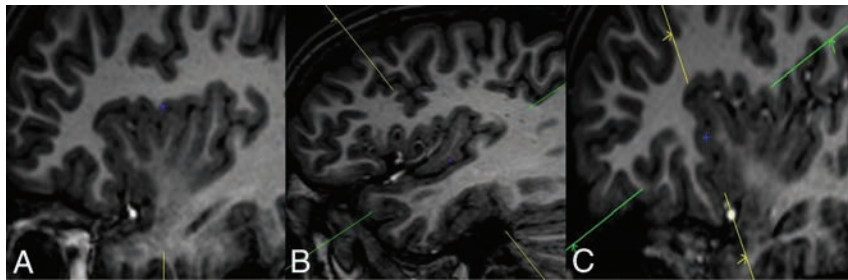


FIG 2. T1WI sagittal view representation of the peri-insular sulci. *A*, Superior peri-insular sulcus. *B*, Inferior peri-insular sulcus. *C*, Anterior peri-insular sulcus.

The following sequences were analyzed for each patient: 3D T1 turbo field echo in the sagittal plane (TR = 9.7 ms, TE = 4.6 ms, matrix = 240 × 240, pixel size = 1 × 1 mm, FOV = 235 × 235 mm, slice thickness = 1 mm, flip angle = 8°, echo-train length = 159); 3D T2 TSE in the sagittal plane (TR = 2500 ms, TE = 252 ms, matrix = 240 × 240, pixel size = 0.7 × 0.7 mm, FOV = 240 × 240 mm, slice thickness = 1 mm, flip angle = 90°, echo-train length = 133).

MRIs were reviewed by 2 experienced neuroradiologists (J.B. and S.K.) working with the knowledge that all patients had insular focal cortical dysplasia (FCD) based on presurgical SEEG and histopathology but blinded to the side and exact location of lesions within the insula. Reviews were first conducted independently, comparing the insulae of both hemispheres in each patient. The results of these reviews were compared. Discordant results were then discussed, and a consensus was reached. A κ score was calculated on the basis of the initial independent reviews.

MR imaging studies were reformatted in oblique reference planes to analyze specific structures using an MPR algorithm integrated in the PACS of our institution. The oblique sagittal plane, parallel to the base of the insula, was used to analyze its gyral architecture (Fig 1). Planes parallel and perpendicular to the superior, inferior, and anterior peri-insular sulci were used to analyze the transitional zones between the insular cortex and its neighboring structures (Fig 2). Images were evaluated for signs of

FCD of the insula, the peri-insular sulci, the opercula, or other structures surrounding the insula. These signs included cortical thickening, increased cortical T2WI signal, blurring of the gray/white matter junction, abnormal white matter signal extending from the cortex to the ventricular surface, the transmante sign,⁵⁻⁷ and abnormal gyral and/or sulcal patterns,⁵ including shallow sulci or underdeveloped gyri (hypoplasia or a poorly defined gyral pattern), unusually deep sulci or broad gyri (pachygyria), and sulci or gyri with an unusual form (dysmorphic or irregular gyral pattern).

RESULTS

The clinical and radiologic data are summarized in Tables 1 and 2, respectively.

The 7 patients selected for our study underwent an operation at a mean age of 8.6 years (range, 3–13 years). SEEG was performed in all patients before the operation and demonstrated an ictal onset zone within the insula (anterior insula in 4, posterior insula in 3). MR imaging was performed at a maximum of 3 months before the operation and showed subtle abnormalities involving the insula in all patients. One patient had FCD limited to the insula, and 6 had FCD involving the adjacent structures as well.

The most commonly observed MR imaging features of insular FCD in our study were insular and peri-insular blurring, found in 6 of the 7 patients, and an abnormal gyral pattern of the insula, found in all 7 patients. On the basis of these features, 1 radiologist found insular FCDs in all 7 patients, and the other radiologist found insular FCD in 6 of the 7 patients. Neither radiologist found such anomalies in the contralateral insula. The rate of interobserver agreement for the detection of insular dysplasia was almost perfect, with a κ score of 0.86.

The presurgical MR imaging, CT–MR imaging coregistration with SEEG electrodes in place, and postsurgical MR imaging of 2 types of patients are shown: one with an isolated insular lesion (patient 1, Fig 3) and one with an insular lesion extending into the peri-insular sulcus (patient 3, Fig 4).

The presurgical MR imaging, CT–MR imaging coregistration with SEEG electrodes in place, and postsurgical MR imaging of 2 types of patients are shown: one with an isolated insular lesion (patient 1, Fig 3) and one with an insular lesion extending into the peri-insular sulcus (patient 3, Fig 4).

DISCUSSION

To our knowledge, this is the first clinical report to describe a method for analyzing MRIs to improve the detection of subtle insular lesions in patients with drug-resistant epilepsy.

In the few studies that have reported insular epilepsy surgery in children, negative findings on MRIs are common, and little attention is given to imaging considerations.^{4,8,9} Lesion identifi-

Table 1: Clinical data

Patient	Sex	Age at Seizure Onset (yr)	Neurologic Status before Surgery	Age at Last Surgery (yr)	Topography of Resective Surgery	Postsurgical Deficit	Pathology	FU Duration (yr)	Engel ^a
1	M	2.5	LH, Special education	13.0	Posterior Ins and posterior Op	0	FCD IIa	4.2	I
2	M	3.2	RH, MoMR	6.2	Anterior Ins and Op, + frontal Disc	Left facial paresis	FCD Ib	4.2	I
3	F	3.5	RH, Normal cognitive function	14.7	Posterior Ins and STG	0	Negative	2.4	I
4	F	0.8	RH, MoMR	3.0	Anterior Ins+ frontal Disc	0	FCD IIa	2.3	III
5	M	0.4	Left hemiparesis SMR, ASD	6.1	Anterior Ins+ frontal Disc	0	FCD IIa	0.9	I
6	F	2.0	LH, MiMR	7.6	Posterior Ins and parietal Op, temporal Op	0	FCD IIb	3.0	III
7	M	1.0	LH, MoMR, ASD	9.7	Anterior Ins and Inferior Frontal	0	FCD IIb	1.8	II

Note:—LH indicates left-handed; RH, right-handed; MiMR, mild mental retardation; MoMR, moderate mental retardation; SMR, severe mental retardation; ASD, autism spectrum disorder; Op, operculum; Ins, insula; STG, superior temporal gyrus; Disc, disconnection; FU, follow-up; yr, year.

^a Engel Surgical Outcome Scale.

Table 2: Review of presurgical MRIs in patients with intractable insular epilepsy with no initial detection of insular lesions

Patient No.	Side	Insula		Peri-Insular Sulcus		Surrounding Structures	
		Gyral Pattern	Blurring	Sulcal Form	Blurring	Gyral Pattern	Blurring
1	R	Supernumerary ALG	+	—	—	—	—
2	R	Poorly defined AL	+	Irregular anterior portion of SPS	Anterior SPS	—	Frontal opercula, orbitofrontal
3	R	Hypoplasia PL	—	—	Posterior IPS	Hypoplasia STG	STG, HG
4	R	Irregular AL	+	Irregular anterior portion of SPS	Anterior SPS	—	—
5	R	Irregular AL	+	—	APS	—	Frontal opercula, orbitofrontal
6	L	Thick PL	+	—	Posterior IPS	—	HG, temporal stem
7	L	Poorly defined AL	+	Poorly defined APS	APS	—	Pars orbitalis

Note:—ALG indicates the anterior long gyrus; R, right; L, left; SPS, superior peri-insular sulcus; PL, posterior lobule; IPS, inferior peri-insular sulcus; STG, superior temporal gyrus; HG, Heschl gyrus; AL, anterior lobule; APS, anterior peri-insular sulcus; —, normal; +, present; —, absent.

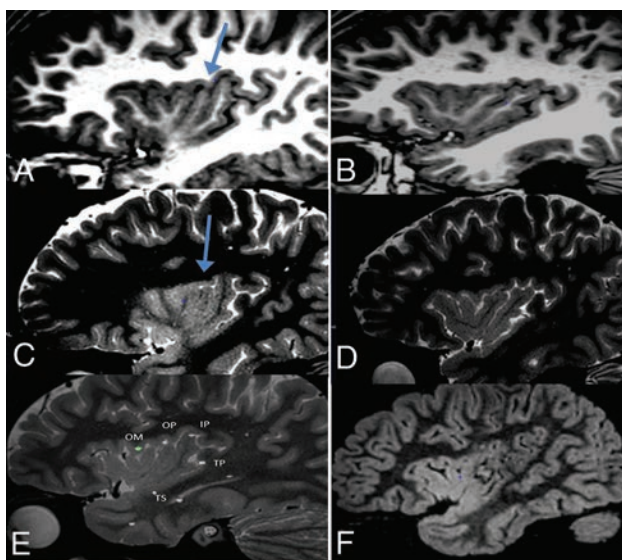


FIG 3. Patient 1. Isolated insular lesion. Oblique sagittal view parallel to the base of the insula. A, T1WI oblique sagittal view shows an unusual gyral pattern of the posterior lobule of the right insula, which shows 3 gyri (arrow). B, T1WI oblique sagittal view shows a normal gyral pattern of the contralateral insula. C, T2WI oblique sagittal view shows blurring of the most anterior long gyrus of the right insula (arrow). D, T2WI oblique sagittal view shows no blurring of the contralateral insula. E, T2WI oblique sagittal view with SEEG electrodes (ictal onset zone around electrode OP). OM, OP, IP, TP, and TS indicate the names of depth electrodes. F, FLAIR sagittal view of the right insula after an operation.

cation on MR imaging increases a patient’s chances of complete resection, which is an essential prognostic factor of successful epilepsy surgery.¹⁰⁻¹²

In this study, 6 of the 7 detected lesions were classified as FCD on histopathologic analysis according to the Blümcke classification.¹³ The 1 case in which no FCD was found (patient 3) may be attributed to the small size of the surgical samples due to the surgical constraints in this region. Those constraints might explain why 2 patients were not seizure-free after the operation (patients 4 and 6).

The MR imaging sequences we chose to analyze are in keeping with the recommended international consensus guidelines for imaging infants and children with recent-onset epilepsy.¹⁴ Apart from high-resolution 3D-T1WI and 3D-T2WI sequences, there is no consensus on the use of other types of sequences in the clinical setting.

Furthermore, it is necessary to use both T1WI and T2WI sequences to detect FCDs in a young pediatric population because maturation of subcortical white matter appears at different ages on T1WI and T2WI, becoming isointense to cortex at times.¹⁵ Beyond 24 months, subcortical white matter maturation is usually complete¹⁵ and FCDs can be detected on both T1WI and T2WI.

The use of MPR postprocessing helped to identify the gyral pattern of the insula and the pattern of the peri-insular sulcus. It also improved the detection of abnormal cortical signal, thickening, and blurring of these structures. All 7 patients were

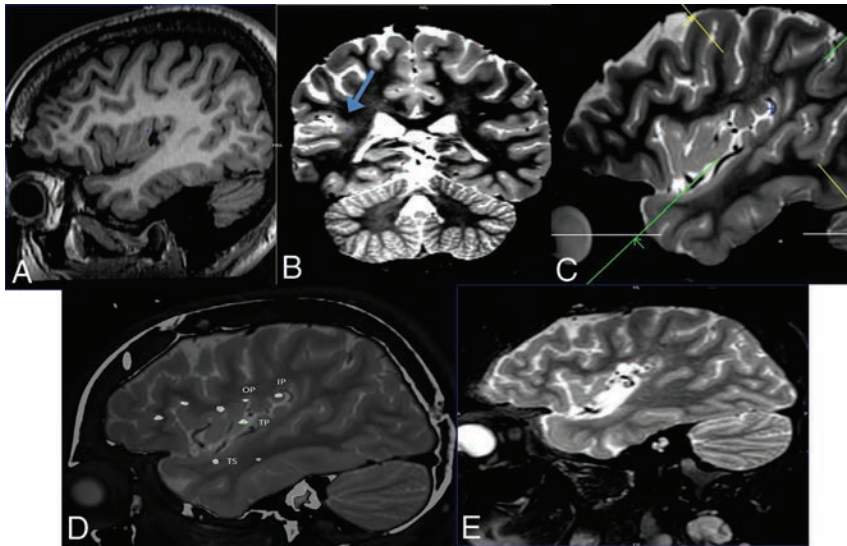


FIG 4. Patient 3. Insular lesion extending into the peri-insular sulcus. *A*, T1WI oblique sagittal view, parallel to the base of the insula, shows hypoplasia of the posterior insular lobule. *B*, T2WI coronal view perpendicular to the inferior peri-insular sulcus shows blurring of the posterior portion of the right inferior peri-insular sulcus (arrow). *C*, T2WI sagittal view shows the cut plane perpendicular to the posterior portion of the inferior peri-insular sulcus, used to obtain the coronal view in *B*. *D*, T2WI sagittal view with SEEG electrodes (ictal onset zone around OP, IP, TP, and TS, representing the depth electrodes). *E*, T2WI sagittal view after surgical resection of the posterior lobule of the insula and the superior temporal gyrus.

found to have subtle abnormal findings on MR imaging involving the insula, while no such anomaly was detected in the contralateral insula. These findings, along with the strong κ score, suggest that the analytic method described in this study is a reliable one, with very few false-positive or false-negative results, while the caveat of a small sample size should be taken into account.

Only patient 1 in our series presented with radiologic signs of FCD limited to the insula itself. Detection of this FCD was made possible through the analysis of the sagittal oblique plane, revealing a posterior lobule with 3 long gyri and blurring of the gray-white matter junction (Fig 3). Literature review of anatomic studies has shown the total number of insular gyri to vary between 4 and 7 (with an average of 5),¹⁶⁻¹⁹ but no study has shown >2 gyri in the posterior lobule of the insula. This unusual gyral pattern in association with localized gray/white matter blurring is suggestive of FCD. Asymmetry of the insular gyral pattern between the 2 hemispheres in the same patient is common¹⁹ and should not be considered an indication of dysplasia.

In the 6 remaining patients, MR imaging signs suggestive of FCD were found in both the insula and the adjacent peri-insular sulcus, stressing the importance of a systematic analysis of these structures.

All of these lesions, identified retrospectively on presurgical MRIs, were found to be epileptogenic on SEEG recordings. The seizure-onset zones, identified on the intracranial electrodes, were in close proximity to the anomalies identified on MR imaging (Figs 3 and 4), while electrode positioning was guided by electro-clinical data before MR imaging detection.

This study has the following limitations: Because refractory insular epilepsy is a rare condition in our experience, a retrospective study design was the most suitable for a preliminary study. As

a consequence of the retrospective nature of the study, the parameters of presurgical MRIs were heterogeneous, with insufficient resolution in a large proportion of the examinations, further reducing the number of patients retained in the study. Furthermore, radiologists were blinded to the side and exact location of lesions within the insula and compared both insulae of each patient with each other. This comparison allowed some degree of evaluation of the level of agreement between the 2 radiologists.

The radiologists knowing that all patients had FCD involving the insula may have created a measurement or expectation bias, increasing their tendency to falsely identify lesions. However, this bias did not seem to influence the outcome of the study because no false-positive results were found.

The results of this preliminary study should be confirmed by a multicentric prospective blinded study on a larger

population of patients with a control group, allowing a more robust statistical analysis.

CONCLUSIONS

In this retrospective study, insular lesions were detected in all 7 patients on MRIs initially considered to have negative findings. This highlights the importance of a rigorous imaging technique and analysis by experienced radiologists to reduce the number of so-called “negative” cases.

When exploring refractory epilepsy, the following criteria should be met to optimize the chances of detecting subtle insular lesions on MR imaging: The radiologist must have a good understanding of the gross anatomy of the insula and its surrounding structures. MR imaging sequences must include high-resolution 3D-T1WI and 3D-T2WI to detect signal anomalies at various stages of myelination in the young pediatric population. Images should be reconstructed in oblique planes using an MPR algorithm to improve the identification of the gyral pattern of the insula and the pattern of the peri-insular sulcus.

Despite proper analysis of the insular region on presurgical MRI, the full extent of certain forms of FCD still escapes detection. Further advances in the detection of these subtle lesions may be expected in light of the technologic progress being made in MR imaging research using ultra-high-field-strength (7T) scanners to improve spatial resolution as well as the possible contribution of advanced MR imaging techniques such as arterial spin-labeling and diffusion tensor imaging.

REFERENCES

1. Isnard J, Guénot M, Sindou M, et al. **Clinical manifestations of insular lobe seizures: a stereo-electroencephalographic study.** *Epilepsia* 2004;45:1079–90 CrossRef Medline

2. Nguyen DK, Nguyen DB, Malak R, et al. **Revisiting the role of the insula in refractory partial epilepsy.** *Epilepsia* 2009;50:510–20 CrossRef Medline
3. Levitt M, Ojemann J, Kuratani J. **Insular epilepsy masquerading as multifocal cortical epilepsy as proven by depth electrode.** *J Neurosurg Pediatr* 2010;5:365–67 CrossRef Medline
4. Dylgjeri S, Taussig D, Chipaux M, et al. **Insular and insulo-opercular epilepsy in childhood: an SEEG study.** *Seizure* 2014;23:300–08 CrossRef Medline
5. Colombo N, Tassi L, Galli C, et al. **Focal cortical dysplasias: MR imaging, histopathologic, and clinical correlations in surgically treated patients with epilepsy.** *AJNR Am J Neuroradiol* 2003;24:724–33 Medline
6. Mellerio C, Labeyrie M, Chassoux F, et al. **Optimizing MR imaging detection of type 2 focal cortical dysplasia: best criteria for clinical practice.** *AJNR Am J Neuroradiol* 2012;33:1932–38 CrossRef Medline
7. Colombo N, Salamon N, Raybaud C, et al. **Imaging of malformations of cortical development.** *Epileptic Disord* 2009;11:194–205 CrossRef Medline
8. Weil A, Le N, Jayakar P, et al. **Medically resistant pediatric insular-opercular/periSylvian epilepsy, Part 2: outcome following resective surgery.** *J Neurosurg Pediatr* 2016;18:523–35 CrossRef Medline
9. Perry M, Donahue D, Malik S, et al. **Magnetic resonance imaging-guided laser interstitial thermal therapy as treatment for intractable insular epilepsy in children.** *J Neurosurg Pediatr* 2017;20:575–82 CrossRef Medline
10. Hauptman J, Mathern G. **Surgical treatment of epilepsy associated with cortical dysplasia: 2012 update.** *Epilepsia* 2012;53(Suppl 4):98–104 CrossRef Medline
11. Rowland N, Englot D, Cage T, et al. **A meta-analysis of predictors of seizure freedom in the surgical management of focal cortical dysplasia.** *J Neurosurg* 2012;116:1035–41 CrossRef Medline
12. Englot D, Raygor K, Molinaro A, et al. **Factors associated with failed focal neocortical epilepsy surgery.** *Neurosurgery* 2014;75:648–55; discussion 655; quiz 656 CrossRef Medline
13. Blümcke I, Thom M, Aronica E, et al. **The clinicopathologic spectrum of focal cortical dysplasias: a consensus classification proposed by an ad hoc Task Force of the ILAE Diagnostic Methods Commission.** *Epilepsia* 2011;52:158–74 CrossRef Medline
14. Gaillard W, Chiron C, Cross J, et al; ILAE, Committee for Neuroimaging, Subcommittee for Pediatric. **Guidelines for imaging infants and children with recent-onset epilepsy.** *Epilepsia* 2009;50:2147–53 CrossRef Medline
15. Barkovich AJ. **Normal postnatal brain development.** In: Barkovich AJ. *Pediatric Neuroimaging*. 2nd ed. New York: Raven Press; 1995:20–35
16. Türe U, Yaşargil D, Al-Mefty O, et al. **Topographic anatomy of the insular region.** *J Neurosurg* 1999;90:720–33 CrossRef Medline
17. Varnavas G, Grand W. **The insular cortex: morphological and vascular anatomic characteristics.** *Neurosurgery* 1999;44:127–36; discussion 136–38 CrossRef Medline
18. Augustine J. **The insular lobe in primates including humans.** *Neurol Res* 1985;7:2–10 CrossRef Medline
19. Naidich T, Kang E, Fatterpekar G, et al. **The insula: anatomic study and MR imaging display at 1.5T.** *AJNR Am J Neuroradiol* 2004;25:222–32 Medline

Quantitative Analysis of Spinal Canal Areas in the Lumbar Spine: An Imaging Informatics and Machine Learning Study

 B. Gaonkar,  D. Villaroman,  J. Beckett,  C. Ahn,  M. Attiah,  D. Babayan,  J.P. Villablanca,  N. Salamon,  A. Bui, and  L. Macyszyn



ABSTRACT

BACKGROUND AND PURPOSE: Quantitative imaging biomarkers have not been established for the diagnosis of spinal canal stenosis. This work aimed to lay the groundwork to establish such biomarkers by leveraging the developments in machine learning and medical imaging informatics.

MATERIALS AND METHODS: Machine learning algorithms were trained to segment lumbar spinal canal areas on axial views and intervertebral discs on sagittal views of lumbar MRIs. These were used to measure spinal canal areas at each lumbar level (L1 through L5). Machine-generated delineations were compared with 2 sets of human-generated delineations to validate the proposed techniques. Then, we use these machine learning methods to delineate and measure lumbar spinal canal areas in a normative cohort and to analyze their variation with respect to age, sex, and height using a variable-intercept mixed model.

RESULTS: We established that machine-generated delineations are comparable with human-generated segmentations. Spinal canal areas as measured by machine are statistically significantly correlated with height ($P < .05$) but not with age or sex.

CONCLUSIONS: Our machine learning methodology demonstrates that this important anatomic structure can be accurately detected and quantitatively measured without human input in a manner comparable with that of human raters. Anatomic deviations measured against the normative model established here could be used to flag spinal stenosis in the future.

ABBREVIATIONS: CPT = Current Procedural Terminology; ERT = ensemble of regression trees; ICD-9 = International Classification of Diseases; ML = machine learning; MRN = medical record number; SVM = support vector machine

Spinal cord or nerve root compression due to narrowing of the spinal canal is thought to underlie the disorders of lumbar radiculopathy and myelopathy, both major causes of morbidity and disability^{1,2} in the United States. Patient screening includes radiologic evaluation of the central canal of the spine using MR imaging alongside labeling of stenosis as none, mild, moderate, or severe. These labels drive risky and often expensive treatment and surgical decisions. Yet, MR imaging-based labeling is known to be highly subjective and shows substantial interrater variability.³⁻⁵ It is necessary to develop objective diagnostic and treatment criteria⁶ to improve treatment.

Canal stenosis by definition is a reduction in the area of the spinal canal. The percentage reduction in canal area compared with a demographically matched control signifies the degree of stenosis. Yet, computing the percentage reduction requires that one can consistently and accurately delineate spinal canals on MR imaging and that one has knowledge of the variation of canal areas in asymptomatic individuals over a wide demography. Our study presents work in both directions by proposing and validating a machine learning (ML) method to automatically delineate spinal canals on axial MR imaging using the validated ML method in conjunction with a large clinical data base to establish a variable-intercept mixed linear model of variation of spinal canal areas.

While computational methods to segment anatomic ROIs have been published in the literature⁷⁻¹⁰ and used to segment several regions in the spine,^{8,9,11-15} we focused on the spinal canal. We established an ML technique to delineate spinal canals on axial MR imaging and to measure their areas at lumbar levels. Subsequently, we established a linear model linking these areas to age, sex, and height using data from 1755 asymptomatic individuals.

Received September 19, 2018; accepted after revision July 3, 2019.

From the Departments of Neurosurgery (B.G., D.V., J.B., C.A., M.A., D.B., L.M.) and Radiology (J.P.V., N.S., A.B., L.M.), University of California, Los Angeles, Los Angeles, California.

Please address correspondence to Bilwaj Gaonkar, PhD, Department of Neurosurgery, 300 Stein Plaza, Ste 554E, Los Angeles, CA, 90095; e-mail: bilwaj@gmail.com; @bilwaj



Indicates article with supplemental on-line appendix and tables.



Indicates article with supplemental on-line photo.

<http://dx.doi.org/10.3174/ajnr.A6174>

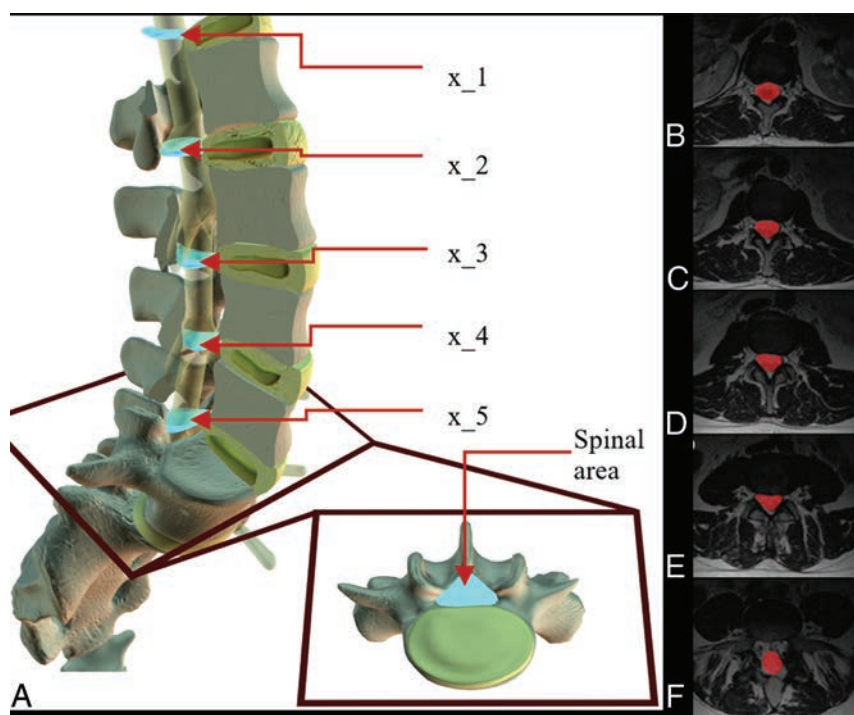


FIG 1. Variation of spinal canal area with level. A, This 3D model represents a generic lumbar spine where light blue objects represent an area of the central canal at each lumbar level at the midsection of a disc. The square frame (red) zooms in on the intervertebral disc (yellow) below L5 to give an axial view of where the central canal area (light blue) is located. In a randomly selected T2-MR imaging, each picture in this series B–F depicts 1 section of spinal cord segmentation (red) from each level. Tissues within the canal but outside the thecal sac are not segmented.

The study was executed in 4 steps:

1. Creating a large data base of lumbar MRI studies.
2. Training and validating ML models for delineating canals and measuring their areas, using subsets of data extracted from the database and manually segmented by experts.
3. Using the ML models to measure canal areas in asymptomatic individuals with MRIs.
4. Using these measurements to establish a linear model linking lumbar spinal canal areas to age, sex, and height.

Many in the radiology community agree that there are numerous advantages of standardized reports,¹⁶ and this study aims to usher in a quantitative era for radiologic interpretation and reporting for lumbar spinal stenosis.

MATERIALS AND METHODS

Institutional Review Board Statement

This study was conducted according to the rules and regulations of our institution and approved by the institutional review board (institutional review board No. 16–000196).

Data Collection for Machine Learning

We queried the PACS of our institution for individuals who had undergone any spine imaging using the corresponding Current Procedural Terminology (CPT)¹⁷ codes (On-line Table 1). This query yielded 39,295 unique medical record numbers (MRNs) and corresponding accession numbers. We extracted

and anonymized the images corresponding to each accession number. The On-line Appendix presents further details of our data collection.

MR Imaging Sequences

Axial T2 MR imaging was used for canal segmentation. Resolutions in the axial plane varied between 0.27×0.27 mm per pixel to 1.5×1.5 mm. Resolutions were perpendicular to the axial plane and ranged between 1 and 10 mm. The mean resolution was 0.53×0.53 mm in the axial plane and 5.13 mm in the perpendicular direction. Corresponding SDs were 0.125×0.125 and 0.5 mm, respectively. The mean TRs and TEs varied as $TR = 3756 \pm 738$ ms and $TE = 107 \pm 12$ ms. Corresponding sagittal images used for disc segmentation had resolutions between 0.5×0.5 and 2×2 mm per pixel in the sagittal plane and 1–5 mm perpendicular to the sagittal plane.

Preprocessing

Preprocessing involved nonparametric bias correction, linear histogram matching to a common template, and intensity normalization to the 0–1 range for each 3D MR image. All scans were oriented into the frame of the template using linear image registration, and resampling was performed in the axial frame to fit each section to a 256×256 pixel frame.

Training Data Generation by Human Raters

A subset of 100 axial MR images was randomly chosen from the 39,295 for algorithmic training purposes and archived alongside corresponding sagittal MR images. Physicians segmented spinal canals and discs with the help of students. A student was first trained by an attending physician to identify spinal canal boundaries and delineate them using ITK-SNAP (www.itksnap.org).¹⁸ The student delineated canals on each section of the 100 axial MRIs and saved the segmentations as NIfTI files. The student also went through the 100 corresponding sagittal MRIs and segmented lumbar discs. The attending physician reviewed each section and corrected the student-generated delineations. The segmented spinal canal region was the area enclosed in the thecal sac, excluding ligaments and structures within the cavity. Segmenting the thecal sac within the spinal canal allows more distinct edges and defines a more clinically relevant area. These scans were used for training the models.

Validation Data Generation

The process of segmenting spinal canals on axial scans was repeated 2 more times on 109 axial images with different student-physician pairs, similar to the training data generation. These

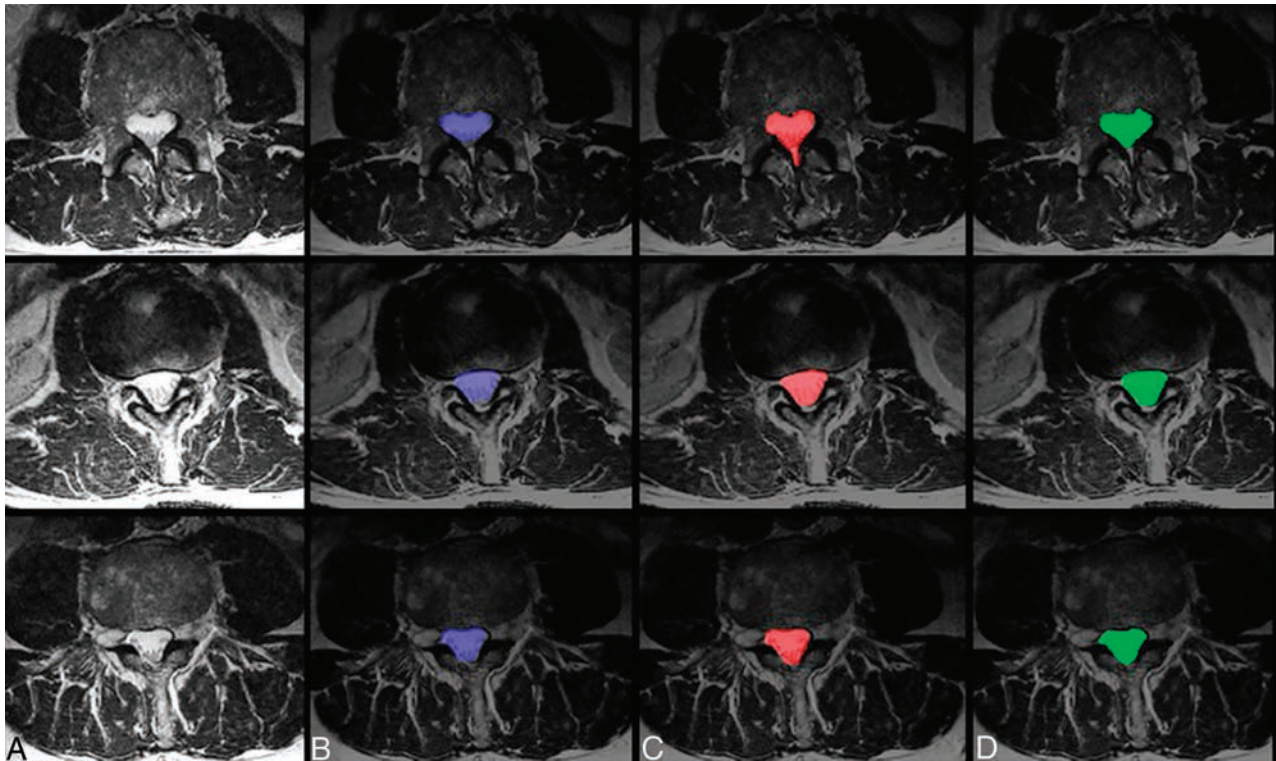


FIG 2. Sample case images of central canal segmentations. Three case images of axial T2 MR imaging (A) randomly selected from the dataset are shown alongside their resulting segmentations (blue) of the spinal canal using the proposed ensemble technique (B), segmentation (red) by manual rater 1 (C), and segmentation (green) by manual rater 2 (D).

Table 1: Comparison of automated spinal canal segmentations in a validation dataset of 109 axial MRIs^a

	Centrality	Auto vs Rater 1	Auto vs Rater 2	Rater 1 vs Rater 2
Dice ratio	Mean	0.84 ± 0.08	0.83 ± 0.08	0.9 ± 0.05
	Median	0.87	0.85	0.92
Hausdorff distance (mm)	Mean	7.89 ± 9.42	9.41 ± 11.2	7.90 ± 9.62
	Median	4.59	5.64	4.66
Average surface distance (mm)	Mean	0.84 ± 0.08	0.83 ± 0.08	0.9 ± 0.05
	Median	0.10	0.14	0.07

^aData are means and medians.

were selected by randomly sampling from the 39,000+ MRNs containing symptomatic and asymptomatic cases.

Training the Machine Learning Model for Segmentation of the Central Canal

We used a hybrid machine learning model to execute segmentation of central canals. In the first step, we detected a 25 × 25 pixel window containing the canal. An ensemble of support vector machine (SVM)-based object detection systems was trained using histogram-of-oriented gradient¹⁹ features and the hard-negative mining paradigm to “classify” whether a particular 25 × 25 pixel window contained a central canal. The SVMs used were linear SVMs with C = 10, 50, 100, 150, 250, 500, 1000. A window classified by ≥4 SVMs as the spinal canal was considered a “positive” detection. The image was cropped along this window and passed on to the second step of segmentation, which was executed using an ensemble of regression trees²⁰ (ERT) shape-regression model. We used the ERT

with $\nu = 0.05$ and a tree depth set to 2 to predict 68 points, which form the contour of each spinal canal. Both steps were implemented using the DLib 1.8.0 software library (<http://dlib.net/>).

Disc Segmentation

A Deep-U-Net⁷ model (On-line Figure) was trained on the designated

100 sagittal MR images to segment discs and was implemented using the Keras API running on top of TensorFlow 1.3.0. A rectified linear unit was used for convolutional neurons throughout the architecture except for the final output layer, which used sigmoidal activation. We used a fixed learning rate (1e-5) and the Adam optimizer with drop-out (probability of .25) regularization. The loss function used was the negative of the Dice score.

Segmentation Measurements

We used Dice scores, the Hausdorff distance, and average surface distance metrics. These compared overlaps for automatic spinal canal segmentations with segmentations generated by manual raters and manual raters among themselves.

Data Collection for Analysis of Normative Cohort

We cross-referenced the 39,295 image accessions with anonymized patient records to eliminate studies associated with the

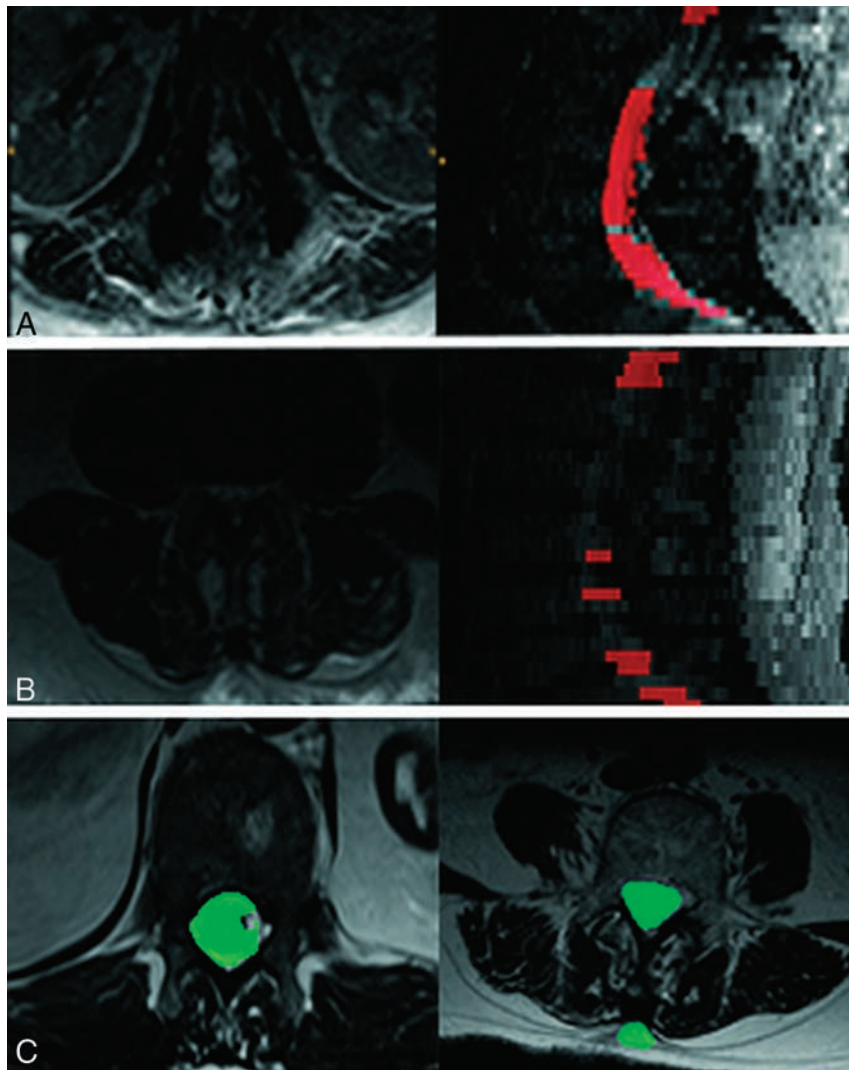


FIG 3. Modes of segmentation failure of the proposed algorithm compared with U-Net results. Two scans using SVM + ERT failed (Dice score <0.7). The mode of failure was complete lack of segmentation as seen in rows A and B, thereby making it easy to eliminate such cases automatically. In contrast U-Net failures are more subtle and can involve under and oversegmentation as shown in row C.

International Classification of Diseases²¹ (ICD-9) codes (listed in On-line Table 2) related to the presence of spinal pathology or symptoms attributable to the spine (eg, sciatica). The filtered dataset contained 3837 unique MRNs. We could not use all the MRNs for analyses due to various factors, such as the unavailability of associated demographic data (670 cases) and failure to meet any of the quality control criteria mentioned in On-line Table 3 (1412 cases). Quality control metrics are required because incomplete acquisition, image corruption, erroneous segmentation, DICOM header mislabeling, and misorientation in data present a challenge to automatically detecting nonstenosed canals at all 5 levels. Our final analysis included 1755 MRNs (797 men and 958 women), in which the mean age of men was 49.6 years ($\sigma = 16.92$ years) with a median of 49.5 years. The mean age of women was 48.25 years ($\sigma = 16.25$ years) with a median of 49.0 years. The age ranges for both men and women were between 19 and 81 years.

tions had a 100% detection rate, we attempted a U-Net algorithm for spinal cord segmentations. This model had parameters identical to the U-Net described for disc segmentation. As opposed to the proposed method, the U-Net failed by mis-segmenting the image (Fig 3C). Because such failures are difficult to track using simple quality control criteria (On-line Table 3), we espoused the SVM + ERT approach.

Time Improvement

Human-driven segmentation of a spinal canal takes between 30 and 40 minutes for each image, while machine-generated segmentation takes between 20 and 25 seconds. Thus, machine segmentation is as efficient as expected.

Relationship between Canal Areas and Height, Sex, and Age

We investigated the relationship between canal areas and demographic factors (height, sex, and age) using a variable-intercept

Area Measurements

We cross-referenced axial MRIs containing segmented canals with their sagittal MRIs containing segmented intervertebral discs to locate slices at each lumbar level in a standard way (Fig 1). At axial slices where the center of a disc was found, we documented canal areas to investigate variation of these areas with respect to age, sex, and height.

RESULTS

Segmentation Results

While central canals may not have a consistent shape (Fig 2A), machine-generated segmentations were qualitatively comparable with those generated by human experts (Fig 2B–D). Quantitative metrics (Dice score, Hausdorff distance, and average surface distance) for the validation dataset are recorded in Table 1. These metrics indicate that machine-generated segmentation agrees almost as well with each human expert as the human experts agree among themselves. Disc segmentations generated by machine achieved a Dice overlap of 0.88 with respect to a single human rater on the validation dataset. All discs detected by the human rater were detected by the U-Net, achieving a detection rate of 100%.

Segmentation Modes of Failure

Figure 3A, -B presents 2 validation set images that had a Dice coefficient <0.7. The proposed model seems to fail by nonsegmentation of entire slices. Given that U-Net-generated disc segmenta-

Table 2: Age, gender, and height were analyzed using a mixed effects model Canal Area ~ age + gender + height + gender*height + (1 | subject). This table represents the Random Effects fit^a

Random Effects			
Groups	Name	Variance	SD
Group	(Intercept)	2868	53.55
Residual		2365	48.63
No. of obs	8775	No. of subjects	1755

Note:—obs indicates observers.

^a The model fit is summarized. Height is the only variable that is statistically significantly related to canal areas.

Table 3: Age, gender, and height were analyzed using a mixed effects model Canal Area ~ age + gender + height + gender*height + (1 | subject). This table represents the Intercept fit - equivalent to traditional regression^a

Fixed Effects	Estimate	Standard Error	T Value	Pr (> t)
(Intercept)	-278.18495	43.20594	-6.439	0.00
Age	0.05158	0.08429	0.612	0.54
Sex	-0.63539	62.56533	-0.01	0.10
Height	8.00079	0.66184	12.089	0.00
Sex:height	-0.46311	0.93188	-0.497	0.62

Note:—Pr (>|t|) indicates p-value.

^a The model fit is summarized. Height is the only variable that is statistically significantly related to canal areas.

Table 4: Age, gender, and height were analyzed using a mixed effects model Canal Area ~ age + gender + height + gender*height + (1 | subject). This table represents the correlation of fixed effects^a

Correlation of Fixed Effects	(Intercept)	Age	Sex	Height
Age	-0.203			
Sex	-0.662	0.001		
Height	-0.995	0.11	0.672	
Sex:height	0.692	-0.009	-0.998	-0.703

^a The model fit is summarized. Height is the only variable that is statistically significantly related to canal areas.

mixed linear model. This is because the canal area measurements at L1 through L5 are not independent within subjects. Canal areas were clustered by subject, and a mixed model of the form: Canal Area ~ Age + Sex + Height + Sex × Height + (1 | Subject) is used. We used the R package lme4 (<https://cran.r-project.org/web/packages/lme4/index.html>) to implement the model. Tables 2–4 summarize the model fit and show that height is the only demographic factor statistically significantly correlated with canal areas at L1 through L5.

DISCUSSION

We describe a computerized pipeline to analyze spinal canal areas with respect to age, sex, and height. Our machine learning algorithm can automatically delineate spinal canals with human-level accuracy in a time-efficient and consistent manner.

We acknowledge that there are certain limitations to the study design. The first is the area of delineation, at the lower levels (L5–S1), was chosen to be the thecal sac rather than the full canal. This was because the thecal sac was most directly relevant to nerve compression and thus to stenotic pathology. Because the

thecal sac is much more difficult to delineate, especially at lower levels, this can yield partial canal segmentations as seen in Fig 1F. A second caveat involves defining asymptomatic images using ICD codes. While these codes are the clinical standard, they can sometimes contain human error. A third limitation of the study was that we could not obtain the demographic data for body mass index and smoking status, both of which could be important covariates in the model.

The high computational burden of training and analysis represented a challenge to the study. More advanced deep learning models could potentially be trained with the use of graphics processing units, which were not available for this study. We would expect such models to perform better than the proposed pipeline. Lack of computational power also held up cross-validation analysis during training. In the future, we intend to obtain additional computational capacity and train more powerful ML models for canal segmentation.

Future work will include shape analysis alongside area measurements. Canal morphology is perhaps as important as canal area to the diagnosis of stenosis. The development of diagnostic shape measures will be an area of focus for future research. Last, in the future, we also hope to investigate how our technique segments spinal canals when severe pathology is present and whether such segmentations can be used for diagnostic purposes.

CONCLUSIONS

We have used state-of-the-art machine learning technology to establish a normative range of spinal canal areas in the lumbar spine from MR images. We have documented the variation of these areas with respect to age, sex, and height. We believe that these measurements and range are the critical first step to usher in an objective paradigm in the radiologic diagnosis of lumbar stenosis.

Disclosures: Bilwaj Gaonkar—UNRELATED: Employment: University of California Los Angeles, RELATED: Passive stock ownership in Theseus AI, a start up being spun out of University of California Los Angeles, Luke Macyszyn - UNRELATED: Employment: University of California Los Angeles, RELATED: Stock ownership and Board membership in Theseus AI, a start up being spun out of University of California Los Angeles, NIH grant R21EB026665 awarded as Principal Investigator; We have plans to apply for patents (Planned, Pending or Issued) and wish to have the right to submit patents based on this work in the future.

REFERENCES

1. Chad DA. Lumbar spinal stenosis. *Neurol Clin* 2007;25:407–18
2. Genevay S, Atlas SJ. Lumbar spinal stenosis. *Best Pract Res Clin Rheumatol* 2010;24:253–65 CrossRef Medline
3. Bankier AA, Levine D, Halpern EF, et al. Consensus interpretation in imaging research: is there a better way? *Radiology* 2010;257:14–17 CrossRef Medline
4. Kamper SJ, Apeldoorn AT, Chiarotto A, et al. Multidisciplinary biopsychosocial rehabilitation for chronic low back pain: Cochrane systematic review and meta-analysis. *BMJ* 2015;350:h444 CrossRef Medline
5. Alpert HR, Hillman BJ. Quality and variability in diagnostic radiology. *J Am Coll Radiol* 2004;1:127–32
6. Brady A, Laoide RÓ, McCarthy P, et al. Discrepancy and error in radiology: concepts, causes and consequences. *Ulster Med J* 2012;81:3–9

7. Ronneberger O, Fischer P, Brox T. **U-Net: convolutional networks for biomedical image segmentation.** May 18, 2015. <https://arxiv.org/pdf/1505.04597.pdf>. Accessed April 15, 2018
8. Gaonkar B, Beckett J, Villaroman D, et al. **Quantitative analysis of neural foramina in the lumbar spine: an imaging informatics and machine learning study.** *Radiology: Artificial Intelligence* 2019;1:180037 CrossRef
9. Ji X, Zheng G, Liu L, et al. **Fully automatic localization and segmentation of intervertebral disc from 3D multi-modality MR images by regression forest and CNN.** In: Yao J, Vrtovec T, Zheng G, et al, eds. *Computational Methods and Clinical Applications for Spine Imaging. CSI 2016. Lecture Notes in Computer Science. Vol 10182.* Cham: Springer; 2016. https://link.springer.com/chapter/10.1007/978-3-319-55050-3_9
10. Tu Z, Bai X. **Auto-context and its application to high-level vision tasks and 3D brain image segmentation.** *IEEE Trans Pattern Anal Mach Intell* 2010;32:1744–57 CrossRef Medline
11. Peng Z, Zhong J, Wee W, et al. **Automated vertebra detection and segmentation from the whole spine MR images.** *Conf Proc IEEE Eng Med Biol Soc* 2005;3:2527–30 Medline
12. Aslan MS, Ali A, Rara H, et al. **A novel 3D segmentation of vertebral bones from volumetric CT images using graph cuts.** In: Bebis, G. et al. eds. *Advances in Visual Computing. ISVC 2009. Lecture Notes in Computer Science. Vol. 5876,* Berlin: Springer; 2009
13. Zukić D, Vlasák A, Dukatz T, et al. **Segmentation of vertebral bodies in MR images.** 2012. <https://diglib.eg.org/handle/10.2312/PE.VMV.VMV12.135-142>. Accessed April 15, 2018
14. Gaonkar B, Xia Y, Villaroman DS, et al. **Multi-parameter ensemble learning for automated vertebral body segmentation in heterogeneously acquired clinical MR images.** *IEEE journal of translational engineering in health and medicine* 2017;5:1–2
15. Mirzaalian H, Wels M, Heimann T, et al. **Fast and robust 3D vertebra segmentation using statistical shape models.** *Conf Proc IEEE Eng Med Biol Soc* 2013;2013:3379–82 CrossRef Medline
16. Hall FM. **The radiology report of the future.** *Radiology* 2009;251:313–16 CrossRef Medline
17. **Current procedural terminology (CPT).** *JAMA* 1970;212:873–74 Medline
18. Yushkevich PA, Piven J, Hazlett HC, et al. **User-guided 3D active contour segmentation of anatomical structures: significantly improved efficiency and reliability.** *Neuroimage* 2006;31:1116–28 CrossRef Medline
19. Dalal N, Triggs B. **Histograms of oriented gradients for human detection.** <https://lear.inrialpes.fr/people/triggs/pubs/Dalal-cvpr05.pdf>. Accessed November 10, 2017
20. Kazemi V, Sullivan J. **One millisecond face alignment with an ensemble of regression trees.** 2014. <http://www.csc.kth.se/~vahidk/papers/KazemiCVPR14.pdf>. Accessed November 10, 2017
21. Centers for Disease Control and Prevention, National Center for Health Statistics. **International Classification of Diseases, Ninth Revision, Clinical Modification (ICD-9-CM).** 2018. <https://www.cdc.gov/nchs/icd/icd9cm.htm>. Accessed April 15, 2018

Automatic Spinal Cord Gray Matter Quantification: A Novel Approach

C. Tsagkas, A. Horvath, A. Altermatt, S. Pezold, M. Weigel, T. Haas, M. Amann, L. Kappos, T. Sprenger, O. Bieri, P. Cattin, and K. Parmar



ABSTRACT

BACKGROUND AND PURPOSE: Currently, accurate and reproducible spinal cord GM segmentation remains challenging and a noninvasive broadly accepted reference standard for spinal cord GM measurements is still a matter of ongoing discussion. Our aim was to assess the reproducibility and accuracy of cervical spinal cord GM and WM cross-sectional area measurements using averaged magnetization inversion recovery acquisitions images and a fully-automatic postprocessing segmentation algorithm.

MATERIALS AND METHODS: The cervical spinal cord of 24 healthy subjects (14 women; mean age, 40 ± 11 years) was scanned in a test-retest fashion on a 3T MR imaging system. Twelve axial averaged magnetization inversion recovery acquisitions slices were acquired over a 48-mm cord segment. GM and WM were both manually segmented by 2 experienced readers and compared with an automatic variational segmentation algorithm with a shape prior modified for 3D data with a slice similarity prior. Precision and accuracy of the automatic method were evaluated using coefficients of variation and Dice similarity coefficients.

RESULTS: The mean GM area was 17.20 ± 2.28 mm² and the mean WM area was 72.71 ± 7.55 mm² using the automatic method. Reproducibility was high for both methods, while being better for the automatic approach (all mean automatic coefficients of variation, $\leq 4.77\%$; all differences, $P < .001$). The accuracy of the automatic method compared with the manual reference standard was excellent (mean Dice similarity coefficients: 0.86 ± 0.04 for GM and 0.90 ± 0.03 for WM). The automatic approach demonstrated similar coefficients of variation between intra- and intersession reproducibility as well as among all acquired spinal cord slices.

CONCLUSIONS: Our novel approach including the averaged magnetization inversion recovery acquisitions sequence and a fully-automated postprocessing segmentation algorithm demonstrated an accurate and reproducible spinal cord GM and WM segmentation. This pipeline is promising for both the exploration of longitudinal structural GM changes and application in clinical settings in disorders affecting the spinal cord.

ABBREVIATIONS: AMIRA = averaged magnetization inversion recovery acquisitions; CV = coefficient of variation; DSC = Dice similarity coefficient; HD = Hausdorff distance; SC = spinal cord

The human spinal cord (SC) can be affected by numerous neurologic disorders of variable pathophysiology (eg, genetic, inflammatory, demyelinating, degenerative, and so forth),^{1,2} and

MR imaging is a valuable part of the diagnostic work-up in patients with suspected intramedullary pathology.^{3,4} SC gray matter and white matter can be involved to a various extent not only among different SC disorders but also among patients with the same disease (eg, multiple sclerosis, amyotrophic lateral sclerosis).^{5,6} Hence, quantification of SC compartments may add to our understanding of SC pathology^{5,6} and hopefully help in the management of individual patients in the future.

However, the SC presents additional challenges for MR imag-

Received November 26, 2018; accepted after revision June 25, 2019.

From the Neurologic Clinic and Policlinic (C.T., M.A., L.K., T.S., K.P.), Department of Medicine and Biomedical Engineering; Translational Imaging in Neurology Basel (C.T., A.A., M.A., M.W., L.K., K.P.), Department of Medicine and Biomedical Engineering; Division of Radiological Physics (M.W., T.H., O.B.), Department of Radiology; and Division of Diagnostic and Interventional Neuroradiology (M.A.), Department of Radiology, University Hospital Basel, University of Basel, Basel, Switzerland; Medical Image Analysis Center (C.T., A.A., M.A.), Basel, Switzerland; Department of Biomedical Engineering (A.H., A.A., S.P., M.W., O.B., P.C.), University of Basel, Allschwil, Switzerland; and Department of Neurology (T.S.), DKD HELIOS Klinik, Wiesbaden, Germany.

C. Tsagkas and A. Horvath contributed equally as first authors.

This work was supported by the Swiss National Science Foundation (grant No. 320030_156860) and the Foundation for Sponsorship of Gastroenterological and General Clinical Research as well as of Medical Imaging (application ID 02/2015).

Please address correspondence to Katrin Parmar, MD, Department of Neurology, University Hospital Basel, Petersgraben 4, CH-4031 Basel, Switzerland; e-mail: katrin.parmar@usb.ch

Indicates open access to non-subscribers at www.ajnr.org

Indicates article with supplemental on-line table.

Indicates article with supplemental on-line photo.

<http://dx.doi.org/10.3174/ajnr.A6157>

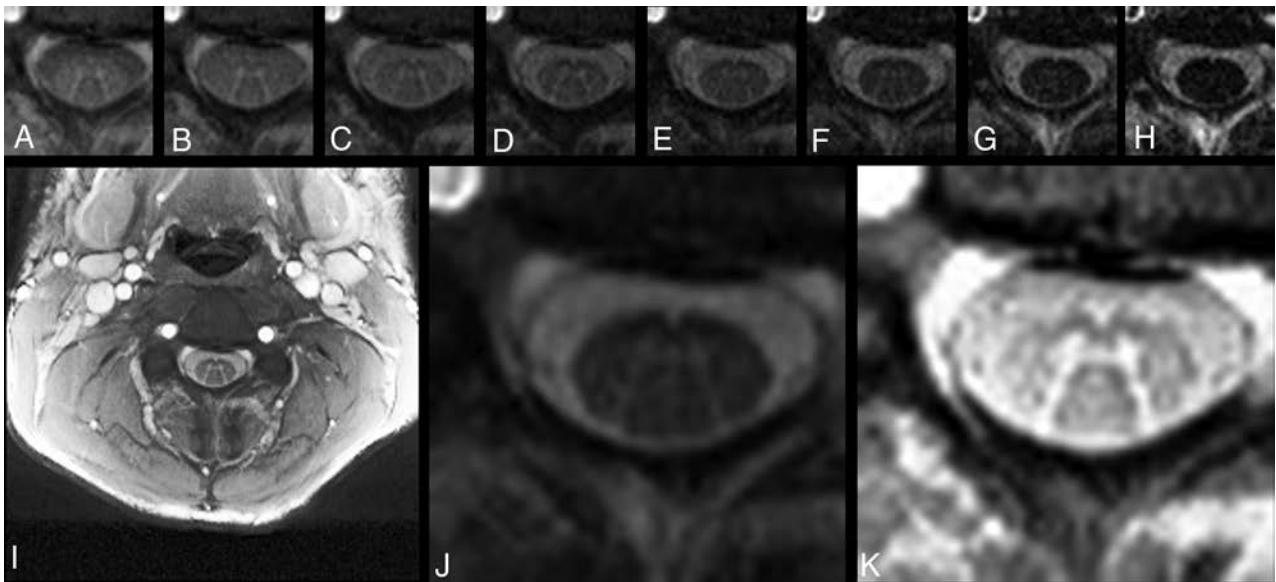


FIG 1. Exemplary axial AMIRA slice of 1 representative volunteer at the C4 level. *A–H*, Eight images of different tissue contrast acquired by the AMIRA sequence, shown in chronologic order from lowest-to-highest TI. *I*, Average image from *A* to *E* in full view, which delivers a high contrast-to-noise-ratio for GM/WM. *J*, Average image from *F* to *H*, which delivers a high contrast-to-noise ratio for SC/CSF. *K*, Same average image as in *I* but histogram-equalized and zoomed.

ing. The SC is surrounded by a number of different tissue types, including CSF, bone, and air. These create considerable signal inhomogeneities along this thin, elongated structure.^{3,4,7,8} As a result, conventional SC MR imaging was—until recently—not able to differentiate sufficiently among SC GM, WM, and CSF. In the past, there were first attempts toward this differentiation using a series of acquisition approaches.^{9–12} More recently an averaged magnetization inversion recovery acquisitions (AMIRA) sequence was proposed, delivering a notable SC GM/WM contrast while maintaining short acquisition times at the same time.¹³ The latter is especially important for imaging small-sized structures (like the SC GM/WM) in patients with disabilities having a short time window in which they can lie still.

Moreover, accurate SC GM segmentation remains challenging. First, manual approaches demonstrated the feasibility of distinguishing between WM and GM.⁹ However, manual approaches require a considerable amount of time, are prone to error, and demonstrate significant interobserver and intraobserver variability. As a result of improvements in image quality and postprocessing techniques, the first fully automatic SC GM segmentation methods were established in the past few years.^{14–17} These methods have deployed atlas-based GM segmentation algorithms, which may, however, lead to misestimations or segmentation errors, especially in case of pathology, image artifacts, or large between-individual anatomic variations.^{18,19} A noninvasive broadly accepted reference standard for accurate and reproducible SC GM measurements is still a matter of ongoing discussion.

In this study, we validate a fully automatic method for SC GM and WM segmentation in terms of its reproducibility and accuracy in segmenting the cervical SC of healthy controls against a manual segmentation. The proposed approach used a variational segmentation algorithm with a shape prior,²⁰ modified for 3D data with a slice similarity prior on AMIRA images.

MATERIALS AND METHODS

Subjects and MR Imaging Acquisition

Twenty-four healthy subjects (14 women; mean age, 40 ± 11 years) were scanned in a test-retest fashion on a 3T whole-body MR imaging system (Magnetom Prisma; Siemens, Erlangen, Germany). All subjects provided written consent. Experimental procedures conformed to the Declaration of Helsinki, and the study protocol was approved by the local ethics committee. We acquired 12 axial AMIRA images¹³ (FOV = $128 \times 128 \text{ mm}^2$, slice thickness = 8 mm, slice overlap = 4 mm, in-plane resolution = $0.67 \times 0.67 \text{ mm}^2$, TE_{balanced steady-state free precession} = 2.14 ms, TR_{balanced steady-state free precession} = 5.13 ms, signal averaging = 1, acquisition time = 51 seconds per slice) over a 48-mm cervical SC segment, extending approximately from the C2–C5 vertebral level.¹³ The most rostrally acquired slice was placed with its lower surface adjacent to the most rostral surface of the C2/C3 intervertebral disc. For precise positioning of each individual slice and its orthogonal angulation to the course of the SC, a strongly T2-weighted TSE with high contrast between CSF and SC was used as a reference. For each slice, the AMIRA approach acquired 8 images of considerably different tissue contrast among GM, WM, and CSF with effective TI = 97.1, 158.7, 220.2, 281.8, 343.3, 404.9, 466.5, 528.0 ms. Averaging the first 5 images enhances the GM/WM contrast-to-noise ratio, whereas averaging the last 3 images clearly improves the WM/CSF contrast-to-noise ratio (Fig 1). For more details on the AMIRA sequence, please see Weigel and Bieri, 2018.¹³

Each subject was scanned 3 times in 1 MR imaging session. The first 2 scans were performed in a back-to-back fashion without repositioning to allow intrasession comparisons. The third scan was obtained after patient repositioning to allow intersession comparisons.

All scans underwent basic preprocessing including 2D and 3D correction for field inhomogeneities using the scanner soft-

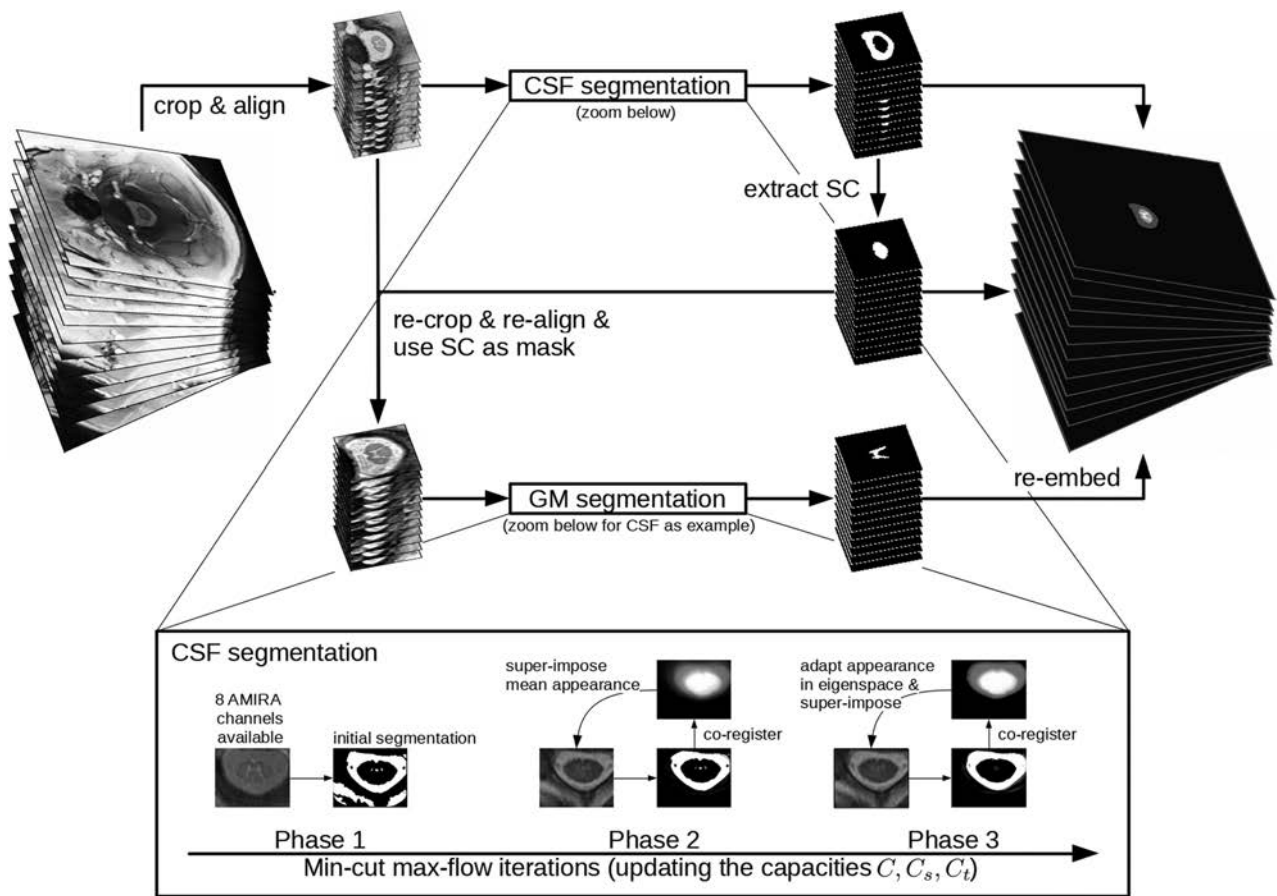


FIG 2. Flow chart of the automatic segmentation pipeline. As a first step of the algorithm to align the 12 slices, the images are center-cropped and slice-wise successively coregistered rostral to caudal using translations in pixel-size steps to prevent further interpolation. Then, the algorithm automatically locates and delineates the ring-shaped CSF from its surroundings and extracts the cross-sectional SC surface. Finally, it uses the previously segmented SC surface as a mask for GM/WM differentiation. The iterative steps of CSF segmentation are shown as a zoomed-in view. GM segmentation uses essentially the same steps and is thus not shown in detail.

ware before segmentation. To minimize numeric errors of the validation metrics, we performed a 5-fold in-slice upsampling of the slices using the Lanczos-3 interpolation kernel.

SC Segmentation

As proposed in a previous study,²⁰ a variational segmentation approach based on the continuous min-cut max-flow framework was used, which includes total variation regularization to segment WM and GM. The min-cut max-flow capacity functions are modeled using edge, region, and prior information as well as an appearance model built from manual segmentations. Aiming for high accuracy, the proposed approach prefers intensities of the actual image and tries to include prior information as little as possible, which regularizes for higher precision. Compared with the previous study,²⁰ we added a slice similarity prior,²¹ included all inversion images of one slice (Fig 1) into the calculation of the max-flow capacity functions, and improved the adaptation of the appearance model with posterior models that reconstruct the most likely appearance only based on well segmented pixels.²²

As a first step of the algorithm to align the 12 slices, the images are center-cropped and slice-wise successively coregistered rostral to caudal using translations in pixel-size steps to prevent further interpolation. Then, the algorithm automatically locates and delineates the ring-shaped CSF from its surroundings and extracts

the cross-sectional SC surface. Finally, it uses the previously segmented SC surface as a mask for GM/WM differentiation. An illustration of the algorithm is shown in Fig 2. Segmentations were achieved in a leave-one-subject-out cross-validation—that is, with the currently segmented subject being left out in the appearance model used.

The segmentation algorithm was implemented in Matlab (MathWorks, Natick, Massachusetts). Processing time on a Xeon CPU E5-2620 v3 @ 2.40GHz (Intel, Santa Clara, California) is around 1 minute for each segmentation step (CSF-SC and WM-GM segmentation), and fewer than 8 GB of RAM is used to segment a stack of 12 slices. Code is available on <https://github.com/neonroehre/AJNR2019>.

Two experienced raters (C.T. and A.A.) were involved in the manual segmentations. Both raters had >4 years' experience in neuroimaging research, including SC volumetric studies. In a first step, segmentations were conducted on the average of the last 3 AMIRA images for the total SC cross-sectional area. Using the already delineated total SC masks, we then performed manual segmentations of the GM and WM cross-sectional areas on the average of the first 5 AMIRA images (On-line Figure). C.T. segmented all images once. These results were further applied as a “manual reference standard.” C.T. also conducted a second

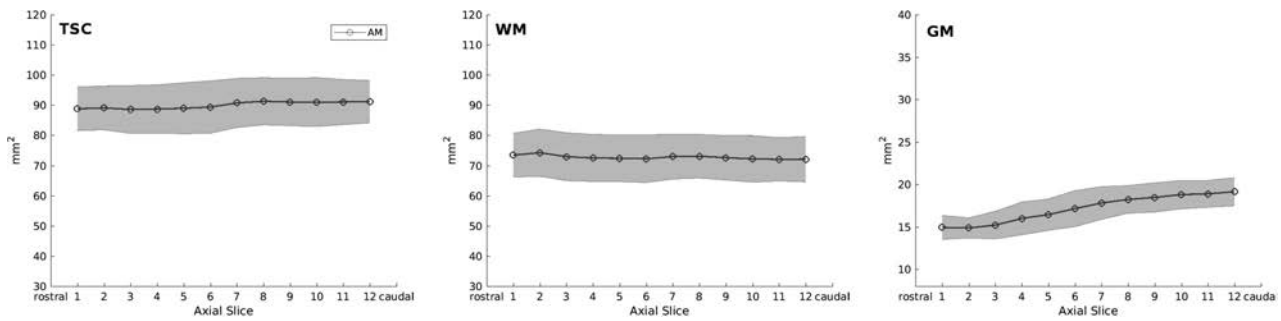


FIG 3. Cross-sectional areas of total spinal cord, white matter, and gray matter per axial slice as measured by automatic segmentations. Notice the slight increase of total spinal cord (TSC) and the marked GM cross-sectional area increase caudally, which corresponds to the cervical SC enlargement. The light gray area depicts the limits of ± 1 SD.

“run” of 60 randomly selected slices to assess intrarater comparisons. This second run was conducted with slightly different contrast adjustments than the first to evaluate the robustness of intrarater manual segmentation. A.A. segmented all images of the first scan of all 24 healthy controls to allow interrater comparisons.

To evaluate the performance of our method on SC slices, in which the fully automatic approach failed (in total 12% of acquired slices, see also Results), we applied a semiautomatic approach as follows: The SC/CSF boundaries were segmented manually (manual reference standard) and segmentation of the GM and WM was then performed using the fully-automatic approach described above, given the manual total SC masks.

To compare our automatic method with currently available algorithms, we tested the iterative nonlocal STAPLE algorithm²³ on our AMIRA images using the algorithm in the SCFusion_Demo package (https://www.nitrc.org/frs/download.php/7666/scfusion_demo.zip). Asman et al²³ used atlases consisting of SC-GM-WM contrast images and SC-GM-WM manual reference standard segmentations, which are rigidly registered to the target slice and fused together with the most fitting manual reference standard segmentation as an estimation of the targeted segmentation. We built our own atlases and tested the iterative nonlocal STAPLE in a leave-one-subject-out fashion.

Statistical Analysis

Intra- and intersession and intra- and interrater reproducibility of the 2 approaches were evaluated using coefficients of variation (CVs), Dice similarity coefficients (DSCs), and Hausdorff distances (HDs). The accuracy of the automatic method compared with the manual reference standard was evaluated using the DSC and HD. CVs between the 2 masks *A* and *B* were calculated with the following formula:

$$CV = \sqrt{2} \times \frac{|A - B|}{|A + B|} \%$$

DSCs were calculated as follows:

$$DSC = 2 \times \frac{|MRS \cap AM|}{|MRS| + |AM|}$$

HDs were calculated as follows:

$$d(X \rightarrow Y) = \max(d_i^{X \rightarrow Y}, i = 1 \dots N_x)$$

$$HD = \max[d(MRS \rightarrow AM), d(AM \rightarrow MRS)],$$

where *d* is the Euclidean distance between voxels *x* and *y*, MRS is the manual reference standard and AM the automatic method.

Because of non-normally distributed data, we performed a square root transformation of the CV, a cubic transformation of the DSC, and a logarithmic transformation of the HD before conducting all *t* test analyses and MANOVA. Two-paired *t* tests were performed for the following comparisons after controlling for normal data distribution: 1) manual segmentation versus automatic method reproducibility, and 2) manual segmentation versus automatic method total SC, WM, and GM cross-sectional area. For the automatic method, differences in measures of reproducibility and accuracy between intrasession and intersession; among GM, WM, and total SC; and among the axial slice levels (1–12) were investigated using MANOVA. Additional Tukey post hoc tests were conducted when applicable.

RESULTS

In total, 864 slices were acquired from 24 volunteers with 12 slices per scan, and each scan was performed a total of 3 times for each subject. Of 864 acquired axial SC slices, 9 were excluded from further analysis because of severe imaging artifacts. The automatic method successfully segmented 88% (752 slices) of all remaining slices. Because of imaging artifacts, localization problems, or posterior gaps of the CSF, 8% of all slice-wise SC segmentations and 4% of GM segmentations would have needed further manual interventions and thus were excluded from the reproducibility analysis.

Cross-Sectional SC Measurements

The mean total SC area was $89.98 \pm 7.88 \text{ mm}^2$, the mean WM area was $72.71 \pm 7.55 \text{ mm}^2$, and the mean GM area was $17.20 \pm 2.28 \text{ mm}^2$ as measured by the automatic method. Compared with the manual reference standard, the automatic method delivered significantly higher total SC and WM area as well as significantly lower GM area (86.88 ± 11.87 , 69.18 ± 10.16 , and $17.77 \pm 3.05 \text{ mm}^2$, respectively; all, $P < .001$). Cross-sectional areas per slice of the automatic method are shown in Fig 3.

Reproducibility

Measurements of intra- and intersession and intra- and interrater reproducibility are shown in the On-line Table. Reproducibility

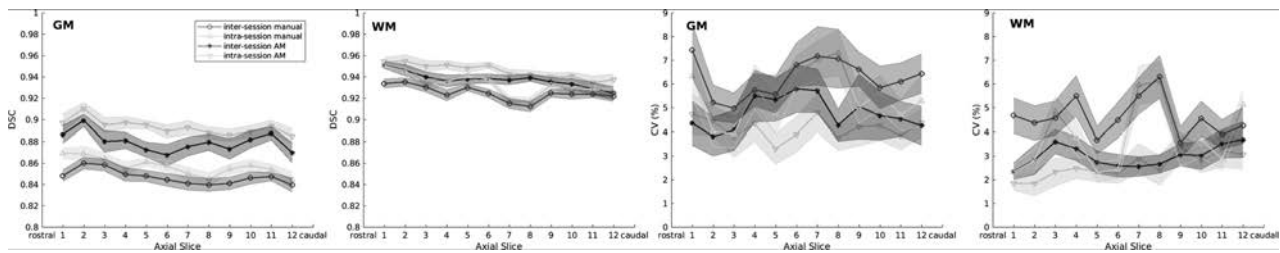


FIG 4. Comparison between the reproducibility of manual and automatic measurements (AM) of spinal cord gray matter and white matter per axial slice. Intrasession and intersession reproducibility is assessed in terms of Dice coefficients (graphics on the left) and coefficients of variation (graphics on the right). Manual and automatic intersession reproducibility is shown in dark gray, whereas manual and automatic intrasession reproducibility is shown in light gray. Error bars display mean values \pm 0.2 SDs.

SC GM, WM, and TSC accuracy of automatic and semiautomatic segmentations against the manual reference standard segmentations^a

	Parameter	GM	WM	TSC
AM (on 88% of acquired slices, nondiscarded from initial analysis)	DSC	0.86 \pm 0.04 (0.87)	0.90 \pm 0.03 (0.91)	0.95 \pm 0.03 (0.95)
	HD (mm)	0.90 \pm 0.44 (0.72)	0.82 \pm 0.22 (0.75)	0.64 \pm 0.27 (0.67)
SAM (on 12% of acquired slices, discarded from initial analysis)	DSC	0.83 \pm 0.04 (0.84)	0.96 \pm 0.01 (0.96)	
	HD (mm)	1.11 \pm 0.55 (0.93)	0.64 \pm 0.15 (0.67)	
AM (on nondiscarded samples) and SAM (on discarded slices), mixed (100% of acquired slices)	DSC	0.86 \pm 0.04 (0.86)	0.91 \pm 0.04 (0.92)	0.96 \pm 0.03 (0.96)
	HD (mm)	0.91 \pm 0.46 (0.81)	0.80 \pm 0.22 (0.75)	0.60 \pm 0.29 (0.55)

Note:—SAM indicates semiautomatic segmentation; TSC, total spinal cord; AM, automatic segmentations; DSC, Dice coefficient; HD, Hausdorff distances.

^a All values are shown as mean \pm SD (median).

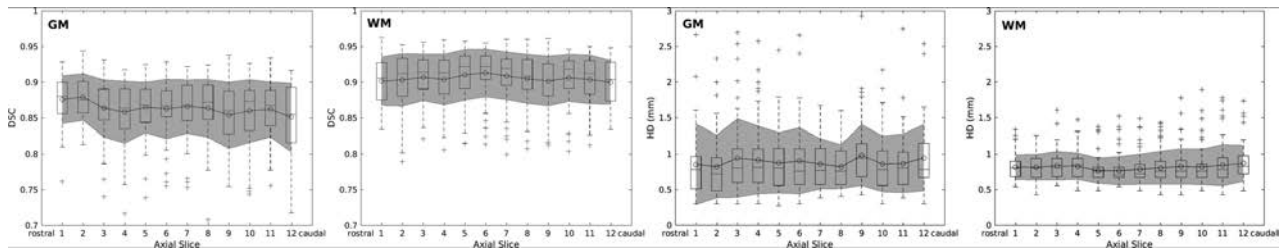


FIG 5. Accuracy measurements in terms of Dice coefficients (graphics on the left) and Hausdorff distances (graphics on the right) of white matter and gray matter per slice. Overlaid boxplots display median values as well as 25th and 75th percentile values. Gray areas depict the mean standard error values \pm 1 SD.

of SC GM and WM is also depicted per slice in Fig 4. All mean CVs of the automatic method were \leq 4.77%, and the mean DSC was \geq 0.88 between scans and raters. The latter was significantly better than for the manual segmentation (all, $P < .001$).

By means of MANOVA with DSC, HD, and CV as multivariate outcomes, a significant difference between intra- and intersession reproducibility for total SC, WM, and GM using the automatic method was shown ($P < .001$ for all 3 models). However, CVs differed only for WM and total SC ($P < .05$ and $P < .001$, respectively), but not for GM. In our automatic method, intra- and intersession reproducibility was significantly decreased in the order total SC \rightarrow WM \rightarrow GM (all $P < .001$), as shown by MANOVA and post hoc tests. No difference was found in intra- and intersession reproducibility among slices for GM, but a significant decrease was found for WM (both $P < .001$) and total SC ($P < .05$ and $P < .001$, respectively) in caudal slices, as shown by MANOVA. However, CVs were similar for all SC metrics among all slices.

Accuracy

Measurements of accuracy of our fully automatic method compared with a manual reference standard are shown in detail in the Table and are also shown per slice in Fig 5. The automatic method showed a mean DSC of \geq 0.86 in all SC metrics. Accuracy was

significantly decreased in the order total SC \rightarrow WM \rightarrow GM (all $P < .001$), as shown by MANOVA and post hoc tests. In MANOVA, accuracy was lower for GM ($P < .05$) and total SC ($P < .001$) in caudal slices, but not for WM. However, the DSC was similar among acquired slices for total SC.

Measurements of accuracy of the initially discarded SC slices (12% of all acquired AMIRA slices) analyzed in a semiautomatic fashion are also shown in the Table. The semiautomatic approach showed a mean DSC of \geq 0.83 in both GM and WM. When we compared it with the fully automatic approach on the initially nondiscarded SC slices, a statistically significant accuracy decrease was observed in the semiautomatic approach (both $P < .001$).

Comparison with the Iterative Nonlocal STAPLE Algorithm

In comparison with the original study²³ performed on T2* MR images, the application of the iterative nonlocal STAPLE algorithm in our AMIRA images showed a higher accuracy. Mean DSC and HD for the total SC, GM, and WM were as follows—total SC: mean DSC = 0.93 \pm 0.03 (median, 0.94), mean HD = 0.96 \pm 0.39 mm (median, 0.84 mm); GM: mean DSC = 0.80 \pm 0.06 (median, 0.82), mean HD = 1.09 \pm 0.42 mm (median, 1.04 mm); WM: mean DSC = 0.87 \pm 0.04 (median, 0.88), mean HD =

0.98 ± 0.37 mm (median, 0.89 mm).²³ Moreover, our proposed automatic method had higher accuracy for all total SC, WM, and GM compared with the iterative nonlocal STAPLE algorithm in our AMIRA images (all, $P < .001$).

DISCUSSION

Visualization of the SC GM in MR imaging has been hampered by technical difficulties until recently.⁸ Despite technologic advancements, segmentation of SC compartments remains a challenge.²⁴ In this work, we successfully deployed the novel MR imaging approach AMIRA and a fully automatic variational segmentation algorithm with a shape prior modified for 3D data with a slice similarity before demonstrating a fully automated approach for segmentation of SC, GM, and WM.

In contrast to brain MR imaging, the environment of the SC presents additional challenges for MR imaging methods and inherently for SC segmentation. The greatest challenges include magnetic field inhomogeneities across the SC, cord curvature, shape and size, contact of the SC and the osseous canal, osteophytes causing focal changes in CSF flow dynamics within the canal, motion artifacts, Gibbs artifacts, partial volume effects, and B_1 inhomogeneity.²⁵⁻²⁷ The AMIRA sequence¹³ used is based on a 2D approach that is, generally, less motion-sensitive than a 3D sequence. It uses a relatively short acquisition time of 51 seconds per slice, which leads to a reduction of motion artifacts and is especially suitable for disabled patients with limited ability to lie still (eg, due to spasticity). The AMIRA approach makes use of a balanced steady-state free precession readout, which is inherently of low-flow sensitivity or inherently flow compensated.¹³ The inversion recovery preparation is global and nonselective; hence, it does not pose an issue for CSF flow sensitivity either.

Furthermore, because the SC has a small cross-section of roughly 1.3×0.7 cm and our slices were located close to the isocenter, effects of B_1 inhomogeneity do not play a significant role for the present AMIRA images. The even smaller size of the SC GM presents additional difficulties for MR imaging methods, requiring submillimeter in-plane resolutions, especially for morphometry. Visualization and segmentation of the SC GM and WM are hampered by the similar relaxation times of the 2 SC compartments, limiting the use of conventional SC MR imaging for that purpose. Finally, the complex butterfly shape of the SC GM makes the segmentation of the structure a rather difficult task for computer-based segmentation methods. The AMIRA approach was able to produce SC images with a high GM/WM contrast in all participants. This was achieved in clinically feasible acquisition times (10.2 minutes for a 48-mm cervical SC segment).

Of 864 slices, only 9 were excluded due to image artifacts, mainly resulting from magnetic field inhomogeneities produced by bone structures (clavicles, scapulae, humeri, ribs, and so forth) as well as due to aliasing and motion artifacts. Although, these artifacts occurred in a rather small percentage of the acquired images (1%), they should be taken into account in future applications of the AMIRA approach. A further argument in favor of the use of AMIRA for SC GM and WM quantification is that our pipeline was able to deliver not only higher accuracy measures compared with a previous study²⁴ demonstrating results from

various MR imaging sequences and segmentation algorithms, but also better accuracy performance of an established algorithm on AMIRA compared with T2* MR images (see also below). This result may be an indirect indication of the superior quality of AMIRA compared with other sequences used so far for spinal cord GM and WM quantification. Nevertheless, due to AMIRA having a nonisotropic resolution, our MR imaging acquisition may have been more prone to partial volume effects, despite our slices being angulated individually in an orthogonal way to the course of the SC.

The proposed automatic segmentation method showed excellent precision in terms of inter- and intrasession reproducibility and was superior to the manual segmentation performed by experienced raters for all SC metrics, as measured by both CV and DSC. Our automatic method was also superior in terms of the HD for total SC, though it did not differ with regard to SC WM and GM. At the same time, the accuracy of the automatic method was high for total SC, GM, and WM, as measured by both the DSC and HD. Comparing the present data with results of the SC GM segmentation challenge,²⁴ we achieved a superior mean GM DSC of 0.86 versus 0.80 performed by the deepSeg (<https://pypi.org/project/deepSeg/>) algorithm in the SC GM segmentation challenge dataset. This achievement could be potentially explained by the high quality of the AMIRA images and/or the use of a multi-center dataset within the challenge with results from various MR imaging sequences and segmentation algorithms. Application of the previously published iterative nonlocal STAPLE algorithm on our AMIRA images showed higher accuracy than the original work of Asman et al²³ (SC GM: median DSC of 0.82 versus 0.75, median HD of 1.04 versus 2.5 mm), which was performed on T2*-weighted 3D gradient-echo images. While our atlases were constructed from a pool of around 800 samples, Asman et al had around 2000 available slices. Thus, the better accuracy seen here can be explained by a possible higher image quality in AMIRA images compared with T2*-weighted 3D gradient-echo images; however, a direct comparison of MR images within the same subjects was not performed. The shallow architecture of the proposed algorithm with only a few parameters may make it less prone to overfitting to the training set compared with a state-of-the-art deep neural network. However, a direct comparison of our method with deepSeg²⁸ was not possible in this study.

Precision and accuracy of our automatic method was decreased in the order of total SC→WM→GM. This decrease may be caused by the accordingly decreasing size of WM and GM compared with total SC because small differences may be translated into a larger variance. Moreover, the more complex geometry of the GM and WM compared with total SC may be more prone to misclassification errors. Finally, despite the good image quality, signal contrast was stronger for SC/CSF compared with GM/WM, which, in turn, could have partly contributed to differences in total SC and GM segmentation. Moreover, a slightly lower reproducibility and accuracy of our measurements in more caudally acquired slices could also be identified, which may reflect a decrease in contrast intensity and a “noise” increase in AMIRA images acquired closer to the lungs and surrounded by overall greater body mass (thorax, shoulders, and arms) compared with the more rostral cervical SC.

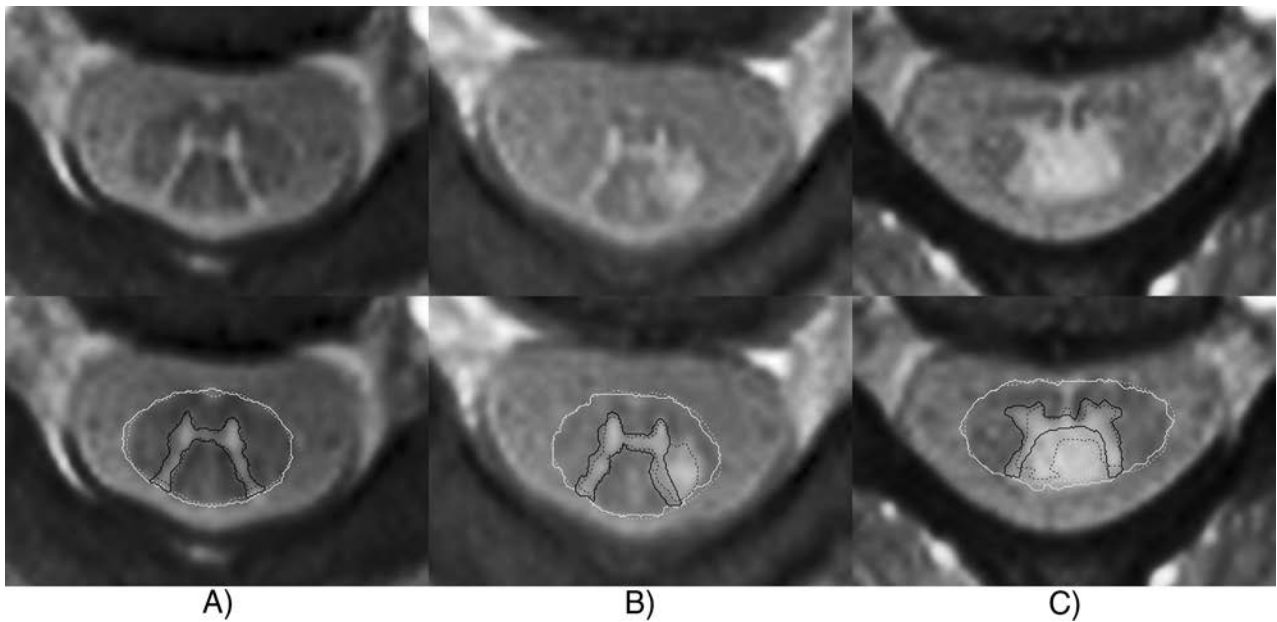


FIG 6. Examples of segmentations of representative patients with MS. *The thick continuous line* indicates automatic segmentation; the *dashed line*, manual reference standard. **A**, A 54-year-old female patient with MS. Rostral cervical SC slices of the C1/C2 level without focal lesions. Automatic segmentation highly corresponds to the manual reference standard. **B**, A 32-year-old male patient with MS. Rostral cervical SC slice of the C2 level with a focal posterolateral lesion fused with the left posterior gray matter horn. Automatic segmentation misclassifies the focal lesion as SC GM. **C**, A 33-year-old female patient with MS. A cervical SC slice of the C3/C4 level with a focal posterior lesion fusing with the posterior SC GM horns and the central SC GM commissure. Automatic segmentation misclassifies the focal lesion as SC GM and CSF.

Our automatic method also showed significantly lower intra-session than intersession variability for all SC metrics. However, GM intra- and intersession CVs were similar, with mean values ranging between 4.10% and 4.77%. Accordingly, our method demonstrated similar mean intra- and intersession CVs between 2.54% and 2.95% for WM. We, therefore, conclude that patient repositioning only slightly influences GM and WM area measurements; this conclusion provides evidence for the suitability of our automatic segmentation method in longitudinal settings.

In our work, minimal contrast adjustment differences in our manual segmentation led to a marked decrease of reproducibility, especially in GM area quantifications, as shown in the manual intra- and interrater measurements (mean CV up to 19.18%). Because the proposed method is fully automatic and requires no user-software interaction, it is devoid of additional variation produced by intra- and interrater variability. Therefore, our method provides significant advantages in large datasets or multicenter studies and, as mentioned above, may also be valuable in the longitudinal evaluation of individual patients (eg, patients with MS).

Compared with the manual reference standard, the automatic method slightly overestimated total SC and WM area, while underestimating the GM area. This result might be due to different intensity-thresholding in the manual segmentation compared with the automatic method. The caudal GM area increase shown in Fig 3 can be explained by the increased volume of motor cells of the cervical SC enlargement in the GM ventral horns, which innervate the upper limb muscles.

Although a fully automatic segmentation was not feasible on 12% of acquired SC slices, a semiautomatic approach with manual total SC segmentation and fully automatic GM and WM segmentation could be performed on those slices. This approach also

showed high-accuracy measurements with mean DSC of ≥ 0.83 in both GM and WM. However, compared with the fully automatic method on the initially nondiscarded slices, a slight accuracy decrease was observed, which could be interpreted in terms of a lower image quality of those AMIRA images. Nevertheless, these results demonstrate a relative robustness of our automatic approach even in MR images of suboptimal quality, which are a rather common phenomenon in clinical routine.

The present work focused on SC GM and WM segmentation using AMIRA images of healthy controls. Nevertheless, the motivation of our research is to deploy this method in patient data (eg, patients with MS) for the development of a potential widely applied MR imaging biomarker. Exemplary segmentation of data of patients with MS (not shown in detail here) showed that lesion appearance was similar to that of GM and therefore challenged the algorithm where lesions did not respect the GM boundaries (Fig 6). In future work, we intend to adjust the current method to address its current limitations. As an alternative approach, we plan to apply a deep learning-based segmentation approach on pathologic images as already performed on the data of healthy subjects.^{28,29}

CONCLUSIONS

The AMIRA sequence is presented as a time-efficient and reproducible MR imaging approach within the cervical cord. Our fully automatic segmentation method for SC GM and WM demonstrated further high reproducibility and accuracy. We were able to show that a shallow algorithm produces state-of-the-art GM-WM segmentation results on the AMIRA data. It is therefore suitable in large longitudinal studies investigating upper cervical SC volumes. Reproducibility measures of this work could be further

used for effect size calculations of SC compartment metrics for studies using the same processing approach. In future work, we will address the use of deep learning approaches, as demonstrated in recent studies.²⁸

Disclosures: Charidimos Tsagkas—RELATED: Grant: Swiss National Science Foundation (grant No. 320030_156860) and the Foundation for Sponsorship of Gastroenterological and General Clinical Research as well as of Medical Imaging (application ID 02/2015); UNRELATED: Grants/Grants Pending: University of Basel, Forschungsfonds für exzellente Nachwuchsforschende, pending. Antal Horvath—RELATED: Support for Travel to Meetings for the Study or Other Purposes: Swiss National Science Foundation.* Simon Pezold—UNRELATED: Grants/Grants Pending: Novartis Research Foundation.* Matthias Weigel—RELATED: Grant: Swiss National Science Foundation, Comments: grant No. 320030_156860, Method Development for MRI of Spinal Cord*; UNRELATED: Employment: Department of Biomedical Engineering, University of Basel, Switzerland, Comments: postdoctorate; Patents (Planned, Pending or Issued): University Hospital Freiburg, Freiburg, Germany, Comments: patent for Optical Motion Correction, neither relevant nor used in the present work; Travel/Accommodations/Meeting Expenses Unrelated to Activities Listed: International Society for Magnetic Resonance in Medicine, European Society for Magnetic Resonance in Medicine and Biology, MR Compact, Comments: travel reimbursement and accommodation for invited, scientific talks about MRI physics. Ludwig Kappos—UNRELATED: Board Membership: Actelion, Almirall, Bayer AG, Biogen, Celgene/Receptos, df-mp, Excemed, Genzyme, Japan Tobacco, Merck, Minoryx, Mitsubishi Tanabe Pharma, Novartis, Roche, Sanofi-Aventis, Santhera, Teva Pharmaceutical Industries, Vianex*; Consultancy: Actelion, Almirall, Bayer AG, Biogen, Celgene/Receptos, df-mp, Excemed, Genzyme, Japan Tobacco, Merck, Minoryx, Mitsubishi Tanabe Pharma, Novartis, Roche, Sanofi-Aventis, Santhera, Teva Pharmaceutical Industries, Vianex*; Grants/Grants Pending: Bayer AG, Biogen, Novartis, Roche, the Swiss MS Society, the Swiss National Research Foundation*; Payment for Lectures Including Service on Speakers Bureaus: Allergan, Almirall, Baxalta, Bayer AG, Biogen, CSL Behring, Desitin, Excemed, Genzyme, Merck, Novartis, Pfizer, Roche, Sanofi-Aventis, Teva Pharmaceutical Industries*; Payment for Development of Educational Presentations: Allergan, Almirall, Baxalta, Bayer AG, Biogen, CSL Behring, Desitin, Excemed, Genzyme, Merck, Novartis, Pfizer, Roche, Sanofi-Aventis, Teva Pharmaceutical Industries.* Till Sprenger—RELATED: Grant: Swiss National Science Foundation*; UNRELATED: Consultancy: Actelion, ATI, Biogen, Desitin, electroCore, Sanofi Genzyme, Novartis, and Mitsubishi Tanabe Pharma Europe*; Grants/Grants Pending: EFIC-Grüenthal, Novartis Switzerland, the Swiss Multiple Sclerosis Society*; Payment for Lectures Including Service on Speakers Bureaus: Sanofi Genzyme, Biogen, Novartis, Teva Pharmaceutical Industries.* Oliver Bieri—RELATED: Grant: Swiss National Science Foundation*; UNRELATED: Grants/Grants Pending: Swiss National Science Foundation.* Katrin Parmar—RELATED: Grant: Swiss National Science Foundation*; UNRELATED: Grants/Grants Pending: Baasch Medicus Foundation; Payment for Lectures Including Service on Speakers Bureaus: Excemed, Novartis Switzerland*; Travel/Accommodations/Meeting Expenses Unrelated to Activities Listed: Novartis Switzerland. *Money paid to the institution.

REFERENCES

- Ginsberg L. Disorders of the spinal cord and roots. *Pract Neurol* 2011;11:259–67 CrossRef Medline
- Cook SA. Spinal disease: neoplastic, degenerative, and infective spinal cord diseases and spinal cord compression. April 10, 2015. <https://clinicalgate.com/spinal-disease-neoplastic-degenerative-and-infective-spinal-cord-diseases-and-spinal-cord-compression/>. Accessed April 4, 2015
- Wheeler-Kingshott CA, Stroman PW, Schwab JM, et al. The current state-of-the-art of spinal cord imaging: applications. *Neuroimage* 2014;84:1082–93 CrossRef Medline
- Kearney H, Miller DH, Ciccarelli O. Spinal cord MRI in multiple sclerosis: diagnostic, prognostic and clinical value. *Nat Rev Neurol* 2015;11:327–38 CrossRef Medline
- Schlaeger R, Papinutto N, Panara V, et al. Spinal cord gray matter atrophy correlates with multiple sclerosis disability. *Ann Neurol* 2014;76:568–80 CrossRef Medline
- Paquin MÉ, Mendili MM, Gros C, et al. Spinal cord gray matter atrophy in amyotrophic lateral sclerosis. *AJNR Am J Neuroradiol* 2018;39:184–92 CrossRef Medline
- Stroman PW, Bosma RL. Spinal cord imaging. In: Weidner N, Rupp R; Tansey K, eds. *Neurological Aspects of Spinal Cord Injury*. Cham: Springer International Publishing; 2017:237–57

- Stroman PW, Wheeler-Kingshott C, Bacon M, et al. The current state-of-the-art of spinal cord imaging: methods. *Neuroimage* 2014;84:1070–81 CrossRef Medline
- Yiannakas MC, Kearney H, Samson RS, et al. Feasibility of gray matter and white matter segmentation of the upper cervical cord in vivo: a pilot study with application to magnetisation transfer measurements. *Neuroimage* 2012;63:1054–59 CrossRef Medline
- Held P, Dorenbeck U, Seitz J, et al. MRI of the abnormal cervical spinal cord using 2D spoiled gradient echo multiecho sequence (MEDIC) with magnetization transfer saturation pulse: a T2* weighted feasibility study. *J Neuroradiol* 2003;30:83–90 Medline
- Papinutto N, Schlaeger R, Panara V, et al. 2D phase-sensitive inversion recovery imaging to measure in vivo spinal cord gray and white matter areas in clinically feasible acquisition times. *J Magn Reson Imaging* 2015;42:698–708 CrossRef Medline
- Weigel M, Bieri O. A simple and fast approach for spinal cord imaging at 3T with high in-plane resolution and good contrast. In: *Proceedings of the Annual Meeting of International Society of Magnetic Resonance in Medicine*, Singapore; May 7–13, 2016:4408
- Weigel M, Bieri O. Spinal cord imaging using averaged magnetization inversion recovery acquisitions. *Magn Reson Med* 2018;79:1870–81 CrossRef Medline
- Prados F, Cardoso MJ, Yiannakas MC, et al. Fully automated gray and white matter spinal cord segmentation. *Sci Rep* 2016;6:36151 CrossRef Medline
- Datta E, Papinutto N, Schlaeger R, et al. Gray matter segmentation of the spinal cord with active contours in MR images. *Neuroimage* 2017;147:788–99 CrossRef Medline
- Dupont SM, De Leener B, Taso M, et al. Fully-integrated framework for the segmentation and registration of the spinal cord white and gray matter. *Neuroimage* 2017;150:358–72 CrossRef Medline
- De Leener B, Lévy S, Dupont SM, et al. SCT: Spinal Cord Toolbox, an open-source software for processing spinal cord MRI data. *Neuroimage* 2017;145:24–43 CrossRef Medline
- Bach Cuadra M, Duay V, Thiran JP. Atlas-based segmentation. In: Paragios N, Duncan J, Ayache N, eds. *Handbook of Biomedical Imaging: Methodologies and Clinical Research*. Boston: Springer US; 2015:221–44
- Wachinger C, Golland P. Atlas-based under-segmentation. *Med Image Comput Comput Assist Interv* 2014;17:315–22 Medline
- Horváth A, Pezold S, Weigel M, et al. Variational segmentation of the white and gray matter in the spinal cord using a shape prior. In: Yao J, Vrtovec T, Zheng G, et al, eds. *Computational Methods and Clinical Applications for Spine Imaging*. Cham: Springer International Publishing; 2016:26–37
- Pezold S, Fundana K, Amann M, et al. Automatic segmentation of the spinal cord using continuous max flow with cross-sectional similarity prior and tubularity features. In: Yao J, Glocker B, Klinder T, et al, eds. *Recent Advances in Computational Methods and Clinical Applications for Spine Imaging*. Cham: Springer; 2015:107–18
- Lüthi M, Albrecht T, Vetter T. Probabilistic modeling and visualization of the flexibility in morphable models. In: Hancock ER, Martin RR, Sabin MA, eds. *Mathematics of Surfaces XIII*. Berlin: Springer-Verlag; 2009:251–64
- Asman AJ, Smith SA, Reich DS, et al. Robust GM/WM segmentation of the spinal cord with iterative non-local statistical fusion. *Med Image Comput Comput Assist Inter* 2013;16(Pt 1):759–67 Medline
- Prados F, Ashburner J, Blaiotta C, et al. Spinal cord grey matter segmentation challenge. *Neuroimage* 2017;152:312–29 CrossRef Medline
- Bhadrelia RA, Bogdan AR, Kaplan RF, et al. Cerebrospinal fluid pulsation amplitude and its quantitative relationship to cerebral blood flow pulsations: a phase-contrast MR flow imaging study. *Neuroradiology* 1997;39:258–64 CrossRef Medline
- Figley CR, Stroman PW. Investigation of human cervical and upper thoracic spinal cord motion: implications for imaging spinal cord

- structure and function. *Magn Reson Med* 2007;58:185–89 CrossRef Medline
27. Piché M, Cohen-Adad J, Nejad MK, et al. **Characterization of cardiac-related noise in fMRI of the cervical spinal cord.** *Magn Reson Imaging* 2009;27:300–10 CrossRef Medline
28. Perone CS, Calabrese E, Cohen-Adad J. **Spinal cord gray matter segmentation using deep dilated convolutions.** *Sci Rep* 2018;8:5966 CrossRef Medline
29. Horvath A, Tsagkas C, Andermatt S, et al. **Spinal cord gray matter-white matter segmentation on magnetic resonance AMIRA images with MD-GRU.** <https://arxiv.org/abs/1808.02408>. Accessed August 7, 2018

Comparative Analysis of Volumetric High-Resolution Heavily T2-Weighted MRI and Time-Resolved Contrast-Enhanced MRA in the Evaluation of Spinal Vascular Malformations

S.K. Kannath, S. Mandapalu, B. Thomas, J. Enakshy Rajan, and C. Kesavadas



ABSTRACT

BACKGROUND AND PURPOSE: Volumetric high-resolution heavily T2-weighted imaging or time-resolved contrast-enhanced MRA is used in the detection and characterization of spinal vascular malformations, though inherent trade-offs can affect their overall sensitivity and accuracy. We compared the efficacy of volumetric high-resolution heavily T2-weighted and time-resolved contrast-enhanced images in spinal vascular malformation diagnosis and feeder characterization and assessed whether a combined evaluation improved the overall accuracy of diagnosis.

MATERIALS AND METHODS: Twenty-eight patients with spinal vascular malformations (spinal dural arteriovenous fistula, spinal cord arteriovenous malformation, and perimedullary arteriovenous fistula) were prospectively enrolled. MR images were separately analyzed by 2 neuroradiologists blinded to the final diagnosis.

RESULTS: Both sequences demonstrated 100% sensitivity and 93.5% accuracy for the detection of spinal vascular malformations. Volumetric high-resolution heavily T2-weighted imaging was superior to time-resolved contrast-enhanced MR imaging for identification of spinal cord arteriovenous malformations (100% versus 90% sensitivity and 96.7% versus 93.5% accuracy), however, for the diagnosis of perimedullary arteriovenous fistula, time resolved contrast enhanced MRI was found to perform better than the volumetric T2 sequence (80% versus 60% sensitivity and 96.7% versus 93.5% accuracy). Both sequences showed equal sensitivity (100%) and accuracy (87%) for spinal dural arteriovenous fistulas. Combined evaluation improved the overall accuracy across all types of spinal vascular malformation. Volumetric high-resolution heavily T2-weighted imaging was superior or equal to time-resolved contrast-enhanced MR imaging for feeder identification of spinal dural arteriovenous fistulas for both observers (90.9% and 72.7% versus 72.7%), which improved to 90.9% when the sequences were combined. Time-resolved contrast-enhanced MR imaging performed better for major and total feeder identification of spinal cord arteriovenous malformation (80% versus 60%) and perimedullary arteriovenous fistula (80% versus 60%–80%).

CONCLUSIONS: Combined volumetric high-resolution heavily T2-weighted imaging and time-resolved contrast-enhanced MR imaging can improve the sensitivity and accuracy of spinal vascular malformation diagnosis, classification, and feeder characterization.

ABBREVIATIONS: ASA = anterior spinal artery; PMAVF = perimedullary arteriovenous fistula; SCAVM = spinal cord arteriovenous malformation; SDAVF = spinal dural arteriovenous fistula; SVM = spinal vascular malformation; TRCE = time-resolved contrast-enhanced; TRICKS = time-resolved imaging of contrast kinetics; VHHT2WI = volumetric high-resolution heavily T2-weighted imaging

Spinal vascular malformations (SVMs) are rare entities at various locations in the spinal cord and its coverings. These include predominantly spinal cord arteriovenous malformation (SCAVM), spinal dural arteriovenous fistula (SDAVF), and perimedullary arteriovenous fistula (PMAVF). The clinical presentation is variable, though typical clinical patterns exist among

certain entities such as acute spinal cord dysfunction due to hemorrhage in SCAVM or slow progressive paraplegia in SDAVFs.^{1,2} There is a variable delay in the diagnosis due to nonspecific clinical symptoms or low clinical suspicion, which often leads to serious morbidity, even after successful treatment. MR imaging is usually the initial investigation of choice based on which diagnosis is suspected, while DSA remains the criterion standard.³ DSA is, however, invasive and has additional risks such as exposure to ionizing radiation, iodinated contrast medium overload, and a

Received May 9, 2019; accepted after revision July 1.

From the Department of Imaging Sciences and Interventional Radiology (S.K.K., B.T., J.E.R., C.K.), Sree Chitra Tirunal Institute for Medical Sciences and Technology, Trivandrum, Kerala, India; and Department of Radiology (S.M.), NRI Medical College, Chinakani, Guntur, Andhra Pradesh, India.

Please address correspondence to Santhosh Kumar Kannath, MD, PDCC, Department of Imaging Sciences and Interventional Radiology, SCTIMST, Medical College PO, Trivandrum, 695011 Kerala, India; e-mail: drsanthoshkannath@gmail.com

Indicates article with supplemental online tables.

Indicates article with supplemental on-line photo.

<http://dx.doi.org/10.3174/ajnr.A6164>

small risk of inducing spinal cord infarction.⁴ DSA also can miss the diagnosis in SDAVF and PMAVF because of operator-dependent factors, and such patients may have a poor prognosis even after successful treatment.^{5,6}

SVMs are suspected on the basis of the presence of flow voids in the subarachnoid space and/or cord parenchyma and are further evaluated using volumetric high-resolution heavily T2-weighted imaging (VHHT2WI), contrast-enhanced MRA, and time-resolved contrast-enhanced (TRCE) MR imaging sequences for characterization and localization of arterial feeders.⁷⁻¹³ VHHT2WI sequences such as Cube (GE Healthcare, Milwaukee, Wisconsin) and sampling perfection with application optimized contrasts by using different flip-angle evolution (SPACE; Siemens, Erlangen, Germany) provide excellent contrast between the cord and CSF along with suppression of CSF flow artifacts. Submillimeter spatial resolution of these sequences allows multiplane reconstruction without artifacts, which would help in the detection and diagnosis of SVM and localization of arterial feeders.¹³ On the contrary, dynamic TRCE MR image sequences such as time-resolved imaging of contrast kinetics (TRICKS) provide good temporal resolution and capture contrast kinetics as it transits through the feeding artery and vascular malformation into the draining vein. While the lack temporal information is a major disadvantage for the former sequence, the latter sequence has poor spatial resolution and a limited FOV; thus, an accurate localization or characterization of an SVM may be difficult or lesions may be missed altogether.¹⁰ We hypothesized that combining these 2 sequences could maximize the overall diagnostic performance while offsetting the trade-offs and thus could potentially improve the overall accuracy of detection and characterization of spinal vascular malformations. In the present study, we used the diagnostic capability and feeder characterization of VHHT2WI (Cube) and TRCE MR (TRICKS) independently and in combination for the assessment of SVM.

MATERIALS AND METHODS

This prospective observational study included all patients with clinically suspected or diagnosed spinal vascular malformations who presented to the radiology department of Sree Chitra Tirunal Institute for Medical Sciences and Technology between May 2015 and October 2017. Patients with contraindications to MR imaging or partially treated SVMs or those who were unwilling to give consent were excluded from the study. MR imaging of the whole spine was performed on a 3T Discovery 750 MR imaging scanner (GE Healthcare) initially, followed by invasive spinal angiography on an Innova 3131 biplane DSA machine (GE Healthcare).

MR Imaging Technique

The MR imaging protocol consisted of initial routine T2 and 3D Cube acquisitions of the whole spine in the sagittal plane, followed by contrast-enhanced TRICKS of the suspected region. The parameters were as follows—Cube: TE/TR, 60–115/2500 ms; echo-train length, 90; FOV, 30 cm with a matrix of 288 × 288 and slice thickness of 1.6 mm in the sagittal plane. The entire spine was covered in 2 or 3 stations. The total acquisition time for each station was 6.08 minutes. For TRICKS, because there is a limita-

tion to the longitudinal area of coverage, the FOV was centered at the region of maximum concentration of flow voids, after evaluating the prior conventional T2 sequence. Initially the TRICKS sequence with a temporal resolution of 4 seconds and 200 milliseconds was used for the first 7 patients, and the parameters were as follows: TE/TR 1.4–11/4 ms; flip angle, 30°; slice thickness, 2 mm with an FOV of 46 cm, matrix of 512 × 256, and NEX of 1 with 20 phases acquired in the sagittal plane in 1 minute and 43 seconds. To shorten the temporal resolution to 3 seconds 100 milliseconds, we reduced the TR to 3.7 ms, the NEX to 0.75, and the flip angle to 20°, resulting in a total scan time of 1 minute 15 seconds, and these parameters were used in the remainder of the study. Gadolinium contrast medium (gadodiamide, Omniscan; GE Healthcare, Piscataway, New Jersey), 0.2 mmol/kg body weight (15–18 mL), was injected at a rate of 3.5 mL/s followed by a 20-mL saline chase follow-through.

The resulting images from both sequences were postprocessed using multiplanar reconstructions and maximum intensity projections in orthogonal and oblique planes on an Advantage Workstation for Windows (GE Healthcare).

Data Analysis

The VHHT2WI and TRCE MR images were independently analyzed after a gap of 2 weeks for the presence of vascular malformations, type (SDAVF, SCAVM, or PMAVF), and feeding arteries (number and their level) by 2 neuroradiologists (S.K.K. with 9 years' experience and S.M. with 3 years' experience) who were blinded to the case particulars. The spinal angiography data were analyzed by a single neuroradiologist (J.E.R. with 14 years' experience) blinded to the MR imaging observations. The technique of identification of the type of vascular malformation and its feeder was discussed previously and is detailed in On-line Table 2.^{10,13} Statistical analysis of the data was performed by calculating the sensitivity, specificity, accuracy, and positive and negative predictive values of VHHT2WI, TRCE, and combined data in identifying the type and location of vascular malformations in comparison with spinal angiography. κ coefficients of intermodality and interobserver variability were also calculated. All analyses were performed on SPSS, Version 21 (IBM, Armonk, New York).

RESULTS

Of 34 patients who met the inclusion criteria, 28 patients were included in the final analysis after exclusions (On-line Figure). The median age of the patients was 48 years (range, 15–78 years), with 22 males and 6 females. Eleven patients had SDAVFs, 10 had SCAVMs, 5 patients had PMAVFs, and the remaining 2 patients had extraspinal arteriovenous malformations. The clinical and demographic characteristics of the subjects are shown in Table 1.

Diagnosis and Characterization of SVMs

Both VHHT2WI and TRCE MR imaging performed equally with a sensitivity of 100% and accuracy of 93.5% for diagnosing the presence of SVMs. The specificity was low (33%), due to a low number of true-negative cases.

For the diagnosis of SDAVF, VHHT2WI and TRCE MR imaging had equal sensitivity, specificity, and accuracy of 100%,

80%, and 87%, respectively. The VHHT2WI sequence misdiagnosed 2 cases of PMAVFs and 1 case of vertebral body AVM as DAVFs. The false diagnosis of the SDAVF was made due to the presence of flow voids without apparent identification of a nidus. False-positives occurred in 3 cases with TRCE MR imaging: In 1 case of an SCAVM, a small nidus was misinterpreted as a draining vein; in another case of PMAVF, the anterior spinal artery (ASA) was not visualized and was misdiagnosed as a DAVF; and in the last, in an extraspinal AVM, the nidus was missed. After we combined both sequences, the specificity and accuracy improved to 84% and 90%, respectively. Thus, cross-confirmation between the 2 modalities improved the overall accuracy of diagnosis.

For SCAVM, the VHHT2WI had excellent sensitivity and accuracy of 100% and 96.7%, respectively, while the TRCE MR imaging had a sensitivity and accuracy of 90% and 93.5%, respectively. Both sequences had an equal specificity of 95.2%. One patient with an extraspinal AVM and one with a spinal cord AVM were misdiagnosed with DAVFs on TRCE imaging. Combining the sequences improved the overall accuracy of TRCE imaging to that of VHHT2WI.

For PMAVFs, TRCE MR imaging performed better, with a sensitivity and accuracy of 80% and 96.7% compared with the VHHT2WI sequence, which had a lower sensitivity and accuracy of 60%, and 93.5%, respectively. Both sequences had a specificity and positive predictive value of 100%. In 2 patients, the PMAVF

was falsely diagnosed as an SDAVF on VHHT2WI. The combined evaluation improved the sensitivity to that of TRCE MR imaging due to better identification of the ASA.

Feeder Identification of SVMs

DAVF. The level of the arterial feeder to a DAVF was exactly identified by the VHHT2WI sequence in 7 and 6 of 11 patients by observers 1 (63.6%) and 2 (54.5%), respectively. When extended to 1 vertebral level, observer 1 identified arterial feeders in 10 of 11 (90.9%) patients, whereas observer 2 identified them in 8 of 11 patients (72.7%). On the TRCE sequence, observers 1 and 2 identified the level in 8 of 11 (72.7%) patients. By combined evaluation, both observers identified feeders in 10 of 11 patients (Table 2). The laterality of the arterial feeder was correctly predicted in all cases by observer 1 but was misinterpreted in 1 case by observer 2. In the presence of multiple feeders to the DAVF, only 1 feeder could be identified by both observers.

AVM. Both the observers identified dominant arterial feeders in 6 of 10 patients on VHHT2WI and 8 of 10 patients on the TRCE sequence (Table 2). On the TRCE sequence, 2 feeders (20%) were falsely localized to an incorrect level by both observers.

Also, TRCE performed better in the assessment of the overall number of feeders by both observers compared with VHHT2WI. More than half the number of feeders were identified by TRCE (54.0%–66.6%), while identification was possible in only 25%–29% with VHHT2WI. Intracranial aneurysms were found on spinal angiography in 4 patients. Both observers were able to identify these in 3 of 4 patients (75%) using both sequences.

PMAVF. The dominant feeder or single feeder could be identified on VHHT2WI in 4 of 5 (80%) patients by observer 1, and in 3 of 5 (60%) patients by observer 2. Similarly, both observers could identify feeders in 4 of 5 (80%) patients with the TRCE sequence.

Of 7 feeders on spinal angiography, on the VHHT2WI sequence, observers 1 and 2 identified 4 (57.1%) and 3 (42.8%) arterial feeders, respectively. Using the TRCE sequence and combined VHHT2WI and TRCE MR images, observers 1 and 2 identified

Table 1: Demographics and clinical features of patients with spinal vascular malformations

	SDAVF	SCAVM	PMAVF
Median age (range) (yr)	57.7 (49–67)	29 (15–53)	52 (27–78)
Sex			
Male	10	6	5
Female	1	4	0
Comorbidities			
Diabetes	4	1	2
Hypertension	2	0	1
Presentation			
Acute/subacute	0	8	1
Chronic	11	2	4
Clinical features			
Initial symptoms			
Low back pain	3	7	3
Sensory symptoms	3	5	2
Motor weakness	5	5	0
Symptoms at diagnosis			
All (motor/sensory/bladder/bowel)	9	7	5
Any symptoms	2	3	0
Time to diagnosis (median) (range) (mo)	11.4 (4–24)	42.6 (0–180)	13.4 (1–24)

Table 2: Feeder characterization and level localization of various spinal vascular malformations using different MR imaging sequences

	VHHT2WI		TRCE MRA		Combined Approach	
	Obs. 1	Obs. 2	Obs. 1	Obs. 2	Obs. 1	Obs. 2
SDAVF						
Exact level	7/11 (64%)	6/11 (54%)	7/11 (64%)	7/11 (64%)	7/11 (64%)	7/11 (64%)
Within 1 vertebral level	10/11 (91%)	8/11 (73%)	8/11 (73%)	8/11 (73%)	10/11 (91%)	10/11 (91%)
SCAVM						
Dominant feeder	6/10 (60%)	6/10 (60%)	8/10 (80%)	8/10 (80%)	8/10 (80%)	8/10 (80%)
All feeders	6/24 (25%)	7/24 (29%)	13/24 (54%)	16/24 (67%)	13/24 (24%)	16/24 (67%)
PMAVF						
Dominant feeder	4/5 (80%)	3/5 (60%)	4/5 (80%)	4/5 (80%)	4/5 (80%)	4/5 (80%)
All feeders	4/7 (57%)	3/7 (43%)	4/7 (57%)	5/7 (71%)	4/7 (57%)	5/7 (71%)

Note:—Obs. Indicates observer.

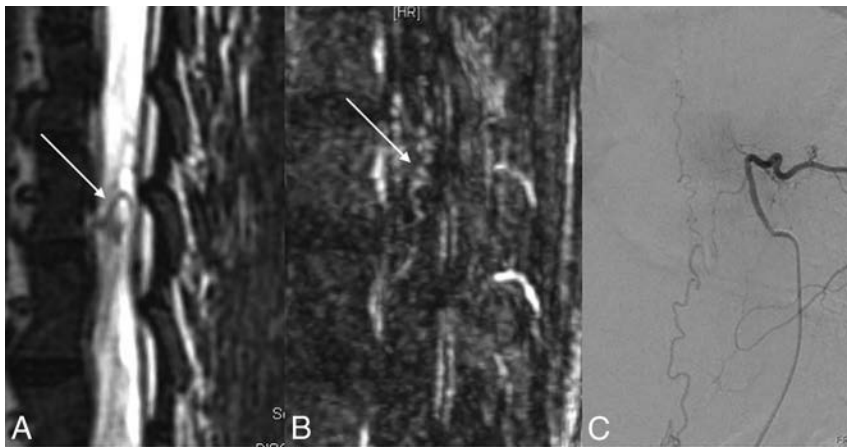


FIG 1. SDAVF. The VHHT2WI (A) shows a radicular vein (arrow) traced to left D8 vertebral foramen. The vein is faintly appreciated in TRCE (arrow in B) as well. The diagnosis is confirmed on DSA (C).

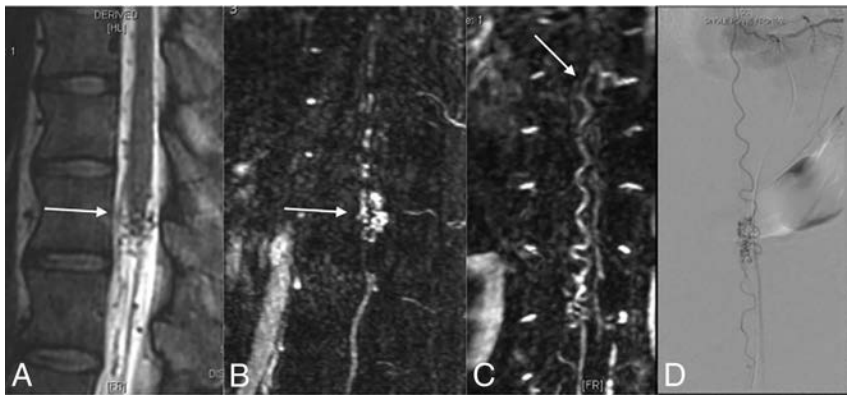


FIG 2. SCAVM. VHHT2WI (A) shows flow voids (arrow) within the conus suggesting the diagnosis of SDAVF. The feeder to the SCAVM was not identified. The parenchymal nidus (arrow in B) and the feeder from the ASA (arrow in C) are well seen in TRCE MR imaging. DSA confirms the observation (D).

tified 4 (57.1%) and 5 (71.4%) feeders, respectively. On the TRCE sequence, 1 false-positive was identified by observer 1 and 2 false-positives were identified by the observer 2. Two of 5 patients had multiple feeders. VHHT2WI could identify only a single feeder level in 2 patients by both observers. However, by TRCE, observer 2 could identify both feeders in 1 patient, and observer 1 could identify only 1 feeder.

The representative cases of the 3 types of SVMs are illustrated in Figs 1–3.

Intermodality and Interobserver Agreement

Moderate-to-substantial agreement was noted between the 2 modalities (VHHT2WI and TRCE MR) among the 2 observers in the evaluation of the feeders or for localization. However, notably, the agreement improved for both the observers when a combined evaluation was performed. Substantial-to-perfect interobserver agreement was also noted across the modalities for all types of SVMs (On-line Tables 1 and 2).

DISCUSSION

Advanced MR imaging techniques used for the evaluation of SVMs include anatomic depiction of the vascular malformation using VHHT2WI (SPACE or Cube) or TRCE MR angiographic

sequences (TRICKS). Most of the earlier studies discuss the utility of a specific MR image for a particular spinal malformation such as an SDAVF or SCAVM. To our knowledge, our series is the first study to report the usefulness of 2 different imaging sequences in the evaluation of spinal vascular malformation and its characterization. Our study found that VHHT2WI and TRCE MR imaging had an overall sensitivity of 100% and accuracy of 93.5% in the evaluation of suspected spinal vascular malformations. Also, the combined evaluation did not improve the accuracy of detection, suggesting that any one of the modalities is sufficient for confirming the presence of a vascular malformation. For feeder identification of an SDAVF, volumetric sequences were found to have higher accuracy, and combined evaluation yielded a detection rate within 1 vertebral level of 90%. However, the major feeders of SCAVMs and PMAVFs were better recognized using the TRCE sequence than the volumetric sequence.

Conventional T2 MR imaging is often the first diagnostic study in the evaluation of spinal vascular malformations. The presence of flow voids and cord hyperintensity in a patient with a suspected spinal vascular malformation is reported to have 100% sensitivity in the diagnosis of SDAVFs.³ Flow voids, however, are observed in only about 70% of cases; more-

over, the detection rate could be very low (<40%) in low-flow shunt lesions.^{3,14} Advanced MR images can improve the sensitivity and diagnostic accuracy for the detection of SVM. Amarourche et al¹⁰ reported the utility of the TRCE MR imaging technique (TRICKS) in the evaluation of different types of SVMs. In this study, 98% sensitivity and 63% specificity were achieved for the diagnosis of SVMs. Although the characterization of SDAVFs was excellent with this technique, when one included the localization of feeders within 1 level (82.8%), a false-positive interpretation was observed for PMAVFs, and the proportion of SCAVMs included in the study was very low (6.4%). Other studies on SDAVFs also reported similar high sensitivity (88%–100%) and specificity (80%–90%) for the detection of SDAVFs and feeder localization (85.7%–100%).^{11,12} The performance of TRCE is affected by several technical parameters, such as positioning of the FOV, delay between scan acquisitions and contrast bolus initiation, and temporal resolution of the sequence.^{10–12} Positioning of the FOV outside the region of the fistula can lead to a false-negative diagnosis, while low temporal resolution can lead to inadequate mapping of high- or low-volume shunts, yielding an erroneous interpretation.^{10–12}

The other sequence used to investigate SVMs is VHHT2WI,

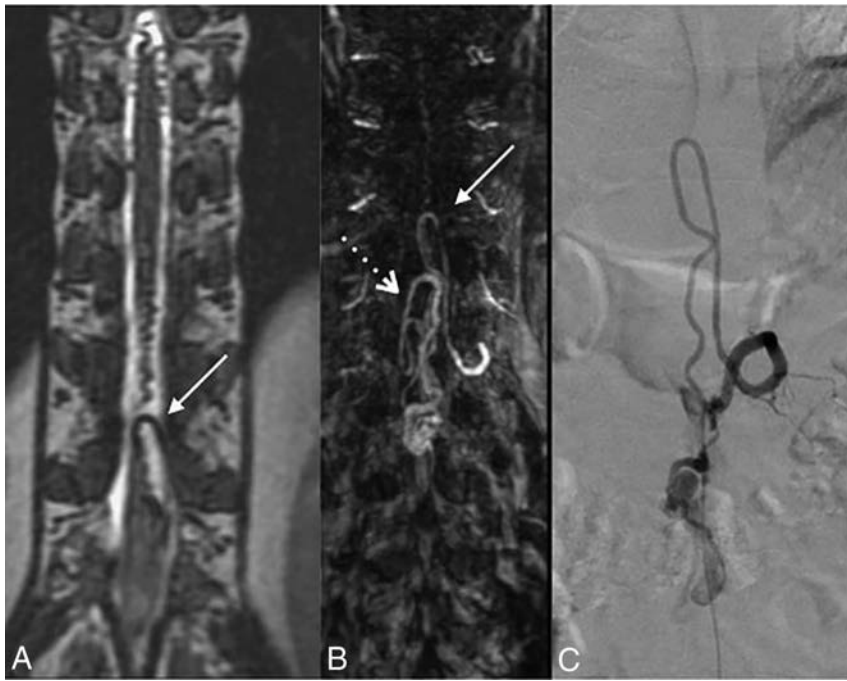


FIG 3. PMAVF. VHHT2WI shows a prominent ASA (arrow in A) supplying the fistula (not shown). TRCE MR image shows 2 ASAs feeding the fistula (arrows in B). A hypertrophied ASA supplying the fistula is demonstrated in C.

which provides superior parenchymal-CSF contrast distinction, thus allowing easy identification of even subtle flow voids and further characterization of the malformations based on the localization of the lesion or the feeder that supplies it.^{13,15} A recent study using this sequence demonstrated 98.1% sensitivity and 90% specificity for the diagnosis of SVMs, which was higher for SDAVFs (100% and 90%) compared with SCAVMs (89% and 71.8%), respectively.¹⁶ Additionally, VHHT2WI could be used for localization of SDAVFs, and the site could be reliably identified within 1 vertebral level in 94% of the cases.¹³ However, the role of this sequence to distinguish intradural vascular malformations such as PMAVFs and SCAVMs and the capability of identifying feeders to these malformations are unknown. Thus, although both VHHT2WI and TRCE MR imaging are excellent tools to evaluate suspected SVMs, due to inherent technical limitations of each of these sequences, whether it is possible to replace a diagnostic spinal angiography or plan limited angiography with therapeutic intent is unclear.^{10,11,17}

In our study, we found that VHHT2WI and TRCE MR imaging had high sensitivity and accuracy in the diagnosis of SVM, concurrent with other reported studies in the literature.¹⁰⁻¹⁵ Although the diagnosis of SDAVF could be confidently made using either sequence, a false-positive diagnosis was a concern for both. In our series, 2 cases of PMAVF and 1 case each of PMAVF and SCAVM were erroneously diagnosed as SDAVFs. Although VHHT2WI has submillimeter resolution, a near-normal-sized ASA feeding a low-flow PMAVF (type A PMAVF) might be missed due to volume averaging and thus could be erroneously reported as an SDAVF. Similarly, due to the low temporal resolution of TRCE MR imaging, optimal capture of different angiographic phases might be a limitation in a slow-flow PMAVF or a small

SCAVM with a near-normal-sized ASA feeder, resulting in an overlap of feeders and draining veins.¹⁰ Combining both sequences led to a higher accuracy of 90%, and this improvement is likely a consequence of improved diagnostic confidence of subtle imaging observations in one technique, which could be cross-confirmed with the other. The higher sensitivity and accuracy of VHHT2WI and TRCE MR imaging in the diagnosis of SCAVMs in our series are not surprising, given both the sequences' ability in direct visualization of the parenchymal nidus, which, in itself, is confirmatory. However, TRCE MR imaging was found to be superior in the depiction of PMAVFs, primarily due to its ability to demonstrate the arterial feeder.

Similar to results of prior reports, our results confirm the role of advanced MR images such as VHHT2WI and TRCE in the detection of arterial feeders to SDAVFs. The detection rate for both sequences within 1 vertebral level was

found to be high and comparable with those reported in the literature.¹⁰⁻¹³ Most interesting, we observed that the rate of identification depended on the readers' experience; however, by using input from both the sequences, high accuracy (90.9%) could be attained. This suggests that the effect of the learning curve on interpretation could be offset by using 2 modalities rather than a single sequence. A similar observation was also noted for PMAVF, in which a combined evaluation detected a higher proportion of the main as well as all feeders. Contrary to the prior report, both sequences could identify main feeders in 60%–80% of the cases and, in more than half, the number of all feeders to SCAVMs.¹⁰ The poor characterization reported by Amarouche et al¹⁰ might be due to limited experience; only 3 patients with SCAVMs were included in their study cohort. High interrater agreement was found for all the parameters in our study, suggesting that the observations are largely unambiguous and reproducible.

In this study, we used 2 disparate MR imaging techniques to evaluate anatomic and flow characteristics of SVMs. Although the performances of these individual sequences are comparable as far as diagnosis and feeder identification of various SVMs is concerned, combined evaluation improved the overall accuracy. The greatest utility of the combined sequence was found in enhancing the specificity and accuracy of SDAVF by discriminating it from PMAVF and identification of the dominant feeders to intradural malformations such as PMAVF and SCAVM. One disadvantage of using both sequences for SVM evaluation is the mild prolongation of the total acquisition time. However, the clinician could opt for any particular sequence for the initial evaluation, and additional sequences could be used only if the findings are confirmatory of the pres-

ence of an SVM. The current favored approach at the authors' institution is to obtain VHHT2WI initially, and perform a TRCE sequence later, centering the FOV at the site of the SVM localized from the earlier sequence. With this approach, false-negative interpretation due to improper placement of the FOV in TRICKS could be avoided and the observations could be confirmed by both modalities. Accurate distinction of spinal vascular malformations and their feeders preoperatively can aid the interventionist in tailoring the spinal DSA and planning endovascular treatment in a single sitting. This approach will have the advantage of reduction in procedural time and the risks of spinal DSA, radiation exposure, and contrast load along with an overall reduced hospital stay.¹⁷

Our study has several strengths. The study design was prospective, blinded, and performed on a 3T MR imaging machine. Spinal vascular malformations were evaluated with 2 different sequences, which enabled characterization of both the anatomic and physiologic aspects of the pathology. Furthermore, we were able to overcome the relative drawback of the limited FOV with the TRCE sequence by planning the FOV on the basis of findings on conventional MR imaging rather than using a fixed position as in prior studies. Also, different types of SVMs were included and separately analyzed to understand the disease-specific performance of the sequences.

There are a few limitations to our study. Due to the rarity of the disease, the number of patients in the study was relatively low. Use of a lower temporal resolution of the TRCE MR imaging in the initial phase of the study may have introduced some heterogeneity, though we believe that its effect on diagnostic accuracy is negligible.

CONCLUSIONS

VHHT2WI is superior in identifying SCAVMs, while the TRCE MR imaging is superior in identifying PMAVFs, with both sequences having equal accuracy in diagnosing SDAVFs. For feeder identification, VHHT2WI is superior in SDAVFs, while the other sequence is more useful in SCAVMs and PMAVFs. The combined evaluation of VHHT2WI and TRCE MR imaging increases the sensitivity and specificity in identifying and classifying spinal vascular malformations and thus could be used for planning targeted DSA and subsequent interventions.

Disclosures: Bejoy Thomas—UNRELATED: Grants/Grants Pending: Department of Science and Technology, Department of Biotechnology, GE Healthcare*; Patents (Planned, Pending or Issued): 2 Indian patent applications pending*; Stock/Stock Options: shareholder Wipro India. Chandrasekharan Kesavadas—UNRELATED: Employment: Sree Chitra Tirunal Institute for Medical Sciences and Technology. *Money paid to the institution.

REFERENCES

1. Aminoff MJ, Logue V. **The prognosis of patients with spinal vascular malformations.** *Brain* 1974;97:211–18 CrossRef Medline
2. Krings T, Geibsprasert S. **Spinal dural arteriovenous fistulas.** *AJNR Am J Neuroradiol* 2009;30:639–48 CrossRef Medline
3. Toossi S, Josephson SA, Hetts SW, et al. **Utility of MRI in spinal arteriovenous fistula.** *Neurology* 2012;79:25–30 CrossRef Medline
4. Chen J, Gailloud P. **Safety of spinal angiography: complication rate analysis in 302 diagnostic angiograms.** *Neurology* 2011;77:1235–40 CrossRef Medline
5. Barreras P, Heck D, Greenberg B, et al. **Analysis of 30 spinal angiograms falsely reported as normal in 18 patients with subsequently documented spinal vascular malformations.** *AJNR Am J Neuroradiol* 2017;38:1814–19 CrossRef Medline
6. Gailloud P. **Isolated aortic origin of the intersegmental spinal branch.** *J Neurointerv Surg* 2013;5:e19 CrossRef Medline
7. Mull M, Nijenhuis RJ, Backes WH, et al. **Value and limitations of contrast-enhanced MR angiography in spinal arteriovenous malformations and dural arteriovenous fistulas.** *AJNR Am J Neuroradiol* 2007;28:1249–58 CrossRef Medline
8. Luetmer PH, Lane JI, Gilbertson JR, et al. **Preangiographic evaluation of spinal dural arteriovenous fistulas with elliptic centric contrast-enhanced MR angiography and effect on radiation dose and volume of iodinated contrast material.** *AJNR Am J Neuroradiol* 2005;26:711–18 Medline
9. Ali S, Cashen TA, Carroll TJ, et al. **Time-resolved spinal MR angiography: initial clinical experience in the evaluation of spinal arteriovenous shunts.** *AJNR Am J Neuroradiol* 2007;28:1806–10 CrossRef Medline
10. Amarouche M, Hart JL, Siddiqui A, et al. **Time-resolved contrast-enhanced MR angiography of spinal vascular malformations.** *AJNR Am J Neuroradiol* 2015;36:417–22 CrossRef Medline
11. Saindane AM, Boddu SR, Tong FC, et al. **Contrast-enhanced time-resolved MRA for pre-angiographic evaluation of suspected spinal dural arterial venous fistulas.** *J Neurointerv Surg* 2015;7:135–40 CrossRef Medline
12. Mathur S, Bharatha A, Huynh TJ, et al. **Comparison of time-resolved and first-pass contrast-enhanced MR angiography in pretherapeutic evaluation of spinal dural arteriovenous fistulas.** *AJNR Am J Neuroradiol* 2017;38:206–12 CrossRef Medline
13. Kannath SK, Alampath P, Enakshy Rajan J, et al. **Utility of 3D SPACE T2-weighted volumetric sequence in the localization of spinal dural arteriovenous fistula.** *J Neurosurg Spine* 2016;25:125–32 CrossRef Medline
14. El Mekabaty A, Pardo CA, Gailloud P. **The yield of initial conventional MRI in 115 cases of angiographically confirmed spinal vascular malformations.** *J Neurol* 2017;264:733–39 CrossRef Medline
15. Kralik SF, Murph D, Mehta P, et al. **Diagnosis of spinal dural arteriovenous fistula using 3D T2-weighted imaging.** *Neuroradiology* 2017;59:997–1002 CrossRef Medline
16. Kannath SK, Rajendran A, Thomas B, et al. **Volumetric T2-weighted MRI improves the diagnostic accuracy of spinal vascular malformations: comparative analysis with a conventional MR study.** *J Neurointerv Surg* 2019 Mar 6. [Epub ahead of print] CrossRef Medline
17. Kannath SK, Thomas B, Sankara Sarma P, et al. **Impact of non-contrast enhanced volumetric MRI-based feeder localization in the treatment of spinal dural arteriovenous fistula.** *J Neurointerv Surg* 2017;9:178–82 CrossRef Medline

Celebrating 35 Years of the AJNR

September 1984 edition

Magnetic Resonance Imaging: Serial Observations in Multiple Sclerosis

M. A. Johnson¹
D. K. B. Li²
D. J. Bryant³
J. A. Payne⁴

Three patients with four or more follow-up magnetic resonance imaging (MRI) examinations over a 15-22 month period are described to illustrate the differing patterns of follow-up seen with MRI in multiple sclerosis (MS). These cases illustrate patterns of remission, exacerbation and remission, and rapid progression. The value of MRI in the follow-up of MS is discussed.

Magnetic resonance imaging (MRI) has been shown to be a very sensitive method of detecting lesions in multiple sclerosis (MS) [1-3]. We illustrate the use of MRI in follow-up by presenting three patients with clinically definite MS examined on four or more occasions each over a 15-22 month period.

Subjects and Methods

Three patients with four or more follow-up studies are described; each had a different clinical pattern of MS. Their clinical histories are presented in detail to correlate with MRI findings. The MRI scanner and basic pulse sequences used in this study have been described [3, 4]. The principal pulse sequences used during the study are listed in table 1 and described according to American College of Radiology nomenclature [5]. Examination times were 60-150 min depending on the number of slices scanned. Up to 15 individual slices were obtained at each examination. Present slice thickness is 10 mm.

All examinations conformed to the guidelines for clinical MRI established by the National Radiological Protection Board [6]. The examinations were performed with the permission of the Ethics Committee of the Royal Postgraduate Medical School, and informed consent was obtained from each patient. No preparation or exogenous contrast agents were required, and no adverse effects were noted during or after the MRI examination.

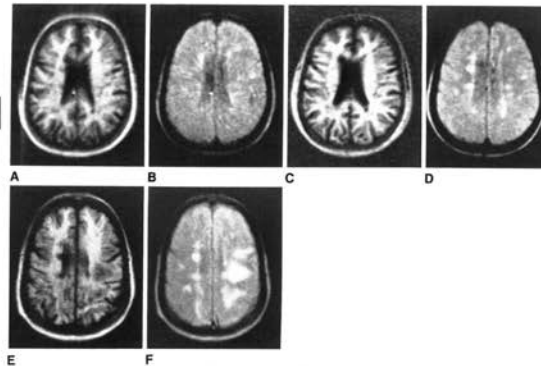
Case Reports

Case 1

A 25-year-old man had acute left hemiplegia that progressed over 1 week and subsequently recovered completely. During the acute phase, he developed reflex and postural changes of an upper motor neuron lesion. Auditory and visual-evoked potentials were normal. Lumbar puncture revealed slight increase in the number of lymphocytes (6/mm³) as well as oligoclonal banding in the cerebrospinal fluid (CSF).

Initial computed tomography (CT) with and without contrast enhancement revealed a low-attenuation, nonenhancing lesion in the right supra- and periventricular region. An MRI inversion-recovery (IR) scan demonstrated a large lesion with long T1 in the corresponding location (Fig. 1A). A smaller lesion with long T1 was also noted in the posterior limb of the right internal capsule.

Follow-up examinations 2 months later when the clinical symptoms had completely resolved revealed the right periventricular lesion to be smaller on CT and MRI scans (Fig. 1B). The third follow-up MRI scan (17 months after the initial scan) included both IR and spin-echo (SE) pulse sequences and showed further diminution of the right periventricular lesion, with long



Received January 4, 1984, accepted after revision March 28, 1984.

M. A. Johnson is a Medical Research Fellow of the Alberta Heritage Foundation.

¹Department of Diagnostic Radiology, MRI Unit, Royal Postgraduate Medical School, Hammenorth Hospital, Du Cane Rd., London W12 3NS, England. Address reprint requests to M. A. Johnson.

²Department of Diagnostic Radiology, University of British Columbia, Vancouver V6T 2S5, British Columbia, Canada.

³Hert Research Laboratory, Wembley, London HA9 7PA, England.

⁴AJNR 8:695-699, September/October 1984
0195-6108/84/0525-0495
© American Roentgen Ray Society

Experimental in vivo Imaging of the Cranial Perineural Lymphatic Pathway

John M. Pile-Spellman¹
Kenneth A. McKusick²
H. William Strauss³
John Cooney⁴
Juan M. Taveras⁵

After intraventricular injection of ^{111m}Tc antimony sulfide in rabbits (n = 12) and cats (n = 14), radiolabeled colloid was imaged passing into the nasal mucosa and subsequently into the cervical lymph nodes. The cervical lymph nodes accounted for about 12% of the injected dose in rabbits sacrificed at 22-24 hr after injection and about 5% of the injected dose in cats sacrificed at 5-6 hr after injection. In both animals this represented at least one-third of the cerebrospinal fluid colloid clearance. This technique is applicable to in vivo imaging studies of the perineural lymphatic pathway for cerebrospinal fluid absorption in primates and, with modifications, in human subjects.

The perineural lymphatic pathway (PLP) has been demonstrated in a variety of animals using a broad array of imaging agents [1-29]. Materials injected into the cerebrospinal fluid (CSF) can be seen passing along the olfactory nerve into the nasal mucosa and cervical lymphatics. Although the PLP or accessory pathway may be present around all nerves to some extent, the olfactory nerve is the predominant site of CSF efflux by the PLP [1-4].

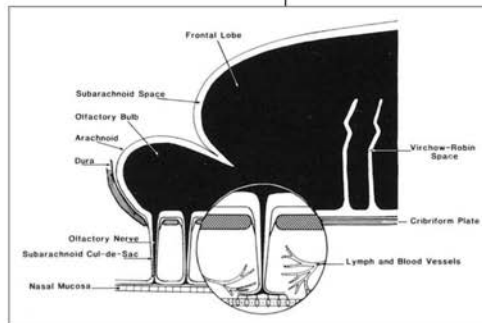
The PLP carries a significant proportion (at least 15%-30%) of CSF efflux under physiologic conditions [17, 21-24]. The PLP behaves as a bulk-flow drainage pathway. Materials of different molecular weights (60,000-150,000) are cleared at nearly identical rates [21-24]. The PLP appears to be pressure-dependent. McComb et al. [30] showed that at higher intracranial pressures, intracisternal dyes and tracers were cleared into the periorbital and nasal tissue at higher rates. The pathophysiology of the PLP is largely unknown, except for its relation to communicating hydrocephalus and central nervous system infections in some animals [31-38].

Evidence for a PLP in primates and humans is conflicting [7, 11, 31, 32, 39-42]. Since researchers have stressed the similarity between primates and cats in CSF absorption dynamics, it is noteworthy that a PLP has been demonstrated in the latter [32, 42]. We report an experimental technique for visualization of the PLP in the intact animal, which has been applied in cats and rabbits. With modifications, this imaging method may be applicable to clinical studies.

Materials and Methods

About 0.20 ml of ^{111m}TcCS₂S₃ (antimony sulfide) colloid (370 MBq/ml) was instilled into the lateral ventricles of rabbits (n = 12) and cats (n = 14) and viewed with a Nuclear Services, Inc. upgraded HP Pho Gamma III camera with a 3-mm-aperture pinhole collimator, interfaced to a Mod Comp III computer.

Regions of interest for the cranial CSF, olfactory bulb, nasal mucosal region, and cervical lymph nodes were assigned and analyzed. The animals were then sacrificed, and relevant tissues were analyzed for radioisotope activity.



Can Trace-Weighted Images Be Used to Estimate Diffusional Kurtosis Imaging–Derived Indices of Non-Gaussian Water Diffusion in Head and Neck Cancer?

We read with great interest the appealing article by Tu et al,¹ aimed at assessing the role of histogram-based descriptors of the non-Gaussian diffusional kurtosis imaging (DKI) model² in treatment-response prediction of nasopharyngeal carcinoma. They found that histogram-based analysis of DKI-derived indices of “kurtosis” and “diffusivity” may potentially predict the neoadjuvant chemotherapy and short-term radiation therapy response in locoregionally advanced nasopharyngeal carcinoma, therefore possibly modifying the treatment regimen. Considering that DKI is a quantitative diffusion MR imaging technique, we think it would be of practical interest to discuss in greater detail the approach used to estimate kurtosis and diffusivity in this study and in various DKI applications in general.

Tu et al¹ used only 3 orthogonal diffusion-weighting directions as is usual in extracranial DKI studies. While a rigorous application of DKI would require the use of at least 15 diffusion-weighting directions and 2 non-null b-values,² this simplification (based on the assumption of a relatively low diffusion anisotropy degree for tumor lesions) allows reducing the scan time, which is a pivotal issue in numerous extracranial applications of diffusion MR imaging. In this context, the estimation of kurtosis and diffusivity as the average of directional kurtosis and diffusivity obtained separately along the 3 orthogonal directions (namely K and D) hence represents the best possible approximation³ for rotational invariant mean kurtosis (ie, the average of directional kurtosis along all spatial directions) and mean diffusivity, respectively.² However, it is likely that Tu et al¹ estimated K and D by fitting the DKI model to trace-weighted images (TWIs) (ie, the geometric means of acquired diffusion-weighted images (DWIs), along the 3 orthogonal diffusion-weighting directions), albeit not explicitly reported.

This fact represents an important methodologic issue that should be adequately discussed. Indeed, while the approach of using TWIs has been widely adopted in many extracranial applications of DKI, it is mathematically as well as theoretically incorrect and yields no advantage in terms of acquisition time.^{3,4} Notably, a simulation study has shown that this approach can potentially affect the estimation of K.³ In particular, even for true K values ~ 1 (as typically observed in human tissue) and a low dif-

fusion anisotropy degree (<0.2), the percentage error in the K estimation caused by the use of TWIs instead of single DWIs along the 3 orthogonal directions can range up to more than 30%, resulting in greater uncertainty introduced by DWIs noise for typical signal-to-noise ratio values. In addition, a recent in vivo study has demonstrated that the fit of the DKI model to TWIs can introduce bias and error in the estimation of K and D of head and neck cancer, which can be non-negligible for single lesions.⁴ The median (95% confidence interval) errors in K and D were 5.1% (0.8%, 32.6%) and 1.7% (–2.5%, 5.3%), respectively.

In conclusion, toward an optimization of methods in quantitative DKI of the head and neck and extracranial regions in general, the use of at least 15 diffusion-weighting directions and 2 non-null b-values would be conceptually recommendable.² Nonetheless, the widespread and growing tendency to obtain K and D by fitting the DKI model to TWIs should possibly be avoided because it can affect the estimation of DKI-derived indices.^{3,4}

REFERENCES

1. Tu N, Zhong Y, Wang X, et al. **Treatment response prediction of nasopharyngeal carcinoma based on histogram analysis of diffusional kurtosis imaging.** *AJNR Am J Neuroradiol* 2019;40:326–33 CrossRef Medline
2. Jensen JH, Helpert JA. **MRI quantification of non-Gaussian water diffusion by kurtosis analysis.** *NMR Biomed* 2010;23:698–710 CrossRef Medline
3. Giannelli M, Toschi N. **On the use of trace-weighted images in body diffusional kurtosis imaging.** *Magn Reson Imaging* 2016;34:502–07 CrossRef Medline
4. Marzi S, Minosse S, Vidiri A, et al. **Diffusional kurtosis imaging in head and neck cancer: on the use of trace-weighted images to estimate indices of non-Gaussian water diffusion.** *Med Phys* 2018;45:5411–19 CrossRef Medline

● M. Giannelli

Unit of Medical Physics

Pisa University Hospital “Azienda Ospedaliero-Universitaria Pisana”

Pisa, Italy

● C. Marzi

Department of Electrical, Electronic, and Information Engineering

“Guglielmo Marconi”

University of Bologna

Cesena, Italy

<http://dx.doi.org/10.3174/ajnr.A6167>

● **M. Mascalchi**

Department of Clinical and Experimental Biomedical Sciences "Mario Serio"
University of Florence
Florence, Italy

● **S. Diciotti**

Department of Electrical, Electronic, and Information Engineering
"Guglielmo Marconi"
University of Bologna
Cesena, Italy

● **C. Tessa**

Unit of Radiology
Versilia Hospital
Lido di Camaione, Italy

REPLY:

We appreciate the comments by Dr Giannelli and colleagues regarding our recent article “Treatment Response Prediction of Nasopharyngeal Carcinoma Based on Histogram Analysis of Diffusional Kurtosis Imaging,” which raised an interesting issue on the influence factors of diffusional kurtosis imaging (DKI) estimation bias.

As they mentioned, DWI with 3 diffusion-weighted directions is currently the de facto standard in the application of DKI in body tumor. There are objective reasons for using 3 perpendicular directions in body application of non-Gaussian diffusional kurtosis imaging rather than >15 directions as in brain white matter evaluations.¹ First, the different anisotropic features between body and head lead to a basic need for >15 directions in white matter applications, while 3 directions may be sufficient in body applications.² Second, the increase of directions will result in a large increase in acquisition time, more likely leading to bulk and respiration motion, which should be avoided in body imaging acquisitions. Third, trace weighted images (TWIs) could increase the low signal-to-noise ratio in body tissue and make images robust to motion.^{3,4}

Giannelli et al have reported that the percentage error in K and D estimation using TWIs in head and neck cancer can be non-negligible for single lesions. They recommended the use of at least 15 diffusion-weighting directions and 2 non-null b-values in quantitative DKI analysis based on a simulation study⁵ and a prospective study.⁶ They drew this conclusion on the basis of a small sample study with a group of 18 patients with significantly different types of head and neck tumors, for example, tongue squamous cell carcinoma and lymphoma, using 3 main diffusion directions (x, y, z) with an acquisition time of 8 minutes 21 seconds (the time of our study is 3 minutes 26 seconds).

As we all know, different types of tumors have remarkably different biologic microstructures, resulting in differing diffusivity. For example, nasopharyngeal carcinoma (NPC) is a special type of head and neck tumor that has remarkably different biologic characteristics than other head and neck tumors. It is relatively isotropic, though the microstructure complexity differs according to treatment response.⁷ Moreover, the acquisition of NPC MR images is relatively more sensitive to bulk and respiratory artifacts; therefore, an appropriate short acquisition time is important. Therefore, the reproductivity and reliability of the recommendation for more directions not only in patients with NPC but also in those with other head and neck tumors remains controversial and needs further validation in unique types of tumors with certain sample sizes. Moreover, it appears that the DKI parameters may differ among different MR imaging systems and different institutions.⁸⁻¹⁰ Further study should be a multicenter large-sample-size prospective validation of this recommendation. The more complex the algorithm, the more error will occur during each step of calculation. Hence, a simplified geometric model may be more feasible in clinical application.¹¹

In conclusion, the use of only 3 perpendicular directions in general DKI body applications may lead to non-negligible bias during calculation. However, in body solid tumors with fewer anisotropic characteristics, 3 directions may be sufficient in clinical application. These comments remind us to pay more attention to the influencing factors of DKI acquisitions. On the other hand, because the imaging biomarkers differ in numerous studies,^{7,8,10,12-14} these comments give us an idea of how to explain the variation among these studies, to modify the parameter calculations, and to increase the possibility of exploring unique, proper, and impactful metrics as image biomarkers for further clinical application.

REFERENCES

1. Giannelli M, Marzi C, Mascalchi M, et al. **Toward a standardized approach to estimate kurtosis in body applications of a non-Gaussian diffusion kurtosis imaging model of water diffusion.** *Radiology* 2017;285:329–31 CrossRef Medline
2. Iima M, Le Bihan D. **Clinical intravoxel incoherent motion and diffusion MR imaging: past, present, and future.** *Radiology* 2016;278:13–32 CrossRef Medline
3. Filli L, Wurnig M, Nanz D, et al. **Whole-body diffusion kurtosis imaging: initial experience on non-Gaussian diffusion in various organs.** *Invest Radiology* 2014;49:773–78 CrossRef Medline
4. Iima M, Yano K, Kataoka M, et al. **Quantitative non-Gaussian diffusion and intravoxel incoherent motion magnetic resonance imaging: differentiation of malignant and benign breast lesions.** *Invest Radiology* 2015;50:205–11 CrossRef Medline
5. Giannelli M, Toschi N. **On the use of trace-weighted images in body diffusional kurtosis imaging.** *Magn Reson Imaging* 2016;34:502–07 CrossRef Medline
6. Marzi S, Minosse S, Vidiri A, et al. **Diffusional kurtosis imaging in head and neck cancer: On the use of trace-weighted images to estimate indices of non-Gaussian water diffusion.** *Med Phys* 2018;45:5411–19 CrossRef Medline
7. Tu N, Zhong Y, Wang X, et al. **Treatment response prediction of nasopharyngeal carcinoma based on histogram analysis of diffusional kurtosis imaging.** *AJNR Am J Neuroradiol* 2019;40:326–33 CrossRef Medline
8. Law BK, King AD, Bhatia KS, et al. **Diffusion-weighted imaging of nasopharyngeal carcinoma: can pretreatment DWI predict local failure based on long-term outcome?** *AJNR Am J Neuroradiol* 2016;37:1706–12 CrossRef Medline
9. Zhang Y, Liu X, Zhang Y, et al. **Prognostic value of the primary lesion apparent diffusion coefficient (ADC) in nasopharyngeal carcinoma: a retrospective study of 541 cases.** *Sci Rep* 2015;5:12242 CrossRef Medline
10. Zheng D, Lai G, Chen Y, et al. **Integrating dynamic contrast-enhanced magnetic resonance imaging and diffusion kurtosis imaging for neoadjuvant chemotherapy assessment of nasopharyngeal carcinoma.** *J Magn Reson Imaging* 2018;48:1208–16 CrossRef Medline
11. Jensen JH, Helpert JA. **MRI quantification of non-Gaussian water diffusion by kurtosis analysis.** *NMR Biomed* 2010;23:698–710 CrossRef Medline
12. Liyan L, Si W, Qian W, et al. **Diffusion kurtosis as an in vivo imaging marker of early radiation-induced changes in radiation-induced temporal lobe necrosis in nasopharyngeal carcinoma patients.** *Clin Neuroradiol* 2018;28:413–20 CrossRef Medline
13. Zhong J, Shi P, Chen Y, et al. **Diffusion kurtosis imaging of a human nasopharyngeal carcinoma xenograft model: Initial experience with pathological correlation.** *Magn Reson Imaging* 2018;47:111–17 CrossRef Medline

14. Fujima N, Yoshida D, Sakashita T, et al. **Prediction of the treatment outcome using intravoxel incoherent motion and diffusional kurtosis imaging in nasal or sinonasal squamous cell carcinoma patients.** *Eur Radiology* 2017;27:956–65 CrossRef Medline

 **N. Tu**

 **L. Bu**

PET-CT/MRI Center
Renmin Hospital of Wuhan University
Wuhan, China

 **G. Wu**

Department of Radiology
Shenzhen University General Hospital and
Shenzhen University Clinical Medical Academy
Shenzhen, China

Vendors Used in CT and MRI Neuroradiology Research

The market for radiology equipment is competitive throughout the world because the gross sales overall may be in the tens of billions of dollars. The vendors of these machines often compete on the basis of price, relationships with purchasers, volume discounting, and convenience of use. However, the perception that one manufacturer has an advantage in advanced technology over the other may also impact sales decisions, particularly at cutting edge research institutions. Assessing the quality of a manufacturer's research and development (R&D) is a difficult process. Industry may show its dedication to advancement by sponsoring research projects with funds and/or providing access to "works-in-process" advanced techniques to interested parties. We sought to determine the relative contributions of manufacturers to the neuroradiology literature in 2018 for the *American Journal of Neuroradiology (AJNR)* and a European-based (*Neuroradiology*) journal. Although this search may not be a true test of the quality of the R&D effort of a company, it may indicate which vendor has an advantage in neuroradiology research publications and, by proxy, institutions.

Thus, we reviewed each original research article published in 2018 in the *AJNR* and *Neuroradiology* and recorded which vendor was specified in the methodology for CT and MR imaging articles. For each technique, the results were aggregated on the whole and into categories for brain, spine, and head and neck to determine the frequencies of vendors mentioned in the articles. For MR imaging (Tables 1 and 2) and CT (Tables 3 and 4) articles, we categorized manufacturers as Siemens (Erlangen, Germany), GE Healthcare (Milwaukee, Wisconsin), Philips Healthcare (Best, the Netherlands) and

"Others." As a retrospective bibliometric analysis that did not involve human subjects, this study was exempt from institutional review board approval and was Health Insurance Portability and Accountability Act compliant.

We found that Siemens (72/190, 37%) led the *AJNR* literature in MR imaging studies overall, including 36% of brain, 40% of spine, and 46% of head and neck publications. For CT, the gap narrowed with Siemens accounting for 38% of CT articles. GE Healthcare and Philips Healthcare competed for second place in *AJNR*. In *Neuroradiology*, similar trends were seen, except in head and neck. Siemens was favored in the *Neuroradiology* MR imaging literature, constituting 42% of brain and 75% of spine articles. For CT, Siemens was dominant with 73% of brain and 75% of spine neuroradiology articles. Taken in total, Siemens had more mentions than other vendors ($P < 0.01$).

Our study noted that research performed on Siemens CT and MR imaging products led overall in the American- and European-based journals we selected for 2018. That advantage was more noteworthy in MR imaging research and in *Neuroradiology*.

Disclosures: David Yousem—UNRELATED: Expert Testimony: medicolegal; Payment for Lectures Including Service on Speakers Bureaus: American College of Radiology; Royalties: Elsevier.

 S. Ramezanpour
 R. Jalilianhasanpour
 D.M. Yousem

Russell H. Morgan Department of Radiology and Radiological Science
 Johns Hopkins Medical Institution
 Baltimore, Maryland

<http://dx.doi.org/10.3174/ajnr.A6180>

Table 1: AJNR MR imaging articles published in 2018

Body Part	Siemens (No./No.) (%)	GE Healthcare (No./No.) (%)	Philips Healthcare (No./No.) (%)	Others (No./No.) (%)	Total
Brain	52/144 (36%)	52/144 (36%)	34/144 (23%)	6/144 (4%)	144
Spine	8/20 (40%)	5/20 (25%)	7/20 (35%)	0/20 (0%)	20
Head and neck	12/26 (46%)	4/26 (15%)	9/26 (34%)	1/26 (3%)	26
Totals	72/190 (37%)	61/190 (32%)	50/190 (26%)	7/190 (3%)	190

Table 2: Neuroradiology MR imaging articles published in 2018

Body Part	Siemens (No./No.) (%)	GE Healthcare (No./No.) (%)	Philips Healthcare (No./No.) (%)	Others (No./No.) (%)	Total
Brain	25/59 (42%)	17/59 (28%)	16/59 (27%)	1/59 (1.6%)	59
Spine	3/4 (75%)		1/4 (25%)		4
Head and neck	4/14 (28%)	4/14 (28%)	6/14 (42%)		14
Totals	32/77 (41%)	21/77 (27%)	23/77 (29%)	1/77 (1.2%)	77

Table 3: CT vendors noted in AJNR articles

Body Part	Siemens (No./No.) (%)	GE Healthcare (No./No.) (%)	Philips Healthcare (No./No.) (%)	Others (No./No.) (%)	Total
Brain	2/8 (25%)	3/8 (37%)	1/8 (12%)	2/8 (25%)	8
Spine	1/6 (16%)	3/6 (50%)	1/6 (16%)	1/6 (16%)	6
Head and neck	5/7 (71%)	2/7 (29%)			7
Totals	8/21 (38%)	8/21 (38%)	2/21 (9%)	3/21 (14%)	21

Table 4: CT vendors noted in Neuroradiology articles

Body Part	Siemens (No./No.) (%)	GE Healthcare (No./No.) (%)	Philips Healthcare (No./No.) (%)	Others (No./No.) (%)	Total
Brain	11/15 (73%)	2/15 (13%)	1/15 (6%)	1/15 (6%)	15
Spine	3/4 (75%)			1/4 (25%)	4
Head and neck	1/6 (16%)	3/6 (50%)		2/6 (33%)	6
Totals	15/25 (60%)	5/25 (8%)	1/25 (4%)	4/25 (16%)	25